MICRO-MANUFACTURING
Design and Manufacturing of Micro-Products

Edited by

MUAMMER KOÇ
Center for Precision Forming (CPF-National Science Foundation IUCRC)
Virginia Commonwealth University
Richmond, VA

Istanbul Sehir University
Istanbul, Turkey

TUĞRUL ÖZEL
Manufacturing Automation Research Laboratory
Industrial and Systems Engineering
Rutgers University
Piscataway, New Jersey

A JOHN WILEY & SONS, INC., PUBLICATION

Published by John Wiley & Sons, Inc., Hoboken, New Jersey
Published simultaneously in Canada

ISBN: 978-0-470-55644-3

Library of Congress Cataloging-in-Publication Data is available.

Printed in Singapore

10 9 8 7 6 5 4 3 2 1

CONTENTS

FOREWORD

Since early 1990s, there has been an increasing demand for compact, integrated and miniature products for use in our daily lives as well as for industrial applications. Consumer products that we use and interact with every day are not only continuously getting smaller, but also are loaded with more integrated multi-functionalities. Similar trends have also taken place in other devices such as portable and distributed power generation devices (batteries, fuel cells, micro-turbines), electronic cooling systems, medical devices (pace makers, catheters, stents), sensors, etc. As a consequence, components for such devices and systems also get smaller down to micro/meso-scales, with a near future expectation into nano-scales. Micro-fabrication techniques for silicon materials have been well established and utilized in manufacturing of micro-electronics devices. There have been hundreds, if not thousands, of books written about semiconductors, micro-electronics and related micro-fabrication processes. Hence, their adaptation is apparent for systems such as Micro-Electromechanical-Systems (MEMS) for use in aforementioned miniature devices and products. However, these techniques are mostly limited to silicon as a starting material. When complex and integrated products are required, for cost effective design and use of metallic components, thus far, well-known macro-fabrication methods such as forming and machining were adapted into micro/meso-scales mainly using intuition and experience.

In this work, a collection of esteemed authors from a broad range of backgrounds and institutions worldwide has prepared, possibly one of the first extensive books on micro-manufacturing processes for mainly non-silicon materials. The main goal was to gather the experience, technological know-how and scientific findings in a wide variety of topics and applications in a synergistic and coherent book for the benefit of students, researchers, engineers, managers and

teachers who would start their investigations studies, preparations or careers with a concise set of information.

The first chapter, written by Drs. M. Koç and T. Özel, summarizes the recent developments and findings on micro-manufacturing, including the size effects, applications, tooling, etc., reported in the literature with examples and applications. In the second chapter, prepared by Dr. K. Teker, a summary of well-known micro-fabrication methods for silicon materials is presented to allow readers to compare them with the processes described in the rest of the book. The third chapter, which is prepared by Drs. T. Makino and K. Dohda, describes the issues in modeling and analysis for micro-manufacturing processes along with a comparison of different modeling approaches. Drs. O. Karhade and T. Kurfess present metrology, inspection and quality control aspects at micro-scales, and describe alternative methods to do so. Dr. A. Bandyophadyay and his colleagues discuss micro-layered manufacturing processes to be used for medical devices, sensors, etc. made out of metals and plastics in Chapter 5. In Chapter 6, Dr. Wu and Dr. Özel describe some of the micro-manufacturing processes based on laser processing with several examples and discuss long and short pulsed laser-material interactions. Micro Injection Molding process for polymers is presented by Dr. Yao in Chapter 7 while Micro-mechanical Machining is introduced in Chapter 8 by Dr. Özel and his associate. Dr. Koç prepared Chapter 9 with his colleague Dr. Mahabunphachai on micro-forming processes such as micro-forging, micro-stamping, micro-hydroforming and size effects. Dr. Rahman and his group cover in Chapter 10 micro-EDM processes including descriptions of equipment development. Dr. Fu Gang explains the micro Metal Injection Molding process in Chapter 11 with several examples of applications.

We would like to thank all of the authors who contributed to this book. We also extend our thanks to Ms. Anita Lekhwani of John Wiley who assisted us in all stages of preparing this book for the publication.

MUAMMER KOÇ and TUĞRUL ÖZEL
June 2010

CONTRIBUTORS

Abu Bakar, Mechanical Engineering Department, National University of Singapore (NUS), Singapore

Ali Asad, Mechanical Engineering Department, National University of Singapore (NUS), Singapore

Vamsi K. Balla, The School of Mechanical and Materials Engineering, Washington State University, Pullman, Washington

Amit Bandyopadhyay, The School of Mechanical and Materials Engineering, Washington State University, Pullman, Washington

Sheldon A. Bernard, The School of Mechanical and Materials Engineering, Washington State University, Pullman, Washington

Susmita Bose, The School of Mechanical and Materials Engineering, Washington State University, Pullman, Washington

Kuniakii Dohda, Professor, Department of Engineering Physics, Electronics & Mechanics, Nagoya Institute of Technology, Nagoya, Japan

Gang Fu, Mechanical Engineering Department, Nanyang Technological University (NTU), Singapore

Muhammad Pervej Jahan, Mechanical Engineering Department, National University of Singapore (NUS), Singapore

Omkar G. Karhade, Process Technology Development Engineer, Intel Corporation, Chandler, Arizona

MUAMMER KOÇ, Associate Professor & Director, Center for Precision Forming, (CPF- National Science Foundation IUCRC), Virginia Commonwealth University (VCU), Richmond, VA; Istanbul SEHIR University, Turkey

THOMAS KURFESS, Professor and BMW Chair of Manufacturing, Clemson University, International Center for Automotive Research, Clemson, South Carolina

NGIAP HIANG LOH, Mechanical Engineering Department, Nanyang Technological University (NTU), Singapore

SASAWAT MAHABUNPHACHAI, National Metal and Materials Technology Center (MTEC), Pathumthani, Thailand

TAKEHIKO MAKINO, Assistant Professor, Department of Engineering Physics, Electronics & Mechanics, Nagoya Institute of Technology, Nagoya, Japan

TAKESHI MASAKI, Mechanical Engineering Department, National University of Singapore (NUS), Singapore

TUĞRUL ÖZEL, Associate Professor & Director, Manufacturing Automation Research Laboratory, School of Engineering, Industrial and Systems Engineering, Rutgers University, Piscataway, New Jersey

MUSTAFIZUR RAHMAN, Professor, Mechanical Engineering Department, National University of Singapore (NUS), Singapore

BEE YEN TAY, Mechanical Engineering Department, Nanyang Technological University (NTU), Singapore

KASIF TEKER, Assistant Professor, Department of Physics & Engineering, Frostburg State University, Maryland, Maryland

THANONGSAK THEPSONTHI, Manufacturing Automation Research Laboratory Industrial & Systems Engineering Rutgers, The State University of New Jersey, Piscataway, New Jersey

SHU BENG TOR, Mechanical Engineering Department, Nanyang Technological University (NTU), Singapore

YOKE SAN WONG, Mechanical Engineering Department, National University of Singapore (NUS), Singapore

BENXIN WU, Assistant Professor, Mechanical Engineering, Laser-based Manufacturing and Applications Laboratory, Illinois Institute of Technology, Chicago, Illinois

DONGGANG YAO, Associate Professor, School of Materials Science and Engineering, Georgia Institute of Technology, Atlanta, Georgia

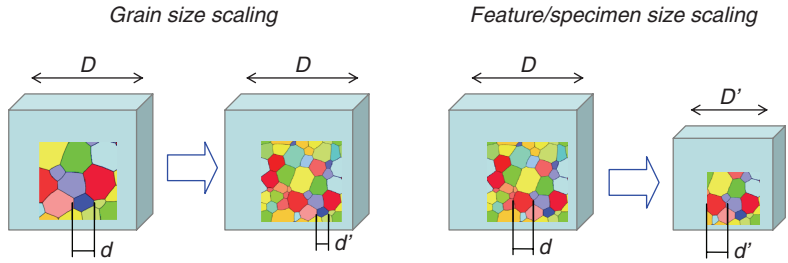

Figure 1.4 Illustration of two types of scaling effects: "grain size effect" and "feature/specimen size effect."

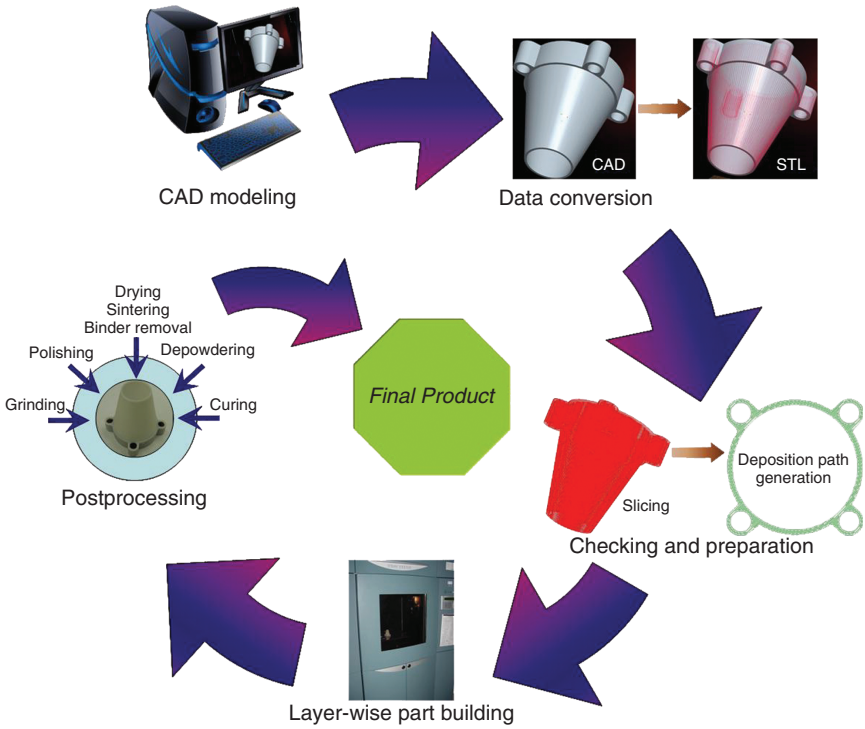

Figure 5.3 Basic processing steps in layered manufacturing.

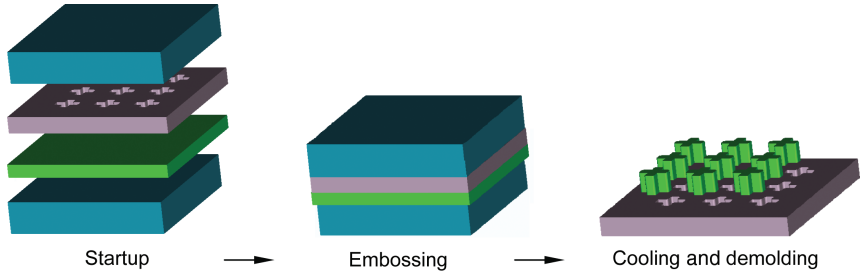

Figure 7.8 Steps involved in through-thickness embossing of discrete microparts.

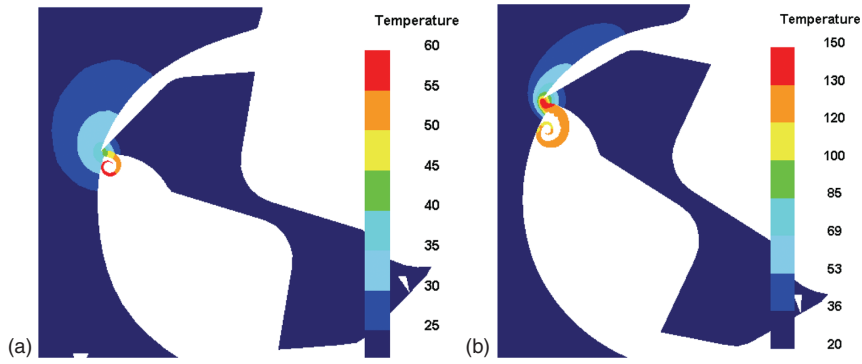

Figure 8.17 FEM simulation of micromilling: (a) AL2024-T6 aluminum and (b) AISI 4340 steel [8].

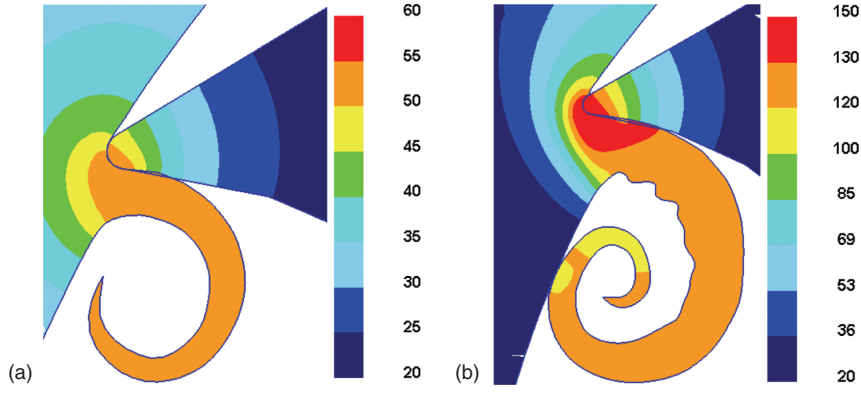

Figure 8.18 Predicted temperature distributions (°C) in the cutting zone during micromilling: (a) AL2024-T6 aluminum and (b) AISI 4340 steel [8].

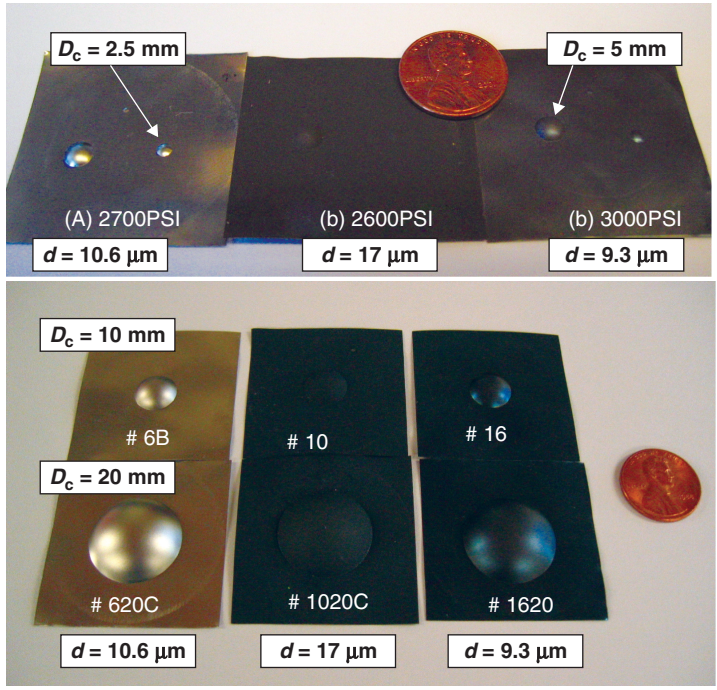

(a)

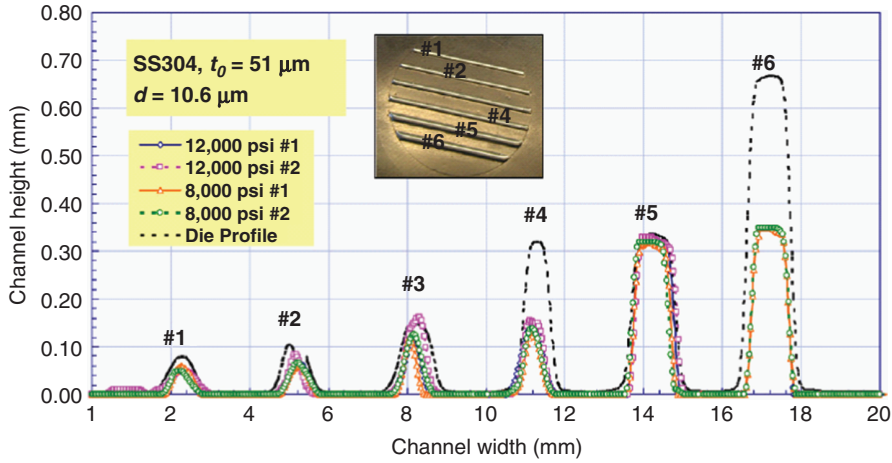

(b)

Figure 9.26 (a) Meso- and micro-scales bulging, and (b) micro-channel hydroforming on thin SS304 blanks [30,31].

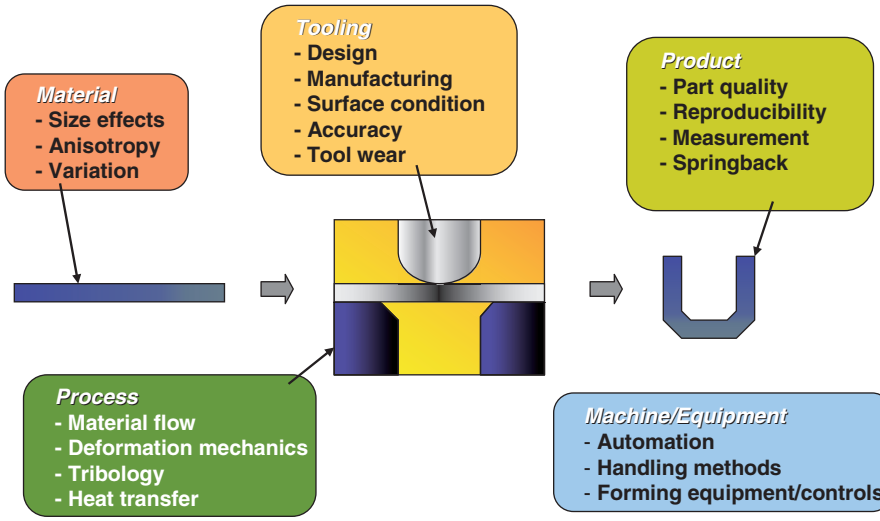

Figure 9.27 Basic elements of a micro-forming system.

CHAPTER 1

FUNDAMENTALS OF MICRO-MANUFACTURING

MUAMMER KOÇ
Center for Precision Forming (CPF — National Science Foundation IUCRC), Virginia Commonwealth University, Richmond, VA
Istanbul Sehir University, Turkey

TUĞRUL ÖZEL
Manufacturing Automation Research Laboratory, School of Engineering, Industrial and Systems Engineering, Rutgers University, Piscataway, New Jersey

1.1 INTRODUCTION

During the last decade, there has been a continuing trend of compact, integrated and smaller products such as (i) consumer electronics—cell phones, PDAs (personal digital assistant), etc.; (ii) micro- and distributed power generators, turbines, fuel cells, heat exchangers [1–4]; (iii) micro-components/features for medical screening and diagnostic chips, controlled drug delivery and cell therapy devices, biochemical sensors, Lab-on-chip systems, stents, etc. [5–8]; (iv) micro-aerial vehicles (MAV) and micro-robots [9–12]; and (v) sensor and actuators [13,14] (Fig. 1.1). This trend requires miniaturization of components from meso- to micro-levels. Currently, micro-electromechanical systems (MEMS), mostly limited to silicon, are widely researched and used for miniaturized systems and components using layered manufacturing techniques such as etching, photolithography, and electrochemical deposition [15,16]. Such techniques are heavily dependent on technologies and processes originally developed for micro-electronics manufacturing. However, MEMS have some limitations and drawbacks in terms of (i) material types (limited to silicon in combination with sputtered and etched thin metallic coatings), (ii) component geometries (limited to 2D and 2.5D), (iii) performance requirements (i.e., types of mechanical motions that can be realized, durability, and strength), and

Micro-Manufacturing: Design and Manufacturing of Micro-Products, First Edition.
Edited by Muammer Koç and Tugrul Özel.

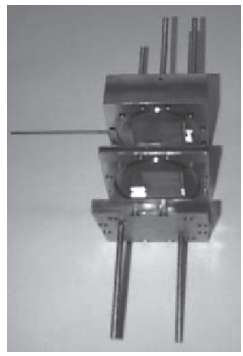

(a)

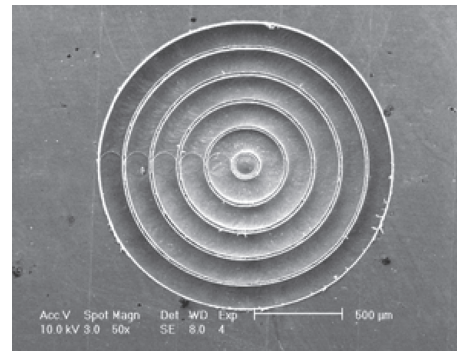

(b)

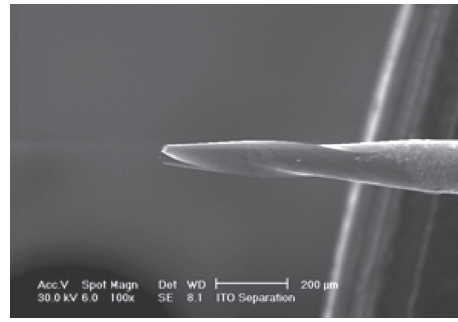

(c)

Figure 1.1 (a) Micro-channel chemical reactor, components are manufactured by laser micro-machining [20]; (b) pattern of concentric 127 µm channels of varying depth up to 125 µm cut into a brass workpiece; (c) SEM photograph of the front view of the 127 µm diameter two-flute end mill [21].

(iv) cost (due to slow and sequential nature of processes that are not amenable to mass production).

These issues lead the way for researchers to seek alternative ways of producing 3D micro-components with desired durability, strength, surface finish, and cost levels using metallic alloys and composites. Micro-machining processes have been widely used and researched for this purpose [15–17]. For instance, the laser micro-machining is used to fabricate micro-structures (channels, holes, patterns) as small as 5 µm in plastics, metals, semiconductors, glasses, and ceramics. Aspect ratios of 10:1 are claimed to be possible with this process. As a result, micro-scale heat exchangers, micro-membranes, micro-chemical-sensors and micro-scale molds can be fabricated with micro-machining. However, these processes are not appropriate for high-volume-low-cost applications [18,19]. Figure 1.2 depicts representative parts and features manufactured using mechanical micro-machining process.

As an alternative, micro-forming (micro-extrusion, micro-embossing, micro-stamping, micro-forging, etc.) processes have been considered and researched

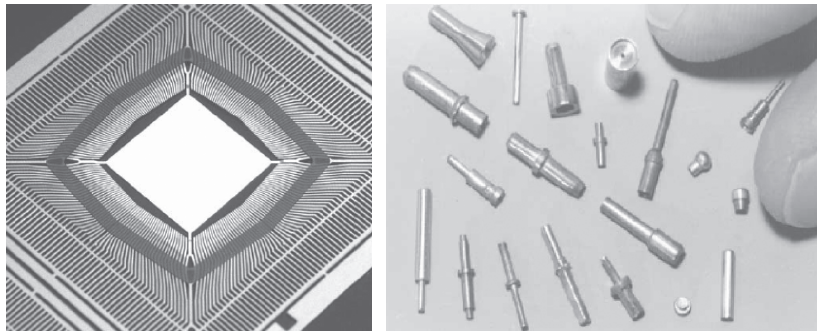

(a) (b)

Figure 1.2 (a) lead frame (pitch 300 μm) blanks stamped for electronic connectors [19]; (b) Sample micro-extruded/forged parts.

as a prominent processing method because of their potential capabilities to produce a large volume of components cost-effectively [19,22–25]. Examples of micro-extruded parts are shown in Fig. 1.2. Micro-forming poses some difficulties because of the size and frictional effects associated with material forming processing. For micro-components in the ranges of interest (0.1–5 mm), the surface area/volume ratio is large, and surface forces play important roles. As the ratio of feature size to grain size becomes smaller, deformation characteristics change abruptly with large variations in the response of material [26]. Thus, new concepts are needed to extend forming processes to micro-levels. Early research attempts indicate that micro-forming is feasible but fundamental understanding of material, deformation, and tribological behavior in micro-/meso-scale is necessary for successful industrialization of micro-forming [24,27].

The development of novel methods and use of alternative instruments for accurate and cost-effective measurement of material properties are needed in micro-forming process and tool and product design. As is well known, both solids and fluids exhibit different properties at the micro-scopic scale. As the size scale is reduced, surface and size effects begin to dominate material response and behavior. Consequently, material properties obtained on regular scale specimens are no longer valid for accurate analysis and further design. Mechanical, tribological, and deformation properties deviate from bulk values as the characteristic size of the micro-components approaches the size scale of a micro-structure, such as the grain size in polycrystalline materials [22,27]. The ultimate challenge and the fundamental underlying barrier in the advancement of micro-forming processes are to be able to characterize these properties at the micro-scale in an accurate and reasonably cost-effective manner.

1.2 MICRO-FORMING (MICRO-SCALE DEFORMATION PROCESSES)

Micro-forming is defined as the production of metallic parts by forming with at least two part dimensions in the submillimeter range [27]. When a forming

process is scaled down from the conventional scale to the submillimeter range, some aspects of the workpiece such as the micro-structure and the surface topology, remain unchanged. This causes the ratio between the dimensions of the part and parameters of the micro-structure or surface to change, and is commonly referred to as the *size effects*.

The trend toward further miniaturization—in particular, in the field of electronics, consumer products, energy generation and storage, medical devices, and micro-systems technology (MST)—will persist as long as consumers still seek for compact devices with heavily integrated functions. Metal forming processes are well known for their high production rate, minimized material waste, near-net-shapes, excellent mechanical properties, and close tolerances. These advantages make metal forming suitable for manufacturing of micro-features, especially where a high-volume-low-cost production is desired [19,28]. However, the well-established metal forming technology at the macro-scale cannot be simply applied in the micro-levels due to the so-called "size effects" on the material behavior. At the micro-level, the processes are characterized by only a few grains located in the deformed area; thus, the material can no longer be considered as a homogeneous continuum. Instead, the material flow is controlled by individual grains, that is, by their size and orientation [29]. As a result, conventional material properties are no longer valid for accurate analysis at this level. Furthermore, the deformation mechanism changes abruptly with large variations in the response of material as the ratio of grain size to the feature size decreases. Surface interaction and friction force become more prominent as the ratio of the surface area to volume increases [26,28]. These issues have been investigated to better understand, define, and model the "size effects." Additional size effects concerning the forming process are forming forces, spring-back, friction, and scatter of the results.

A micro-forming system comprises five major elements: material, process, tooling, machine/equipment, and product as illustrated in Fig. 1.3. The size effect is a dominant factor in design, selection, operation, and maintenance of all these elements. For example, a major problem in micro-forming lies in the design and manufacturing of the tools (i.e., dies, inserts, and molds). Small and complex geometries needed for the tools are difficult to achieve, especially when close tolerances and good surface quality are desired. Special tool manufacturing techniques are required to overcome these difficulties. Carefully selected tool material and simple shaped/modular tools can help reduce the cost of tool making and the degree of difficulty regarding the tool manufacturing, and increase tool life.

A vital challenge for micro-machine and equipment is the required precision at a high-speed production. In general, positioning of the micro-parts during the production process requires an accuracy of a few micrometers to submicrometers depending on the part type and ultimate use. In addition, as the part size is extremely small and the part weight is too low, handling and holding of micro-parts becomes very difficult due to adhesive forces (van der Waals, electrostatic, and surface tension). Therefore, special handling and work holding equipment need to be developed to overcome these difficulties in placing, positioning, and assembling the micro-parts. Also, clearance or backlash, between a die and a

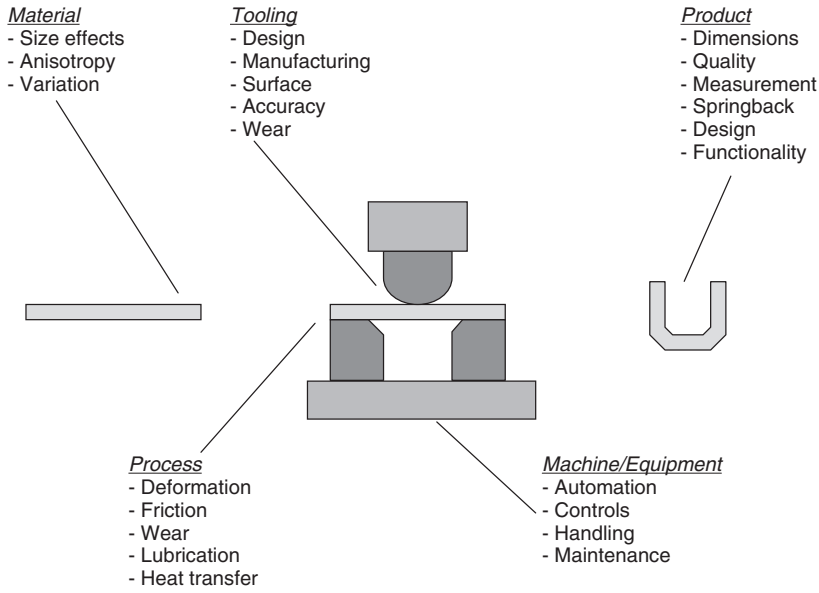

Figure 1.3 Micro-forming system.

punch that could be negligible at the conventional scale, can be a problem when the total required stroke to form the micro-part and clearance lies in the range of a few hundred micrometers [27]. Another challenge concerns the accurate measurement, inspection, and monitoring system of the process and dimensional parameters during and after the forming process. Automation systems for the micro-manufacturing are another issue that will eventually need to be studied and improved for the high-volume-low-cost production process.

1.2.1 Size Effects in Micro-forming Processes

For the accurate analysis and design of micro-forming processes, proper modeling of the material behavior at the micro-/meso-scale is necessary by considering the size effects. Two size effects are known to exist in metallic materials. One is the "grain size" effect and the other is the "feature/specimen size" effect (see Figure 1.4). The former is generally represented by the Hall–Petch law, which states that the material strengthens as the grain size decreases. The latter is observed when the miniaturization of the part occurs resulting in the decrease of the flow stress. Although the first studies on "feature/specimen size" effect were as early as the 1960s, up until now, no models quantitatively describe the phenomena. In order to implement the miniaturization effect into simulation tools, a quantitative description of the phenomena is necessary. In this chapter, an attempt has been made to quantify the size effect on the flow stress by considering the fundamental properties of single and polycrystal plasticity.

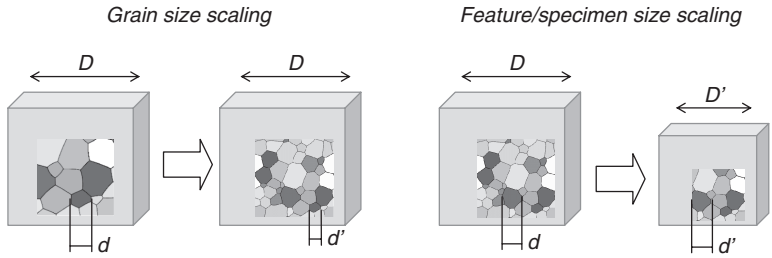

Figure 1.4 Illustration of two types of scaling effects: "grain size effect" and "feature/specimen size effect." (A full color version of this figure appears in the color plate section.)

According to Armstrong [30] and Kim *et al.* [31], the size effects can be investigated under two categories—the "grain size effect" and the "feature/specimen size effect." The "grain size effect" has been known to follow the Hall–Petch equation [32,33]. This effect purely depends on the average size of the material grains and is the dominant effect on the material response at the macro-levels. However, as the feature/specimen size reduces to the micro-scales, the "feature/specimen size effect" has also been reported to have considerable impact on the material response, and thus manufacturability.

Depending on the material testing methods or metal forming processes, the "feature/specimen size effect" could be further divided into two distinctive effects: the "feature size effect" and the "specimen size effect." In general, the "specimen size" can be referred to as the diameter of a billet (rod) or the thickness of a blank (sheet) to be tested or formed, while the "feature size" could be regarded as the smallest feature (channels, radii, protrusions, etc.) on the final part that these specimens will be formed into. For example, in an extrusion process of micro-pins, the specimen size would be the initial diameter of the rod/billet, while the feature size would be the diameter of the reduced section. In the case of micro-channels formed on an initially flat thin sheet blank, specimen size will be regarded as the thickness of the blank, while micro-channels will be the feature of interest and their dimensions (i.e., width and height) will represent the feature size. Similarly, in a bulge test of thin sheet blank, the specimen size will be the blank thickness, while the feature size will be the bulge diameter. With this distinction between the specimen size and the feature size effects, it is obvious that a tensile test could be used only to study the effect of the specimen size but not the feature size on the material behavior.

Even though these size effects can be distinguished based on the above discussion, as the grain, specimen, and feature sizes get smaller and smaller into the micro-scales, their effects are coupled, and therefore should be considered together. Koç and Mahabunphachai [34] proposed the use of two characteristic parameters N and M to couple and represent these interactive effects, where N is defined as the ratio between the specimen and the grain sizes, and M is the ratio between the feature and the specimen sizes. By defining N and M, all

TABLE 1.1 Type of Size Effects and Characteristic Parameters

	Size Effects		
	Grain Size	Specimen Size	Feature Size
Tensile test	d	t_0, D_0	—
Bulge test	d	t_0	D_c
Stamping process	d	t_0	D_c
Extrusion process	d	D_0	D_c
Characteristic parameter	$N = t_0/d$ or D_0/d		$M = D_c/t_0$ or D_c/D_0

combinations of the interactive effects, that is, grain-to-specimen, specimen-to-feature, and grain-to-feature sizes, can be represented and quantified using N, M, and $N \times M$, respectively. A summary of different types of size effects and their corresponding characteristic parameters is presented in Table 1.1, where d is material grain size, t_0 the specimen thickness, D_0 the specimen diameter, and D_c the die cavity.

The "specimen size effect" (t_0 or D_0) on the material flow curve as a measure of material response was observed in various tensile test conditions for a variety of materials such as CuAl alloy [35], CuNi18Zn20, CuZn15 [36], CuZn36 [37], and aluminum [38,39]. While the grain size shows a strong effect on the material response at all length scales (i.e., from macro- to micro-scale), it is not until the N value is around 10–15 that the "specimen size effect" starts to influence the material response [31,38,40]. In general, the tensile test results showed a decreasing trend of the flow stress with the decreasing specimen size (i.e., decreasing N value) as illustrated in Fig. 1.5a and 1.5b. Similar observations were reported in upsetting tests of copper, CuZn15, and CuSn6 [19] as illustrated in Fig. 1.5c, and in bulging test of CuZn36 [37] as illustrated in Fig. 1.5d. This trend of decreasing flow stress with decreasing N value was rather consistent based on the results of various studies. However, as N is reduced close to a range of 2–4, several researchers had reported an increase in the flow stress as N is decreased further. For instance, the tensile test results of 99.999% Al rods by Hansen [38] showed an increase in the flow stress as N decreases from 3.9 to 3.2 (Fig. 1.5a). Similar results were also observed in micro-/meso-scale hydraulic bulge testing of thin CuZn36 blanks [37], where the flow stress was found to increase as N value decreases from 5 to 3.3 ($d = 60$ μm, t_0 reduced from 0.3 to 0.2 mm) as shown in Fig. 1.5. An increase in the flow stress was also observed as N is reduced close to 1 (single crystal deformation) as reported in bending tests of CuZn15 and aluminum 99.0–99.5% [36,39]. Nevertheless, in the tensile test results of CuNi18Zn20 specimens by Kals and Eckstein [36], a continuous decrease in the flow stress was reported as N decreased from 25 to 2.5 (i.e., $d = 40$ μm, $t_0 = 1.0$, 0.5, and 0.1 mm) as shown in Fig. 1.5b. A summary of the effect of N on the flow stress based on the findings reported in the literature is presented in Fig. 1.6.

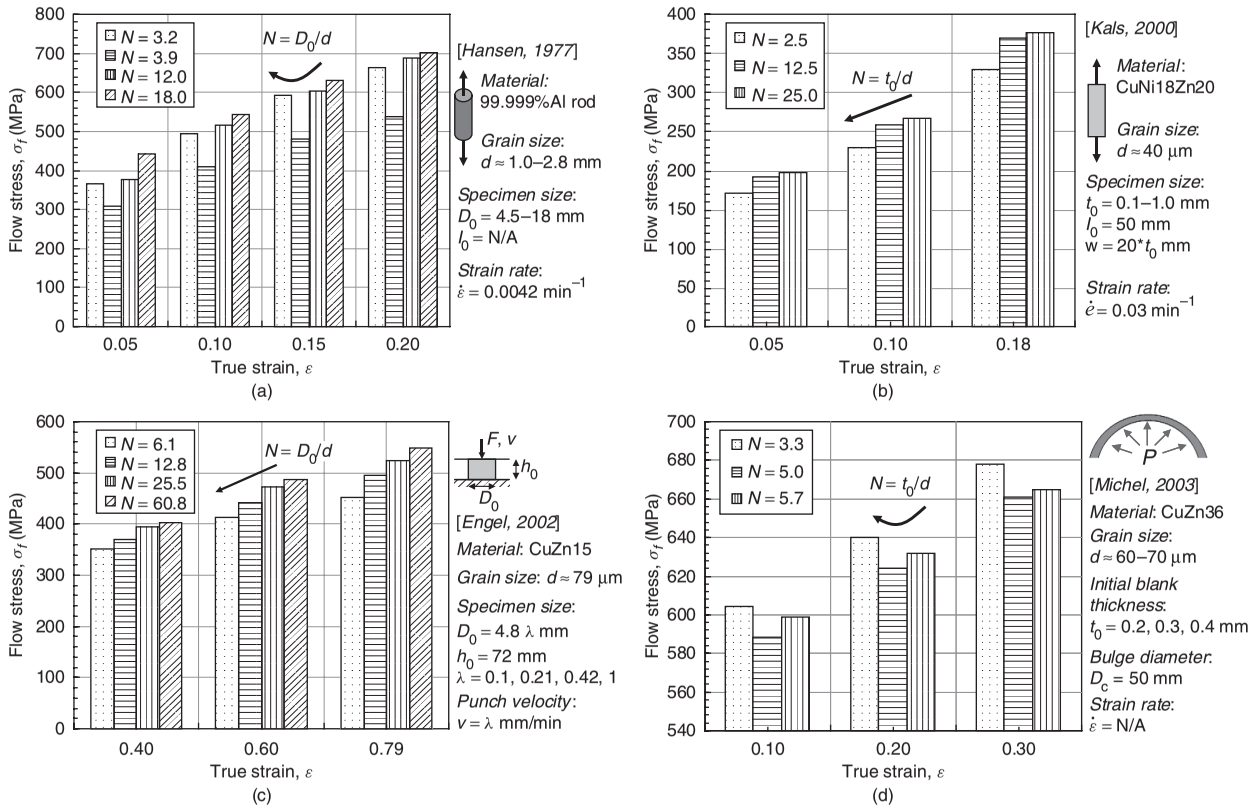

Figure 1.5 Effect of N on material flow stress under different testing conditions.

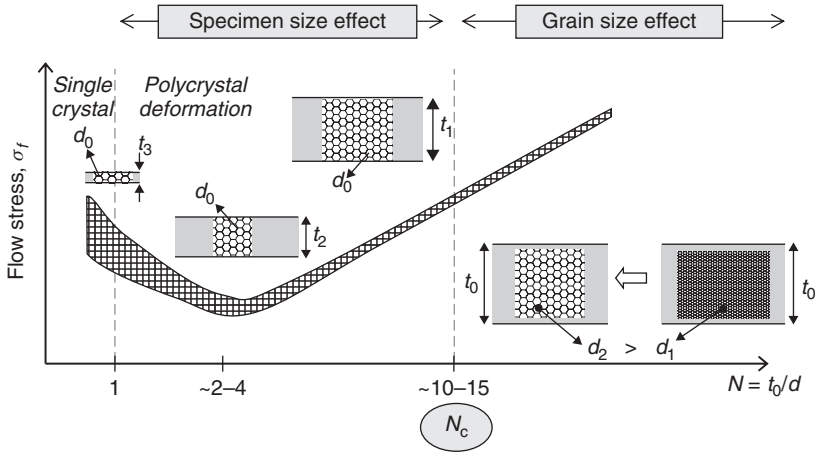

Figure 1.6 Grain versus specimen size effect on the flow stress as a function of N.

In contrast, studies on the "feature size effect" are only few and quite recent. In a study by Michel and Picart [37], thin blanks of CuZn36 with initial thickness of 0.25 mm were bulged using two different bulge diameters of 20 and 50 mm, corresponding to $M = 80$ and 200, respectively. They observed a decrease in the material flow stress when smaller bulge diameter was used. Their results revealed the effect of the feature size on the material response. Unfortunately, no discussion or explanation for this phenomenon was provided in their publication regarding the feature size effect (i.e., bulge diameter). A comprehensive understanding of the feature size effect (D_c or M) is still lacking and requires further investigations, both qualitatively and quantitatively, due to an impressing fact that micro-/meso-scale channel or feature arrays on a large surface area are increasingly used and needed for a wide range of end products for enhanced heat/mass transfer purposes.

1.2.2 Numerical Modeling of Micro-scale Deformation

Finite element analysis (FEA) is an important and respected research tool used to support, and in some cases, explain the results obtained from the experiment or derived from traditional approaches of theory. As with any tool, its effectiveness depends heavily on the skill and dedication of the researcher who guides its use. This is especially true in micro-forming research where properties of material differ from conventional scale, and the ambiguous characterization of the deformation mechanism and surface interaction is not fully understood. Since the length scale of the micro-forming processes is in the range of a few hundred micrometers, which is between the macro-scale (millimeter) and the molecular scale (angstrom), both continuum mechanics and molecular dynamics (MD) simulations appear to be legitimate candidates.

MD deals with simulating the motion of molecules to understand the physical phenomena that derive from dynamics molecular interactions. The goal of MD simulations is to understand and to predict macro-scopic phenomena from the properties of individual molecules making up the system. With continuing advances in the methodology and the speed of computers, MD studies are being extended to larger systems, greater conformational changes, and longer time scales. The results available today make it clear that the applications of MD will play an even more important role in the future [41].

On the other hand, in continuum mechanics, material and structural properties are assumed to be homogeneous throughout the entire structure for a simplifying approximation of physical quantities such as energy and momentum. Differential equations are employed in solving problems in continuum mechanics. Some of these differential equations are specific to the materials being investigated, and are called constitutive equations, while others capture fundamental physical laws such as conservation of mass or conservation of momentum. The physical laws of solids and fluids do not depend on the coordinate system in which they are observed. Despite the fact that continuum mechanics completely ignores the heterogeneity in a structure, the continuum mechanics simulation has been successfully used in a wide range of application in many research fields. Continuum mechanics was originally intended to model the behavior of structural components, with dimensions of order 0.1–100 m or so. To apply the continuum mechanics in micro-scale analysis, the issue we need to address is the actual fact that the material is highly inhomogeneous at this micro-level, and that as a result the stress and strain fields are nowhere being near uniform and homogeneous.

The obvious advantage of the MD simulation over the continuum mechanics simulation is that it gives a route to dynamical properties of the system: transport coefficients, time-dependent responses to perturbations, rheological properties, and spectra. The predictions are "exact" in the sense that they can be made as accurate as we like, subject to the limitation imposed by the computer budget [42]. However, since MD simulations start at the scale of an atom and the time on the order of femtoseconds, running simulations to large size and times is prohibitive. In fact, in terms of computing power, there is a competition between the time and size scales as illustrated in Fig. 1.7 [43]. Note that nonlocal continuum mechanics theories involve adding strain gradients or dislocation density evolution equations that include a spatial length scale.

Figure 1.7 shows that as the simulation time (inversely related to the applied strain rate) increases, the computational power is the main constraint that limits the size of the block material. Similarly, as the block size increases, the computational times require fairly large applied strain rates (i.e., short simulation time). Strain rates lower than the order of $10^6\ s^{-1}$ are not feasible at this time in atomistic simulations. For example, a 10-nm cubic domain of a metal can be simulated only for times less than around 10^{-10} s, even on very large parallel machines [43]. This computational limitation is the major factor that prevents the extensive use of MD simulations in an analysis of structures larger than nanometer scale.

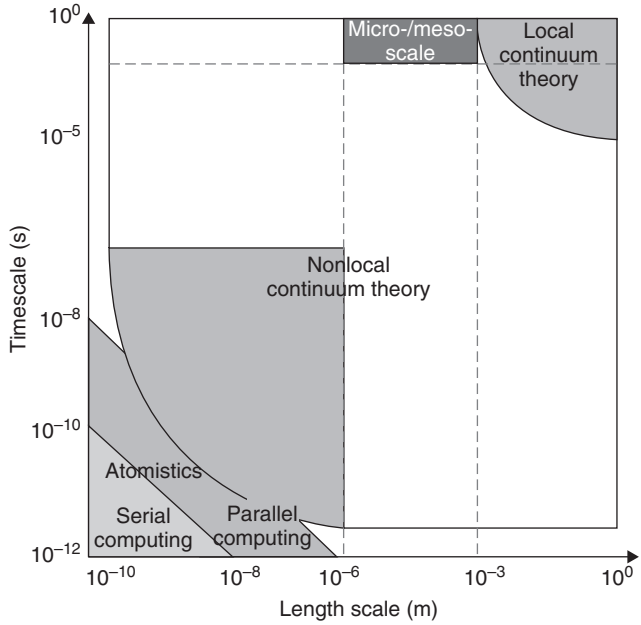

Figure 1.7 Schematic of strain rate and spatial size scale effects on computing and the regions where local and nonlocal continuum theories are applicable [43].

1.3 MICRO-MACHINING FOR DISCRETE PART MICRO-MANUFACTURING

There is a growing need for fast, direct, and mass manufacturing of miniaturized functional products from metals, polymers, composites, and ceramics. The demand for miniaturized meso-(1–10 mm)/micro-(1–1000 μm) devices with high aspect ratios and superior surfaces has been rapidly increasing in aerospace, automotive, biomedical, optical, military, and micro-electronics packaging industries [44,45].

In the last two to three decades, the micro-manufacturing processes such as *wet etching, plasma etching, ultrasonic, and LIGA (German acronym for lithography, electroplating, and molding*), which are a result of the explosion of activities in MEMS, have been developed and widely used for manufacturing micro-parts [44,46]. However, most of these methods are slow, and limited to a few silicon-based materials [46]. Also, the MEMS-based methods are typically planar; that is, 2.5D processes that are not capable of fabricating many of the miniature parts that consist of true three-dimensional (3D) features, for example a micro-mold for a plastic injection of micro-parts [46]. Moreover, a majority of these processes require a high setup time and cost, hence they are not economical for small batch size production. In short, the limitations of the MEMS-based methods in terms

of material choices, part dimensions, and production sizes make these processes unsuitable for manufacturing of many complex miniature parts.

Since the MEMS-based methods are not capable of meeting every demand, other alternative processes such as mechanical micro-machining (e.g., micro-milling) combined with numerical control (NC) machine tool technology [47–49]—*micro-electro-discharge machining* (Micro-EDM), *laser beam micro-machining* (LBM), and *focused ion beam* (*FIB*) *machining*—offer alternative fabrication methods [50] to bridge the gap between meso- and micro-scale direct manufacturing of discrete parts or dies and molds for micro-forming micro-injection-molding-type massmanufacturing micro-parts (Fig. 1.8).

Mechanical micro-machining (or tool-based micro-machining) as scaled down versions of turning, milling, and drilling is rapidly gaining momentum in industrial applications because of its viability to directly produce miniature 3D functional parts from a wide range of materials with high precision [48,52–54].

LBM is another alternative to produce features in micron sizes using long (*nanosecond*) and short (*femtosecond*) pulsed lasers as shown in Figure 1.9 on transparent/translucent, nonconductive, and elastic polymers (acrylic, polycarbonate, PEEK (polyetheretherketone), PMMA (polymethylmethacrylate), PDMS (polydimethylsiloxane), elastomers, and others) and difficult-to-process materials (hard metals, ceramics, diamond, and glass) for a variety of applications ranging from biosensors to micro-fluidic devices, solar-cell surfaces (see Figure 1.10), metallic medical devices (coronary stents) to optical and photonic devices.

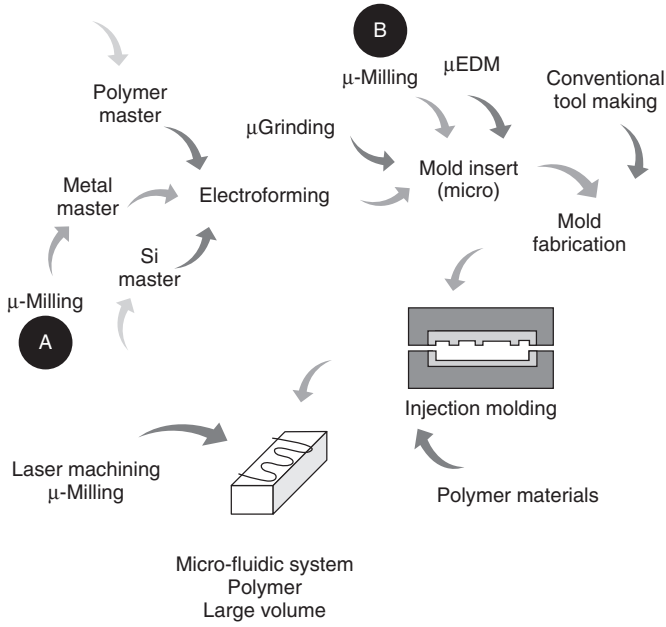

Figure 1.8 Micro-machining processes for micro-injection molding [51].

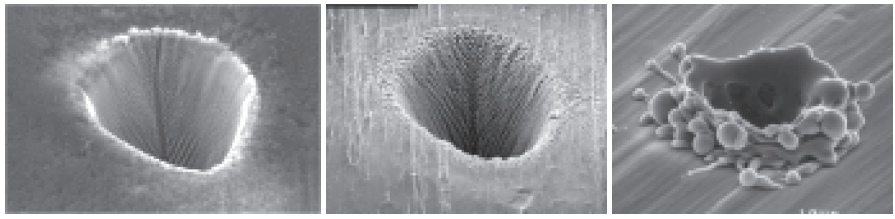

Figure 1.9 Pulsed laser beam micro-machining: (a) Holes drilled with a Ti sapphire system (120 femtoseconds) in air and (middle) in vacuum. (b) A hole drilled by an Nd: YAG laser ($\lambda = 1.06$ μm; pulse width = 100 ns, $P = 50$ mW, 2 kHz). *Source:* All images were taken from the entry side of the Kovar foil. (Courtesy of Sandia Manufacturing Science and Technology Center, http://mfg.sandia.gov).

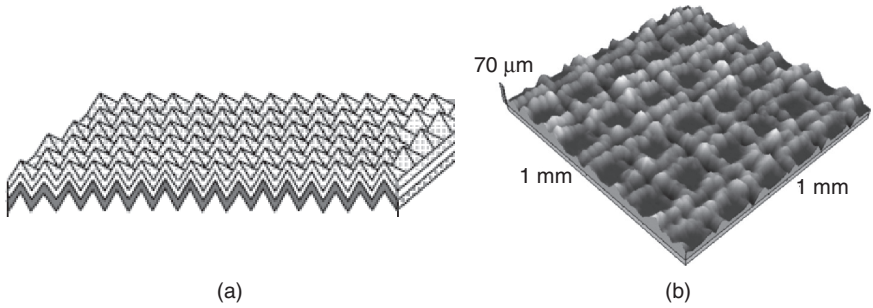

Figure 1.10 (a) Design of multifunctional solar cell surfaces and (b) surface texturing with laser scribing [45,50].

Micro-manufacturing processes have different material capabilities and machining performance specifications. Machining performance specifications of interest include *minimum feature size, feature tolerance, feature location accuracy, surface finish*, and *material removal rate* (Table 1.2). Mechanical micro-machining utilizes miniature cutting tools, ultra-high-speed spindles and high precision machine tools. However, there exist some technological barriers. These can be on the size of the cutting tool; for instance, the diameter of small production micro-drills is about 25 μm, and the diameter of micro-milling tools is about 20 μm [17,48,52,53,55–57]. It can have limitations on feature tolerance with error compensation between 250 and 500 nm, or on the flat and round surface produces; for example, roughness of micro-drilled hole walls is about 10–50 nm and roughness of diamond machined surfaces is about 5 nm [17,48,52,53,55–60]. These limitations are a result of several factors such as lack of technologies to fabricate viable and economical smaller cutting tools, accuracy and repeatability of machine tool drives, tool deflections and

vibrations (especially in micro-milling process), size effect, and minimum chip thickness requirements in mechanical micro-machining processes, which is always a problem in ductile- and coarse-grained polycrystalline micro-structure metals [48,53,59,61].

There is also a growing need in parallel for high precision and accuracy metrology instruments. Capability of metrology instruments can be summarized as resolution limit of many *optical instruments* is about 1 μm, of *scanning electron micro-scopes* is about 1–2 nm, of *laser interferometers* is about 1 nm, and of *scanning probe micro-scopy* is about 0.1 nm [45,50].

However; despite its benefits, scaling down the mechanical machining process from the macro- to micro-scale is not as easy as it sounds. Many factors that can be neglected in macro-scale machining suddenly become significant in micro-scale machining; for example, material structure, vibration, and thermal expansion [52–54,60]. As a result, the application of micro-mechanical machining process is still limited. Many technological obstacles need to be resolved, and many physical phenomena need to be well understood. In this chapter, a brief review of micro-mechanical machining is presented.

1.3.1 Size Effects in Micro-machining Processes

Despite its success in manufacturing macro-scale parts, scaling down the mechanical machining process into micro-scale production encounters several difficulties(see example of micro-parts in Figure 1.11). It is important to note that as the mechanical machining is scaled down, many physical and mechanical properties of material removal process, which are less pronounced in macro-mechanical machining, play very important roles in micro-mechanical machining. As a result, there are some specific issues that occur only in mechanical machining at micro-scale; for example, size effect and minimum uncut chip thickness.

The term *size effect* in metal cutting (chip formation) processes is often referred to as nonlinear increase in the specific cutting energy with decreasing undeformed chip thickness. Vollertsen *et al.* [62] presented a decreasing trend in shearing energy per unit volume for machining processes with data for SAE 1112 steel from Taniguchi *et al.* [63] and tensile tests from Backer [64] as shown in Fig. 1.12.

Given that flow stress, in most metals, increases as strain rate increases, the strain rate sensitivity of flow stress also increases rapidly in the range applicable to machining type processes ($>10^4\ s^{-1}$); therefore, specific cutting pressure could increase as undeformed chip thickness decreases.

Performance of mechanical micro-machining processes is influenced by work material micro-structure; for example, anisotropy, crystalline orientation, grain size, and boundaries [65–67]. Most commonly used engineering materials such as steel and aluminum have the length of crystalline grain size between 100 nm and 100 μm, which is comparable to the size of micro-feature. Therefore, in micro-mechanical machining, shearing takes place inside the individual grain

TABLE 1.2 Fundamental Principle, Capabilities, and Performance Specifications of Micro-manufacturing Processes

Process	Principle	Minimum Feature Size	Tolerance	Production Rates	Materials
Micro-extrusion	Plastic deformation by force	50 μm	5 μm	High/mass Fair accuracy	Ductile metals
Micro-molding/ casting	Melting and solidification by heat	25–50 μm	5 μm	High/mass Fair accuracy	Polymers/ metals
Mechanical micro-machining	Chip formation by force	10 μm	1 μm	High MRR High accuracy	Metals/ polymers/ ceramics
Micro-EDM	Melting/ breakdown	10 μm	1 μm	High MRR High accuracy	Conductive materials
Excimer laser	Ablation by laser beam	6 μm	0.1–1 μm	Low MRR High accuracy	Polymers/ ceramics
Short-pulse laser	Ablation by laser beam	1 μm	0.5 μm	Low MRR High accuracy	Almost any
Focused ion beam	Sputtering by ion beam	100 nm	10 nm	Very low MRR High accuracy	Tool—steels, nonferrous, plastics

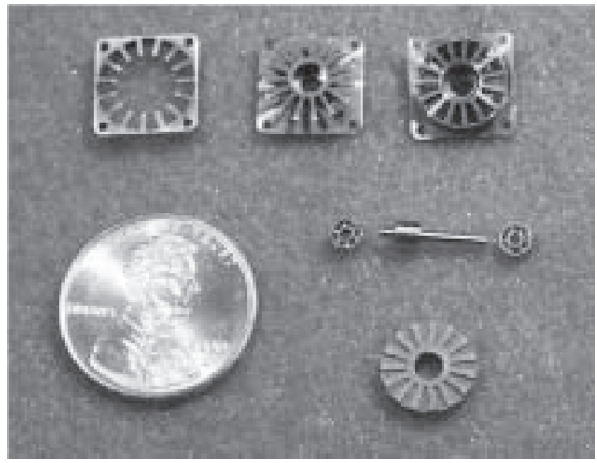

Figure 1.11 Meso-scale stepper motor (10 mm × 10 mm × 5 mm) machined by Micro-EDM process. *Source:* Courtesy of Sandia Manufacturing Science and Technology Center.

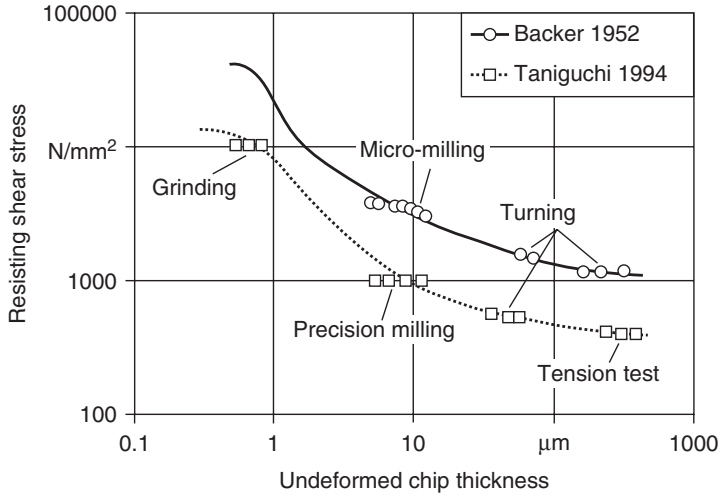

Figure 1.12 Increasing shear stress during material separation for decreasing undeformed chip thickness in several micro-manufacturing processes [62].

instead of along the grain boundary as in macro-mechanical machining. Characteristic dimesions of crystals (grains) on polycrystalline metarials, and phases on multiphase materials, are commensurate with the tool dimensions and uncut chip thickness values. Both elastic and plastic behavior of individual crystals are anisotropic, and therefore the cutting action experiences different mechanical properties when passing through different grains [56,66–68]. Thus, machining force magnitudes, rake face friction, and elastic recovery will vary during the process. In summary, micro-structure of work material plays an important role in mechanical micro-machining.

As an example, the size effect is demonstrated with measured specific forces in flat end milling process using miniature end mills with decreasing feed per tooth, and hence undeformed chip thickness in Fig. 1.13. As it can be seen, the undeformed chip thickness values less than 1 μm create a nonlinear increase in specific cutting forces measured [60].

In micro-mechanical machining, owing to limited strength of the edge of the micro-cutting-tool, the uncut chip thickness is constrained to be comparable or even less than the size of the tool edge, and as a result a chip will not be generated. The chips will be generated, and material removal will be achieved only when the uncut chip thickness reaches a critical value, the so-called *minimum chip thickness* [69]. Minimum (or critical) uncut chip thickness is considered to be a measure of the highest attainable accuracy [70,71]. No chip is produced with a chip thickness less than a critical value, and the entire material is forced under the cutting tool and deformed. Especially, in micro-milling, the elastic portion of the deformation recovers after the tool passes [52,72,73].

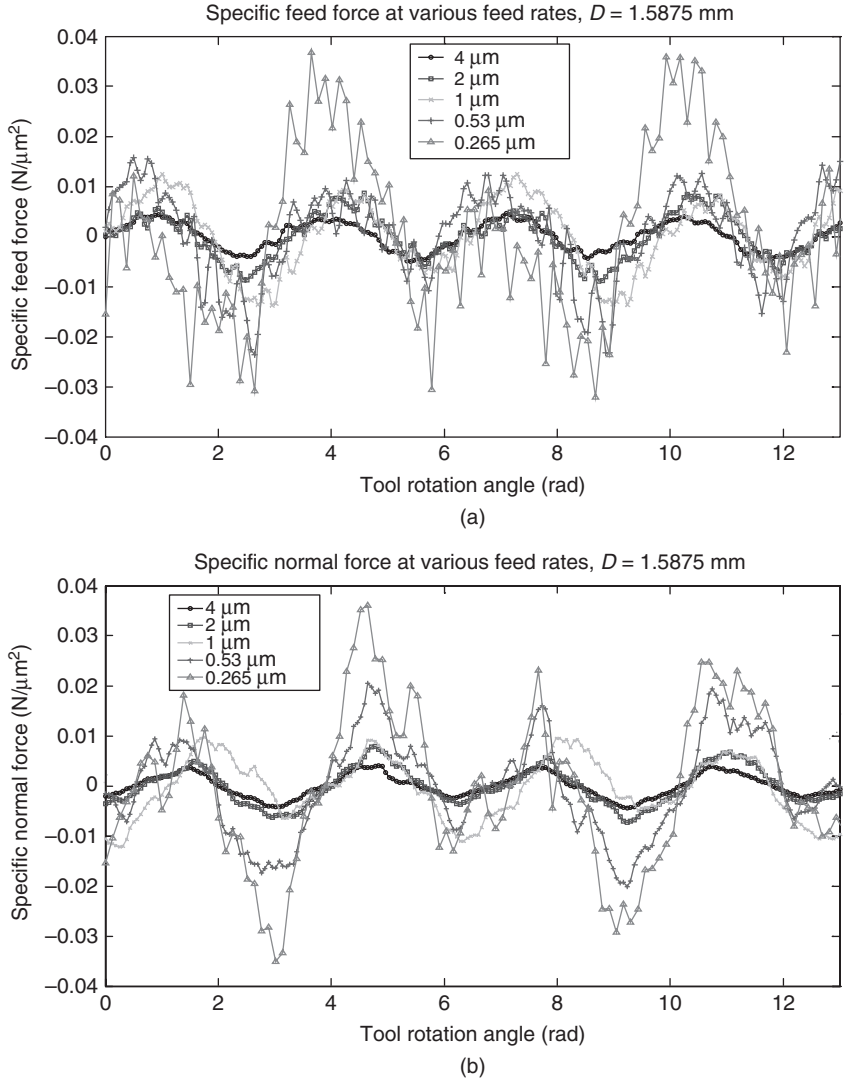

Figure 1.13 Size effect on the forces acting on the flat end milling tool during full immersion milling: (a) effect of reduction in feed per tooth on feed force; (b) effect of reduction in feed per tooth on normal force (two-flute end mill, 30 helix angle, $N = 6000$ rpm) [60].

The minimum chip thickness requirement significantly affects machining process performance in terms of cutting forces, tool wear, surface finish, process stability, etc. [55,72,73]. Hence, knowledge of the minimum chip thickness is important for the selection of appropriate machining conditions. In order to estimate the normalized minimum chip thickness, researchers have resorted to

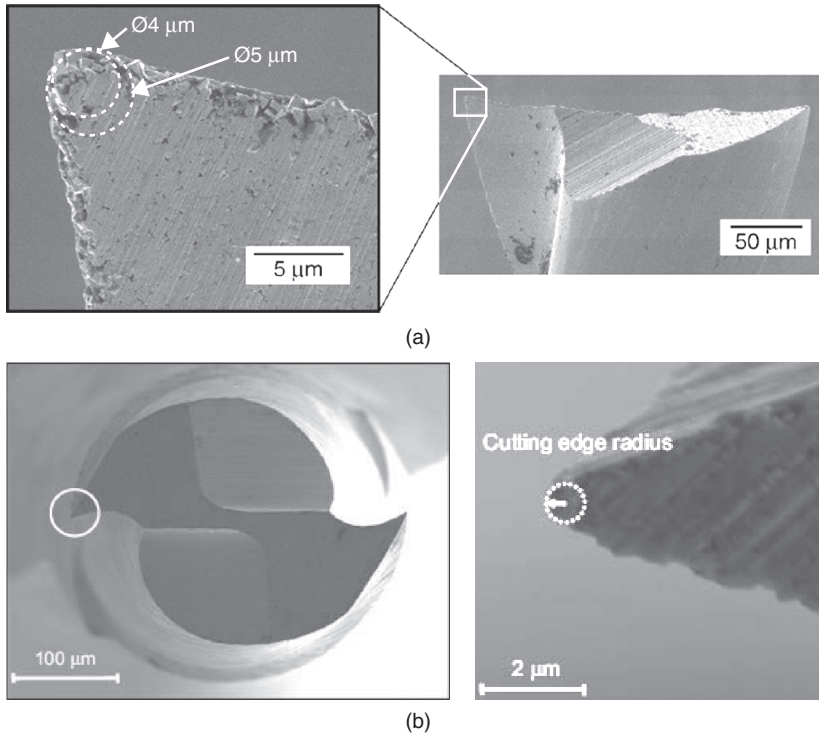

Figure 1.14 (a) Cutting edge of a tungsten carbide (WC) micro-end-mill under SEM indicating a large cutting edge and corner radius [59]; (b) 500 µm diameter micro-end-mill and edge radius [76].

experimentation [72,73], MD simulations [74], and micro-structure-level force models [56], as well as to analytical slip-line plasticity-based models [75].

The minimum chip thickness is considered to be related to the resistivity of the material against plastic deformation, such as indentation hardness. It is found to be strongly dependent on the ratio of chip thickness to cutting edge radius and on the workpiece material/tool combination. Some images depicting tool edge radius are given in Fig. 1.14 as examples. It was seen to be between 5% and 38% of the edge radius for different materials [75].

Numerical models have been created for micro-machining of single crystalline materials (copper and aluminum) and polycrystalline materials (aluminum alloys, cast iron, and steels) with an aim to understanding of deformations including micro-structure and grain size effects and the influence of tool edge radius on micro-milling [56,60,74,76–78]. Micro-machining-induced plastic deformation, white layer formation, subsurface alteration, and residual stresses on the fabricated materials are analyzed through the FEM (finite element method)-based process simulations. Furthermore, by using FEM-based process

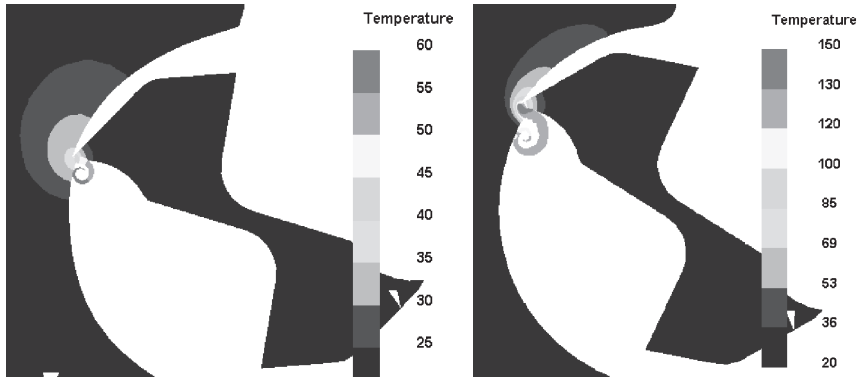

Figure 1.15 FEM simulation of micro-milling: (a) AL2024-T6 aluminum and (b) AISI 4340 steel [60].

simulations, micro-end-mill tool geometry and machining parameters can be investigated (Fig. 1.15) [60].

REFERENCES

1. Rachkovkij DA, *et al.* Heat exchange in short micro tubes and micro heat exchangers with low hydraulic losses. J Microsyst Technol 1998;4:151–158.
2. Lee SJ, *et al.* Design and fabrication of a micro fuel cell array with flip-flop interconnection. J Power Sources 2002;112:410–418.
3. Meng DS, Kim J, Kim CJ. A distributed gas breather for micro direct methanol fuel cell. Proc IEEE 2003:534–537.
4. Khanna R. MEMS fabrication perspectives from the MIT microengine project. Surf Coat Technol 2003;163–164:273–280.
5. Trackenmueller R, *et al.* Low cost thermoforming of micro fluidic analysis chip. J Micromech Microeng 2002;12:375–379.
6. Aoki I, *et al.* Trial production of medical micro tool by metal deformation processes using moulds. Proc IEEE 1995:344–349.
7. Chu M. Design and Fabrication of Active Microcage [MS thesis]. Los Angeles (CA): Mechanical and Aerospace Engineering Department, University of California; 1998.
8. Chovan T, Guttman A. Microfabricated devices in biotechnology and biochemical processing. Trends Biotechnol 2002;20(3):116.
9. Yeh R, Kruglick EJJ, Pister KSJ. Surface-micro machined components for articulated micro robots. J MEMS 1996;5(1):10–17.
10. Hayashi I, Iwatsuki N. Micro moving robotics. International Symposium on Micro mechatronics and Human Science; 1998 Nov. 25–28; Nagoya. 1998. pp 41–50.

11. Dudenhoeffer DD, Bruemmer DJ, Anderson MO, McKay MD. Development and implementation of large-scale micro-robotic forces using formation behaviors. Idaho National Engineering and Environmental Laboratory (INEEL), ID 83415 INEEL Long-Term Research Initiative Program under DOE Idaho Operations Office Contract DE-AC07-99ID13727 and through DARPA Software For Distributed Robotic program contract J933.
12. Kim J, Koratkar NA. Effect of unsteady blade motion on the aerodynamic efficiency of micro-rotorcraft. Proceedings of the 44th AIAA/ASME/ASCE/AHS Structures, Structural Dynamics and Materials Conference; 2003 Apr 7–10; Norfolk, VA. 2003.
13. Eddy DS, Sparks DR. Application of MEMS technology in automotive sensors and actuators. Proc IEEE 1998;86:1747–1755.
14. Fujita H. Micro actuators and micro machines. Proc IEEE 1998;86:1721–1732.
15. Choundhury PR, editor. Handbook of microlithography, micromachining and microfabrication. Volume 2: Micromachining and microfabrication. Bellingham (WA): SPIE Press; 1997.
16. Fukuda T, Menz W, editors. Micro mechanical systems: principles and technology. Amsterdam: Elsevier; 1998. pp 260–271.
17. Friedrich CR, Vasile MJ. Development of the micro milling process for high aspect-ratio micro structures. J MEMS 1996;5:33–38.
18. Ashida K, *et al.* Development of desktop machining micro factory—trial production of miniature machine products. Proceedings of Japan-USA Flexible Automation Conference; 2000 Jul 23–26; Ann Arbor, MI. 2000.
19. Engel U, Eckstein E. Microforming-from basics to its realization. J Mater Process Technol 2002;125–126:35–44.
20. Pacific Northwest National Laboratory Web Site. Available at www.pnl.gov.(accessed on May 1, 2010).
21. Ni J. Meso scale mechanical machine tools and micro milling process development for future micro factory based manufacturing. Proceedings of SATEC ’03; China. 2003.
22. Geiger M, Messner A, Engel U. Production of micro parts–size effects in bulk metyaal forming, similarity theory. Prod Eng 1997;4(5):15.
23. Raulea L, *et al.* Grain and specimen size effects in processing metal sheets. Volume II, Proceedings of the 6th ICTP: Advanced Technology of Plasticity; 1999 Sep 19–24; Nuremberg, Germany. 1999. pp 939.
24. Saotome Y, Iwazaki H. Superplastic backward micro extrusion of micro parts for micro-electro-mechanical systems. J Mater Process Technol 2001;119:307–311.
25. Ike H, Plancak M. Coining process as a means of controlling surface microgeometry. J Mater Process Technol 1998;80–81:101–107.
26. Tiesler N, Engel U. Microforming-effects of miniaturization. In: Pietrzyk M, *et al.*, editors. Proceedings of the International Conference on Metal Forming. Rotterdam, Netherlands: Balkema; 2000. pp. 355.
27. Geiger M, Kleiner M, Eckstein R, Tiesler N, Engel U Microforming. Ann CIRP 2001;50(2):445. Keynote paper.
28. Vollertsen F, Hu Z, Schulze Niehoff H, Theiler C. State of the art in micro forming and investigations into micro deep drawing. J Mater Process Technol 2004;151:70–79.

29. Engel U, Egerer E. Basic research on cold and warm forging of microparts. Key Eng Mater 2003;233–236:449–456.
30. Armstrong RW On size effects in polycrystal plasticity. J Mech Phys Solids 1961;9:196–199.
31. Kim G, Koç M, Ni J. Modeling of the size effects on the behavior of metals in micro-scale deformation processes. J Manuf Sci Eng 2007;129:470–476.
32. Hall EO. Deformation and ageing of mild steel. Phys Soc Proc 1951;64(B381): 747–753.
33. Petch NJ. Cleavage strength of polycrystals. J Iron Steel Inst 1953;174:25–28.
34. Koç M, Mahabunphachai S. Feasibility investigations on a novel micro-manufacturing process for fabrication of fuel cell bipolar plates: Internal pressure-assisted embossing of micro-channels with in-die mechanical bonding J Power Sources 2007;172:725–733.
35. Miyazaki S, Fujita H, Hiraoka H. Effect of specimen size on the flow stress of rod specimens of polycrystalline Cu-Al alloy. Scripta Metall 1979;13:447–449.
36. Kals TA, Eckstein R. Miniaturization in sheet metal working. J Mater Process Technol 2000;103:95–101.
37. Michel JF, Picart P. Size effects on the constitutive behaviour for brass in sheet metal forming. J Mater Process Technol 2003;141:439–446.
38. Hansen N. The effect of grain size and strain on the tensile flow stress of aluminium at room temperature. Acta Metall 1977;25:863–869.
39. Raulea LV, Goijaerts AM, Govaert LE, Baaijens FPT. Size effects in the processing of thin metals. J Mater Process Technol 2001;115:44–48.
40. Onyancha RM, Kinsey BL. Investigation of size effects on process models for plane strain microbending. Proceedings of the International Conference on Manufacturing Science and Engineering (MSEC); 2006 Oct 8–11; Ypsilanti, MI. 2006.
41. Karplus M. Molecular dynamics of biological macromolecules: a brief history and perspective. Biopolymers 2003;68:350–358.
42. Allen JP, *et al.* Nested stamped sheet metal plates to make an internal chamber. US patent 6,777,126. 2004.
43. Horstemeyer MF, Baskes MI, Plimpton SJ. Computational nanoscale plasticity simulations using embedded atom potentials. Theor Appl Fract Mech 2001;37:49–98.
44. Alting L, Kimura F, Hansen HN, Bissacco G. Micro engineering. Ann CIRP 2003;52(2):635–657.
45. De Chiffre L, Kunzmann H, Peggs GN, Lucca DA. Surfaces in precision engineering, microengineering and nanotechnology. Annals of the CIRP 2003;52/2:561–577.
46. Madou M Fundamentals of microfabrication. Boca Raton, FL: CRC Press; 1997.
47. Masuzawa T, Tonshoff HK. Three-dimensional micro-machining by machine tools. Ann CIRP 1997;46(2):621–628.
48. Dornfeld D, Min S, Takeuchi Y. Recent advances in mechanical micromachining. Ann CIRP 2006;55(2):745–768.
49. Liow JL. Mechanical micromachining: a sustainable micro-device manufacturing approach? J Clean Prod 2009;17:662–667.
50. Rajurkar KP, Levy G, Malshe A, Sundaram MM, McGeough J, Hu X, Resnick R, DeSilva A. Micro and nano machining by electro-physical and chemical processes. Ann CIRP 2006;55(2):643–666.

51. Bissacco G, Hansen HN, Tang PT, Fugl J. Precision manufacturing methods of inserts for injection molding of microfluidic systems. Proceedings of the ASPE Spring Topical Meeting; Columbus, OH. 2005. pp 57–63.
52. Cao J, Krishnan N, Wang Z, Lu H, Liu WK. Microforming-experimental investigation of the extrusion process for micropins and its numerical simulation using RKEM. J Manuf Sci Eng 2004;126:642–652.
53. Chae J, Park SS, Freiheit T. Investigation of micro-cutting operations. Int J Mach Tools Manuf 2006;46:313.
54. Asad ABMA, Masaki T, Rahman M, Lim HS, Wong YS. Tool-based micromachining. J Mater Process Technol 2007;192–193:204.
55. Wuele H, Huntrup V, Tritschle H. Micro-cutting of steel to meet new requirements in miniaturization. Ann CIRP 2001;50(1):61–64.
56. Vogler MP, DeVor RE, Kapoor SG. Microstructure-level force prediction model for micro-milling of multi-phase materials. J Manuf Sci Eng 2003;125:202–209.
57. Asad ABMA, Masaki T, Rahman M, Lim HS, Wong YS. Tool-based micromachining. J Mater Process Technol 2007;192–193:204.
58. Eda H, Kishi K, Ueno H. Diamond machining using a prototype ultra-precision lathe. Precis Eng 1987;9:115–122.
59. Filiz S, Conley CM, Wasserman MB, Ozdoganlar OB. An experimental investigation of micro-machinability of copper 101 using tungsten carbide micro-endmills. Int J Mach Tools Manuf 2007;47:1088–1100.
60. Dhanorker A, Özel T. Meso/micro scale milling for micromanufacturing. Int J Mechatronics Manuf Syst 2008;1:23–43.
61. Özel T, Liu X. Investigations on mechanics based process planning of micro-end milling in machining mold cavities. Mater Manuf Process 2009;24(12):1274–1281.
62. Vollertsen F, Biermann D, Hansen HN, Jawahir IS, Kuzman K. Size effects in manufacturing of metallic components. CIRP Ann—Manuf Technol 2009;58:566–587.
63. Backer WR, Marshall ER, Shaw MC. The size effect in metal cutting. Transact ASME 1952;74:61–72.
64. Taniguchi N. The state-of-the-art of nanotechnology for processing ultra-precision and ultra-fine products. Precis Eng 1994;16(1):5–24.
65. vonTurkovich BF, Black JT. Micro-machining of copper and aluminum crystals. J Eng Ind Transact ASME 1970;92:130–134.
66. Ueda K, Manabe K. Chip formation mechanism in microcutting of an amorphous metal. Ann CIRP 1992;41:129–132.
67. Zhou M, Ngoi BKA. Effect of tool and workpiece anisotropy on microcutting processes. Proc Inst Mech Eng (IMechE) 2001;215:13–19.
68. Egashira K, Mizutani K. Micro-drilling of monocrystalline silicon using a cutting tool. Precis Eng 2002;26:263–268.
69. Ikawa N, Shimada S, Tanaka H. Minimum thickness of cut in micromachining. Nanotechnology 1992;3:6–9.
70. Lucca DA, Rhorer RL, Komanduri R. Energy dissipation in the ultraprecsion machining of copper. CIRP Ann—Manuf Technol 1991;40:69–72.
71. Lucca DA, Seo YW, Rhorer RL, Donaldson RR. Aspects of surface generation in orthogonal ultraprecision machining. CIRP Ann—Manuf Technol 1994;43:43–46.

72. Vogler MP, DeVor RE, Kapoor SG. On the modeling and analysis of machining performance in micro-endmilling. Part I: Surface generation. ASME J Manuf Sci Eng 2004;126:685–694.
73. Vogler MP, DeVor RE, Kapoor SG. On the modeling and analysis of machining performance in micro-endmilling. Part II: Cutting force prediction. ASME J Manuf Sci Eng 2004;126:695–705.
74. Shimada S, Ikawa N, Tanaka H, Ohmori G, Uchikoshi J, Yoshinaga H. Feasibility study on ultimate accuracy in microcutting using molecular dynamics simulation Ann CIRP 1993;42:91–94.
75. Liu X, DeVor RE, Kapoor SG. An analytical model for the prediction of minimum chip thickness in micromachining. ASME J Manuf Sci Eng 2006;128:474–481.
76. Torres CD, Heaney PJ, Sumant AV, Hamilton MA, Carpick RW, Pfefferkorn FE. Analyzing the performance of diamond-coated micro end mills. Int J Mach Tools Manuf 2009;49:599–612.
77. Lai X, Li H, Li C, Lin Z, Ni J. Modelling and analysis of micro scale milling considering size effect, micro cutter edge radius and minimum chip thickness. Int J Mach Tools Manuf 2008;48:1–14.
78. Woon KS, Rahman M, Neo KS, Liu K. The effect of tool edge radius on the contact phenomenon of tool-based micromachining. Int J Mach Tools Manuf 2008;48:1395–1407.

CHAPTER 2

MICRO-FABRICATION PROCESSES IN SEMICONDUCTOR INDUSTRY

KASIF TEKER
Department of Physics & Engineering, Frostburg State University, Frostburg, Maryland

2.1 INTRODUCTION

The electronics industry has been growing rapidly in the past several decades. This growth has been driven by new developments in integrated circuit (ICs). Silicon has been the most popular material to build ICs. The micro-fabrication techniques used for IC fabrication have also been used to fabricate a variety of structures such as thin film devices and circuits, micro-magnetics, optical devices, micro-mechanical structures, and micro-electromechanical systems (MEMS). In some applications, these devices and structures have been integrated into chips containing electronic circuits.

This chapter discusses the common micro-fabrication techniques used for both ICs and micro-machines. The first part introduces the crystal structure of Si, crystal growth, wafer production, oxidation of silicon, and other semiconductor substrates (SiC and GaAs). Next, chemical vapor deposition (CVD) is introduced. In this technique, source gases are introduced into a reactor to form a desired film on the surface of a wafer. Furthermore, thin film deposition techniques based on the physical process are discussed (sputtering and evaporation). Later, lithography, the technique used to transfer patterns onto a substrate surface using a photosensitive material (photoresist, PR) is discussed. Finally, subtractive pattern transfer techniques, dry etching and wet etching, are presented.

Micro-Manufacturing: Design and Manufacturing of Micro-Products, First Edition.
Edited by Muammer Koç and Tugrul Özel.

2.2 SEMICONDUCTOR SUBSTRATES

2.2.1 Silicon

Silicon has been the most important semiconductor material for the electronics industry and is likely to retain this position in the foreseeable future. Silicon comprises about 26% of the earth's crust.

Solids exist in crystalline and amorphous forms. In crystalline solids, atoms are arranged in a periodic array over large atomic distances, that is, a long-range order exists. This long-range atomic order is absent for amorphous materials. Crystalline materials can be classified as single crystals and polycrystals. If the periodic arrangement is perfect and extends throughout the entire solid, it is called a single crystal. However, if the solid is composed of many small crystals or grains, it is named polycrystalline material. The silicon starting materials for ICs have the single-crystal form.

Crystals are described by their most basic structural element, which is called unit cell. The unit cell represents the symmetry of the crystal structure in which all the atomic positions in the crystals may be generated by translations of the unit cell integral distances along each of its edges. In crystalline materials, it is very convenient to describe directions and planes. Labeling conventions have been established in which three indices or integers are used to designate planes and directions. Crystal planes are described by Miller indices as (hkl). Any two planes parallel to each other are equivalent and have identical indices. The Miller indices are determined as follows:

1. The intercepts of a plane are expressed as integral multiples of the lattice parameters a, b, and c.
2. The reciprocals of the three integers found in step 1 are taken.
3. These three numbers are changed to the set of smallest integers by division or multiplication using a common factor.

Similarly, the crystallographic directions are expressed as three integers in a bracket [uvw]. For cubic crystals, the direction [hkl] is perpendicular to a plane with the same there integers (hkl). If either a direction or a plane is known, its perpendicular counterpart can readily be determined.

Silicon has a diamond-cubic crystal structure, a structure that can be thought of as two interlocking face-centered cubic lattices. The three-dimensional exhibit of a Si crystal structure is shown in Fig. 2.1. Each atom has four nearest neighbors, which determine the electronic structure of silicon. Si is a group IV element and has four valence electrons. Each of these four electrons is shared with one of its four nearest neighbor atoms by forming a covalent bond for each shared electron pair. Since all valence electrons in a Si crystal are involved in bonding, no free electrons are available for the conduction of electrical current. However, these covalently bonded electrons can be excited (thermally or optically), and thus can be made available as free electrons for electrical conduction. A common

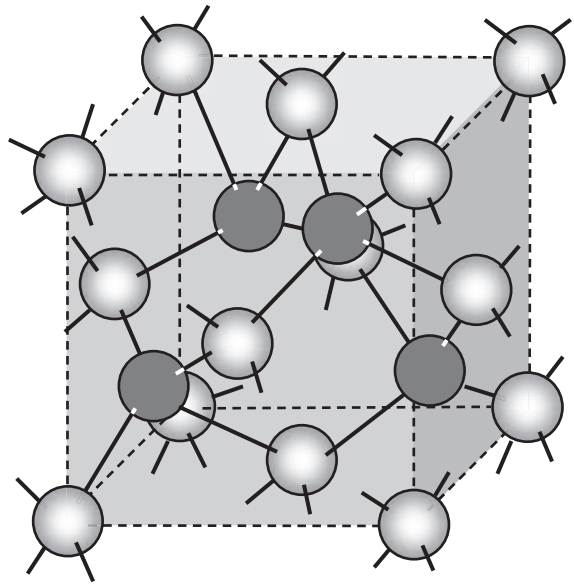

Figure 2.1 Silicon unit cell (diamond-cubic crystal structure).

method of changing the electrical conductivity of a semiconductor is introducing electrically active impurities into it by a method named *doping*. Group V elements are used as substitutional donors (n-type), while group III elements are used as acceptors (p-type). Upon incorporation into the Si crystal, donors give up an electron, whereas acceptors receive an electron. Both positive (holes) and negative charge (electrons) carriers contribute to the electrical conductivity. Fabrication of ICs and micro-machines requires a method for n- or p-type doping of the semiconductor substrate, usually in selective regions of the substrate. Two common doping methods are diffusion and ion implantation.

2.2.2 The Manufacture of Silicon Wafer

The fabrication of ICs takes place on silicon substrates having very high crystal quality. The importance of using single-crystal material for the transistor regions of ICs was reported by Teal in 1949 [1]. He stated that defects at the grain boundaries of the polycrystalline material reduce the performance of the devices dramatically. Therefore, it is very critical to use a high-quality single-crystal Si substrate to fabricate semiconductor devices. The method of achieving a high-quality single-crystal Si wafer involves the following steps:

1. The raw material (e.g., quartzite, a type of sand) is refined to produce electronic grade polysilicon (EGS).
2. This EGS is used to grow single-crystal silicon by Czochralski (CZ) growth or float-zone (FZ) crystal growth.

The CZ growth involves the solidification of a crystal from molten silicon. The EGS is loaded into a fused silica crucible in an evacuated chamber. The loaded crucible is heated to about 1500°C under inert gas ambient. Then, a small seed crystal (about 5 mm in diameter and 10 cm in length) is lowered into the crucible so that it comes into contact with the molten silicon. The seed crystal must be properly oriented, because it will be a template for the larger crystal, called the boule. The seed crystal is pulled up at a controlled rate. Both the seed crystal and the molten silicon crucible are rotated in opposite directions during the pulling process. It is very critical not to stir the melt to prevent incorporation of oxygen from the crucible into the silicon crystal during growth. The FZ process is another major technique to grow single-crystal silicon. A high-purity polysilicon rod is passed through an RF heating coil, which creates a localized molten zone from which the single crystal ingot grows. The Si comes into contact only with the ambient gas in the chamber. Thus, the FZ-grown crystals have higher purity than the CZ-grown crystals. FZ-grown Si is ideal for applications requiring low doping levels (e.g., detectors and power devices). Today, boules of silicon can be up to 300 mm in diameter and 1–2 m in length [2]. In Fig. 2.2, the basic processing steps for silicon wafer are summarized.

2.2.3 Oxidation of Silicon

One of the most significant advantages that makes silicon a superior semiconductor material is its ability to form chemically stable silicon dioxide. When silicon is exposed to an oxidizing ambient (oxygen or stream of steam) at elevated temperatures (between 700 and 1300°C), a stable oxide forms. This process is known as thermal oxidation. Silicon can even oxidize at room temperature forming a thin native oxide having a thickness of about 2 nm. When the oxidation takes place under water vapor, it is called wet oxidation, and when the source is pure oxygen, it is called dry oxidation. The oxidation reaction takes place at the SiO_2–Si interface. Thus, as the oxide grows, silicon is consumed and the SiO_2–Si interface moves into silicon. The high temperature helps diffusion of oxidant through the surface oxide layer to the SiO_2–Si interface to form oxide rapidly. The thermal oxidation process involves three steps: (i) gas-phase transport of oxidizing species to the surface; (ii) diffusion of oxidizing species through the formed oxide to the

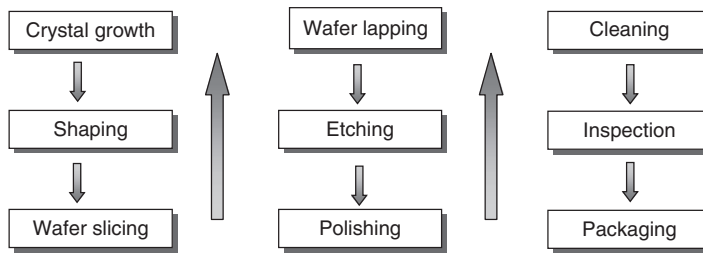

Figure 2.2 Basic processing steps for silicon wafer.

SiO_2–Si interface; and (iii) oxidation reaction at the SiO_2–Si interface [3]. The oxidation rate depends on the crystallographic orientation of the Si, doping level, and the pressure of the oxidizing gas. For example, a (111) surface oxidizes about 1.7 times more rapidly than a (100) surface. SiO_2 formed by thermal oxidation is used as an insulator layer, a mask, and as a sacrificial layer.

2.2.4 Silicon Carbide (SiC) and Gallium Arsenide (GaAs)

Silicon carbide (SiC) with many superior characteristics, such as wide bandgap, high thermal conductivity, high saturated electron drift velocity, high breakdown electric field, chemical stability, and resistance to radiation damage, has been expected to meet the requirements for high-temperature, high-frequency, and high-power applications. Moreover, its electrical stability well over 300°C, makes it an excellent material for micro-machines. It also exhibits piezoresistive properties. SiC can be doped by both n- and p-type impurities, and it allows a natural oxide to be grown on its surface. SiC has many different polytypes, and the two most common SiC polytypes are 3C-SiC (cubic) and 6H-SiC. Currently, 6H-SiC substrates are commercially available for high-temperature and high-power applications.

Gallium arsenide (GaAs) is an important III–V semiconductor material that is used in the fabrication of devices such as microwave frequency ICs, infrared light-emitting diodes, laser diodes, solar cells, and optical windows. GaAs circuits have been manufactured commercially for applications requiring high speed and low power. Although, GaAs enables production of faster devices in the IC industry, its use is partly limited because of its high cost. GaAs is used as a substrate for the epitaxial growth of other III–V semiconductor compounds. Table 2.1

TABLE 2.1 A Comparison of the Properties of Some Common Semiconductor Materials

	Si	GaAs	3C-SiC	6H-SiC	GaN	Diamond
Lattice constant (Å)	5.43	5.65	2.36	$a = 3.09$ $c = 15.12$	$a = 3.189$ $c = 5.185$	— —
Band gap (eV) at 300 K	1.11	1.43	2.23	3.02	3.39	5.5
Maximum operating temperature (°C)	250	150	>600	>600	—	1000
Melting point (°C)	1420	1238	Sublimes	>1800	—	Phase change
Breakdown voltage (10^8 V/cm)	0.3	0.4	—	3	5	10
Electron mobility ($cm^2/(V\ s)$)	1400	8500	1000	600	900	2200
Hole mobility ($cm^2/(V\ s)$)	600	400	40	40	150	1600
Saturated electron drift velocity (10^7 cm/s)	1	2	2.7	2	2.7	1.5
Thermal conductivity (W/cm)	1.5	0.5	5	5	1.3	20

compares several properties of the common semiconductor materials used in ICs and micro-machining.

2.3 CHEMICAL VAPOR DEPOSITION (CVD)

CVD refers to the formation of a condensed phase from a gaseous medium of a different chemical composition [4]. The reactant gases are introduced into a reaction chamber and are reacted at a heated surface to form a solid film (Fig. 2.3). It is distinguished from physical vapor deposition (PVD) processes such as evaporation or sputtering, where condensation occurs in the absence of a chemical change. CVD is used extensively in semiconductor industry for deposition of a wide range of materials from insulators to metals. A CVD process can be summarized in the following steps:

1. Transport of reactant and carrier gases in the main gas flow region from the reactor inlet to the deposition zone.
2. The reactant gas species are transported to the wafer surface. This transport takes place in the gas phase.
3. The reactants are adsorbed to the growth surface, and these adsorbed species are named as *adatoms*.
4. The adatoms migrate to the growth sites on the surface on which chemical reactions take place to form a solid film.
5. The gaseous by-products are desorbed from the deposition surface. These by-products diffuse through to the main gas flow region away from the deposition zone toward the reactor outlet.

2.3.1 Types of CVD

CVD can be categorized according to the type of heating, the operating pressure, the reactant sources, etc. On the basis of the type of heating used, the reactors are classified as hot-wall and cold-wall reactors. In hot-wall reactors, the whole

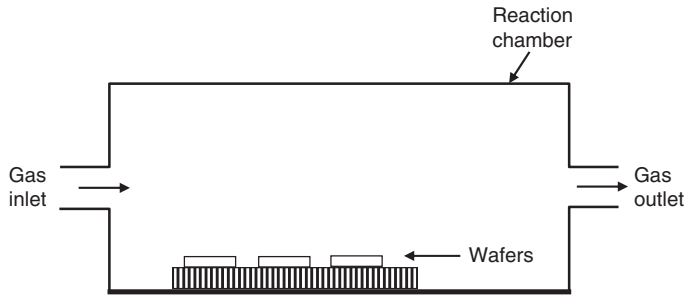

Figure 2.3 A simple CVD reaction chamber.

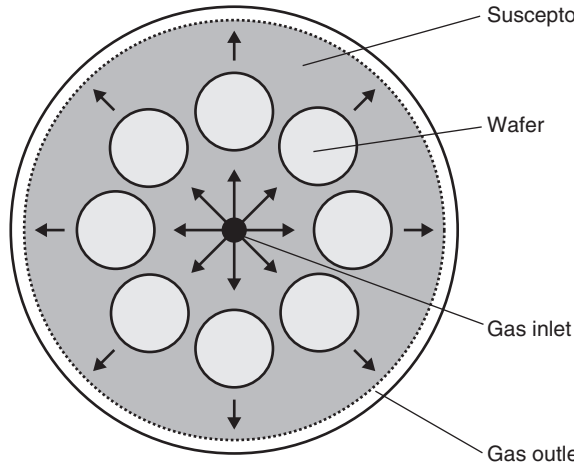

Figure 2.4 Top view of a multi-wafer CVD reactor with radial flow configuration. Arrows show gas flow distribution inside the reaction chamber.

tube is heated up along with its content, with the source of heating usually being resistance heating. Thus, the film-forming reactions take place on the reaction chamber walls as well as on the substrate. Cold-wall reactors are usually heated up by means of RF induction or infrared radiation of the substrate, leaving the chamber walls reasonably cool. In addition, on the basis of the reactants used, the process is called metalorganic CVD (MOCVD) if one of the reactants is a metal organic. Figure 2.4 shows the top view of a multi-wafer MOCVD reactor with radial flow configuration. On the basis of the operating pressure, CVD reactors may be grouped as atmospheric pressure CVD (APCVD) or reduced pressure CVD. Also, the reduced pressure group is divided into two groups: (i) low-pressure CVD (LPCVD), in which the energy source is entirely thermal and (ii) plasma-enhanced CVD (PECVD), in which the energy source is partially plasma. In some cases, the use of a plasma lowers the growth temperature. Figure 2.5 illustrates the CVD reactor types graphically [5].

2.3.2 Advantages and Disadvantages of CVD Growth

The advantages of CVD growth are as follows:

- Flexible
- Abrupt interface
- High purity
- Simple reactor
- Uniform
- Large scale

- High growth rate
- Selective growth
- *In situ* monitoring

However, there are disadvantages too:

- Expensive reactants
- Many parameters to control accurately
- Possibly hazardous precursors

Flow through an isothermal, constant-diameter tube at relatively low flow velocities usually used in CVD reactors will be laminar, with parallel flow velocity vectors in the direction parallel to the walls. The magnitude of the gas velocity will be a smooth function of its radial position with a value of zero at the walls. Laminar flow has a characteristic Reynolds number and given by

$$N_{\mathrm{Re}} = \frac{v\rho d}{\mu} \tag{2.1}$$

where v is the velocity along the pipe, d is the tube diameter, μ is the absolute viscosity, and ρ is the fluid density. The crossover point for the transition between laminar and turbulent flows is typically between 2000 and 3000. Thus, in order to ensure that CVD reactors operate in a laminar flow regime, the Reynolds number should usually be two decades below the critical value.

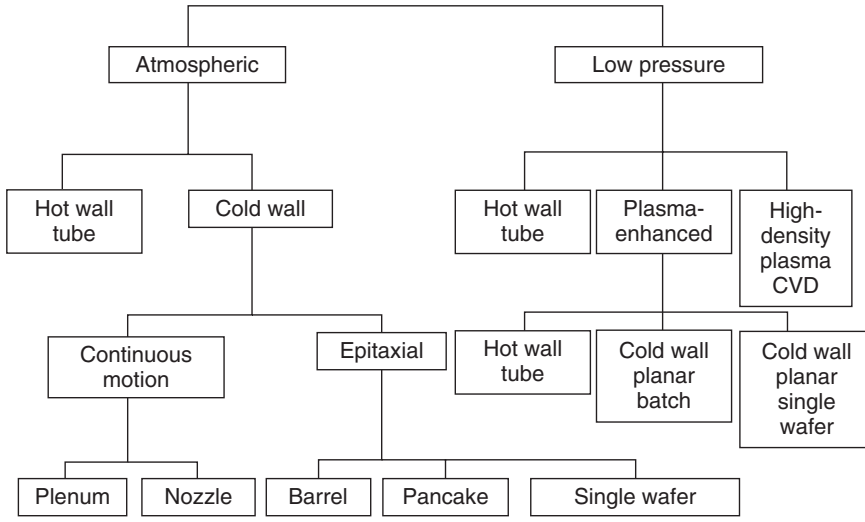

Figure 2.5 CVD reactor types.

The boundary-layer model may provide insight for the everyday operation and reactor design. This is the most widely used model for the calculation of the growth rate in the mass-transport-limited regime for most vapor phase crystal growth systems. It takes the velocity boundary layer (a transition region between the solid surface and the free gas stream) as a truly stagnant layer through which mass transport takes place only by diffusion. The boundary-layer thickness, $\delta(x)$, is defined as the distance from the interface at which the velocity component parallel to the wall becomes 99% of its free stream value, v, and is given by the condition that for $x > \delta(x)$

$$\delta(x) \cong 5\left(\frac{\mu x}{\rho v}\right)^{1/2} \tag{2.2}$$

where x is the distance measured from the leading edge of the substrate. The thickness of the boundary layer decreases with increasing flow velocities. Also, the boundary-layer thickness increases with distance from the leading edge of the substrate. These led to the idea of tilting the susceptor to compensate for gas-phase depletion effects and an increasing boundary-layer thickness along the flow direction because of the developing concentration profile. This model has proved to be a useful approximation for analysis and interpretation of experimental results [6].

2.4 LITHOGRAPHY

IC and micro-machine fabrication require lithography, the technique used to transfer patterns onto a surface of substrate. The most widely used type of lithography is photolithography. An advanced IC can have more than 20 masking layers. Therefore, a significant portion of the total cost in semiconductor manufacturing is due to lithographic processes.

The basic steps of lithographic process are shown in Fig. 2.6. As an example, an oxidized Si wafer and a positive PR (a thin layer of photosensitive material) combination were used. The PR is applied as a thin film to the substrate by spin coating. Subsequently, the coated PR is exposed to a form of radiation (e.g., ultraviolet light) through a mask. The mask contains clear and opaque features that define the pattern to be created in the PR layer. The regions in the PR exposed to the radiation are made soluble in a developing solution known as a developer. The radiation-exposed wafer is rinsed with a developer to remove the PR from the exposed areas leaving a pattern of bare and PR-covered oxide on the wafer surface. The PR pattern is the positive image of the pattern on the mask. If the unexposed regions are removed by the developer, then a negative image results. The resist is called a negative resist. Following development, the wafer is immersed in a solution of HF acid to remove the oxide selectively from the bare oxide regions without attacking the PR and the underlying Si. The PR protects the underlying oxide layer. Following the oxide etching, the remaining PR can

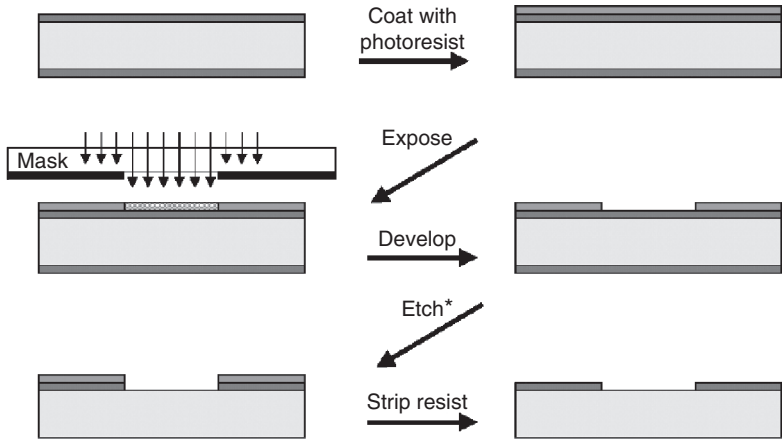

Figure 2.6 Basic steps of a lithographic process with positive photoresist and an oxidized Si wafer. The asterisk shows the stage of etching or adding process.

be removed with a strong acid such as H_2SO_4 or organic solvents. The oxidized Si wafer with etched windows can be used in further fabrication. The PR has two primary roles: (i) precise pattern formation in the resist and (ii) protection of the substrate during a variety of subtractive (e.g., etching) or additive (e.g., ion implantation) processes. Although both positive and negative PRs are used in semiconductor micro-fabrication, the better resolution capabilities of positive PRs make them a superior choice for smaller features.

A mask is defined as a substrate that contains patterns that can be transferred to a wafer surface. A photomask consists of a very flat glass or quartz plate (transparent to UV light) with a thin chromium pattern (absorber), which is opaque to UV light. The absorber pattern on the mask is fabricated by e-beam lithography, which can produce higher resolution than photolithography.

2.5 PHYSICAL VAPOR DEPOSITION (PVD)

The PVD technique is based on the formation of the vapor of the material to be deposited as a thin film. PVD techniques such as evaporation and sputtering are widely used for deposition of many kinds of thin layers in ICs and micro-machines. In general, the PVD process sequence can be described as follows:

1. The source material (solid or liquid) is converted to the vapor phase.
2. The vapor is transported from the source to the substrate surface across a region of low pressure.
3. The vapor can condense on the substrate surface to form a solid film.

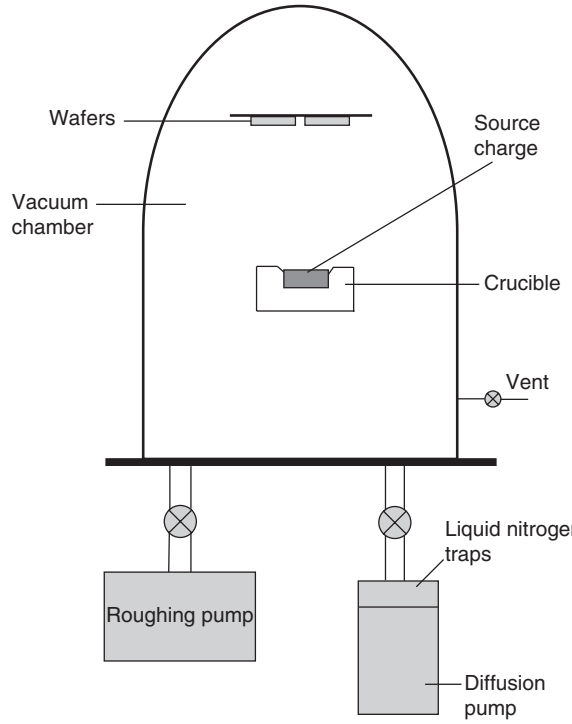

Figure 2.7 A simple diffusion-pumped evaporation system for thin film deposition.

Thermal evaporation was extensively used for the deposition of metal layers in early semiconductor technologies. Currently, sputtering is used more often compared to evaporation because of (i) better step coverage ability and (ii) better alloy composition. Evaporation involves molten samples because of the need for high vapor pressures required for high deposition rates. Figure 2.7 shows a simple diffusion-pumped evaporation system for thin film deposition. A sample vapor pressure of 10 mtorr or higher is required for reasonable deposition rates. Evaporation can be classified into three groups: (i) resistive, (ii) inductive, and (iii) electron beam evaporation. In the resistive method, a metal is evaporated by passing a high current through a highly refractory metal filament or a boat. The resistive evaporation is very susceptible to contaminations from the heating filament or boat. The resistive evaporation is not widely used in industrial applications. In inductive evaporation, a water-cooled RF coil surrounds a crucible with the source material to be evaporated. Inductively heated systems are very good and efficient for higher temperature refractory metals deposition. Nevertheless, contamination is still a problem due to crucible heating. This adverse effect can be avoided by heating only the source and cooling the crucible. The method for improving the contamination issue is electron beam evaporation. In electron beam (e-beam) evaporation, an electron beam gun (3–20 keV) is focused on the

source material that is situated in a recess in a water-cooled copper hearth. The electron beam is magnetically deflected onto the source material, which melts locally. Thus, the source metal forms its own crucible resulting in less crucible contamination problems. E-beam can produce high-quality deposition at very high deposition rates. Despite these advantages, e-beam evaporation can cause X-ray damage to the substrate and the equipment is very complex compared to the other two techniques.

Sputtering is a major technique for metal layer deposition in ICs and micromachines. It was first discovered by Grove in 1852 [7], and developed by Langmuir in 1923 [8]. It is a parallel-plate plasma reactor in a vacuum chamber (Fig. 2.8). The target material to be deposited is bombarded with high-energy ions created in plasma. The cathode and anode in a sputtering system are closely spaced (less than 10 cm) to collect a great number of ejected target atoms. Sputtering is preferred to evaporation because of (i) wider choice of materials, (ii) better step coverage, (iii) its being better at producing alloys, and (iv) better adhesion to the substrate. For elemental metal deposition, DC sputtering is preferred because of high deposition rates. However, an RF plasma technique is used for insulating layers [9]. The sputter deposition rate depends on the ion flux to the target material, the target material, and the transport of the ejected atoms to the substrate. A minimum ion energy is required for each target material. This energy is in the range of 10–30 eV [10], below which sputtering does not occur. The sputter yield (described as the number of atoms ejected per incident ion)

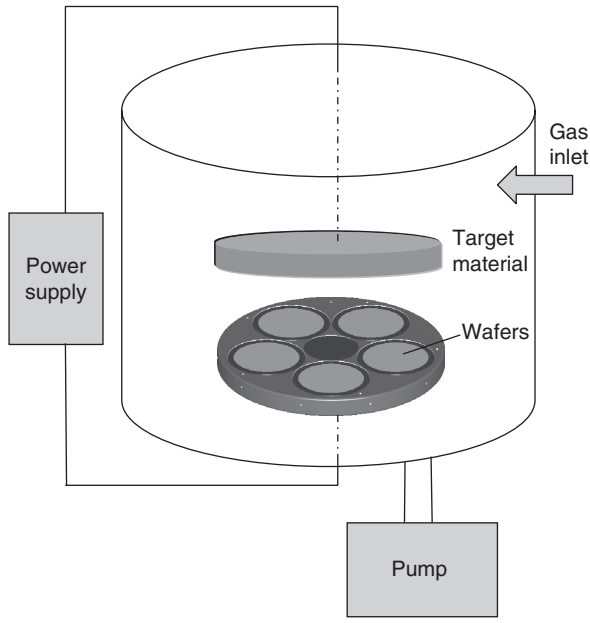

Figure 2.8 A parallel-plate sputtering system chamber.

is strongly dependent on the ion energy. In the range of sputtering, the yield increases with the incident ion energy and mass. The sputter yield increases as the square of the ion energy up to about 100 eV, and linearly with the energy up to 750 eV. The yield increases very little until the start of ion implantation [11]. Furthermore, the maximum sputter yield takes place at an ionic energy of about 1 keV. Target materials such as Cu, Pt, and Au have high sputter yields, whereas Ta and Mo have low sputter yields.

When an energetic ion strikes the surface of a material, several events can take place. The ion energy dictates the type of interaction. Ions with very low energies (< 5 eV) may get reflected by the surface of the target material. At energies about 10 eV, the ion may get adsorbed to the surface of the target material. At much higher energies (>10 keV), the ion penetrates into the bulk of the sample before slowing down and depositing its energy. Thus, these high-energy ions are embedded in the target. At intermediate incident ion energies, part of the ion energy is transferred to the solid in the form of heat and crystal damage; another portion of the energy ejects atoms from the surface of the target material. The ejected atoms and clusters have energies of about 10–50 eV, which is about one hundred times more than the energy of the evaporated atoms. Therefore, the sputtered atoms have higher surface mobility compared to the evaporated atoms. This results in improved step coverage of the deposited atoms on the substrate surface in sputtering. It is desirable that as many of the sputtered atoms as possible be deposited on the substrate. For a deposition rate of 40 nm/min, two layers of deposited film will form about every second. As the complexity of deposited compounds and materials for devices increases, sputtering can still provide solutions for the semiconductor industry.

2.6 DRY ETCHING TECHNIQUES

Etching is a selective material removal from the substrate by physical or chemical processes with an etchant. The main objective of etching, in general, is to transfer the pattern created by the mask onto the wafer surface precisely by selectively removing the material from the uncovered regions. Dry etching involves gas or vapor phase and includes physical, chemical (plasma etching), and physical–chemical etching (ion-enhanced etching). The efficiency of etching is evaluated by etch rate, selectivity, uniformity, surface quality, reproducibility, surface damage, and pattern transfer precision. Etch rate can be defined as the rate of removal of material from the selected regions.

Physical etching occurs by accelerating argon or other inert ions in an electrical field toward the substrate. Etching mechanism is due to momentum transfer from incident ions to the etch surface. Since physical etching involves high-energy ions, etching rate is almost material nonselective, that is, the etch rates of various materials are close. In general, the physical etch rate is very small (only $\sim$20–50 nm/min) relative to the chemical etching methods. Moreover, ion striking can create dramatic damage to the substrate surface. This could be

reversed by annealing. Another limitation of the physical etching is the lack of precise pattern transfer onto the substrate surface. This could be due to a number of factors that can be caused by the nonvolatility of reaction products or ion–surface interactions. Some of these limitations in physical etching are: (i) faceting (angled walls and features), (ii) ditching or trenching (due to glancing incidence of ions), and (iii) redeposition of etched material on the walls (especially for high-aspect ratio features). Despite these limitations, physical etching continues to find applications in semiconductor fabrication.

In chemical (plasma) etching, reactive chemical species produced in the plasma are transported to the substrate surface for etching. The etching gas is chosen to generate species that react chemically with the substrate to be etched. The reaction products are removed by the vacuum system. The function of the plasma is to supply reactive etchant species. The advantages of the plasma etching are: (i) high etching rates, (ii) isotropic etching, (iii) very selective etching, (iv) eliminating high-energy ion damage, and (v) no need for high vacuum (pressure >1 mtorr). Effective plasma etching takes place in several steps: (i) reactive chemical species are generated from the feed gas by the plasma; (ii) these reactive species must diffuse to the surface of the substrate and be adsorbed; (iii) a chemical reaction takes place resulting in a volatile by-product; and (iv) the by-product must be desorbed, diffused away from the substrate, and be exited by the main gas flow out of the etch reactor. The smallest rate determines the overall etching rate. In some cases, plasma may not be required to generate reactive neutrals. For example, etching of Si with xenon difluoride (XeF_2) does not need plasma to generate the etching reactive species. A Si etch rate as high as 10 μm/min has been reported with XeF_2 [12]. It has also been reported that XeF_2 exhibits very high etching selectivity over silicon dioxide, silicon nitride, aluminum, and PR. One of the biggest shortcomings of the solely chemical etching is the problem of undercutting associated with the isotropic etching. Thus, purely chemical etching is not suitable for etch features smaller than 1 μm. Therefore, adding a physical component to a chemical etching can provide better etching solutions.

Dry etch processes based on a combination of physical and chemical etching offer controlled anisotropic etching and higher selective etching than physical etching. In ion-enhanced etching, ion bombardment can induce a reaction by making the surface more reactive for the reactive plasma species (e.g., by creating surface damage). The etch rate achieved by ion-enhanced etching is significantly higher than in physical etching. For instance, the etch rate of Si in Ar physical etching is about 10 nm/min, while the etch rate is about 200 nm/min for a reactive gas such as CCl_2F_2. Furthermore, ion-enhanced etching can generate precise transfer of the mask pattern to the substrate with good etching selectivity with various materials. Chlorine-based plasmas are often used for anisotropic etching of Si, GaAs, and aluminum-based metallizations. Chlorinated sources such as CCl_4, BCl_3, and Cl_2 have high vapor pressures. Moreover, both these sources and their etch products are easier to handle than the bromides and iodides. Etching rates as high as 1.0 μm/min is possible in ion-enhanced etching.

2.7 WET BULK MICRO-MACHINING

In wet bulk micro-machining, features are created in the bulk of the substrates such as silicon, SiC, GaAs, and InP by isotropic or anisotropic wet etchants. Wet etching is the main processing for bulk micro-machining [13–15]. The common isotropic etchant solution for Si is a combination of HF and nitric acid (HNO_3) in water. The overall reaction is given by

$$Si + HNO_3 + 6HF \rightarrow H_2SiF_6 + HNO_2 + H_2 + H_2O \tag{2.3}$$

Mostly, acetic acid is used as a diluent instead of water. Nevertheless, the etch profiles created by isotropic wet etchants are difficult to control and usually cause undercutting of the etch mask (Fig. 2.9). The significant undercutting can limit the use of isotropic etchants in micro-machining.

Anisotropic etchant allows the formation of features defined by the crystallographic planes in the silicon substrate. The most common anisotropic etchant for Si is potassium hydroxide (KOH). The etching is called *anisotropic*, because the etching rate is high in <100> direction and low in <111> direction. Etch ratios for these two directions can be several hundred. In single-crystal Si, the angle between the {100} and the {111} planes is 54.74°. If a mask opening is properly aligned with the primary orientation flat (the [110] direction), only the {111} planes will be introduced as side walls from the beginning of the etching.

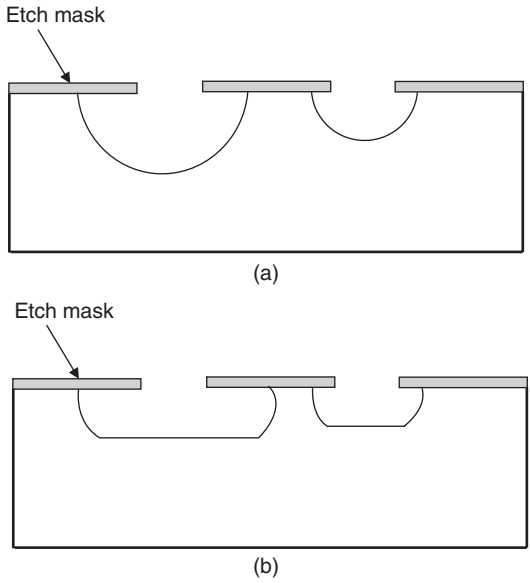

Figure 2.9 Isotropic etch profiles of Si with (a) and without (b) etchant solution agitation. Both etch profiles also show significant undercutting of the etch mask.

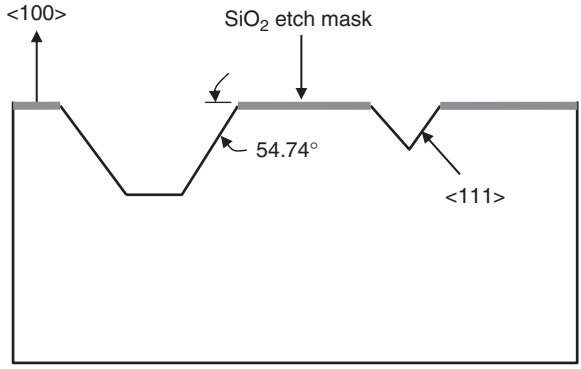

Figure 2.10 Cross section of anisotropically etched features in a (100) Si wafer.

A square mask opening will result in an etch feature in the shape of an inverted pyramid, and the etch depth is determined by the intersection of the {111} planes. If the etch is stopped before the intersection of the {111} planes, then a truncated pyramidal etch cavity is formed (Fig. 2.10). The anisotropic etchants along with the proper mask alignment provide practical solutions in commercial applications. For example, a membrane of a piezoresistive pressure sensor is formed using anisotropic wet etching of Si wafer.

2.8 SUMMARY

Micro-fabrication processes used in both ICs and micro-machines have been discussed. Thin film deposition techniques such as CVD and PVD have been presented. Further, subtractive pattern transfer techniques, and dry etching and wet etching, have been discussed. Finally, lithography, the technique used to transfer patterns onto a substrate surface, has been presented.

REFERENCES

1. Teal GK. IEEE Trans Elect Dev 1976;ED 23:621.
2. Campbell SA. Fabrication engineering at the micro- and nanoscale. New York (NY): Oxford University Press, Inc.; 2008.
3. Deal BE, Grove AS. J Appl Phys 1965;36:3770–3778.
4. Shaw DW. J Cryst Growth 1975;31:130.
5. Wolf S, Tauber RN. Silicon processing for the VLSI era. Sunset Beach (CA): Lattice Press; 2000.
6. Stringfellow GB. Organometallic vapor phase epitaxy: theory and practice. San Diego (CA): Academic Press; 1999.
7. Grove RW. Philos Trans Faraday Soc 1852; 87.

8. Langmuir I. General Electric Rev 1923;26:731.
9. Wehner GK. Adv Electron Phys 1955;VII:253.
10. Stuart RV, Wehner GK. J Appl Phys 1962;33:2345.
11. Wehner GK. Phys Rev 1956;102:690.
12. Hoffman E, Warneke B, Kruglick E, Weigold J, Pister KSJ. Proceedings of IEEE Micro Electro Mechanical Systems (MEMS 1995); Amsterdam, the Netherlands. 1995. pp 288–293.
13. Madou M. Fundamentals of micro-fabrication. Boca Raton (FL): CRC Press; 2002.
14. Kovacs G. Micro-machined transducers sourcebook. Boston (MA): WCB McGraw-Hill; 1998.
15. Kendall DL, Fleddermann CB, Malloy KJ. Volume 17, Semiconductors and semimetals. New York (NY): Academic Press; 1992.

CHAPTER 3

MODELING AND ANALYSIS AT MICRO-SCALES

TAKEHIKO MAKINO and KUNIAKI DOHDA
Department of Engineering Physics, Electronics & Mechanics, Nagoya Institute of Technology, Nagoya, Japan

3.1 INTRODUCTION

Why does micro-scale manufacturing have to be distinguished from macro-scale manufacturing? In this chapter, the answer is presented by showing how phenomena occurring in micro-scale manufacturing have to be treated differently from those in macro-scale. Of course, if scaling down can be completely applied to conventional macro-scale manufacturing and the relative precision of the products is high enough compared to the case of macro-scale manufacturing, the physical world in micro-scale is considered to be totally the same as that in macro-scale. Micro-manufacturing does not simply mean the manufacturing of small-sized materials. It means the manufacturing of materials the micro- or smaller-scale phenomena of which have to be directly considered in modeling and analysis.

Modeling and analysis have two aims, as summarized in Table 3.1. One is numerical prediction of practical processes. It is useful for promoting the efficiency of product design. In this case, phenomenological models usually involve many parameters so that the calculated results match as much as possible with the experimental findings. In this case, the physical meaning of the parameters tends to be unclear. The other aim is to understand the mechanism of the key phenomenon related to a process. For this purpose, the physical origin of the phenomenon has to be well described in the model. The model requires less number of parameters the physical meaning of which is clear. In this chapter, the focus is on the investigation into the latter aim.

The manufacturing process discussed in this chapter is limited to micro-scale, to be more accurate, micro/meso (between macro and micro)-scale metal forming. "Metal forming" is a process in which metals are shaped through deformation

Micro-Manufacturing: Design and Manufacturing of Micro-Products, First Edition.
Edited by Muammer Koç and Tugrul Özel.

TABLE 3.1 Aims of Modeling and Analysis

Aim	Numerical Prediction	Elucidation of Mechanism
Model	Phenomenological model	Physical model
Scale	Macroscopic	Microscopic
Parameters	Fitted to experimental value	With physical meaning

by a harder tools that have opposite shape of the desired part. The forming process involves the flow of material, plastic deformation, along the tool surface without loss of the material's volume. The micro-structure of the material changes after forming. Forging and extrusion are the typical processes of metal forming. In metal forming, as shown in Fig. 3.1, plastic deformation characteristics of polycrystal of metallic element, friction behavior of material/tool interface, and the interrelationship between these two factors have to be considered. Micro/meso-scale metal forming applies conventional macro-scale techniques to sub-millimeter-scale metal forming with modifications. Hereafter, the term micro/meso-scale will be rephrased as micro-scale for simplicity.

In the following sections, how these factors are treated in macro-scale and how these should be expressed in micro-scale are shown.

3.2 LIMITATION OF CONTINUUM MODELS AT MICRO-SCALES

In macro-scale metal forming, the deformation characteristics can be treated by a continuum model. Plastic deformation is described by a criterion of yielding and a constitutive equation (stress–strain relationship). Von Mises' (Huber–Mises)

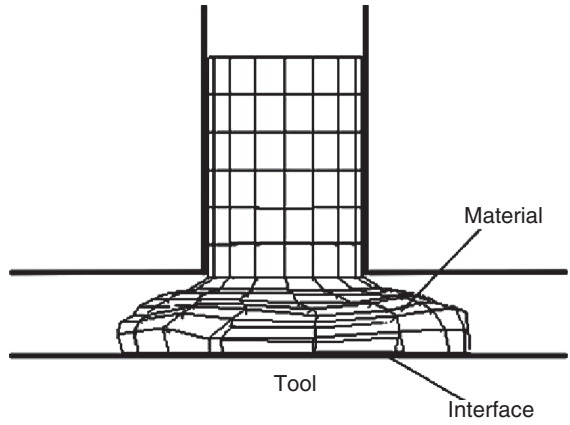

Figure 3.1 Important elements of a typical metal forming process.

criterion of yielding is

$$(\sigma_y - \sigma_z)^2 + (\sigma_z - \sigma_x)^2 + (\sigma_x - \sigma_y)^2 + 6(\tau_{yz}^2 + \tau_{zx}^2 + \tau_{xy}^2) = 6k^2 \qquad (3.1)$$

where σ and τ are stress components, and k is a material-yielding parameter. This criterion physically means that yielding begins when the elastic energy of distortion reaches a critical value. Constitutive equations indicate the relationship between stress and strain as of a macroscopic physical value in materials. Reuss' equation is

$$\mathrm{d}\varepsilon_{ij}^{\mathrm{p}} = \sigma_{ij}' \mathrm{d}\lambda \qquad (3.2)$$

where $\mathrm{d}\varepsilon^{\mathrm{p}}$ and σ' are plastic strain-increment and deviatoric stress, respectively, and $\mathrm{d}\lambda$ is a scalar factor of proportionality obtained by the experimental stress–strain curve. This indicates a relationship between stress and plastic strain-increment.

The models are categorized as phenomenological ones. In that sense, the continuum model of plasticity is usually expressed by the parameters obtained by pilot experiments such as tensile tests.

Both from the physical and the microscopic points of view, plastic deformation is caused by slips of close-packed crystallographic planes of crystals. The slips are caused by the movement of dislocations, which is one type of lattice defects, line defect, formed in crystals. The dislocations move along the close-packed direction (slip direction) on the close-packed plane (slip plane) of the atoms in a crystal. Activation of a slip system (a combination of slip plane and slip direction) occurs when the shear stress acting at the slip system is high enough. If five independent slip systems activate at the same time, deformation of a crystal in a polycrystalline, in which mutual restriction exists, can occur in any direction. Therefore, if there are enough crystals in a material that have well-dispersed orientations, the characteristics of plastic deformation of the outer shape can be considered to be uniform and isotropic.

In micro-scale, materials are not assumed to be uniform, because the crystal grains in small-sized materials are relatively large, compared to the outer size of the material as shown in Fig. 3.2. In this case, the number of crystals is limited and nonuniformity of deformation is pronounced. Whether the stress and strain can be treated as having a macroscopic value, from start to finish, depends on the ratio of the size of the crystals to the outer size of the material. If the ratio is small (close to zero), the material under deformation behaves uniformly, even if the outer size is smaller than 0.1 mm.

Each crystal grain having various crystallographic orientations deforms by slips along the crystallographic planes in it. Therefore, further deformation causes nonuniformity in the stress–strain relationship among individual crystal grains. If a process is planned to manufacture a metal part by using deformation, usually some preforming processes (steps) are applied before the final forming process. Deformation applied to the material previously is accumulated as "texture" in the

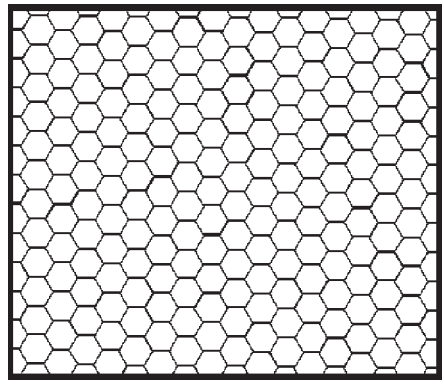

Figure 3.2 Crystal grains and the outer size of materials.

material during consequent processes. If the final process is to be simulated by using a conventional continuum model, experimental results of multiaxial tensile tests are necessary as input parameters after the series of preforming processes before the simulation of the final forming process. For example, anisotropy in plastic deformation is expressed for yield criterion in terms of parameters and stress components, as

$$F(\sigma_y - \sigma_z)^2 + G(\sigma_z - \sigma_x)^2 + H(\sigma_x - \sigma_y)^2 + 2L\tau_{yz}^2 + 2M\tau_{zx}^2 + 2N\tau_{xy}^2 = 1 \tag{3.3}$$

where F, G, H, L, M, and N are anisotropic coefficients, and σ and τ are stress components (if material is isotropic, $L = M = N = 3F = 3G = 3H$) [1]. The relationship between stress and plastic strain-increment also contains anisotropic coefficients. Similarly, if several consequent processes are to be simulated one by one, experimental results in each case need to be gathered and applied to each simulation step as input parameters. These approaches, particularly the latter case, are obviously impractical. The history of deformation applied to the material can hardly be treated in conventional models. However, the history affects the micro-scale forming more strongly than the macro-scale forming, because small-sized materials usually undergo more processes than large-sized materials do (e.g., further rolling passes). Hence, the developed texture during such processing before the final shaping operation strongly affects the final shape, quality, and micro-structure of the small-sized product.

Similar to the case of deformation characteristics, the friction in macro-scale metal forming is usually described by a phenomenological model. The friction can be treated as uniform so as to be expressed using a constant as

$$F = \mu N \tag{3.4}$$

where F is the frictional force, μ is the coefficient of friction, and N is the normal force. This expression comes from the friction law in the case of friction without macroscopic deformation. The experiments needed for determining the coefficient are such as ring compression test for friction with plastic deformation. The friction between the material and the tool affects the sliding and deformation of the material at the interface. The effect of friction on deformation is more significant in micro-scale than in macro-scale because the ratio of the area of the contact surface to the volume of the workpiece is larger.

Microscopically, friction during relative sliding is caused mainly by adhesion of a softer material on the contacting points of the bumped surface of a harder tool. If the material deforms macroscopically during metal forming, the adhesion occurs on a wider area of the surface of the tool. In this case, the adhesion behavior keenly affects the friction. Nonuniformity in friction between the material and the tool is averaged and weakened in macro-scale, if not diminished. However, in micro-scale, the difference in friction appears significant from one part to another because the tool surface manufactured by another mechanical process, such as cutting and polishing, is not uniform microscopically. Additionally, the friction changes as the process progresses. The characteristics are hardly fitted to the parameters that will be expressed in a simple function as usually done in modeling on macro-scales. The nonuniformity of contact surfaces and the consequent variations in friction condition have to be taken into account seriously in micro-scale. However, the problem is how to take into a model accurately and appropriately.

To model the deformation and friction in micro-scale, the physics of the forming should be captured better than in macro-scale. There is no established way of modeling micro-scale metal forming. In Sections 3.3 and 3.4, possible ways of modeling of deformation and friction are discussed, respectively.

3.3 MODIFIED CONTINUUM MODELS

To modify the limitations of continuum models in micro-scale deformation analysis, crystal plasticity is the most important factor to be considered. Attempts to apply crystal plasticity to macroscopic stress–strain relation were started by Taylor [2]. He assumed the following three points:

1. Plastic strain in each crystal is equal in a polycrystalline aggregate.
2. Yield shear stress for each slip system is equal (Taylor's isotropic hardening rule).
3. A combination of slip systems acts so that the total amount of the slips is minimized.

As a result of these assumptions, the total shear strain of a crystal in a polycrystalline is related to the macroscopic plastic strain by using a Taylor factor,

$$\sum_r \left| \mathrm{d}\gamma^{(r)} \right| = M \, \mathrm{d}E_{ij}^{\mathrm{p}} \tag{3.5}$$

where $\mathrm{d}\gamma^{(r)}$ is the shear strain-increment of the rth slip system, M is a Taylor factor, and $\mathrm{d}E^{\mathrm{p}}$ is the macroscopic plastic strain-increment. In contrast to the continuum model seen in Section 3.2, the yielding condition is determined by the critical shear stress for each slip system.

As a combined approach of the Taylor's crystal plasticity model and a finite-element method, the finite-element polycrystal method (FEPM) has been developed [3,4]. Each element in the finite-element method is accounted for each crystal that has a unique crystallographic orientation in a polycrystalline. The FEPM can simulate polycrystal plasticity by introducing a virtual external force, which is treated as a kind of initial strain, acting on each node, expressed as

$$\mathbf{K}\dot{\mathbf{u}} = \mathbf{F} + \mathbf{F}^{\mathrm{p}} \tag{3.6}$$

where $\mathbf{K}$ is a stiffness matrix, $\dot{\mathbf{u}}$ is a matrix of nodal displacement increment, $\mathbf{F}$ is a nodal force matrix, and $\mathbf{F}^{\mathrm{p}}$ is a matrix of the virtual external force caused by plastic strain and plastic spin (rigid rotation of crystallographic orientation). Change in the crystallographic orientation of crystals is determined by a mathematical rotation rule. In the FEPM, the successive integration method is utilized to determine the combination of active slip systems and the amount of the slip (shear strain).

By using the information of crystal plasticity, the FEPM can treat deformation history of a material. The FEPM has been used for analyzing the development of anisotropy in macro-scale materials; however, this method is now applied for analyzing the shape of materials after micro-scale forming. In this approach, the parameter needed is limited to the critical shear stress acting at slip systems. The physical meaning of the parameter is clear. Micro-scale phenomena have been considered to represent crystal plasticity. The phenomena were rationalized to the macroscopic stress and strain by combining the macro- and micro-scale. In the next section, friction is considered as smaller-scale phenomena.

3.4 MOLECULAR DYNAMICS MODELS AND DISADVANTAGES

Modeling and analysis of the material/tool interface for the understanding and estimation of frictional behavior in micro-scale is not straightforward. The behavior of relatively moving heterogeneous surfaces cannot be described as "continuum" any more. Besides, the experimental results available for modeling are very limited because the actual interface consists of the tool and material surfaces plus miscellaneous constituents such as oxides and oil. Even if enough experimental results under strict condition can be obtained, the modeling other than continuum approximation is not fairly under way. As described in Section 3.2, friction that acts at the interface relates to the adhesion process. The adhesion process is

considered to be understandable on the atomic scale rather than on a micro-scale. A possible way of modeling is to go back to the atomic scale.

Molecular dynamics method is a calculation method that chases the movement of "discrete" atoms or molecules by setting interatomic potentials that act on each atom. The potential expresses the interaction between atoms. If the potential can be determined appropriately for the material/tool interface, the dynamics of atomistic interface will be predicted. The movement of the atoms (nuclei) under interactions can be determined by classical mechanics using the Newtonian equation

$$m\frac{\mathrm{d}^2 r_i}{\mathrm{d}t^2} = F = \frac{\mathrm{d}\phi}{\mathrm{d}r_i} \tag{3.7}$$

where m is the mass of an atom, r_i is the position coordinate of atom i, t is time, F is the force acting on atom i, and ϕ is the interatomic potential. The interactions between atoms are determined by the electrons around nuclei. The states of electrons are determined by quantum mechanics using Schrödinger equation

$$\hat{H}\psi = E\psi \tag{3.8}$$

where $\hat{H}$ is a Hamiltonian that contains the operations associated with kinetic and potential energies, ψ is a wave function that express electronic density, and E is the energy of a system.

To determine the state of electrons, electronic-state calculations have been developed. The electronic-state calculation is carried out by solving Schrödinger equation by setting potentials that act on each electron. If the potentials are decided only by the atomic numbers, the calculations are from first principles (*ab initio*). In practical calculations, the potentials used are not usually true first-principle potentials but "pseudo potentials" that concern only valence electrons and contain some adjusting parameters. However, the practical calculations using a set of pseudo potentials can predict a fairly wide range of physical properties.

To construct the atomic potentials from the electronic-state calculations, at first, the electronic states were calculated for the arrangement of atoms that simulates an interface, for example, a surface and adhesive atoms, with changing the distance between the surface and the atoms. Then, the changes in energies calculated in the electronic-state calculations are fitted to atomic-potential functions. In this case, the arrangement of atoms and the potential functions selected decides the degree of approximation of the proposed model. The results are easily visualized and analyzed because the change of coordinates of each atom with time step progressed is recorded.

Modeling using minimal amount of experimental results is important in the present approach. Advantage of this method is that the parameters to be input are only atomic numbers. Any combination of tool/material can be considered. This means that the searching the tool material for lowering the friction is possible.

There are no essential disadvantages in this approach. There are obvious problems that come from treating on the atomic scale. The problems of the present approach are limited number of atoms and short time scale. Although in the case of plastic deformation, the microscopic strain is related to the macroscopic strain by simple summation, until now the atomistic behavior at the frictional interface has not been found to be directly related to the macroscopic view of friction. This is a kind of "missing link" between scales.

In the following section, the atomistic behavior related to adhesion is viewed and the proposal of how the atomistic behavior and micro-scale deformation behavior are combined is presented.

3.5 EXAMPLES OF MICRO-SCALE MODELING APPROACHES AND CROSS-COMPARISONS

(i) FEPM for anisotropy of plasticity under uniform friction, (ii) molecular dynamics using interatomic potential derived by the first-principle electronic-state calculation for frictional interface, and (iii) finite-element crystal plasticity combined with molecular dynamics for anisotropy of plasticity under nonuniform friction are presented as examples of micro-scale modeling approaches, with a comparison between modeling and experimental results.

3.5.1 Finite-Element Polycrystal Method for Anisotropy of Plasticity under Uniform Friction

In micro-scale metal forming, deformation characteristics of crystallites as opposed to that of a macro-scale continuum object appear [5]. There is a risk of undesirable distortion of the shape formed and worse tolerance because of the strong anisotropy of the deformation of crystallites. It is, however, common that the small-sized materials go through heavy deformation processes, for example, drawing, as a result of being so small just prior to a final forming. The crystal grain size and its orientation as a result of the thermomechanical history of the material are factors crucial to prediction of the deformational characteristics and the shape of the small parts. Therefore, an analysis method that can treat the grain size, the crystal orientation, and its changes is required to follow the history and predict the resultant deformational behavior. If the macro-scale procedure is not applicable at micro-scale without modification, necessary modifications will be proposed for the application. The purpose of this section is to clarify the effect of a number of crystals in a material and the effect of predeformation on deformation. The key results are confirmed by experiments.

3.5.1.1 Methods. Here, a ring shape is employed because any variation in the shape can be distinguished easily because of its large free surface. Moreover, ring compression test is a well-known method for estimating the friction coefficient

TABLE 3.2 Parameters of Materials

Crystal structure	Face-centered cubic
Crystallographic orientation	Random, textured
Number of elements	288, 384, 600, 900, and 1728
Young's modulus, Poisson's ratio	110 GPa, 0.34
Work hardening rule	$\sigma = 320\,\varepsilon^{0.14}$
Friction	Zero
Amount of compression	50%

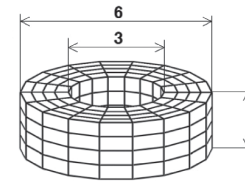

between a tool and the material. By using the information of crystal plasticity, the FEPM can treat the mechanical history of the material. The FEPM software developed by Takahashi [4] was used in the present study.

The material parameters for copper are listed in Table 3.2. The work hardening rule obtained by a tensile test is directly related to the yield shear stress of single crystal. The profile ratio of the ring is 6:3:2 (outer diameter:inner diameter:height). The free surface of this ring is 57% of the entire surface. The numbers of elements that are equal to the numbers of grains are 288, 384, 600, 900, and 1728. These numbers are also related to the grain sizes of the rings when the sizes of the ring are the same. In the case where the ring's outer diameter is 0.6 mm, if the grain size assumes to be uniform, the estimated sizes correspond accordingly to 52, 48, 41, 36, and 29 μm, respectively. The rings were compressed by 50% using parallel flat tools having a rigid body. In this section, the substance is focused on deformation behaviors in micro-scale. Therefore, the friction between the material and the tool is assumed to be zero. To examine the effect of predeformation on the shape after the final compression, ring-shaped materials were deformed by various degrees of both tensile and compression strain prior to the final deformation. After the predeformation, only the information of the crystal orientation was applied to the original-sized (6:3:2) ring for the final compression. A simple example for checking the crystal plasticity is shown by compressed shape with changing the number of crystals in the same initial outer shape.

3.5.1.2 Results. As the first step of the application of the FEPM for the analysis of compressed shape, the orientations of the crystals prior to the compression are set to be random. Figure 3.3 shows the (111) pole figures of randomly oriented crystals in the rings prior to the compression and the shape of the rings after the compression. The numbers in the figure indicate the number of the elements. The ring shape becomes more isotropic as the number of elements increases. However, a roughness is found at both outer and inner circumferences.

To examine the possibility of controlling the shape, the crystallographic texture is introduced by predeformation. Figure 3.4 shows the (111) pole figures of

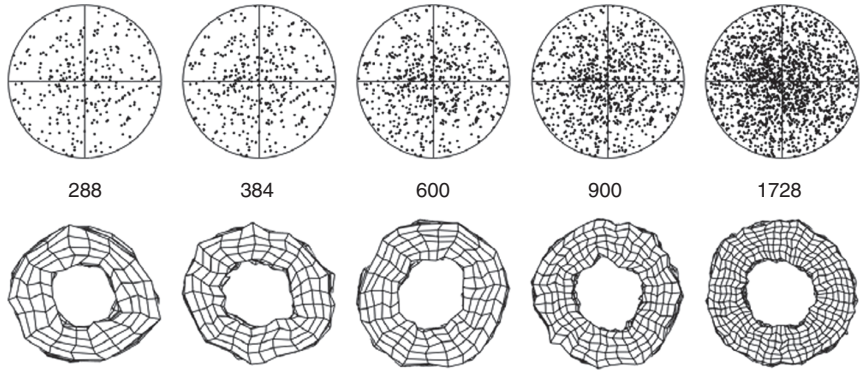

Figure 3.3 The (111) pole figures of randomly oriented crystals and the final shape of the rings.

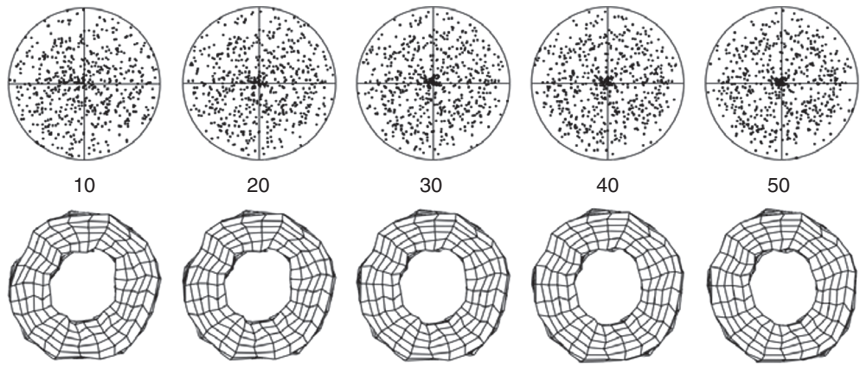

Figure 3.4 The (111) pole figures of pre-tensioned samples and the final shape of the rings.

pre-tensioned rings prior to the compression and the shape of the rings after the compression. The number of the elements in the ring is 600. The numbers in the figure indicate the percentage of the nominal strain as a result of the pre-tension. The (111) plane directions concentrate on the tensile axis gradually as the pre-tensile strain increases. The final shape of the pre-tensioned ring becomes smooth as the pre-tensile strain increases.

Figure 3.5 shows the (111) pole figures of precompressed rings prior to the compression and the shape of the rings after the compression. The initial orientation of the ring is the same as that of the ring used in the pre-tensioned ring. Almost half of the (111) plane directions concentrate around the compression axis gradually as the compression strain increases. The final shape of the pre-compressed ring becomes more distorted as the precompression strain increases.

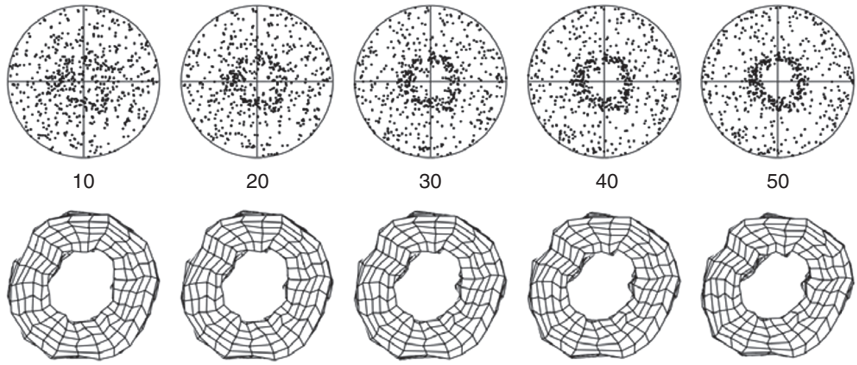

Figure 3.5 The (111) pole figures of precompressed samples and the final shape of the rings.

3.5.1.3 Comparison with Experimental Results. As a typical face-centered cubic metal, copper was chosen because its deformation characteristics are simple compared to brass-type materials that tend to form more twins under compression. The profile of the ring was 0.6 mm:0.3 mm:0.2 mm (outer diameter:inner diameter:height). The ring shape was fabricated by drawing the tube and cutting it. Both end planes were polished so that the surface roughness would be 0.05 μm. Some of the rings were annealed at 873 K for 2 h to make the grains larger and to weaken the strong texture produced by drawing. The other rings were used in their as-drawn state. The micro-structures of the rings are observed by means of optical microscopy before compression. One of the end planes was polished using water-resistant paper and diamond paste and then etched using iron chloride. The rings were compressed by 50% using parallel flat tools having a surface roughness of 0.1 μm. To obtain the plastic deformation characteristics unrelated to the friction, the friction occurring between the material and the tool was set to be as small as possible by using both PTFE (Polytetrafluoroethylene) sheets about 25 μm thick and lubricant oil with a kinetic viscosity of 430 mm^2/s. Figure 3.6 shows the optical micro-graphs of the rings before and after the 50% compression. The micro-structure of the annealed ring shows that the size of equiaxed grains is distributed from 20 to 60 μm (Fig. 3.6b). The grains in the as-drawn ring are heavily deformed and the grain diameter that is observed at the end surface is about 8 μm (Fig. 3.6e). The shape of the annealed sample after compression is coarse (Fig. 3.6c), compared to the as-drawn sample (Fig. 3.6f). The dark contrast seen in (c) and (f) comes from the adhesion of the PTFE sheet. Even after the compression, the as-drawn sample is highly isotropic.

It is found that the pre-tension is the most effective to reduce anisotropy. To compare the effect of the predeformation on the relation between the number of elements and anisotropy, the materials that have various numbers of randomly oriented grains are pre-tensioned by 50% and compressed. Figure 3.7 shows the (111) pole figures of pre-tensioned rings prior to the compression and the shape of the rings after the compression. Compared to the results shown in Fig. 3.3, the

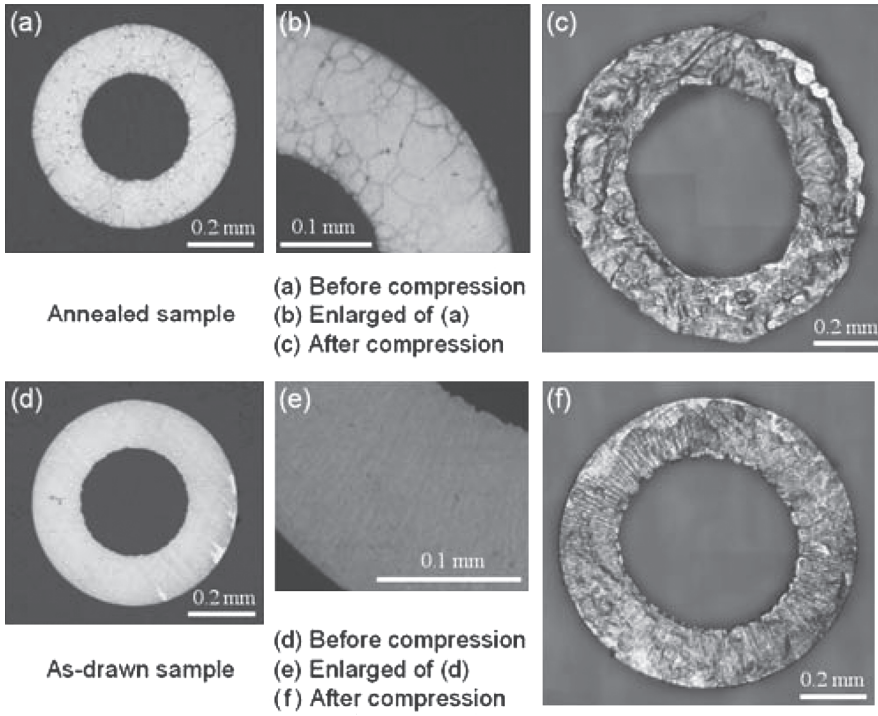

Figure 3.6 The optical micro-graphs of the annealed and as-drawn rings before and after the compression.

final shapes are smoother. This result suggests that the suitable predeformation could potentially improve the accuracy of the shape of the deformed material.

The small number of crystallites in the material enhances anisotropy in micro-scale deformation. Crystallographic texture can also enhance and, contrarily, diminish the anisotropy. Precompression can enhance the anisotropy of compressed rings. Pre-tension can diminish the anisotropy. Therefore, the appropriate thermomechanical history facilitates control of micro-scale metal forming.

The micro-structure of the annealed ring (Fig. 3.6b) shows that the size of equiaxed grains is distributed from 20 to 60 μm. In the FEPM analysis in the present study, the volumes of the elements were set to be almost equal. Therefore, to plot the experimental result in the figure of the predicted one, it is necessary to count the number of grains. The number of the grains at the end surface can be estimated to be about 160 (about 40 in one fourth of the surface). The numbers of elements at the end surface of the rings, in which the total numbers of elements are 600 and 900, are 120 and 180, respectively.

High isotropy of the as-drawn ring after the compression (Fig. 3.6f) comes from a large number of grains and the strong texture. Taking into account that the small-sized materials usually go through heavy deformation processes prior

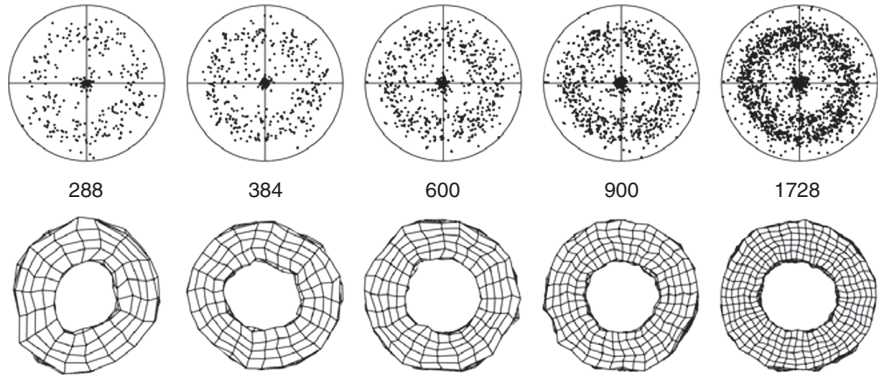

Figure 3.7 The (111) pole figures of 50% pre-tensioned samples and the final shape of the rings.

to a final forming, the micro-scale phenomena hardly occur in general processes. However, it is noted that the present results show the importance of the crystallographic texture as a result of the mechanical history in micro-scale forming.

For macro-scale forming, anisotropy of the material has been treated by using anisotropy parameters estimated by the experiments after each step of the forming process. For the history-sensitive micro-scale forming, application of FEPM enables the prediction of the deformation without using experimental measurements. This is one specific advantage of the FEPM. It is possible to enhance the accuracy of prediction by using EBSP (electron back scattering pattern) data for the initial crystal orientation. However, the virtue of the present analysis is the use of less number of parameters. It will be required to obtain more information even if it is qualitative. This method is to be used for the analysis of micro-scale deformation of materials that have strong anisotropy such as hexagonal close-packed systems. Additionally, analyses of processes that are sensitive to mechanical history, for example, micro-scale multistage forming, will be promising.

3.5.1.4 Summary. The micro-scale deformation characteristics were investigated by means of simple ring compression and an analysis method that concerns polycrystal plasticity. The conclusions are as follows:

1. The FEPM analysis illustrates that the shape distorts in the case of the small metal part containing a small number of crystallites that are randomly orientated. The annealed ring was distorted in shape after compression.
2. The texture produced by tension is an effective means to control the shape formed by compression. Conversely, the texture produced by compression is not well suited for controlling the shape. The compressed as-drawn ring showed very high isotropy. Appropriate thermomechanical history facilitates the control of micro-scale metal forming.

3.5.2 Molecular Dynamics Using Interatomic Potential Derived by the First-Principle Electronic-State Calculation for Frictional Interface

Using the atomistic model described in the previous section, adhesion behavior occurring at frictional interface was investigated [6]. Figure 3.8 shows the atomic model simulating ironing process by letting the rigid tool move parallel to the material surface. The crystallographic plane of the rigid tool surface is (100). In this model, periodic boundary condition is applied to the width direction and semi-infinite flat plate is implemented. To apply the periodic condition to both the material and the tool that have different lattice constants, the least common multiple of the constants have to be considered. Difference between the modeled and actual lattice constants is less than 1%. As constituent materials in the model, TiC, TiN, and VC for rigid tool (hard coatings of tool surface), and Al and Cu for deforming material are chosen. The interatomic potentials that can express interface between heterogeneous materials are obtained by the following procedures. Using a first-principle electronic-state calculation software, ABINIT [7], the total energy of the arrangement of atoms shown in Fig. 3.9. The atoms in the calculating cell are aligned as surface and adhering atoms. The electronic calculation is executed for the infinitely aligned cells and the change in total energy with varying distance between the adhering atoms (constituent of deforming material) and the surface. To extract the interatomic potential from calculated total energy, it is assumed that the total energy difference consists of nine nearest neighbors for each material's atom as shown in Fig. 3.10, the interatomic potential that act between a pair of atoms (two-body potential), and the potential function can be approximated as a Morse-type function, that is,

$$\phi(r) = D_1 e^{-\lambda_1(r-r_0)} - D_2 e^{-\lambda_2(r-r_0)} \tag{3.9}$$

where D_1, D_2, λ_1, and λ_2 are parameters, r is interatomic distance, and r_0 is its cutoff distance. By fitting these parameters in the function so as to simultaneously satisfy the energy difference with replacing centered atom, as shown in Fig. 3.10,

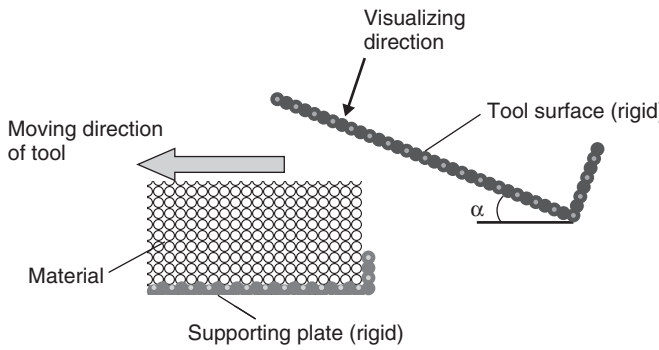

Figure 3.8 Atomic model simulating ironing process.

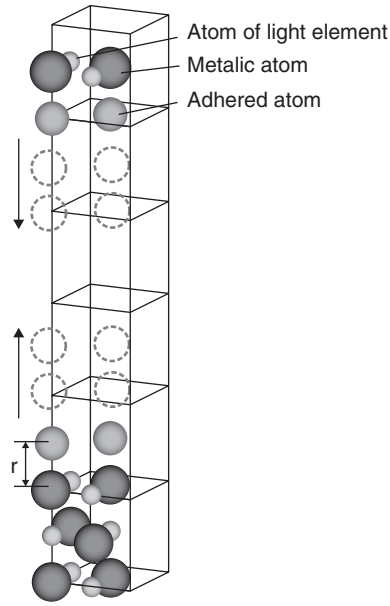

Figure 3.9 Configuration of atoms constituting tool and material for first-principle calculation.

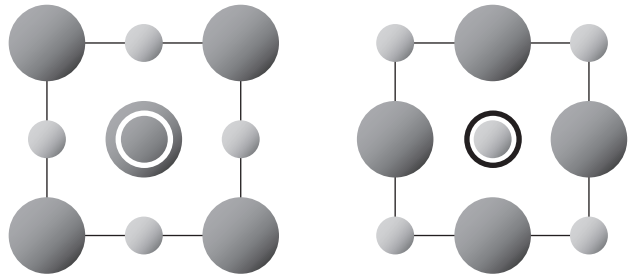

Figure 3.10 Configuration of atoms: (a) an adhered atom is on a metallic atom and (b) an adhered atom is on a light-element atom.

the potential curve is obtained as in Fig. 3.11. Figure 3.12 shows the extracted interatomic potentials for heterogeneous pairs. Applying the potentials to the ironing-process model, the movement of atoms at material–tool interface can be chased.

Calculated results are visualized to be able to observe adhered atoms through the rigid die from the direction perpendicular to the die. Material constituent

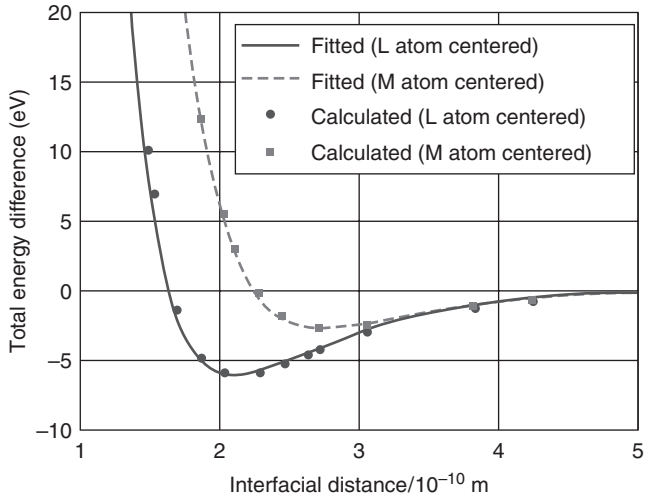

Figure 3.11 Change in total energy with interfacial distance. L: light-element. M: metallic.

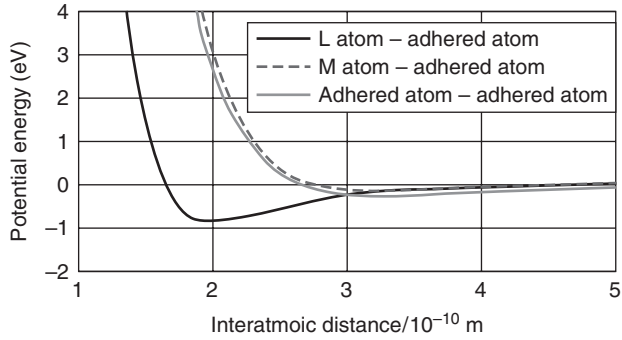

Figure 3.12 Change in potential energy with atomic distance.

atoms are determined as adhered atoms when the atoms lie just below the die and move at the same speed with the die for a certain period of time.

Figure 3.13 shows a snapshot of an ironing process at a certain moment. Figure 3.14 shows adhered Al atoms at various die surfaces (TiC, TiN, and VC) at the same time since the ironing started. In each surface, adhered atoms are found on the whole contacting area and are arranged regularly. In this figure, gray atoms are on the first layer and black atoms are on the second layer. In order to check regularity, radial distributions of the atoms on the first layer for various die are shown in Fig. 3.15. The regularity is ascertained by the existence of peaks in the radial distribution, although the number of atoms is limited. There is a relation between the arrangement of the first layer and the pattern of growth

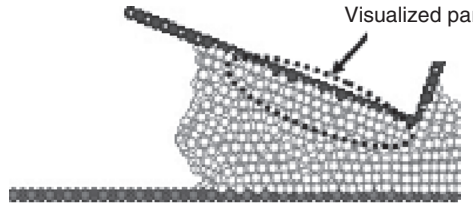

Figure 3.13 Snapshot of ironing process.

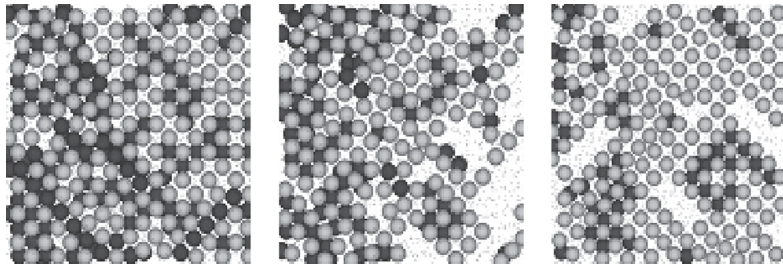

Figure 3.14 Arrangement of adhered atoms viewed through die.

of adhesion of the second layer. For example, in a TiC/Al system in which the number of second-layer atoms is largest, the arrangement of the first-layer atoms is very close to the array of crystal lattice of die surface. It is implied that the arrangement of the first layer that is close to an fcc structure of Al triggers the growth of the second or of more layers. On the other hand, in radial distribution of other systems, TiN/Al and VC/Al, the number of second-nearest-neighbor atoms is smaller than that of first-nearest-neighbor atoms. This implies that the arrangement is different from the array of crystal lattice of die surface. Compared to TiC/Al system, in these two systems, the arrangement of the first layer that is different from the fcc structure of Al causes no further growth of adhesion.

Figure 3.16 shows adhered Cu atoms on various die surfaces (TiC, TiN, and VC). The tendency of the adhesion on the first layer is different between the three systems. In VC/Cu system, adhered atoms are found at whole contacting area and are arranged regularly. In TiC/Cu system, the adhesion of the first layer is not stable according to dynamical observation. In TiN/Cu system, no stable adhesion is observed. It is expected that Cu atoms do not form stable arrangement on these die surface. Figure 3.17 shows a radial distribution of Cu atoms on the first layer for VC surface. Although the periodicity of the arrangement is recognized, the arrangement of the first-layer atoms is not related to the array of crystal lattice of the die surface. And it is hardly observed in the second-layer atoms. Because of the difference in the fcc structure of Cu in the first-layer arrangement, no further growth of adhesion is allowed.

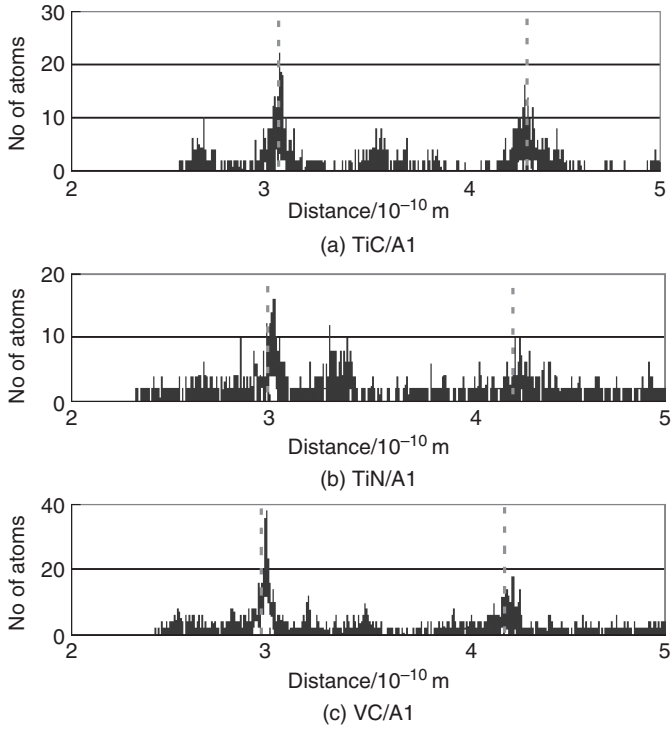

Figure 3.15 Radial distribution of first-layer atoms on various die surface.

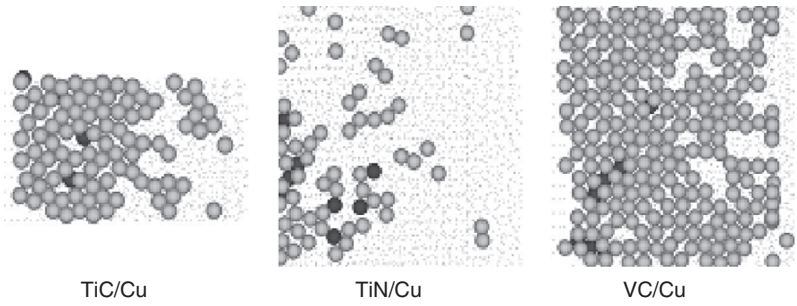

Figure 3.16 Arrangement of adhered atoms viewed through die.

These calculated results are usually difficult to compare with experimental results. However, the following route has possibilities; the surface conditions of the die during or after friction can be measured by Kelvin probe. Kelvin probe measures a difference in contact potential. The value is the difference in work function between surfaces of probe material and subject material. The work function, a minimum energy of removing an electron from a material's

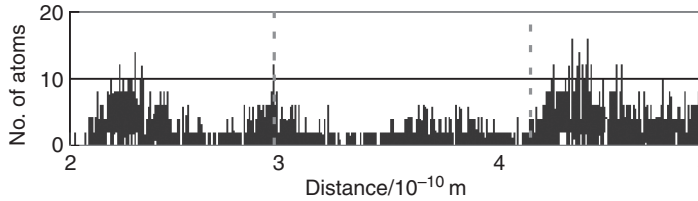

Figure 3.17 Radial distribution of first-layer atoms on various die surface.

surface, is very sensitive to surface conditions. The work function of surfaces with adhered atoms can be predicted by the first-principle calculation. Therefore, the combination of molecular dynamics calculation and first-principle calculation is useful for comparing calculated and experimental results.

3.5.2.1 Summary. In this section, using the first-principle calculation and molecular dynamics calculation, the atomic movement of material at material–tool interface is tracked and the following are found:

1. Adhesion behaviors are found in various tool/material systems.
2. Adhered atoms on the first layer are regularly aligned. The arrangement is affected by the array of crystal lattice of the die surface.
3. Growth of adhesion after the second layer is affected by the arrangement of atoms on the first layer. When the arrangement of first layer is different from the array of crystal lattice of the die surface, the growth of adhesion is suppressed.

3.5.3 Finite-Element Crystal Plasticity Combined with Molecular Dynamics (Injection Upsetting)

In Section 3.5.1, how anisotropy of plastic deformation occurs in simple ring compression was discussed. In this section, applicability of FEPM to more complex deformation, for example, the history of deformation with no axial asymmetry, is described. Then, a model in which the coefficient of friction that is derived by atomistic modeling presented in Section 3.5.2 is applied to the interface is proposed [8,9].

As mentioned in Section 3.5.1, in micro-scale forming, materials are usually formed by many steps before a final forming process. Although the state of the material before forming very much affects the shape after forming, the state is difficult to be identified. In order to identify the state before the final forming, the effect of deformation history has to be predicted. An equal-channel angular pressing (ECAP), which is one of the typical severe-plastic-deformation processes, can be utilized to make a history of deformation. The ECAP is a process in which specimens with a circular or rectangle cross section are extruded through

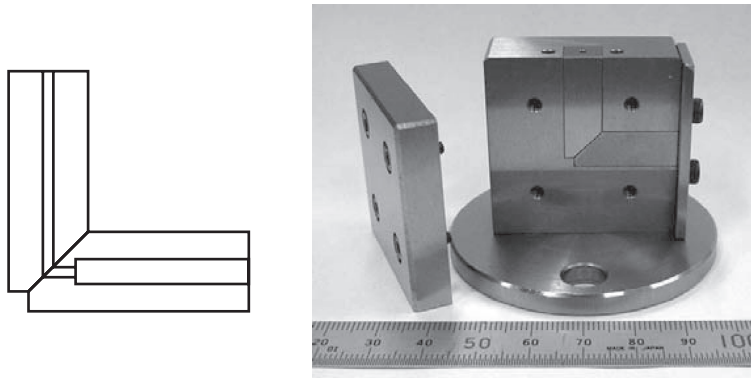

Figure 3.18 ECAP apparatus (a) schematic of dies and (b) appearance of apparatus.

a bent channel and given a strong shear deformation at the corner. The advantage of ECAP is that the deformation mode is not of axial symmetry. Another advantage of ECAP is that the cross section of the specimens does not change. From these features, the degree of deformation can be controlled by using only one set of dies and the process can be repeated several times with or without changing the direction of deformation. Figure 3.18 shows the micro-scale ECAP apparatus. The important part of this apparatus is the connection of the two channels at a specific angle. At the present stage, the diameter of the channels was 1.50 mm. The angle between the channels was set to be 90° by attaching two cutoff edged blocks (dies) having small channels with high accuracy. To eject the specimen, the following new specimen was fed to press the previous one to complete the deformation of its entire length. Multipass (4-pass) routes in ECAP are route A—repeat same orientation, Ba—repeat $+90^\circ$ and -90° of angular rotations alternately (+: counterclockwise), route Bc—repeat $+90^\circ$ of angular rotations, and route C—repeat 180° of angular rotations, as shown in Fig. 3.19. In experiments, forward extrusion, a typical forging process for parts with axial symmetry, was done as a subsequent forming process. Forward extrusion is the process in which cylindrical specimens are pushed into a stepped (wide to narrow) die.

3.5.3.1 Apparatus for Evaluating Anisotropy. For evaluating the anisotropy of the final deformation, the use of an injection-upsetting test was proposed. Injection upsetting is a process in which cylindrical specimens are upset by being pushed through the channel in the upper die against the lower die and injected to a gap between these dies. The typical shape after the process is like the head of a nail. In the test apparatus, a flange-shaped upper die that has an inlet channel is attached to a disk-shaped lower die with a clearance. The cylindrical specimen in the channel is pressed against the disk-shaped die and the injection-upsetting deformation can occur without buckling, even with the

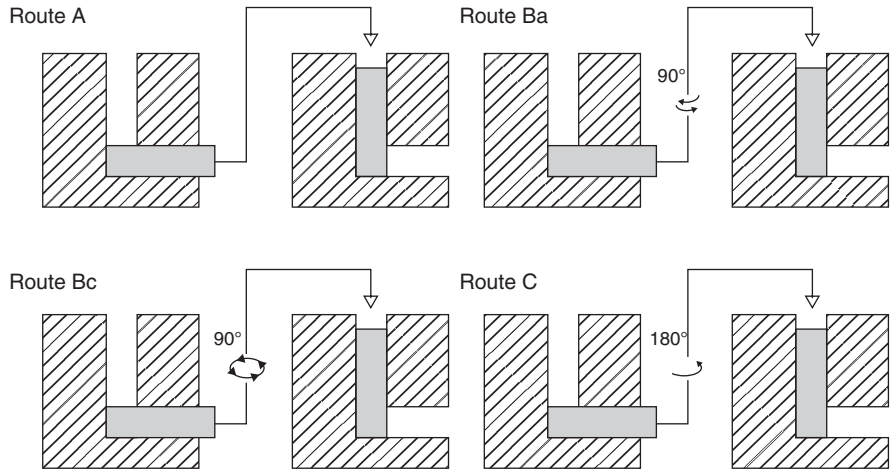

Figure 3.19 Multipass routes in ECAP process.

thinness. From the shape of the end face of the injection-upset specimens, the anisotropy is evaluated by the deviation from a circular form because the end face can deform radially without restraint of tool. For this test, it is not necessary to change the shape of the specimens formed by prior deformation. Only the end faces of the specimens have to be polished to ensure perpendicularity between the faces and specimen axis after prior deformation. The apparatus attached to a die set with a punch and shape of model for the injection-upsetting process are shown in Fig. 3.20.

3.5.3.2 Experimental Conditions. The dimensions of the channel in each apparatus are summarized in Table 3.3. The experiments were carried out by a Shimadzu AG-IS 50 kN. The pressing speed was 1.0 mm/min. As-received (as-drawn) pure aluminum with a 1.5-mm diameter was used as a starting material.

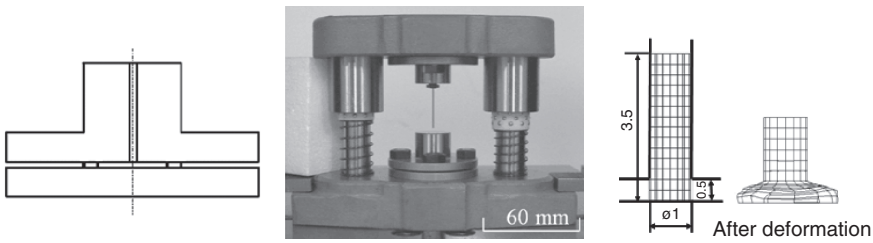

Figure 3.20 Injection-upsetting test apparatus for evaluating anisotropy of pins: (a) schematic of dies, (b) appearance of apparatus including die set, and (c) shape of the model for the injection-upsetting process.

TABLE 3.3 Dimension of Channels in Three Apparatuses

Apparatus	Diameter (mm)	Length (mm)
ECAP	1.50/1.50	20/2
Extrusion	1.50/1.00	15/1
Injection-upsetting test	1.00	0.50 (clearance)

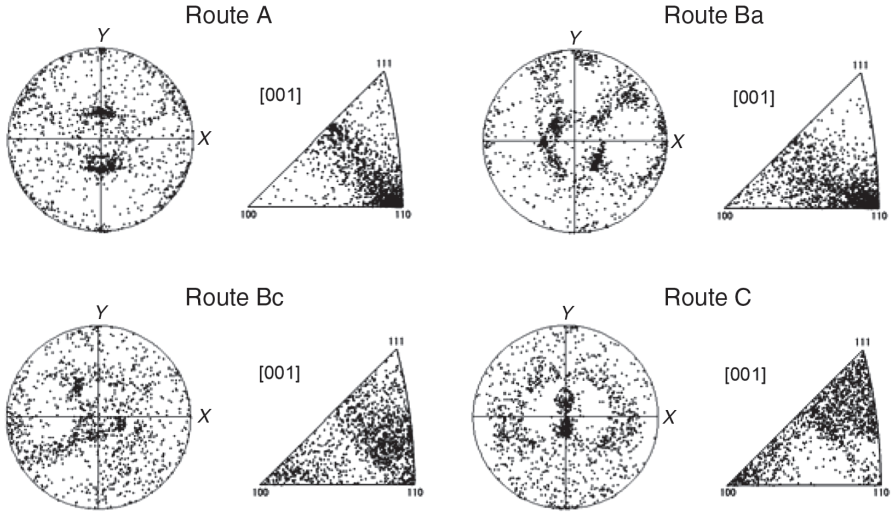

Figure 3.21 Crystal orientations in entire specimen after ECAP processes of various routes.

In all processes, a lubricant oil of high kinematic viscosity (430 mm^2/s at 313 K) was used to lower the friction.

Figure 3.21 shows the results of crystal orientations in the entire specimen after ECAP processes of various routes. As a result of route A, zonal distribution from [211] to [111] was distinguished. In route A and Ba, a strong texture at [111] was observed. In route Bc and C, different distributions were observed. However, a strong concentration at one orientation was not observed. Figure 3.22 shows the calculated and experimental results of the shape of the end face after ECAP processes of various routes. In experiments, the strong tendency in calculation was not observed; however, the same tendency is seen in strong anisotropy in route A and Ba. Especially in route Ba, the angle of inclination of anisotropy in calculation corresponds to the experimental result. In route Bc and C, weak anisotropy is observed in both calculated and experimental results. It is confirmed that the FEPM calculation is applicable to prediction of the effect of complex history on the final deformation.

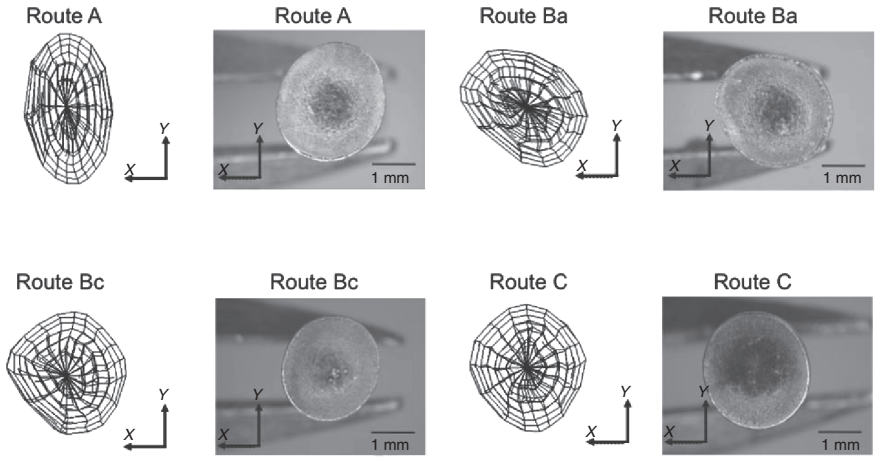

Figure 3.22 Calculated and experimental results of shape of end face after ECAP processes of various routes.

3.5.3.3 Modeling of Friction. In macro-scale modeling, the condition of contact between the tool and the material is assumed as uniform. On the other hand, in micro-scale real world, the condition is nonuniform. Since the ratio of surface to volume of material is large, the effect of contact conditions on deformation is not negligible. Therefore, a new analysis method that can treat the nonuniformity is needed.

As already shown in the previous sections, materials in micro-scale forming have to be treated as polycrystalline. The distribution and the change in crystal orientation of the material at the interface are likely to have an influence on the interfacial friction. As a proposal of calculating method, condition of contact between tool and material derived in atomic scale modeling is related to information about crystal orientation. Although it is difficult that the adhesion behavior in atomic scale is directly related to micro-scale friction behavior, crystal orientation can be a setting condition in atomistic calculation, and the difference in friction from the crystal orientation will appear.

In the rest of this section, the method that connects the atomistic model for friction and the micro-scale model for deformation by means of crystal orientation is proposed, and the effect of nonuniform contacting condition on deformation will be discussed. The friction coefficients are evaluated in atomistic calculation by changing the crystal orientation of material, using the interatomic potentials derived in Section 3.5.2, and a numerical table of friction coefficients is produced in advance. In crystal plasticity calculation for an injection-upsetting process, the movement of interface, at which each crystal has a different crystal orientation, is calculated under the condition of the precalculated friction coefficients.

3.5.3.4 Friction Coefficient Calculation. In Section 3.5.2, a method dealing with the adhesion behavior in atomic scale is presented. In this section, the forces

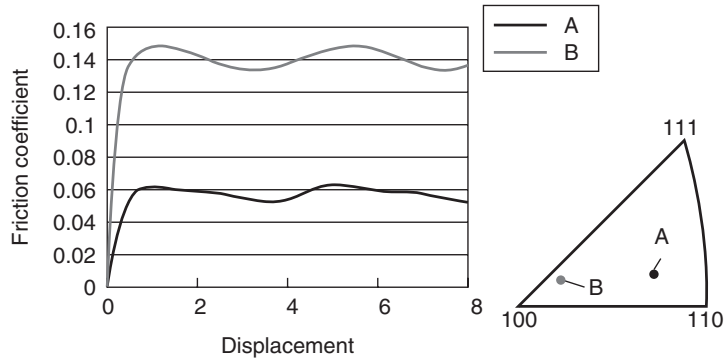

Figure 3.23 Example of a coefficient of friction for a crystal orientation of material.

acting at the interface are evaluated by using interatomic potentials derived in Section 3.5.2 related to coefficients of friction. The friction coefficients are calculated from the normal and the lateral (frictional) forces acting between the atoms in a rigid material (Al) and between the atoms in a rigid tool (TiC) by letting the material slide on the tool. Because the atoms in the material and the tool are not allowed to move, the calculation is static. Plastic deformation and adhesion of material are important factors to be considered in estimating the friction during forming. However, these two factors are essentially too dynamic to be introduced to the pre-estimation of the friction coefficient, at the present stage of investigation. The friction coefficients are obtained by changing the crystal orientation of the material. The calculated coefficient is fluctuated periodically because of a periodicity of the crystals as shown in Fig. 3.23. A coefficient for a crystal orientation is obtained by averaging over the fluctuating part. The precalculated coefficients of friction are utilized for the friction of crystal contacting at the interface at each step of deformation calculation. The number of segmentations of the crystal orientation is limited to 123.

3.5.3.5 Condition of Calculation. As a model to be calculated, injection-upsetting process in which the cylinder with diameter of 1 and length of 3.5 is injected to a space with clearance of 0.5 by upsetting up to 1.3. This process is suitable to examine the effect of friction on deformation because the friction at the contacting plane greatly affects the deformation. The initial crystal orientations, shown in Fig. 3.24, are produced by the tension of a specimen with random orientations, on the assumption that the specimen is in the as-drawn state. The material used is pure aluminum the properties of which are Young's modulus—70 GPa, Poisson ratio—0.3, and hardening rule $\sigma = 160\varepsilon^{0.25}$. Number of elements is 1568 (radial directional $\times$ circumferential $\times$ height wise $= 7 \times 16 \times 14$).

3.5.3.6 Results and Discussion. Shape of end face of an injection-upset specimen with applying friction coefficients depending on crystal orientations

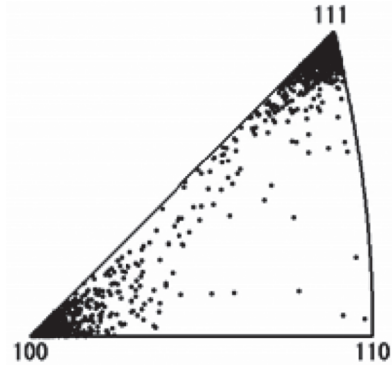

Figure 3.24 Initial orientations of crystals in the material for the injection-upsetting process.

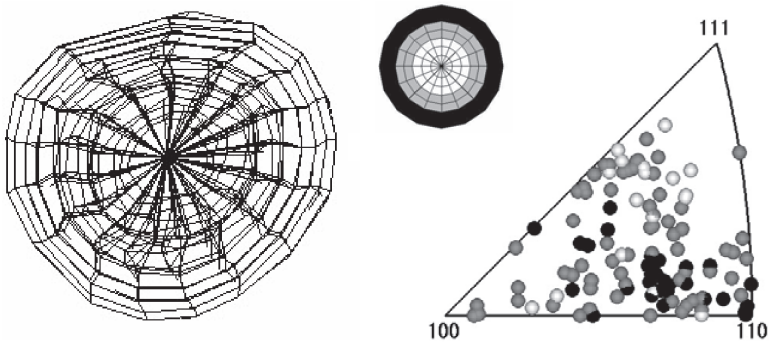

Figure 3.25 (a) Shape of end face after the injection-upsetting process and (b) the resultant orientations of crystals at end face when friction coefficients depending on crystal orientations are applied.

are shown with orientations of the crystals located at the end face in Fig. 3.25. The orientations of the crystals are coded by gray level depending on the position from the center of the end face. Figure 3.26 shows the shape and orientations of a specimen with a uniform friction coefficient, for comparison. In both cases, after injection upsetting, the orientations tend to incline from plane [211] to plane [111]. Although the central part of the end face keeps in a concentric fashion in both cases, the shape of outer circumference in Fig. 3.25 is more anisotropic than that in Fig. 3.26. It was observed that the crystal orientations change with displacement of upsetting and the amount of change in a crystal depends on the position of the crystal at end face. In order to examine the effect of orientation change on friction coefficient, the change in averaged friction coefficient for the entire area, outer circumference, and central area of the end face is plotted

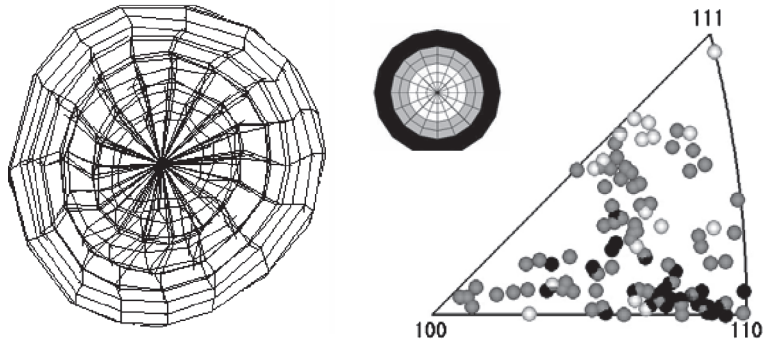

Figure 3.26 (a) Shape of end face after the injection-upsetting process and (b) the resultant orientations of crystals at end face when uniform friction coefficient is applied.

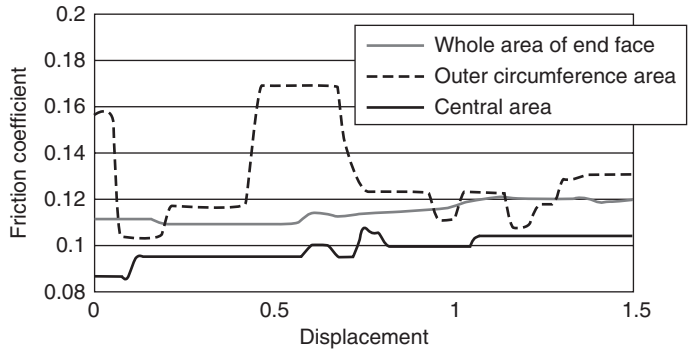

Figure 3.27 Change in averaged friction coefficient with displacement of upsetting.

against the displacement of upsetting in Fig. 3.27. Even considering that the change in averaged friction coefficient is not continuous because of the limited number of segmentations of orientation, it is confirmed that the averaged friction coefficient for the entire area increases slightly and especially at the beginning of upsetting, difference in the coefficients between the areas is large. As a result of the difference, it is considered that the lack in uniformity of friction coefficient causes the anisotropic shape of the end face in Fig. 3.25.

3.5.3.7 Summary. A method that connects the atomistic model for friction and the micro-scale model for deformation by means of crystal orientation was proposed, and the effect of nonuniform contacting conditions on deformation was discussed. It was confirmed that the change in friction coefficient that depends on the change in crystal orientation affects the deformation behavior. At the present

stage, the method deriving friction coefficient from atomistic calculation needs to be improved in the future.

3.6 SUMMARY, CONCLUSIONS AND REMAINING RESEARCH ISSUES

In this chapter, modeling and analysis needed in micro-scale metal forming was discussed from the point of view of a mechanism-elucidation-oriented approach. By the approach shown above, the following points can be investigated:

1. effect of crystal plasticity on deformation;
2. effect of deformation history on deformation;
3. search of good combination of tool/material and surface modification;
4. relationship between material and its crystal state, and friction.

The knowledge obtained in modeling study can be applied to structure design of micro-scale machines constructed by the parts made by micro-scale metal forming. The control of inner structure such as orientation of crystals in parts becomes more important in micro-scale design. In the field of nanotechnology, calculation experiments have been already accepted. Molecular structures are predicted by calculations and the function is discussed before experimental confirmation. Selection of materials and its combination will become significant in future; therefore the development of the model using less experimental results is required.

Remaining issues are related to interfacial phenomena. Modeling of friction still has a long way to go. Combining deformation and friction is also a difficult task. In the present case, the difference in crystal orientation was chosen to be a variable that determines the frictional coefficient. This is nothing but a choice. The adhesion phenomena are important for surface modification in surface science and also for reducing friction in forming engineering.

From the point of view of a mechanism-elucidation-oriented approach, it is more important to develop modeling of key phenomena than to enhance the accuracy of numerical prediction.

REFERENCES

1. Hill R. The mathematical theory of plasticity. New York: Oxford University Press; 1950. pp 317–321.
2. Taylor GI. Plastic strain in metals. J Inst Metals 1938;62:307–324.
3. Takahashi H, Motohashi H, Tokuda M, Abe T. Elastic-plastic finite element polycrystal model. Int J Plasticity 1994;10:63–80.
4. Takahashi H. Polycrystal plasticity. Tokyo: Colona Publishing; 1999.

5. Makino T, Dohda K, Ishitani A, Endo C. Finite element polycrystal method analysis of micro/meso-scale ring compression Proceedings of the 2nd International Conference on Micro-Manufacturing (ICOMM 2007); Greenville, SC. 2007. pp 207–212.
6. Makino T, Dohda K, Ishikawa M. Atomistic elementary process of galling on tool surface. The Proceedings of the 2008 Japanese Spring Conference for the Technology of Plasticity; Tsudanuma, Japan. 2008. pp 369–370.
7. Gonze X. First-principles computation of material properties: the ABINIT software project. Comput Mater Sci 2002;25:478–492. Available at http://www.abinit.org/.
8. Makino T, Dohda K, Ishitani A, Zhang H. Anisotropy of plastic deformation in micro/meso-scale metal forming. Transact North Am Manuf Res Inst SME 2009;37:333–340.
9. Makino T, Dohda K, Ishikawa M. Analysis of deformation behavior at tool/material interface in micro/meso-scale metal forming. The Proceedings of the 60th Japanese Joint Conference for the Technology of Plasticity; Nagano, Japan. 2009. pp 261–262.

CHAPTER 4

METROLOGY, INSPECTION, AND PROCESS CONTROL IN MICRO-SCALES

OMKAR G. KARHADE
Intel Corporation, Chandler, Arizona

THOMAS R. KURFESS
International Center for Automotive Research, Clemson University, Clemson, South Carolina

4.1 INTRODUCTION

Advances in micro-machining technology have enabled the design and development of ever smaller and complex miniaturized products. To address this miniaturization requirement, smaller dimensions, precise material properties, precise fabrication, stress-free components, and high reliability are being targeted. Various metrology techniques are used for the measurement of these properties. These techniques are critical also during component fabrication for monitoring production processes, to ensure a high yield.

Quantification of these properties is very challenging as the measurement needs to be taken on a micro-scale. On a micro-scale, the properties of material differ from those of the bulk material. Furthermore, dimensional precision required for micro-machined parts is more stringent as the overall dimensions are reduced. Fabrication techniques are also significantly different from bulk machining techniques (e.g., chemical deposition, oxidation and annealing are used in micro-machining). These techniques may introduce high stresses in different components in the micro-machined parts, which may have a significant impact on the functionality or reliability of those parts.

Conventional macro-scale metrology techniques can partially address these issues. Extensive research is being done to develop newer metrology techniques.

Micro-Manufacturing: Design and Manufacturing of Micro-Products, First Edition.
Edited by Muammer Koç and Tugrul Özel.

Some of these techniques are derived from macro-scale metrology and some are fundamentally different from macro-scale techniques.

The metrology techniques are generally offline, meaning that the part needs to be taken out of the production line and moved to the metrology tool in order to be measured. This has a negative impact on the production cycle time and early detection of defect cannot be achieved. Hence, significant research efforts are directed towards enabling in-line metrology.

This chapter presents different metrology techniques for micro-scale components. The techniques are mainly divided into spatial metrology, thermometry, and characterization of material properties. Spatial metrology targets the external and internal dimensions of the components. It also explores different metrology techniques used for the measurement of dynamic quantities such as displacement and vibrations. The methods include different approaches such as optical, tactile, acoustic, and destructive. Thermal imaging is also discussed in detail for micro-scale systems, as different thermal profiles during fabrication lead to different mechanical properties of the micro-machined parts. Techniques used in the metrology of mechanical properties of micro-machined components are also reviewed.

4.2 SPATIAL METROLOGY

4.2.1 Optical Methods

4.2.1.1 Optical Microscopy. Optical microscopy is one of the oldest metrology methods for the detection and measurements of micro-scale objects. It is a fast and nondestructive metrology method enabling a submicrometer-scale resolution. When combined with appropriate image-processing instrumentation, the method is capable of measuring static and dynamic spatial dimensions. In optical microscopy, a magnified optical image of the surface under observation is generated using a lens system. The image gives information mainly about the object surface on the focal plane of the microscope. Hence, the dimensional information is limited to the lateral dimensions.

The resolution limit of the image is governed by optical diffraction, which can be empirically determined by the Rayleigh criterion. For digital analysis, the image is usually captured by some hardware such as a charge-coupled device (CCD) camera. The hardware and lighting conditions (e.g., coaxial and ring lighting) may also affect the effective resolution of the metrology.

The metrology of micromachined components often requires locating the edge of a part. This is difficult, as the observed location varies with lighting condition, noise, and assumptions made in the edge position algorithm [1]. Other significant errors of optical techniques typically stem from interference, resonance, shadowing, secondary reflections, and lens distortions [2,3].

An important limitation of optical microscopes for the inspection of micro-scale parts is the inability to acquire true three-dimensional data. Some optical microscopes are integrated with software that employs image-processing

techniques to determine the Z-height at which the scan is taking place. The state-of-the-art software uses a projected Ronchi grid to determine the height at which the microscope is focused on one region of the image [4]. If the region selected has multiple focus points (i.e., the region selected is not in a single plane), the algorithm assigns the average value to the Z-height. Further edge detection algorithms are run to extract the X and Y data from the microscope image. This technique, in theory, produces three-dimensional data from an image; however, the algorithms used after finding the Z-height in one location of the image assume that all of the data are in the same plane.

While most measurements using optical microscopy target a static part, many micro-devices are dynamic and their dynamics must be characterized. The dynamic measurement of out-of-plane dimensions is difficult. Stroboscopic methods can be used in conjunction with optical microscopy to detect dynamic displacements in the plane of interest. For example, optical metrology has been combined with a phase shifting stroboscopic interferometer to obtain a three-dimensional dynamic measurements [5].

4.2.1.2 Confocal Microscopy. Optical microscopy is designed to look at the reflection of light from the surface at the focal plane. In cases such as three-dimensional and/or semitransparent parts, where there is a significant signal from the plane out of focus, optical microscopy does not yield good contrast. Confocal microscopy is adapted from optical microscopy to eliminate out-of-focus light to increase image contrast. This also enables three-dimensional image-slicing of the object.

The confocal laser scanning microscope (CLSM) is currently the most widely used confocal variation. It combines a confocal microscope with a scanning system in order to gather a three-dimensional data set. A typical setup is shown in Fig. 4.1. A CLSM consists of point illumination, point detection, and a confocal lens system. Scanning is done mostly by moving the beam, which alleviates focusing problems caused by objective lens scanning and is faster than specimen scanning [6]. Different planes can be imaged by moving the detection pinhole. With a scanning system added, the CLSM system has the ability to scan multiple times on different imaging planes, resulting in a three-dimensional data set. The CLSM enables measurement of dimensions that are in the range of microns with nanometer accuracy.

A significant advantage that confocal microscopy has over other optical metrology techniques is its ability to measure steep slopes of up to almost 90° on a part with minimal surface roughness. Such a measurement requires a high-resolution, high numerical aperture objective, which has a limited lateral measuring field unsuitable for measuring the entire object. Because of this limitation, a stitching procedure is needed to combine scans taken with several objectives to form a global picture of the component being inspected. Mechanical scanning has two disadvantages. First, it slows down the inspection process significantly. Second, the accuracy of the results is limited by the variations in the involved mechanical motions. Shin *et al.* developed a single-fiber-optic confocal

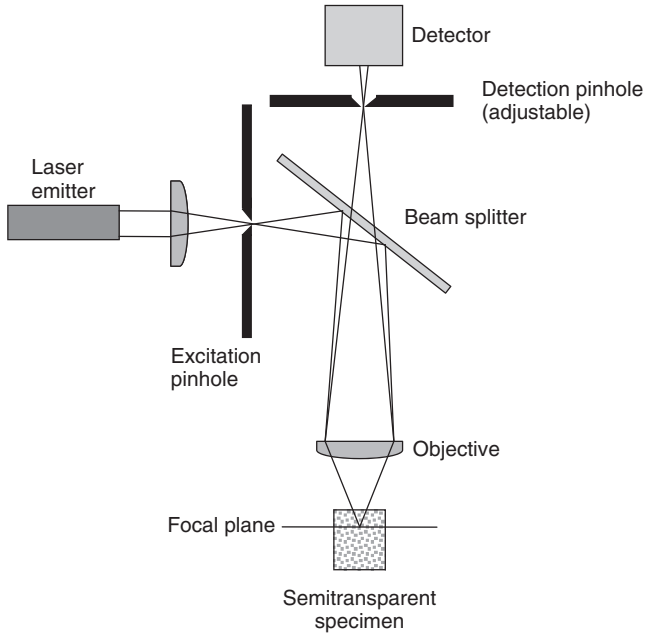

Figure 4.1 Schematic of optics in confocal microscope.

microscope (SFCM) with a micro-electromechanical system (MEMS) scanner and a miniature objective lens to overcome these disadvantages [7]. Riza *et al.* demonstrated a CSLM without mechanical scanning, using an electronically controlled liquid-crystal lens [8].

4.2.1.3 Fringe Projection Microscopy. Three-dimensional information can be generated using a two-dimensional image by projecting known gridlines on the surface and interpreting the gridline distortions. Fringe projection microscopy makes use of this principle. This method is well known for surface roughness metrology and has the advantage of high rates of data acquisition [9]. In fringe projection microscopy, a known grid (optical fringes) is projected on to the surface of interest. The surface nonuniformities distort the grid lines, the distorted two-dimensional image is captured by an image-capturing device, and the data is processed to interpret the surface roughness. An image-capturing surface height variation using fringe projection imaging is shown in Fig. 4.2.

Resolution is dependent on the optical system and the data acquisition hardware and is primarily dictated by the magnification and the aperture size of the system. Typical resolutions are on the order of a 100 nm, though the technique has been used to reach resolutions of 20 nm [11]. Fringe projection is viable for semirough surfaces ($>$300 nm RMS) because of its speed, but not as good as confocal microscopy or white light interferometry for out-of-plane resolution [12]. Despite the limitations in resolution, work has been done to use

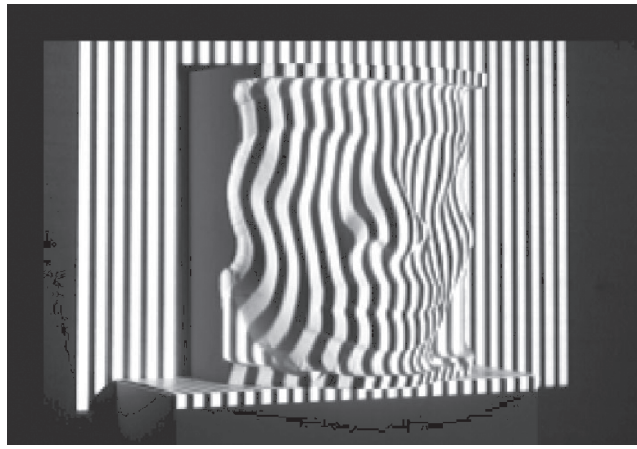

Figure 4.2 Fringe projection image-capturing surface height variation in the sample [10].

fringe projection in the metrology of micro-machined parts. Dynamic imaging of parts using fringe projection microscopy is also feasible [13]. This technique also enables long working distances and can be used for in-line metrology.

4.2.1.4 Auto Focusing Probing. Another means of generating Z-height (out-of-plane) information is to use the well-developed autofocusing technique commonly used in CD and DVD players. The autofocusing probe tracks the z-height of a surface by scanning the area. At each point on the surface, the probe is moved in the z direction, using a voice coil mechanism to focus on the surface. A schematic of the setup of autofocusing probe is shown in Fig. 4.3. If the specimen surface goes out of focus, the shape of the spot formed on the quadrant photo-diode changes. This is used as a feedback signal to the voice coil and the probe is moved until the specimen comes in to focus. The signal in voice coil corresponds to the z-height variation on the specimen surface, as the focal length of the optical system is constant.

Submicron accuracy in the z dimension can be obtained using this technique [14]. This method has been incorporated to a three-dimensional noncontact coordinate measurement machine (CMM) [15]. The displacement of a number of discrete points can be captured into an image showing the surface of the sample [16]. The dynamic bandwidth of a single point is shown to be about 10 kHz, which is limited by the bandwidth of the voice coil and control algorithm.

Similar to many measurement techniques that rely on reflected light, the DVD probe cannot focus on areas from which the light is not directly reflected back to the probe, such as in the case of chamfers, fillets, and relatively steep walls ($<20^\circ$ from horizontal). Additionally, relatively high reflectivity is required to achieve focus. Dynamic imaging of the surface is also difficult because of slower scanning speeds.

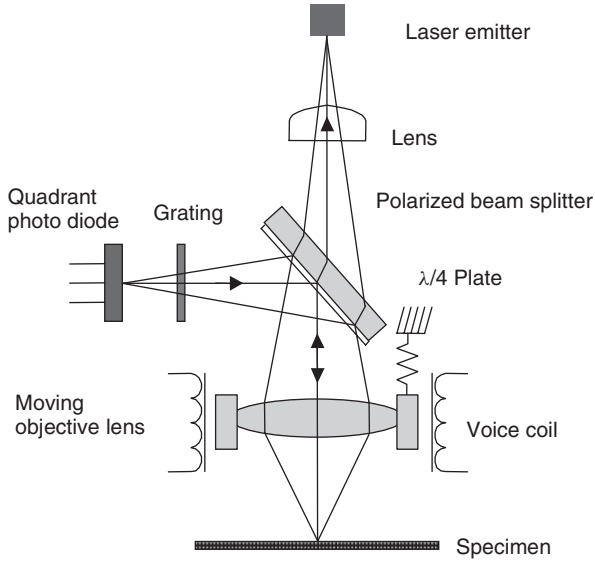

Figure 4.3 Schematic of optics and mechanism in autofocusing probe.

4.2.1.5 Scanning Interferometry. Interferometry enables measurement of the z dimension more precisely. The intensity of the interference of waves originating from different heights is highly sensitive to the difference between the heights. Height differences smaller than wavelength of radiation used can be easily measured by this method. Scanning laser interferometry and scanning white light interferometry (SWLI) make use of this principle.

In an interferometer, as shown in Fig. 4.4, within the objective, a light beam is split, with one beam going to the sample surface and the other to a reference surface. These light waves get reflected and interfere with each other, forming a pattern of light and dark bands, called fringes. For scanning interferometers, a piezoelectric crystal is used to create small movements in the objective in a direction perpendicular to the surface of interest. As the reference surface within the objective moves, the result of the combination of the reflected light varies. On the basis of the interference pattern, or fringes, and the wave length of the light employed, coordinate data can be extracted [17].

SWLI is currently used to perform dimensional measurement of micromachined parts [18]. White light interferometers have a subnanometer resolution in the scanning direction, at best a submicrometer resolution in the lateral directions, and can be used on a multitude of parts with different surface finishes [19]. White light is commonly used in scanning interferometers because it allows for higher resolution by comparing data from multiple wavelengths. Additionally, it is possible to resolve step height changes greater than $\lambda/4$ [20]. This technique has the ability to quickly measure step height changes and deflections. Additionally, when integrated with an image-processing system, it

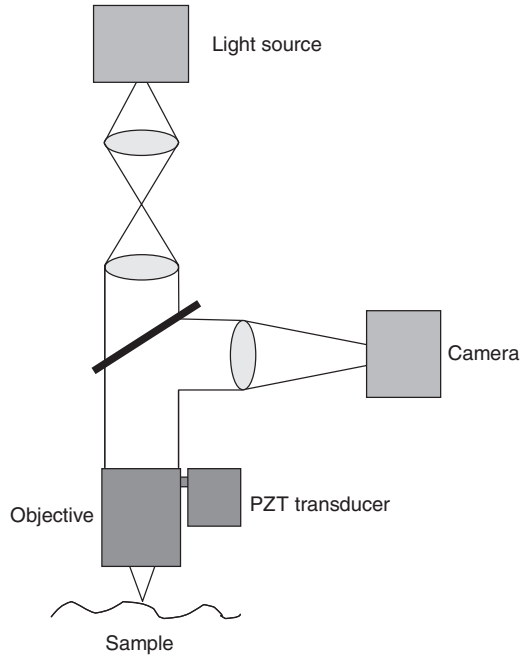

Figure 4.4 Schematic of scanning laser interferometer.

can provide lateral dimensions. However, the lateral resolution of commercially available systems is inadequate, except when equipped with high-power objectives, which severely limit the field of view. Additionally, these tools are limited in their ability to measure sloped surfaces. As the objective power decreases, the degree of identifiable slopes also decreases.

Despite these limitations, white light interferometry is heavily used in the MEMS industry to determine surface roughness, structural support analysis, deflection curve verification, and analysis of material properties. SWLI has also been reported to be used to measure meso-scale devices with relative success [21]. Dynamic metrology can be achieved with a white light interferometer using stroboscopic illumination techniques. Veeco's DMEMS system offers 15 Hz to 1 MHz frequencies and a 0.1-nm scale resolution [22]. The synchronized capture of a set of three-dimensional measurement data is used to generate a video of the moving system. An example of a 3D image of a micro-machined grating structure captured by SWLI is shown in Fig. 4.5.

4.2.1.6 Micro-Fabricated Scanning Grating Interferometer — μSGI.

The micro-fabricated scanning grating interferometer, or μSGI, has been developed to allow parallel scanning of dynamic and static devices [23,24]. The μSGI is based on traditional laser interferometry, but operates on the micro-scale. The system, manufactured using standard silicon processing techniques, measures

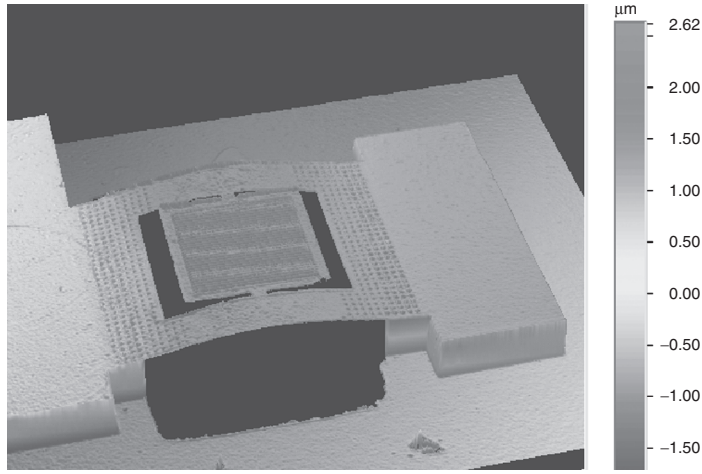

Figure 4.5 3D image of a micro-machined actuable grating structure captured by SWLI.

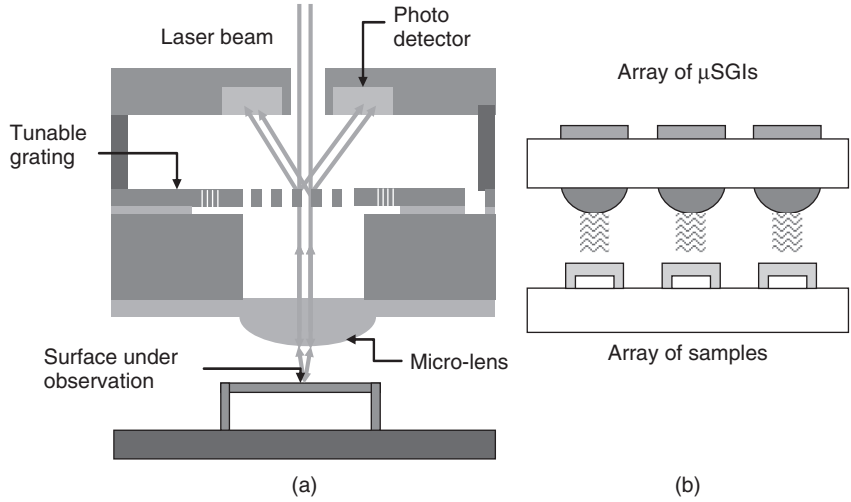

Figure 4.6 (a) Schematic of micro-fabricated scanning grating interferometer. (b) Schematic showing an array implementation.

distance by using a reflective diffraction grating. The diffraction grating is located on a transparent substrate with a micro-lens, fabricated using a reflow technique. The light is reflected from the diffraction grating, and the sample is collected by photo diodes. The system is shown in Fig. 4.6. The diffraction grating is fabricated on a membrane that can be actuated, which allows active noise reduction.

As with all interferometers, the intensity change due to displacement takes the shape of a sine wave. The diffraction grating is made deformable to enable higher

vertical displacement sensitivity by staying within the linear portion of the sine wave, allowing a vertical resolution of 0.5 nm. The lateral resolution is 1 μm.

This system has several distinct advantages over traditional interferometry. First, it has been designed to be produced in an array to permit faster inspection by using several μSGI units in parallel. Second, the system has the ability to perform both static and dynamic measurements. Noise reduction in the μSGI has been achieved by a recurrent calibration-based method using high-bandwidth tunable grating actuation. This algorithm shows more than 40 dB noise reduction at low frequencies and a 6.5 kHz noise reduction in bandwidth. The μSGI shows 2×10^{-5} $nm_{rms}/\sqrt{Hz}$ over a wide bandwidth (GHz) limited by the photodetector [25]. This is further modified to measure long-range distances [26]. An example of vibrating AFM scanned by a μSGI is shown in Fig. 4.7.

4.2.1.7 Scanning Laser Doppler Vibrometry. Laser Doppler vibrometry (LDV) is a noncontact vibration measurement technique using the Doppler Effect.

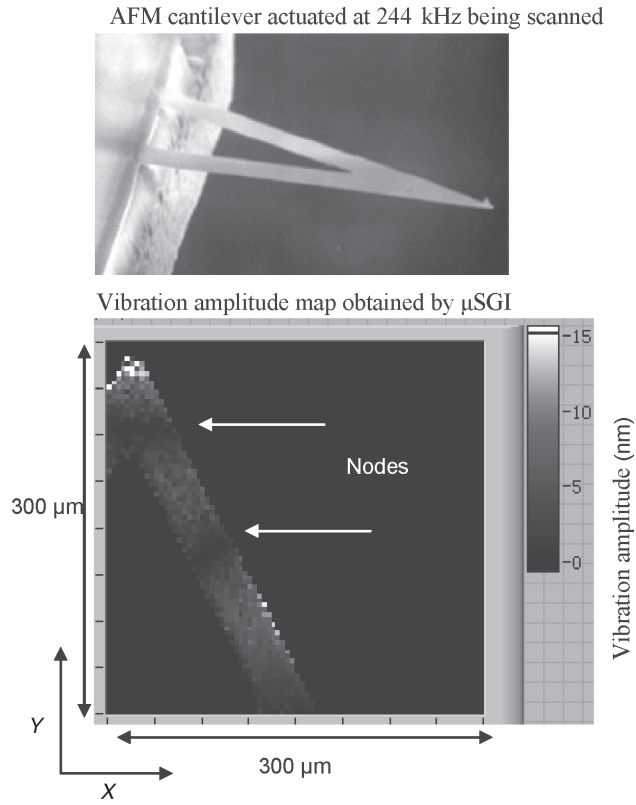

Figure 4.7 AFM cantilever actuated at its third resonance frequency is scanned by μSGI and vibration amplitude is mapped showing two nodes.

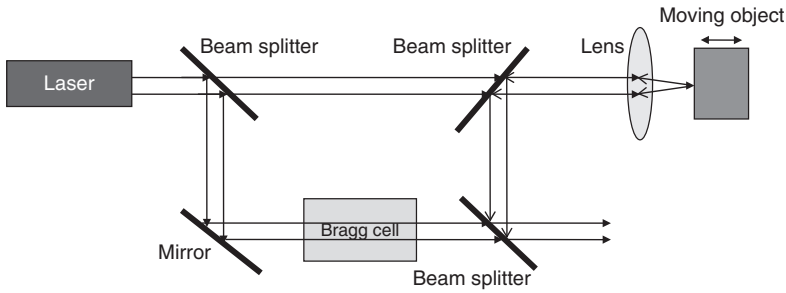

Figure 4.8 Schematic of scanning Doppler vibrometry.

LDV is designed to measure the dynamic displacements of components. A frequency shift is observed when a beam is reflected by a moving object. If the object is moving away from the source, then the reflected beam shows a lower frequency. When it is moving toward the source, it exhibits a higher frequency. This shift can be measured by making the reflected beam interfere with a reference beam. A scanned laser spot measures the dynamic profile of the surface under observation.

A coherent laser light is passed through a set of beam splitters and lenses as shown in the schematic in Fig. 4.8. The part of the beam from a fixed mirror serves as the reference beam. The other part gets reflected by the moving object, which carries the information about the displacement and the velocity of the moving object. A Bragg cell, an acousto-optic device, is used to introduce a frequency shift to the reference frequency. This prevents directional ambiguity typical of interferometers [27].

LDV permits long working distances and is commonly used for nondestructive dynamic metrology. The signal is dependent on the reflectivity of the sample surface. Hence, measurement of dynamics of steep slopes is difficult. The lateral resolution is limited by the diffraction optics. Lawrence *et al.* used LDV to measure the dynamic vibrations of a two-axis micro-mirror MEMS [28]. LDV can be combined with a scanning white light interferometer to measure the topography of a sample surface [29].

4.3 DIGITAL HOLOGRAPHIC MICROSCOPE SYSTEMS

Digital holographic systems have been employed for many years to measure the displacements of vibrating devices. In this technique, a digital camera is used to record a hologram produced by making a reference beam interfere with a beam reflected by the sample under test. The hologram is stored and then compared with the hologram generated after object displacement or deformation. The deformation is quantified using standard phase shifting or other interferometric techniques. These systems can achieve nanometer-level measurement of out-of-plane motion of devices. The ability to measure motions up to several megahertz can be achieved by combining holographic techniques with stroboscopic methods [30].

Holographic systems with an off-axis configuration enable capturing information of the entire part by single image acquisition. The image can be reconstructed at any object plane and the digital holographic microscope (DHM) can be used even at long stand-off distances (20–30 cm). The lateral resolution for the DHM is relatively high (~300 nm) and vertical resolution can be subnanometer [31]. However, this resolution is suitable either for static or for a low bandwidth measurement [32].

There are different methods of image reconstruction, including the Fresnel-approach, Fourier approach, and convolution-approach. Lensless Fourier holography is the fastest and most suitable algorithm for small objects. Lateral resolution ranges from a few micrometers to hundreds of micrometers without any additional optics [33]. Phase unwrapping is still necessary in digital holography since the fringe-counting problem remains.

In time averaged electro-optic holographic microscope (EOHM), the sample is exposed for an extended period of time (relative to the time period of the frequency of vibration) to capture a single image. It is easy to use this method to find the resonant frequencies and mode shapes using this method. The bandwidth of operation is not limited, but in the time domain only one frequency can be analyzed in a given measurement. The DHM method may also suffer from aberrations such as spherical (for off-axis configuration), coma or astigmatism, field curvature, or distortion [34].

4.3.1 Scanning Electron Microscopy

The lateral and vertical resolution of any optical metrology methods is limited mainly by the wavelength of the light used. A shorter wavelength enables higher resolution. The electron microscope uses electron beams, which are capable of generating angstrom-scale resolution. Electron microscopes are mainly classified as transmission electron microscope (TEM) and scanning electron microscope (SEM). In TEM, the electron beam is passed through a thin slice of specimen and it is imaged on the other side. SEM, on the other hand, operates by scanning a focused beam of high energy electrons across a conductive sample contained in a vacuum. As the electron beam hits the conductive surface, secondary electrons are emitted. These secondary electrons are counted and used to create an image of the sample. A schematic of SEM is shown in Fig. 4.9. Current commercial SEMs offer a subnanometer lateral resolution and up to 2 million times magnification. SEM is one of the commonly used metrology methods to image micro-machined parts for visualization of three-dimensional structure and finer details [35].

SEMs scan the sample at video rate and hence measurement of high-frequency dynamic vibrations becomes difficult. The frequencies that are multiples of the video rate can be strobed with SEMs. For other frequencies, the amplitude of lateral vibrations can be estimated by the blur area to find the Q-factor of dynamic devices in a vacuum [36]. Wong and Wong implemented dynamic stroboscopic in-plane imaging by time-gating the secondary electron detector signal. Dynamic measurements with instantaneous velocities can be obtained by pixel blurring analysis [37].

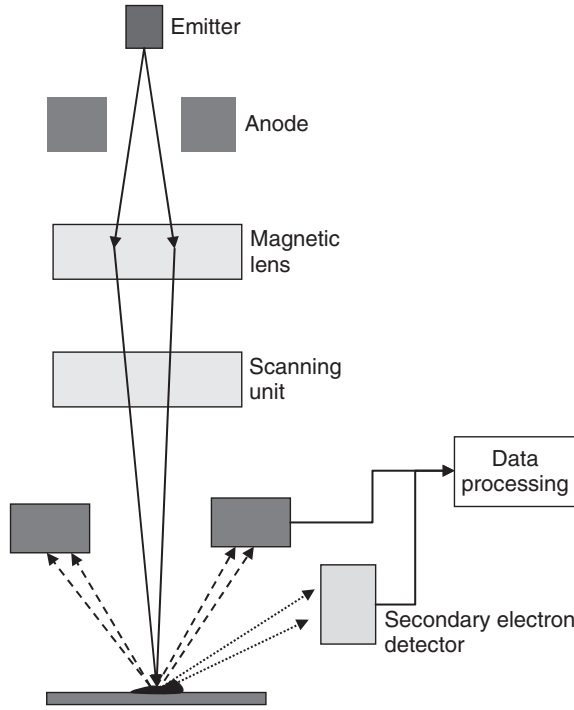

Figure 4.9 Schematic of scanning electron microscope.

The accuracy of the images captured by the SEM is highly dependent on machine capability and the specific part being examined [38]. Beam-sample interactions (i.e., charging) can greatly influence the results. Additionally, despite high resolution of the SEM, the output is typically generated from the electron detector and displayed on a screen as a two-dimensional image. Since no coordinate data are directly output from the SEM, performing any analysis other than line width measurements directly with the SEM software becomes difficult. Thus, SEMs are ideal for visualizing MEMS parts, but are inadequate for the quantitative analysis of MEMS devices (Fig. 4.10).

SEM-based metrology has a number of other drawbacks. For the SEM, an edge appears as an intensity change in the image [3]. Thus, the location of the edge can vary greatly, depending on the image analysis technique used. This can result in widely varying metrology results. The vacuum pressure in the SEM can also induce warping in delicate MEMS devices under scan [39]. The vacuum requirement and the need for a conductive target add to the complexity of SEM-based micro-metrology.

An alternative SEM process is called X-SEM. This process is destructive and requires the sample to be cross-sectioned. The cross section is then imaged in an SEM. Often this technique is used to determine sidewall and height characteristics

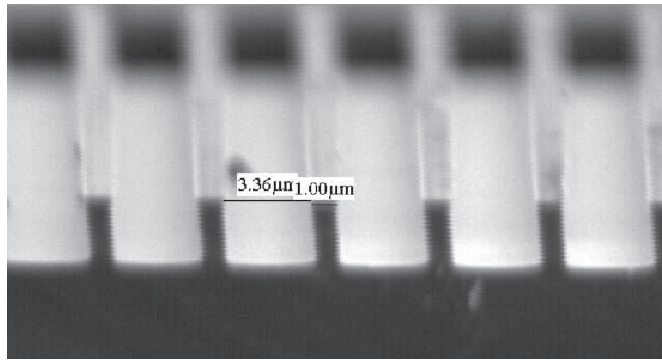

Figure 4.10 A sample image of micro-machined grating.

[40]. Top-down X-SEM process is used to characterize SEM images, which require interpretation of intensity and the process is sensitive to sidewall geometry [41]. Top-down SEMs are commonly used to characterize micro-structures.

4.4 MICRO COORDINATE MEASURING MACHINES — μCMM

A CMM is a contact method for measuring the surface topology of a part. A probe scans the surface of the part and generates coordinates for surface points at the location of contact. Small-scale CMMs are being investigated for their possible use in geometric characterization of micro-machined parts [42]. These devices have working volumes up to $400 \times 400 \times 100$ mm [43]. Submicrometer uncertainties are being targeted with nanometer resolutions [44]. Various approaches are being taken to scale down components of a traditional CMM [45,46]. The main issues yet to be addressed are the size, quality, and calibration of the probe tip used for inspection. In addition, the design of a sensing system to detect the small displacement forces of the probe still proves to be a challenge. Optical probes are also used to achieve nanometer-level resolution over $25 \times 25 \times 10$ mm commercial three-dimensional CMM uses laser scanners with multiple microscopes [47,48].

4.5 SCANNING PROBE MICROSCOPY

Scanning probe microscopy (SPM) is another form of contact technique that offers high resolution. The two most widely used SPMs are scanning tunneling microscope (STM) and atomic force microscope (AFM). In STM, a metallic probe is brought into close proximity of a conductive surface so that a small current flows between them. The current is held constant by a feedback control scheme, allowing the probe to track the height of the surface [3]. Subangstrom

resolution is attainable in the normal direction of the surface, and angstrom-scale resolution is attainable in the lateral direction.

AFM has a resolution similar to that of STM, but it's use is not limited to conductive surfaces [49]. Measurement using an AFM is performed with a sharp probe that collects a series of line scans across the surface of a part. The topography of the part is measured by bringing the probe close to the specimen and measuring the repulsive and attractive forces on the probe tip. Figure 4.11 shows a schematic of an AFM. The AFM cantilever has a sharp probe, which is brought into close vicinity of the sample surface. Different surface forces such as van der Waal's force, mechanical contact force, and capillary force cause deflection in the cantilever. These are detected by measuring deflection of an optical beam. This signal is used as feedback to drive the AFM cantilever to track the sample surface and record the topology of the sample surface.

Depending on the feedback force, an AFM is capable of working in both contact and noncontact modes to collect surface data. In contact mode, the method of data acquisition is similar to that for a profilometer, where the probe tip slides along the surface of the specimen to measure the relative height changes. Shear stresses that arise from sliding the probe tip across the surface of a part can be eliminated by using a setup in which the probe tip oscillates as it traverses across the surface, which is called the tapping mode. In noncontact mode, the van der Waals forces between the probe tip and specimen are measured and converted to coordinate data. Thus, it enables noncontact method and therefore eliminates tip erosion [50]. This method has lower resolution and is less stable than the sliding and the tapping modes.

There are certain limitations to SPMs, particularly in measuring high aspect ratio parts. STMs, as previously mentioned, are limited to parts with conductive surfaces. Electronic inhomogeneities can also have significant effects on the

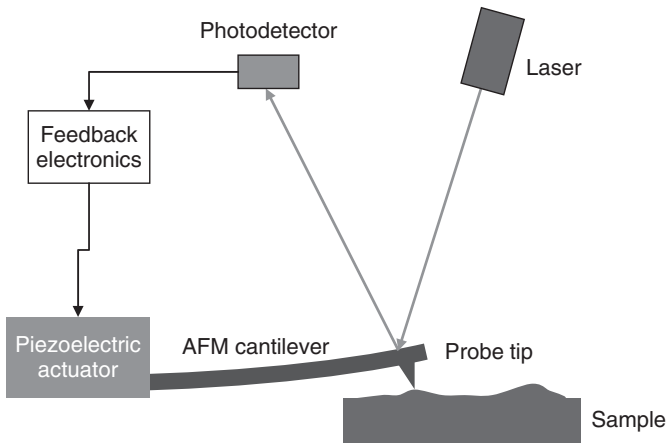

Figure 4.11 Schematic of an atomic force microscope.

topographical image generated from the probe [51]. Vibrations in the probing mechanism also limit gap-width stability which, in turn, can affect the fidelity of the measurements. All SPMs are limited, in the same sense as white light interferometers, to the maximum measurable slope changes in a surface or between surfaces. When features with perpendicular sidewalls are scanned, the data typically exhibit a slope or curtain that is actually not present [52]. SPMs have atomic resolution in the z (out-of-plane) direction, but are limited to a few micrometers [53]. This limitation severely prohibits the inspection of high aspect ratio parts with dimensions on the order of millimeters. Though these tools have extremely high resolution, it is not feasible to collect scans that cover entire surface of a part, given the limited scan range they offer.

Recently, AFMs have been successfully used to measure the sidewalls of parts with a height of 2 μm [54,55]. Dynamic measurements can be achieved by high-speed AFMs scanning using a mechanical feedback loop and resonant scanning mechanism; however, this is a contact method [56]. An AFM with force sensing integrated readout and active tip (FIRAT) uses high-bandwidth micromachined actuator, high interferometric resolution and possesses an extended range [57,58].

4.5.1 Micro-computed Tomography

Computed tomography (CT) is a radiographic technique for nondestructive three-dimensional testing. This technique was initially developed for medical imaging and then evolved to image micro-machined components. CT inspection consists of measuring a complete set of line-integrals involving the physical parameter of interest over the designated cross section. Different mathematical algorithms are used to reconstruct an estimate of the spatial variation of the parameter over the desired slice [59]. The two-dimensional imaging planes are then stacked and a three-dimensional image is rendered using software.

Figure 4.12 shows a schematic of a CT system. The specimen is placed on a stage that can be translated and rotated. The X-rays passing through the target can be magnified by optics and are then detected by a scintillator-camera detection system. The acquired images are processed and reconstructed by a computer and are displayed.

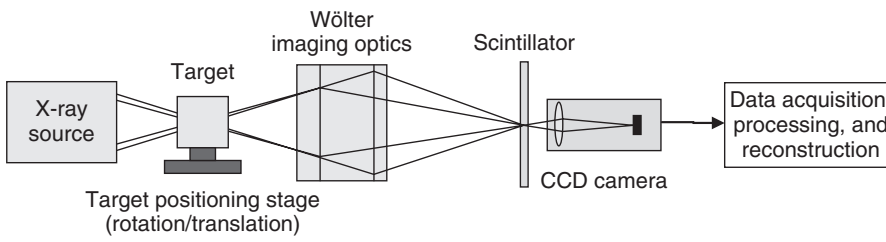

Figure 4.12 Schematic of computed tomography system.

CT provides nondestructive characterization of the internal structures of meso-scale devices. Also, it can be used to inspect metallic or nonmetallic, solid or fibrous, smooth- or irregular-surfaced specimens; however, some materials such as Teflon cannot be viewed by CT scan [60]. The results can be used for quality control, flaw detection, dimensional measurement, and reverse-engineering. There is a possibility, however, that artifacts appearing in the resulting image due to the physics of the system cannot be removed. The scan provides micrometer-level resolution but complete scans are quite time consuming and require a significant amount of data processing [61,62]. The processing that is done on the raw data directly affects the outcome of an inspection, and current algorithms are not well calibrated or verified to any internationally recognized metrology standard.

4.5.2 Scanning Acoustic Microscopy

Nondestructive inspection of the internal features of a micro-machined part is challenging with optical methods or most of the contact methods. Scanning acoustic microscopy (SAM) offers a way to penetrate through solid structures and image the interfaces between different layers (Fig. 4.13). This technique is being extensively used in semiconductor manufacturing industry for detecting delamination, crack defects in Silicon, and underfill voiding [63]. Many of the micro-machining techniques are derived from semiconductor industry, and acoustic microscopy can be used to visualize the internal features of micro-machined components.

SAM uses acoustic waves in the frequency range of mega- to gigahertz. The waves are generated by a transducer and are focused on to a specimen using acoustic lenses. The waves usually need a medium, to travel through and hence the parts to be scanned are either immersed in water or a column of water is

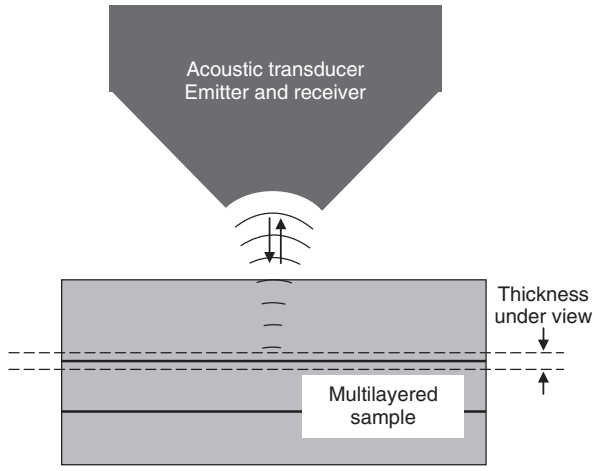

Figure 4.13 Schematic of scanning acoustic microscopy.

created in the path of acoustic wave. At each interface between the layers, part of the acoustic wave is reflected back. If the difference between the acoustic impedance of the two materials at the interface is high, then most of the wave is reflected. Hence, voids in the structure can be easily detected by the reflection mode SAM. The reflected waveform enables viewing different interfaces as they are separated in time. The whole reflected waveform is called A-scan. If only part of the waveform is gated to generate an image, then it is called C-scan. A C-scan enables viewing a thin layer inside the specimen. In another mode of scanning, the signal transmitted through the specimen is received by a sensor underneath the transducer (T-scan). This enables viewing the defects throughout the thickness.

SAM enables a nondestructive technique for reliability inspection of micro-machined components. Cracks, delamination, voids, and stiction can be detected by SAM [64–66]. A lateral resolution of a few microns and depth of field of few millimeters can be obtained. However, the parts need to be immersed into or exposed to some medium such as water. This may cause corrosion, stiction, and other undesirable changes in the test parts. Acoustic Microscopy has also been modified to scanning near-field microscopy (SNAM) to detect subsurface defects of submicron size [67].

4.5.3 Thermometry of Micro-Machined Components

Many of the micro-machined electromechanical parts (MEMS) have heating elements (e.g., AFM cantilever with heated tip, heatuaters) [68,69]. Thermometry (temperature measurement) of these parts is critical to ensuring their functionality. Several different methods are used to detect the temperatures of micro-machined components during and after fabrication.

4.5.3.1 Infrared Microscopy. Components at higher temperature emit higher infrared radiation intensity. Micro-infrared radiation thermometry techniques detect the infrared radiation emitted by the specimen and interpret the temperature on the basis of the emissivity of the specimen. Typically these systems are calibrated at different temperatures to account for changes in emissivity with temperatures. Minimum spot size is dependent on the diffraction limit as in optical microscopy and is usually about a few microns. Temporal resolution of the order of 1 μs can be obtained for dynamic readings. This method is typically used in the IC (integrated circuits) industry where the temperature map of the heated device can be obtained by this method [70].

The drawback of using this method in scanning micro-fabricated parts is that Silicon is one of the most commonly used materials in micro-fabrication and is semitransparent to IR (infrared) radiation, which introduces uncertainties. Typically the IR receivers are cooled to reduce noise, however the cooled receivers are usually bulky and not easy to use. New studies make use of bimaterial micro-cantilevers to detect energy absorbed [71]. These are limited to a resolution of 3–5°C.

4.5.3.2 Thermal Reflectance Thermometry. This technique makes use of small change in the reflectance of the material surface with the change in temperature. The system is precalibrated for the material under observation. A visible laser is used to measure the reflectivity of the specimen. A submicron spatial resolution can be obtained by thermal reflectance thermometry as the spot size depends on the diffraction limit of the visible radiation. Temperature map of the specimen can be obtained with a dynamic response in picoseconds [72]. A temperature resolution of few millikelvin can be obtained using this technique [73]. Surface properties such as roughness and coatings introduce uncertainties in the calibration affecting the temperature reading accuracy.

4.5.3.3 Scanning Thermal Microscopy (SThM). Scanning thermal microscopy (SThM) utilizes the principle of AFM. A temperature sensor (thermocouple) is fabricated on the tip of the AFM cantilever. The cantilever is scanned over the surface of the specimen and temperature map is recorded [74]. The main advantage of SThM is high spatial resolution of a few nanometers, which is enabled by the AFM tip [75]. However, scanning rates are lower compared to optical techniques and dynamic metrology over the entire surface is difficult. Lack of good calibration techniques, contact resistance between the tip and the specimen surface, friction effect and hysteresis limit the accuracy of SThM.

4.5.3.4 Laser-Induced Fluorescence. Laser-induced fluorescence technique is used for thermal metrology of micro-machined and fluidic devices. In this technique the specimen is seeded with a temperature-sensitive phosphor dye and the fluorescence is monitored to measure temperature. A wide range of temperatures can be measured using this technique [76]. The fluorescing intensity is proportional to illuminating light intensity, dye concentration, and the optical constant of the dye. Hence, measurement is highly dependent on the setup [77]. For micro-machined parts, the need for surface modification also limits the use of this method.

4.5.3.5 Laser Interferometric Thermometry. Another technique used for thermal imaging is laser interferometric thermometry. This technique utilizes the change in the refractive index of the material caused by changing temperature. For IR radiation, a significant change in the refractive index of Silicon is observed with temperature, which can be measured interferometrically [78]. Operationally, an IR laser beam is projected on the surface of specimen. The reflections from the top surface and bottom surface of the specimen interfere with each other to generate constructive or destructive interference depending on the length of the optical path between the top and the bottom surfaces. With change in temperature, the length of the optical path changes and the change can be detected by measuring the intensity of the light interference by a photo-diode. Subkelvin temperature changes can be detected by this technique. The readings are confounded with the

strain in the specimen. Absolute temperature measurement is not possible. Also, thermal imaging of a surface becomes difficult as the thickness of the specimen must be constant over the region of interest.

4.6 METROLOGY OF MECHANICAL PROPERTIES

Mechanical properties such as Young's modulus, fracture toughness, yield strength, and relevant physical measurements such as stress and strain are critical to design and reliability of the micro-machined components. For micro-machined parts the properties of the bulk material are significantly different from the thin film materials. Hence, the micro-machined components need to be tested for the material properties. However, fabrication and handling of a specimen and application of direct force on it is a challenging task. Different testing methods are developed to measure the mechanical properties of the micro-machined parts.

4.6.1 Raman Spectroscopy

Raman spectroscopy is an optical technique used for stress and temperature measurement in which light is scattered from the surface of the specimen. The scattering is a function of the stress and the temperature on the surface. This technique is specifically suited for micro-machined components fabricated with Silicon because of its high scattering cross section. In this method, a laser is projected on the surface of the specimen. Part of this incident laser is scattered because of the interaction of photons with phonons. This scattering is spectroscopic measure of these photons and gives information about the resonance frequencies of the phonons. The phonon resonance can be interpreted to measure temperature and stress in the material close to the surface. Optical diffraction limit based micron level spatial resolution can be obtained with this method. Also, it is limited to a submicron penetration depth. A stress resolution of 10 MPa and a thermal resolution of 5 K is reported [79,80].

4.6.2 Bending Test

For force measurement, a beam bending approach can be employed. In this test, a micro-cantilever beam is deflected using a probe (Fig. 4.14). The applied force is measured on the probe side and the deflection of the beam is measured optically. Knowing the geometry of the beam and using the theory of bending, Young's modulus can be obtained. Further bending the beam until it fails in fracture provides information about the yield strength and fracture toughness of the sample material.

An AFM probe with known spring constant can be used to measure these properties [81]. This is a relatively simple method to test the mechanical properties of micro-machined parts. Electrostatic pull-in is another form of bending

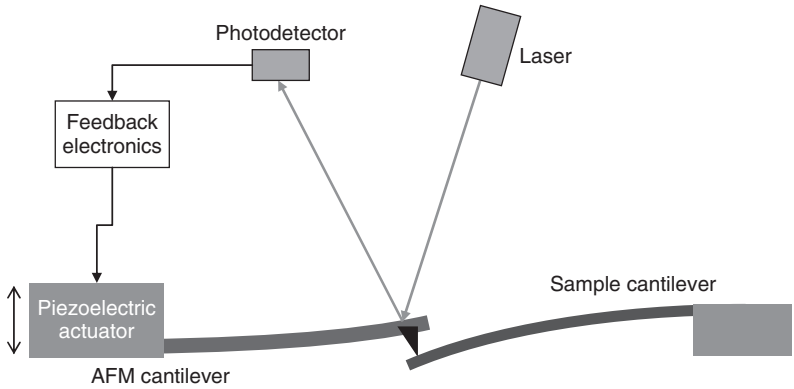

Figure 4.14 Schematic of bending test using an AFM probe to deflect a micro-cantilever.

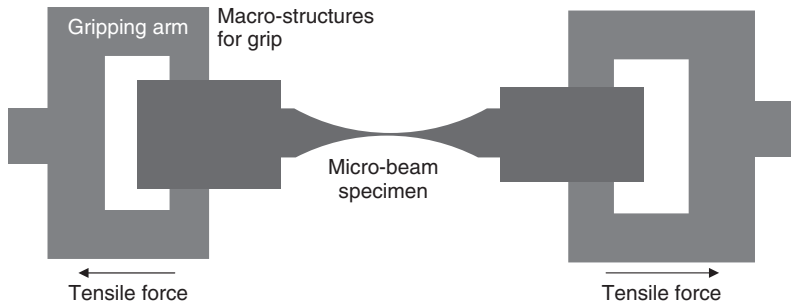

Figure 4.15 Schematic of a tensile testing apparatus for micro-specimen.

test that can also be used to determine the mechanical properties of thin film materials [82]. However, in most of the cases, linear bending theory can not be applied because of high beam curvatures. Hence, data analysis becomes relatively difficult and numerical analysis is required.

4.6.3 Tensile Test

In a tensile test, the specimen is pulled with known force from two sides and the strain is measured to determine Young's modulus, Poisson's ratio, yield strength and fracture strength (Fig. 4.15). The handling of the specimen and application of a known force are challenging because of specimen's small size. Different gripping structures and mechanisms are used to overcome this problem. MEMS-based grippers and loading structures are often employed. These use torsion-based setups and electrostatic and piezoelectric actuators [83,84]. Better accuracy in strain measurements can be obtained by using reflective lines deposited on the material to generate fringes [85]. Digital image correlation (DIC) method is also used to measure strain [86].

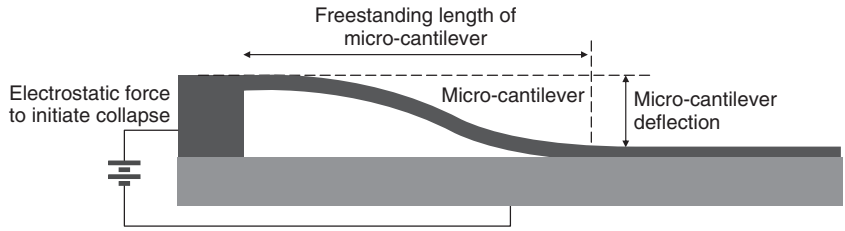

Figure 4.16 Schematic of experimental setup used for measuring the stiction effect.

4.6.4 Interfacial Properties

Micro-machined components often have freestanding surfaces that lead to friction and stiction. These properties depend on the environmental conditions, especially humidity. Measurement of these interfacial properties is important for the reliability of these components. In one of the methods used for the determination of stiction force, the freestanding cantilever is retracted using electrostatic force, and as it collapses due to the stiction force the electrostatic force is released. This leaves an S-shaped beam where the freestanding length of the cantilever beam can be used to calculate the stiction force (Fig. 4.16) [87] Electrostatic pull-in force can also be transformed into a translational motion and friction force can be determined [88,89].

REFERENCES

1. El-Hakim SF. Some solutions to vision-dimensional metrology problems. SPIE Proceedings, Close-Range Photogrammetry Meets Machine Vision; 1935 Sep 3–7; Zurich, Switzerland; 1990.
2. Svetkoff DJ, Kilgus DB. Influence of object structure on the accuracy of 3-D systems for metrology. Proc SPIE 1992;1614:218.
3. Marchman HM, Dunham N. AFM: a valid reference tool? Proc SPIE 1998;3332:4.
4. VIEW. 2008. Ronchi grid. Available at http://www.vieweng.com/ronchi_grid.jsp.
5. Petitgrand S, Bosseboeuf A. Simultaneous mapping of out-of-plane and in-plane vibrations of MEMS with (sub) nanometer resolution. J Micromech Microeng 2004;14(9):97–101.
6. Corle TR, Kino GS. Confocal scanning optical Microscopy and related imaging systems. Academic Press, San Diego; 1996.
7. Shin HJ, Pierce MC, Lee D, Ra H, Solgaard O, Richards-Kortum R. Fiber-optic confocal microscope using a MEMS scanner and miniature objective lens. Opt Express 2007;15(15):9113–9124.
8. Riza NA, Sheikh M, Webb-Wood G, Kik PG. Demonstration of three-dimensional optical imaging using a confocal microscope based on a liquid-crystal electronic lens. Opt Eng 2008;47:063201.
9. Seitz G, Tiziani HJ. Resolution limits of active triangulation systems by defocusing. Opt Eng 1993;32:1374.

10. Blasi F. Review of 20 years of range sensor development. J Electron Imaging 2004;13:231.
11. Leonhardt K, Droste U, Tiziani HJ. Microshape and rough-surface analysis by fringe projection. Appl Opt 1994;33(31/1):7477–7488.
12. Windecker R, Franz S, Tiziani HJ. Optical roughness measurements with fringe projection. Appl Opt 1999;38(13):2837–2844.
13. Tay CJ, Quan C, Shang HM, Wu T, Wang S. New method for measuring dynamic response of small components by fringe projection. Opt Eng 2003;42:1715.
14. Fan KC, Chu CL, Mou JI. Development of a low-cost autofocusing probe for profile measurement. Meas Sci Technol 2001;12:2137–2146.
15. Fan KC, Fei YT, Yu XF, Chen YJ, Wang WL, Chen F, Liu YS. Development of a low-cost micro-CMM for 3D micro/nano measurements. Meas Sci Technol 2006;17(3):524–534.
16. Kirkland E. A nano coordinate machine for optical dimensional metrology [MS thesis]. Atlanta (GA): Georgia Institute of Technology; 2003.
17. St. Clair LES, Mirza AR, Reynolds P. Metrology for MEMS manufacturing. Sens Mag 2000;17(7).
18. O'Mahony C, Hill M, Brunet M, Duane R, Mathewson A. Characterization of micromechanical structures using white-light interferometry. Meas Sci Technol 2003;14(10):1807–1814.
19. de Groot PJ, Deck LL. Surface profiling by frequency-domain analysis of white light interferograms. Proc SPIE Int Soc Opt Eng 1994;2248:101.
20. Wyant JC. White light interferometry. Proc SPIE Int Soc Opt Eng 2002;4737:98–107.
21. Shilling KM. Two dimensional analysis of meso-scale parts using image processing techniques [Masters thesis]. Atlanta (GA): Mechanical Engineering, Georgia Institute of Technology; 2003.
22. Veeco. 2008. DMEMS NT3300, Available at http://www.veeco.com/pdfs.php/395 (last accessed 2008).
23. Kim B, Degertekin FL, Kurfess TR. Micromachined scanning grating interferometer for out-of-plane vibration measurement of MEMS. J Micromech Microeng 2007;17:1888–1898.
24. Karhade OG, Degertekin FL, Kurfess TR. SOI-based micro scanning grating interferometers: device characterization, control and demonstration of parallel operation. J Micromech Microeng 2008;18(4):045007.
25. Karhade OG, Degertekin FL, Kurfess TR. Active control of microinterferometers for low-noise parallel operation. IEEE/ASME Trans Mechatron 2010;15(1):1–8.
26. Karhade OG, Degertekin FL, Kurfess TR. Active control of grating interferometers for extended-range low-noise operation. Opt Lett 2009;34(19):3044–3046.
27. Lawrence EM. MEMS characterization using Laser Doppler vibrometry. Proc SPIE 2003;4980(51). DOI: 10.1117/14.478195.
28. Lawrence EM, Speller KE, Yu D. MEMS characterization using Laser Doppler Vibrometry. Proc SPIE 2003;4980:51.
29. Polytec I. 2008. MSA-500 micro system analyzer. Available at http://www.polytec.com/usa/_files/OM_BR_MSA-500_2008_06_US_draft.pdf. Retrieved 2008 Sep 24.
30. Novak E. MEMS metrology techniques. Proc SPIE 2005;5716:173.
31. Coppola G, Ferraro P, Iodice1 M, De Nicola S, Finizio A, Grilli S. A digital holographic microscope for complete characterization of microelectromechanical systems. Meas Sci Technol 2004;15(3):529–539.

32. Emery Y, Cuche E, Marquet F, Aspert N, Marquet P, Kühn J, Botkine M, Colomb T, Montfort F, Charriére F, Depeursinge C. Digital holography microscopy (DHM): fast and robust systems for industrial inspection with interferometer resolution. Optical Measurement Systems for Industrial Inspection IV; Munich, Germany, SPIE; 2005.
33. Seebacher S, Osten W, Baumbach T, Jüptner W. The determination of material parameters of microcomponents using digital holography. Opt Lasers Eng 2001;36(2): 103–126.
34. Hariharan P. Optical holography. Cambridge University Press New York; 1984.
35. Hitachi. 2008. S-5500 In-Lens FE SEM. Available at http://www.hitachi-hta.com/pageloader~type~product~id~389~orgid~44.html (last accessed 2008).
36. Gilles JP, Megherbi S, Raynaud G, Parrain F, Mathias H, Leroux X, Bosseboeuf A. Scanning electron Microscopy for vacuum quality factor measurement of small-size MEMS resonators. Sens Actuators A Phys 2008;145:187–193.
37. Wong CL, Wong WK. In-plane motion characterization of MEMS resonators using stroboscopic scanning electron microscopy. Sens Actuators A Phys 2007;138(1):167–178.
38. Postek M. The scanning electron. Handbook of charged particle optics; CRC press, Florida; 1997.
39. Storment CW, Borkholder DA, Westerlind V, Suh JW, Maluf NI, Kovacs GTA. Flexible, dry-released process for aluminum electrostatic actuators. J Microelectromech Syst 1994;3(3):90–96.
40. Opsal JL, Chu H, Wen Y, Chang YC, Li G. Fundamental solutions for real-time optical CD metrology. Proc SPIE 2002;4689:163.
41. Lagerquist MD, Bither W, Brouillette R. Improving SEM linewidth metrology by two-dimensional scanning force microscopy. Proc SPIE 1996;2725:494.
42. Peggs GN, Lewis AJ, Oldfield S. Design for a compact high-accuracy CMM. CIRP Ann Manuf Technol 1999;48(1):417–420.
43. Shiozawa H, Fukutomi Y, Ushioda T, Yoshimura S. Development of ultra-precision 3D-CMM based on 3D metrology frame. Proc ASPE 1998;18:15–18.
44. Peggs GN, Lewis A, Leach RK. Measuring in three dimensions at the meso-scopic scale. Proceedings of ASPE; 2003 Jan 22–23, Florida; 2003.
45. Takamasu K, Fujiwara M, Yamaguchi A, Hiraki M, Ozono S. Evaluation of thermal drift of nano-CMM. Proceedings of 2nd EUSPEN International; 2001.
46. Cao S, Brand U, Kleine-Besten T, Hoffmann W, Schwenke H, Bütefisch S, Büttgenbach S. Recent developments in dimensional metrology for microsystem components. Microsyst Technol 2002;8(1):3–6.
47. Fan KC, Fei YT, Yu XF, Chen YJ, Wang WL, Chen F, Liu YS, Development of a low-cost micro-CMM for 3D micro/nano measurements. Meas Sci Technol 2006;17(3):524–534.
48. Shapegrabber. 2008. SG2 series scan heads. Available at http://28189.vws.magma.ca/sol-products-3d-scan-heads-specs-metric.shtml.
49. Binnig G, Quate CF, Gerber C. Atomic force microscope. Phys Rev Lett 1986; 56(9):930–933.
50. Marchman HM. Nanometer-scale dimensional metrology with noncontact atomic force microscopy. Proc SPIE 1996;2725:527.
51. Binnig G, Rohrer H. Scanning tunneling microscopy. IBM J Res Dev 2000;44(1–2):279–293.

52. Griffith JE, Marchman HM, Miller GL, Hopkins LC. Dimensional metrology with scanning probe microscopes. J Vac Sci Technol B Microelectron Nanometer Struct 1995;13:1100.
53. Veeco. 2008. Innova SPM. Available at http://www.veeco.com/pdfs/datasheets/B67_RevA1_Innova_Datasheet.pdf (last accessed 2008).
54. Rizvi SA, Meyyappan A. Atomic force microscopy: a diagnostic tool (in) for mask making in the coming years. Proc SPIE 1999;3677:740.
55. Walch K, Meyyappan A, Muckenhirn S, Margail J. Measurement of sidewall, line, and line-edge roughness with scanning probe microscopy. Proc SPIE 2001;4344:726.
56. Humphris ADL, Miles MJ, Hobbs JK. A mechanical microscope: high-speed atomic force microscopy. Appl Phys Lett 2005;86:034106.
57. Onaran AG, Balantekin M, Lee W, Hughes WL, Buchine BA, Guldiken RO, Parlak Z, Quate CF, Degertekin FL. A new atomic force microscope probe with force sensing integrated readout and active tip. Rev Sci Instrum 2006;77:023501.
58. Van Gorp B, Onaran AG, Degertekin FL. Integrated dual grating method for extended range interferometric displacement detection in probe microscopy. Appl Phys Lett 2007;91:083101.
59. STM. ASTM Standard Guide for Computed Tomography (CT) Imaging, Designation: E1441-9; 1993.
60. Fisher RF, Hintenlang DE. Micro-CT imaging of MEMS components. J Nondestruct Eval 2008;27:115–125.
61. Shilling KM. Meso-scale Edge Characterization [PhD thesis]. Atlanta (GA): Georgia Institute of Technology; 2006.
62. Rapiscan. 2008. CT systems. Available at http://www.rapiscansystems.com/ctsystems.html (last accessed 2008).
63. Semmens JE. Flip chips and acoustic micro imaging: an overview of past applications, present status, and roadmap for the future. Microelectron Reliab 2000;40(8–10):1539–1543.
64. Wei J, Xie H, Nai ML, Wong CK, Lee LC. Low temperature wafer anodic bonding. J Micromech Microeng 2003;13(217). DOI: 10.1088/0960-1317/13/2/308.
65. Dragoi V, Glinsner T, Mittendorfer G, Wieder B, Lindner P. Adhesive wafer bonding for MEMS applications. Proc SPIE 2003;5116:160–167.
66. Janting J. In: Leondes CT, editor. Techniques in scanning acoustic microscopy for enhanced failure and material analysis of microsystems, MEMS/NEMS Handbook. Springer; 2007. pp. 905–921.
67. Günther P, Fischer UC, Dransfeld K. Scanning near-field acoustic microscopy. Appl Phys B Lasers Opt 1989;48(1):89–94.
68. Mamin HJ. Thermal writing using a heated atomic force microscope tip. Appl Phys Lett 1996;69(433). DOI: 10.1063/1.118085.
69. Moulton T, Ananthasuresh GK. Micromechanical devices with embedded electro-thermal-compliant actuation. Sens Actuators A Phys 2001;90(1–2):38–48.
70. Trigg A. Applications of infrared microscopy to IC and MEMS packaging. IEEE Trans Electron Packaging Manuf 2003;26(3).
71. Zhao Y, Mao M, Horowitz R, Majumdar A, Varesi J, Norton P, Kitching J. Optomechanical uncooled infrared imaging system: design, microfabrication, and performance. J Microelectromech Syst 2002;11(2):136–146.

72. Cahill DG, Goodson K, Majumdar A. Thermometry and thermal transport in micro/nanoscale solid-state devices and structures. J Heat Transfer 2002;124(2): 223–242 DOI: 10.1115/1.1454111.
73. Christofferson J, Shakouri A. Thermoreflectance based thermal microscope. Rev Sci Instrum 2005;76:024903. DOI: 10.1063/1.1850634.
74. Mills G, Zhou H, Midha A, Donaldson L, Weaver JMR. Scanning thermal microscopy using batch fabricated thermocouple probes. Appl Phys Lett 1998;72:2900. DOI: 10.1063/1.121453.
75. Luo K, Shi Z, Varesi J, Majumdar A. Sensor nanofabrication, performance, and conduction mechanisms in scanning thermal microscopy. J Vac Sci Technol B 1997;15(2):349–360.
76. Goss LP, Smith AA, Post ME. Surface thermometry by laser-induced fluorescence. Rev Sci Instrum 1989;60:3702–3706. DOI: 10.1063/1.1140478.
77. Hassan I. Thermal-fluid MEMS devices: a decade of progress and challenges ahead. J Heat Transfer 2006;128(11):1221–1234. DOI: 10.1115/1.2352794.
78. Donnelly VM, McCaulley JA. Infrared-laser interferometric thermometry: A non-intrusive technique for measuring semiconductor wafer temperatures. J Vac Sci Technol A 1990;8(1):84–94.
79. Srikar VT, Swan AK, Unlu MS, Goldberg BB, Spearing SM. Micro-Raman measurement of bending stresses in micromachined silicon flexures. J Microelectromech Syst 2003;12(6):779–787.
80. Abel ML, Graham S, Serrano JR, Kearney SP, Phinney LM. Raman thermometry of polysilicon microelectro- mechanical systems in the presence of an evolving stress. J Heat Transfer 2007;129(3):329–335.
81. Serrea C, Pérez-Rodrígueza A, Morantea JR, Gorostizab P, Estevec J. Determination of micromechanical properties of thin films by beam bending measurements with an atomic force microscope. Sens Actuators A Phys 1999;74(1–3):134–138.
82. Osterberg PM, Senturia SD. M-TEST: a test chip for MEMS material property measurement using electrostatically actuated test structures. IEEE J Microelectromech Syst 1997;6:107–118.
83. Haque MA, Saif MTA. A review of MEMS-based microscale and nanoscale tensile and bending testing. Exp Mech 2006;43(3):248:255.
84. Ando T, Shikida M, Sato K. Tensile-mode fatigue testing of silicon films as structural materials for MEMS. Sens Actuators A Phys 2001;93(1):70–75.
85. Sharpe WN Jr, Yuan B, Vaidyanathan R. Measurements of Young's modulus, Poisson's ratio, and tensile strength of polysilicon. Proceedings of the 10th IEEE International Workshop on Microelectromechanical Systems; Nagoya, Japan; 1997. pp. 424–429.
86. Chasiotis I, Knauss WG. A new microtensile tester for the study of MEMS materials with the aid of atomic force. Exp Mech 2006;42(1):51–57.
87. de Boer MP, Knapp JA, Mayer TM, Michalske TA. Role of interfacial properties on MEMS performance and reliability. Proc SPIE 1999;3825(2).
88. de Boer MP, Mayer TM. Tribology of MEMS. MRS Bull 2001;4:302–304.
89. Corwin AD, Street MD, Carpick RW, Ashurst WR, Starr MJ, de Boer MP. Friction of different monolayer lubricants in MEMs interfaces. Sandia Report SAND2005-7954, Sandia National Laboratories, Albuquerque, CA; 2006.

CHAPTER 5

MICRO-LAYERED MANUFACTURING

AMIT BANDYOPADHYAY, VAMSI K. BALLA, SHELDON A. BERNARD, and SUSMITA BOSE
The School of Mechanical and Materials Engineering, Washington State University, Pullman, Washington

5.1 INTRODUCTION

Layered manufacturing technologies (LMTs) produce complex-shaped three-dimensional (3D) objects directly from a computer-aided design (CAD) model by successive addition of material(s) in a layer-by-layer fashion without the use of specialized tools, molds, or dies. These technologies also bridge the gap between product conceptualization and product realization and are reasonably fast. LMTs are also known as additive fabrication, solid freeform fabrication (SFF), and sometimes also called, in the industry, by the names of specific applications such as rapid prototyping (RP), rapid tooling (RT), and rapid manufacturing (RM). These technologies are relatively new and have been developed since the late 1980s. In the past, layered manufacturing (LM) applications were limited to the development of prototypes and casting inserts, since mechanical properties of parts and surface finish were inadequate for actual applications. However, with the recent advances in the field coupled with postprocessing, a variety of methods of production tooling, low-volume structural parts, customized implants and parts, architectural designs, archaeological replicas, and artwork in wider range of materials have been developed. To date, more than 40 LM processes have been developed and many more are under development. The basic paradigm is the same for all these processes, although specific process details can vary widely. In the process, a 3D CAD model of the object is first created and then decomposed into horizontal cross-sectional layer representations.

Micro-Manufacturing: Design and Manufacturing of Micro-Products, First Edition.
Edited by Muammer Koç and Tugrul Özel.

Then trajectories will be generated for guiding material additive processes to physically build/stack up these layers in an automated fabrication machine to form the 3D object. Similarly, all LM processes have similar features such as (i) arbitrarily complex 3D geometries can be built, (ii) automatic process planning based on a CAD model, (iii) no part-specific tooling is required, but a generic fabrication machine is used, and (iv) minimal or no human intervention is required. In terms of practical use, the application of LM can be organized into three separate categories:

- *Rapid Prototyping (RP).* molds, casting patterns, dies, medical modeling, etc.
- *Rapid Tooling (RT).* sharp tests for the products and materials, saves lead times (bridge tooling), and tools complex geometries (conformal cooling channels).
- *Rapid Manufacturing (RM).* manufacture of artifacts for end-use, low-volume production, for small series, complex geometries, customized products, and products that would not be possible otherwise.

The introduction of these technologies has opened up exciting new possibilities in product design, development, and manufacturing. The capabilities of LM for competitive usage for prototypes, tooling, and end-use purposes are being improved rapidly. Therefore, knowledge of these technologies and their effective application are vital for the manufacturing and design industry.

5.1.1 History

The conceptual foundations of LM lie in topography and photosculpture techniques dating back almost 150 years. These early technologies can be categorized as manual "cut and stack" approaches to building a freeform object in a layer-wise fashion. As early as in 1890, a layered method for making a mold for topographical relief maps was suggested by Blanther [1]. In the nineteenth century, photosculpture was developed to create 3D replicas of any object [2]. One somewhat successful realization of this technology was designed by Frenchman François Willème in 1860. Development of modern LMT started with a system proposed by Munz [3] in 1951 with the similar features of the present stereolithography process. In his process, a transparent photo emulsion is selectively exposed and fixed in a layer-wise representation of a cross section of an object. When the process is repeated, the final transparent cylinder contains an image of the object. Subsequently, the object is manually carved or photochemically etched out to create a 3D object. Later in 1968, parallel work on developing this technique was reported by Swainson [4] and Battelle Laboratories [5]. In 1971, Ciraud first proposed a successful LM process that has all the features of the modern LMT [6]. This process is essentially a powder deposition method with an energy beam. Figure 5.1 shows the historical development of LM and related technologies [7], and early parts produced by these techniques [8–10].

Topography & Photosculpture	
1860 – Willeme photosculpture	1951 – Munz patent
1890 – Blanther patent	1962 – Zang patent
1902 – Baese patent	1971 – Gaskin patent
1922 – Montheah patent	1972 – Matsubara patent
1933 – Morioka patent	1974 – DilMatteo patent
1937 – Perera patent	1979 – Nakagawa laminated tool
1940 – Morioka patent	
Modern LM Processes	
1968 – Swainson patent	1990 – Levant patent, Quadrax and DMEC founded
1972 – Ciraud patent	1991 – Teijin Seiki, Foeckele & Schwartze, Soliegn, Meiko, Mitsui founded
1979 – Housholder patent	1992 – Quadrax acquired by 3D, Kira and Laser 3D founded, First shipment by DTM
1981 – Kodama patent	1994 – Snaders prototyping started
1982 – Herbert patent	1995 –Aaroflex started
1984 – Maruntani, Masters, Andre, and Hull patents	1997 – AeroMet, Optomec, ZCorp started
1985 – Helysis founded and Denken venture started	1998 – Object founded
1986 – Pomerantz, Feygin and Deckard patents, 3D founded	1999 – POM founded
1987 – Fudim, Arcella patents, Cubital, DTM and Dupont's Somos founded	2000 – Helisys cloased and Solidica founded
1988 – First commercial shipment by 3D, CMET and Stratasys founded	2001 – 3D and DTM merge
1989 – Crump, Helsinki, Marcus, Sachs patents, EOS and BMP Tech. founded.	

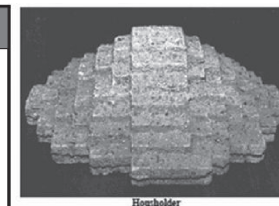
Housholder

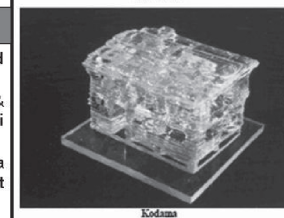
Kodama


Herbert

Figure 5.1 Historical development of layered manufacturing [7] (left) and parts produced by early LM techniques [8–10] (right).

The advent of CAD and programmable tools based on mathematical representations of 3D solids devised by Herbert Voelcker in 1970, and developments in several basic technologies such as lasers, materials, computing technologies, computer-aided manufacturing (CAM), between 1960 and 1980, have also been crucial in the birth of today's LMTs. In 1986, Charles Hull patented a breakthrough process, which he named "stereolithography," (SLA) for automated manufacture of accurate plastic prototypes, using an ultraviolet (UV) laser and photo-curable liquid polymers [11]. The process was commercialized in 1988. In 1987, Carl Deckard, a researcher form the University of Texas, came up with layer-based manufacturing processes for metals, wherein he printed 3D models by utilizing laser light for fusing metal powder in solid prototypes, single layer at a time and this process was named "selective laser sintering" (SLS). In the early 1990s, a number of new LM processes had been successfully commercialized, which included, laminated object manufacturing (LOM), solid ground curing (SGC), and fused deposition modeling (FDM). Early materials were primarily polymeric and ceramic and metal-based systems were developed later. In the mid-to-late 1990s, a major push was made in the area of generating tooling for injection molding and other mold-based mass-production processes, leading to the development of a number of processes that involved the use of an additively manufactured part somewhere in the process chain of making a tool.

Fabrication of functional metallic components was also recognized soon. Laser cladding-based metal fabrication technologies, laser and electron beam melting (EBM) of powder beds, and ultrasonic consolidation (UC) of metal foils were successfully commercialized in late 1990s. Current LMTs operate with an incredibly high precision and create novel designs/parts at a fraction of the expense of a full-scale manufacturing. In addition to creating the actual components for product testing, LM is used to produce display models using alternative materials. LM capabilities are becoming less and less of an exclusive domain of corporate organizations as lower-end LM systems are already within the financial range of committed individuals as the cost of LM steadily drops.

5.1.2 Process Steps

Basic fabrication processes used for making parts are of three types, namely subtractive, formative, and additive [12], as shown in Fig. 5.2. The subtractive process starts with a large single block of solid material and the material is removed at specific locations until the final desired shape is obtained. Subtractive fabrication processes include turning, sawing, drilling, milling, planning, grinding, electrical discharge machining (EDM), laser cutting, and water-jet cutting. An additive process is the exact reverse of subtractive process, wherein the material is manipulated and successive portions of it are combined to form the desired part. Also, in additive process the end product is much larger than the feedstock material. Majority of LM processes, welding, soldering, and brazing, fall under the additive fabrication processes category. Examples of formative fabrication processes include forging, press working, and injection molding, wherein a mechanical force is applied to a raw material to mold it into a desired shape. Hybrid machines combining two or more fabrication processes are also possible.

Although process details may vary from one LM process to another, all LMTs share common basic operating principles and process steps. Figure 5.3 shows the flow diagram of the basic processing steps, which are

- CAD modeling
- Data conversion

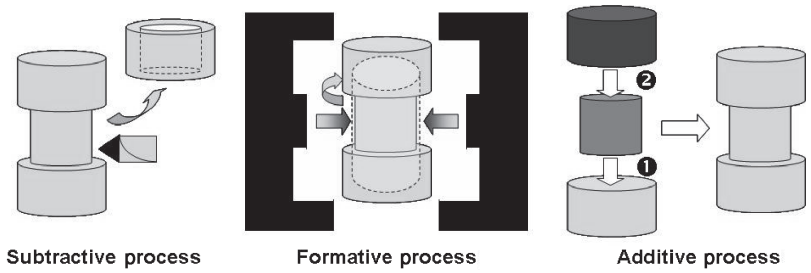

Figure 5.2 Basic fabrication processes.

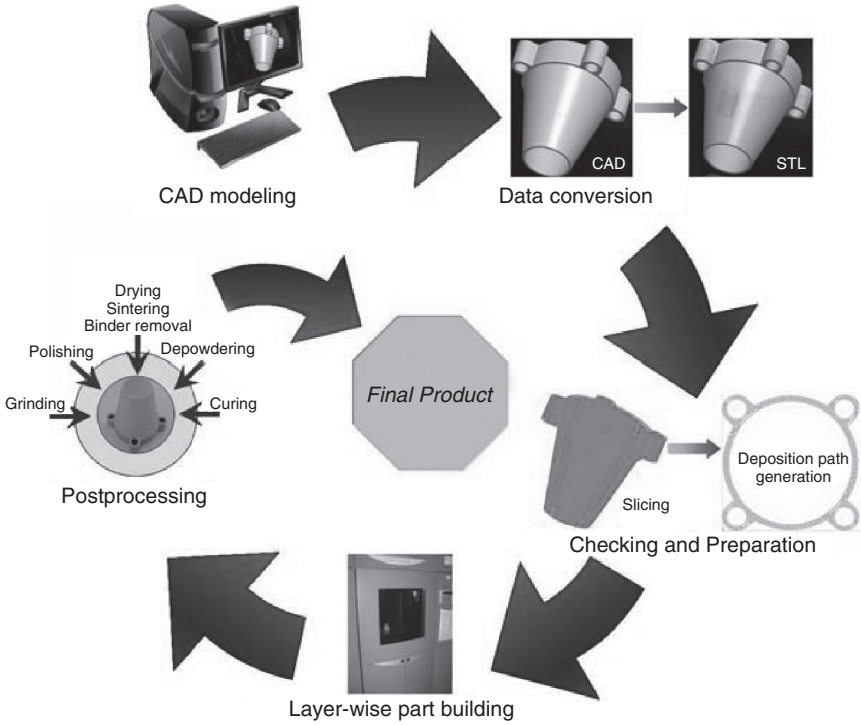

Figure 5.3 Basic processing steps in layered manufacturing. (A full color version of this figure appears in the color plate section.)

- Checking and preparation
- Layer-wise part building
- Postprocessing.

A number of iterations between processing steps 3 and 5 are required to achieve a satisfactory model or the final part. As with other fabrication processes, process planning is also an important step in LM processes. These five steps are discussed in the following sections.

5.1.2.1 CAD Modeling. Layered manufacturing requires 3D digital data describing a physical object as an input. Therefore, 3D CAD modeling is an important prerequisite for LM and is one of the most time-consuming steps. Many modern CAD or CAM systems can be used to generate the model. Off-the-shelf parts for which no technical data are available, data acquisition is made via reverse engineering using coordinate measuring machine (CMM) or a laser digitizer, to capture the data points of the physical model and reconstruct it in a CAD system. For LM, the CAD model must be a closed volume with surfaces and solids as basic elements. This ensures that all

horizontal cross sections, essential for LM, are closed curves to create the final solid object. Invariably, the final part produced by LM will be slightly different from that produced by the CAD model, depending on the LM process. Therefore, care must be taken in designing the part and in specifying the parameters for LM systems, to avoid poor utilization of the systems. For example, difficult-to-build structures such as thin walls, small holes/slots, porous scaffolds, overhangs, and supports have to be carefully considered during CAD modeling. Therefore, designers and LM system users must closely work with the systems to gain experience, with which they can utilize LM effectively. However, availability of many different commercial LM systems with different capabilities and requirements may pose some difficulties to CAD modeling or the designers.

5.1.2.2 Data Conversion. The 3D CAD model is then converted into *ST*ereo*L*ithography (STL) format, which has been conceived by 3D Systems, USA [13–15]. The STL format is industry standard because slicing a part, a next LM processing step, is easier with STL format. The STL format allows us to transfer the slicing operation into a routine of finding the interactions between lines and triangles. Besides, the format makes the process reliable and robust, and data processing tools to repair surfaces and STL files are readily available in the market. The STL file format approximates the surfaces of the model, using tiny triangles. A surface normal and a vector indicating the outward direction perpendicular to the triangle's surface represents the boundary of the solid model. Currently, almost all CAD/CAM systems have the CAD–STL interface and allow the user to adjust the maximum allowable deviation between the original CAD model and the STL model. The maximum allowable deviation depends on the desired feature resolution and the maximum STL size that a system can handle. As with any system, the STL format is also not free from inherent problems, which has led to the discovery of several new formats for LMTs [16]. Some of the proposed formats are StereoLithography Contour (SLC) [17], common layer interface (CLI) [14,18], rapid prototyping interface (RPI) [19,20], and layer exchange ASCII format (LEAF) [21]. A detailed discussion of these formats can be found in Chua *et al*. [16]. However, STL is still a dominant file format for LMTs.

Application of LM in medicine utilizes computerized tomography (CT) scan data to make models and customized implants, and some of the implants have been successfully implanted in patients. The CT scan data can be converted to models suitable for LM, using special CAD systems, STL-interfacing, and direct interfacing. The main advantage of using CT data as an interface of LM is its ability to make implants to suit specific sites and specific patients. However, a specialized software is required to process CT data.

5.1.2.3 Checking and Preparation. STL files generated from CAD models often suffer from various defects and contain no topological data. The defects may arise from errors in the CAD models and tessellation algorithms in the CAD–STL

interface. Typical errors include gaps (missing facets), overlapping facets, degenerate facets (all edges are collinear), and nonmanifold topology conditions [16]. These problems, if not fixed, can result in failure of subsequent operations on the models. Therefore, it is always necessary to perform model checks before it is being sent to LM systems for part building. Repairing invalid models is very difficult [20]. However, manual repair of defective models is now routinely being performed using specialized software such as MAGICS®, software developed by Materialise, N.V., Belgium [22]. Other possible solutions are provided in Chua *et al*. [16]. Once the STL files are made error-free, the LM system's software applies machine/process-dependant geometry corrections (such as shrinkage, distortions, postprocessing) to the STL files. Other LM process/machine-dependant setup steps to prepare STL files for actual part building include (i) part orientation, (ii) generation of support structures, (iii) slicing, (iv) selection of the deposition path and the process parameters, and (v) build layout.

Part Orientation. Also known as build orientation, part orientation is very important to achieving best part quality, reduction of build time, the support structures, and the desired final properties in different orientations. Because the parts are built layer by layer, the number of layers, decided by the height of the part, determines the total build time. Also, machine-dependent operations such as wide/narrow tool paths, calibration, and deposition head positioning contribute to the total build time. The extent and location of the support structures required for a model depends on part/build orientation. Depending on the materials and the LM processes, the final parts may show clear boundaries between each individual layers. These layer boundaries may result in anisotropy in properties when measured parallel or normal to the layers. Therefore, decision upon part/build orientation should consider part quality, support structures, build time, and strength anisotropy.

Generation of Support Structures. Not all LM processes require generation of support structures. For example, powder-bed-based processes, in which the loose powder bed supports the overhang features during the build process. Other processes, based on extrusion, often require support structures during part building to prevent slumping or sagging of overhang features. In general, LM systems come with system-specific software capable of automatic support-structure generation based on part orientation. The downside of these support structures is that they add to material cost, postprocessing time, and build time. However, minimum support structures are required to ensure best feature quality with reasonable build times.

Slicing. Generation of a series of closely spaced 2D cross sections, by intersecting a ray of virtual lines with the 3D object, of a 3D part is known as slicing. The STL file along with the support structures is sliced into thin, horizontal cross sections. The user can specify the layer thickness, usually between 0.05 and 0.5 mm. The surface finish in the Z-direction depends on slice/layer thickness, as the main error associated with slicing is the staircase error, as shown in Fig. 5.4. Staircase error can be minimized by

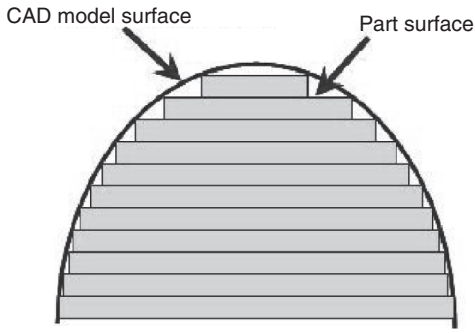

Figure 5.4 Staircase error.

smaller layer thicknesses, but at the expense of increased build time. New techniques such as "adaptive slicing" to minimize staircase error are under development [23].

Deposition Path and Process Parameters. After slicing, the user can decide how these cross sections are made. LM processes that use point- or line-based deposition heads, for example FDM, require creation of a deposition path that the machine will use to build each layer. An internal crosshatch structure is generated between the inner and the outer surface boundaries of the part. Support structures are generally created using coarser settings. The deposition path allows the user to achieve the desired part strength, build time, and surface finish. Important variables include orientation, deposit width, and the distance between deposits. For other processes, the build file is created with an appropriate choice of build/technological parameters, which may include cure depth, laser power, drying time, drying temperature, and other physical parameters. The cross sections created thus are systematically built, typically fully automatic and unattended, and then combined to form a 3D object.

Build Layout. LM can build multiple parts concurrently in one operation, and to fully utilize this capability, one should carefully consider the placement of parts in the overall build layout, which can significantly affect the overall efficiency of the process. It is generally desirable to arrange parts in such a way that the uppermost parts in a build end at the same Z height, as this offers the greatest operational efficiency. The number of identical parts that can be built is subject to the overall build size constrained by the build volume of the LM system.

5.1.2.4 Layer-wise Part Building. For most LM systems, this step is fully automated and can run almost without human intervention. Building time can vary from few hours to few days, depending on the size and the number of parts. Figure 5.5 shows typical parts built using different LM machines at Washington

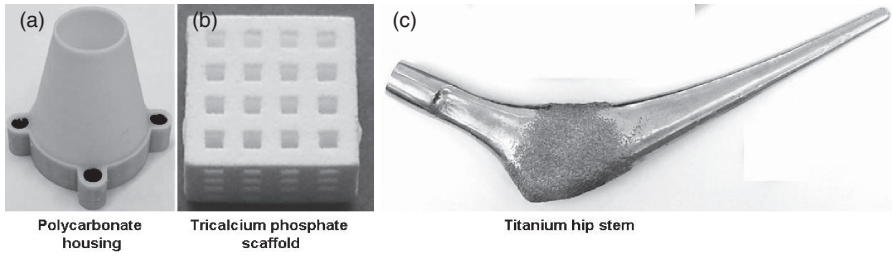

Figure 5.5 Typical parts built using different LM machines at WSU (a) fused deposition modeling (FDM-TITAN, Stratasys), (b) 3D printing (Imagene, ExOne), and (c) laser-engineered net shaping (LENS, Optomec).

State University (WSU), Pullman. The support material, shown dark in Fig. 5.5a, has to be removed from the parts produced using FDM. The method of support material removal can be different for different LM systems. For example, some processes require simple tools to breakaway the supports, some supports can dissolve in water, some require grinding, and others can melt at low temperatures. Part building details vary from process to process and application dependant, and are discussed in detail in the subsequent sections of this chapter.

5.1.2.5 Postprocessing. Generally, at the final stage some manual operations with possible part damage are required. Therefore, utmost care has to be taken in postprocessing. As with part building, the details of postprocessing also vary from process to process and are discussed later. However, mandatory post-processing steps required for some layered manufacturing systems are listed in Table 5.1. Cleaning refers to removal of excess materials from the part inside and outside. For example, this refers to removing excess powder from SLS parts. Similarly, resin residing in the holes and supports has to be removed from the parts produced via stereolithography (SLA). Table 5.1 indicates that SLA requires highest number of postprocessing tasks. Also, the cleaning of SLA parts requires special recommendations for safety reasons. It has been reported that accuracy is closely related to the postprocessing treatments [24]. The final finish needs secondary processes such as additional machining, milling to add the necessary features to the parts, and sanding and painting to improve the appearance of the parts.

TABLE 5.1 Essential Postprocessing Steps for Some LM Technologies

Postprocessing	Selective Laser Sintering (SLS)	Stereolithography (SLA)	Fused Deposition Modeling (FDM)
Cleaning	Required	Required	Not required
Postcuring	Not required	Required	Not required
Finishing	Required	Required	Required

Considering the numerous details involved in preparing the necessary input for LM systems, proper documentation of all the geometrical and process details is extremely important.

5.1.3 Advantages of Layered Manufacturing

Product design, concept realization/testing, product and material development, and product manufacture can benefit from LMTs. The first direct benefit is its ability to fabricate geometrically complex/intricate parts in a straightforward manner and in a relatively short duration. Some LM processes allow us to produce parts with different materials at different locations to meet site-specific service requirements. In industry, the application of LM has been categorized into three major groups and the specific advantages of LM in each group are summarized below.

5.1.3.1 Rapid Prototyping (RP). Advantages of making a prototype of a new design prior to actual production are very well established [16,25,26]. The most significant benefit is savings on cost and time in the product development/improvement cycle, as these technologies can produce parts quickly and inexpensively. Savings on time and cost could range from 50% to 90%, depending on the size of production. Without significantly affecting the cost of lead time, part design, size, and features can be optimized to meet customer requirements. Profits can be realized earlier on new products as fixed costs are lower. Marketing as well as the customers can also benefit from the utilization of RP technologies. RP is useful also in styling and product ergonomics. For example, products such as a helmet, breathing apparatus, and driving masks require trial and error to ensure best fit and comfort, and thus RP will provide immediate feedback to accelerate the development process. Layered manufacturing techniques are powerful tools to take a right and quality product to the market sooner. Product visualization, communication, and functional/performance testing are also possible with RP.

5.1.3.2 Rapid Tooling (RT). Instead of making an RP part, LMTs can also be used to make the mold that can be used to make a tool using other processes. For example, an investment casting mold can be directly made from a thermal plastic model. These technologies can be used to make various kinds of tooling instruments such as dies, mold inserts, conformal cooling channels in an injection molding tool, and other complex tool geometries, which are not possible with any other techniques. Other benefits include the speed of fabrication and the ability to fabricate tools from multiple materials, which can potentially increase the productivity by 25–50%.

5.1.3.3 Rapid Manufacturing (RM). LMTs are increasingly used to make functional parts via direct or indirect methods. The indirect method makes a negative mold of the part to be built using other processing techniques. Examples

include patterns to make molding and die-casting for volume production. In this way LMTs can be indirectly used to fabricate functional parts with metals, ceramics and other materials. Direct fabrication of functional parts is also feasible using latest LMTs such as direct metal deposition (DMD), laser material deposition (LMD), and hybrid RM processes combining laser deposition and machining. Since the processes can produce complex parts, design restrictions based on manufacturability are completely eliminated with additional cost and time savings involved in tool making. Customized products to suit individual customers can be easily fabricated, which significantly benefit the implant manufacturing area. Advanced materials and other composite materials that are difficult to process can be easily utilized to make functional end-use parts. Finally, heterogeneous and functionally graded parts can be built without much difficulty.

LMTs are being used also to repair worn or defective metallic components by depositing precise amounts of materials at desired locations. It is also possible to add features to existing parts. This allows efficient unification of LM capabilities and conventional processing techniques for efficient material utilization and economical part production. Effective usage of LM for prototyping, tooling, and end-use purposes depends on a complete understanding of these technologies.

5.2 LAYERED MANUFACTURING PROCESSES

5.2.1 Classification

Layered manufacturing processes are characterized by great miscellany in terms of feedstock form, basic principle, and the process by which the part is built. Numerous LM processes available in the market can be classified in many ways and here the major LM processes are classified according to the fundamental process by which the part is built, as shown in Fig. 5.6.

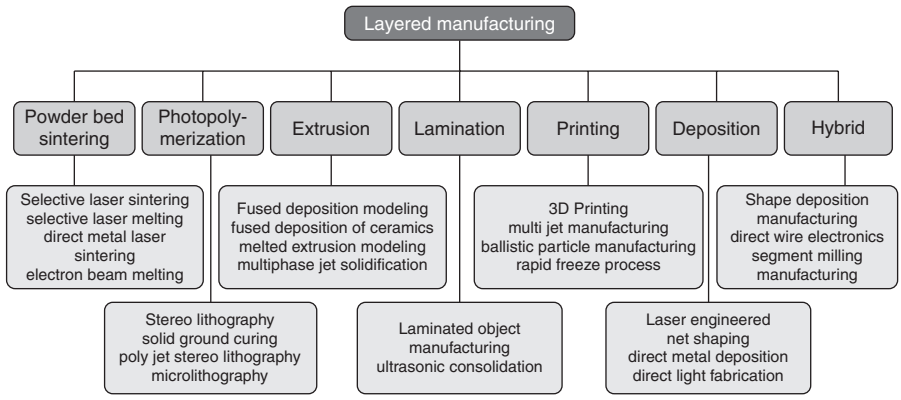

Figure 5.6 Classification of layered manufacturing processes.

5.2.2 Process Details

Various vendors of LM machines offer different machine-specific details for the same LM process. In this section, only process-specific details are emphasized.

5.2.2.1 Powder Bed Sintering/Melting Processes. The technology of powder bed sintering/melting processes, using a laser to bond powdered materials into a solid part, was developed at the University of Texas at Austin, USA, in 1989. This process, also known as SLS, was originally developed to create plastic parts using thermoplastic powdered materials because of their low melting temperatures, and the principle was later extended to metallic and ceramic powders. Currently, the SLS technology and machines are commercially available from 3D Systems, USA and EOS GmbH, Germany.

In SLS, parts are built by focusing a fine laser beam onto a thin layer of loose powder bed, which sinters/melts the particles with one another and with the previous layer to form a solid layer. Then, the next layer is directly built on top of this solid layer after another thin layer of loose powder bed is deposited. The SLS process starts with deposition of a thin layer of fusible powder onto a platform in fabrication chamber, using a counter-rotating roller. The first cross-sectional slice of the CAD object is precisely drawn/scanned on this preplaced powder layer by a finely focused laser beam under the guidance of an X–Y scanner system. A schematic of a typical powder bed sintering process is shown in Fig. 5.7. The heat generated due to the interaction between the laser beam and the powder material is controlled to melt the powder to form the solid slice cross section (Fig. 5.7a, right). The surrounding material remains loose and serves as a built-in support for subsequent layers and overhang structures in the object. After completing the first cross section, the build platform is lowered one layer/slice thickness (typically 0.1 mm) to accommodate the powder for the next layer. Feed piston in the powder delivery system is moved up by one layer thickness and

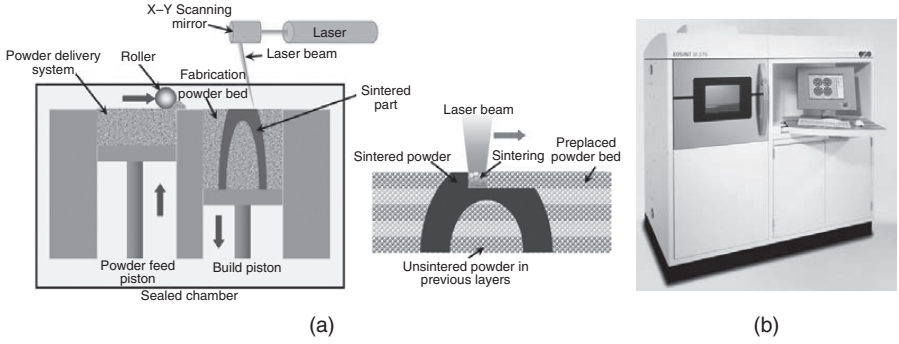

Figure 5.7 Powder bed sintering process (a) Schematic showing various components of SLS (left) and layer-by-layer sintering process (right) (b) Commercial SLS unit. *Source:* courtesy EOS GmbH

the powder is deposited and leveled on top of the previous layer in the build platform, using a roller mechanism preparing the next layer for sintering. These steps are repeated and successive layers are fused together to form a 3D object represented by the CAD model.

The fabrication chamber is sealed and maintained in an inert atmosphere, which prevents oxidation and contamination of the final parts and explosion of the loose powder. Once the building process is complete, the parts are allowed to cool in the chamber and the excess powder is brushed away, and the final finishing operations may be carried out depending on the application of the part. As the sintering process requires high amount of heat, the energy required during SLS of similar layer thickness is approximately 300–500 times higher than that required for photopolymerization process [27,28]. To minimize the laser power requirements of the process and to prevent warping of the parts, the powder beds are maintained at temperatures just below the sintering/melting temperature of the power, using auxiliary heaters [29]. The performance and the properties of the final parts produced by SLS depend on various process parameters such as laser parameters (power, spot size, pulse duration, and frequency), powder characteristics (size, shape, size distribution, and packing density), scan parameters (layer thickness, scan spacing, and travel speed), and temperature-related parameters (powder bed temperature and chamber temperature) [29]. It is important to understand the interdependency and interactive influence of these parameters on part quality. For example, the required laser power increases with increasing melting point of the material, but decreases with the laser absorption capacity and the particle size of the material. To maximize the surface finish, mechanical properties, and dimensional accuracy of the parts, powder characteristics, laser power, scan speed, and powder bed temperatures are to be carefully balanced. Several studies [30–39] have been performed focusing on the influence of the parameters involved in laser sintering on the properties of the final parts. Also, the process does not require support structures, as overhangs and undercuts are supported by the solid powder bed, which considerably reduces the build and cleaning cycle times compared to other LM processes. However, finer particle sizes (typically below 20 μm) pose problems in terms of spreading and handling, although they produce more accurate and smoother parts.

Conceptually, SLS is the only technology that offers the capability to directly process a wide variety of engineering materials, including thermoplastics, metals/alloys, ceramics, and their composites. Depending on the materials being processed, the basic bonding methods in a powder bed process can be categorized into two groups, namely direct and indirect methods. In direct method, the powder bed consists of either single or two components [40]. In the single-component direct method, the powder material is directly fused and sintered together using a high-power laser beam. This method is widely used to process majority of polymeric materials/composites and some low-melting-point metals/alloys. In this case, sintering occurs as a result of incipient melting and solidification of powder particles, whereas in conventional sintering, the bonding occurs predominantly by solid-state diffusion. The two-component method consists of a mixture of two

metal powders, one with a high melting point constituting the main structural part and the other with a low melting point acting as a binder. The laser energy is modulated to ensure complete melting of the low-melting constituent only, which fills the pores between the high-melting-point solid powder particles, resulting in a dense product upon solidification. This process is similar to classical liquid phase sintering and is used to fabricate high-melting-point metallic parts. The two-component indirect method uses a polymer-coated metallic/ceramic powder or a dry mixture of polymer and metallic/ceramic powder as a feedstock. The polymer melts and binds the particles together during laser irradiation and the ceramic/metallic powder remains virtually unaffected by the laser heat. Because of the polymer binder, the parts are usually porous and require subsequent debinding/infiltration with a metal to produce dense parts. This process is best suited for making ceramic parts, as majority of the ceramic materials are not suitable for direct melting.

Several processes have been developed on the basis of the powder bed sintering/melting principle exclusively to produce direct functional metallic parts, as the presence of low-melting-point components in the parts, produced by direct or indirect two-component methods discussed above, is detrimental to their physical, mechanical, and chemical properties. Processes developed for direct metallic component fabrication include selective laser remeling (SLM) developed at Fraunhofer Institute for Laser Technology, Aachen, Germany, direct metal laser sintering (DMSL), and EBM developed at Chalmers University in Sweden in the 1990s and commercialized in 2001 by Arcam AB, Sweden. All these processes use significantly high-power lasers, the latest X–Y scanning technologies, and precise atmosphere controls. EBM uses a focused electron beam as the heat source in place of a laser beam. The kinetic energy of the projected electron, at half the speed of light, on the powder bed induces melting. As in SLS, the electron-beam gun initially preheats the powder layer to reduce the distortion in the final parts. Then the preheated layer is selectively melted at high beam power or by decreasing the travel speed. Some of the advantages of EBM over SLS include high energy efficiency, high-quality melts, high vacuum to eliminate impurities, ability to process refractory and dissimilar metals, and rapid beam manipulation and movement (in place of part movement). Some disadvantages include requirement of high vacuum and electrically conductive materials, and production of γ rays during processing. So far, EBM has been extensively used to create a wide variety of complex structures, using pure Ti and the Ti-6Al-4V alloy [41–45]. Laser sintering process has been used to create structures, using a wide range of metallic, polymer, ceramic, and composites powders [46–56].

5.2.2.2 Photopolymerization Processes

5.2.2.2.1 Stereolithography. The Stereolithography process is the first commercialized LM process developed and patented by Charles W. Hull in 1986. Stereolithography is still regarded as a benchmark by which other technologies are judged. The process works on polymerization of a photo-curable liquid resin—a polymer that solidifies as a result of electromagnetic irradiation, layer

by layer to develop 3D objects. Many types of liquid photopolymers are available that can be solidified by exposure to electromagnetic radiation, including γ rays, X-rays, electron beam, UV, and visible range [57]. However, majority of photo-curable polymers used in commercial SLA systems are curable in the UV range. There are a wide variety of photosensitive polymers containing fillers and other chemical modifiers to meet the desired chemical and mechanical requirements. Although the basic SLA process is the same, commercial SLA machines have wide variation with respect to the photopolymerizable materials, type of radiation, method of exposure or scanning, and other aspects. Several companies offer SLA machines and the most popular is 3D Systems, USA.

In SLA processes, the photopolymer is cured point by point, line by line, and layer by layer on a build platform in a vat filled with a photo-curable liquid resin, as shown in Fig. 5.8. The process takes place at room temperature and does not require any controlled atmosphere. The process begins with the elevator setting the build platform just below the surface of the liquid resin. The computer-controlled X–Y scanning mirror then directs the focused laser beam on the surface of the photo-curable liquid resin to polymerize, forming a solid two-dimensional cross section corresponding to the first slice represented in a CAD model of the object. The laser beam causes the polymer to harden precisely at the point where the light hits the liquid polymer surface. The build platform is then lowered by an elevation control system to cover the first solid layer with another layer of liquid resin and a leveling sweeper moves across the surface to recoat the next layer of resin on top of the previously cured layer. The laser beam then scans the surface of the liquid resin according to the next slice cross section, forming the next layer of the part. This process continues building the part in a bottom-up fashion, until the system completes the part represented by a 3D CAD model.

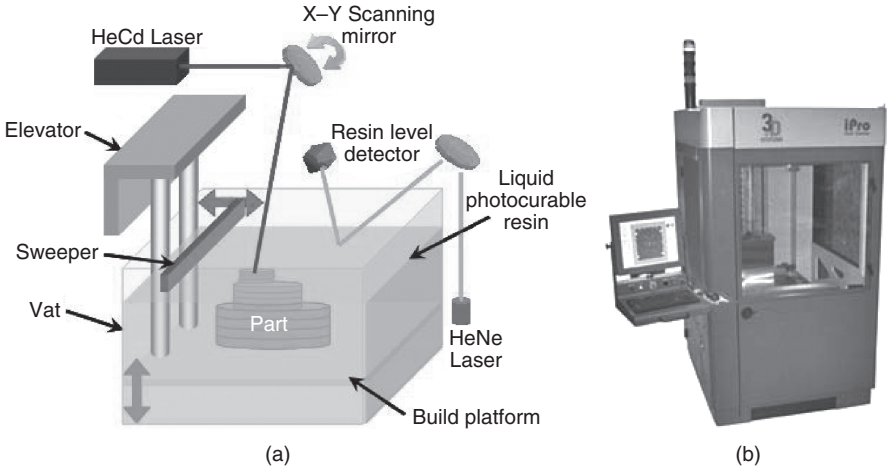

Figure 5.8 (a) Schematic of stereolithography process, (b) Commercial SLA unit. *Source:* courtesy 3D Systems, Inc.

The part is then raised out of the vat, cleaned of excess polymer and support structures, and then placed in a UV oven for complete curing. Depending on the part geometry, the process builds support structures simultaneously with the part.

The key strength of SLA is its ability to rapidly direct focused radiation of appropriate power and wavelength onto the surface of the liquid photopolymer resin [58]. The beam is focused on the surface of a liquid photopolymer, curing a predetermined depth of the resin after a controlled time of exposure (inversely proportional to the laser scanning speed). To ensure scan-to-scan and layer-to-layer bonding during part building, the cure depth and the cured line width must be controlled. Exposing the liquid polymer to a threshold with an appropriate focused spot size is essential. Typically, the cure depth of the laser must be slightly more than the layer thickness. Layer thickness typically varies between 0.025 and 0.5 mm and is user defined. Early SLA processes produced parts that were fairly brittle and prone to distortion and warpage during curing. However, recent advances in the technology have largely eliminated these problems. Also, recent machines are equipped with high-power soli-state or semiconductor lasers with adjustable beam size to accelerate the building process. The process can achieve excellent surface finish and good dimensional accuracy on the order of ± 100 μm. Some commercial systems (E-Darts, Autostrade Co. Ltd., Japan, and COLAMM, Mitsui Zosen Corp., Japan) build parts on an ascending platform, using a laser light transmitted through a transparent window at the bottom of the resin chamber.

For various applications, a wide range of photo-curable resins are commercially available with varying physical, chemical, and mechanical properties. These can be classified as epoxy-, vinylether-, and acrylate-based resins. Acrylics cure about 75% and 80% when exposed to UV light and epoxies continue to cure once the polymerization is initiated by the light. Acrylate resins generally exhibit higher viscosity and higher curl distortion. Epoxies and vinylethers exhibit almost negligible curling tendency and superior mechanical properties, and are therefore considered more suitable for most prototyping applications. Desirable characteristics of a photo-curable liquid resin include high photo speed, good wettability with the cured resin, low viscosity and shrinkage, low curling tendency, long shelf life, and good mechanical properties. Parameters that influence performance and functionality of SLA-processed parts are the physical and chemical properties of the resin, the power, spot size and wavelength of the laser, the speed and resolution of the optical scanning system, layer thickness, the recoating system, and the type of postcuring process. Also, cure depth and cured line width must be controlled, which are a function of laser power, spot size, and scan speed. A number of studies are available describing the parameter effects [59–63].

Postprocessing steps include solvent cleaning; removal of support structures; postcuring in UV oven; and finishing operations such as sanding, milling, polishing, and bead-blasting. Infusion of liquid monomers into the semicured part results in swelling and therefore, the parts must be removed from the vat as soon the building process is complete. A matter of concern in SLA is that the parts

usually have some uncured regions, as a result of the cone features generated by the laser during curing process, and require a postcuring process. Also, the postcuring usually results in shrinkage leading to dimensional changes and distortion in the parts [58]. Concept models and prototypes for design verification and form and fit issues are generally made using SLA. Rarely, the process is used to make prototype tooling and low-volume production tooling. The SLA areas of applications are restricted by the properties of the given material. End-use metal parts can be produced through investment casting and sand casting processes using patterns fabricated from these processes. The main limitation of SLA is that only photo-curable resins are usable for part construction, which are expensive and some of which exhibit bad odors and are toxic. Another disadvantage is that the parts with enclosed and hollow structures are trapped in the resin.

5.2.2.2.2 Solid Ground Curing. SGC is developed and commercialized by Cubital Ltd., Israel in 1991. This process has the advantage of curing the entire layer of a photo-curable resin at a time, which overcomes the speed limitation of SLA, where a point energy source is used for curing. SGC uses several kinds of liquid and cured resins to create objects. A water-soluble wax is used to create support structures and ionographic solid tones are used to create an erasable image of the computer-generated cross section on a glass mask. SGC consists of two main steps namely mask generation and layer fabrication, which are repeated a number of times to complete the part. In the mask generation step, the first cross-sectional image of the part is generated on a transparent substrate (glass mask) by ionographic printing process, a technique similar to photocopying. The image is formed by depositing a black electrostatic toner that adheres to the ion-charged portions of the substrate. This is used to mask the uniform illumination of the collimated UV lamp. Figure 5.9 shows the various stages of the SGC process.

The layer fabrication stage starts with spraying a photosensitive resin on the build platform as it passes under the resin application station. Then the build platform is transferred to the UV light curing station, where the photo mask

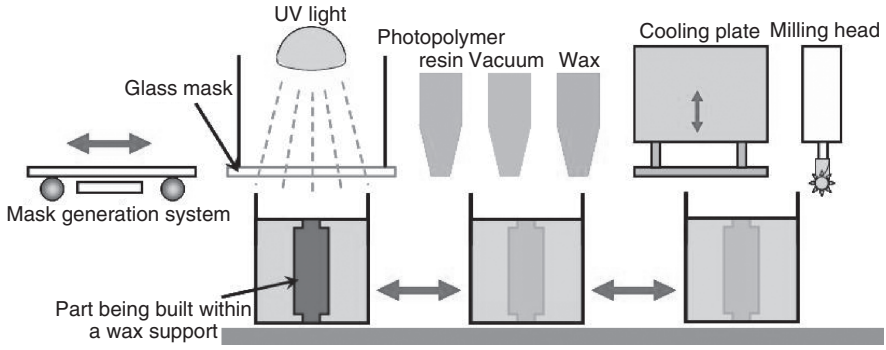

Figure 5.9 Schematic of solid ground curing (SGC) process.

from the mask generator is placed above the build platform and aligned under UV light. A shutter is opened allowing the photosensitive resin layer to be exposed to UV light through the photo mask. When UV light is passed through this glass mask onto the liquid resin, the resin is polymerized wherever light is allowed to pass. The surrounding unexposed resin remains liquid, which is removed using a vacuum. The glass mask is cleaned and a new mask is generated on the plate for the next layer. Molten wax is spread into the empty space created after collecting the unsolidified resin and the wax is solidified under a cooling plate. Then the surface of the layer is milled to its exact thickness. This step also produces a roughened surface of cured photopolymer, assisting adhesion of the next layer to it. A new layer of photopolymer is then applied to this milled surface and the cycle is repeated until the object is completely formed within a wax matrix. As each layer is surface milled before generating a new layer, the SGC process facilitates a high degree of accuracy in the Z direction. The process is self-supporting and does not require external support structures as continuous structural support for the parts is provided by the wax. The supporting wax is melted away or dissolved during postprocessing.

In contrast to SLA, the SGC process is considered a high-throughput production process and the high throughput is achieved by hardening each layer of the photosensitive resin at once. Multiple parts can be created simultaneously on the sample platform because of the large work space and the milling step maintains vertical accuracy. Because the parts are completely cured during the build process itself, no postcuring is necessary and associated shrinkage, warping, and curling problems are completely eliminated in SGC. The process lacks widespread market acceptance because of high acquisition and operating costs and the complex nature of the process requiring skilled workers to monitor. However, the benefits of this process have been utilized in other photopolymerization processes by simplifying the fabrication procedures. One such process is Objet's polyjet process—a hybrid of material printing and stereolithography, developed by Objet Geometries, Inc., Israel. The process uses printing technology to deposit supports and build material combined with UV-curable materials. As shown in Fig. 5.10, the machine consists of a multinozzle print head that slides back and forth along the X-axis and deposits a thin layer of liquid polymer resin onto a build platform according to the slice information. Immediately after deposition, a UV bulb fitted to the print head emits UV light, which cures and hardens each layer. The internal build tray moves down and the print head begins building the next layer. Support structures are printed and cured simultaneously using a different gel-like photopolymer that is water soluble. As with SGC, this process requires no postcuring. Similar technology has since been introduced by 3D Systems as part of their InVision line of 3D Printers.

5.2.2.2.3 Micro-Fabrication. In micro-fabrication, several processes have been developed over the last few years whereby miniature objects are built using lamps, lasers, and X-ray as energy sources [64–66]. The parts built by these processes are highly complex and typically less than 1 mm in size.

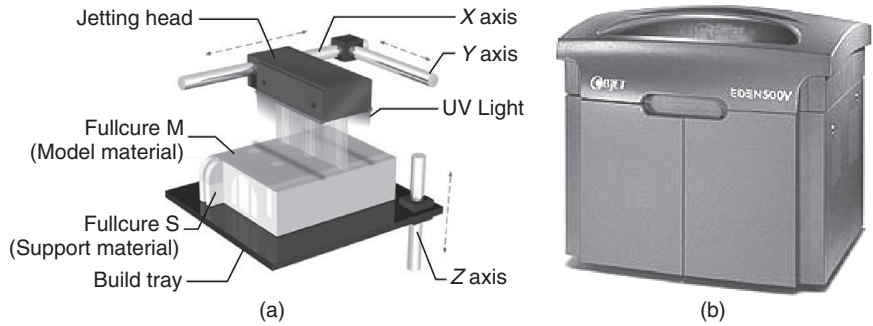

Figure 5.10 (a) The Objet PolyJet process and (b) actual machine. *Source:* courtesy Objet, Inc.

These processes are known as micro-stereolithography (μSL) processes. The μSL technique differs from conventional SLA method in that the focus point of the laser beam remains fixed on the surface of the resin, while an $x-y$ positioning stage moves the build platform on which the part is made. One μSL process has been commercialized by Micro-TEC GmbH, Germany. Their machines use a He–Cd laser and are capable of constructing small parts with layers as thin as 1 μm, with submicron precision and a feature definition of less than 10 μm. μSL processes are widely used for building micro-parts in micro-mechanics, micro-biotics (micro-actuators), micro-fluidics, and bone scaffolds using polymers, ceramics, and composites [67–74]. The fabrication of micro-ceramic parts uses homogeneous ceramic suspensions of monomer, photoinitiator, dispersant, dilutents, etc. The green body ceramic micro-parts are then postprocessed by binder burnout and sintering to obtain fully dense ceramic parts.

5.2.2.3 Extrusion-Based Processes. Unlike photopolymerization processes, where the feedstock material changes from liquid into a solid final object, the extrusion-based processes use materials in a solid form, which are melted, extruded, and then deposited into a desired shape. Extrusion-based processes were originally developed for making plastic prototypes and currently these processes have also been used to make functional metallic and ceramic parts. There are three commercial systems available in this group: (i) FDM, (ii) multiphase jet solidification (MJS), and (iii) melted extrusion modeling (MEM). The FDM process was originally developed by Advanced Ceramics Research (ACR) in Tucson, Arizona, and the technology has been significantly developed by Stratasys, Inc. USA. MEM was jointly developed by Beijing Yinhua Co. Ltd., China, and Tsinghua University, China. The unique advantage of MJS is that it can be used to produce metallic or ceramic parts. The process uses low-melting-point alloys or a powder-binder mixture that is melted and extruded through a computer-controlled nozzle to build the parts layer by layer. The Fraunhofer Institute for Applied Materials (IFAM) Research and

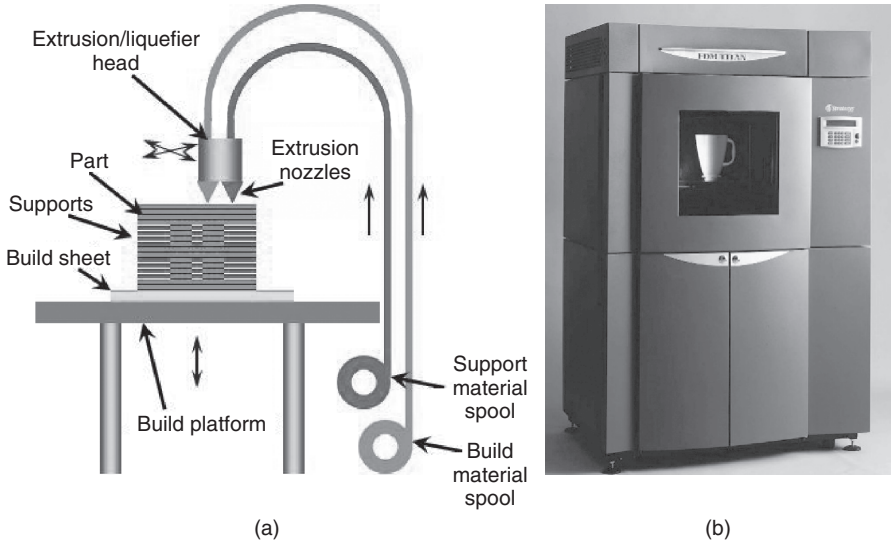

Figure 5.11 (a) Fused deposition modeling process and (b) Stratasys FDM Titan. *Source:* courtesy Stratasys, Inc.

the Fraunhofer Institute for Manufacturing Engineering and Automation (IPA) joined together in developing MJS. Extrusion-based processes are currently the best-selling processes for prototyping applications especially FDM machines by Stratasys, Inc.

FDM fabricates parts by extruding molten thermoplastic material through a small nozzle to form a thin "road" in a predetermined pattern on a build sheet to complete the part layer by layer. The machine uses specialized software to create user-defined tool paths and automatic support structures. Different materials are used for support structures and building the part. A schematic of the FDM process is shown in Fig. 5.11.

The process starts with feeding the extrusion head (or the liquefier) with a thin filament of build material (typically ϕ 1 mm) by a roller mechanism. The filament is then heated to a semiliquid state, then extruded through a nozzle, and deposited on the build sheet as per the tool path in the $X-Y$ plane. The solid filament is used as a linear piston to extrude the material. The surrounding air in the build envelop is maintained at a temperature below the build/support materials' melting point and the extruded material quickly solidifies and bonds to the previous layer and the adjacent roads. The build chamber temperature control is very important as it keeps the material already deposited warmer and ensures efficient interlayer and inter-road bonding, which decides the mechanical strength of the part. When the layer is completed, the build platform is lowered precisely to maintain the constant standoff distance between the working surface and the extrusion tips. The support and build materials are extruded using separate tips. The build process deposits both the build and support materials in separate steps for each layer at a

time. During switching between the build and support materials, one nozzle will rise up so that it will not interfere with the material being laid down. The width of the extruded material called "road width" can be controlled by the feed rate of the filament. The layer thickness typically varies between 0.1 and 0.5 mm and the road width between 0.25 and 2.5 mm. In some extrusion designs, with the same basic operating principle of FDM, liquid-based slurries and other precursor materials can be used in place of thermoplastic materials. The support structures are removed during postprocessing, which are either mechanically removed or dissolved in a water-based solvent.

FDM uses a wide range of thermoplastic build materials including acrylonitrile butadiene styrene (ABS), polycarbonate (PC), polyphenylsulfone (PPSF), investment grade waxes, polyolefins, polyamides, elastomers, nylon, and various versions of these materials to meet various application requirements. These materials are also available in different colors. The most popular materials are PC, a high-performance plastic, and PPSF, a high-performance plastic with excellent chemical resistance, strength, and rigidity, typically used for medical applications. A bioresorbable polymer poly(ε-caprolactone) (PCL) has also been developed and used in FDM processes for tissue engineering applications [75]. Various metallic and ceramic materials have been used to create fully dense and tailored porosity functional parts, using FDM [76–80]. Normally, when working with metals and ceramics, separate extrusion heads with heater settings, drive mechanisms, and nozzle diameters are used. Important process parameters that affect the performance and quality of the parts are road width, deposition speed, nozzle tip diameters, filament feed rate, liquefier temperature and material viscosity, chamber temperature, standoff distance, positioning accuracy, build material properties, and part geometry. Several investigations show the importance of these parameters [81,82]. FDM has been extensively used to create designed, micro- and macro-structured 3D porous structures. By changing the deposition angle in each successive layer and the spacing between the material roads, parts with controllable pore morphology, size and connectivity, and complex internal structures can be produced [75,79]. Similarly, 3D honeycomb ceramic structures with precisely controlled pore size, volume, and geometry have been produced using a sacrificial wax mold [80]. The extrusion-based process produces parts for functional/concept models for almost every industry, including automotive, aerospace, business, medical, consumer products, and architecture. The advantages of the extrusion-based process include easy-to-use, cost/time-effective, relatively inexpensive materials, and in some cases its water-soluble support material. Important concerns are limited materials, wavy surface finish, limited size, and unpredictable shrinkage of thermoplastics, leading to part inaccuracies. Appropriate shrinkage compensation factors [83] and optimized deposition strategies [84] are necessary to achieve high dimensional accuracy. The wavy surface finish of the parts results from the elliptical nature of the material road and the surface finish can be improved by using thinner layers and small nozzle sizes. The total build time depends on the volume of the part being built and the support structures.

MEM works on the same basic principle as that of FDM, where the extruded build material is deposited on a build sheet, using a three axis ($X-Y-Z$) controlled extrusion head. The extrusion head is capable of moving upwards between the layers, which gives added capabilities. The MJS process uses low-melting-point alloys or a powder-binder mixture, which is melted and extruded to build the part in a layer-by-layer fashion [85]. In MJS, the feedstock material is in the form of a mixture or liquefied alloy and therefore, the feeding and nozzle systems are somewhat different from those of FDM. The material mix consists of 50% low-viscosity wax and 50% metal or ceramic powder. Initially, the feedstock is heated to a semisolid state in a confined chamber and is then squeezed through a computer-controlled nozzle by a high-pressure pumping system, and deposited on a platform layer by layer [85]. The extruded material solidifies as it is deposited on the previous layer because of heat conduction. The bonding between the layers is achieved by partial remelting of the previous layer during deposition of a fresh layer of the liquefied material. The main components of MJS are personal computer, a computer-controlled positioning system, and a heated chamber with a jet and a hauling system. The extrusion temperature of the molten material can reach up to 200°C and extrusion orifices vary from 0.5 to 2.0 mm. Important process parameters include layer thickness, feedstock material (liquefied alloys or powder-binder mixture), chamber pressure, build speed, jet specification, material flow, and operating temperature. So far, the process has been used to create functional parts for various industries (automotive, aerospace, biomedical, and machine tools) from silicon carbide, stainless steel 316L, titanium, alumina, and bronze powder.

5.2.2.4 Sheet Lamination Processes. LOM is a sheet lamination process in which 3D objects are constructed by sequentially laminating the part cross sections represented by a computer-generated slice. The process was developed by Feygin in 1985 and the first LOM machines were manufactured in 1991 by Helisys, Inc. USA (currently Cubic Technologies, USA). In this process [86–88], layers of sheet materials such as paper, plastics, or composites are attached to a stack and cut using a laser according to the one cross-sectional layer of the part. Later, several processes have been developed using this principle, but with different laminating/cutting methods and build materials. Some processes use glues/adhesives for bonding the laminated sheets together, while others use welding or brazing techniques. The sheet laminating processes can be classified into to two groups (i) processes that first bond the laminates to the substrate and then form the desired shape ("bond-then-form" processes) and (ii) processes that form the shape in each laminate and then bond it to the substrate ("form-then-bond" processes).

5.2.2.4.1 Bond-Then-Form Processes. The LOM and paper lamination technology (PLT, Kira Corp. Ltd., Japan) using kraft paper as the build material, and UC (Solidica, Inc., USA), which uses thin metal foils as the build material, fall under this category. There are three basic steps involved in these

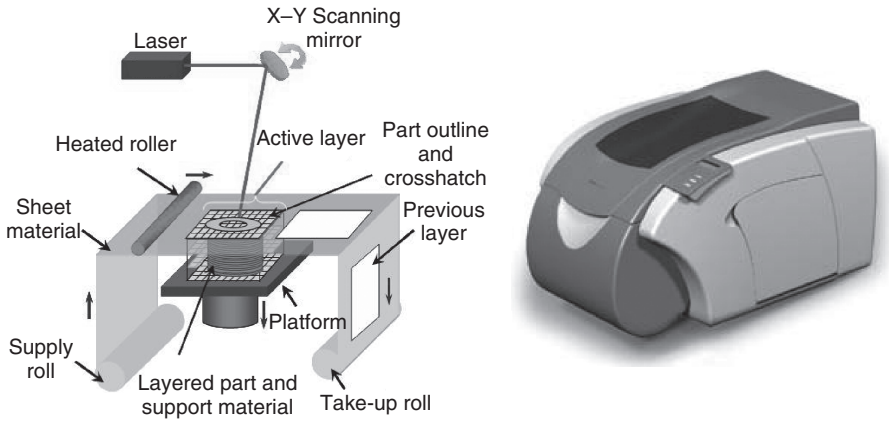

Figure 5.12 (a) Laminated object manufacturing process and (b) actual printer. *Source:* courtesy Cubic Technologies, Inc.

processes: placing the laminate, bonding the laminate, and cutting the laminate into slice shape. LOM uses adhesive-backed paper laminates as the build material and employ a heated roller to bond the laminates together. The sheet thicknesses vary between 0.02 and 0.2 mm and continuous feeding of the material is achieved with the help of winding and unwinding rolls. Figure 5.12 shows the schematics of a LOM process. The metallic build platform is initially covered with a double-sided adhesive tape on which the first layer of the part is built. The build sheet is fed to the platform from a supply roll and bonded to the substrate/or to the previous layer, using a heated roller. The roller melts the plastic adhesive on the bottom side of the build sheet and produces bonding between the laminates. Computer-generated cross-sectional outline, the crosshatches, and the model's perimeter are then cut using a controlled laser to a depth equal to the sheet thickness. The areas that are to be removed from the final object are diced into small pieces, using a crosshatch pattern, which act as support material and can be easily removed during postprocessing. The model is freed from the remaining sheet by a perimeter cut. The build platform with the stack of previously formed layers is lowered and a new section of material advances on top of the previously bonded layer. Then the platform is again raised up and the heated roller bonds the fresh sheet material to the previous layer. These steps are repeated until all the layers are completed. The part comes out of the machine in an enclosed rectangular block of laminates. PLT is another variation of LOM, wherein a laser printer prints the binder/resin according to the cross-sectional data on a plain paper and then bonds it to the substrate/previous layer with a pressure-assisted hot plate. A knife then cuts the deposited paper as per the slice profile. In this process, the removal of the support material is easy as it is not bonded to the previous layers as in LOM. Commercial machines based on these technologies are manufactured

by Solidimension, Israel (SD300 and XD700) and 3D Systems, USA (InVision LD 3D Printer) [89].

Postprocessing of LOM parts involves removing the crosshatched pieces, sanding, polishing, etc. Because the parts are made of paper, sealing with epoxy or silicon spay is necessary to prevent moisture absorption, expansion, and warpage. Some studies [90] indicate that the interlaminate strength of LOM-fabricated parts depends on roller temperature, bonding speed, contact area between the paper and the roller, and sheet deformation. Maintaining the working envelope temperature is critical in achieving uniform lamination across the entire laminate area. Finished parts do not experience any shrinkage, warpage, or other deformations, as the process does not involve any physical or chemical changes of the sheet materials. Potentially, any sheet material including plastics, metal, and ceramics, with an adhesive backing can be used in LOM. Fully dense ceramic and functionally graded materials have also been made using LOM [91,92]. In these studies, a low-melting-point polymer has been used as a binder between the laminates. After the part construction, the green parts were debinded and sintered at high temperatures by reaction bonding.

The basic principle of LOM has been successfully extended to create complex 3D parts from metal foils/sheets by employing ultrasonic welding. The process is known as Ultrasonic Consolidation (UC). The UC technology was developed and commercialized by Solidica, Inc., in 2000 [93]. Figure 5.13 illustrates the UC process.

The UC machine consists of two basic systems namely an ultrasonic metal welding system and a CNC milling platform. By alternate bonding and selective machining, the UC process creates solid objects with complex internal and external geometries. The process uses a rotating ultrasonic "sonotrode" (textured cylinder) that travels, with appropriate normal load, along the length of a thin

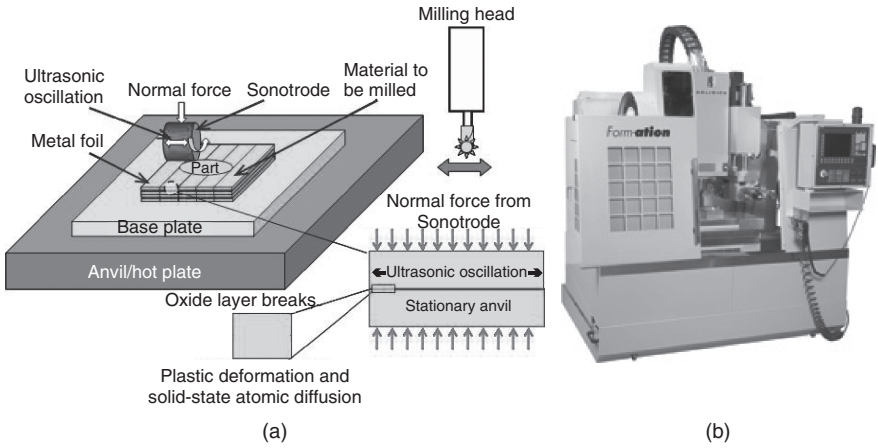

Figure 5.13 (a) Schematic illustration of ultrasonic consolidation process and (b) Solidica's "Form-ation" UC machine. *Source:* courtesy Solidica, Inc.

metal foil placed over a metallic substrate. The sonotrode oscillates, at ultrasonic frequencies and micron-scale amplitudes, transversely in the direction of welding, while traveling over the metal foil (typically 25 mm wide and 100 μm thick). The dynamic stresses generated at the interface between the two mating surfaces, as a result of oscillating shear and normal forces, produce plastic deformation at the interface and breaks up the oxide film. The clean metal surfaces thus generated metallurgically bond together under the influence of plastic flow and atomic diffusion. Then another foil/strip is deposited and welded adjacent to the previously welded strip. These steps are repeated until a complete layer is formed. At the end of each layer, a CNC milling head shapes the layer to its slice contour. Certain geometric features of the part are milled after several layers have been made. The chips generated during milling are blown away using compressed air and then foil for the next layer is deposited. The process is carried out at room temperature or slightly elevated temperatures between 93 and 150°C, using a heated platen/anvil.

The UC process can produce complex metal parts with excellent dimensional control and material properties because of the solid-state fabrication process and ultrasonic bond quality characterized by fine grain structures. It is also possible to insert miniature components such as sensors, strain gauges, computational devices, and thermocouples into the machined cavities of the part prior to encapsulation by subsequent material deposition, thus creating structures with embedded functionality. UC has been successfully used to make parts, using many metals/alloys including Al, Mg, Ti, Cu, and steel, and dissimilar materials such as glass-metals, Al–Ti, and Cu–Al [94–97]. In addition to forming metallurgical bonds, plastic flow generated by ultrasonic excitation is strong enough to encapsulate a variety of reinforcing materials [98–100]. Amplitude of oscillation, contact pressure, sonotrode texture, temperature, and weld speed are the most important parameters that control the interfoil and foil–substrate bonding [101–103]. Achieving 100% bonding during UC is difficult, but removal of surface roughness of the previous layer prior to the deposition of a layer has been shown to achieve 100% linear weld densities [104,105]. Some of the advantages of UC include (i) incorporation of complex internal geometries, cavities, channels, fibers, sensors, etc.; (ii) high feature accuracy (±0.05–0.12 mm) and surface finish; (iii) negligible shrinkage, residual stresses, and distortion due to solid-state processing; (iv) high fabrication speed; (v) minimal secondary machining operations; and (vi) the fact that the build can be stopped and restarted at any time. The main disadvantage is that not all materials are suitable for UC, especially those with high melting point and high strength and prone to oxidation. Several research groups are working to extend this technique to a wide variety of metals/alloys. The applications of the UC process include investment casting, vacuum forming, blow molding, injection molding, and direct aluminum prototype parts.

5.2.2.4.2 Form-Then-Bond Processes. In these processes, the contour of the cross section is first cut from the sheet material and the sectioned contours are

then stacked and bonded together. Form-then-bond processes are more popular for making parts, using metallic or ceramic sheet materials. There are two commercially available technologies that use the principle of form-then-bond: (i) offset fabbers—by Ennex Corp., USA [106], and (ii) computer-aided manufacturing of laminated engineering of materials (CAM-LEM)—developed by Case Western Reserve University, USA. "Offset fabbers" uses an adhesive-backed sheet material that is cut to represent the desired cross section, using a plotting knife. The shaped laminate, along with parting lines and outlines of support structures, is then placed on top of the previous layer and bonded to it. In the CAM-LEM process, the contours of individual slices are laser cut from a sheet stock of desired material, for example, a green ceramic tape. Figure 5.14 shows the step-by-step process of CAM-LEM. The sliced sections are extracted from the sheet stock and precisely stacked to form the original CAD model. After assembly, the layers are laminated by warm isostatic pressuring (or other suitable method) to ensure firm contact between individual layers, which promotes strong bonding in the subsequent sintering. The laminated green parts are then fired into a monolithic structure, using optimized sintering cycle. For 3D metallic parts, laser-cut shapes/sheets have been bonded using diffusion boding, laser spot welding, and brazing techniques [107–109]. From-then-bond processes allow multiple material types to be deposited in a single build, creating functionally graded materials/structures. Also, the process can use adjustable build layer thicknesses, allowing large volumes to be built with thicker sheets and regions that require smooth surface finish with thinner sheets. The process also allows construction of parts with internal voids and channels without manual waste removal, which overcomes the problem of entrapped volume that plagues most of other LM processes. The distinct characteristic of separate geometric formation step and material bonding step eliminates the danger of cutting into the previous layers and entrapment of fine unwanted foreign materials between the laminates, which are associated with bond-then-form processes. As with other LM processes, these

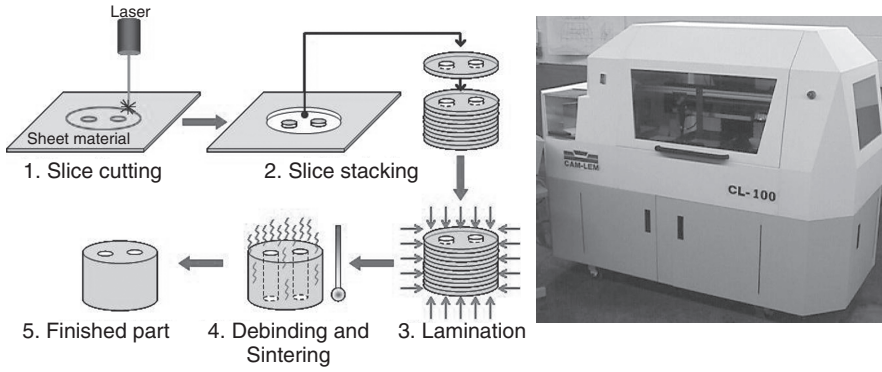

Figure 5.14 Schematic of CAM–LEM process and a CAM–LEM machine. *Source:* courtesy CAM–LEM, Inc.

processes also require support structures for overhanging structures and a precise tooling/alignment system to ensure proper stacking of individual layers. Important factors affecting the quality of the parts are the laser cutting, the indexing and tacking, the alignment of the stacking process, the binding process, and the sintering process.

In general, sheet lamination processes are characterized by little shrinkage, residual stresses, and distortion problems compared to other processes. The main advantages of these processes include (i) wide range of organic and inorganic materials such as paper, plastics, metals, composites, and ceramics that are nontoxic, stable, and easy to handle, (ii) high building speeds for large parts, and (iii) high-precision and low material, machine, and process costs. The main disadvantages are (i) difficult to make parts with delicate thin walls and to control parts' accuracy in the Z-direction, (ii) integrity of the parts depends on the adhesive strength of the glue used—low and inhomogeneous mechanical strength for functional prototypes, and (iii) require elaborate postprocessing including sealing.

5.2.2.5 Printing Processes. Printing-based LM processes can be classified into two main groups—binder printing and direct printing. In binder printing processes, the liquid binder is selectively printed on a powder bed that solidifies and creates the shape of the desired cross-sectional slice by binding the powder together. Direct printing processes involve creating the part by direct printing of build material through a print head. Three-dimensional printing (3DP) was representative of binder printing process, originally developed by faculty and students of Massachusetts Institute of Technology (MIT) in 1993. This process is very similar to powder bed sintering technology, but uses printing of liquid binder, in place of laser, to bind the powder together and thus can operate at very high speeds and low costs. The process begins with laying a thin layer of powder bed in the build box (Fig. 5.15). A roller mechanism spreads the powder from the feed box onto the build platform. Then the print head moves across the loose powder bed selectively printing/spraying the fine liquid binder droplets, according to the cross-sectional area of the first slice, onto the previously laid

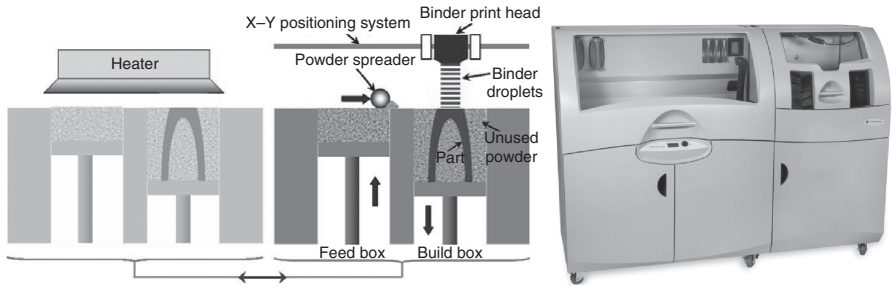

Figure 5.15 Binder printing process and commercial 3D printer. *Source:* courtesy Z Corp.

powder bed. The printed binder upon solidification binds the powder together and to the previous layer. The powder outside the part geometry remains loose and acts as a support for subsequent layers. Typical print head contains a large number of parallel nozzles that enable the head to print 50–80 mm of the layer profile in a single pass. The build platform is then lowered (typically between 0.02 and 0.4 mm, depending on the powder size) by one layer thickness and a new layer of powder is spread on top. The print head applies the binder according to the data for the next layer. This process is repeated for all the layers to complete the part at or near room temperature in ambient atmosphere. After part construction, the binder is allowed to harden, loosely adhering powder is removed, and the part is further processed. Some manufacturers (e.g., ExOne LLC) use certain type of binders that require elevated temperatures to activate the binder forming a green body and an interlayer drying step (under a heated plate) to expel the moisture and to control binder spreading between the layers. Green parts generally exhibit a low mechanical strength and should be handled with care. Parts made from starch or plaster are often infiltrated with wax or epoxy, and sealed to prevent moisture absorption.

It is extremely important to control the amount of binder sprayed/printed to achieve high dimensional accuracy and part quality. Binder materials also vary depending on the build material and final application. The typical binder volume ranges between 10% and 20% of the part volume and depends on layer thickness, type of material, and powder characteristics such as size, shape, size distribution, and packing density. Other process parameters are binder characteristics (viscosity, chemistry, wettability), powder bed packing density, binder droplet size, drying temperature/time, and printing rate. For concept models, plaster and starch are widely used as building materials. Metallic and ceramic powders can also be used for generating tooling and patterns for various applications.

3DP LM machines are available from Z Corp., USA; ExOne Corp., USA; Soligen Technologies, USA; and Therics, Inc., USA. The machines from ExOne Corp. are designed for fabricating metal parts and Z Corp. machines use starch and plaster formulations for part construction. Therics, Inc. produces machines that are exclusively designed for manufacture of implantable drugs, solid oral tablets, and tissue engineering products by printing micro-drops of binders, drugs, and other materials. Soligen Technologies manufactures direct shell production casting (DSPC) machines, which involve a patternless casting process for metal parts and are used also for direct production of ceramic investment shells/cores. In all 3DP processes, the parts' accuracy depends on the ability to jet when and where required, which depends on the jet size and motion control. Among LM processes, 3DP is least expensive, five times faster, easy to operate, and can build complex parts with complex color schemes. No support structures are required and unused powder can be reused after screening, which minimizes waste. The use of an off-the-shelf print head allows for inexpensive, quick replacement of the system's primary consumable component. Poor surface finish, textured surface roughness, feature resolution, liquid binder spreading, and fragile nature of green parts are some of the concerns associated with binder printed parts. Several

studies have been carried out using binder printing technology to make metallic, ceramic, and composite parts and functionally graded structures [110–118].

Two LM processes have been developed on the basis of direct printing technology, where the build material is directly printed on a substrate in a layer-by-layer fashion to complete the part. One of the processes, the ModelMaker, was developed and commercialized by Sanders Prototype Inc., USA (now Solidscape, Inc.) in 1994. The other one, called rapid freeze prototyping (RFP), was developed at University of Missouri-Rolla, USA by Dr. Ming Leu. RFP can make three-dimensional ice parts of arbitrary geometry layer by layer by freezing water droplets. The ModelMaker uses two print heads (one for the thermoplastic build material and one for the supporting wax) that are used to melt and print the build and support materials onto the build platform to form a layer cross section. Then a cutter removes a ~25-μm-thick layer from the top surface of the layer. The wax is printed in the areas adjacent to the part, which serves as the support material. Although the build times are high, a high degree of precision and surface finish can be achieved in this process. Ballistic particle manufacturing (BPM) is yet another process, in which molten thermoplastic material is sprayed onto the substrate, using a multiaxis print head. Other commercial system based on direct printing technology is 3D Systems' MultiJet modeling technique. Low-melting-point metals such as Sn, Zn, and Pb have been used in these direct printing technologies [119,120]. Another interesting LM process is RFP, in which a cold source is used to freeze the water point by point in a layer-by-layer manner to create 3D ice parts from a CAD model [121,122] and the process has not yet been commercialized. The most promising industrial application of RFP is investment casting and silicon molding [123–125]. The advantages of ice patterns instead of plastic/wax patterns are (i) elimination of shell cracking, (ii) easier to remove without pattern expansion, and (iii) close dimensional tolerances, and cost savings between 35% and 65%.

5.2.2.6 Metal Deposition Processes. In metal deposition processes, the metal in the form of power or wire is completely melted, using a high-power laser beam, and deposited layer by layer to form 3D objects. Various versions of this technology are direct laser deposition (DLD), DMD, direct light fabrication (DLF), laser-engineered net shaping (LENS), and others. LENS, the first commercially available metal deposition technology, was originally developed by Sandia National Laboratories, USA, and was commercialized by Optomec Design Company, USA, in 1998. POM Group, Inc., USA, also manufactures DMD machines with five-axis capability. Controlled metal buildup (CMB), a metal deposition process that uses metal wire as the feedstock, was developed by RoderTec GmbH and Fraunhofer Institute. This process also involves high-speed cutting of each deposited layer to suit its corresponding slice contour and thickness. Complete melting and solidification of feedstock material results in fully dense parts in a single step in contrast to the porous and partially sintered parts produced in powder bed processes. However, for specific application such as load-bearing metal implants, fabrication of controlled porosity structures has

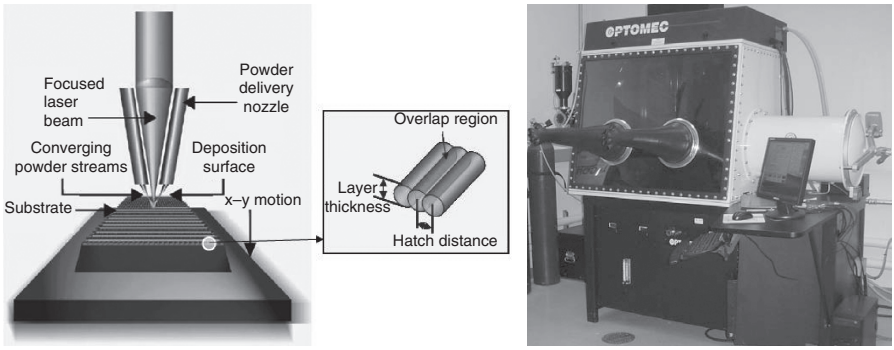

Figure 5.16 (a) Schematic representation of metal deposition process and (b) Optomec's LENS-750 system.

been demonstrated [126,127]. The deposition process begins with directing a focused laser beam on to a metal substrate placed on a numerically controlled X–Y table, as shown in Fig. 5.16.

The laser beam generates a small molten metal pool on the substrate and a predetermined amount of metal powder is then injected into the metal pool, which melts and solidifies rapidly as the laser beam moves away. The substrate is then scanned relative to the deposition head to write a thin line of solidified metal along the line of laser scanning, strongly bonded to the substrate or previous layer, with a finite width and thickness. As in FDM, each layer is formed by a number of consecutive overlapping tracks. After each layer is formed, the laser head, along with the powder delivery nozzle, moves up by one layer thickness from the deposit (keeping the same standoff distance throughout the deposition process) and the subsequent layer is generated. This procedure is repeated many times until the entire object represented in the three-dimensional CAD model is produced on the substrate, which can be a tailored to be a solid or a porous object. The amount of overlap between consecutive tracks is generally 25% of the track width (to create dense parts) and typical layer thicknesses are between 0.25 and 0.5 mm. The entire building process occurs inside a glove box filled with inert gas, or in some versions the liquid metal pool is shielded with inert gas. In general, these processes require support structures for building overhanging features, but latest machines with 5- to 6-axis capability can easily generate overhanging features without support structures [128].

Metal deposition processes are designed to produce fully dense functional parts in metals and ceramics, and many metallic, intermetallic, ceramic, and composite materials have been successfully processed [129–137]. The process can use either prealloyed or a blend of elemental powders with size ranging between 20 and 100 μm as feedstock materials. Multiple powder feeding system can be effectively used to generate new alloys and composites *in situ* [138]. Major process parameters for metal deposition processes include (i) laser beam diameter

and power, (ii) laser focus point, (iii) laser travel speed, (iv) powder feed rate, (v) scan spacing (laser beam overlap), (vi) time delay between successive scans, and (vii) layer thickness. Other parameters such as the nozzle-to-surface distance (standoff distance), nozzle gas flow rate, absorptivity, and depth of focus with respect to the substrate also play important roles. Studies focusing on the effects of the process parameters are available [139]. Laser power, laser travel/scan speed and powder feed rate are interdependent and must be carefully balanced to achieve constant standoff distance, between the deposit and the deposition head and satisfactory builds. Similarly, the laser focus point has to be buried into the substrate ($\sim$1 mm) to ensure adequate substrate/previous layer melting and strong interlayer bonding. However, for minimal dilution at the interface, the focus point should be adjusted on or just above the substrate surface. Latest machines are equipped with sophisticated accessories such as closed-loop melt pool control system and automatic Z-height control system [140,141]. These systems also facilitate fabrication of materials with functional gradient in composition across the fabricate parts [142–145].

The intrinsic feature of laser-based metal deposition processes is that, at certain time, only a small volume of the material is thermally treated resulting in extremely high-temperature gradients and cooling rates (typically between 10^3 and 10^5 K/s) leading to several micro-structural benefits [146] such as (i) suppression of diffusion-controlled solid-state phase transformations, (ii) formation of supersaturated solutions and nonequilibrium phases, (iii) formation of extremely fine, refined micro-structures with little elemental segregation, and (iv) formation of very fine second phase particles. By utilizing high cooling rates, it has been recently demonstrated that bulk amorphous components, without losing the amorphous structure of the feedstock, can be fabricated using laser-based direct manufacturing techniques [147]. Depending on the process parameters, the extremely complex nature of solidification during metal deposition produces a wide variety of grain structures (columnar and equiaxed) [148,149]. Thermal histories associated with metal deposition processes, being layer-based deposition processes, involve remelting and numerous low-temperature reheating cycles. Both experimental and modeling/simulation results showed that the deposited materials experience significant rapid quenching during the initial stages of deposition and the quenching effect decreases with an increase in the deposit thickness or number of layers [150–153]. The reheating cycles can lead to stress relieving, precipitation of secondary phases, etc. A number of research articles describe micro-structural evolution in laser-deposited metal parts [154,155]. Significant amounts of residual stresses can be generated during laser deposition and can lead to cracking, especially in brittle and dissimilar material combinations. The mechanical properties of laser-deposited materials are always superior to their equivalent wrought or cast materials [156–158].

These processes can be used throughout the life cycle of the product for applications ranging from materials/alloy development to functional prototyping and low-volume production. The main strength of laser-powder deposition processes lies in their ability to produce fully dense parts with good metallurgical properties

at reasonable speeds, without subsequent furnace processing. In addition to economic advantages, the process enables fabrication of novel shapes, hollow structures, and material gradients that are not otherwise feasible. An additional benefit is its unique ability to add material to existing components for service and repair applications. Objects fabricated are of a near-net shape, but will generally require finish machining. The major limitations are poor resolution, build speeds, difficulty in the production of parts with complex geometries, and surface finish.

5.2.2.7 Hybrid and Other Processes

5.2.2.7.1 Hybrid Layered Manufacturing Processes. Hybrid layered manufacturing processes have been developed to address some of the issues related to metal-deposition-based LMTs. For example, laser-based deposition techniques, which can produce functional metal parts with complex geometries, are currently limited in terms of surface finish, geometric inaccuracies, and the need for support structures. The shape deposition manufacturing (SDM) process, developed by Dr. Fritz Prinz at Carnegie Mellon University and later Stanford University, is a hybrid layered manufacturing process that overcomes the above difficulties by combining the flexibility of the additive layer manufacturing process with the precision and accuracy attained with the subtractive CNC machining process [159]. In SDM of metals, one of the three important deposition processes is used to deposit individual segments of the parts at a deposition state to form the layer of the part. Deposition processes include plasma spraying with droplet diameters on the order of 1–10 μm, micro-casting (using conventional arc welding processes) with droplets of size 5–10 μm, and laser deposition [160–162]. After depositing each layer, the part is transferred to the shaping station, where the deposited layer is milled to shape the layer contour, layer thickness, or net shape, using a five-axis CNC machine. After milling, the part may be subjected to shot-peening to control/relieve the stress buildup due to repeated thermal deposition and machining. The part is then transferred back to the deposition stage for the deposition of the next layer or sacrificial support material deposition. The sequence of deposition of part material or support material depends on the parts' geometry. These steps are repeated until the part is complete, after which, the sacrificial support material is removed and the final part is revealed. The process is schematically shown in Fig. 5.17.

The major difference between SDM and normal LM processes is that the CAD model of the part is decomposed into slices or segments, each maintaining the full 3D geometry of the outer surface. The advantage of decomposing the part into segments (or "compacts") is that it eliminates the need for machining undercut features and the features are formed by deposition support or part material onto previous layers or segments. The layer thickness depends on the local geometry of the part and the constraints of the deposition process. The additive and subtractive nature of SDM show considerable promise for producing dense metallic parts in a quick and more economical way, and it has been used to embed electronics and other components within the structure [163]. The advantages of SDM include a wide variety of processable materials, variable layer

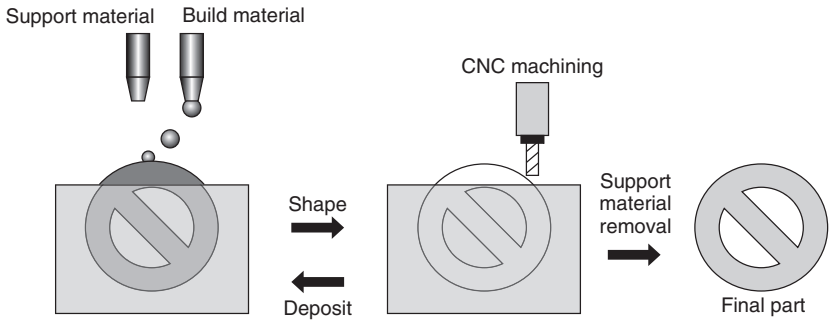

Figure 5.17 Shape deposition manufacturing process steps.

thickness, ability to make heterogeneous structures and undercut features, and disadvantages are required controlled atmosphere, large floor space and precise position, and transfer mechanism [16].

5.2.2.7.2 Other Processes. Several processes have been developed on the basis of the above described or other additive manufacturing approaches. Some of the important processes are very briefly discussed below. Very similar to SDM, segment milling manufacturing (SMM) is a new approach to construction of parts segment by segment. In SMM processes, the part is split into segments (or plate-like free partial bodies) and each segment is shaped using a milling machine in combination with a deposition system. The shaped individual segments are assembled to form the final 3D object. The segmentation process eliminates the stair-case effect and produces parts with a smooth surface finish. Another advantage of SMM processes is their achievable accuracy. The restricted part geometries that can be segmented are a matter of concern. Commercially available systems based on SMM include (i) layer milling manufacturing (Zimmermann GmbH, Germany), (ii) stratoconception (Charlyrobot, France), and (iii) stratified object manufacturing (MEC GmbH, Germany).

In recent years, advances in integration and processing techniques have enabled micro-electronic and micro-electromechanical devices to shrink in size dramatically. The use of lithographic techniques for micro-fabrication of these electronic and mechanical devices/structures at the submillimeter level requires expensive facilities, extreme processing conditions, and timescales on the order of weeks to go from design to completed device. Direct write (DW) technologies are a group of technologies that are capable of depositing, dispensing, or processing (including subtractive) different types of materials over various surfaces following a preset pattern or layout in a simple, fast, economical, and highly versatile way. DW processes are characterized by the use of computer-generated patterns and shapes for direct fabrication without part-specific tooling. DW has the ability to fabricate micron-scale active and passive functional devices directly onto structural parts and assemblies. The benefits of utilizing these techniques are increased functionality, reduced size and

weight, reduced cost, design simplification, reduction in component number, and a reduction in time to market. The potential applications of DW technologies include RF devices; displays; stealth materials; metamaterials; packaging; sensors and harnesses; and electrical, microwave, and optical components. Over the years, many different DW technologies have been developed [164], which include inkjet DW, DW thermal spray, aerosol, laser direct etching, matrix-assisted pulsed laser evaporation (MAPLE), nScrypt 3De (nano/micro pen), and maskless meso-scale materials deposition (M3D). DW processes use some sort of 3D programmable dispensing or deposition head to accurately apply small amounts of material (10–25 μm wide and ~5 μm thick) automatically to form circuitry or other useful mesoscopic devices. Using these technologies, a variety of materials can be deposited (metals, dielectrics, ferrites, semiconductor and dielectric polymers, resistors, composites, and chemically reactive materials) onto a variety of substrates (plastic, metal, ceramic, glass, and even cloth) [164]. Integration of DW processes with other additive manufacturing processes makes it possible to produce parts with completely embedded electrical circuitry and other electronic devices with a huge application potential in electronics, aerospace, and satellite industries.

Laser direct-write is a general term that encompasses modification, subtraction, and addition processes capable of creating patterns of materials directly on substrates without the need for lithography or masks. For laser direct-write modification (LDWM) or subtraction (LDW-), the material of interest is directly irradiated and is either removed (laser micro-machining) or modified (melting, sintering, and so on). In both cases, either pulsed or CW lasers can be effective. One method of laser direct-write addition process (LDW+) is MAPLE (Fig. 5.18). The process begins with the material of interest in powder form and combines it with a liquid carrier to form an ink (Fig. 5.18). This ink is spread on a glass plate fixed approximately 100 μm from the substrate. A pulsed UV laser irradiates the ink from behind the glass plate to propel a mass of material forward onto the substrate below. A pattern of material is created on the substrates either by $x-y$ translation of the substrate or by raster scanning the laser beam.

The M3D process involves ultrasonic/pneumatic atomization of a liquid molecular precursor or a colloidal suspension of metals, dielectric, ferrite, or resistor powder, and the aerosol stream is delivered through a deposition head orifice directed at the substrate that moves under computer control, so that intricate geometries may be deposited [165]. Either laser chemical decomposition or thermal treatment, often by a coaxial laser system, is used to process the deposit to the desired state. Pen-based processes, such as Micropen and nScrypt 3De, use dispensing nozzles (50 μm–2.5 mm in diameter) and a variety of metallic and ceramic slurries or "inks," to write intricate patterns. The electronic inks are heated at low temperatures to evaporate any fluid, leaving behind the dried metal or ceramic, and then fired to sinter the powders together. Two aspects of the pen-based processes make them extremely useful: (i) fine line traces can be deposited on nonplanar substrates and (ii) inks can be custom-designed for specific functional needs. Thermal spray techniques for DW applications have been demonstrated by researchers at the State University of New York at Stony

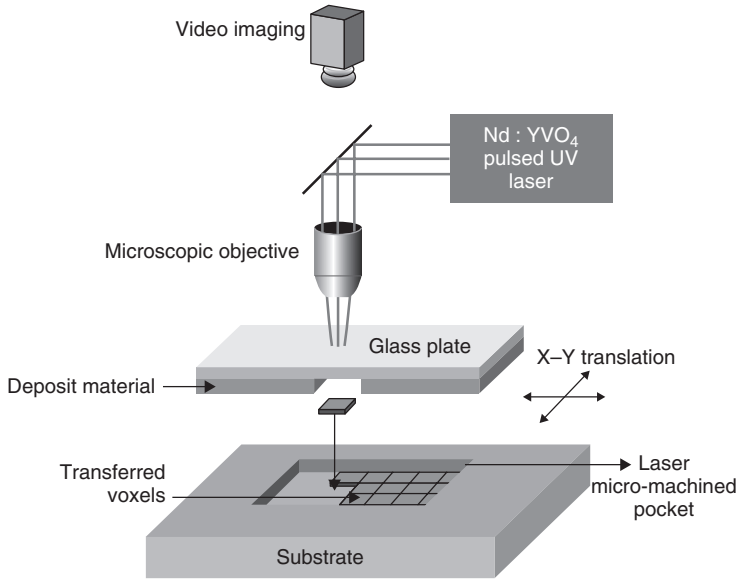

Figure 5.18 Schematic of MAPLE process.

Brook [166,167]. With appropriate torch designs and powder particle size distribution, these processes were shown to result in satisfactory deposits (as thin as 5 μm) of a wide range of materials. Thermal spray techniques offer certain unique advantages in DW applications: (i) high writing speed, (ii) flexibility with spray materials (metals, ceramics, polymers, or any combinations of these materials and incorporation of mixed or graded layers), (iii) useful material properties in the as-deposited state, and (iv) very low thermal input during processing.

5.3 MATERIALS AND LAYERED MANUFACTURING CAPABILITIES

5.3.1 Materials

Several materials including thermoplastics, polymers, metals, and ceramics have been used in a variety of layered manufacturing techniques (Table 5.2). Use of composites (polymeric, ceramic, and metallic) in making functionally graded materials is now being researched actively in a number of research laboratories and universities. However, plastics/polymer-based materials dominate the materials used in LM systems because of their availability and ability of a large number of LM processes to handle/process plastics [35,52,53,55,70,75,82,115]. PC is an industry-standard engineering thermoplastic and is suitable for creating concept and function models and prototypes, investment casting patterns for metal prototypes and casting tooling, etc. Owing to its high impact strength, tensile strength, and compressive strength, PC and blends of it are used in myriad products such as car interiors, toys, and medical-equipment cabinetry. In today's auto industry, many car interiors are built from the material. Hubcaps, too, are often made of

TABLE 5.2 List of the Materials Currently being Used in Various LM Techniques

LM Technique	Materials Used
Stereolithography	Photocurable resins simulating engineering thermoplastics such as polycarbonate (PC), nylon, acrylonitrile butadiene styrene (ABS), polyphenylsulfone (PPSF), elastomers, and electro ceramics.
Fused deposition modeling	PC, nylon, ABS, PPSF, PC/ABS blend, natural and synthetic polymers for biological applications such as polyglycolic acid (PGA), poly(L)-lactat (PLA), poly(DL)glycolacatat (PLGA), polyvinyl alcohol (PVA), Polyhydroxyethylmethacrylate (PHEMA), majority of ceramics including PZT, Al2O3, and ZrO2, $ZrO_2-Al_2O_3$ composites, alumino-silicates, silicon carbides, ceramic-metal composites.
Selective laser sintering	Thermoplastics, polyamides, elastomers, polymer composites, metals/alloys, ceramics, and metal–ceramic and ceramic–ceramic composites. For example, nylon, glass/Al-filled nylon, polystyrene, steel, calcium phosphate ceramics, PZT, Ti, carbon fiber, Ti, CoCr, Al, NiTi, Ta, etc.
3D printing	Polyamides, nylon, thermoplastics, ceramics (engineering, structural, electronic, and biological), metals such as steel, Ti, Ti alloys, CoCrMo alloy, etc.
Metal-deposition techniques	Stainless steel, brass, CoCrMo alloys, Ni-based super alloys, copper, aluminum alloys, tantalum and metallic matrix composites, *in situ* composites and ceramets (WC–Co), etc.
Laminated object manufacturing	Plastics and ceramic sheets.

a chrome-plated PC due to the high level of stress exerted on them at highway speeds. Other applications include cell phones, business equipment, computer products, and a wide variety of consumer products, such as appliances. Nylon is another industry-standard engineering thermoplastic. This material is suitable for creating models and prototypes that can withstand and perform in demanding environments. It is one of the most durable RP materials currently available in the industry, and it offers substantial heat and chemical resistance. Other thermoplastics similar to nylon include ABS, PPSF, and a PC/ABS blend. Polyamide-based powders (such as DuraForm PA and DuraForm GF from 3D Systems) are used to create rigid and rugged plastic parts for functional applications. Polystyrene-based materials with low residual ash content (such as PS 1500 and PS 2500 from EOS GmbH) are particularly suitable for making patterns for investment casting. A number of proprietary polyamide-based composite materials reinforced with glass, metal shots, and other nano-sized fibers are also available for production of parts with superior heat and chemical resistance. For biomedical applications, several natural polymers such as collagen networks, alginate, chitosan, fibrin, and hyaluronic acids or synthetic polymers such as polyglycolic acid (PGA), poly(L)-lactat (PLA), poly(DL)glycolacatat (PLGA), polyvinyl alcohol (PVA), Polyhydroxyethylmethacrylate (PHEMA), and chitosan (a chitin

derivate) have been used. LM systems such as FDM, 3DP, stereolithography (SLA), and SLS have used plastic/polymer-based materials and their composites [54,56,67,69,79,92, 98–100,105,113,114,116,117,137,138].

A number of proprietary metal powders are available from machine manufacturers for producing functional tools through the two-component indirect process. The most common powder combination is a stainless steel powder mixed with a combination thermoplastic/thermoset binder, which is subsequently infiltrated with bronze. Similarly, a number of commercially available binder-coated ceramic powders (zirconia- and silica-based) can be used for producing molds and cores for metal casting. However, a large number of investigators have used a wide variety of metals, alloys, ceramics, and their combinations to make functional end-use parts or rapid tools useful parts, using high-power laser-based LMTs. The strength of these technologies lies in their ability to fabricate fully dense metal parts with good metallurgical properties at reasonable speeds. A variety of materials can be used such as stainless steel, brass, CoCrMo alloys, Ni-based super alloys, copper, aluminum, tantalum, and composites [98–100, 105,113,114,116,117,137,138] can also be made by combining metal particles [36,40–48,71,76,94–97,101,111,112,126–132,135,139,144,145,147,148]. Of particular interest are reactive materials such as titanium. Most systems use a powder feedstock, but there has also been work done with material provided as fine wires. Material composition can be changed dynamically and continuously, leading to objects with properties that might be mutually exclusive using classical fabrication methods. Stucker *et al* [167] have successfully employed the SLS process to produce complex-shaped ZrB_2–Cu composite EDM electrodes with a more homogeneous micro-structure compared to a hot pressing route. Similarly, Lu *et al*. [168] produced *in situ* TiC reinforced Cu electrodes, using Cu, Ti, Ni, and C powder mixtures and employing a laser sintering process. A number of investigators have extensively studied the formation of metallic, ceramic, and composite functional parts, using laser sintering processes [169,170]. Das and coworkers [171] employed a novel approach for fabricating fully dense parts using the SLS process. Initially, the SLS process was used to produce 3D parts with a gas impermeable skin, which encapsulates the porous internal volume, by carefully controlling the process parameters. These parts were then directly postprocessed to full density by containerless hot isostatic pressing (HIP). The SLS/HIP approach was successfully used to produce complex 3D parts in Inconel 625 and Ti–6Al–4V for aerospace applications.

The application of LMT to ceramics manufacturing is motivated by the advances in engineering where methods of creating complex shapes are limited. A particular advantage is the ability to create functional gradients in electroceramic applications and to assist in metal–ceramic joining [172]. Ceramics often incur high machining costs for low production numbers and high tooling costs in injection molding of large batches. The use of solid free-forming as a RP method enables a designer to evaluate new ceramic materials and designs under different test conditions. Among the techniques used for LM of ceramic materials for structural and functional applications are stereolithography, FDM, SLS, LOM, 3DP,

direct ceramic ink-jet printing, and laser chemical vapor deposition [173,174]. Some ceramic materials [173] used in these processes include $ZrO_2-Al_2O_3$ composites, alumino-silicates, silicon carbides, ceramic ink, and ceramic–metal composites such as tungsten carbide cobalt, WC–Co, known as ceramet.)

5.3.2 Layered Manufacturing Capabilities

The capabilities of current LMTs can easily meet the industry requirements of prototypes and models for visualization, form-fit, and ergonomic studies. However, the mechanical and functional properties of direct-manufactured end-use products and rapid tools vary depending on the type of the LM process and the material used for construction. Quantitative understanding of the effects of process parameters, build style, support structures, and other factors on the surface finish, dimensional accuracy, magnitude of shrinkage, residual stresses, distortion, and mechanical properties of a part produced using each LM process is necessary to enhance product performance. Each LM process has its own merits and demerits in terms of resolution, accuracy, required secondary/finishing operations, build speed/total build time, usable materials, etc. Depending on the construction material, part size/shape, required accuracy, final application, etc., an appropriate LM process has to be selected after a careful comparison of all the available processes. Accuracy and surface finish are two important considerations that must be traded when choosing the build orientation during RM. LMTs produce parts in layers, which invariably results in the "stair-case or stair-stepping" effect as a result of finite thickness. Smooth surface finish with a less strain-stepping effect can be achieved with the processes that produce thinnest layers—increases the total build time. Among LM processes, inkjet-based and stereolithography processes can achieve thinnest layers in the range of 10–15 μm with good surface finish as well. The minimum layer thickness of powder-bed-based processes such as SLS and 3DP depends on the minimum powder size that can be uniformly spread without agglomeration or static self- charging or sticking to the spreader roller. Also, these processes produce a rough and sandy surface appearance. Surface finish also depends on the process-dependant parameters such as scanning pattern and scanning speeds. Resolution is one of the factors that determine finish, appearance, and accuracy. Currently, most layered manufacturing machines have "few mils" resolution range that differs in different directions (X, Y, and Z). Advanced systems with specialized scanning and motion control systems can achieve much finer features, but they are limited in the size of the parts they can fabricate. The inkjet-based system from Solidscape is capable of very high resolution. In all cases, the parts require postprocessing operations such as sanding, painting, polishing, infiltration, and machining. A brief comparison of the available layer thicknesses and achievable feature resolution in various LM processes is presented in Table 5.3. Surface finish and dimensional accuracy are influenced not only by the materials and the postprocesses but also by the other factors such as the machine, software algorithms, building accuracy, and shrinkage compensation [175]. Accuracy is the greatest challenge of future LM processes.

TABLE 5.3 Comparison of Layer Thickness and Resolution of Different LM Techniques

Technique	Resolution (mm)		Layer	Accuracy (mm)
	$X-Y$ axis	Z axis	Thickness (mm)	
Stereolithography	0.2–0.3	0.025–0.762	0.010–0.05	±0.1
Solid ground curing	0.1–0.15	0.1–0.15	0.1–0.2	±0.5
3D printing	0.12–0.5	0.07–0.17	0.1–0.2	±0.02
Fused deposition modeling	0.25–0.5	0.05–0.75	0.05–0.76	±0.13
Selective laser sintering	0.07–0.5	0.076–0.5	0.08–0.15	±0.13–0.7
Metal-deposition techniques	0.02–0.5	0.1–0.4	0.08–0.4	±0.1–0.5
Inkjet	0.03	0.1–0.2	0.03–0.1	±0.13
Laminated object manufacturing	0.07–0.25	0.05–0.5	0.07–0.3	±0.1–0.25

All LMTs are fairly slow and typically take few hours to even days to complete a part. Nevertheless, this is still considered as faster compared to conventional subtractive processing, especially for complex parts. The total build time depends on build speed and pre- and postprocessing steps required, which vary from process to process. LM processes that are raster based are generally faster than the processes that fabricate each layer in a vector fashion, and thicker layers considerably reduce the build time. Thus, 3DP is faster than SLA, which is quicker than FDM and inkjet-based processes. However, when accounting for the extra pre- and postrun operations required for SLA and SLS (such as cleaning, curing, warm-up, or cool-down), the overall time to produce the unfinished test part using SLA or SLS will be significantly higher than in FDM. Because FDM does not require additional pre- or postrun operations, it is very competitive in the overall time to produce the part. Assessment of different LMTs in terms of building speed, surface finish, and dimensional accuracy has been made quantitatively for plastics [176–178] and qualitatively for ceramics [179–181]. Parts from processes such as 3DP, SLS, and MJM are generally very fragile and require infiltration or binder burnout or sintering, depending on the construction material. Even direct-manufactured end-use parts require final machining and other secondary operations before acceptable finishes and tolerance are achieved. Powder-based methods are self-supporting and do not require additional supporting structures for overhangs and undercuts. All other methods require a support structure of some kind which is fabricated right along with the part and require longer build and postprocessing times. Different LMTs are compatible with a variety of materials including plastics, ceramics, and metals. Powder-bed-based processes, such as 3DP and SLS, are very versatile compared to other processes and can use any material that is available in power form. SLA and SGC processes are limited to

photocurable polymers. Similarly extrusion-based processes are limited to materials with relatively low melting points. LOM was originally limited to papers and being used with plastics, ceramics, and composites as well. Today's LMTs are being widely used for RT and direct manufacturing of end-use parts. The appropriate selection of process depends on process capability to provide desired characteristics to the specific tooling or final part and construction material. It is important to note that there are no specifications available for important parameters such as accuracy and resolution for the rapid tools and final parts. One reason for this is that these results, for all LMTs, significantly change depending on the part geometry, material, and other factors. The comparison of different LMTs to make RT and metal parts is presented in Table 5.4. Each technology has its own advantages and market niche, which has allowed each of the machines' producers to survive as a viable commercial enterprise.

5.4 APPLICATIONS OF LAYERED MANUFACTURING TECHNOLOGIES

The use of LMTs span the spectrum of industries including automotive, aerospace, medical, toys, and consumer products. The automotive and consumer products industry are the largest users of LMTs (Fig. 5.19a). The possible application of these technologies is virtually unlimited and can be categorized into three major groups: RP, RT, and rapid/direct manufacturing. So far, RP (functional models) has been the largest application class (Fig. 5.19b) for these technologies, followed by rapid/direct manufacturing of parts, which is growing rapidly and should eventually dominate the industry. Over the years, the LM industry has grown into a billion-dollar industry (1.2 billion in 2008) and in the last three years an average annual growth of 13.8% has been estimated [182,183].

5.4.1 Rapid Prototyping

The successful launch of a new product into today's competitive markets depends on fast, efficient product development, coupled with quick and flexible manufacturing processes. In the recent years, the benefits of layered manufacturing processes are being increasingly realized and the LMTs have become an integral part of product design, development, and manufacture for various industries using production materials ranging from plastic and nylon to ceramic, composites, and powdered metals. Clear communication is crucial during the design process to prevent unexpected costs and delays in the production due to design flaws. Rapid prototypes are being widely used as models for concept realization and effective communication among various people, including designers, manufacturers, and customers. Rigorous iterative testing for form, fits, ergonomics, and functionality of a new design is possible, using functional prototypes, before going into time-consuming and expensive traditional manufacturing. Several case studies enumerating the benefits in terms of cost and time savings associated

TABLE 5.4 Comparison of LM Technologies for Rapid Tooling and Direct Part Manufacturing

Process	Lead Time	Part/Build Materials	Maximum Part Size	Tool Life	Strengths	Weaknesses
Electron-beam melting	2–4 weeks	H13 tool steel, low alloy steel, titanium alloy (Ti-6Al-4V), pure titanium	$200 \times 200 \times 200$ (mm^3)	100,000–1 million	Fully dense parts, energy efficient, many processable materials, conformal cooling	Limited part size, slow cool-down, requires finishing
Directed metal-deposition technique	2–4 weeks	H13 tool steel, 304 and 316 stainless steels, nickel-based alloys such as Inconels, and cobalt-chrome and Ti-6Al-4V alloys	$460 \times 460 \times 1100$ (mm^3)	10 to millions	Fully dense parts, repair and feature addition possible, multiple/gradient materials, conformal cooling, can use any powdered material, properties identical with intrinsic material	Geometric limitations on overhangs, poor surface finish, require finish machining
Ultrasonic consolidation	< 1 week	aluminum, copper and other soft metals	$610 \times 915 \times 254$ (mm^3)	> 5000	Conformal cooling, dissimilar materials, laminated composites, fully dense, embedded components, good surface finish	Soft materials, shorter tool life
Conventional processing	4–16 weeks	All	None	50–100,000 s	Excellent accuracy/finishes, long tool life	Slow, expensive for complex parts

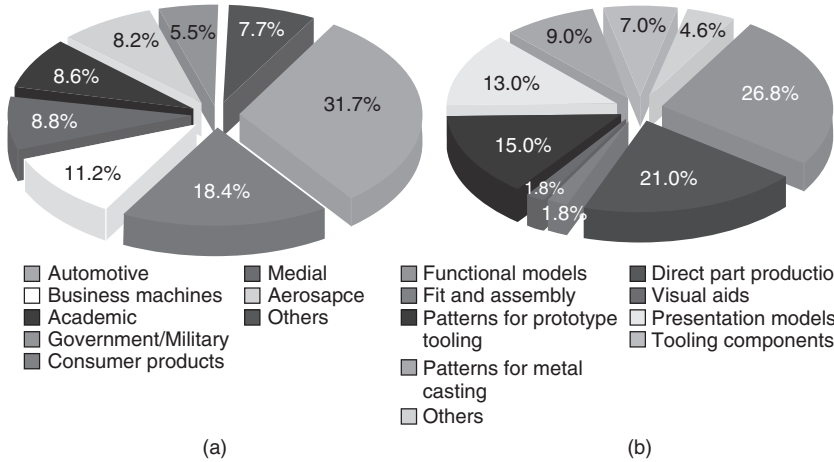

Figure 5.19 Percentage use of layered manufacturing worldwide (a) company/sector wise usage and (b) application-wise usage [182,183].

with product development using LMTs are provided in Grimm [184]. Typical prototypes made using different LMTs from different material and colors are presented in Fig. 5.20. Photopolymerization processes such as stereolithography (SLA), PolyJet and SGC, 3DP, SLS, and FDM are the most popular LM manufacturing technologies used for prototype development. The prototypes made of plastics/polymers can also serve as effective tools to analyze stress [185], fluid flow [186], etc. Also, the ability to make prototypes in multiple colors helps visualization of finite element analysis data in a physical model of the part/design (Fig. 5.21a), which can be used to enhance communication and identify critical design changes. In healthcare applications, the prototypes are used for presurgical planning—to reduce operating room time, implant precontouring, physician–physician and physician–patient communication and education (Fig. 5.21b). Similarly, physical models of complex molecules make visualization and understanding of the structure and interactions of different molecules simple for education, research, and development of drugs (Fig. 5.21c).

5.4.2 Rapid Tooling

Tooling is one of the slowest and most expensive steps in the manufacturing processes and the tools are often complex in shape and require high dimensional accuracy and surface finish. Fabrication of tooling by LMTs can make conventional manufacturing processes faster, cheaper, and better. RT aims at producing tools that last long with improved mechanical and thermal properties, incorporating shorter lead times and significant cost savings. Typically, RT can save 75% or more of tooling cost and development times [187]. LMTs are used in two different ways to make production quality machine tools: (i) *Direct tooling*—molds and other tools are directly fabricated by a LM system and (ii) *Indirect tooling*—LM-generated parts are used as patterns for making molds

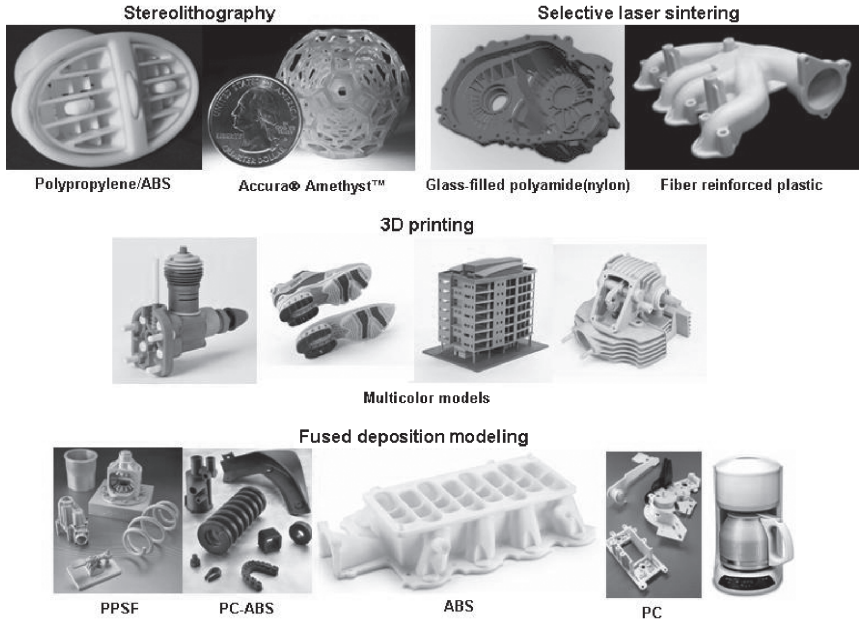

Figure 5.20 Typical prototype parts build using stereolithography (*Source:* courtesy 3D Systems, Inc.), selective laser sintering (*Source:* courtesy 3D Systems, Inc.), 3D printing (*Source:* courtesy Z Corp.), and fused deposition modeling (*Source:* courtesy Stratasys, Inc.).

or tools. Typical tooling include (i) dies and inserts for injection molding, die-casting, vacuum casting, and metal forming operations, (ii) sacrificial patterns or shells for investment casting, (iii) patterns, cores, and molds for sand casting, (iv) jigs and fixtures for automatic assembly lines, and (v) other tooling for series production of plastic and metallic parts.

5.4.2.1 Direct Tooling. Direct tooling eliminates the inaccuracies associated with replication techniques involved in indirect tooling techniques for making molds or dies. The most significant advantage of using LMTs in direct tooling is the ability to include additional features in the tool that are impossible by conventional tooling techniques, such as conformal cooling/heating channels that allow appropriate cooling/heating of the tool at desired locations. Some studies have shown that these conformal channels can cut injection mold cycle times by up to 40%. Specialized LM processes and materials have been developed to meet specific application and material requirements for molding, casting, and jigs/fixtures. The processes include SLA, SLS, LENS, DMLS, EBM, 3DP, and LOM. Figure 5.22 shows some tools produced using LMTs.

SLA tools are generally produced with commercially available materials such as Polypropylene, ABS, PC, Nylon 6:6 and composites. These tools are typically used for injection molding of high- and low-density polyethylene, polystyrene, polypropylene, and ABS plastics. Up to 500 parts have been molded from a

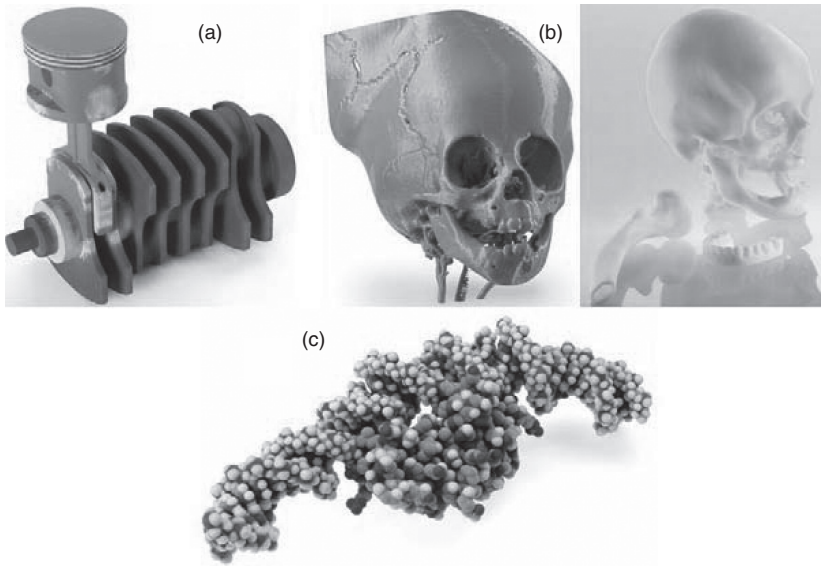

Figure 5.21 (a) Finite element stress analysis of piston-connecting rod-crank shaft assembly represented in a 3D physical model (*Source:* courtesy Z Corp.), (b) skull, femur, and tooth models derived from patients' CT or MRI scan data (*Source:* courtesy Stratasys, Inc.), and (c) a physical molecular model of a drug (*Source:* courtesy Z Corp.).

single tool, although 10–50 parts is more typical. The composites reinforced with aluminum shots, etc. are more durable and can run for 1000–5000 parts. Research into the development of high-temperature and filled resins is also being undertaken by several organizations. Metallic molds that are durable for injection molding and die-casting are produced by SLS, LENS, EBM, and DMLS using H13 tool steels, steel infiltrated with bronze, bronze, Inconel 625, tungsten carbide, and titanium carbide cermets, and other alloys. These fully dense molds with complex geometries have been used to cast hundreds of aluminum, zinc, and magnesium parts. For making plastic parts, these molds can last up to 100,000 or more cycles. UC has also been used to make metallic tools for injection molding. Ceramic tooling produced by LOM, SLS, and 3DP are very strong and durable, and could be used as tooling in a variety of manufacturing processes.

5.4.2.2 Indirect Tooling. Most of the RT types that are used today are indirect—LM parts are used as patterns for making molds and dies for conventional manufacturing processes. Almost all LM processes have been used to create rapid indirect tooling for various applications. Several processes have been developed to create a mold using LM-generated parts/tools and their accuracy depends on the accuracy of LM processes that are used to create the pattern/part. One of the most popular tooling applications of RP is the production of room temperature vulcanizing (RTV) silicone rubber molds. Silicone rubber molds are used to produce urethane-, epoxy-, and zinc-based alloy parts/prototypes.

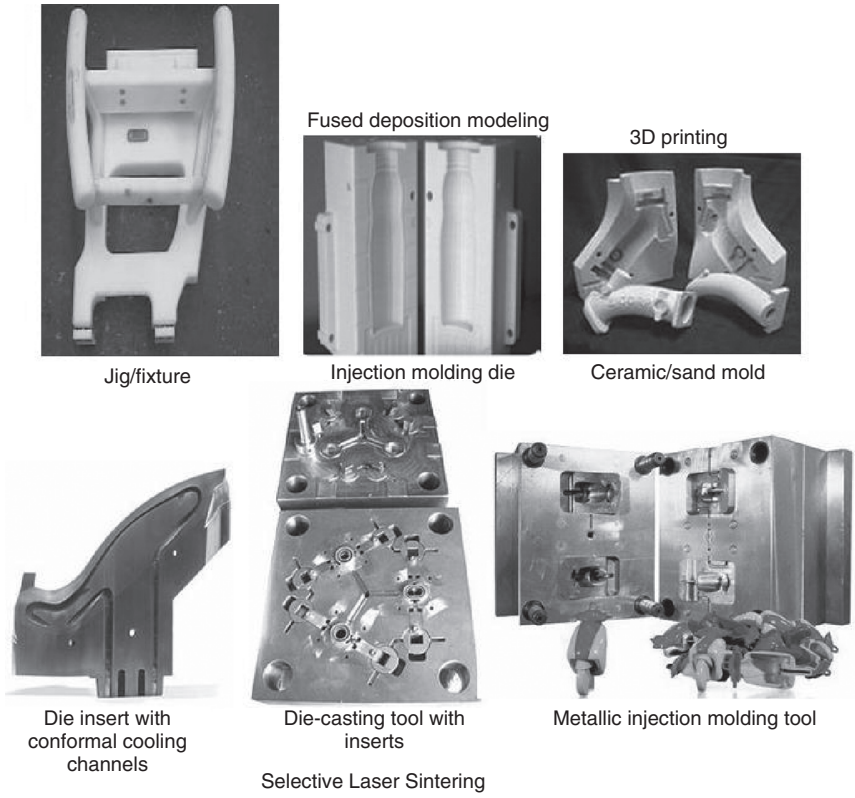

Figure 5.22 Production tooling made using fused deposition modeling (*Source:* courtesy Stratasys, Inc.), 3DP (*Source:* courtesy Z Corp.), and selective laser sintering (*Source:* courtesy EOS GmbH).

RTV molds are being used in vacuum casting, reaction injection molding, wax injection molding, cast resin tooling, etc. to make thermoplastic parts such as polypropylene and ABS. The patterns generated using LM processes are also used to make soft and hard metallic molds, using spray metal tooling processes. In these processes, an atomized metal is deposited onto a pattern using a spray gun to make molds. Typical metals include lead/tin-based alloys, Al, Cu, and steels. Spray metal tools have been used in many applications, including sheet metal forming, injection molding, compression molding, and blow molding. Various plastics including polypropylene, ABS, and polystyrene and difficult process materials such as reinforced nylon and PC have been molded. Some companies have used investment casting with RP models to produce metal tooling. Most of the tools cast so far have been in aluminum, but there are some examples of tool steel molds. By making a sacrificial RP model of the desired cavity, the lost wax process can be used to replicate the part in a metal.

5.4.3 Rapid/Direct Manufacturing

Rapid or direct manufacturing of end-use parts using LMTs is a natural extension of RP. The number/type of products that are produced by LM machines is continuously increasing as new materials are being developed by various companies. For large production runs, LMTs are not economical, but for short production runs, LM processes are much cheaper as these do not require tooling. LMTs are also ideal for producing custom parts tailored to the user's exact specifications. As with RT, the use of LMTs for rapid/direct manufacturing falls into two categories: indirect and direct. As discussed earlier, indirect manufacturing involves manufacture of a pattern or a mold, and has been successfully adopted for manufacture of end-use parts of plastics, ceramics, and metals [188]. In contrast, direct manufacturing methods create final end-use components in a single operation. Direct manufacturing of functional parts using LMTs is rapidly growing as many manufacturers have begun to realize the unique capabilities of additive processes for direct part production. Some unique characteristics of LM processed functional parts include complex geometries, multiple materials, controlled local geometric meso- and micro-structures, lower costs and mass customization. Virtually all LMTs are being used presently for RM. The processes that use end-use materials for part construction are most popular including 3DP, SLS, FDM, metal deposition, and related technologies. Photo-curable resins used in photopolymerization-based processes (SLA, SGC, etc.) can simulate engineering materials but can not replace them. Major LMTs used to make end-use final parts are listed in Table 5.5. There are other technologies that are being adopted for specific applications, for example, micro-stereolithography for the manufacture of MEMS and DW technologies for electronic and other nano-devices. Typical end-use parts produced by LMTs are shown in Fig. 5.23.

Aerospace and Automotive. The aerospace industry has been one of the early adopters of LMT, because the aerospace parts are made of expensive materials in small quantities, are complex, and must meet stringent functional requirements, which is ideal for the best utilization of LMTs. Fabrication of jet engine components such as turbine blades with internal cooling channels is a major area of interest. Several metal-deposition-based technologies have been used to fabricate components using high-strength, high-temperature, Ni-based super alloys with single-crystal structures [148,149]. Layered

TABLE 5.5 LM Technologies being Used for Rapid/Direct Manufacturing

Metal Parts	Ceramic Parts	Plastic Parts
Selective laser sintering	Three-dimensional printing	Selective laser sintering
Selective laser melting	Fused deposition modeling	Fused deposition modeling
Laser-engineered net shaping	Selective laser sintering	Stereolithography
Direct metal deposition	Stereolithography	Three-dimensional printing
Electron-beam melting		
Three-dimensional printing		

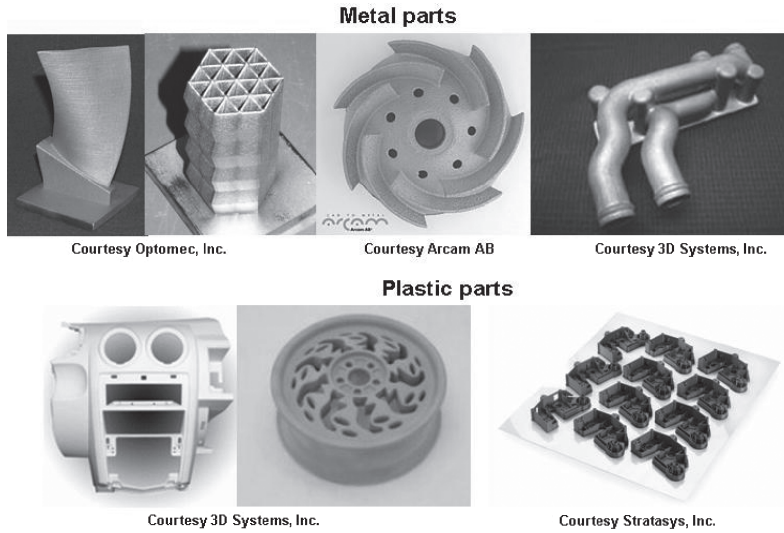

Figure 5.23 Functional parts produced using LM technologies.

manufacturing is being applied also to the manufacture of composites for aerospace use. Long-term applications include active skin materials for drag reduction and spare part manufacturing for space missions. NASA has identified additive manufacturing as an enabling technology for future space missions. The vision is to make use of additive manufacturing for large structures (including moon and Mars dwellings) and replacement parts as well as for repair of damaged components in space [189].

The automotive industry also has great application potential for LMTs. The ability to make complex parts using multiple materials for automotive application can provide improved fuel efficiency, longer engine life, and lower assembly costs. Several automotive manufacturers such as General Motors, Ford, Daimler-Benz, Honda, BMW, and Volkswagen have already been using these techniques for the manufacture of functional parts [190,191].

Electronics. In this area, the number of LM processes being used is more than that in other application area. Direct manufacturing, using LMTs, is very attractive for electronic parts because of their unique characteristics such as small size, huge quantities, and batch fabrication. Elimination of tooling in layered manufacturing is another strong driving force for low-volume production of electronic components. Many electronic devices, components, and transducers are made of repeated simple geometric shapes, and the ability of LMT to create complex, compositionally/structurally graded materials offers the field more design flexibility and powerful fabrication techniques. Many electronic materials are amenable to deposition techniques and many polymer-based materials with electronic properties are commercially available. A number of commercially available DW technologies offer the possibility of making meso-scale passive/active

devices (semiconductor devices, resistors, conductive elements, capacitors) directly integrated to any substrate materials (mechanical devices) and these devices have very important applications in military, aerospace, medical, and RF communication areas [163]. Antennas and waveguides are among the less-typical components that can also be fabricated. Semiconductor packaging and ceramic devices are being fabricated using SLA. UC is being widely applied to make components with embedded sensors, devices, and antennas for various applications (Fig. 5.24a).

Medical. A large number of research studies have documented the use of LM in medical applications, which can be grouped in to four major categories: (i) visualization and surgical planning, (ii) customized prosthetic implants, (iii) tissue engineering and scaffolds, and (iv) drug delivery and micro-medical devices. LM systems are now routinely used to produce physical models of biological structures and human anatomy to assist in surgical planning, testing, and communication (Fig. 5.21b). Compared to conventional MRI assessment, medical models allow a more precise diagnosis and procedural planning.

Prosthetic devices and implants for hip, knee, and spinal joints are now routinely made using LMTs. Layered manufacturing processes have also been employed to produce various artificial joints and load-bearing implants in biocompatible materials such as titanium, CoCrMo, NiTi alloy, and others [126,127, 130–133, 144,145]. Customized prosthetics and implants based on the anatomical data from imaging systems such as computed tomography have been investigated [192–195]. These custom-made implants with exact anatomical shape of the femoral/bone canal have been shown to have better *in vivo* life [196–199] and reduce surgical time [192,193]. Plastic Surgery and craniomaxillofacial

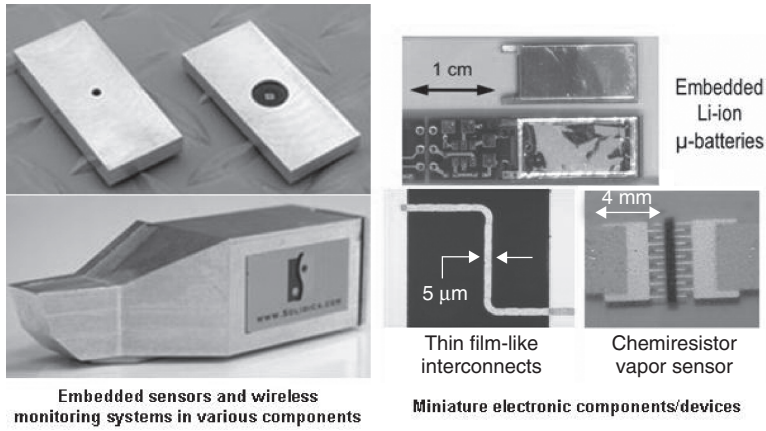

Figure 5.24 Metal-encased smart sensors fabricated using ultrasonic consolidation (*Source:* courtesy Solidica, Inc.) and miniature electronic devices made using the MAPLE technology (*Source:* courtesy Naval Research Laboratory).

reconstruction prosthetics are also of very great interest. Some implants and prosthetic devices fabricated using LMTs are shown in Fig. 5.25.

Fabrication of designed porous and bioresorbable scaffolds that mimic natural bone are being made with calcium phosphate based ceramics, using SLS, 3DP, FDM, and stereolithography. LMTs are ideal for generating scaffolds or bone grafts with complex pore structure and dopants such as enzyme inhibitors and diffusion barriers. In addition to bone, tissue scaffolds are being made using LMTs for replacement or regeneration of other organs. Most tissue engineering strategies for creating functional replacement tissues or organs rely on a design that closely resembles the natural extracellular structure, a highly porous micro-structure with interconnected pore networks that allow cell in-growth and reorganization, and special surface chemistry and material characteristics that are spatially variable, favor cellular attachment and proliferation, and exhibit controlled degradation. Additive manufacturing technologies offer several advantages over conventional techniques for producing scaffolds with these characteristics, and various processes and biocompatible materials have been demonstrated [200–205]. There are long-term prospects for entire, complex, vascularized organs to be fabricated by such methods. The direct printing of living tissues is also being adopted. Groups in both the US and Europe are using the inkjet technology to deposit live cells. Envisiontec GmbH (Germany) produces the Bioplotter (TM), the first

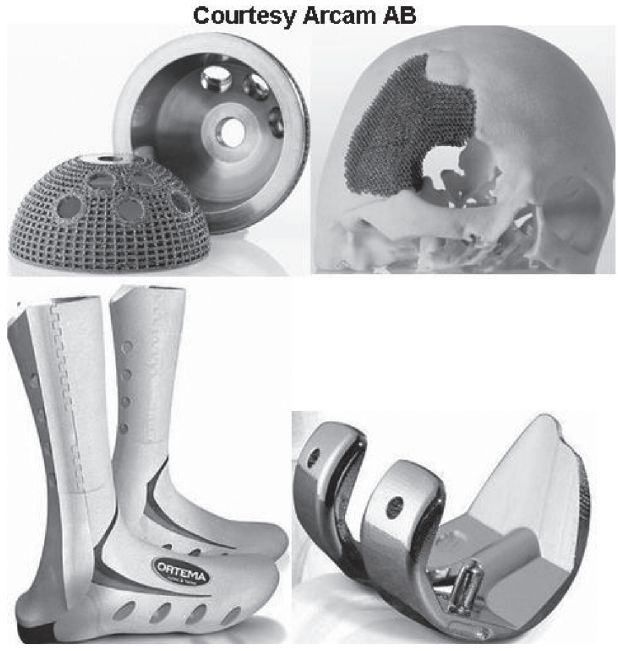

Figure 5.25 Typical prosthetic devices and metal implants fabricated by LM technology.

commercially available system expressly designed for depositing living cells. Another important application of LMTs is fabrication of drug delivery systems. Several articles describe functional benefits that can be achieved with current drugs by LMTs [206–210]. Several types of oral dosage forms such as pulsed, rapid, monotonic, or constant release can be produced. Incorporation of multiple drugs in the same pill to synchronize the multiple functions is also being investigated. Complex devices with micron-level features that would deliver medicine directly to the organ are being developed.

5.5 FUTURE DIRECTIONS

LMTs are changing the way companies design, develop, and manufacture the products. A large number of organizations in various fields are exploring the benefits of LMT to open up new opportunities in research, business, and education. The use of LMTs for prototyping and modeling is well developed and accepted in the industry and it is now being extended and researched for creating fully functional end-use products. Also, the use of LMTs in the product design, development, and manufacturing sectors has increased from ~25% to ~39% over the last four years [89,183]. While the application of LMTs to date has been significant, there is much to be done before LMTs realize their full potential, specifically improvements in terms of (i) long build time for low- to high-volume production, (ii) tight dimensional accuracy and surface finish, (iii) lack of material options and their unsatisfactory properties, (iv) consistency in process and product characteristics, (v) short-term and long-term property data of rapid manufactured parts, and (vi) build envelope size [175] are necessary.

LM machines are still considered slow by some industry standards, as it can take up to a day or more to make an average size part of few tens of cubic inches with acceptable resolution. LM machine manufacturers are reducing the build time on a continuous basis by utilizing faster computers, complex control systems, and improved materials, which potentially make RM economical for a wide range of products and materials. Improvements are also needed in build envelope size and the fine performance parameters of additive manufacturing are more important for RM than for RP applications.

Current commercial machines are accurate up to ~0.08 mm in the $x-y$ direction, but less in the build or in the z direction. Software improvements in terms of errors generated during slicing such as strain-stepping effects, approximation errors, and accurate compensation for material shrinkage are required to achieve high dimensional accuracy and surface finish [211,212]. Development of closed-loop and adaptive control systems with feed-forward and feedback capabilities for LM machines can resolve repeatability issues and eliminate the requirement for operator skills. Improvements in laser optics and motor controls are expected to increase accuracy, and new polymers that are being developed are less prone to curing and temperature-induced warpage.

The plastic prototypes produced from currently available plastic materials are good for fit/form tests and visualization, but they are too weak for functional testing. Stronger plastic materials and other novel materials such as composites will

greatly expand the range of functional products that can be made by LMTs. The mechanical properties of end-use plastic parts made by LMTs fall short of their molded, machined, or cast counterparts. Also, the properties vary with the type of machine, build orientation, and the type of material used. In addition, a quantitative understanding of the effects of process parameters, build style, support structures, and other factors on the magnitude of shrinkage, residual stresses, and distortion is rarely used to enhance product performance. Another material issue involves freedom of choice. For example, there are thousands of commercial thermoplastic grades available in the market, but only few graded thermoplastics and photopolymers are available for LM systems. Many LM machine manufacturers and research labs are working to develop new materials including plastics, photopolymers, ceramics, and metal matrix composites. While developing new materials, sustainable (green) materials that are recyclable, reusable, and biodegradable must also be identified. It will take a very long time, though, before LMTs will have access to a wide range of materials that are available for conventional manufacturing processes.

Unlike prototypes or models, both short- and long-term properties are important for the utilization of direct-manufactured products. The materials/products developed from LMTs must be extensively characterized and tested. Lack of such design data for the products manufactured using LMTs presents another barrier to the adoption of direct manufacturing. Local composition control and microstructural design are two strong points of additive manufacturing that merit additional study. To support this, additional improvements in the current CAD softwares are necessary to accommodate the use of complex local changes in properties such as geometry, graded and mixed material, and colors. New LMTs and machines with better tolerances and speeds, multiaxis deposition, and wider range of materials are being developed around the world. Greater benefits might be realized by developing application-specific or material-specific machines for direct manufacturing rather than all-purpose machines, as is the tradition with additive manufacturing companies. All the above improvements will help the layered manufacturing industry continue to grow worldwide. However, it should be noted that LMTs can never eliminate the need for conventional manufacturing technologies such as casting, forging, and injection molding for high-volume manufacturing.

REFERENCES

1. Blanther JE. Manufacture of contour Relief Maps. US patent 473,901. 1892.
2. Bogart M. In art the end don't always justify means. Smithsonian 1979;9:104–110.
3. Munz OJ. Photo-glyph recording. US patent 2,775,758. 1956.
4. Swainson WK. Method, Medium and Apparatus for Producing Three-Dimensional Figure Product. US patent 4,041,476.
5. Schwerzel RE, *et al* Three-dimensional photochemical machining with lasers. Appl Lasers Ind Chem SPIE 1984;90–97.
6. Ciraud PA. Process and device for the manufacture of any objects desired from any meltable material. FRG Disclosure Publication, 2,263,777. 1972.

7. Bourell DL, Beaman JJ, Leu MC, Rosen DW. A brief history of additive manufacturing and the 2009 roadmap for additive manufacturing: looking back and looking ahead. RapidTech 2009: US-TURKEY Workshop on Rapid Technologies; 2009 Sep 24–25. Macka, Istanbul, Turkey: Istanbul Technical University; 2009.
8. Housholder RF. Molding process. US patent 4,247,508. 1981.
9. Kodama H. Automatic method for fabricating a three-dimensional plastic model with photo hardening polymer. Rev Sci Instrum 1981;52:1770–1773.
10. Herbert AJ. Solid object generation. Jour Appl Photo Eng 1982;8(4):185–188.
11. Hull C. Apparatus for the production of three dimensional objects by stereolithograph. US patent 4575330. 1986.
12. Burns M. Automated fabrication. New Jersey: PTR Prentice Hall; 1993.
13. Jacobs PF. Rapid prototyping and manufacturing. Deaborn (MI): Society of Manufacturing Engineers; 1992.
14. Jamieson R, Herbert H. Direct slicing of CAD models for rapid prototyping. Rapid Prototyping Journal 1995;1(2):4–12
15. Donahue RJ. CAD model and alternative methods of information transfer for rapid prototyping systems. Proceedings of the 2nd International Conference on Rapid Prototyping; 1991. pp 217–235.
16. Chua CK, Leong KF, Lim CS. Rapid prototyping: principles and applications. 2nd ed. Singapore: World Scientific Publishing Co. Pte. Ltd.; 2003.
17. Vancraen W, Swawlwns B, Pauwels J. Contour interfacing in rapid prototyping—tools that make it work. Proceedings of the 3rd European Conference on Rapid Prototyping and Manufacturing; Dayton (OH): 1994. pp 25–33.
18. Smith-Moritz G. 3D Systems. Rapid Prototyp Rep Rapid Prototyp Manuf 1994;4(12):3.
19. Wozny MJ. Systems issues in solid freeform fabrication. Proceedings, Solid Freeform Fabrication Symposium; 1992, Aug 3–5; Texas: 1992. pp 1–15.
20. Rock SJ, Wozny MJ. A flexible format for solid freeform fabrication. Proceedings of Solid Freeform Fabrication Symposium; 1991 Aug 12–14; Texas: 1991. pp 1–12.
21. Dolenc A, Malela I. A data exchange format for LMT processes. Proceedings of the 3rd International Conference on Rapid Prototyping; Dayton (OH): 1992. pp 4–12.
22. Materialise NV. Magics 3.01 Materialise User Manual. Materalise Software Department, Kapeldreef 60, B-3001 Heverlee, Belgium; 1994.
23. Hope RL, Roth RN, Jacobs PA. Adaptive slicing with sloping layer surfaces. Rapid Prototyp J 1997;3:89–98.
24. Peiffer RW. The laser stereolithography process—photosensitive materials and accuracy. Proceedings of the First International User Congress on Solid Freeform Manufacturing; 28–30, Oct 1993. Germany: 1993.
25. Stucker BE, Janaki Ram GD. Layer-based additive manufacturing technologies. In: Groza JR, Shackelford JF, Lavernia EJ, Powers MT, editors. Volume 26, Materials processing handbook. Florida: CRC Press; 2007. pp 1–32.
26. Liou FW. Rapid prototyping and engineering applications: a toolbox for prototype development. Florida: CRC Press; 2008.
27. Hug WF, Jacobs PF. Laser technology assessment for strereolithographic systems. Proceedings of the 2nd International Conference on Rapid Prototyping; Dayton (OH): 1991. pp 29–38.

28. Barlow JJ, Sun MSM, Beaman JJ. Analysis of selective laser sintering. Proceedings of the 2nd International Conference on Rapid Prototyping; Dayton (OH): 1991. pp 29–38.
29. Stucker BE. The selective laser sintering process. In: Ready JF, *et al.*, editors. LIA handbook of laser materials processing. Orlando (FL): Laser Institute of America & Magnolia Publishing, Inc.; 2001. p 554.
30. Senthilkumaran K, Pulak M, Pandey and Rao PVM. Influence of building strategies on the accuracy of parts in selective laser sintering. Mater Des 2009;30:2946–2954.
31. Wang RJ, Wang L, Zhao L, Liu Z. Influence of process parameters on part shrinkage in SLS. Int J Adv Manuf Technol 2007;33:498–504.
32. Hardro PJ, Wang JH, Stucker BE. Determining the parameter settings and capability of a rapid prototyping process. Int J Ind Eng 1999;6:203.
33. Ning Y, Wong YS, Fuh JYH, Loh HT. An approach to minimize build errors in direct metal laser sintering. IEEE Trans Autom Sci Eng 2006;3(1):73–80.
34. Wang X. Calibration of shrinkage and beam offset in SLS process. Rapid Prototyp 1999;5(3):129–133.
35. Shi Y, Li Z, Sun H, Huang S, Zeng F. Effect of properties of polymer materials on the quality of selective laser sintering parts. Proc IME: J Mater Des Appl 2004;218:247–252.
36. Chatterjee AN, *et al.* An experimental design approach to selective laser sintering of low carbon steel. J Mater Process Technol 2003;136:151.
37. Venuvinod PK, Ma W. Rapid prototyping—laser based and other technologies. London: Kluwer Academic; 2004.
38. Jain PK, Pandey PM, Rao PVM. Experimental investigations for improving part strength in selective laser sintering. Virt Phys Prototyp 2008;3(3):177–188.
39. Hur SM, Choi KH, Lee SK, Chang PK. Determination of fabricating orientation and packing in SLS process. J Mater Process Technol 2001;112:236–243.
40. Kathuria YP. Microstructuring by selective laser sintering of metallic powder. Surf Coat Technol 1999;643:116–119.
41. Harrysson OLA, Cansizoglu O, Marcellin-Little DJ, Cormier DR, West HA II. Direct metal fabrication of titanium implants with tailored materials and mechanical properties using electron beam melting technology. Mater Sci EngC 2008;28:366–373.
42. Murr LE, Gaytan SM, Medina F, Martinez E, Martinez JL, Hernandez DH, Machado BI, Ramirez DA, Wicker RB. Characterization of Ti-6Al-4V open cellular foams fabricated by additive manufacturing using electron beam melting. Mater Sci Eng A 2008. DOI: 10.1016/j.msea.2009.11.015.
43. Heinl P, Muller L, Korner C, Singer RF, Muller FA. Cellular Ti–6Al–4V structures with interconnected macro porosity for bone implants fabricated by selective electron beam melting. Acta Biomater 2008;4:1536–1544.
44. Strondl A, Fischer R, Frommeyer G, Schneider A. Investigations of MX and γ'/γ'' precipitates in the nickel-based superalloy 718 produced by electron beam melting. Mater Sci Eng A 2008;480:138–147.
45. Cormier D, Harrysson O. Electron beam melting of gamma titanium aluminide. In: Bourell DL, *et al.*, editors. Proceedings of 16th Solid Freeform Fabrication Symposium. Austin (TX): University of Texas at Austin; 2005.

46. Tang Y, Loh HT, Wong YS, Fuh JYH, Lu L, Wang X. Direct laser sintering of a copper-based alloy for creating three-dimensional metal parts. J Mater Process Technol 2003;140:368–372.
47. Simchi A. Direct laser sintering of metal powders: mechanism, kinetics and microstructural features. Mater Sci Eng A 2006;428:148–158.
48. Guo Z, Shen P, Hu J, Wang H. Reaction laser sintering of Ni–Al powder alloys. Opt Laser Technol 2005;37:490–493.
49. Bertrand P, Bayle F, Combe C, Goeuriot P, Smurov I. Ceramic components manufacturing by selective laser sintering. Appl Surf Sci 2007;254:989–992.
50. Slocombe A, Li L. Selective laser sintering of TiC-Al2O3 composite with self propagating high-temperature synthesus. J Mater Process Technol 2001;118:173–178.
51. Shishkovsky I, Yadroitsev I, Bertrand P, Smurov I. Alumina–zirconium ceramics synthesis by selective laser sintering/melting. Appl Surf Sci 2007;254:966–970.
52. Goodridge RD, Hague RJM, Tuck CJ. An empirical study into laser sintering of ultra-high molecular weight polyethylene (UHMWPE). J Mater Process Technol 2010;210:72–80.
53. Yan C, Shi Y, Yang J, Liu J. Preparation and selective laser sintering of nylon-12 coated metal powders and post processing. J Mater Process Technol 2009;209:5785–5792.
54. Tan KH, Chua CK, Leong KF, Cheah CM, Cheang P, Abu Bakar MS, Cha SW. Scaffold development using selective laser sintering of polyetheretherketone–hydroxyapatite biocomposite blends. Biomaterials 2003;24: 3115–3123.
55. Salmoria GV, Klauss P, Paggi RA, Kanis LA, Lag A. Structure and mechanical properties of cellulose based scaffolds fabricated by selective laser sintering. Polym Test 2009;28:648–652.
56. Chung H, Das S. Functionally graded Nylon-11/silica nanocomposites produced by selective laser sintering. Mater Sci Eng A 2008;487:251–257.
57. Reiser A. Photosensitive polymers. New York: John Wiley & Sons, Inc.; 1989.
58. Jacobs PF. Rapid prototyping & manufacturing, fundamentals of stereolithography. 1st ed. Dearborn (MI): Society of Manufacturing Engineers; 1992.
59. Zhou JG, Herscovici D, Chen CC. Parametric process optimization to improve the accuracy of rapid prototyped stereolithography parts. Int J Mach Tools Manuf 2000;40:363.
60. Schaub DA, Montgomery DC. Using experimental design to optimize the stereolithography process. Qual Eng 1997;9:575.
61. West AP, Sambu SP, Rosen DW. A process planning method for improving build performance in Stereolithography. Comput Aided Des 2001;33:65–79.
62. Chockalingama K, Jawahara N, Chandrasekarb U, Ramanathana KN. Establishment of process model for part strength in stereolithography. J Mater Process Technol 2008;208:348–365.
63. Wang WL, Cheah CM, Fuh JYH, Lu L. Influence of process parameters on stereolithography part shrinkage. Mater Des 1996;17:205–213.
64. Yi F, Wu J, Xian D. LIGA technique for microstructure fabrication. Microfab Technol 1993;4:1.

65. Ikuta K, Maruo S, Kojima S. New microstereolithography for freely movable 3D micro structures—Super IH process for submicron resolution. Proceedings of the IEEEMicro Electro Mechanical Systems, The 11th IEEE International Workshop on Micro Electro Mechanical Systems (MEMS '98); 1998 Jan 25–29; Heidelberg, Germany: 1998. pp 290–295.
66. Rapid prototyping report. Microfabrication 1994;4(7):4–5.
67. Basrour S, Majjad H, Coudevylle JR, de Labachelerie M. Complex ceramic-polymer composite microparts made by microstereolithography. Proceedings of SPIE Vol. 4408, Design, Test, Integration, and Packaging of MEMS/MOEMS; Cannes, France: 2001. pp 535–542.
68. Kim JY, Lee JW, Lee S-J, Park EK, Kim S-Y, Cho D-W. Development of a bone scaffold using HA nanopowder and micro-stereolithography technology. Microelectron Eng 2007;84:1762–1765.
69. Lee JW, Ahn G, Kim DS, Cho D-W. Development of nano- and microscale composite 3D scaffolds using PPF/DEF-HA and micro-stereolithography. Microelectron Eng 2009;86:1465–1467.
70. Zhang X, Jiang XN, Sun C. Micro-stereolithography of polymeric and ceramic microstructures. Sens Actuators 1999;77:149–156.
71. Lee JW, Lee IH, Cho D-W. Development of micro-stereolithography technology using metal powder. Microelectron Eng 2006;83:1253–1256.
72. Sun C, Zhang X. The influences of the material properties on ceramic microstereolithography. Sens Actuators A 2002;101:364–370.
73. Carroza MC, *et al.* Piezoelectric-drive stereolithography fabricated micropump. J Micromech Microeng 1995;5:177.
74. Varadan VK, Varadan VV. Microstereolithography for fabrication of 3D polymeric and ceramic MEMS. In: Behringer UF, Uttamchandani DG, editors. Volume 4407, Proceedings of the Conference on SPIE: MEMS Design, Fabrication, Characterization and Packaging. Edinburgh: SPIE Publishing, Bellingham; 2001. p 147.
75. Zein I, *et al.* Fused deposition modeling of novel scaffold architectures for tissue engineering applications. Biomaterials 2002;23:1169.
76. Wu G, *et al.* Solid freeform fabrication of metal components using fused deposition of metals. Mater Des 2002;23:97.
77. Grida I, Evans JRG. Extrusion freeforming of ceramics through fine nozzles. J Eur Ceram Soc 2003;23:629.
78. Cornejo IA. Development of bioceramic tissue scaffolds via fused deposition of ceramics. In: George L, *et al.*, editors. Proceedings of the Conference on Bioceramics: Materials and Applications III. Westerville (OH): American Ceramic Society; 2000. pp 183.
79. Kalita SJ, *et al.* Development of controlled porosity polymer-ceramic composite scaffolds via fused deposition modeling. Mater Sci Eng C 2003;23:611.
80. Bose S, Suguira S, Bandyopadhyay A. Processing of controlled porosity ceramic structures via fused deposition. Scr Mater 1999;41:1009.
81. Anita K, Arunachalam S, Radhakrishnan P. Critical parameters influencing the quality of prototypes in fused deposition modeling. J Mater Process Technol 2001;118:385.
82. Lee BH, Abdullah J, Khan ZA. Optimization of rapid prototyping parameters for production of flexible ABS object. J Mater Process Technol 2005;169(1):54.

83. Dao Q, *et al.* Calculation of shrinkage compensation factors for rapid prototyping (FDM). Comput Appl Eng Edn 1999;1650:186. ISBN: 0-9754429-1-0.
84. Ziemian CW, Crawn PM. Computer aided decision support for fused deposition modeling. Rapid Prototyp J 2001;7:138.
85. Greulick M, Greul M, Pitat T. Fast, functional prototypes via multiphase jet solidification. Rapid Prototyp J 1995;1(1):20–25.
86. Feygin M. Apparatus and method for forming an integral object from laminations. US patent 4,752,352. 1988 Jun 21.
87. Feygin M. Apparatus and method for forming an integral object from laminations. European patent 0,272,305. 1994 Feb 3.
88. Feygin M. Apparatus and method for forming an integral object from laminations. US patent 5,354,414. 1994 Nov 10.
89. Wohlers T. Wohlers Report 2005, Rapid Prototyping and Tooling State of the Industry Annual Worldwide Progress Report. Fort Collins (CO): Wohlers Associates, Inc.; 2005.
90. Pak SS, Nisnevich G. Interlaminate strength and processing efficiency improvements in laminated object manufacturing. Proceedings 5th International Conference Rapid Prototyping; Dayton (OH); 1994. pp 171–180.
91. Klosterman D, *et al.* Interfacial characteristics of composites fabricated by laminated object modeling. Compos A 1998;29A:1165.
92. Zhang Y, *et al.* Rapid prototyping and combustion synthesis of TiC/Ni functionally gradient materials. Mater Sci Eng A 2001;A299:218.
93. White DR. Object consolidation employing friction joining. US patent 6,457,629. 2002 Oct 1.
94. Kong CY, Soar RC, Dickens PM. Characterization of aluminium alloy 6061 for the ultrasonic consolidation process. Mater Sci Eng A 2003;A363:99.
95. White DR. Ultrasonic consolidation of aluminium tooling. J Adv Mater Process 2003;161:64.
96. Robert B. Tuttle, feasibility study of 316L stainless steel for the ultrasonic consolidation process. J Manuf Process 2007;9(2):87–93.
97. Janaki Ram GD, Robinson C, Yang Y, Stucker BE. Use of ultrasonic consolidation for fabrication of multi-material structures. Rapid Prototyp J 2007;13(4):226–235.
98. Kong CY, Soar RC, Dickens PM. Ultrasonic consolidation for embedding SMA fibres within aluminium matrices. Compos Struct 2004;66:421–427.
99. Yang Y, Janaki Ram GD, Stucker B. An experimental determination of optimum processing parameters for Al/SiC metal matrix composites made using ultrasonic consolidation. J Eng Mater Technol 2007;129:538–549.
100. Kong CY, Soar RC. Fabrication of metal–matrix composites and adaptive composites using ultrasonic consolidation process. Mater Sci Eng A 2005;412:12–18.
101. Kong CY, Soar RC, Dickens PM. Optimum process parameters for ultrasonic consolidation of 3003 aluminium. J Mater Process Technol 2004;146:181–187.
102. Li D, Soar R. Influence of sonotrode texture on the performance of an ultrasonic consolidation machine and the interfacial bond strength. J Mater Process Technol 2009;209:1627–1634.
103. Janaki Ram GD, Yang Y, Stucker BE. Effect of process parameters on bond formation during ultrasonic consolidation of aluminum alloy 3003. J Manuf Syst 2007;25(3):221–238.

104. Brent E. Stucker and Durga Janaki Ram Gabbita, Surface roughness reduction for improving bonding in ultrasonic consolidation rapid manufacturin. US patent US2007/0295440 A1. 2007 Dec.

105. Yang Y, Janaki Ram GD, Stucker BE. Bond formation and fiber embedment during ultrasonic consolidation. J Mater Process Technol 2009;209:4915–4924.

106. Burns M, Heyworth KJ, Thomas CL. Offset fabbing. In: Marcus H, *et al.*, editors. Proceedings of Solid Freeform Fabrication Symposium. Austin (TX): University of Texas at Austin; 1996.

107. Himmer T, Nakagawa T, Anzai M. Lamination of metal sheets. Comput Ind 1999;39:27.

108. Himmer T, *et al.* Metal laminated tooling—a quick and flexible tooling concept. In: Bourell DL, *et al.*, editors. Proceedings of the Solid Freeform Fabrication Symposium. Austin (TX): University of Texas at Austin; 2004. p 304.

109. Wimpenny DI, Bryden B, Pashby IR. Rapid laminated tooling. J Mater Process Technol 2003;138:214.

110. Dimitrov D, Schreve K, De Beer N. Advances in three dimensional printing—state of the art and future perspectives. Rapid Prototyp J 2006;12(3):136–147.

111. Turker M, Godlinski D, Petzoldt F. Effect of production parameters on the properties of IN 718 superalloy by three-dimensional printing. Mater Charact 2008;59:1728–1735.

112. Cao WB, *et al.* Development of freeform fabrication method for Ti–Al–Ni. Intermetallics 2002;10:879.

113. Kernan BD, Sachs EM, Oliveira MA, Cima MJ. Three-dimensional printing of tungsten carbide–10wt% cobalt using a cobalt oxide precursor. Int J Refract Metals Hard Mater 2007;25:82–94.

114. Rambo CR, Travitzky N, Zimmermann K, Greil P. Synthesis of TiC/Ti–Cu composites by pressureless reactive infiltration of TiCu alloy into carbon preforms fabricated by 3D-printing. Mater Lett 2005;59:1028–1031.

115. Czyzewski J, Burzynski P, Gawel K, Meisner J. Rapid Prototyping of electrically conductive components using 3D printing technology. J Mater Process Technol 2009;209(12–13):5281–5285.

116. Sun W, *et al.* Freeform fabrication of Ti3SiC2 powder-based structures—Part I: integrated fabrication process. J Mater Process Technol 2002;127:343.

117. Moon J, *et al.* Fabrication of functionally graded reaction infiltrated SiC–Si composite by three-dimensional printing (3DP™) process. Mater Sci Eng A 2001;A298:110–119.

118. Jackson TR, Liu H, Patrikalakis NM, Sachs EM, Kima MJ. Modeling and designing functionally graded material components for fabrication with local composition control. Mater Design 1999;20(2–3):63–75.

119. Sachs E, *et al.* Three-dimensional printing: Rapid tooling and prototyping directly from a CAD model. Trans ASME J Engl Ind 1992;114:481.

120. Orme M, Willis K, Cornie J. The development of rapid prototyping of metallic components via ultra fine droplet deposition. Proceedings of the 5th Internation Conference on Rapid Prototyping; Dayton (OH): 1994. p 27.

121. Zhang W, Leu MC, Ji Z, Yan Y. Rapid freezing prototyping with water. Mater Des 1999;20:139–145.

122. Leu MC, Zhang W, Sui G. An experimental and analytical study of ice part fabrication with rapid freeze prototyping. Ann CIRP 2000;49(1):147–150.
123. Liu Q, Leu MC, Richards V, Schmitt S. Dimensional accuracy and surface roughness of rapid freeze prototyping ice patterns and investment casting metal parts. Int J Adv Manuf Technol 2004;24(7–8):485–495.
124. Sui G, Leu MC. Investigation of layer thickness and surface roughness in rapid freeze prototyping. ASME J Manuf Sci Eng 2003;125(3):556–563.
125. Leu MC, Liu Q, Bryant FD. Study of part geometric features and support materials in rapid freeze prototyping. Ann CIRP 2003;52(1):185–188.
126. Krishna BV, Bose S, Bandyopadhyay A. Low stiffness porous Ti structures for load bearing implants. Acta Biomater 2007;3:997–1006.
127. Krishna BV, Xue W, Bose S, Bandyopadhyay A. Engineered porous metals for implants. JOM 2008;60(5):45–48.
128. Lewis GK, Schlienger E. Practical considerations and capabilities for laser assisted direct metal deposition. Mater Des 2000;21:417.
129. Krishna BV, Bose S, Bandyopadhyay A. Laser processing of net-shape NiTi shape memory alloy. Metall Mater Trans A 2007;38A:1096–1103.
130. Krishna BV, Bose S, Bandyopadhyay A. Fabrication of porous NiTi shape memory alloy samples using laser engineered net shaping. J Biomed Mater Res Part B—Appl Biomater 2009;89B:481–490.
131. Krishna BV, Xue W, Bose S, Bandyopadhyay A. Laser assisted Zr/ZrO_2 coating on Ti for load-bearing implants. Acta Biomater 2009;5:2800–2809.
132. Krishna BV, Banerjee S, Bose S, Bandyopadhyay A. Direct laser processing of tantalum coating on Ti for bone replacement structures. Acta Biomaterialia 2010;6:2329–2334.
133. Roy M, Krishna BV, Bandyopadhyay A, Bose S. Laser processing of bioactive tricalcium phosphate coating on titanium for load bearing implant. Acta Biomater 2008;4:324–333.
134. Krishna BV, Bose S, Bandyopadhyay A. Processing of bulk alumina ceramics using laser engineered net shaping. Int J Appl Ceram Technol 2008;5:234–242.
135. Griffith ML, *et al.* Understanding the microstructures and properties of components fabricated by LENS. Proceedings of the Materials Research Society Symposium, Volume 625; San Francisco; 2000. p 9.
136. Brice CA, *et al.* Characterization of laser deposited niobium and molybdenum silicides. Proceedings of the Materials Research Society Symposium, Volume 625; San Francisco; 2000, 31.
137. Liu W, DuPont JN. Fabrication of functionally graded TiC/Ti composites by Laser Engineered Net Shaping. Scr Mater 2003;48:1337.
138. Banerjee R, *et al.* In-situ deposition of Ti-TiB composites. In: Keicher D, *et al.*, editors. Proceedings of the Conference on Metal Powder Deposition for Rapid Manufacturing. San Antonio (TX): Metal Powder Industries Federation at Princeton (NJ); 2002. p 263.
139. Srivastava D, *et al.* The optimization of process parameters and characterization of microstructure of direct laser fabricated TiAl alloy components. Mater Des 2000;21:425.
140. Hofmeister W, *et al.* Solidification in direct metal deposition by LENS processing. J Metals 2001;53(9):30–34.

141. Hofmeister W. Melt pool imaging for control of LENS process. In: Keicher D, *et al.*, editors. Proceedings of the Conference on Metal Powder Deposition for Rapid Manufacturing. San Antonio (TX): Metal Powder Industries Federation at Princeton (NJ); 2002. p 188.

142. Bandyopadhyay PP, Krishna BV, Bose S, Bandyopadhyay A. Compositionally graded aluminum oxide coatings on stainless steel using laser processing. J Am Ceram Soc 2007;90:1989–1991.

143. Krishna BV, Bandyopadhyay PP, Bose S, Bandyopadhyay A. Compositionally graded yttria stabilized zirconia coating on stainless steel using laser engineered net shaping (LENS™). Scr Mater 2007;57:861–864.

144. Krishna BV, Xue W, Bose S, Bandyopadhyay A. Functionally graded Co-Cr-Mo coating on Ti-6Al-4V alloy structures. Acta Biomater 2008;4:697–706.

145. Krishna BV, DeVasConCellos P, Xue W, Bose S, Bandyopadhyay A. Fabrication of compositionally and structurally graded Ti-TiO_2 structures using laser engineered net shaping (LENS). Acta Biomater 2009;5:1831–1837.

146. Krishna BV, Bandyopadhyay A. Laser Processing of Fe Based Bulk Amorphous Alloy. Surface and Coatings Technology 2010;205:2661–2667.

147. Gaumann M, *et al.* Single crystal laser deposition of superalloys: processing-microstructure maps. Acta Mater 2001;49:1051.

148. Liu W, DuPont JN. Effects of melt-pool geometry on crystal growth and microstructure development in laser surface-melted superalloy single crystal: mathematical modeling of single-crystal growth in a melt pool (Part 1). Acta Mater 2004;52:4833.

149. Zheng B, Zhou Y, Smugeresky JE, Schoenung JM, Lavernia EJ. Thermal behavior and micro structural evolution during laser deposition with laser-engineered net shaping. Part I. Numerical calculations. Metall Mater Trans A 2008;39A:2228.

150. Zheng B, Zhou Y, Smugeresky JE, Schoenung JM, Lavernia EJ. Thermal Behavior and Microstructure Evolution during Laser Deposition with Laser-Engineered Net Shaping: Part II. Experimental Investigation and Discussion. Metall Mater Trans A 2008;39A:2237.

151. Kelly SM, Kampe SL. Microstructural evolution in laser-deposited multilayer Ti–M–4V builds: Part I. Microstructural characterization. Metall Mater Trans A 2004;35A:1861.

152. Kelly SM, Kampe SL. Microstructural evolution in laser-deposited multilayer Ti–6AI–4V builds: Part II. Thermal modeling. Metall Mater Trans A 2004;35A:1869.

153. Banerjee R, *et al.* Microstructural evolution in laser deposited Ni-25 at % Mo alloy. Mater Sci Eng 2003;A347:1.

154. Brooks JA, Headley TJ, Robino CV. Microstructures of laser deposited 304L austenitic stainless steel. In: Danforth SC, Dimos DB, Prinz F, editors. Volume 625, Proceedings of the Materials Research Society Symposium. Pittsburgh (PA): Materials Research Society; 2000. p 21.

155. Xue L, Islam M. Laser consolidation—a novel one-step manufacturing process from CAD models to net-shape functional components. In: Keicher D, *et al.*, editors. Proceedings of the Conference on Metal Powder Deposition for Rapid Manufacturing. San Antonio (TX): Metal Powder Industries Federation at Princeton (NJ); 2002. p 61.

156. Wu X, *et al.* Microstructure and mechanical properties of a laser fabricated Ti alloy. In: Keicher D, *et al.*, editors. Proceedings of the Conference on Metal Powder Deposition for Rapid Manufacturing. San Antonio (TX): Metal Powder Industries Federation at Princeton (NJ); 2002. p 96.

157. Keicher DM, Smugeresky JE. The laser forming of metallic components using particulate materials. J Metals 1997;49:51–54.

158. Merz R, Prinz FB, Ramaswami K, Terk M, Weiss LE. Shape deposition manufacturing. Paper Presented at Solid Freeform Fabrication Symposium. Texas: University of Texas at Austin; 1994.

159. Song Y, *et al.* 3D welding and milling: Part I—a direct approach for freeform fabrication of metallic prototypes. Int J Mach Tools Manuf 2005;45:1057.

160. Zhang Y, *et al.* Weld deposition-based rapid prototyping: a preliminary study. J Mater Process Technol 2003;135:347.

161. Fessler JR, *et al.* Laser deposition of metals for shape deposition manufacturing. In: Bourell DL, *et al.*, editors. Proceedings of the Solid Freeform Fabrication Symposium. Austin (TX): University of Texas at Austin; 1996. p 117.

162. Li X, Prinz F. Metal embedded fiber bragg grating sensors in layered manufacturing. J Manuf Sci Eng 2003;125:577.

163. Pique A, Chrisey DB. Direct-write technologies for rapid prototyping applications: sensors, electronics, and integrated power sources. San Diego (CA): Academic Press; 2002.

164. Essien M, Renn MJ. Development of meso-scale processes for direct write fabrication of electronic components. In: Keicher D, *et al.*, editors. Proceedings of the Conference on Metal Powder Deposition for Rapid Manufacturing. San Antonio (TX): Metal Powder Industries Federation at Princeton (NJ); 2002. p 209.

165. Sampath S. Thermal spray techniques for fabrication of meso-electronics and sensors. In: Danforth SC, Dimos DB, Prinz F, *et al.*, editors. Volume 625, Proceedings of the Materials Research Society Symposium. Pittsburgh (PA): Materials Research Society; 2000. p 181.

166. Chen Q, Tong T, Longtin JP, Tankiewicz S, Sampath S, Gambino RJ. Novel sensor fabrication using direct-write thermal spray and precision laser micromachining. Trans ASME 2004;126:830–836.

167. Stucker BE, *et al.* Manufacture and use of ZrO2/Cu composite electrodes. US patent 5870663. 1999 Feb 9.

168. Lu L, *et al. In situ* formation of TiC composite using selective laser melting. Mater Res Bull 2000;35:1555.

169. Sercombe TB. Sintering of freeformed maraging steel with boron additions. Mater Sci Eng A 2003;A363:242.

170. Simchi A, *et al.* On the development of direct metal laser sintering for rapid tooling. J Mater Process Technol 2003;141:319.

171. Das S, *et al.* Processing of titanium net shapes by SLS/HIP. Mater Des 1999;20:115.

172. Cawley JD. Proceedings, ASME international gas turbine and aeroengine congress and exhibition; 1997; Orlando (FL). New York: AmericanSociety of Mechanical Engineers; 1997. 1–6.

173. Tay BY, Evans JRG, Edirisinghe MJ. Solid freeform fabrication of ceramics. Int Mater Rev 2003;48(6):341–370.

174. Subramanian PK, Marcus HL. Selective laser sintering of alumina using binder. Mater Manuf Process 1995;10:689–706.
175. Kruth JP, Leu MC, Nakagawa T. Progress in Additive Manufacturing and Rapid Prototyping. CIRP Ann 1998;47:525–540.
176. Kruth JP. Material Incress Manufacturing by Rapid Prototyping Techniques. CIRP Ann 1991;40:603–614.
177. Pham DT, Gault RS. A comparison of rapid prototyping technologies. Int J Mach Tools Manuf 1998;38:1257–1287.
178. Ippolito R, Luliano L, Gatto A. Benchmarking of Rapid Prototyping Techniques in Terms of Dimensional Accuracy and Surface Finish. CIRP Ann 1995;44:157–160.
179. Halloran JW. Freeform fabrication of ceramics. Br Ceram Trans 1999;98:299–303.
180. Wang G, Krstic VD. Rapid prototyping of ceramic components–review.. J Can Ceram Soc 1998;67:52–58.
181. Paul BK, Baskaran S. Issues in fabricating manufacturing tooling using powder-based additive freeform fabrication. J Mater Process Technol 1996;61:168–172.
182. Wohlers T. Worldwide trends in additive manufacturing. Us–Turkey Workshop on Rapid Technologies; 2009 Sep 24–25 Macka, Istanbul, Turkey, September 24–25.
183. Wohlers T. Wohlers Report 2009, Rapid Prototyping and Tooling State of the Industry Annual Worldwide Progress Report. Fort Collins (CO): Wohlers Associates, Inc.; 2009. ISBN: 0-9754429-5-3.
184. Grimm T. User's guide to rapid prototyping. Michigan (MI): Society of Manufacturing Engineers; 2004.
185. Ashley S. Rapid prototyping is coming of age. Mech Eng 1995;117:62–69.
186. Langdon R. A decade of rapid prototyping. Automot Eng 1997;22(4):44–59.
187. (a) Hilton P. Making the leap to rapid tool making. Mech Eng 1995;117(7):75–77; (b) Ashley S. From CAD art to rapid metal tools. Mech Eng 1997;119(3): 82–88.
188. Hongjun L, *et al.* A note on rapid manufacturing process of metallic parts based on SLS plastic prototype. J Mater Process Technol 2003;142:710.
189. Karen M, et al. Solid freeform fabrication: an enabling technology for future space missions. In: Keicher D, *et al.*, editors. Proceedings of the Conference on Metal Powder Deposition for Rapid Manufacturing. San Antonio (TX): Metal Powder Industries Federation at Princeton (NJ); 2002. p 51.
190. Prototyping Report. Volume 5(2), Volkswagen uses laminated object manufacturing to prototype complex gear box housing. CAD/CAM Publishing Inc.; San Diego, CA; 1995: 1–2.
191. Muller H, Sladojevic J. Rapid tooling approaches for small lot production of sheet metal parts. J Mater Process Technol 2001;115:97.
192. Winder J, Cooke RS, Gray J, Fannin T, Fegan T. Medical rapid prototyping and 3D CT in the manufacture of custom made cranial titanium plates. J Med Eng Technol 1999;23(1):26–28.
193. D'Urso PS, Earwaker WJ, Barker TM, Redmond MJ, Thompson RG, Effeney DJ, Tomlinson FH. Custom cranioplasty using stereolithography and acrylic. Br J Plast Surg 2000;53(3):200–204.
194. He J, Li D, Lu B. Custom fabrication of a composite hemiknee joint based on rapid prototyping. Rapid Prototyp J 2006;12(4):198–205.

195. Kruth J-P, Vandenbroucke B, Van Vaerenbergh J, Naert I. Digital manufacturing of biocompatible metal frameworks for complex dental prostheses by means of SLS/SLM. Virtual prototyping and rapidmanufacturing - advanced research in virtual and rapid prototyping. London: Taylor & Francis; 2005. pp 139–146.
196. Bargar WL. Shape the implant to the patient. A rationale for the use of custom-fit cementless total hip implants. Clin Orthop Relat Res 1989;249:73–78.
197. Stulberg SD, Stulberg BN, Wixson RL. The rationale, design characteristics, and preliminary results of a primary custom total hip prosthesis. Clin Orthop Relat Res 1989;249:79–96.
198. McCarthy JC, Bono JV, O'Donnel PJ. Custom and modular components in primary total hip replacement. Clin Orthop Relat Res 1997;344:162–171.
199. Reize P, Giehl J, Schanbacher J, Bronner R. Clinical and radiological results of individual hip stems of the type Adaptiva® without cement. Z Orthop Ihre Grenzgeb 2002;140:304–309.
200. Leong KF, *et al.* Solid freeform fabrication of three-dimensional scaffolds for engineering replacement tissues and organs. Biomaterials 2003;24:2363.
201. Sachlos E, *et al.* Novel collagen scaffolds with predefined internal morphology made by solid freeform fabrication. Biomaterials 2003;24:1487.
202. Lam CXF, *et al.* Scaffold development using 3D printing with a starch-based polymer. Mater Sci Eng 2002;C20:49.
203. Yeong W-Y, Chua C-K, Leong K-F, Chandrasekaran M. Rapid prototyping in tissue engineering: challenges and potential. TRENDS Biotechnol 2004;22(12):643–652.
204. Sun W, Lal P. Recent development on computer aided tissue engineering—a review. Comput Methods Programs Biomed 2002;67:85–103.
205. Yang S, Leong K-F, Du Z, Chua C-K. The design of scaffolds for use in tissue engineering. Part II. Rapid Prototyp Tech Tissue Eng 2002;8(1):1–11.
206. Lu Y, Chen SC. Micro and nano-fabrication of biodegradable polymers for drug delivery. Adv Drug Deliv Rev 2004;56:1621–1633.
207. Katstra WE, Palazzolo RD, Rowe CW, Giritlioglu B, Teung P, Cima MJ. Oral dosage forms fabricated by Three Dimensional Printing. J Control Release 2000;66:1–9.
208. Leong KF, Chua CK, Gui WS, Verani. Building porous biopolymeric microstructures for controlled drug delivery devices using selective laser sintering. Int J Adv Manuf Technol 2006;31:483–489.
209. Low KH, Leong KF, Chua CK, Du ZH, Cheah CM. Characterization of SLS parts for drug delivery devices. Rapid Prototyp J 2001;7(5):262–268.
210. Rowe CW, Katstra WE, Palazzolo RD, Giritlioglu B, Teung P, Cima MJ. Multimechanism oral dosage forms fabricated by three dimensional printing. J Control Release 2000;66:11–17.
211. Yan X. A review of rapid prototyping technologies and systems. Comput Aided Des 1996;28:307.
212. Balsmeier P. Rapid prototyping: state-of-the-art manufacturing. Ind Manage 1997;39:55.

CHAPTER 6

MICRO-LASER PROCESSING

BENXIN WU
Department of Mechanical Engineering, Illinois Institute of Technology, Chicago, Illinois

TUĞRUL ÖZEL
Manufacturing Automation Research Laboratory, School of Engineering, Department of Industrial and Systems Engineering, Rutgers University, New Jersey

6.1 INTRODUCTION

The use of laser technology in the processing of materials for micro-products has been reported over the last decade. Laser-based material processing on a micro-scale has been used in thermal processing, shock peening, surface treatment, cleaning of surfaces, welding, melting and polishing, scribing, as well as micro-machining of basic geometric features on a variety of materials [1–12].

Lasers are usually categorized as two groups: continuous wave (cw) and pulsed lasers. Conventional cw and pulsed laser irradiation and ablation is used in many fields, such as material processing, machining, etching, deposition, sintering, micro-fluidics, medical, and many other applications [13–19].

The use of lasers in micro-manufacturing is closely connected to the characteristics of the laser. The main laser parameters to be chosen and controlled are wavelength, λ (nm); average power (W) or energy (J); intensity (W/m^2) or fluence, (Φ) (J/m^2); pulse duration, τ(s); pulse repetition rates (Hz); and peak power (pulse energy/pulse duration) [9,11,16,20,21].

Pulsed lasers achieve much higher intensities than cw lasers and are the preferred solution for the fabrication of micro-sized structures. Long-pulsed (nanosecond, ns), short-pulsed (picoseconds, ps), and ultrashort-pulsed (femtosecond, fs) lasers that are commonly used for repairing, trimming, marking, scribing, texturing, welding, ablation, cutting, and drilling include among others (i) Excimer lasers with ultraviolet (UV) wavelengths, (ii) Ti:sapphire lasers

Micro-Manufacturing: Design and Manufacturing of Micro-Products, First Edition.
Edited by Muammer Koç and Tugrul Özel.

mode-locked, oscillator-amplified based on chirped-pulsed-amplification (CPA) technique, with extreme peak powers usually in the order of 10^6 W with 700–980 nm wavelengths, (iii) copper vapor lasers with wavelengths between 578 and 611 nm, (iv) neodymium-doped yttrium aluminum garnet (Nd:YAG) lasers with near-infrared, visible, and UV wavelengths at 1064, 533, 355, and 266 nm. Specific laser parameters for these lasers are given in Table 6.1.

Laser-beam machining uses an intensely focused, coherent stream of light (a laser) to vaporize or chemically ablate materials. In general, pulsed lasers produce a small heat-affected zone and a small recast layer on the machined surface by causing material vaporization through high peak power and shorter interaction time (Fig. 6.1). The differences between the long- (nanosecond) and short-pulsed (picoseconds and femtoseconds) laser micro-machining are well experimented (Figs. 6.2 and 6.3).

TABLE 6.1 Most Common Lasers Used for Laser Processing on a Microscale and Their Parameters [4–6,9,14,22]

Laser Type	Wavelength (nm)	Power (W)	Pulse Energy (mJ)	Fluence (J/cm^2)	Pulse Duration	Repetition Rate
Q-switched	1064	1–35 W	8 mJ	—	5–100 ns	1–400 kHz
Nd:YAG	532	0.5–20 W	5 mJ	—	5–70 ns	1–300 kHz
	355	0.2–10 W	3 mJ	—	5–50 ns	15–300 kHz
	266	0.5–3 W	<1 mJ	—	5–30 ns	15–300 kHz
Ti:sapphire	800 (central)	0.5–2 W	0.25–0.9 mJ	—	100–150 fs	1–5 kHz
	(700–980)	—	—	—	—	—
Excimer-	—	—	—	—	10–20 ns	5–10 Hz
XeF	351	—	—	1.8–9.1	—	—
XeCl	308	—	—	1.2–9.8	—	—
KrF	248	—	—	0.9–9.8	—	—
ArF	193	—	—	0.7–4.0	—	

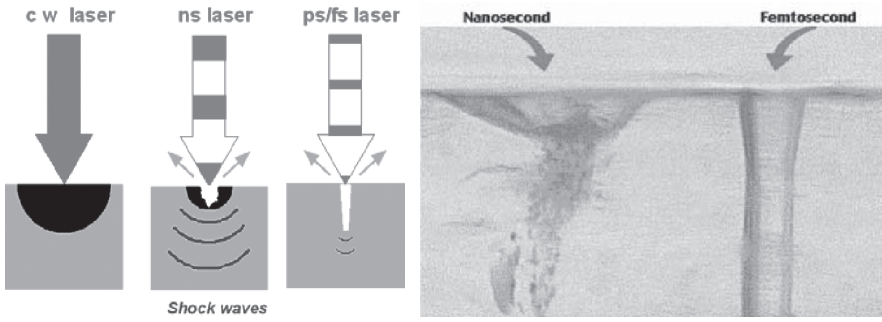

Figure 6.1 Illustration of heat-affected zones subjected to different laser types. *Source*: courtesy of Clark/MXR corp.

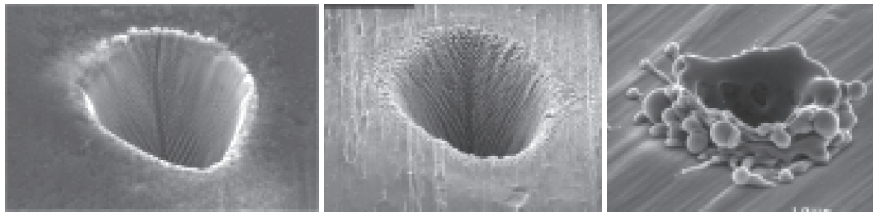

(a) (b) (c)

Figure 6.2 Pulsed laser-beam micro-machining holes drilled with a Ti:sapphire system (120 fs) (a) in air and (b) in a vacuum, and (c) a hole drilled by an Nd:YAG laser ($\lambda = 1.06$ μm; pulse width = 100 ns, $P = 50$ mW, 2 kHz). All images were taken from the entry side of the kovar foil. *Source*: Courtesy of Sandia Manufacturing Science and Technology Center, http://mfg.sandia.gov.

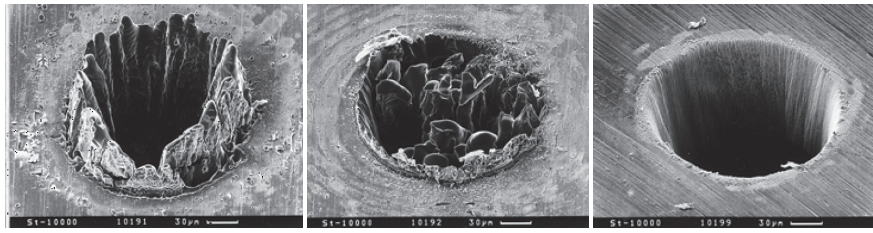

(a) (b) (c)

Figure 6.3 Laser ablation with (a) nanosecond pulse (3.3 ns and 1 mJ), (b) picosecond pulse (80 ps and 900 μJ), and (c) femtosecond pulse (200 fs, 120 μJ) at 780 nm wavelength [3].

Laser micro-machining is an alternative micro-manufacturing process used for the production of micrometer-sized structures, using long- (*nanosecond*) and short-pulsed (*femtosecond*) lasers on absorptive metals with applications including hole drilling, removal of surface defects, and mask repair (Fig. 6.4) and transparent materials such as glass and polymers with applications including fabrication of optical waveguides, micro-fluidic channels, and fabrication of photonic devices.

6.2 LASER RADIATION, ABSORPTION, AND THERMAL EFFECTS

In ablation, the chemical bonds between atoms are broken by the excess amount of laser energy absorbed by the valence electrons in the material. In laser radiation regimes, the dominant process involved is the heating of the target material through the liquid phase to the vapor phase, resulting in the expansion and expulsion of the desired target material [3,4,16,20]. This is accompanied by heating and collateral damage to the surrounding area, the degree of which is determined

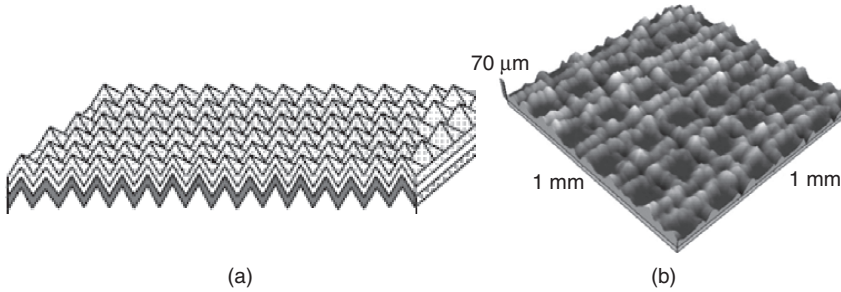

Figure 6.4 (a) Design for multifunctional solar cell surfaces and (b) surface texturing with laser scribing [23,24].

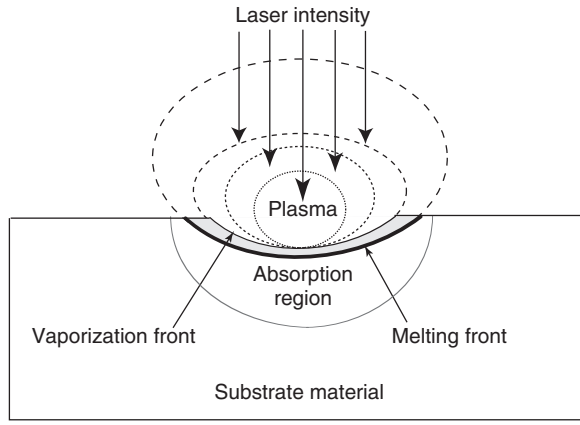

Figure 6.5 Illustration of laser–material interaction [25].

by the rate of energy absorption and the rate of energy loss through thermal conduction in the material. This collateral damage is often detrimental and is a limiting factor when high-precision ablation is required or when it may present a hazard, for example, laser surgery.

The advent of short-pulsed lasers opens up a new area for research and applications in material processing. In laser micro-machining, short-pulsed and ultrashort-pulsed lasers produce a very small heat-affected zone compared to cw lasers (Fig. 6.1), enabling extremely localized laser heating on the micro-scale. Localized micro-scale heating reduces thermal damage to the bulk material. This damage is often detrimental and is a limiting factor when high precision is required. The major processes in the laser–material thermal interaction include radiation absorption and the associated thermal effects (Fig. 6.5).

In general, the limiting factor in the spatial resolution of laser ablation is the diffusion of the heat coming out of the irradiated spot in metals. According to Ivanov and Zhigilei [16], the laser energy is absorbed by the electrons and

within femtoseconds is equilibrated among the electrons and slowly (within a few picoseconds) transferred to the atomic vibrations, depending on the strength of the electron–phonon coupling in the lattice.

A thermal equilibrium is formed within the lattice between the electrons and the phonons. The heat flow from the irradiated surface to the bulk of the lattice is considered as common thermal diffusion, and when the laser pulse duration is comparable to or less than the duration of this equilibrium formation, a state of thermal nonequilibrium is created by the laser irradiation, where the electrons and the lattice have different temperatures (Fig. 6.6). At the continuum level, the time of evolution of the lattice and electron temperatures, (T_l and T_e), can be described within a so-called *two-temperature model* (*TTM*) by the two coupled nonlinear differential equations given below.

$$C_e(T_e)\frac{\partial T_e}{\partial t} = \nabla[K_e(T_e)\nabla T_e] - G(T_e - T_l) + S(z,t)$$
$$C_l(T_l)\frac{\partial T_l}{\partial t} = \nabla[K_l(T_l)\nabla T_l] - G(T_e - T_l) \tag{6.1}$$

where C and K are the heat capacities and the thermal conductivities of the electrons and the lattice as denoted by the subscripts e and l, respectively, and G is the electron–phonon coupling constant. The source term *S(z,t)* is used to describe the local laser energy deposition per unit area and unit time during the laser pulse duration. These equations can be solved by a finite-difference method and the spatial and time evolution of the electron and lattice temperatures can be obtained. The TTM is discussed in detail later.

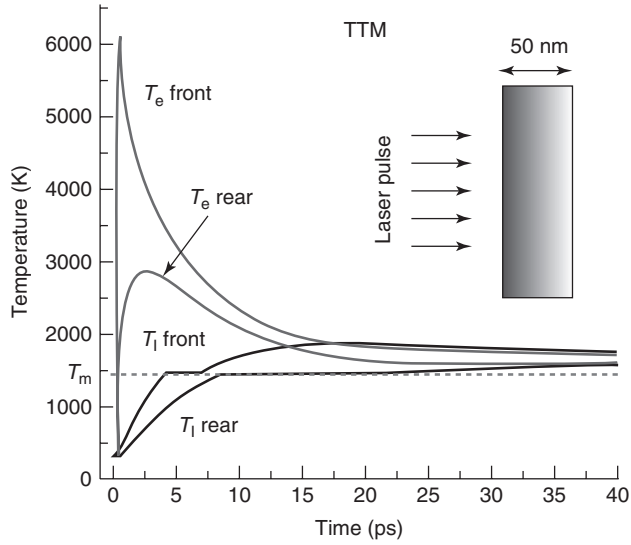

Figure 6.6 Predicted lattice and electron temperatures with TTM [16].

Modeling thermal diffusion during laser ablation of materials has been of great interest for researchers. The publications by Chichkov *et al*. [3], Momma *et al*. [4], Ramanathan and Molian [12], and Ki and Mazumder [20] are just to name a few in this field. Often, the two-temperature coupled equations are solved under the assumption that the electron and the lattice heat capacities and the thermal conductivity remain constant in the laser ablation process. The solution is usually valid for ultrashort to nanosecond pulse-width regimes.

Researchers have utilized the TTM to compute the temperatures of the lattice and the electron with respect to short time period (from femto- to nanoseconds) in order to determine the transient behavior of the temperature fields with the lattice of the work material which is induced by the pulsed laser irradiation.

Numerical models are established for simulating ultrashort laser interaction with the work material. The TTM is utilized to simulate the energy transport of electrons and lattices. Specifically, ultrafast laser radiation is simulated by solving heat conduction equations and using the finite-difference time-domain method. The temperature histories of electrons and lattices are presented to demonstrate the basic phenomenon of thermal energy generation and complex laser-beam propagation with the targeted work material.

6.3 LASER PROCESSING OF MATERIALS

Selection of the optimum laser wavelengths is influenced by the minimum feature size and the optical properties of the work material. The characteristics of absorption, reflectivity, and thermal diffusion of different kinds of materials are shown in Fig. 6.7 and are summarized subsequently.

6.3.1 Laser Processing of Metals and Alloys

When radiation interacts with metals, the energy absorbed raises the temperature level. However, if much of the radiation is reflected because of the surface characteristics, the energy absorbed may not be sufficient to achieve the softening of the material to substantially affect the process of removal of the material. The use of short-pulsed lasers with a proper choice of laser parameters may still achieve thermal softening in highly reflective metals. The mechanism is similar to those related to laser-induced phase transformations, as reviewed by Grigoropoulos *et al*. [26]. As shown in Fig. 6.7, aluminum is highly reflective. However, copper and steel have better absorption at UV wavelengths. Zhang *et al*. [27] studied laser micro-machining of copper, using a frequency tripled pulsed single-mode Nd:YAG laser of 50-ns pulse duration and reported favorable experimental results. The reflectivity of metals often decreases with temperature, and they are effectively machined by Nd:YAG and CO_2 lasers. Zhao *et al*. [6] reported favorable results on micro-machining of aluminum, using a femtosecond Ti:sapphire laser.

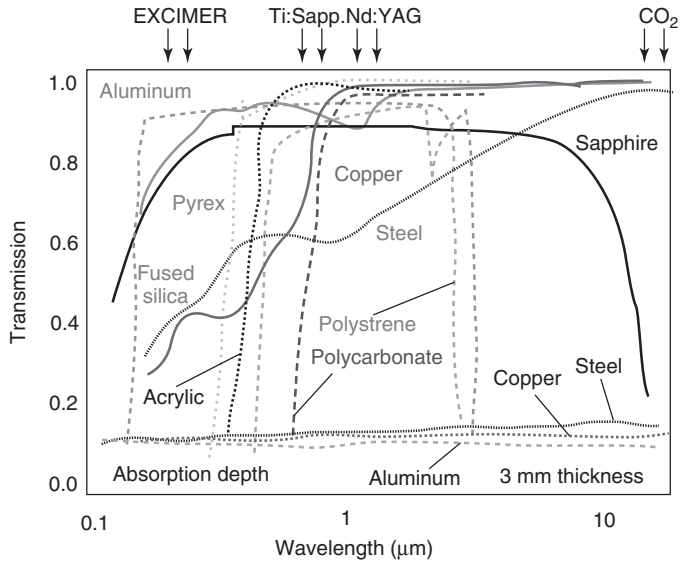

Figure 6.7 The relationship between wavelength and transmission for some metals, polymers, glass, and ceramics [25].

6.3.2 Laser Processing of Polymers and Composites

Polymers exhibit strong absorption in the UV and deep infrared (IR) wavelengths, but weak absorption at visible wavelengths. However, the reaction to lasers is somewhat different in polymers, compared to that seen in metals. It is believed that UV produces a cooler excitation in polymers. On the other hand, IR causes the most molecular vibration and material change through thermal process. However, the properties of most polymers and composites are very strong functions of temperature. This implies that even slight changes in temperature can have a strong effect on machining and localized laser heating can be used effectively for increasing the productivity and the product characteristics. At UV wavelengths (200–400 nm), the material removal mechanism in polymers is generally thermal evaporation. Below 200 nm, the polymeric material is removed typically by chemical ablation.

6.3.3 Laser Processing of Glasses and Silica

Micro-machining of hard and brittle glasses finds applications in biochemistry, biomedicine, lab-on-chip devices, sensors, and Bio-MEMS devices. Many crystals and glasses exhibit strong optical absorption at deep UV and IR wavelengths, with much weaker absorption at visible and near-infrared wavelengths. The absorption of light by some glasses can have a very nonlinear behavior. For example, the transmission wavelength of Pyrex ranges from 300 nm to 3 μm, but at 2.5 μm, the material has the best absorption. However, since glass is

nonopaque, absorption occurs largely within the volume of the material, rather than on the surface. Zhang *et al*. [28] studied micro-machining of glass materials by laser-induced plasma-assisted ablation using a 532-nm laser and reported the experimental results. Zhao *et al*. [6] applied a femtosecond Ti:sapphire laser for micro-machining of fused silica successfully.

6.3.4 Laser Processing of Ceramics and Silicon

Synthetic CVD diamond is an attractive material, since it has various applications such as IR optical applications, detectors, sensors, and thermal management systems. Among all materials, diamond is the most difficult one to be machined because of its hardness and inertness, and, like glass, it is highly transparent over a broad range of the optical spectrum. Laser etching of silicon permits a wide variety of structures to be made, since it is independent of the crystal plane orientation unlike wet etching. Various pulse lasers such as IR Nd:YAG [9] and femtosecond (Ti:sapphire) lasers [17,29] have been used for machining of diamond and silicon [20] for a number of years. Similarly, crystal growth from the melt in the manufacture of silicon chips is followed by several processes of laser machining to obtain the desired shape, size, and other characteristics of silicon wafers. The focus in these processes is on melting and ablation caused by lasers. The use of lasers with micro-machining techniques has not received much attention, though this approach enables better control of the product characteristics and lower costs.

6.4 LASER PROCESSING PARAMETERS

There are several key parameters influencing laser ablation and directly affecting the energy working on materials. Larger reduction in laser power or increases in cutting speed will result in incomplete penetration of the cut zone, or poor quality in laser ablation. Chen and Yao [18] investigated pulsed laser micro-machining and its influence on dross attachment, burn, and recast layer thickness by using designed experiments and statistical analysis. They identified that the significant factors affecting dross attachment are average power, orifice size, and tracking speed. They found that when the average power increases, the dross attachment rating number decreases. Bordatchev and Nikumb [21] investigated the relationship of energy with crater diameter, depth, and volume in pulsed laser micro-machining by using designed experiments and statistical analysis. They considered only pulse energy as a major controlled parameter. Shallow craters were created in copper foil with a thickness of 70 μm by applying a single pulse to one location and then moving the part to a new position for the subsequence pulse. They obtained approximate relations between geometric parameters and pulse energy. Many other research findings indicate the main parameters in laser processing which will be discussed briefly next.

6.4.1 Laser Spot Size and Beam Quality

Beam quality is measured by its energy, focus ability, and homogeneity. If the beam is not of a controlled size, the laser-affected region may be larger than the desired size with excessive slope in the sidewalls. Ho and Ngoi [30] reported a subspot size micro-machining technique utilizing the phenomenon of short-pulsed laser interference.

6.4.2 Peak Power

The peak power must be able to soften the workpiece for thermal processing, but must not be strong enough to cause direct ablation. There exist optimum values of laser-beam intensity such that extremely localized material softening will occur. A higher peak power is required to cause ablation or melting and vaporization of the target material. Peak power is the most important limiting parameters for pulsed lasers and can be increased by reducing the pulse duration.

6.4.3 Pulse Duration

The effect of pulse duration on feature quality is significant in laser ablation. Although the achievable average laser power and laser intensity decrease with decreasing pulse duration, the peak power increases, effectively providing fast irradiation and ultrashort laser–matter interaction. The short pulse duration can maximize peak power and minimize thermal diffusion to the surrounding bulk work material, leading to localized heating as discussed by Pronko *et al*. [2], Malshe *et al*. [31], and Choi *et al*. [19]. Theoretically, the pulse duration should not be longer than the thermal relaxation time for thermal diffusion. The advantages of short-pulsed lasers such as very small heat conduction and very thin liquid phase thickness are promising for future applications in precision thermal processing of materials with minimal damage. Lasers with pulse durations of few femtoseconds and high repetition rates are available for micro-processing applications (Table 6.1) though femtosecond laser ablation is still thermal in nature, and cannot completely avoid heat affected zone, recast layer, chemical contamination, etc.

6.4.4 Pulse Repetition Rate

When the energy is sufficient, every pulse has a thermal effect on the workpiece. It is necessary for successive spots to overlap for successful material removal e.g., in a series of drill operations. If the pulse rates were low, the energy would leave the thermal zone and would be of no use. If the residual heat were retained by a rapid repetition rate (limiting the time for thermal conduction), the thermal effect on the work material would be more efficient. On the other hand, a pulsed laser has an upper limit in pulse repetition (Table 6.1). A very high pulse repetition rate (100 kHZ and above) may result in pulse laser irradiation behaving similar to cw laser irradiation on some materials.

Direct laser ablation can be performed by controlling laser-beam properties such as laser energy, intensity, pulse duration, and wavelength. However, this method requires additional capabilities for a typical laser beam generation and delivery system. With the laser-beam interference technique, micro-machining of even smaller features that are typically not achievable is possible. Ho and Ngoi [30] reported a subspot size micro-machining technique by utilizing the phenomenon of ultrafast pulse laser interference. The results show much more reduction in machined feature size compared to the case of a noninterfered laser beam. Holes of 300 nm were successfully drilled on a 1000-Å thick gold, using the interfered laser beam.

Most of these methods are for fabrication of 2D or 2.5D features such as holes and channels. Micro-machining of 3D geometrical features such as spherical, conical, and cylindrical surfaces remains a challenge. Malshe and Deshpande [29] studied femtosecond-pulsed laser micro-machining on optoelectronic materials with 2D and 3D periodic patterns in the form of ripples, clusters, and combination of features. They found that the amorphous and defective areas in the nanolaser region enable selective light trapping and surface passivation without contaminating the surface. Choi *et al*. [19] proposed a 3D micro-machining method called *hole area modulation* (*HAM*). They reported that the laser ablation depth was influenced by hole diameter on the mask, pitch, transferring velocity, transferring distance, and the number of pulses. The machined cavity could be converted to 2D distribution with depth information, and then the 3D cavity will be generated. When the laser-beam properties cannot be altered, the HAM method can be made an alternative solution by controlling the density of the holes and the step size to improve the accuracy of the 3D geometry.

6.5 ULTRASHORT-PULSED LASER ABLATION

Nanosecond (ns) and ultrashort-pulsed (femtosecond to picosecond) lasers have many current and potential applications in micro-machining of metals, semiconductors, and dielectrics for the manufacturing of electronic, medical, optical, and other devices, and they have the advantage of extremely high achievable radiation intensities (and hence can ablate almost any material) and extremely short pulse durations (and hence can realize precise material removal with a very small heat-affected zone). The laser–material interaction and ablation mechanisms are different for nanosecond and ultrashort-pulsed lasers because of the significantly different pulse durations, which are discussed separately.

A lot of efforts have been devoted to the experimental and theoretical studies of the ultrashort laser–matter interactions in recent years, and numerical models based on comprehensive hydrodynamics [32–35] or molecular dynamics [23,36–43] have been developed. Ultrashort laser ablation is a very complicated process, and further work is still needed to completely understand the fundamental ablation mechanisms. Earlier investigations show that material removal during ultrashort laser ablation may be realized through one or a combination of the

following mechanisms, such as spallation, Coulomb explosion, phase explosion, critical-point phase separation (CPPS), and fragmentation [23,33–46]. The actual mechanisms depend on laser intensity, wavelength, material types, etc.

Multiple complicated physical processes may occur on different time scales during and after an ultrashort laser pulse interaction with a target, which are discussed subsequently.

6.5.1 Two-temperature Heat Transfer

When an ultrashort laser pulse irradiates a solid, the laser energy will be absorbed. For metals, this is realized mainly through free carrier absorption [47], that is, electrons in the conduction band absorb photons and obtain higher energy. In semiconductors and dielectrics, electrons can be excited from the valance bands to the conduction bands through photon (or multiphoton) ionization process. Following the absorption of the laser energy by electrons, the energy will be transferred from electrons to the lattice through electron–photon collision. The typical timescale for the electrons and the lattice to reach thermal equilibrium is around ~1–10 ps, depending on the material. Hence, for laser pulses of shorter than this characteristic time, the initial heat transfer process during laser–matter interaction cannot be described by the commonly used one-temperature heat transfer equation. Instead, the so-called two-temperature heat transfer equation needs to be used. The one-dimensional (1D) form of the equation can be given as follows [24,33,34,46]:

$$\frac{\partial E_{\mathrm{e}}}{\partial t} = \frac{\partial}{\partial z}\left(k_{\mathrm{e}}\frac{\partial T_{\mathrm{e}}}{\partial z}\right) - \mathrm{G}(T_{\mathrm{e}} - T_{\mathrm{i}}) + S \tag{6.2}$$

$$C_{\mathrm{i}}\frac{\partial T_{\mathrm{i}}}{\partial t} = \mathrm{G}(T_{\mathrm{e}} - T_{\mathrm{i}}) \tag{6.3}$$

where $T_{\mathrm{e}}, T_{\mathrm{i}}$, and C_{i} are the electron temperature, the lattice temperature, and the volumetric heat capacity of the lattice respectively, t is the time, z is the spatial coordinate, S is the source term, k_{e} is the electron thermal conductivity of an electron, and G denotes the electron–phonon coupling constant, given by $\mathrm{G} = C_{\mathrm{e}}/\tau_{\varepsilon}$, where τ_{ε} is the mean energy exchange time for the electrons and the lattice. The electron thermal energy per unit volume, E_{e}, is given by $\frac{\partial E_{\mathrm{e}}}{\partial t} = C_{\mathrm{e}}\frac{\partial T_{\mathrm{e}}}{\partial t}$, where $\mathrm{C_e}$ is the electron heat capacity, and for semiconductors and dielectrics, it also depends on the density of free electrons generated through photon ionization and avalanche ionization. The lattice thermal conductivity is neglected in Eq. (6.3). The two-temperature heat conduction equations are based on the assumption that the energy distributions of both the phonons and the electrons are thermal distributions characterized by distinct temperatures, that is, the lattice temperature and the electron temperature, respectively [47]. Hence, the TTM is valid only for times longer than the thermalization time for the electrons and the phonons (i.e., the time needed for the electrons and the phonons to establish the energy distribution to make their temperature definition meaningful). For times shorter than the thermalization time, the electron and phonon temperatures lose their

meaning and the use of the TTM is questionable. The source term S is given by [24]:

$$\begin{aligned} S &= \frac{\partial I(z,t)}{\partial z} - E_g \frac{\partial n_e}{\partial t} \quad \text{(semiconductor and dielectrics)} \\ &= \frac{\partial I(z,t)}{\partial z} \quad \text{(metal)} \end{aligned} \tag{6.4}$$

where I is the laser intensity and E_g is the band gap of semiconductors or dielectrics. The last term on the right hand side of Eq. (6.4) for semiconductor and dielectrics represents the energy consumed in overcoming the band gap during free electron generation through the ionization process.

The laser-beam propagation, strictly speaking, is governed by Maxwell's wave equation. For the 1D situation, the following simplified equation is often used [24,46]:

$$\begin{cases} \dfrac{\partial I(z,t)}{\partial z} = aI(z,t) & \text{(metal)} \\ \left[(\sigma_1 + \sigma_2 I(z,t))\dfrac{n_a}{n_a + n_i} + a\right] I(z,t) & \text{(semiconductor)} \\ \sigma_N I^N \dfrac{n_a}{n_a + n_i} \mathrm{h}wN + aI(z,t) & \text{(dielectrics)} \end{cases} \tag{6.5}$$

where σ_1 and σ_2 are one- and two-photon ionization cross sections, h is Planck's constant, w is the laser frequency, n_a and n_i are number densities of neutral and ionized atoms, σ_N is the cross section for multiphoton ionization with N photons (e.g., $N = 6$ for Al_2O_3 at 800 nm), and a is the free electron absorption coefficient.

The free electron absorption coefficient a can be calculated on the basis of the complex dielectric function, which can be calculated by [46,48–50]:

$$\varepsilon = 1 + (\varepsilon_g - 1)\left(1 - \frac{n_e}{n_0}\right) - \frac{n_e e^2}{\varepsilon_0 m_e w^2} \frac{1}{1 + iv/w} \tag{6.6}$$

where n_0 is the valence band electron density, v is the collision frequency, ε_0 is the permittivity of vacuum, e is the electron charge, ε_g is the dielectric constant of the unexcited material, and m_e is the mass of an electron. The material complex index of refraction n can also be obtained from the complex dielectric function [50].

The free electron number density for metals can be obtained from the material equation of state (EOS) model. For semiconductors (e.g., silicon), the electron density can be described by the rate equation [46,48]:

$$\frac{\partial n_e}{\partial t} = \left[(\sigma_1 + 0.5\sigma_2 I)\frac{I}{\mathrm{h}w} + \delta n_e\right] \frac{n_a}{n_a + n_i} - \frac{n_e}{\tau_0 + 1/Cn_e n_i} \tag{6.7}$$

where δ is the impact ionization coefficient [46]. The last term on the right hand side of Eq. (6.7) describes the electron loss due to Auger recombination process with $C = 3.8 \times 10^{-31}\text{cm}^6/\text{s}$ and $\tau_0 = 6 \times 10^{-12}\text{s}$ for silicon [46,48].

For dielectrics, the evolution of electron number density is described by [46,49]:

$$\frac{\partial n_\text{e}}{\partial t} = [\sigma_N I^N + \alpha I n_\text{e}] \frac{n_\text{a}}{n_\text{a} + n_\text{i}} - \frac{n_\text{e}}{\tau} \tag{6.8}$$

where α is the avalanche coefficient and σ_N is the cross section for multiphoton ionization with N photons (e.g., $N = 6$ for sapphire at 800 nm). The last term on the right side describes the free electron loss with the relaxation time τ. It should be noted that in Eqs. (6.7) and (6.8), for simplicity the electron spatial transport through drift and diffusion has been neglected.

The free electron generation during laser interaction with dielectrics and semiconductors significantly affects the laser-beam propagation and energy absorption. Figure 6.8 shows the calculated normalized laser intensity distribution in a silicon target at $t = 100$ fs (laser full-width-at-half-maximum (FWHM) pulse duration: 100 fs, wavelength: 800 nm). If optical absorption due to the generated free electrons is considered, most of the laser energy is absorbed at a depth of several hundred nanometers. However, if free electron absorption is neglected, the absorption depth increases significantly to several microns. Therefore, the laser-induced free electrons play a key role in laser-beam propagation and energy absorption.

6.5.2 Electron Emission from the Surface and Coulomb Explosion

Owing to the temperature increase and the excitation by laser photon flux, free electrons may be emitted from the target surface. The total current density of electrons emitted from a metal target surface can be calculated on the basis of the target surface temperature [52]:

$$J = \sum_{n=0}^{\infty} J_n \tag{6.9}$$

where J_0 is the thermionic emission, J_1 is one-photon photoemission, and J_n is n-photon emission given by Bechtel *et al*. [52]:

$$J_n = \text{a}_n (\text{e}/\text{h}\nu)^n \text{A} I^n (1-R)^n T_\text{e}^2 F\left(\frac{n\text{h}\nu - \phi}{\text{k}T_\text{e}}\right) \tag{6.10}$$

where I is the laser intensity, R is the surface reflectivity, A is the Richardson coefficient, hν is the laser photon energy, ϕ is the surface work function, k is Boltzmann's constant, T_e is the electron temperature, a_n is a constant, and *F(x)*

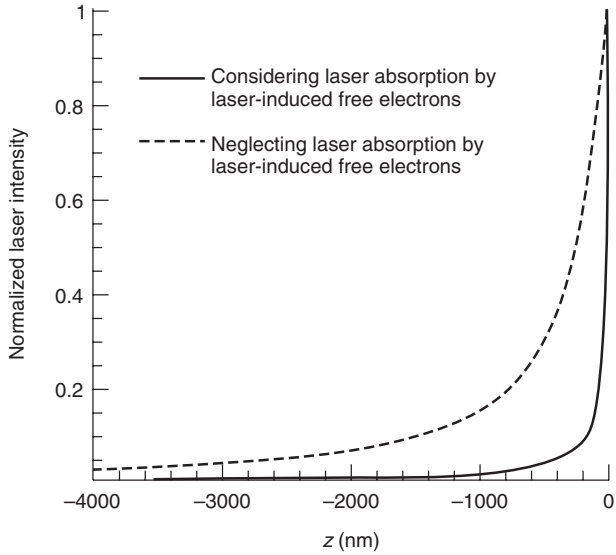

Figure 6.8 The calculated normalized laser intensity distribution in a silicon target at $t = 100$ fs (laser pulse duration: 100 fs, wavelength: 800 nm). *Source*: Reprinted from Appl Surf Sci, 255(9), Wu B, Shin YC., A simplified predictive model for high-fluence ultrashort pulsed laser ablation of semiconductors and dielectrics, 4996–5002, Copyright (2009), with permission from Elsevier [51].

is the Fowler function. Typically, only the first few terms on the right side of Eq. (6.10) are important, and the other terms are generally negligible.

The surface electron emission may break the quasi-neutrality in the near-surface region. As a result, an electric field will be generated, which can be described by the well-known Poisson equation [46]. The charging of target surfaces may cause a subpicosecond electrostatic rupture of the superficial layers, that is, the so-called Coulomb explosion process. Relatively speaking, this effect occurs for dielectrics more easily, and it is often strongly inhibited for metals and semiconductors because of their superior carrier transport properties [46]. Figure 6.9 shows the temporal profiles of the laser-induced electric field on the surface (100-fs and 800-nm laser pulses). It can be seen that the electric field induced in the sapphire target is much higher than that in the silicon and gold targets. It also exceeds the critical electric field for Coulomb explosion, and can induce the electrostatic rupture of a surface layer with a thickness on the order of nanometers.

6.5.3 Formation of Early Plasma Due to Electron Emission

During ultrashort laser–material interaction, the emitted electrons from the target surface may cause the breakdown of the ambient gas because of cascade ionization and may form a so-called "early plasma," which occurs within a few picoseconds after laser pulse starts. It was experimentally observed by Mao *et al*.

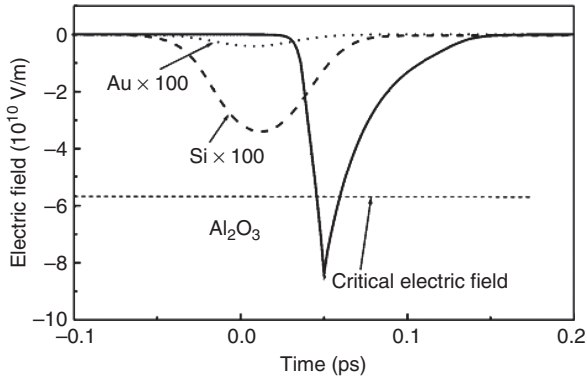

Figure 6.9 Temporal profiles of the laser-induced electric field in the surface region of the targets (100-fs and 800-nm laser pulses; *Source*: plot taken from Bulgakova *et al*. [46] With kind permission from Springer Science+Business Media: Appl Phys A Mater Sci Process, A general continuum approach to describe fast electronic transport in pulsed laser irradiated materials: the problem of Coulomb explosion, 81, 2005, 345–356, Bulgakova NM, Stoian R, Rosenfeld A, Hertel IV, Marine W, Campbell EEB, Figure 2).

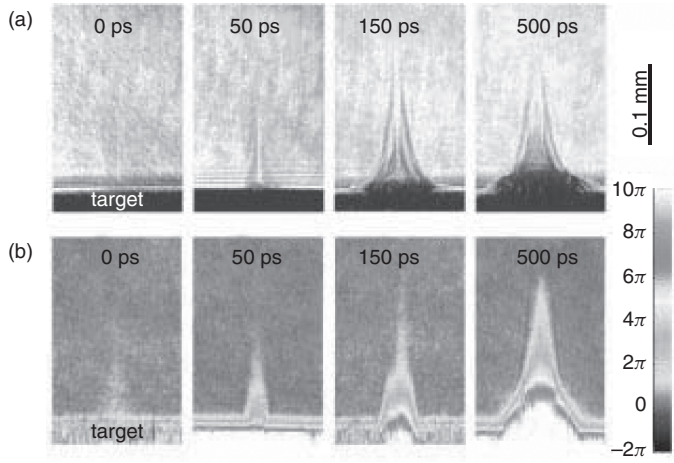

Figure 6.10 (a) Shadowgrams and (b) phase shift maps of the plasma at four different delay times (35-ps and 1064-nm laser pulse and copper target; *Source*: Reprinted with permission from [Mao SS, Mao X, Greif R, Russo RE., Appl Phys Lett, 77(16), 2464–2466, (2000)]. Copyright [2000], American Institute of Physics [54].).

[53,54] as shown in Fig. 6.10. The early plasma is generated because of the ambient air breakdown instead of the ionization of the target vapor. It is formed before significant vaporization or hydrodynamic expansion of the target occurs.

The evolution of the early plasma in the ambient gas can be described by the conservation equations of mass, momentum, and energy for each species (electrons, ions, and neutral atoms). For electrons, the equations in 1D form are

given by [53–55]:

$$\frac{\partial n_e}{\partial t} + \frac{\partial (n_e v_e)}{\partial z} = S_e \tag{6.11}$$

$$\frac{\partial (n_e m_e v_e)}{\partial t} + \frac{\partial (n_e m_e v_e^2)}{\partial z} = -\frac{\partial P_e}{\partial z} + n_e f_e \tag{6.12}$$

$$\frac{\partial \varepsilon_e}{\partial t} + \frac{\partial (\varepsilon_e v_e)}{\partial z} = -\frac{\partial (P_e v_e)}{\partial z} + W_e + Q_e + W_L \tag{6.13}$$

where t is time; z is the spatial coordinate; v_e is the electron velocity; S_e is the source term for electron generation, which is mainly due to cascade ionization; m_e is the electron mass; P_e is the electron pressure; f_e is the force term including three components: the force due to electric field, the force that has resulted from elastic collisions between the electrons and the ions, and the nonlinear ponderomotive force [55]; ε_e is the electron energy per unit volume, which is given by $\varepsilon_e = 1.5kT_e n_e + 0.5 n_e m_e v_e^2$ [53]; W_e is the work done by the forces exerted on electrons; Q_e is the contribution from electron heat conduction; and W_L is the energy source term due to the absorption of laser energy. The governing equations for the ions and the atoms are similar with a few minor differences, one of which is that for neutral atoms no force (and hence no work done by the force) is induced by the electric field.

6.5.4 Hydrodynamic Expansion

During ultrashort laser–material interaction, the absorbed laser energy will increase the target material pressure near the surface. Hydrodynamic motion may be driven by the pressure gradient. The target hydrodynamic expansion process should be described by two-temperature hydrodynamic equations. For metals, the equations in the 1D form are given by [34,56,57]:

$$\frac{\partial \rho}{\partial t} + \frac{\partial (\rho u)}{\partial z} = 0 \tag{6.14}$$

$$\frac{\partial \rho u}{\partial t} + \frac{\partial (\rho u^2 + P)}{\partial z} = 0 \tag{6.15}$$

$$\begin{aligned} &\frac{\partial \left(E_e + \frac{1}{2}\rho_e u^2 \right)}{\partial t} + \frac{\partial \left[u \left(E_e + \frac{1}{2}\rho_e u^2 + P_e \right) \right]}{\partial z} \\ &= -\frac{\partial q_e}{\partial z} + \frac{\partial}{\partial z}\left(k_e \frac{\partial T_e}{\partial z} \right) + \frac{\partial I}{\partial z} - Q_{e\text{-}i}(T_e - T_i) \end{aligned} \tag{6.16}$$

$$\begin{aligned} &\frac{\partial \left(E_i + \frac{1}{2}\rho_i u^2 \right)}{\partial t} + \frac{\partial \left[u \left(E_i + \frac{1}{2}\rho_i u^2 + P_i \right) \right]}{\partial z} \\ &= Q_{e\text{-}i}(T_e - T_i) \end{aligned} \tag{6.17}$$

where t is time, z is the spatial coordinate, ρ_e is the electron mass density (generally negligible), ρ_i is the ion mass density, ρ is the total density and can be expressed as $\rho = \rho_e + \rho_i \cong \rho_i, u$ is the velocity, P_e is the electron pressure, P_i is the ion pressure, P is the total pressure and can be expressed as $P = P_e + P_i, E_e, T_e, E_i$, and T_i, are the volumetric internal energies and temperatures for electrons and ions, respectively, k_e is the electron thermal conductivity, I is the net laser radiation flux in the z-direction, Q_{e-i} is the electron–ion coupling constant, and q_e is the radiative heat flux in the z direction, which is particularly important for the high-temperature region and can be obtained by solving the radiative transfer equation [58]. It should be noted that for simplicity some terms (e.g., the deviatoric stress terms) are not shown in the above equations. When the pressure gradient and the velocity are negligible, the above equations can be simplified into two-temperature heat conduction equations (Eqs. 6.2 and 6.3).

The evolution of the thermodynamic state of the target material near the surface can be obtained by solving the hydrodynamic equations or by using molecular dynamic simulations. Vidal *et al*. [33] solved hydrodynamic equations and showed that under high laser intensities, the dominant material removal mechanism is the so-called "critical-point phase separation" process. Figure 6.11 is the hydrodynamic simulation result from Vidal *et al*. [33], which shows that the

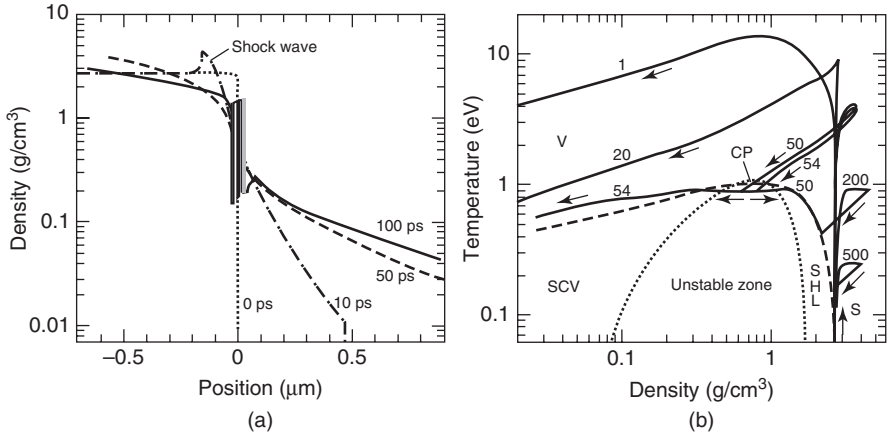

Figure 6.11 (a) Density profiles as a function of position at 0, 10, 50, and 100 ps with respect to the laser pulse. Laser pulse has 500 fs, 1 μm, normal incidence, and 10 J/cm^2. The initial distance between the boundaries of the Lagrangian cells is 1 nm. (b) Trajectories of a few Lagrangian cells in the density–temperature plane. The total simulation time is 400 ps. The cells are numbered inward starting from the interface between the matter and the vacuum. Dashed curve, binodal; dotted curve, spinodal; SHL, superheated liquid; SCV, supercooled vapor; S, solid phase; V, vapor phase; and CP, critical point. Aluminum target. *Source*: Reprinted figure with permission from [Vidal F, Johnston TW, Laville S, Barthelemy O, Chaker M, Drogoff BL, Margot J, Sabsabi M., Phys Rev Lett, 86(12), 2573–2576, 2001], Copyright (2001) by the American Physical Society, http://link.aps.org/doi/10.1103/PhysRevLett.86.2573, [33].

thermodynamic trajectories of the material cells near the surface can be roughly divided into two stages. During the first heating stage, the cells are heated very rapidly to their maximum temperatures without any obvious density change. After that, the density will decrease roughly following the relation $T \propto \rho^{2/3}$. The simulation shows that the material cells, whose expansion trajectories enter the unstable zone near the critical point (CP), will transform into a bubbles–droplets transition layer as a result of thermodynamic instabilities. The mass above these cells will be ablated, whereas the mass below will condense back onto the target. This process is called critical-point phase separation (CPPS).

The MD simulation results from Cheng and Xu [36] also indicate that during ultrashort laser ablation of nickel, the dominant ablation mechanism is CPPS for high fluence, whereas for lower fluence it is phase explosion (the explosive phase change process due to the homogeneous bubble nucleation and growth when material liquid is superheated close to the CP in the thermodynamic two-phase region). Assuming the CPPS mechanism, simplified physics-based models based on the two-temperature heat transfer equations have been developed by Wu and Shin [24,51] for high-fluence ultrashort laser ablation of metals, semiconductors, and dielectrics, which have shown good agreement with the experimental measurements for the laser ablation rate. Some sample results are given in Fig. 6.12.

However, the MD simulation results obtained by some researchers suggest that CPPS may not be the dominant material removal mechanism for high-fluence ultrashort laser ablation [40,41]. Therefore, further experimental and theoretical studies are still needed to understand the exact material removal mechanism for ultrashort laser ablation.

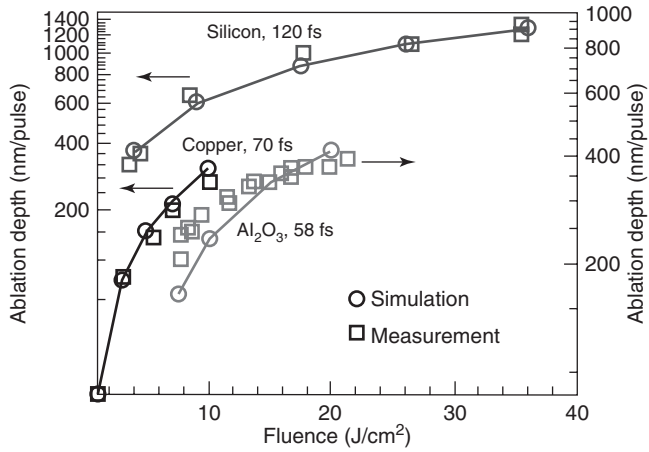

Figure 6.12 The ultrashort laser ablation rate: measurements versus predications by the simplified models of Wu and Shin [24,51]. *Source*: plot is taken from Wu and Shin [24]; the measurement is taken from Hashida *et al*. [44], Meunier *et al*. [59], and Guizard *et al*. [60].

6.6 NANOSECOND-PULSED LASER ABLATION

6.6.1 Ablation Mechanisms

It has been found from the earlier research that nanosecond-pulsed laser ablation involves one or several physical mechanisms for material removal among surface vaporization, phase explosion, and hydrodynamic expansion.

Surface vaporization is the liquid–vapor phase transformation across the liquid–vapor interface. The vapor molecules that leave the liquid surface (the melted surface of the target) are initially in a nonequilibrium velocity distribution, and the distribution changes into equilibrium within a very thin layer at the liquid–vapor interface, which is often called Knudsen layer [61,62].

Phase explosion is the homogeneous bubble nucleation and growth in the target material superheated close to the thermodynamic critical temperature T_c in the two-phase region of the thermodynamic diagram. The nucleation rate strongly depends on the extent to which the target material is superheated [63,64].

Hydrodynamic expansion is the material removal process due to macro-scopic hydrodynamic motion [65,66]. It should be noted that "normal boiling" ("the appearance of heterogeneously nucleated bubbles which diffuse toward the outer surface of a liquid and, if the surface is reached, may possibly escape" [63]) is generally not important for the nanosecond-pulsed laser ablation process [63,64].

For low-intensity laser ablation, surface vaporization is typically the dominant physical mechanism for material removal. However, as the laser intensity gets higher, the target material may be superheated close to the thermodynamic critical temperature, and homogeneous bubble nucleation and growth (phase explosion) occurs. The ejection of liquid droplet–vapor mixture generated because of *phase explosion* generally occurs at a delay time of several hundred nanoseconds [67,68] after the laser pulse starts, and the ejection is through hydrodynamic motion and therefore can be regarded as a *hydrodynamic expansion* process. Another situation where hydrodynamic expansion becomes the dominant mechanism is when the target substrate is driven by a sufficiently intense laser pulse to a temperature above the thermodynamic temperature T_c. In this case, the sharp interface between the condensed and gaseous phases disappears [65] and is smeared into a macro-scopic transition layer (this is because when the target material temperature is higher than T_c, it can be in only one phase—the supercritical state, and thus the sharp interface between different phases disappears). Under such conditions, the condensed target phase should contribute mass to the target vapor phase mainly through hydrodynamic expansion, during which the target material moves from the condensed phase region to the vapor region with its density decreasing continuously to the vapor density. This mechanism is verified through the experimental and modeling work by Wu *et al*. [66].

In summary, nanosecond-pulsed laser ablation can be divided into two stages in terms of material removal mechanisms: the surface vaporization stage and the subsequent hydrodynamic expansion stage (which results in the ejection of vapor and/or liquid–vapor mixture). Homogeneous bubble nucleation and growth (phase explosion) may also take place during these two stages, the significance of

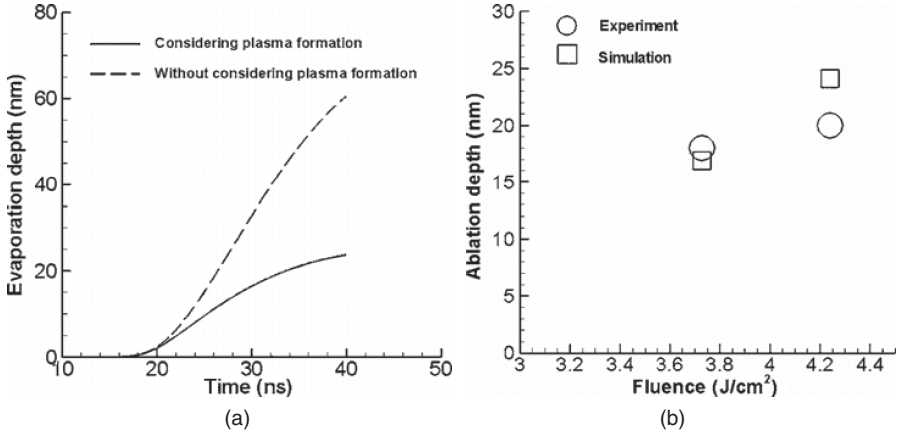

Figure 6.13 (a) The calculated transient evaporation depth in the ablation of nickel by a 248-nm and 26-ns excimer laser pulse with a fluence of 4.24 J/cm^2 and (b) the ablation depth in the ablation of nickel by a 248-nm and 26-ns excimer laser pulse. *Source*: Reprinted with permission from [Wu B, Shin YC., J Appl Phys, 99(8), 084310, (2006)], Copyright [2006], American Institute of Physics [69]; measurement from Xu [70].

which strongly depends on the extent to which the target material is superheated. For low-intensity laser pulses, only the first stage occurs, while for very high-intensity laser pulses, the second stage may dominate over the first stage.

For low-intensity nanosecond-pulsed laser ablation where surface evaporation is the dominant mechanism, the process can be simulated by solving the heat transfer equation in the condensed target and the gas dynamic equations in the vapor and ambient gas phases. The governing equations in the condensed and gaseous phases are coupled through the Knudsen layer relations at the target surface. Figure 6.13 shows the evaporation depth calculated by Wu and Shin [69], which agrees well with the measured ablation depth.

For nanosecond-pulsed laser ablation, the transition of material removal mechanism from surface evaporation to explosive phase change process is often characterized by a jump of ablation rate above a certain threshold laser fluence or intensity. This is because the material removal efficiency will be higher for phase explosion than for surface evaporation. Some previous experimental results for nanosecond-pulsed laser ablation of aluminum and silicon are shown in Fig. 6.14, where the ablation rate jumps at a certain laser fluence or irradiance.

The ejection of liquid droplet–vapor mixture generated because of *phase explosion* generally occurs at a certain delay time after the laser pulse starts. The studies [67,68] show that this delay time is around several hundred nanoseconds. Figure 6.15 shows the time-resolved shadowgraph image of nanosecond-pulsed laser ablation of silicon, and liquid droplet ejection is not observed until around 400 ns. However, some investigations, such as by Xu [70] and Porneala and Willis [71], show that the delay time may be much shorter. Hence, further experimental and theoretical studies are still needed to clarify this issue.

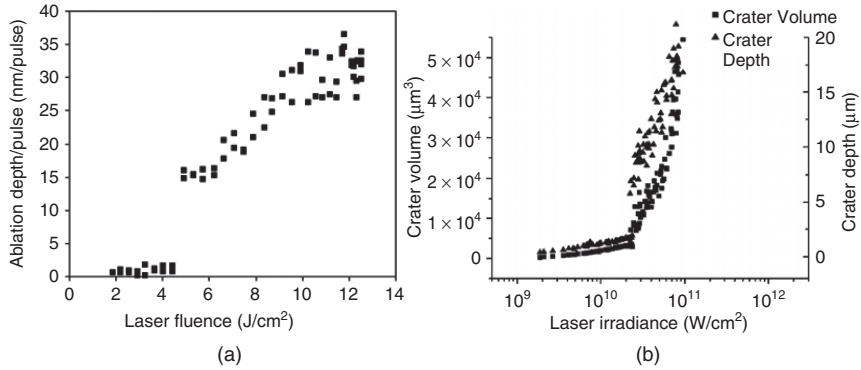

Figure 6.14 (a) The ablation depth per pulse for aluminum as a function of laser fluence (5-ns and 1064-nm laser pulse; *Source*:Reprinted with permission from [Porneala C, Willis DA, Appl Phys Lett, 89, 211121, (2006)], Copyright [2006], American Institute of Physics [71]). (b) The ablation depth and volume for silicon (3-ns and 266-nm laser pulse; *Source*: Reprinted with permission from [Yoo JH, Jeong SH, Greif R, Russo RE., J Appl Phys, 88(3), 1638–1649, (2000)], Copyright [2000], American Institute of Physics [67]).

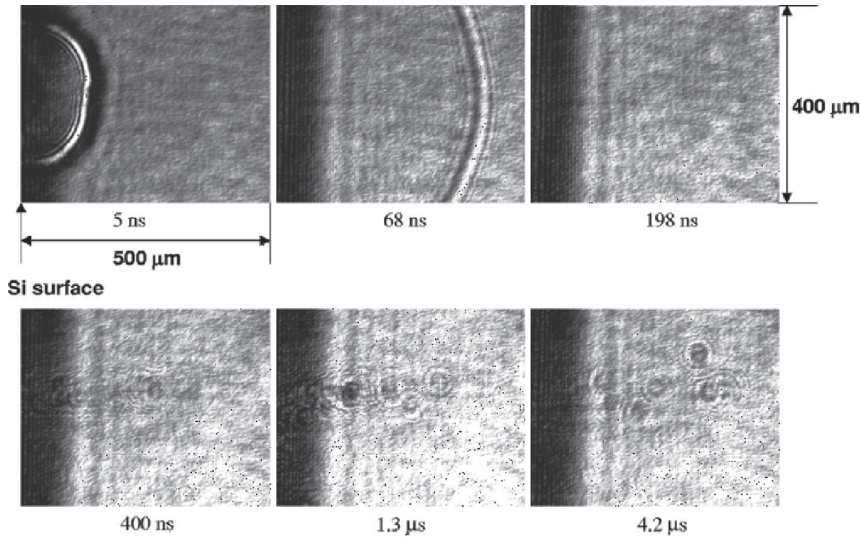

Figure 6.15 Sequence of mass ejection images obtained by laser shadowgraphy for the laser irradiance of 3.9×10^{10} W/cm^2 during laser ablation of silicon (3-ns and 266-nm laser pulse; *Source*: Reprinted with permission from [Yoo JH, Jeong SH, Greif R, Russo RE., J Appl Phys, 88(3), 1638–1649, (2000)], Copyright [2000], American Institute of Physics [67]).

6.6.2 Double-Pulsed Laser Ablation

In Forsman *et al*. [72], an interesting "double-pulse" effect has been observed in nanosecond-pulsed laser ablation of metals. The feature of the effect is that when

two nanosecond laser pulses, separated by a delay time of 30–150 ns, are applied to ablate materials, the average ablation rate per pulse is significantly enhanced compared to the conventional laser ablation situation, where laser pulses are separated by ~100 μs or longer. Figure 6.16 shows the laser pulse train in the double-pulse (superpulse) format and the quality and efficiency enhancement due to superpulse for nanosecond laser drilling of steels.

A hypothesis has been presented in Forsman *et al*. [72] to explain the fundamental mechanism for the double-pulse effect: the first laser pulse ablates the target, generating a high-temperature plasma plume. The second pulse does not directly strike the surface of the target condensed phase. Instead, it mainly interacts with the plasma plume, and raises the temperature and the velocity of the ablated material in the plume lingering above the target surface. As proposed by Forsman *et al*. [72], this energetic plasma drives very rapid fresh material ablation and inhibits ablated material redeposition, and the relative importance of each process depends on the material and the depth of the hole being drilled. This hypothesis has been supported by the simulation results using a physics-based hydrodynamic model proposed by Wu *et al*. [73].

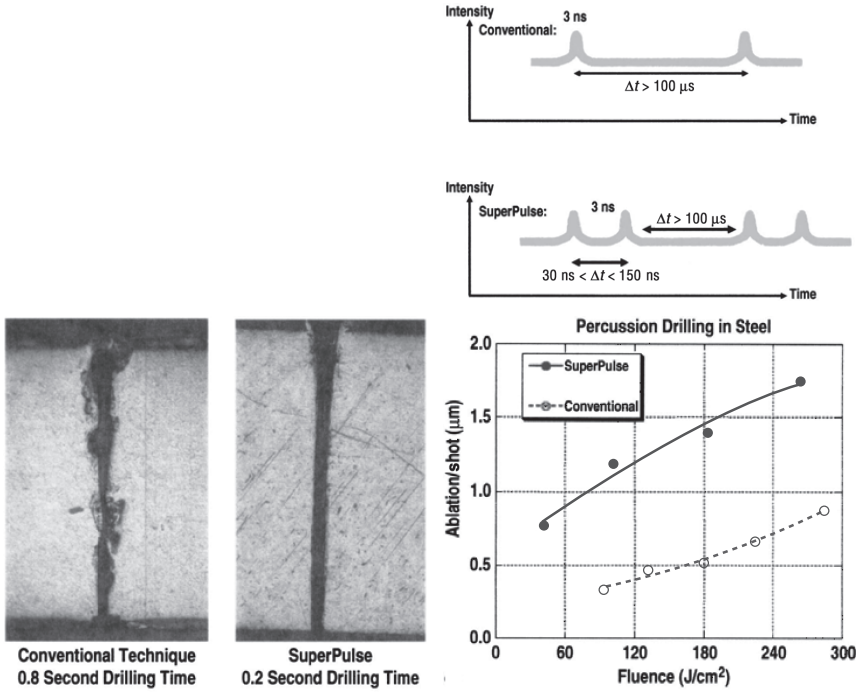

Figure 6.16 Top: laser pulse trains in conventional and superpulse (double-pulse) format. Bottom left: quality enhancement due to superpulse for laser drilling of steel. Bottom right: efficiency enhancement due to superpulse for laser drilling of steel. *Source*: Reprinted with permission from [Forsman AC, Banks PS, Perry MD, Campbell EM, Dodell AL, Armas MS, J Appl Phys, 98, 033302, (2005)], Copyright [2005], American Institute of Physics [72].

6.6.3 Nanosecond Laser-Induced Plasma

During nanosecond-pulsed laser–material interactions, the ablated material (and even ambient air) may be ionized at sufficiently high laser intensities, generating a plasma plume. The plasma may strongly affect laser propagation and energy absorption, and hence its evolution plays an important role in laser ablation. Many techniques directly utilize laser-induced plasma, such as laser-induced breakdown spectroscopy, laser thin-film deposition, and laser synthesis of nanomaterials. Therefore, the understanding of nanosecond laser-induced plasma is very important, and extensive experimental and theoretical work has been performed in this area.

The geometric evolution of laser-induced plasma can be observed with approximately nanosecond resolution using an ICCD (intensified charge-coupled device) camera. Figure 6.17 shows the ICCD images of plasma plume at different delay times produced during nanosecond-pulsed laser ablation of aluminum in air.

The plasma temperature and the electron density can be deduced from the plasma optical emission spectrum. The spectrum can be collected using a spectrometer. The plasma at nanosecond-scale delay times (or longer) is typically in local thermodynamic equilibrium (LTE) [74]. If the plasma is also optically thin, the method most commonly used for the determination of plasma excitation temperatures is finding the ratio of relative intensities of spectral lines from the same

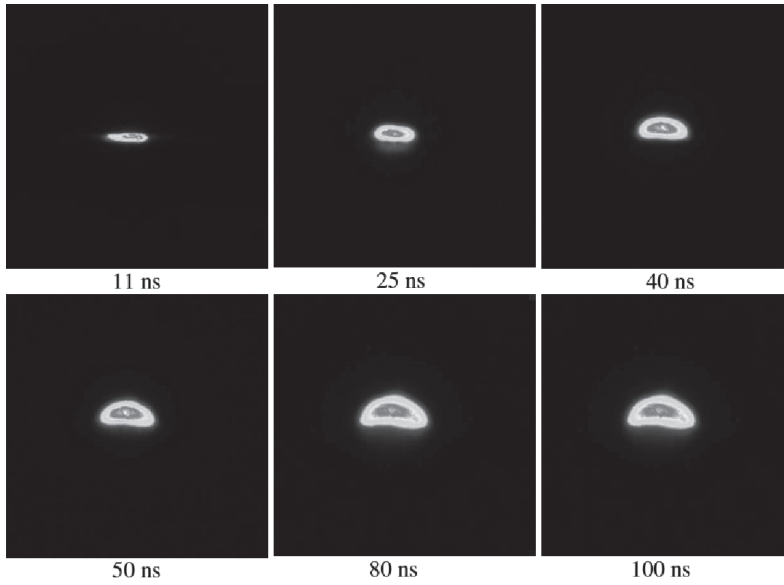

Figure 6.17 ICCD images of plasma plume produced during laser ablation of aluminum in air (6-ns, 532-nm, and 8.1 GW/cm^2 laser pulse; *Source*: Reprinted figure with permission from [Wu B, Shin YC, Pakhal H, Laurendreau NM, Lucht RP, Phys Rev E, 76, 026405, 2007], Copyright (2007) by the American Physical Society, http://link.aps.org/doi/10.1103/PhysRevE.76.026405, [66]).

element and ionization stage. The Stark broadening of spectral lines can be used to determine the electron number density. Neglecting the contribution from the ion broadening, the relation between the FWHM (full-width at half-maximum) of Stark broadened lines $\Delta\lambda_{1/2}$ and the electron number density is given by Griem [75,76] and Bekefi [77]:

$$\Delta\lambda_{1/2} = 2w\left(\frac{n_e}{10^{16}}\right) \tag{6.18}$$

where w and n_e (cm^{-3}) are the electron impact parameter and the electron number density, respectively. The electron number density can be obtained from Eq. (6.18).

The plasma induced by high-intensity nanosecond laser pulses at its early stage is often optically thick leading to radiative trapping, and the continuum emission may also be dominant. In this case, the above approach is not applicable. Pakhal *et al*. [78] developed a radiative transfer model, which can calculate the emission spectrum on the basis of the given electron number density and temperature. The actual electron number density and temperature are the ones that produce the best fit between the calculated and measured spectra. The relevant important electronic transitions (e.g., bound–bound, bound–free, and free–free transitions) have been considered in the model. Figure 6.18 shows the measured and fitted plasma emission spectra.

The plasma induced by high-intensity nanosecond laser pulse has been simulated by solving hydrodynamic equations supplemented by wide-range equations

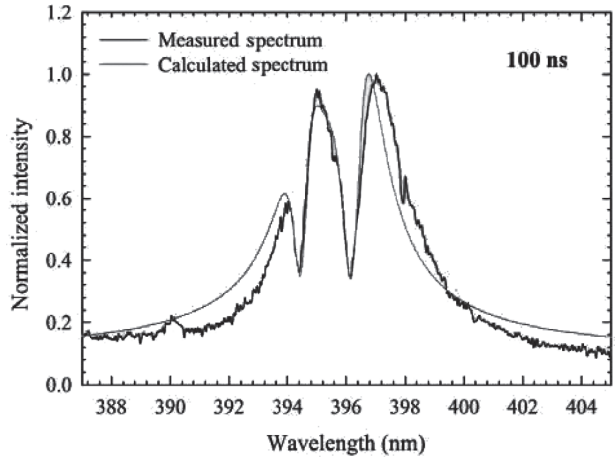

Figure 6.18 Emission spectrum of laser-induced plasma at $t = 100$ ns (aluminum target, ~6-ns, 532-nm, and 3.9 GW/cm^2 laser pulse; *Source*: plots taken from Pakhal *et al*. [78], With kind permission from Springer Science+Business Media: [Appl Phys B, Spectral measurements of incipient plasma temperature and electron number density during laser ablation of aluminum in air, 90, 2008, 15–27, Pakhal HR, Lucht RP, Laurendeau NM, Figure 7b].).

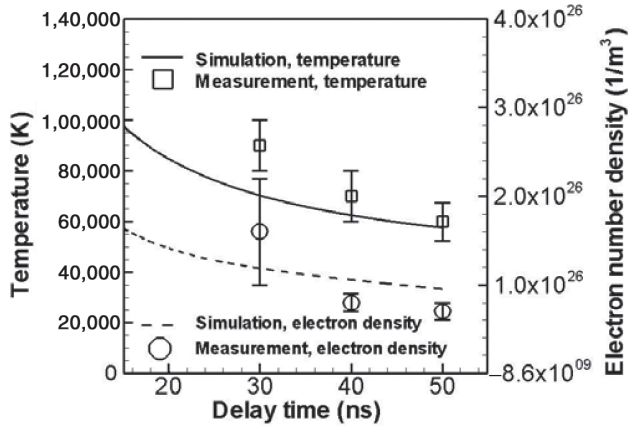

Figure 6.19 Comparison of model predictions with measurements of temperature and electron number density of the plasma induced during aluminum ablation by a 6-ns laser pulse at 8 GW/cm^2. *Source*: Reprinted with permission from [Wu B, Zhou Y, Forsman A, Appl Phys Lett, 95, 251109, (2009)], Copyright [2009], American Institute of Physics [73], and measurements from Wu *et al*. [66].

of state (EOS) [66,73]. The model-predicted plasma temperature and electron density agree reasonably well with experimental measurements as shown in Fig. 6.19.

6.7 LASER SHOCK PEENING

6.7.1 The Process of Laser Shock Peening

Laser shock peening (LSP), also called laser peening in literature, is a process to impart compressive residual stress into the near-surface region of metallic workpieces, utilizing the high pressure of the laser-induced confined plasma at the interface between the coating layer and the confining transparent layer (typically water). The compressive residual stress generated can help improve fatigue and other surface mechanical properties.

Figure 6.20 shows a schematic of the LSP process. The workpiece is coated with a thin opaque coating layer, on which another transparent confining layer (typically water) is applied. A laser beam, which typically has nanosecond (ns) pulse durations and intensities in the range of GW/cm^2, passes through the transparent water layer and is absorbed at the coating–water interface, where a "confined plasma" will be generated. The "confined plasma" can generate a pressure pulse in gigapascal range (with a duration of two to three times laser pulse length [82]) onto the workpiece surface. This will send a shock wave into the workpiece and generate plastic deformation and compressive residual stress in the near-surface region. During LSP, the workpiece experiences a very high strain rate on the order of 10^6 1/s or higher [7].

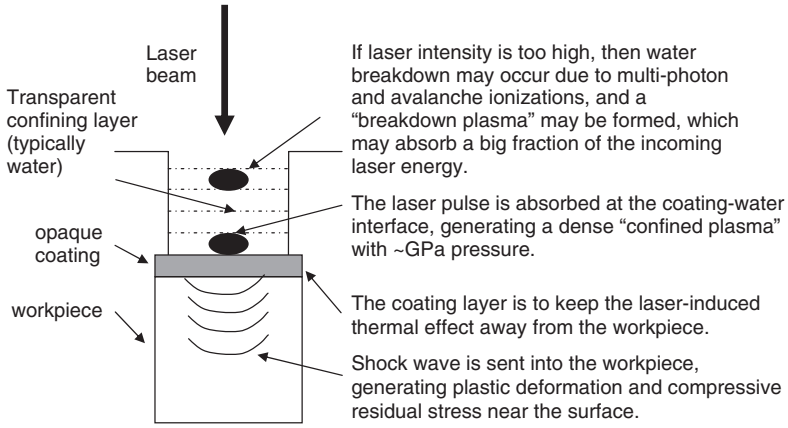

Figure 6.20 Schematic diagram for laser shock peening and the relevant physical processes [81–83].

The coating layer serves to block the thermal effect from the laser pulse so that the workpiece remains relatively cold during the process (otherwise thermally induced tensile residual stress may be generated near the surface). The coating material employed can be black paint or a metal foil, such as zinc, aluminum, or copper foil [7,79]. In many scientific investigations, aluminum has often been chosen as the coating material because of its relatively well-known properties. In practical industrial applications, the water layer can be simply applied through a nozzle.

The laser spot size at the coating surface can vary between ~10 μm (also called micro-LSP in this case; [80]) and a few millimeters. However, a larger laser spot requires a higher pulse energy to obtain the required intensities of ~1–10 GW/cm^2.

6.7.2 Physics of Laser Shock Peening

Figure 6.20 also shows the major relevant physical processes involved in LSP. A model that considers the major physical processes involved has been developed by Wu and Shin [81–83], which can simulate the LSP process (without involving free adjustable variables) starting with the laser pulse parameters and ending with the residual stress generated.

During the LSP process, under sufficiently high laser intensities the dielectric breakdown process may occur in the originally transparent confining layer (e.g., water) through the multiphoton and avalanche ionization processes [81]. A "breakdown plasma" will be generated in this case, limiting the laser energy that can reach the coating–water interface. Hence, it is not helpful to use too high laser intensities during LSP. The laser power density employed in LSP with nanosecond pulses is typically around 1–10 GW/cm^2 for 1064 nm and 1–6 GW/cm^2 for 532 nm [7]. The laser-induced pressure may saturate at higher intensities.

The laser pulse energy that reaches the coating–water interface is absorbed there, creating a "confined plasma." The confined plasma pressure has a peak magnitude in gigapascal range and a duration of approximately two to three times the laser pulse length. Figure 6.21 shows the pressure variation with time based on the experimental measurements [84] and hydrodynamic simulation [82], where the coating material is aluminum. Compared with laser-induced plasma in air and vacuum, the laser-induced plasma in water during LSP has much higher densities, as shown in the hydrodynamic simulation results by Wu [86] in Fig. 6.22. The "confined plasma," strictly speaking, should be simulated by solving the hydrodynamic equations supplemented by the wide-range EOS for water and the coating material. In practical applications, the following simple analytical expression can be applied to estimate the induced pressure in a confining medium by a laser pulse with constant intensity I_0 [85]:

$$P\,(\text{GPa}) = 0.01\sqrt{\frac{\alpha}{\alpha+3}}\sqrt{Z\,(\text{g cm}^{-2}s^{-1})}\sqrt{AI_0(\text{GW cm}^{-2})} \tag{6.19}$$

where P is the pressure; α is the ratio of thermal energy to internal energy for confined plasma (typically around 0.2–0.5, but the exact value can be obtained by fitting the measured pressure); A is the surface optical absorptivity to the laser beam; and Z is the reduced shock impedance defined by $Z = 2/(1/Z_1 + 1/Z_2)$, where Z_1 and Z_2 are the shock impedance of the coating and the confining transparent layer, respectively.

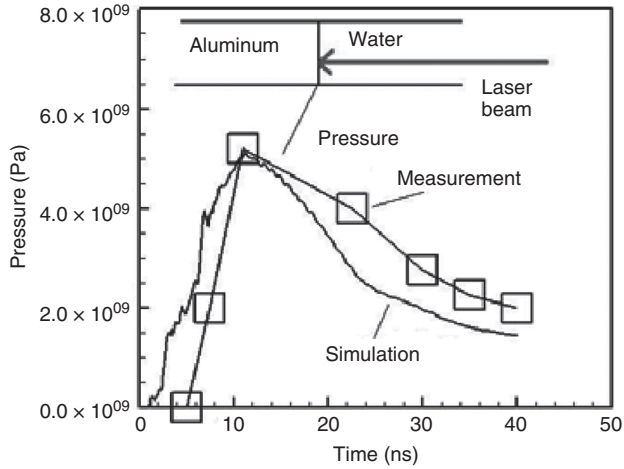

Figure 6.21 Pressure of the confined plasma induced during a 10-ns laser pulse–aluminum interaction in water (simulation from Wu and Shin [82], and measurements from Peyre *et al*. [84]; The figure is reprinted with permission from [Wu B, Shin YC, J Appl Phys, 101(2), 023510, (2007)], Copyright [2007], American Institute of Physics [82].).

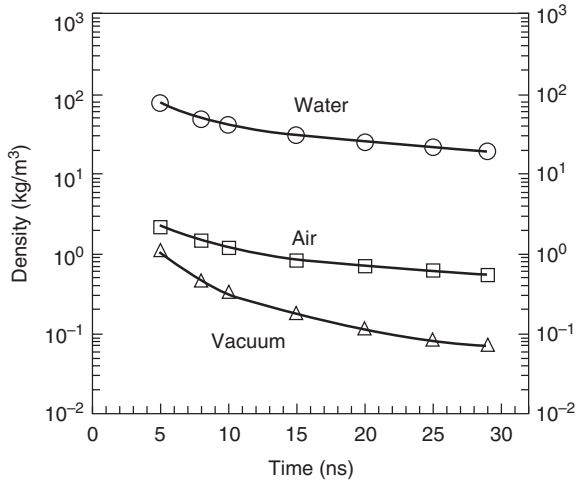

Figure 6.22 The density at the peak temperature location for the plasma induced by 532-nm and 3-ns pulsed laser–aluminum interaction in air, vacuum, and water at 5 GW/cm^2 *Source*: the figure is reprinted with permission from [Wu B., Appl Phys Lett, 93(10), 101104, (2008)], Copyright [2008], American Institute of Physics [86].

Owing to the high pressure of the confined plasma, a shock wave will be sent into the workpiece. The plastic deformation occurs up to a depth at which the pressure of the shock wave no longer exceeds the metal's Hugoniot elastic limit (HEL), which is defined as, under uniaxial strain conditions, the highest elastic stress level in the direction of shock wave propagation. HEL is related to the dynamic yield strength of the material as [84,87,88]:

$$\sigma_{\text{dyn}} = \text{HEL}\frac{1-2\upsilon}{1-\upsilon} \tag{6.20}$$

where υ is the Poisson's ratio.

The transient elastic–plastic deformation and residual stress generation process in the workpiece during LSP can be simulated using the finite element method [84,87–90] based on material high strain rate constitutive relations and/or data. The residual stress can be measured using the X-ray diffraction or incremental hole-drilling method. Figure 6.23 shows the simulated and measured LSP-induced residual stress in a 12Cr steel workpiece. It can be seen that a very large compressive residual stress can be generated in a thick layer of $\sim$1 mm near the workpiece surface. The dislocation activities induced by LSP have also been studied using the dislocation dynamics (DD) approach [91]. It should also be noted that for micro-LSP, where laser spot size is comparable to the material grain size, the material cannot be regarded as homogeneous and isotropic. The effects of specific micro-structures on LSP need to be considered during the study and planning of the LSP process [92].

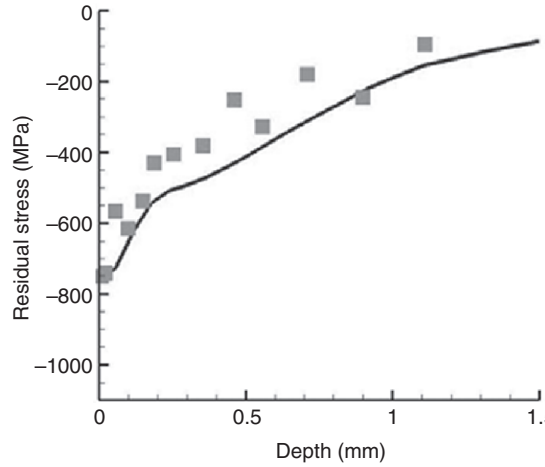

Figure 6.23 Residual stress variation with depth for 12Cr steel workpiece after three LSP impacts using 25-ns laser pulses (simulation (the line) from Wu and Shin [81], and measurements (rectangles) from Peyre *et al*. [84]; *Source*: the plot is taken from Wu [81]).

For a quick estimation, the following simple analytical expressions can be used for plastically affected depth, L_p, and the surface residual stress, σ_{suf}, induced by LSP [93]:

$$L_p = \frac{C_{el} C_{pl} \tau}{C_{el} - C_{pl}} \tag{6.21}$$

$$\sigma_{suf} = -\frac{P}{2[1 + \lambda/(2\mu)]} \left[1 - \frac{4\sqrt{2}}{\pi r}(1 + \nu) \frac{C_{el} C_{pl} \tau}{C_{el} - C_{pl}} \right] \tag{6.22}$$

where C_{el} and C_{pl} are the elastic and plastic shock velocities, respectively; r is the radius of the impact; P is the shock wave pressure; τ is the pressure pulse duration; and λ and μ are the elastic Lame's constants of the target. The equations are valid only when the shock pressure is greater than twice the material's HEL.

Owing to plastic deformation, a dent will be left on the workpiece surface, which is typically around a few hundred nanometers to a few microns. Therefore, the induced surface roughness is generally less than that achieved by conventional shot peening. Figure 6.24 shows the surface profile of 7075 aluminum workpiece after one LSP shot, measured by white light interferometer, which is also compared with the result from finite element simulation [94].

6.7.3 The Effects of LSP on Material Mechanical Properties

LSP can effectively increase the fatigue life and the strength of many common metal materials, such as steel alloys [95], aluminum alloys [96], and titanium alloys [97].

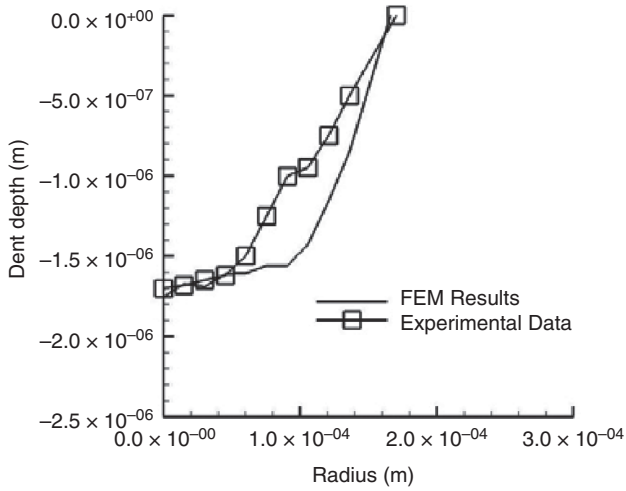

Figure 6.24 Comparison of model predictions and experimental measurements for LSP-induced dent profile on a 7075 aluminum workpiece; *Source*: the plot is taken from Wu [94].

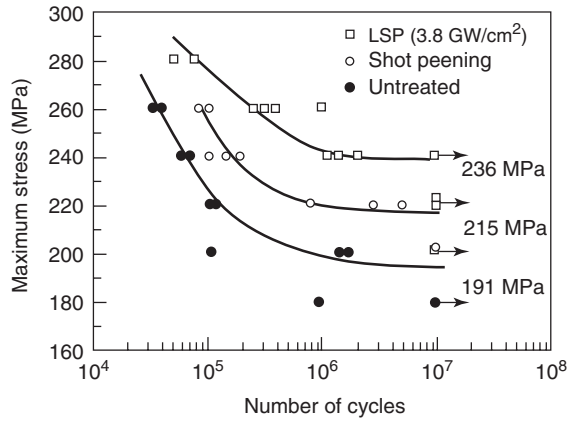

Figure 6.25 The comparison of $\sigma_{max} - N$ curves for untreated, shot-peened, and laser-peened 7075-T7351 alloys [96]. *Source*: The plot is reprinted from Int J Fatigue, 24, Montross CS, Wei T, Ye L, Clark G, Mai YW, Laser shock processing and its effects on microstructure and properties of metal alloys: a review, 1021–1036, Copyright (2002), with permission from Elsevier [7].

Figure 6.25 shows the $\sigma_{max} - N$ curves for untreated, shot-peened, and laser-peened 7075-T7351 alloys [96]. Compared with the untreated specimens, shot peening provided an 11% increase in fatigue strength at 10^7 cycles whereas LSP provided a 22% increase. The improvement with LSP should be due to the greater depth of the induced compressive residual stress field [7].

It has also been found that LSP can increase the fatigue strength of the welds [7]. For example, the fatigue strength of welded joints of 18Ni(250) maraging steel showed a 17% increase at 2×10^6 cycles after processing the heat-affected zones by LSP [98]. LSP can also enhance the fatigue life of 5456 aluminum alloy welds [99].

Besides fatigue life and strength, LSP has also been found to be more effective than shot peening in enhancing the stress corrosion cracking resistance of the thermally sensitized type 304 stainless steel [100]. It has also been demonstrated that LSP can significantly improve the hardness properties of aluminum alloys [101] and 304 stainless steel [99]. The surface hardness increase with the number of laser shots in LSP for 304 stainless steel is shown in Fig. 6.26.

6.7.4 Advantages, Disadvantages, and Applications of LSP

Compared with conventional shot peening, LSP has many advantages. As discussed earlier, under suitable process parameters, it may produce higher compressive residual stress with greater plastic deformation depth and less surface roughness increase [7,102]. This will lead to better enhancement of the mechanical properties. LSP, because of its noncontact nature, can process workpiece locations that are not accessible to shot peening. It can also process very thin sections, where the shot peening can easily generate undesirable damage. The LSP process can be controlled by varying the laser pulse intensity, focal spot size and location, and the pulse number at each peening location.

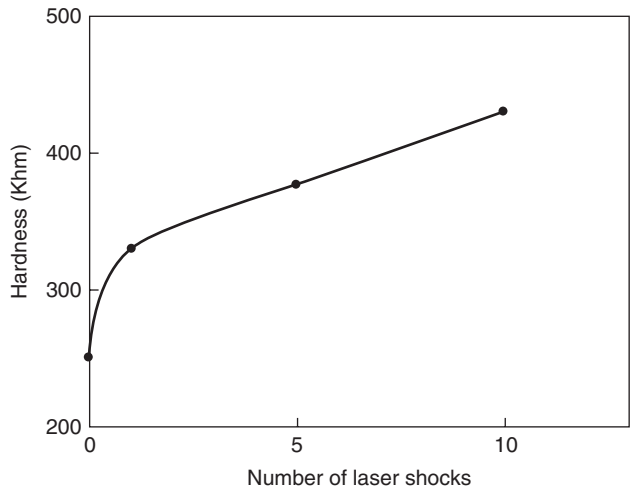

Figure 6.26 The increase of surface hardness for 304 stainless steel with the number of laser shots in LSP [99]. *Source*: The plot is reprinted from Int J Fatigue, 24, Montross CS, Wei T, Ye L, Clark G, Mai YW, Laser shock processing and its effects on microstructure and properties of metal alloys: a review, 1021–1036, Copyright (2002), with permission from Elsevier [7].

One of the major disadvantages of LSP is its relatively low speed and high cost in terms of the processed surface area. In order to realize the intensities of the order of gigawatts per square centimeter, the laser pulse energy has to be sufficiently large (hence the laser pulse repetition rate cannot be very high for a given average laser output power) and the laser spot size has to be sufficiently small (hence the area processed by each laser pulse is small). Therefore, LSP is mainly applied for critical components/devices and situations where shot peening is not applicable. For example, LSP has been applied in the aerospace industry to process many aerospace products, such as rotor components, turbine blades, discs, and gear shafts, and also in biomedical industries for implants and other medical devices [7]. However, with the rapid development of laser technologies, lasers with higher power and lower costs are becoming more and more available. This will widen the LSP applications to higher volume components, such as automobile parts, and other industrial equipment [7].

REFERENCES

1. Gresser HD. Laser sawing of diamonds. SME Technical Paper, Dearborn (MI);MR76-855;1976.
2. Pronko PP, Dutta SK, Squier J, Rudd JV, Du D, Mourou G. Machining of sub-micron holes using a femtosecond laser at 800 nm. Opt Commun 1995;114:106–110.
3. Chichkov BN, Momma C, Nolte S, von Alvensleben F, Tunnermann A. Femtosecond, picosecond and nanosecond laser ablation of solids. Appl Phys 1996; A 63:109–115.
4. Momma C, Nolte S, Chichkov BN, von Alvensleben F, Tünnermann A. Precise laser ablation with ultrashort pulses. Appl Surf Sci 1997;109–110:15–19.
5. Gower M, Rizvi N. Applications of laser ablation to microengineering. Proc SPIE, High-power laser ablation III 2000;4065:452–460.
6. Zhao J, Huettner B, Menschig A. Microablation with ultrashort laser pulses. Opt Laser Technol 2001;33:487–491.
7. Montross CS, Wei T, Ye L, Clark G, Mai YW. Laser shock processing and its effects on microstructure and properties of metal alloys, a review. Int J Fatigue 2002;24:1021–1036.
8. Jaluria Y. Thermal processing of materials: from basic research to engineering. ASME J Heat Transf 2003;125:957–979.
9. Rizvi NH. Femtosecond laser micromachining: current status and applications. RIKEN Rev 2003;50:107–113.
10. Kim KH, Guo Z. Ultrafast radiation heat transfer in laser tissue welding and soldering. Numer Heat Transf Part A Appl 2004;46/1:23–46.
11. Zhang J, Wang Y, Cheng P, Yao YL. Effect of pulsing parameters on laser ablative cleaning of copper oxides. J Appl Phys 2006;99:064902-1–11 .
12. Ramanathan D, Molian P. Ultrafast laser micromachining of latex for balloon angioplasty. J Med Dev 2010;4:014501 1–3.

13. Gomez D, Goenaga I, Lizuain I, Ozaita M. Femtosecond laser ablation for microfluidics. Opt Eng 2005;44(5):0511050–1–8.
14. Nakata K, Umehara M, Tsumura T. Excimer laser ablation of sintered hydroxyapatite. Surf Coat Technol 2007;201:4943–4947.
15. Phipps C. Laser applications overview: the state of the art and future trend in the United States. RIKEN Rev 2002;50:11–19.
16. Ivanov D, Zhigilei S. Combined atomistic-continuum modeling of short-pulse laser melting and disintegration of metal films. Phys Rev B 2003;68:064114, 1–22.
17. Ramanathan D, Molian PA. Micro- and sub-micro-machining of type II a single crystal diamond using a Ti:Sapphire femtosecond laser. ASME J Manuf Sci Eng 2002;124:389–396.
18. Chen K, Yao YL. Process optimization in pulsed laser micromachining with applications in medical device manufacturing. Int J Adv Manuf Technol 2000;16:243–249.
19. Choi KH, Meijer J, Masuzawa T, Kim DH. Excimer laser micro-machining for 3-D microstructure. J Mater Process Technol 2004;149:561–566.
20. Ki H, Mazumder J. Numerical simulation of femtosecond laser interaction with silicon. J Laser Appl 2005;17/2:110–117.
21. Bordatchev EV, Nikumb SK. An experimental study and statistical analysis of the effect of laser pulse energy on the geometric quality during laser precision machining. Mach Sci Technol 2003;1/1:83–104.
22. Li M. Micromachining by single mode diode-pimped solid-state lasers. SME Technical Paper, Dearborn (MI); TP04PUB136; 2004.
23. Schafer C, Urbassek HM, Zhigilei LV. Metal ablation by picosecond laser pulses: a hybrid simulation. Phys Rev B 2002;66:115404.
24. Wu B, Shin YC. A unified simple predictive model for high fluence ultra-short pulsed laser ablation of metal, semiconductor and dielectric. Proceedings of 2009 ASME International Conference on Manufacturing Science and Engineering (MSEC); 2009 Oct 4–7; West Lafayette (IN); 2009.
25. Lee W-H, Özel T. An experimental method for laser micro-machining of spherical and elliptical 3-D objects. Int J Nanomanuf 2009;3(3): 264–278.
26. Grigoropoulos CP, Bennett TD, Ho JR, Xu X, Zhang X. Heat and mass transfer in pulsed-laser-induced phase transformation. Adv Heat Transf 1996;28:75–134.
27. Zhang W, Yao YL, Chen K. Modeling and analysis of UV laser micro-machining of copper. Int J Adv Manuf Technol 2001;18:323–331.
28. Zhang J, Sugioka K, Midorikawa K. High-speed machining of glass materials by laser-induced plasma-assisted ablation using a 532-nm laser. Appl Phys A 1998;67:499–501.
29. Malshe A, Deshpande D. Nano and micro-scale surface and sub-surface modifications induced in optical materials by femtosecond laser machining. J Mater Process Technol 2004;149:585–590.
30. Ho SF, Ngoi BKA. Sub-micro-drilling with ultrafast pulse laser interference. Appl Phys B 2004;79:99–102.
31. Malshe A, Deshpande D, Stach E, Rajurkar K, Alexander D. Investigation of Femtosecond laser-assisted micro-machining of Lithium Niobate. Ann CIRP 2004;;53(1):187–190.

32. Komashko AM, Feit MD, Rubenchik AM, Perry MD, Banks PS. Simulation of material removal efficiency with ultrashort laser pulses. Appl Phys A Mater Sci Process 1999;69(7):S95–S98.
33. Vidal F, Johnston TW, Laville S, Barthelemy O, Chaker M, Drogoff BL, Margot J, Sabsabi M. Critical-point phase separation in laser ablation of conductors. Phys Rev Lett 2001;86(12):2573–2576.
34. Laville S, Vidal F, Johnston TW, Barthelemy O, Chaker M, Drogoff BL, Margot J, Sabsabi M. Fluid modeling of the laser ablation depth as a function of the pulse duration for conductors. Phys Rev E 2002;66:066415.
35. Colombier JP, Combis P, Bonneau F, Harzic RL, Audouard E. Hydrodynamic simulations of metal ablation by femtosecond laser irradiation. Phys Rev B 2005;71:165406.
36. Cheng C, Xu X. Mechanisms of decomposition of metal during femtosecond laser ablation. Phys Rev B 2005;72:165415.
37. Imamova SE, Atanasov PA, Nedialkov NN, Dausinger F, Berger P. Molecular dynamics simulation using pair and many body interatomic potentials: ultrashort laser ablation of Fe. Nucl Instrum Methods Phys Res B 2005;227(4):490–498.
38. Nedialkov NN, Imamova SE, Atanasov PA, Berger P, Dausinger F. Mechanism of ultrashort laser ablation of metals: molecular dynamics simulation. Appl Surf Sci 2005;247:243–248.
39. Nedialkov NN, Imamova SE, Atanasov PA. Ablation of metals by ultrashort laser pulses. J Phys D Appl Phys 2004;37:638–643.
40. Garrison BJ, Itina TE, Zhigilei LV. Limit of overheating and the threshold behavior in laser ablation. Phys Rev E 2003;68:041501.
41. Lorazo P, Lewis LJ, Meunier M. Short-pulse laser ablation of solids: from phase explosion to fragmentation. Phys Rev Lett 2003;91(22):225502.
42. Lorazo P, Lewis LJ, Meunier M. Thermodynamic pathways to melting, ablation, and solidification in absorbing solids under pulsed laser irradiation. Phys Rev B 2006;73:134108.
43. Perez D, Lewis LJ. Molecular-dynamics study of ablation of solids under femtosecond laser pulses. Phys Rev B 2003;67:184102.
44. Hashida M, Semerok AF, Gobert O, Petite G, Izawa Y, Wagner JF. Ablation threshold dependence on pulse duration for copper. Appl Surf Sci 2002; 197–198:862–867.
45. Stoian R, Rosenfeld A, Ashkenasi D, Hertel IV. Surface charging and impulsive ion ejection during ultrashort pulsed laser ablation. Phys Rev Lett 2002;88(9):097603.
46. Bulgakova NM, Stoian R, Rosenfeld A, Hertel IV, Marine W, Campbell EEB. A general continuum approach to describe fast electronic transport in pulsed laser irradiated materials: the problem of Coulomb explosion. Appl Phys A Mater Sci Process 2005;81:345–356.
47. Rethfeld B, Sokolowski-Tinten K, Von Der Linde D, Anisimov SI. Timescales in the response of materials to femtosecond laser excitation. Appl Phys A Mater Sci Process 2004;79(4–6):767–769.
48. van Driel HM. Kinetics of high-density plasmas generated in Si by 1.06- and 0.53-μm picosecond laser pulses. Phys Rev B 1987;35(15):8166.

49. Stuart BC, Feit MD, Herman S, Rubenchik AM, Shore BW, Perry MD. Nanosecond-to-femtosecond laser-induced breakdown in dielectrics. Phys Rev B 1996;53:1749.
50. Born M, Wolf E. Principles of optics: electromagnetic theory of propagation, interference, and diffraction of light. Oxford: Pergamon Press; 1986.
51. Wu B, Shin YC. A simplified predictive model for high-fluence ultrashort pulsed laser ablation of semiconductors and dielectrics. Appl Surf Sci 2009;255(9):4996–5002.
52. Bechtel JH, Lee Smith W, Bloembergen N. Two-photon photoemission from metals induced by picosecond laser pulses. Phys Rev B 1977;15(10):4557–4563.
53. Mao SS, Mao X, Greif R, Russo RE. Simulation of a picosecond laser ablation plasma. Appl Phys Lett 2000;76(23):3370–3372.
54. Mao SS, Mao X, Greif R, Russo RE. Initiation of an early-stage plasma during picosecond laser ablation of solids. Appl Phys Lett 2000;77(16):2464–2466.
55. Kruer WL. The physics of laser plasma interactions. Redwood City (CA): Addison-Wesley; 1988.
56. Itina TE, Vidal F, Delaporte P, Sentis M. Numerical study of ultra-short laser ablation of metals and of laser plume dynamics. Appl Phys A Mater Sci Process 2004a;79:1089–1092.
57. Itina TE, Hermann J, Delaporte P, Sentis M. Modeling of metal ablation induced by ultrashort laser pulses. Thin Solid Films 2004b;453–454:513–517.
58. Zel'dovich YB, Raizer PR. Physics of shock waves and high temperature hydrodynamic phenomena. New York, London: Academic Press; 1966.
59. Meunier M, Fisette B, Houle A, Kabashin AV, Broude SV, Miller P. Processing of metals and semiconductors by a femtosecond laser-based micro-fabrication system. SPIE 2003;64978–32:1–11.
60. Guizard S, Semerok A, Gaudin J, Hashida M, Martin P, Quere F. Femtosecond laser ablation of transparent dielectrics: measurement and modelisation of crater profiles. Appl Surf Sci 2002;186:364–368.
61. Jeong SH, Greif R, Russo RE. Numerical modeling of pulsed laser evaporation of aluminum targets. Appl Surf Sci 1998;127–129:177–183.
62. Gusarov AV, Smurov I. Gas-dynamic boundary conditions of evaporation and condensation: numerical analysis of the Knudsen layer. Phys Fluids 2002;14(2):4242–4255.
63. Kelly R, Miotello A. Does normal boiling exist due to laser-pulse or ion bombardment? J Appl Phys 2000;87(6):3177–3179.
64. Miotello A, Kelly R. Critical assessment of thermal models for laser sputtering at high fluences. Appl Phys Lett 1995;67(24):3535–3537.
65. Anisimov SI, Galburt VA, Ivanov MF, Poyurovskaya IE, Fisher VI. Analysis of the interaction of a laser beam with a metal. Sov Phys Tech Phys 1979;24(3):295–299.
66. Wu B, Shin YC, Pakhal H, Laurendreau NM, Lucht RP. Modeling and experimental verification of plasmas induced by high-power nanosecond laser-aluminum interactions in air. Phys Rev E 2007;76:026405.
67. Yoo JH, Jeong SH, Greif R, Russo RE. Explosive change in crater properties during high power nanosecond laser ablation of silicon. J Appl Phys 2000;88(3):1638–1649.

68. Fishburn JM, Withford MJ, Coutts DW, Piper JA. Method for determination of the volume of material ejected as molten droplets during visible nanosecond ablation. Appl Opt 2004;43(35):6473–6476.
69. Wu B, Shin YC. Modeling of nanosecond laser ablation with vapor plasma formation. J Appl Phys 2006;99(8):084310.
70. Xu X. Phase explosion and its time lag in nanosecond laser ablation. Appl Surf Sci 2002;197:61–66.
71. Porneala C, Willis DA. Observation of nanosecond laser-induced phase explosion in aluminum. Appl Phys Lett 2006;89:211121.
72. Forsman AC, Banks PS, Perry MD, Campbell EM, Dodell AL, Armas MS. Double-pulse machining as a techniques for the enhancement of material removal rates in laser machining of metals. J Appl Phys 2005;98:033302.
73. Wu B, Zhou Y, Forsman A. Study of laser-plasma interaction using a physics-based model for understanding the physical mechanism of double-pulse effect in nanosecond laser ablation. Appl Phys Lett 2009;95:251109.
74. Drogoff BL, Margot J, Vidal F, Laville S, Chaker M, Sabsabi M, Johnston TW, Barthelemy O. Influence of the laser pulse duration on laser-produced plasma properties. Plasma Sources Sci Technol 2004;13:223–230.
75. Griem HR. Plasma spectroscopy. New York: McGraw-Hill; 1964.
76. Griem HR. Semiempirical formulas for the electron-impact widths and shifts of isolated ion lines in plasmas. Phys Rev 1968;165:258–266.
77. Bekefi G, editor. Principles of laser plasmas. New York: Wiley; 1976.
78. Pakhal HR, Lucht RP, Laurendeau NM. Spectral measurements of incipient plasma temperature and electron number density during laser ablation of aluminum in air. Appl Phys B 2008;90:15–27.
79. Fairand BP, Clauer AH, Jung RG, Wilcox BA. Quantitative assessment of laser-induced stress waves generated at confined surfaces. Appl Phys Lett 1974;25:431–433.
80. Zhang W, Yao YL, Noyan IC. Micro-scale laser shock peening of thin films, part 1: experiment, modeling and simulation. J Manuf Sci Eng Trans ASME 2004;126(1):10–17.
81. Wu B, Shin YC. From incident laser pulse to residual stress: a complete and self-closed model for laser shock peening. J Manuf Sci Eng Trans ASME 2007;129:117–125.
82. Wu B, Shin YC. A one-dimensional hydrodynamic model for pressures induced near the coating-water interface during laser shock peening. J Appl Phys 2007;101(2):023510.
83. Wu B, Shin YC. Two-dimensional hydrodynamic simulation of high pressures induced by high power nanosecond laser-matter interactions under water. J Appl Phys 2007;101(10):103514.
84. Peyre P, Sollier A, Chaieb I, Berthe L, Bartnicki E, Braham C, Fabbro R. FEM simulation of residual stresses induced by laser peening. Eur Phys J Appl Phys 2003;23:83–88.
85. Fabbro R, Fournier J, Ballard P, Devaux D, Virmont J. Physical study of laser-produced plasma in confined geometry. J Appl Phys 1990;68(2):775–784.

86. Wu B. High-intensity nanosecond-pulsed laser-induced plasma in air, water, and vacuum: A comparative study of the early-stage evolution using a physics-based predictive model. Appl Phys Lett 2008;93(10):101104.
87. Braisted W, Brockman R. Finite element simulation of laser shock peening. Int J Fatigue 1999;21(7):719–724.
88. Ding K, Ye L. Three-dimensional dynamic finite element analysis of multiple laser shock peening processes. Surf Eng 2003;19(5):351–358.
89. Hu Y, Yao Z. Numerical simulation and experimentation of overlapping laser shock processing with symmetry cell. Int J Mach Tools Manuf 2008;48(2):152–162.
90. Warren AW, Guo YB, Chen SC. Massive parallel laser shock peening: simulation, analysis, and validation. Int J Fatigue 2008;30(1):188–197.
91. Cheng GJ, Shehadeh MA. Multiscale dislocation dynamics analyses of laser shock peening in silicon single crystals. Int J Plast 2006;22:2171–2194.
92. Chen H, Wang Y, Kysar JW, Yao YL. Study of anisotropic character induced by microscale laser shock peening on a single crystal aluminum. J Appl Phys 2007;101:024904.
93. Ballard P, Fournier J, Fabbro R, Frelat J. Residual stresses induced by laser shocks. J Phys IV 1991;1:487–494.
94. Wu B. Numerical modeling and analysis of laser-matter interactions in laser-based manufacturing and materials processing with short and ultrashort lasers [PhD dissertation]. Purdue University; 2007.
95. Peyre P, Berthe L, Scherpereel X, Fabbro R. Laser-shock processing of aluminum coated 55C1 steel in water-confinement regime, characterization and application to high-cycle fatigue behavior. J Mater Sci 1998;33:1421–1429.
96. Peyre P, Fabbro R, Merrien P, Lieurade HP. Laser shock processing of aluminum alloys. Application to high cycle fatigue behavior. Mater Sci Eng 1996;A210:102–113.
97. Ashley S. Powerful laser means better peening. Mech Eng 1998;120:12.
98. Banas G, Elsayed-Ali HE, Lawrence FV, Rigsbee JM. Laser shock-induced mechanical and microstructural modification of welded maraging steel. J Appl Phys 1990;67:2380–2384.
99. Clauer AH, Holbrook JH, Fairand BP. Effects of laser induced shock waves on metals. In: Meyers MA, Murr LE, editors. Shock waves and high-strain- rate phenomena in metals. New York: Plenum Publishing Corporation; 1981. pp 675–702.
100. Obata M, Sano Y, Mukai N, Yoda M, Shima S, Kanno M. Effect of laser peening on residual stress and stress corrosion cracking for type 304 stainless steel. Presented at International Conference on Shot Peening. Warsaw, Poland;7; 1999.
101. Fairand BP, Clauer AH. Laser generated stress waves: their characteristics and their effects to materials. Presented at Proceedings American Inst. of Physics Conf. on Laser Solid Interactions and Laser Processing. Boston; 1978.
102. LSP Technology Company, www.lspt.com and http://lsptechnologies.com/questions/.

CHAPTER 7

POLYMER MICRO-MOLDING/FORMING PROCESSES

DONGGANG YAO
School of Materials Science and Engineering, Georgia Institute of Technology, Atlanta, Georgia

7.1 INTRODUCTION

The use of polymeric materials in micro-devices and micro-systems has been growing rapidly in the recent years. The advantages of using polymers as a replacement for more conventional lithography-based materials, such as silicon and its derivatives, are evident considering the versatile properties and mass-production capabilities of polymers. There are more than several thousand different grades of polymeric materials available for designers to choose from. More importantly, owing to the macro-molecular nature and consequently an infinite number of possible molecular assemblies, polymeric materials hold large degrees of freedom in structural formation. The resulting material properties are extremely versatile, and different mechanical, optical, and electrical functions can be achieved with these materials. Competing or even contradictory functionalities (e.g., insulative vs. conductive, hydrophilic vs. hydrophobic, and transparent vs. opaque) needed by a product may be easily realized with appropriate formulation and selection of polymers. The recent developments in semiconductive polymers, piezoelectric polymers, polymeric electrolytes, and other functional polymers, not only allow polymers to be used as a substitute for silicon, metals, and ceramics in many miniature devices and systems but also make possible applications that could not be realized before.

Owing to their macro-molecular organic structures, polymers have processing properties vastly different from those of their low-molecular-weight inorganic counterparts, such as metals and silicon-based materials. In general, material removal processes using mechanical means are not recommended for processing

Micro-Manufacturing: Design and Manufacturing of Micro-Products, First Edition.
Edited by Muammer Koç and Tugrul Özel.

polymers. The primary difficulty in machining polymers arises from their large elasticity and high sensitivity to heat, by virtue of which their machinability is poor, and it is difficult to produce accurate dimensions and good surface finishes by mechanical machining. Instead, material ablation processes using high-energy beams such as ultrashort-pulsed laser have generated moderate interest in polymer micro-fabrication; however, owing to relatively slow production rates and poor control of dimensions in the depth direction, these radiation-based processes are mostly suitable for prototyping purposes. An improved approach is to employ photolithography for processing radiation-sensitive polymers. There has been huge success in lithographic processing of polymer photo resists, particularly with short-wavelength UV sources or X-rays. After developing the exposed resist in appropriate media, high-aspect-ratio micro-structures can be obtained even with tapered walls. However, this method is suitable only for a limited number of specially formulated photo sensitive polymers.

Traditionally, polymers are processed by deformation and flow processes in a softened state or in a liquid state. Unlike most ductile metallic materials, solid polymers are either too brittle or too elastic, making controllable permanent deformation a challenge. Even worse, a deformed polymer solid is subject to a large amount of viscoelastic recovery over a long period of time [1]. Therefore, a preferred approach is to use chemical or physical phase transitions to control the polymer deformability during processing. For a polymer solid, this requires a first transition from the solid state to a semisolid or even a liquid state before deformation and a second transition to secure the shape after deformation. Since most polymers are thermoplastic, this can be accomplished by heating the polymer above its softening temperature (i.e., glass transition temperature (T_g) for amorphous polymers and melting temperature (T_m) for crystalline polymers) before deformation and subsequently cooling it below the softening temperature after deformation. An important alternative approach is to start with monomers or prepolymers in a liquid state. After flow and shaping, chemical reaction can be activated by heat or by radiation to cure and solidify the material.

Because of their unique processing properties, polymers distinguish themselves from silicon, metals, and ceramics in process development and product realization. Volume production in the polymer industry is primarily by thermoplastic shaping and forming processes. In terms of different process dynamics, these processes can be further classified into three major categories: extrusion, molding, and stretch forming. While extrusion is a continuous die forming process for long profiles, molding is suitable for producing discrete parts by stuffing a resin into a sealed mold cavity. In both extrusion and molding, the polymer is processed in a liquid state primarily by shear deformation at a temperature well above the polymer transition temperature. By contrast, stretch forming processes are characterized by the elongational deformation of a shell-type membrane in a semisolid state. To create a semisolid, rather than a liquid, the polymer is only heated to a temperature slightly above T_g if it is amorphous or slightly below T_m if it is semicrystalline. Among all commercially viable processes in polymer processing, one of the most important processes is injection molding. Three-dimensional

parts with compound curvatures, undercuts, threaded holes, bosses, reinforcing ribs, and other intricate features can be produced in a single molding operation.

Over the past three decades, a considerable amount of work has been done worldwide on adaptation of conventional polymer processing techniques, particularly molding processes, to micro-fabrication or even to nanofabrication. The resulting technology is often referred to as micro-molding [2]. Three most widely used micro-molding processes are micro-injection molding, hot embossing, and casting [2–4]. These processes are able to deliver a replication resolution down to 10 nm [2,5]. This is indeed surprising, considering the relatively large size of polymer molecules. It is generally believed that the macro-molecule of a size similar to that of the feature tends to adapt to the form of the mold. So far, micro-molded parts have shown great commercial potential for a variety of applications, including micro-fluidics, diffractive optics, LCD panels, sensors, actuators, all-polymer electronics, and many others [2,4,6–8].

While earlier investigations into micro-molding were directed toward testifying the ability of conventional molding processes for producing micro-structured surfaces, the recent endeavors are more focused on process improvement, optimization, and analysis. It should be acknowledged that micro-molding benefits greatly from the broad knowledge base supported by the affluence of expertise in the traditional polymer processing industry, which has led to standardized process sequences, high level of automation, short cycle times, as well as to computer-aided engineering [9]. However, a general consensus has also been reached in the micro-molding community that rethinking is often required in order to successfully adapt a macro-scale molding process for micro-scale applications. Because of the so-called size effects, the considerations of process setup, tooling, material structuring, and simulation in micro-molding are quite different from those in conventional molding. Therefore, appropriate handling of these size effects is critical in successful micro-molding. On the one hand, special techniques need to be developed for overcoming some scaling-caused processing difficulties, for example, rapid cooling of a tiny polymer melt. On the other hand, more capable micro-molding processes may be invented if the unique material behavior and process dynamics in micro-scale can be judiciously utilized. Research on the development of hybrid processes under this framework has been conducted [10–15]. Some newly developed processes [10,12] have also integrated the benefits from other processing techniques, such as thermoforming and blow molding, into micro-molding. The resulting processes may be more appropriately called micro-molding/forming processes.

This chapter provides an overview of the state of the art in the micro-molding technology, highlighting common micro-molding techniques, particularly injection- and embossing-based micro-molding processes. To accommodate readers not familiar with polymer processing, a brief account of conventional molding processes as well as the processing properties of polymers is included. The focus of this chapter is placed on describing the differences between micro-molding processes and their macro-counterparts and the rationales for the necessary modifications and improvements. Some basic process dynamics

on micro-molding is also provided, aiming at gaining a more quantitative understanding of these newly emerged processes.

7.2 POLYMERS FOR MICRO-MOLDING

Polymers, on the basis of their different hardening processes, can be divided into two distinct groups: thermoplastic polymers and thermosetting polymers. Heating and cooling can make a thermoplastic polymer undergo reversible phase transitions from a solid state to a melt and then back to the solid state. Thermoplastic polymers can be further classified into amorphous polymers and semicrystalline polymers, depending on their ability to crystallize. By comparison, a thermosetting polymer is hardened by irreversible cross-linking reactions under heat or radiation. A cross-linked polymer cannot be melted but would degrade at an elevated temperature. In terms of the degree of cross-linking, thermosetting polymers can be further divided into two major groups: highly cross-linked rigid thermosetts and lightly cross-linked elastomers. For elastomeric applications, the glass transition temperature has to be substantially lower than room temperature.

Figure 7.1 shows typical modulus versus temperature curves for thermoplastic polymers. An amorphous polymer experiences a large decrease in modulus, approximately three orders of magnitudes, at T_g. Above T_g, the amorphous polymer becomes a rubbery material. The width of the rubber plateau is dependent on the degree of chain entanglement. When the rubber plateau termination temperature (T_t) is reached, the polymer turns into a liquid. For a semicrystalline polymer, the importance of T_g depends on the amount of crystallinity. For a highly crystalline polymer, the effect of T_g is suppressed; in this case, the polymer behaves as a typical crystalline material with a distinct melting temperature, T_m, which marks the solid–liquid boundary in the phase diagram. On the basis of the thermomechanical behavior of polymers, an appropriate processing temperature window can be determined for micro-scale molding and forming. In the case of micro-injection molding, a genuine polymer liquid is needed. This requires that an amorphous polymer be heated above its T_t and a semicrystalline polymer be heated above T_m. In hot embossing, on the other hand, a semisolid or semiliquid material is more desired. For this purpose, a polymer is only heated to a temperature slightly above T_g if it is amorphous and to a temperature slightly below T_m if it is semicrystalline. Such a low-temperature processing is considered helpful in achieving accurate dimensions because of more controllable deformation patterns as well as reduced influences from thermal shrinkage. As amorphous polymers are not subject to large volumetric changes at the crystalline melting temperature, they may be more suitable for precision molding. In fact, most reported micro-molding research has been focused on several common amorphous polymers including poly(methyl methacrylate) (PMMA), acrylonitrile-butadiene-styrene (ABS) copolymers, polycarbonate (PC), and polystyrene (PS). More recently, cyclic olefin copolymers (COC), because of their excellent dimensional stability, have

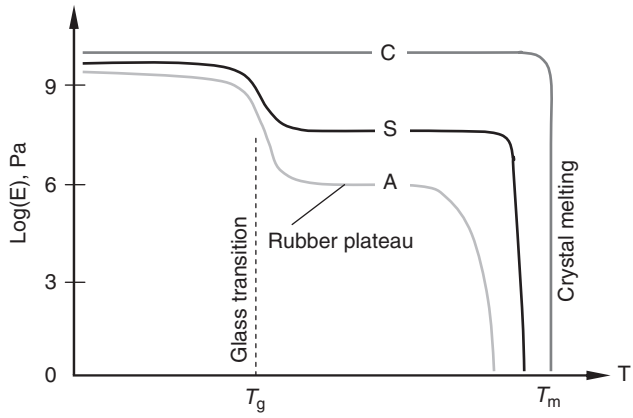

Figure 7.1 Temperature dependency of modulus for A, amorphous polymer; C, highly crystalline polymer; and S, semicrystalline polymer.

been widely reported in the micro-molding community [16–20]. Most amorphous polymers as mentioned above are also highly transparent materials with excellent light-transmission properties and are thus suitable for optical devices. However, it is worth mentioning that semicrystalline polymers are often desired in structural applications, because of their better mechanical performance and improved resistance to chemical/solvent attacks. High-performance semicrystalline polymers such as aromatic nylons, poly(ether ether ketone) (PEEK), poly(phenylene sulfide) (PPS), and liquid crystalline polymers (LCP) may be processed above their melting temperature, using micro-injection molding. For achieving good dimensional accuracy of these polymers, the holding stage needs to be carefully controlled for shrinkage compensation. It should also be noted that thermoplastic polymers, especially amorphous polymers, may be dissolved in appropriate solvents. The resulting solution can then be used in casting processes such as spin coating and film casting. However, owing to extremely large volume shrinkage during solvent extraction or evaporation, these processes find only limited interest in forming thin film patterns.

While thermoplastic polymers dominate in micro-molding applications, thermosetting polymers are advantageous in some special problems. For weak templates, such as a brittle silicon master or a soft biological pattern, a low-viscosity thermosetting prepolymer helps protect the master template from damage and distortion caused by a high molding pressure [21–25]. Rigid thermosetting polymers that have been successfully tested in micro-molding include rigid polyurethane [21], epoxy [23], and various UV-curable resins [26–31]. The viscosity of the prepolymers or oligomers for these polymers is exceptionally low compared with that of thermoplastic polymers, and therefore low forces such as gravitational forces, centrifugal forces, or even capillary forces can be used in micro-molding. These low-pressure micro-molding processes are often referred to as casting processes. Lightly cross-linked elastomeric thermosetts

including elastomeric polyurethane [32] and poly(dimethyl siloxane) (PDMS) [33–36] are also commonly used in micro-molding. Because of their excellent demolding capabilities, these elastomers are also used for making soft molds by transferring the original master pattern on a weak or fragile template to a more durable elastomeric substrate. The elastomeric template is then used for casting-based micro-molding. Soft molding with PDMS stamps [35,37,38] is an example of this technology that has been successful.

7.3 TAXONOMY OF MICRO-MOLDING PROCESSES

Micro-molding has been a multidisciplinary field; the development of this field has been contributed by researchers with diverse background in engineering (including polymer engineering, mechanical engineering, electronics, chemical engineering, and biomedical engineering) and science (including physics, chemistry, and biology). This diversity has allowed expertise from different areas of micro-molding to be cross-fertilized on the same platform, thus enabling the development of innovative processes. However, because of the multidisciplinary nature, different terminologies have been communicated by different researchers. It is thus important to classify the existing micro-molding processes on the basis of their common features from different perspectives. Understanding a group of similar processes would facilitate the development of new processes in a similar cluster.

As in conventional molding, the polymer in micro-molding undergoes coupled mechanical and thermal influences in liquid, rubbery, and solid states. The resulting thermomechanical history determines the structure and the state of stresses and thus determines the properties and performance of the micro-molded part. Like conventional molding, micro-molding mainly uses three mechanisms for applying the molding forces, namely, injection, compression, and casting. In the injection mode, the process is called micro-injection molding, similar to conventional injection molding, but with modified tooling and process setup. The hot embossing process, operated in the compression mode, is basically a hot-mold compression molding process. It is used not only for the fabrication of micro-parts and micro-structured surfaces but also as a lithographic step for patterning resist-coated silicon wafers. The latter case is often referred to as imprinting, for example, nanoimprinting, suitable for patterning low aspect ratio surface structures. In the casting mode, low viscosity resins (e.g., monomers for PDMS) are used. Because of the diminishing gravitational forces in micro-scale, micro-casting is often assisted by vacuum or pressurized gases. Besides the three major mechanisms, micro-molding also utilizes micro-scale surface forces. One widely used surface force is surface tension. For example, casting can be facilitated by the capillary effect. More interestingly, surface tension has been used as a reflow force for creating smoother surfaces, for example, smoother micro-channels [39] and curved surfaces, for example, micro-lense arrays [14,15].

The above classification is done on the basis of the loading configuration at the boundary of the geometry and the body force acting in the domain of the material. These boundary and body loads provide driving forces for deformation but do not indicate the actual deformation mode. From the fundamental point of view, these processes may be directly grouped in terms of different deformation processes into three types: convective flow processes, bulk deformation processes, and membrane stretching processes. Casting and injection molding fall into the first type because these processes rely on fluidic convection for transferring the material to individual micro-features in the mold cavity. The stresses developed in these processes are primarily contingent upon the deformation rate or the strain rate, but not on the amount of strain. In bulk deformation processes, the 3D deformation is controlled mostly by the strain and the locus of an individual material point can be tracked on the basis of the strain history. Hot embossing of amorphous polymers at temperatures close to T_g fits into this category. Membrane stretching is widely used in conventional polymer processing for structuring shell-type structures. Examples are thermoforming and blow molding. Some hybrid micro-molding/forming processes such as rubber-assisted hot embossing [10,40,41] and roll-to-roll shell embossing [42], in fact, can be better described by membrane stretching. Understanding the basic deformation modes and their different roles in micro-molding is an important step toward better control of process dynamics for enhancing micro-molding quality.

For the end users of the micro-molding technology, the geometrical replicability is often among the first few considerations in process selection. Figure 7.2 illustrates four types of representative structures that can be encountered in micro-devices and micro-systems: surface micro-structures, discrete micro-parts, shell micro-structures, and continuous micro-profiles. As different processes can have different capabilities in replicating these geometries, micro-molding processes may be arranged in terms of these geometrical patterns into four groups: surface micro-structuring, shell micro-structuring, discrete micro-cavity molding, and micro-profiling. For surface micro-structuring, the characteristic size of the micro-structure is much smaller than the substrate thickness. During patterning, surface micro-structures undergo localized deformation at the surface of the substrate. Hot embossing is an excellent process for surface micro-structuring, even with thin film substrates with a micrometer thickness. Injection molding may also be used for surface structuring, but limited to relatively thick substrates. In contrast, shell structuring experiences deformation over dimensions larger than the film thickness, and the patterned film is marked by shell-type geometry with a relatively uniform shell thickness. Both injection molding and hot embossing may be used for shell structuring, but with limited success. In particular, a matching pair of mold surfaces is needed to define the shell pattern. This can cause an alignment difficulty when the feature size reduces to micrometers. Furthermore, it is difficult to injection mold into a shell with a micrometer thickness. Research is being conducted in this area to develop more efficient, hybrid processes for uniform shell structuring [10,40,41]. Discrete micro-parts are often referred to as parts with a

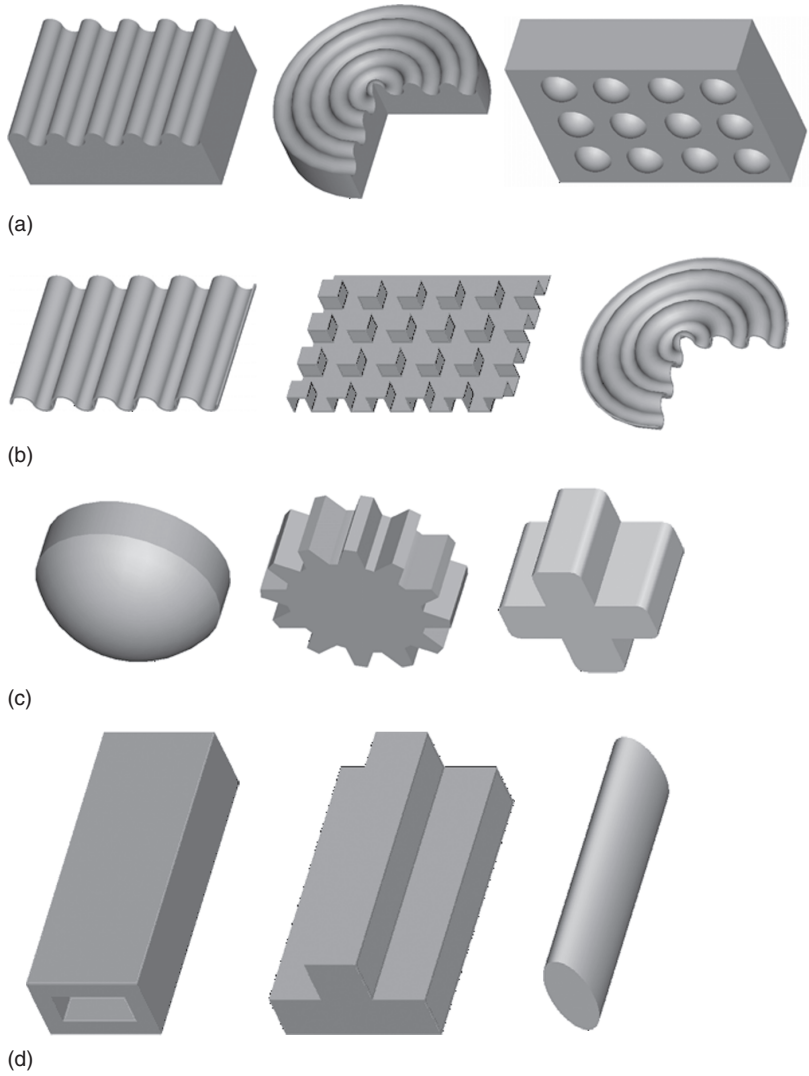

Figure 7.2 Four different types of micro-structures typically involved in micro-molding/forming: (a) surface micro-structures, (b) shell micro-structures, (c) discrete micro-parts, and (d) continuous micro-profiles.

three-dimensional shape and a total weight in the order of a milligram or smaller. Currently, micro-injection molding is considered the most effective process for producing these parts. Hot embossing may also be adapted to this area of applications with relatively simple part geometries, but some modifications on tooling are needed to provide a through-thickness action [11,43]. For the fourth type of structuring, micro-profiling, the structure involved has a constant cross section, but

with an extremely large or even continuous length. Examples are micro-cantilever beams, noncircular optical waveguides, and high-wicking conduits. If the aspect ratio is not large, these micro-profiles may be treated as discrete micro-parts and injection molded or hot embossed; otherwise, continuous processes are needed. Although profile extrusion is a well-established industrial practice, extruding of micro-profiles is a difficult task because of the increased difficulty in shape compensation for die swell at smaller sizes, as well as the increased surface tension effect. Therefore, new processing techniques for overcoming these extrusion difficulties are awaited. Micro-profiles may be alternatively produced by continuous micro-molding processes, such as roll-to-roll embossing; however, research needs to be performed to test the technical feasibility.

From the materials perspective, the solidification or hardening mechanism of the molding polymer notably affects the design and setup of the molding process. Micro-molding processes may thus be categorized on the basis of different solidification mechanisms. The three major solidification mechanisms in conventional molding, namely thermoplastic (either by vitrification for amorphous polymers or by crystallization for semicrystalline polymers), reactive (with monomers or oligomers), and thermosetting (with prepolymers), also dominate in micro-molding. However, other mechanisms that cannot be realized in conventional molding may now work for micro-molding. Given the small amount of polymer needed by a micro-part or micro-structured film and thus the easy removal of the solvent by drying or coagulation, polymer solutions can become suitable materials for selective micro-molding applications. Besides solution casting, a thin solid polymer film can also be plasticized by absorbing solvent vapors and then resolidified by solvent extraction [44,45].

With regard to the types of thermal control, micro-molding can be grouped into variothermal processes and constant-temperature processes. For thermoplastic micro-molding, it is an established fact that a high mold temperature close to the softening temperature of the polymer is required, particularly for molding high-aspect-ratio micro-structures [46–48]. This thermal cycling may be eliminated by employing a nonthermoplastic plastication method, for example, a solvent vapor-assisted method. Yao *et al*. [49] recently showed that constant-temperature embossing can be achieved for slowly crystallizing polymers by embossing the polymer at its amorphous phase and subsequently crystallizing the polymer at the same mold temperature. For reactive and thermosetting polymers, constant-temperature or even room-temperature micro-molding can be performed by employing a nonthermal curing method, for example, UV radiation.

In conventional molding, the mold is typically made of a steel material. Although a hard and durable mold material is desired in micro-molding, fabrication of a metallic micro-mold with well-defined micro-structures or even nanostructures is costly and challenging. Therefore, silicon-based lithographic materials are sometimes directly used as tooling materials in micro-molding. However, silicon is rather brittle and thus may be used only for prototyping purposes. To produce multiple molds, the silicon structures can be replicated by casting to a relatively softer but tougher material, for example, acrylic, epoxy,

and PDMS [50]. This soft tool is not hard and durable enough for micro-injection molding, but is very much suitable for low-force processes, for example, casting. In particular, PDMS has been widely used as a tooling material for soft molding [37,38]. In terms of these different tooling materials, micro-molding processes may be divided into two groups: hard mold processes and soft mold processes.

7.4 GENERAL PROCESS DYNAMICS OF MICRO-MOLDING

In this section, the general process dynamics of polymer molding/forming processes are described first. Scaling analyses are then performed to understand the size effects in miniaturization of these processes. This approach allows a logical comparison between micro-molding/forming processes and their macro-scale counterparts. On the one hand, a huge knowledge base has been developed in the traditional polymer-processing industry and has to be utilized fully. On the other hand, new strategies for material processing and process development, based on the understanding of the size effects in process dynamics, need to be developed to overcome any new processing difficulties caused by scaling, and the potential scaling advantages need to be utilized for developing more effective processes. This practice would therefore help define a useful paradigm for the adaption of known processes to miniature applications and more importantly for creating new hybrid processes better serving the new applications.

Polymer molding and forming processes are transient processes involving coupled momentum and heat transfer. Assuming the validity of the continuum hypothesis, these processes can be modeled using the conservation equations for mass, momentum, and energy, with appropriate boundary conditions representing the processing constraints imposed on the polymer and suitable constitutive models describing the complex rheological behavior. The conservation equations can be written as

$$\frac{\partial \rho}{\partial t} + \nabla \cdot (\rho \mathbf{v}) = 0 \tag{7.1}$$

$$\frac{\partial (\rho \mathbf{v})}{\partial t} + \mathbf{v} \cdot \nabla (\rho \mathbf{v}) = \nabla \cdot \boldsymbol{\sigma} + \mathbf{b} \tag{7.2}$$

$$\rho c_{\mathrm{p}} \left(\frac{\partial T}{\partial t} + \mathbf{v} \cdot \nabla T \right) = \nabla \cdot (k \nabla T) + w \tag{7.3}$$

where ρ, k, and c_{p} are the density, the thermal conductivity, and the specific heat, respectively, $\mathbf{v}$ is a velocity vector, $\boldsymbol{\sigma}$ is a stress tensor, $\mathbf{b}$ is the body force, t is time, T is temperature, and w is heat generation. The primary body force in the momentum equation is the gravitational force. The main heat generation in the energy equation is the permanent work converted into heat.

For thermoplastic polymer processing, the primary contribution to momentum exchange comes from the stress tensor. Thus the inertial and gravitational effects may be neglected. For the mold-filling stage, the effect of compressibility may

also be neglected. Therefore, the mass and momentum conservation equations can be simplified to

$$\nabla \cdot \mathbf{v} = 0 \tag{7.4}$$

$$-\nabla p + \nabla \cdot \boldsymbol{\tau} = 0 \tag{7.5}$$

where p is the pressure and $\boldsymbol{\tau}$ is a deviatoric stress tensor. In fact, these two equations and the energy conservation equation (i.e., Eq. (7.3)), together with an appropriate constitutive model for the stress tensor, have been successfully used in modeling traditional molding, forming, and die flow processes including injection molding, compression molding, thermoforming, blow molding, and extrusion. In a general format, the deviatoric stress tensor can be written as a function of the strain rate history or strain history. The Weissenberg number and the Deborah number can be calculated using the molding/forming geometry and processing conditions, and then the Pipkin diagram [51] can be used to determine a suitable constitutive model. Consider injection molding a polymer liquid at a temperature well above T_m or T_t. The small relaxation time at this high temperature leads to a small Deborah number; however, the Weissenberg number can still be large because of the large strain rate occurring in the process. The resulting material can be best modeled as a generalized Newtonian liquid, its viscosity being dependent on the strain rate. Now consider a different case: thermoforming. The thermoforming temperature is typically set between T_g and T_t for an amorphous polymer, or slightly below T_m for a semicrystalline polymer. This processing temperature yields a long relaxation time, much longer than the processing time. Therefore, a large Weissenberg number and a large Deborah number would be obtained for stretch forming processes. The resulting material can be treated as a nonlinear elastic material. For any molding and forming process, a cooling process is needed. A holding stage under pressure is also desired after the primary deformation stage, in order to compensate for thermal shrinkage during cooling. These stages are characterized by a small deformation rate but with an increasing relaxation time. Thus a linear viscoelastic behavior of the material is expected. In general, these three types of constitutive models are quite sufficient in describing most problems in polymer processing. Some micro-molding processes, however, due to the new processing strategies involved, may require the consideration of more complex rheological behavior involving nonlinear viscoelasticity. Yet, the above-mentioned three relatively simple models would be good starting models for the analysis of the scaling behavior from conventional molding/forming to micro-scale molding/forming.

It is desirable to perform the deformation/flow under an isothermal molding/forming condition [52–55]. This prohibits the stress to freeze into the part during the deformation stage. When an adequate holding stage is subsequently applied at the same isothermal condition, the stress can be relaxed. A scaling analysis can start from this relatively simple isothermal molding problem. Without losing generality, the analysis can also start with a generalized Newtonian liquid

with the stress tensor being a function of the velocity gradient and its transpose:

$$\boldsymbol{\tau} = \mathbf{F}\left(\nabla \mathbf{v}, \nabla \mathbf{v}^{\mathrm{T}}\right) \tag{7.6}$$

Equation (7.5) can then be written as

$$-\nabla p + \nabla \cdot \mathbf{F}\left(\nabla \mathbf{v}, \nabla \mathbf{v}^{\mathrm{T}}\right) = 0 \tag{7.7}$$

To study the scaling behavior of Eq. (7.7), one approach is to normalize the position vector, $\mathbf{x}$, in the Cartesian coordinate system by the characteristic size of the cavity, L, and to obtain a new position vector, velocity vector, and gradient operator expressed as

$$\tilde{\mathbf{x}} = \frac{\mathbf{x}}{L}; \tilde{\mathbf{v}} = \frac{\mathbf{v}}{L}; \text{ and } \tilde{\nabla} = \frac{\nabla}{L}$$

Equation (7.7) can then be written as

$$-\tilde{\nabla} p + \tilde{\nabla} \cdot \mathbf{F}\left(\tilde{\nabla}\tilde{\mathbf{v}}, \tilde{\nabla}\tilde{\mathbf{v}}^{\mathrm{T}}\right) = 0 \tag{7.8}$$

Note that the normalization does not change the velocity gradient, that is, $\tilde{\nabla}\tilde{\mathbf{v}} = \nabla \mathbf{v}$. It should be further noted that pressure and time are not affected by the normalization. This simple analysis thus leads to the following important scaling property:

$$p(t) \rightarrow \tilde{\mathbf{v}}(t) \text{ and } \boldsymbol{\tau}(t) \tag{7.9}$$

This relation depicts a fact that if the same pressure is applied to cavities having the same shape but different sizes, the same stress history and the same normalized velocity history result. This relation is useful in developing scalable processes in miniaturization.

The equation can be normalized differently to obtain different scaling relations. For example, if the deformation in hot embossing can be considered as creep flow with a constant viscosity η, the following useful equation can be derived:

$$-\nabla \hat{p} + \nabla^2 \hat{\mathbf{v}} = 0 \tag{7.10}$$

where the normalized variables are defined as $\hat{\mathbf{v}} = \frac{\partial \mathbf{x}}{\partial \hat{t}}, \hat{t} = t/t_{\mathrm{p}}$, and $\hat{p} = (t_{\mathrm{p}}/\eta)p$, and t_{p} is the processing time. This equation gives a master curve for the isothermal compression molding process with a shear-rate-independent viscosity. Particularly, the following process dynamics can be predicted from this master-curve equation:

- The flow pattern is the same at the same $\tilde{t}$. For example, consider two different molding times (or two different processes), 1 and 10 s. Then, the flow pattern is the same at the end of 0.5 s for the first process and at the end of 5 s for the second process.
- If the molding time is reduced 10 times, the pressure will be increased 10 times.

A more useful scaling analysis is one on the thermal process. Creation of an isothermal molding apparatus is more expensive than conventional molding with a cold mold. It is understood that heat conduction, as a diffusion process, dominates in small sizes, and therefore substantially increased cooling effects are expected upon miniaturization. Hence, strategies for overcoming this scaling-related processing difficulty need to be developed. For simplicity, viscous flow with a constant viscosity is again assumed, and the energy generation is neglected. In this case, the energy conservation equation can be rewritten as

$$\left(\frac{\partial \tilde{T}}{\partial \tilde{t}} + \tilde{\mathbf{v}} \cdot \tilde{\nabla}\tilde{T}\right) = \left(\frac{t_f}{L^2}\alpha\right)\tilde{\nabla}^2\tilde{T} \tag{7.11}$$

where α is the thermal diffusivity. Thus, the normalized thermal response can be written as a function of $(t_f/\alpha L^2)$, $\tilde{\mathbf{x}}$, and $\tilde{t}$:

$$\tilde{T}(\tilde{\mathbf{x}}, \tilde{t}) = F\left(\frac{t_f}{L^2}\alpha, \tilde{\mathbf{x}}, \tilde{t}\right) \tag{7.12}$$

To achieve a similar thermal history, t_f needs to be approximately equal to L^2. This indicates that the filling time should be reduced 100 times if the size gets reduced 10 times. Therefore, extremely rapid filling is needed in order to avoid premature freezing of the polymer in the tiny cavity.

More complex constitutive models and other thermal effects including viscous heating can be included in the above analyses but will result in more lengthy derivations. However, the above exercises entail two important aspects in scaling. First, the development of scalable processes should be considered so that the knowledge from conventional processing can be gracefully adapted to new miniaturization problems. For this purpose, a scaling objective can be set up, for example, to reach the same deformation stress field as used for deriving Eq. (7.7), and a scaling analysis can be performed to achieve this objective. Second, from scaling analysis, strategies to overcome scaling-caused processing difficulty can be developed. The exercise leading to Eq. (7.12) is an example.

Besides the mold-filling stage, the holding stage plays a significant role in quality control. If an isothermal holding stage is assumed, as typically involved in hot embossing, the analysis is indeed simple. As the deformation rate is minimal in this stage, the whole holding stage can be deemed as an isothermal stress

relaxation stage with a step strain at the start of the holding stage. A linear viscoelastic model can be used to predict the stress relaxation process:

$$\tau(\tilde{\mathbf{x}}, t) = \int_0^t M(t - t')\gamma_0(\tilde{\mathbf{x}})\mathrm{d}t' \tag{7.13}$$

where $M(t - t')$ is a memory function and $\gamma_0(\tilde{\mathbf{x}})$ is the starting strain at the beginning of the holding stage. If the starting strain is the same, the size of the cavity does not affect the stress relaxation process.

The continuum hypothesis is followed throughout all the analyses in this section. It should be noted that polymer molecules are quite large with the gyration radius easily reaching tens of nanometers. Wall slip can also occur at small sizes approaching the gyration radius [56]. Therefore, when the feature size drops to such a scale, molecular effects need to be included in the prediction. Surface tension is not considered in the above analyses either. It is generally accepted that in thermoplastic micro-molding, surface tension is not important [56,57], but these effects can become overwhelming in low-viscosity casting processes.

7.5 MICRO-INJECTION MOLDING

The process sequence in micro-injection molding is similar to that in conventional injection molding, involving mold closing, injection, holding, cooling, plastication, mold opening, and part ejection, as illustrated in Fig. 7.3. Some of these stages, such as cooling and plastication, may occur concurrently. After the mold closes, a ram or piston is used to inject a plasticized material into a sealed mold, preferably air vacuumed before injection. The speed control mode is then switched to the pressure control mode. The pressure-controlled holding stage lasts until the gate freezes. The machine then plasticates a prescribed amount of new material for the preparation of the next shot. At the same time, cooling continues until a set ejection temperature is reached. The mold is then opened, and the molded part is ejected. Figure 7.3 illustrates molding of only surface micro-structures. The technology for molding micro-parts is considered similar. As in the substrate for hosting surface micro-structures, runner and gates are used to connect the micro-cavities. The runners are typically much larger than an individual micro-cavity and are separated from the molded micro-parts by degating. Because of the small size of a micro-part, special care is needed during ejection. Ejection pins can be installed at the thick sections, for example, runners, near the micro-part and the part can be pulled out during ejection. Alternatively, ejection pads surrounding the micro-part can be used for more balanced ejection.

Note that the molding stages involved in micro-injection molding are almost the same as those in conventional injection molding. However, owing to the presence of micro-scale or even nanoscale features, different considerations on machine and process setup are needed in order to achieve the necessary feature replication.

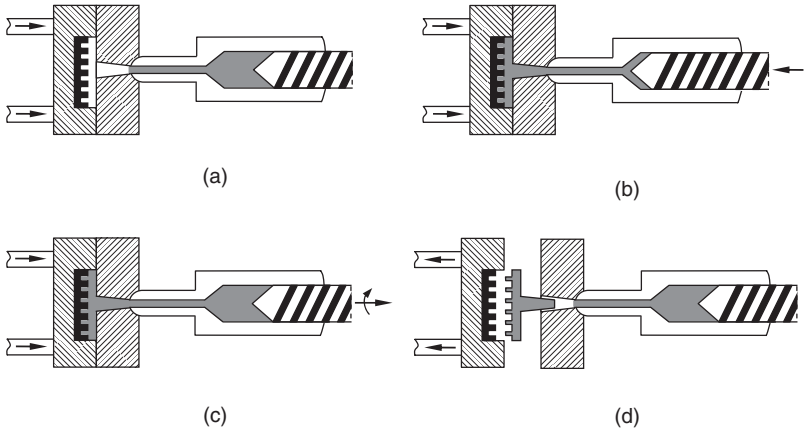

Figure 7.3 Typical stages involved in micro-injection molding: (a) mold closing, (b) injection and holding, (c) cooling and plastication, and (d) mold opening and part ejection.

7.5.1 Micro-Injection Molding Machines

Compared to a bulkier injection molding machine used in conventional molding, the following characteristics are desired for a micro-injection molding machine: (i) accurate metering or dosing, (ii) small shot size, (iii) high injection rate, (iv) short response time, (v) small but accurate clamping force, and (vi) excellent stability and repeatability. Micro-injection molding machines typically employ servo motors with precision ball bearing to achieve accurate movement of the injection plunger. There are mainly four types of injection units used: (i) reciprocating type, (ii) screw-plunger type, (iii) screw-plunger-plunger type, and (iv) plunger type. For a relatively large shot size, for example, around 5 g, a reciprocating injection unit works well. This type of injection unit can be used in molding of micro-structured parts with a relative large substrate or a plurality of micro-parts at a single shot. At smaller shot sizes, a separate plunger for dosing and injection can be used. In this case, the screw is used only for plastication. However, it is difficult to accurately control the dose when a single plunger is used both for dosing and for injection. An improved design employs two separate plungers, one for dosing and one for injection. This screw-plunger-plunger type injection unit is currently adopted in some well-known commercial micro-injection molding machines, for example, Battenfeld Micro-system 50. For prototype micro-injection molding, single-plunger screwless machines can be used. During each shot, a premeasured amount of material is charged into the plunger chamber, softened by conduction heating (often assisted by compression and spreading), and then injected into the mold. Efforts were also made to develop new plastication and injection mechanisms for micro-injection molding, for example, ultrasonic plastication [58] and impact injection molding [59]. For more details on micro-injection

molding machines, the reader is referred to recent articles by Chang *et al*. [60] and Giboz *et al*. [8].

7.5.2 Rapid Thermal Cycling of Injection Molds

Macro-sized parts with low aspect ratio micro-structures, for example, compact disks, can be molded using conventional molding processes without significant modification of the tooling and the process. As the aspect ratio increases, both mold filling and feature ejection become more difficult. One particular obstacle in micro-injection molding comes from the difficulty in filling high-aspect-ratio micro-structures. A conventional mold temperature significantly below the softening temperature of the material would cause a premature freezing problem; the polymer melt would prematurely solidify before the full feature depth could be filled. This molding difficulty can be reduced by increasing the mold temperature. This, however, may result in substantially increased or intolerably long cycle time. To resolve the conflict, a mold with a rapid heating and cooling capability is needed. An elevated mold temperature close to or above the polymer softening temperature is used for mold filling, and a cold mold temperature is used for cooling. Different names have been coined for the technique as seen in the literature, for example, variothermal processes [61–63], rapid thermal response molding [64], and dynamic mold temperature control [65] but all deal with rapidly heating and cooling the mold.

As repeatedly heating and cooling a relatively massive mold mass takes considerable time and energy, means for rapidly heating only the mold surface prior to the injection stage is desirable. To facilitate this, the thermal mass on the mold surface needs to be reduced. This can be achieved by thermally insulating the surface layer from the bulk of the mold by a layer of thermal insulation. At the same time, thermal mismatching between the surface portion and the remaining mold should be minimized. Although a considerable amount of work [55,66,67] in mold rapid heating dealt with a multilayer mold design involving heterogeneous materials, recent developments [64,68] have focused more on the use of a single metallic material for mold construction. In particular, Xu *et al*. [69] proposed a single metallic mold design with a low thermal inertia by employing air pockets inside the mold. These air pockets function as thermal insulations, and thus a separate thermal barrier layer made of a solid dielectric material can be eliminated.

The methods used for mold rapid heating basically fall into three categories: (i) electrical resistive heating, (ii) convective heating, and (iii) radiation heating. When electrical resistive heating is used, an electrical current is directed to flow at the mold surface. Confinement of the current density at the surface of a bulky metallic mold can be achieved by known methods such as induction heating and proximity heating. In the case of induction heating, an electrical coil passing high-frequency current is placed near the mold surface to induce eddy current.

Because of the so-called skin effect [70] at high frequencies, the Joule heating is confined to the mold surface. At present, the induction heating method is probably the most popular method for mold rapid heating in micro-injection molding [61–63,68]. The presence of the external coil as used in induction heating can be eliminated by proximity heating [64]. In proximity heating, the facing mold halves serve as a coil. The elimination of the external coil makes this method useful in *in situ* mold temperature control after the mold is closed. Convective mold heating with oil is an established practice in conventional injection molding. Convective heating is usually much slower than surface resistive heating because convective heating is energy limited while the power input in resistive heating can be easily changed. In conventional molding, electrical cartridge heaters are also used for mold heating. Like oil heating, cartridge heating is a slow heating method. However, the performance of these heating methods may be improved in micro-injection molding applications, given the smaller size of the mold. Smart engineering designs may be developed for enhancing the productivity of these methods for heating smaller molds. Radiation heating is typically not used in conventional injection molding but represents a common practice in other polymer processes such as thermoforming. In micro-injection molding, infrared radiation has been used for heating relatively small mold inserts [71,72]. For this application, a transparent window is incorporated in the mold design.

The above description covers the basic methods used in mold rapid heating. Compared with rapid heating, rapid mold cooling is relatively easier to achieve as long as a low thermal mass is presented. When the energy from heating is confined at the mold surface, the total energy to be taken away by cooling is minimal. Thus, a rapid heating capability of the mold typically also infers a rapid cooling capability. For such a mold, rapid cooling can be simply achieved in a conventional way, for example, by circulating water in the mold base. When air pockets or conformal air channels are used as thermal insulation near the mold surface, the cooling medium can be directed into these air voids during cooling, thus enhancing the cooling performance [52,64].

7.5.3 Processing Strategies for Micro-Injection Molding

Micro-injection molding frequently involves a large variation in flow thickness, particularly for micro-structured articles, where micro-structures are placed on the surface of a considerably thick substrate. This causes race tracking among different flow fronts with different flow thicknesses. As a result, the material fills the thick section first, and the flow may hesitate at the entrance to the micro-structures, as shown in Fig. 7.4. If the mold should be cold and the hesitation time should be longer than the freezing time of the polymer, short shot of micro-structures would occur.

One feasible processing strategy for alleviating the premature freezing problem is to increase the injection rate. The higher injection speed reduces the contact

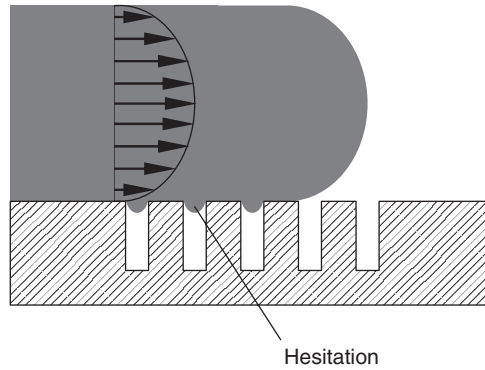

Figure 7.4 Race tracking of flow fronts caused by a vast difference in flow thicknesses.

time between the polymer melt and the mold. Additionally, the amount of viscous dissipation increases at the higher injection speed, and further offsets the unwanted cooling effect. According to numerical simulations [73] and experimental measurements [74], the shear rate in high-speed micro-injection molding could reach as high as 10^6 s^{-1}, two orders of magnitude higher than that used in conventional injection molding. Such high shear rates actually exceed the endurance limit of most thermoplastic polymers. However, molecular characterization of micro-injection molded polyoxymethylene at such high shear rates did not show a significant reduction in molecular weight [74]. This finding is somewhat surprising, but may be attributed to the rapid cooling effects occurring as the material fills the cavity. It should be noted that the rheological properties of polymer melts including the endurance limit are typically characterized on a much longer time scale. Further, the measured shear rate is an apparent shear rate; the actual shear rate could be significantly lower because of the possible presence of wall slip at an extremely high injection speed.

There are some limitations associated with the high-speed injection method. First, owing to the inertia of the plunger, there is a response time or a delay time in the speed buildup process. In micro-injection molding, this response time could be an important portion in the entire injection stage. Second, accurate control of the switchover from speed control to pressure control is difficult for a small shot size, again because of the inertia effect of the ram at a high speed. This could result in inconsistent part quality. When micro-structured thick substrates are molded, the micro-structures are not actually filled during the speed-controlled injection stage but during the pressure-controlled holding stage. In the entire speed-controlled injection stage, the material mainly fills the substrate. Therefore, if designed appropriately, a pressure control scheme starting from the beginning of the injection stage may be advantageous in micro-injection molding applications. A commercially available process called X-melt, developed by Engel Machinery [75], uses the energy stored in the polymer melt to force the polymer melt into the mold cavity. To put simply, the polymer melt is compressed to build

up the pressure. During the compression stage, a shutoff valve is used to avoid flow of the polymer melt from the barrel to the mold cavity. When the shutoff valve is opened, the statically pressurized polymer melt expands into the mold cavity, driven by the energy stored in the melt. Owing to this characteristic, the process may be named expansion injection molding, but should not be confused with expansion processes for foaming, which involves internal gas pressure in the polymer melt. The main advantage of this method over the high-speed method is that no injection ram is used and thus the inertia effect is minimal. Further, the highest injection pressure is attained at the beginning of the injection stage. This allows the polymer to flow at the highest speed at the beginning of the injection stage, thus most effectively suppressing the premature freezing problem. Note that in the speed control scheme, the injection pressure is nearly zero at the startup. Because of the limited compressibility of the polymer melt, a possible limitation of the expansion molding process is the large cushion material used and thus an increased potential for thermal degradation.

The above discussion is rooted in the use of a cold mold in micro-injection molding. When a mold with a rapid heating and cooling capability is available and the mold can be rapidly heated to the polymer softening temperature prior to the injection stage, the premature freezing problem can be eliminated. Yao and Kim [54] proposed a different injection strategy for a near-isothermal molding condition during filling. They proposed the use of a low-speed filling strategy in hot mold filling instead of increasing the injection speed. At a low speed, low pressure is involved, and the molecular orientations can be reduced. Further, filling of cavities with different characteristic thicknesses becomes more scalable. This helps reduce flow imbalance in the mold cavity.

7.6 HOT EMBOSSING

The standard hot embossing process is essentially an open-die compression molding process, involving several sequential steps, as shown in Fig. 7.5. First, a preheated thermoplastic film is placed between two heated mold platens at a temperature above the softening temperature of the polymer. The elevated mold temperature is considered necessary for pattern transferring because a cold mold would result in premature freezing of the polymer. Next, the polymer film is pressurized and shaped by closure of the mold and the micro-features on one of the platens is transferred to the polymer film. Finally, the entire embossing including the polymer and the mold is cooled to below the polymer softening temperature, and the platens are separated for the removal of the embossed film. Owing to its simplicity in tooling and process setup, hot embossing has been widely used in polymer micro/nanofabrication. Another advantage over micro-injection molding is the low stress developed in the process. In the compression mode, the polymer melt flows a much shorter distance than in the injection mold. The reduction in flow stresses helps improve the dimensional accuracy and the stability of the molded part, and at the same time, protects the tool from

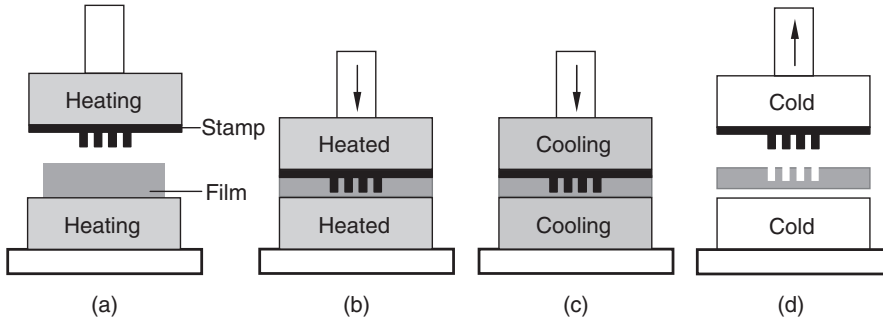

Figure 7.5 Sequential stages involved in hot embossing: (a) preheating, (b) embossing, (c) holding and cooling, and (d) ejection.

damage caused by large strains. Therefore, relatively brittle and/or soft materials, for example, glass, silicon, or even rubber, may be used as mold materials.

While offering the benefits of its simple process and tooling setup, the hot embossing process is subject to some processing difficulties. Because of the open-die setup, significant lateral flow may occur when high embossing pressure is needed for embossing high-aspect-ratio micro-structures, resulting in a large reduction of the substrate thickness. The actual thickness of the embossed film typically ranges from 20 to 200 μm, depending on the process parameters, the polymer material, and the geometry of the mold [76]. When the target thickness is larger than this range, it is difficult to build up high embossing pressure. For this reason, thicker parts with high-aspect-ratio micro-features are often produced by micro-injection molding. Furthermore, the standard hot embossing process is designed for replicating surface features onto polymer substrates. Shell patterns and discrete features (e.g., micro-gears, waveguides, micro through holes, among others) are difficult to fabricate.

Some embossing-based process variants have been developed for addressing the above limitations and enhancing the performance and productivity of the standard hot embossing process. A brief account on these new developments is given in the following sections.

7.6.1 Efficient Thermal Cycling

Thermal cycling of mold temperature is a built-in feature in hot embossing. Unlike injection molding, hot embossing relies mainly on a hot mold for feature transfer. Other strategies such as high-speed injection and expansion molding used in micro-injection molding are difficult to implement in hot embossing. Thus, the productivity of the hot embossing process hinges largely on the efficiency of the thermal cycling. The three main types of heating approaches, namely resistivity heating, convective heating, and radiation heating, as used in micro-injection molding have also been investigated in hot embossing and have greatly

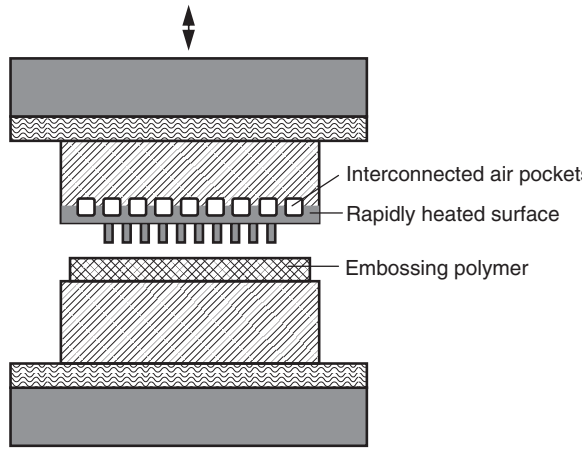

Figure 7.6 Schematic setup of rapid thermal response hot embossing with proximity heating and conformable air pockets.

enhanced the productivity. In particular, Kimberling *et al*. [77] implemented the proximity heating method in hot embossing and reduced the standard cycle time of several minutes or above to below 10 s. The embossing apparatus they used is schematically shown in Fig. 7.6. The high-frequency proximity effect allows the electrical current, and consequently the heating power, to get concentrated at the mold surface. The conformable pockets at the mold surface not only work as air insulation during the embossing stage but also provide channels for forced convection of cold air during cooling. Additionally, owing to the simplified tool design, other methods that cannot work in injection molding may now become feasible in hot embossing. A fluid-based embossing process has been developed by Chang and Yang [13], where a fluid (steam, gas, and oil) is used both as a pressure medium for uniform pressing and as a heating and cooling medium for the polymer film. The cycle time in this fluid-based system is approximately 30 s or shorter. Ultrasonic heating has also been introduced to hot embossing for cycle time reduction [50,78]. With ultrasonic heating, the surface layer of the embossing polymer can be rapidly heated in less than 10 s. The limitations of this method, however, are the difficulty in replicating concaved features and the fact that only extremely small area can be heated [13].

All the above methods for rapid thermal cycling involve heating and cooling a single embossing mold. Yao *et al*. [79] have investigated the use of two stations, one hot and one cold, for rapid thermal cycling. This embossing technique does not rely on the complex design of the mold insert in achieving a low thermal inertia, but rather it is developed as a processing strategy for enhancing productivity. As illustrated in Fig. 7.7, two upper mold bases are employed; one is maintained at a constant hot temperature and the other at a constant cold temperature. During the embossing stage, the hot base is used as the backing for the stamp. When the embossing stage finishes, the backing switches to the cold base. With this

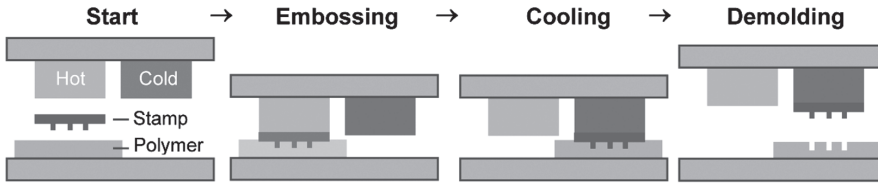

Figure 7.7 Process sequence in two-station embossing.

tool-setup strategy, the heating and cooling stages are decoupled, and thus rapid thermal cycling is achieved. The attachment and separation of the stamp and the two stations can be achieved in a nonmechanical manner, for example, using vacuum force. The cycle time using this two-station approach is in the order of 10 s.

7.6.2 Constant-Temperature Embossing

The thermal cycling problem may also be tackled from the materials perspective. In theory, any material (not necessarily a thermoplastic) that can be softened and solidified during processing can be used in embossing. If softening and solidification could occur at the same temperature, constant-temperature embossing would be possible. The recently developed solvent-assisted embossing method [44,45] may be considered as a specific method in this category. As diffusion is an efficient process at micrometer sizes, solvents including supercritical fluids can rapidly diffuse into the thin polymer layer at the time scale of the process. The absorbed solvent works as a plasticizer and allows the polymer to soften. After the solvent is removed, the polymer is hardened again. In this case, the polymer is processed at a constant mold temperature. Constant-temperature embossing can also be achieved through chemical curing of monomers or oligomers. Among such processes, the most noteworthy process is the UV-curing embossing process [2,7], in which a UV-curable resin is cured by UV radiations. Rather than using solvents or a chemical curing process, Yao *et al*. [49] have investigated the feasibility of utilizing the unique property of slowly crystallizing polymers for achieving constant-temperature embossing. Crystallizable amorphous polymer films were embossed above the polymer's glass transition temperature for pattern transfer and subsequently crystallized for solidification at the same temperature. The total cycle time with this processing strategy was found to be in the order of half the time of crystallization of the polymer.

Solid-state forming is a standard method used by the metal forming industry. The polymer is subjected to a large amount of elastic recovery if forged at a temperature below its softening temperature. Earlier investigations [1,80] showed that the dimensional recovery of the forged polymer micro-structures is significantly affected by the process conditions as well as by properties of the material used. However, it is worth mentioning that the method can be used for devices with relatively low dimensional accuracy requirement, such as scaffolds

for tissue engineering and heat convective surfaces for electrical packaging. This process may be better controlled with enhanced prediction capabilities and process optimization schemes. When imprinting micro-channels on a Teflon substrate, Yao and Nagarajan [1] found that a combination of high forging speed and proper dwell time can be used to effectively reduce the amount of dimensional recovery. Recently, the interest in micro-feature embossing using solid-state forming is growing. Superplastic materials, including amorphous metals, in place of polymeric materials have been investigated by [81,82].

7.6.3 Through-Thickness Embossing

Currently, precise 3D micro-parts are produced mainly using micro-injection molding. The molding results, however, are often compromised because of the complex tool setup and the high amount of stresses introduced to the part during injection molding. It is thus advantageous to use hot embossing, a low-stress process with a simpler tool and process setup, for precision fabrication.

Heckele and Durand [83] developed a technique for producing through holes by hot embossing. They used a substrate with two layers of different materials. After embossing, the tool features protruded through the upper layer into the lower layer. After removal of the lower layer, through holes were left on the upper layer. Werner [84] described a process involving identical top and bottom mold halves, both containing pins, whose top surfaces are attached to each other upon mold closure. By this process, through holes with only a thin residual layer remaining can be embossed. Mazzeo *et al*. [85] developed a tool set for punching thin plastic films. They were able to emboss holes as small as 500 μm in diameter. All the methods described above involve a through-thickness action for fabricating through holes. Nagarajan *et al*. [43] prototyped a hybrid punching and embossing process for through-thickness embossing of 3D parts. The embossing tool included a punching head and to-be-replicated features in the socket behind the punching head. The built-in punching head allowed a through-thickness action and provided a close-die environment for embossing pressure buildup. The method was used to successfully emboss multi-channel millimeter waveguides each of which weighed approximately 0.5 g. This process can be further developed for through-thickness embossing of true micro-parts. Kuduva-Raman-Thanumoorthy and Yao [11] used an embossing stamp with through-thickness micro-cavities and performed a through-thickness embossing step for fabrication of discrete micro-parts (Fig. 7.8), about 1 mg each. After embossing, the embossed parts are attached to thin residual films of a thickness less than 10 μm on both sides. The residual films are then mechanically detached from the micro-parts during ejection.

7.6.4 Embossing of Shell Patterns

Polymer thin films patterned with micro-structures at a characteristic size greater than the film thickness are difficult to fabricate using standard hot embossing.

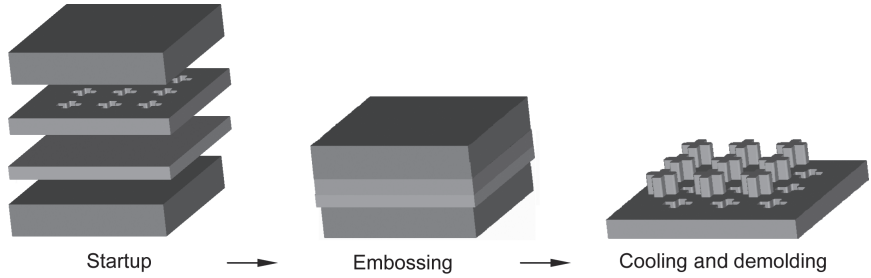

Figure 7.8 Steps involved in through-thickness embossing of discrete micro-parts. (A full color version of this figure appears in the color plate section.)

Such shell micro-structures experience deformation over dimensions larger than the film thickness, and the patterned film is marked by the shell-type geometry with little change in the film thickness during the patterning process [42]. To emboss shell patterns, a pair of matching dies is needed. Such a matching pair requires extremely precise alignment of the mating surfaces. Small misalignment in a micrometer level could cause a tool failure. Furthermore, the tiny space between the matching surfaces may be easily jammed by the polymer, resulting in an ejection difficulty and in worse cases, damage of the micro-structures on the tool.

Figure 7.9 shows the reported methods for patterning shell-type micro-geometries. A modified hot embossing method involving a soft countertool was discussed by Dreuth and Heiden [42]. In this method, the second die is replaced by a cushion material, as shown in Fig. 7.9b. The cushion material and the polymer film are both softened by heat during embossing. After cooling of the two materials, the cushion material is sacrificed, for example, dissolved by a solvent, to recover the structured polymer film. The advantage of this process is that alignment of mating surfaces is not needed. Ikeuchi *et al*. [86] used this method for fabricating polymer membrane micro-channels. Paraffin was used as a cushion material, and membrane micro-channels were fabricated with two polymer films: PMMA film and poly(lactic acid) film. There are some issues involved in the use of a sacrificial countertool. The thermoplastic cushion material needs to be softened together with the embossing film, and therefore the two materials need a similar softening temperature. Moreover, the cushion material should have appropriate deformability. To address these issues, a rubber-assisted embossing using rubber as a soft countertool was recently developed by Nagarajan and Yao [10,40,41]. The sequential stages involved in this process are schematically shown in Fig. 7.10. The rubber countertool further helps with part releasing during ejection.

There also exist continuous processes for patterning/texturing thin polymer films. These processes are based on roll-to-roll setups, involving a heated embossing roll and a pressure roll (Fig. 7.9d) for transferring the surface textures on the embossing roll to a continuous film. The surface texture of the film modifies

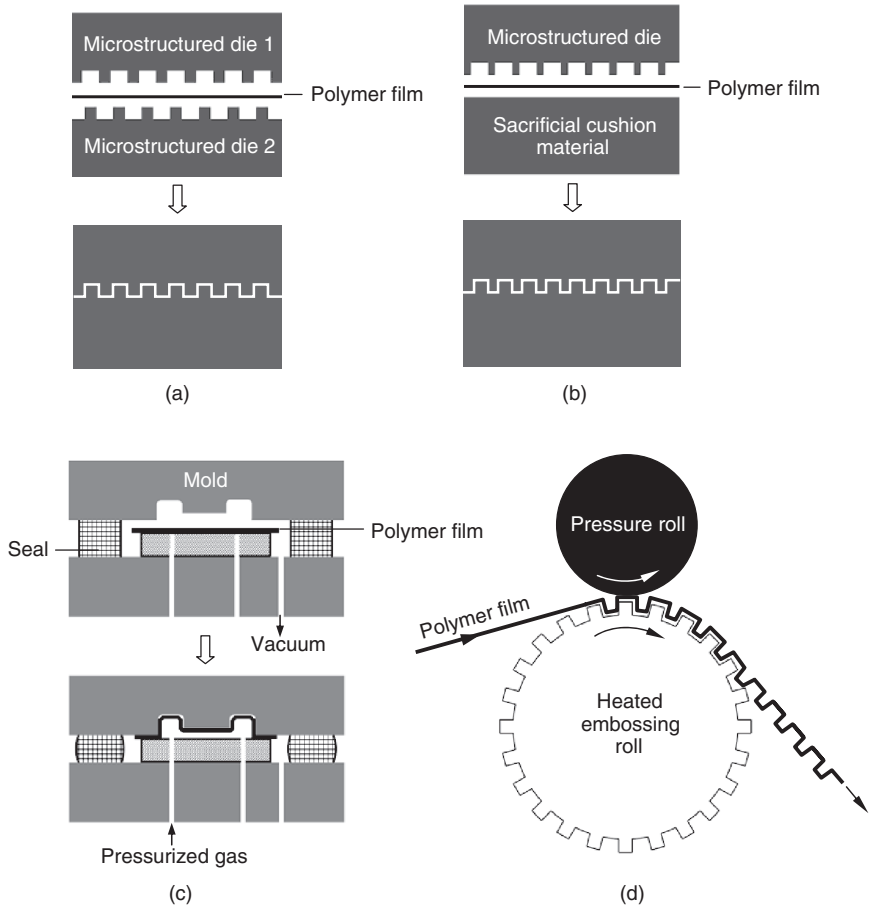

Figure 7.9 Different techniques for fabricating shell micro-structures: (a) hot embossing using a pair of micro-structured dies, (b) hot embossing using a micro-structured die and a countertool made of a deformable polymer, (c) micro thermoforming, and (d) roller embossing.

its feel and appearance and is therefore desired in many end-use applications, including packaging, diapers, raincoats, and disposable goods. However, in order to use a roll embossing process for precision film structuring, accurate and spatial control of the roll surface temperature is needed [87].

Efforts have also been made to scale down conventional thermoforming techniques for precision structuring of polymeric films [2,88]. Truckenmuller *et al*. [88] used a micro thermoforming process to pattern a 25-μm-thick PS film with 125-μm-deep and 250-μm-wide micro-channels. During this micro thermoforming process, the film was held between a structured mold insert and a flat mold platen and then thermoformed under the action of pressurized gas. Although this method was successfully employed for thermoform micro-fluidic analysis chips,

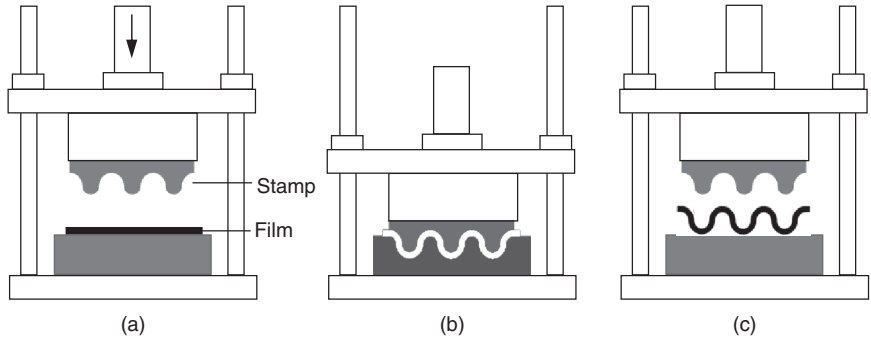

Figure 7.10 Rubber-assisted embossing process involving several sequential stages: (a) startup; (b) embossing, holding, and cooling; and (c) mold opening.

it is not suitable for achieving a high aspect ratio of the channel [2]. Further, uniform film thickness is difficult to accomplish.

7.6.5 Embossing Pressure Buildup

Standard hot embossing is an open-die compression molding process, as shown in Fig. 7.11a. The process window is skewed toward very thin polymer films at a thickness of tens of microns or smaller. In this case, the pressure is not indeed an independent process parameter, but rather it depends on rheological properties of the embossing polymer and the residual film thickness needed. This coupling can be clearly seen in a simple axisymmetric embossing case with a Newtonian viscosity:

$$p(r) = 3\eta \frac{u}{H^3}(R^2 - r^2) \tag{7.14}$$

where r is a radial coordinate, R is the radius of the polymer disk, H is the film thickness, u is the embossing velocity, and η is the viscosity. The standard embossing setup may be slightly modified to create a close-die or near-close-die environment, as shown in Fig. 7.11b–d. The first variation is to use a large polymer film, allowing the polymer to be squeezed and accumulated at the periphery of the stamp, as shown in Fig. 7.11b. Because a long embossing time, about 5 min, is typically used in hot embossing, the accumulated material at the periphery can be cooled significantly because of natural convection. The cooled material, in turn, provides a flow resistance to the material inside the embossing area. The resulting process would be more like a close-die process with less radial variation in pressure. In the second case, a cold polymer substrate can be used, as shown in Fig. 7.11c. In this case, the out-squeeze flow is restrained by the surrounding cold polymer. As a result, only a restricted amount of polymer can escape, typically flowing upward along the wall [89]. Another case is shown in Fig. 7.11d

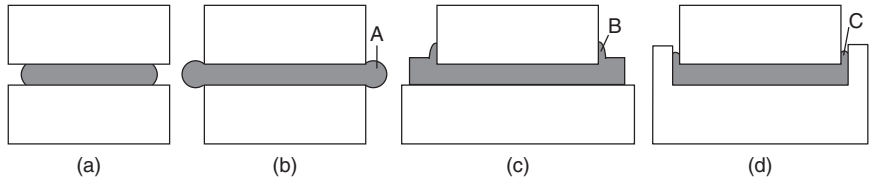

Figure 7.11 Different hot embossing modes: (a) direct open-die embossing, (b) open-die embossing with cooled polymer beads at location A, (c) nonisothermal embossing with wall climbing flow at location B, and (d) near-close-die embossing with squeeze flow in the clearance gap at location C.

where the embossing tool is modified to use a clearance gap for reducing the out-squeeze flow.

Yao and Kuduva-Raman-Thanumoorthy [90] recently proposed that a stepped landing area be employed for better pressure control and thickness control, as shown in Fig. 7.12. The micro-structure stamp is placed in the recess cavity. When a high embossing pressure is applied, a thin film is formed at the landing area between the shoulder and the lower mold platen. With this tooling setup, the embossed thickness is approximately equal to the recess depth. The accuracy increases with the increase of the recess depth, thus favoring the replication of micro-structures on thicker polymer substrates. The strategy described above allows thickness control to be decoupled from pressure control.

Analytical solutions can be obtained for embossing with a stepped landing area. Considering the much larger thickness in the cavity than in the landing area, a uniform pressure inside the cavity can be assumed. With the coordinate system in Fig. 7.12, the pressure field can be analytically solved, given a constant viscosity:

$$p = \begin{cases} 3\eta(v_z/H_s^3)(R_s^2 - r^2), & \text{for } r \geq R \\ 3\eta(v_z/H_s^3)(R_s^2 - R^2), & \text{for } r < R \end{cases} \tag{7.15}$$

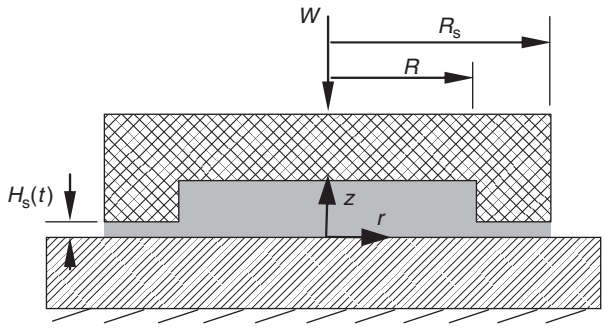

Figure 7.12 A polymer layer embossed by an embossing master with a landing shoulder.

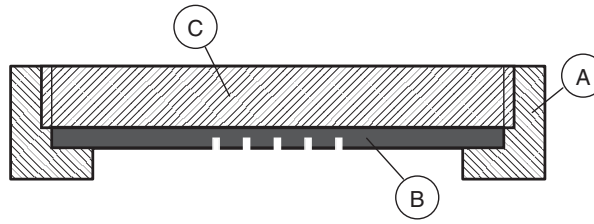

Figure 7.13 An embossing mold using a locating ring as a shoulder, comprising (a) locating ring, (b) stamp, and (c) locking plate.

where p is the pressure, η is the viscosity, R_s and H_s are the radius and thickness of the shoulder, and R is the radius of the embossing disk. From the above equation, it can be seen that, with the shoulder, the embossing pressure is no longer a parameter dependent on the residual film thickness. Rather than that, the pressure can be adjusted by changing the dimensional parameters of the shoulder, that is, R_s and H_s. The extra polymer at the shoulder also works as a cushion material for shrinkage composition in the cavity during the holding stage. The size of this cushion material can be varied by varying R_s. Last but not the least, a uniform cavity pressure is obtained with the inclusion of the shoulder.

Often, the embossing stamp, the major component of the embossing mold, is made of a lithographic material, such as silicon and quartz. These materials are brittle, and therefore it would be difficult to fabricate a shoulder directly on this material. In this case, a locating ring can be used, as shown in Fig. 7.13.

7.7 MICRO-MOLD FABRICATION

Micro-molding represents a cluster of replication-based processes. The final part quality in micro-molding is therefore largely dependent on the quality of the master pattern.

Many methods have been proposed for making stamps/molds for micro-molding, including lithographic methods, replication methods, and material ablation or removal methods. Lithography is a well-established technique, particularly for patterning micro-structured silicon wafer. If only shallow features are needed, lithography can also be used for patterning steel and other more isotropic materials. For example, in the mold-making industry, for many years, a wax coating and acid itching process has been used for creating shallow micro-textures on mold surface. The micro-structures on a soft or brittle substrate made of polymer resist, silicon, or glass can be transferred to a more durable metallic material by the replication method. Different coating-based techniques, including electroplating or electroforming, physical vapor deposition, and chemical vapor deposition, can be used for feature transfer. In particular, the well-known LiGA process is based on lithography and

electroforming. Replication has also been used for transferring the pattern from silicon to a polymeric material, and the patterned polymeric material is used as a prototyping mold. With multiple soft molds created from a silicon template, more parts can be replicated. However, these soft tools are mostly useful for low-pressure and low-temperature processes. The soft molding method based on PDMS is one such process. Studies of micro-mold making have also been performed using hot embossing with a thermoplastic polymer [91]. A recent review on micro-molds made of nonconventional materials is given by Malek *et al*. [50]. For making a durable metallic micro-mold, material ablation or removal methods are used more commonly. Micro-scale material removal can be performed by mechanical micro-machining processes (e.g., micro-milling), electrical discharge machining, electrochemical machining, and high-energy beam machining processes (e.g., with ultrashort-pulsed laser, focused ion beam, electron beam, and plasma). A comparison between different processes usable for metallic mold insert fabrication has been given by Giboz *et al*. [8].

Smooth surface finishes are highly desired for a micro-mold. The surface finish of the structures produced by material removal processes is typically rough, compared with the size of the feature. In conventional mold making, burs and unexpected asperities can be reduced by various types of no-contact polishing processing, for example, ultrasonic polishing and electrochemical erosion. These traditional methods may be adapted to micro-mold polishing, but so far there has been little effort reported. Surface smoothness may also be improved by taking advantage of some natural processes, for example, surface tension caused reflow. For instance, Shiu *et al*. [39] created a pattern with a smooth surface finish by embossing a polymer only half way into a mold with micro-channels. The polymer pattern is then used as a stamp for embossing smooth micro-channels on a second material. Alternatively, the smooth pattern on the polymer template can be transferred to a metallic material by a coating-based replication method as described earlier. In the case of a lens array pattern, different processes [14,92,93] can be used to create a smooth surface.

As in convention molding, draft angles are also desired in demolding. As pointed out by Heckel and Schomburg [2], most problems in micro-molding are not caused by the filing of the mold, but by demolding. It is indeed a difficult task to eject micro-features with an aspect ratio greater than 10 if no draft angle and lubrication agents are employed. Some techniques, including inclined lithography [94,95], underdosing lithography [96], and femtosecond laser machining, are available for incorporating draft angles to a straight wall. In addition to the draft angle, the mold surface often needs to be treated with fluorinated coating material to lower its surface energy [29], thus improving feature releasing during ejection.

7.8 SUMMARY AND ONGOING RESEARCH

After three decades of research, micro-molding has evolved into a useful tool for realization of polymer-based micro-devices and micro-systems. The primary

advantages of using polymers in micro-fabrication arise from their versatile properties and mass production capabilities. While thermoplastic polymers dominate in micro-molding applications, thermosetting polymers are advantageous in some special problems, particularly when a low-viscosity material is needed in casting into weak master templates. The two major thermoplastic micro-molding processes are hot embossing and injection molding, both of which have demonstrated their great potential in precision, large volume production of micro-components. The micro-molding technology has led to many innovations in the emerging MEMS and lab-on-a-chip applications. For example, Fig. 7.14 shows a gallery of micro-molded parts produced by the author and collaborative workers. These successfully micro-molded parts fall into three categories: surface micro-structures, shell micro-structures, and micro-parts. They are used in a wide range of applications including telecommunication, functional optics, lab-on-a-chip applications, biomimetics, and tissue engineering.

Appropriate handling of size effects is an important step toward adaption of conventional molding processes to miniature applications and development of hybrid, innovative micro-molding processes. For successful micro-molding, a logical comparison between micro-molding processes and their macro-scale counterpart is needed. On the one hand, a huge knowledge base has been developed in the traditional polymer-processing industry and has to be utilized fully. On the other hand, new strategies for material processing and process development, based on the understanding of the size effects in process dynamics, need to be developed to overcome any new processing difficulties caused by scaling, and the potential scaling advantages need to be utilized for developing more effective processes. Following this framework, a number of new, more effective micro-molding processes have been developed recently, including expansion injection molding, ultrasonic-assisted micro-molding, variothermal injection molding, rapid-thermal-response embossing, through-thickness hot embossing, rubber-assisted hot embossing, and UV-curing roll embossing. These processes facilitate better quality control in terms of replication fidelity and structural optimization and also enable production of different types of micro-structures and micro-parts more effective than by standard micro-injection molding and standard hot embossing.

However, compared with the two-century industrial endeavor in plastics processing, the history of micro-molding is relatively short. There are still a number of problems waiting to be solved. In particular, new techniques have yet to be developed in the area of process control, process modeling, and morphological characterization. Processing-structure-property relations are of great importance in polymer processing. However, many well-developed characterization protocols for conventional molding fail in micro-molding applications because of the resolution problem. Process control and monitoring is also difficult in micro-molding. For example, measurement of pressure and temperature distribution in a micro-cavity requires an extremely high resolution [97–100]. From the materials point of view, there also exist huge opportunities for improvement. Applications of stronger polymer composites including nanocomposites in micro-molding and

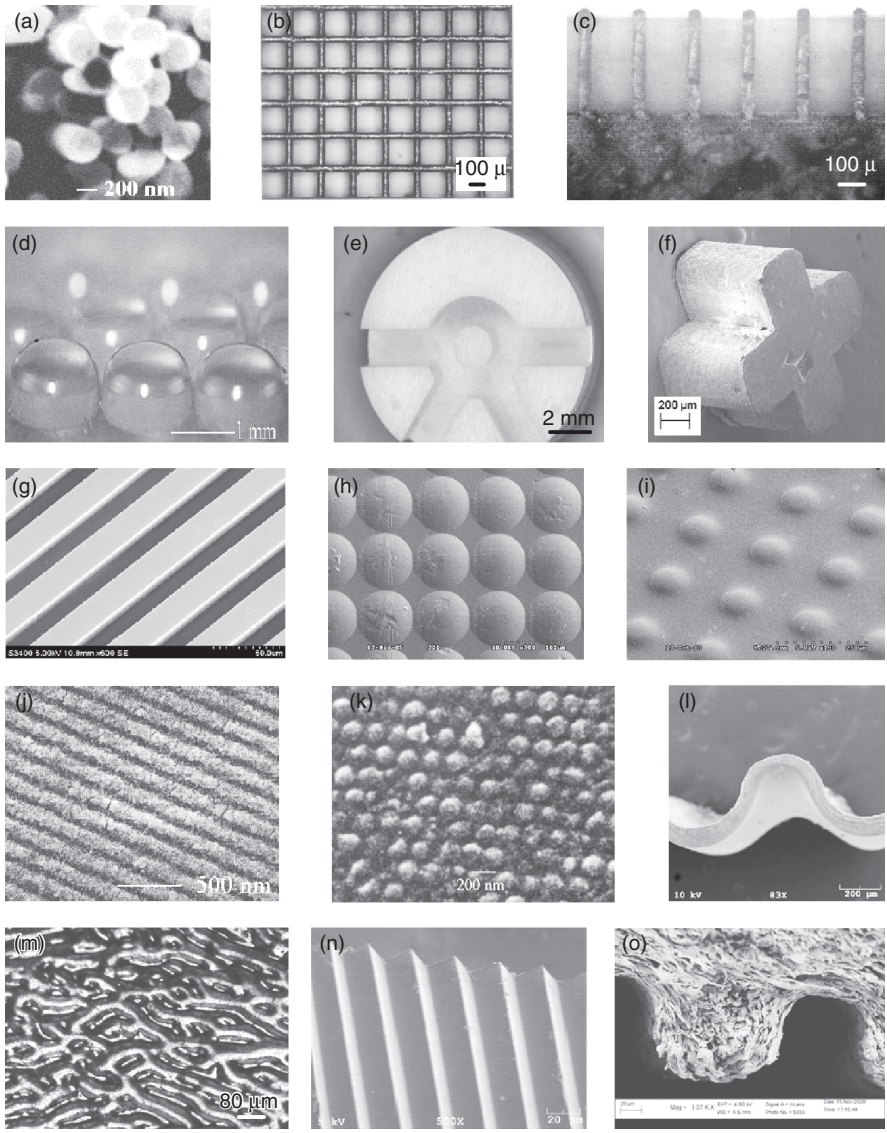

Figure 7.14 A gallery of micro-molded micro-components: (a) injection-molded PS submicron posts, (b) injection-molded HDPE micro-wells, (c) injection-molded high aspect ratio HDPE micro-features, (d) hot-embossed PMMA lenses, (e) through-thickness embossed ABS multichannel waveguide, (f) through-thickness embossed ABS micro-part, (g) hot-embossed PET grooves, (h) two-station embossed micro-lens array, (i) lens array from hybrid compression molding and reflow, (j) hot-embossed holographic surface, (k) hot-embossed antirefractive surface, (l) rubber-assisted embossed ABS shell pattern, (m) hot-embossed biomimetic surface, (n) UV roll embossed V-grooves, and (o) hot-embossed porous PLGA scaffold.

utilization of unique polymer behaviors to realize more effective micro-molding processes are just among important future endeavors. Last but not the least, there is much ongoing research in process modeling and simulation. The more complex rheological behavior and more 3D geometries encountered in hybrid micro-molding processes call for the inclusion of nonlinear viscoelasticity in the modeling procedure, which is still a challenge for high Weissenburg number deformation. Even more challenging is the modeling of nanomolding processes, in which discrete effects may take place. Possible size effects on constitutive relations and their consequences on the micro-molding behavior are still unknown. Therefore, an important future research direction in micro-molding is projected into the fundamental understanding of these size effects.

REFERENCES

1. Yao D, Nagarajan P. Cold forging method for polymer microfabrication. Polym Eng Sci 2004;44:1998–2004.
2. Heckele H, Schomburg WK. Review on micro molding of thermoplastic polymers. J Micromech Microeng 2004;14:R1–R14.
3. Mekaru H, Yamada T, Yan S, Hattori T. Microfabrication by hot embossing and injection molding at LASTI. Microsyst Technol 2004;10:682–688.
4. Rotting O, Ropke W, Becker H, Gartner C. Polymer microfabrication technologies. Microsyst Technol 2002;8:36–32.
5. Gross GLW. The production of nanostructures by mechanical forming. J Phys D Appl Phys 2006;39:R363–R386.
6. Becker H, Locascio LE. Polymer microfluidic devices. Talanta 2002;56:267–287.
7. Gates BD, Xu Q, Stewart M, Ryan D, Willson CG, Whitesides GM. New approaches to nanofabrication: molding, printing, and other techniques. Chem Rev 2005;105:1171–1196.
8. Giboz J, Copponnex T, Mélé P. Microinjection molding of thermoplastic polymers: a review. J Micromech Microeng 2007;17:R96–R107.
9. Bauer HD, Ehrfeld W, Paatzsch T, Smaglinski I, Weber L. Advanced micromolding of optical components. SPIE 1999;3878:261–270.
10. Nagarajan P, Yao DG. Rubber-assisted micro forming of thin polymer films. Microsyst Technol 2009;15:251–257.
11. Kuduva-Raman-Thanumoorthy R, Yao D. Hot embossing of discrete microparts. Polym Eng Sci 2009;49:1894–1901.
12. Hocheng H, Wen TT, Yang SY. Replication of microlens arrays by gas-assisted hot embossing. Mater Manuf Process 2008;23:261–268.
13. Chang JH, Yang SY. Development of fluid-based heating and pressing systems for micro hot embossing. Microsyst Technol 2005;11:396–403.
14. Pan LW, Shen XJ, Lin LW. Microplastic lens array fabricated by a hot intrusion process. IEEE/ASME J Microelectromech Syst 2004;13:1063–1071.
15. Yang HH, Chao CK, Wei MK, Lin CP. High fill-factor microlens array mold insert fabrication using a thermal reflow process. J Micromech Microeng 2004;14:1197–1204.

16. Ito H, Suzuki H, Kazama K, Kikutani T. Polymer structure and properties in micro- and nanomolding process. Curr Appl Phys 2009;9:e19–e24.
17. Hung KY, Chen YK, Huang SH, Shye DC. Molding and hot forming techniques for fabricating plastic aspheric lenses with high blue-light transmittance. Microsyst Technol 2009. Online on Nov. 5, 2007.
18. Angelov AK, Coulter JP. The development and characterization of polymer microinjection molded gratings. Polym Eng Sci 2008;48:2169–2177.
19. Lippmann JM, Geiger EJ, Pisano AP. Polymer investment molding: method for fabricating hollow, microscale parts. Sens Actuator A Phys 2007;134:2–10.
20. Appasamy S, Li WZ, Lee SH, *et al*. High-throughput plastic microlenses fabricated using microinjection molding techniques. Opt Eng 2005;44:123–401.
21. Tanaka H, Matsumoto K, Shimoyama I. Fabrication of a three-dimensional insect-wing model by micromolding of thermosetting resin with a thin elastomeric mold. J Micromech Microeng 2007;17:2485–2490.
22. Choi CG. Fabrication of optical waveguides in thermosetting polymers using hot embossing. J Micromech Microeng 2004;14:945–947.
23. Sethu P, Mastrangelo CH. Cast epoxy-based microfluidic systems and their application in biotechnology. Sens Actuators B 2004;98:337–346.
24. Chung S, Im Y, Choi J, Jeong H. Microreplication techniques using soft lithography. Microelectron Eng 2004;75:194–200.
25. Qin D, Xia YN, Whitesides GM. Rapid prototyping of complex structures with feature sizes larger than 20 μm. Adv Mater 1996;8:917–917.
26. Jin YH, Cho YH, Schmidt LE, Leterrier Y, Manson JAE. A fast low-temperature micromolding process for hydrophilic microfluidic devices using UV-curable acrylate hyperbranched polymers. J Micromech Microeng 2007;17:L1147–L1153.
27. Vogler M, Wiedenberg S, Muhlberger M, *et al*. Development of a novel, low-viscosity UV-curable polymer system for UV-nanoimprint lithography. Microelectron Eng 2007;84:984–988.
28. Chang CY, Yang SY, Chu MH. Rapid fabrication of ultraviolet-cured polymer microlens arrays by soft roller stamping process. Microelectron Eng 2007;84:355–361.
29. Nezuka O, Yao DG, Kim BH. Replication of microstructures by roll-to-roll UV-curing embossing. Polym Plast Technol Eng 2008;47:865–873.
30. Kalima V, Vartialinen I, Saastamoinen T, *et al*. UV-curable ZnS/polymer nanocomposite for replication of micron and submicron features. Opt Mater 2009; 31:1540–1546.
31. Jeon NL, Choi IS, Xu B, *et al*. Large-area patterning by vaccum-assisted micromolding. Adv Mater 1999;11:946–950.
32. Piccin E, Coltro WKT, da Silva JAF, *et al*. Polyurethane from biosource as a new materials for fabrication of microfluidic devices by rapid prototyping. J Chromotagr A 2007;1173:151–158.
33. Niu XZ, Peng SL, Liu LY, *et al*. Characterizing and patterning of PDMS-based conducting composites. Adv Mater 2007;19:2682–2686.
34. Mi YL, Chan YN, Trau D, *et al*. Micromolding of PDMS scaffolds and microwells for tissue culture and cell patterning: A new method of microfabrication by the self-assembled micropatterns of diblock copolymer micelles. Polymer 2006;47:5124–5130.

35. Brehmer M, Conrad L, Funk L. New developments in soft lithography. J Dispers Sci Technol 2003;24:291–304.
36. Klemic KG, Klemic JF, Reed MA, *et al*. Micromolded PDMS planar electrode allows patch clamp electrical recordings from cells. Biosens Bioelectron 2002;17:597–604.
37. Michel B, Bernard A, Bietsch A, *et al*. Printing meets lithography: soft approaches to high-resolution patterning. IBM J Res Dev 2000;45:697–717.
38. Xia Y, Whitesides GM. Soft-lithography. Angew Chem Int Ed Engl 1998;37:550–575.
39. Shiu PP, Knopf GK, Ostojic M, Nikumb S. Rapid fabrication of tooling for microfluidic devices via laser micromachining and hot embossing. J Micromech Microeng 2008;18:025012.
40. Nagarajan P, Yao DG. Uniform shell patterning using rubber-assisted hot embossing process—Part I: experimental. Polym Eng Sci 2011. in press.
41. Nagarajan P, Yao DG. Uniform shell patterning using rubber-assisted hot embossing process—Part II: process analysis. Polym Eng Sci 2011. in press.
42. Dreuth H, Heiden C. Thermoplastic structuring of thin polymer films. Sens Actuators 1999;78:198–204.
43. Nagarajan P, Yao DG, Ellis TS, Azadegan R. Through-thickness embossing process for fabrication of three-dimensional thermoplastic parts. Polym Eng Sci 2007;47:2075–2084.
44. Khang DY, Lee HH. Room temperature embossing lithography. Appl Phys Lett 2000;76:870–872.
45. Wang Y, Liu ZM, Han BX, *et al*. Compressed-CO2-assisted patterning of polymers. J Phys Chem B 2005;109:12376–12377.
46. Despa MS, Kelly KW, Collier JR. Injection molding of polymeric LIGA HARMs. Microsyst Technol 1999;6:60–66.
47. Wimberger-Friedl RW. Injection molding of sub- μm grating optical elements. J Inject Mold Technol 2000;4:78–83.
48. Yao D, Kim B. Injection molding high aspect ratio microfeatures. J Inject Mold Technol 2002;6:11–17.
49. Yao D, Nagarajan P, KRT R. Constant-temperature microfeature embossing with slowly crystallizing polymers. Int Polym Process 2007;22:375–377.
50. Malek CK, Coudevylle JR, Jeannot JC, Duffait R. Revisiting micro hot-embossing with moulds in non-conventional materials. Microsyst Technol 2007;13:475–481.
51. Pipkin AC. Lecture notes in viscoelasticity. New York: Springer; 1972.
52. Yao DG, Chen SC, Kim BH. Rapid thermal cycling of injection molds—an overview on technical approaches and applications. Adv Polym Technol 2009;27:233–255.
53. Yao D, Kim B. Scaling analysis of the injection molding process. ASME J Manuf Sci Eng 2004;126:733–737.
54. Yao D, Kim B. Increasing flow length in thin wall injection molding using a rapidly heated mold. Polym Plast Technol Eng 2002;41:819–832.
55. Kim B, Suh N. Low thermal inertia molding. Polym Plast Technol Eng 1986;25:73–93.
56. Yao D, Kim B. Simulation of the filling process in micro channels for polymeric materials. J Micromech Microeng 2002;12:604–610.

57. Li JH, Young WB. Study on mold filling behaviors of micro channels in injection molding. Int Polym Process 2009;24:421–427.
58. Michaeli W, Spennemann A, Gartner R. New plastification concepts for micro injection moulding. J Polym Eng 2004;24:81–93.
59. Nian SC, Yang SY. Molding of thin sheets using impact micro-injection molding. Int Polym Process 2005;20:441–448.
60. Chang PC, Hwang SJ, Lee HH, Huang DY. Development of an external-type micro-injection molding module for thermoplastic polymer. J Mater Process Technol 2007;184:163–172.
61. Michaeli W, Spennemann A. Injection moulding microstructured functional surfaces. Kunststoffe Plast Eur 2000;90:52–57.
62. Schinkothe W, Walther T. Reducing cycle times—alternative mould temperature control for microinjection moulding. Kunststoffe Plast Eur 2000;90:62–68.
63. Weber L, Ehrfeld W. Micromoulding. Kunststoffe Plast Eur 1999;89:192–202.
64. Yao D, Kimberling TE, Kim B. High-frequency proximity heating for injection molding applications. Polym Eng Sci 2006;46:938–945.
65. Chen SC, Jong WR, Chang JA. Dynamic mold surface temperature control using induction heating and its effects on the surface appearance of weld line. J Appl Polym Sci 2006;101:1174–1180.
66. Jansen KMB, Flaman AAM. Construction of fast-response heating elements for injection molding applications. Polym Eng Sci 1994;34:894–897.
67. Yao D, Kim B. Development of rapid heating and cooling systems for injection molding applications. Polym Eng Sci 2002;42:2471–2481.
68. Chen SC, Jong WR, Chang YJ, *et al*. Rapid mold temperature variation for assisting the microinjection of high aspect ratio micro-feature parts using induction heating technology. J Micromech Microeng 2006;16:1783–1791.
69. Xu XR, Sachs E, Allen S. The design of conformal cooling channels in injection molding tooling. Polym Eng Sci 2001;41:1265–1277.
70. Brown GH. Theory and application of radio-frequency heating. New York: D. Van Nostrand Company; 1947.
71. Chang PC, Hwang SJ. Experimental investigation of infrared rapid surface heating for injection molding. J Appl Polym Sci 2006;102:3704–3713.
72. Yu MC, Young WB, Hsu PM. Micro-injection molding with infrared assisted mold heating system. Mater Sci Eng A 2007;460–461:288–295.
73. Zhao J, Mayes RH, Chen G, Chan PS, Xiong ZJ. Polymer micomould design and micromoulding process. Plast Rubber Compos 2003;32:240–247.
74. Whiteside BR, Martyn MT, Coates PD, Allan PS, Hornsby PR, Greenway G. Micromoulding: process characteristics and product properties. Plast Ruber Compos 2003;32:231–237.
75. Herlihy G. X-melt—a precision technology for micro-moulding and thin-wall parts. In: Coates PD, editor. Polymer process engineering 07—enhanced polymer processing. Bradford: University of Bradford; 2007.
76. Worgull M, Hetu JF, Kabanemi KK. Modeling and optimization of the hot embossing process for micro- and nanocomponent fabrication. Microsyst Technol 2006;12:947–952.

77. Kimberling TE, Liu W, Kim BH, Yao D. Rapid hot embossing of polymer microfeatures. Microsyst Technol 2006;12:730–735.
78. Liu SJ, Dung YT. Ultrasonic vibration hot embossing—a novel technique for molding plastic microstructure. Int Polym Process 2005;20:449–452.
79. Yao D, Nagarajan P, Li L, Yi AY. Two-station embossing process for rapid fabrication of surface microstructures on thermoplastic polymers. Polym Eng Sci 2007;47:530–537.
80. Xu J, Locascio L, Gaitan M, Lee CS. Room-temperature imprinting method for plastic microchannel fabrication. Anal Chem 2000;72:1930–1933.
81. Bohm J, Schubert A, Otto T, Burkhardt T. Micro-metalforming with silicon dies. Microsyst Technol 2001;7:191–195.
82. Yeh MS, Lin HY, Lin HT, Chang CB. Superplastic micro-forming with a fine grained Zn-22Al eutectoid alloy using hot embossing technology. J Mater Process Technol 2006;180:17–22.
83. Heckele M, Durand A. Micro-structurede through-holes in plastic films by hot embossing. Proceedings of 2001 Euspen's 2nd International Conference Torino, Italy; 2001. pp 196–198.
84. Werner M. Hot embossing of through-holes in cyclo-olefin copolymer [Diploma thesis]. Technical University of Denmark; 2005.
85. Mazzeo AD, Dirckx M, Hardt DE. Single-step through-hole punching by hot embossing. SPE ANTEC Proceedings Cincinnati, OH; 2007. pp 2977–2981.
86. Ikeuchi M, Ikuta K. Development of membrane micro embossing (MeME) process for self-supporting polymer membrane microchannel. Proceedings of the IEEE International Conference on Micro Electro Mechanical Systems Miami, FL; 2005. pp. 133–136.
87. Michaeli EHW, Fink B, Blomer P. Dynamic control of roll temperature. Kunststoffe Plast Eur 2005;95:51–53.
88. Truckenmuller R, Rummler Z, Schaller T, Schomburg WK. Low-cost thermoforming of micro fluidic analysis chips. J Micromech Microeng 2002;12:375–377.
89. Yao D, Virupaksha VL, Kim B. Study on squeezing flow during nonisothermal embossing. Polym Eng Sci 2005;45:652–660.
90. Yao DG, Kuduva-Raman-Thanumoorthy R. Enlarged process window for hot embossing. J Micromech Microeng 2008;18:045023.
91. Dirckx M, Mazzeo AD, Hardt DE. Production of micro-molding tooling by hot embossing. Proceedings of the ASME International Manufacturing Science and Engineering Atlanta, GA; 2007. pp. 141–150.
92. Chen Y, Yi AY, Yao D, Klocke F, Pongs G. A reflow process for glass microlens arrays fabrication by use of precision compression molding. J Micromech Microeng 2008;18:055022.
93. Jiang LT, Huang TC, Chiu CR, Chang CY, Yang SY. Fabrication of plastic microlens arrays using hybrid extrusion rolling embossing with a metallic cylinder mold fabricated using dry film resist. Opt Exp 2007;15:12088–12094.
94. de Campo A, Greiner C. SU-8: a photoresist for high-aspect-ratio and 3-D submicron lithography. J Micromech Microeng 2007;17:R81–R95.
95. Turner R, Desta Y, Kelly K, Zhang J, Geiger E, Cortez S, Mancini DC. Tapered LIGA HARMs. J Micromech Microeng 2003;13:367–372.

96. Yang SP, Young WB. Microinjection molding with LIGA-like process. Int Polym Proc 2004;19:180–185.
97. Ono Y, Whiteside BR, Brown EC, Kobayashi M, Cheng CC, Jen CK, Coates PD. Real-time process monitoring of micromoulding using integrated ultrasonic sensors, Trans Inst Meas Control 2007;29:383–401.
98. Whiteside BR, Martyn MT, Coates PD, Greenway G, Allen P, Hornsby P. Micromoulding: process measurements, product morphology and properties. Plast Rubber Compos 2004;33:11–17.
99. Whiteside BR, Spares R, Howell K, Martyn MT, Coates PD. Micromoulding: extreme process monitoring and inline product assessment. Plast Rubber Compos 2005;34:380–386.
100. Whiteside BR, Brown EC, Ono Y, Jen CK. Coates PD. Real-time ultrasonic diagnosis of polymer degradation and filling incompleteness in micromoulding. Plast Rubber Compos 2005;34:387–392.

CHAPTER 8

MECHANICAL MICRO-MACHINING

TUĞRUL ÖZEL
Manufacturing Automation Research Laboratory, School of Engineering, Industrial and Systems Engineering, Rutgers University, Piscataway, New Jersey

THANONGSAK THEPSONTHI
Manufacturing Automation Research Laboratory Industrial & Systems Engineering Rutgers, The State University of New Jersey, Piscataway, New Jersey

8.1 INTRODUCTION

Mechanical micro-machining is a scaled-down version of tool-based traditional material removal processes such as turning, drilling, and milling. Therefore, this chapter is concerned with tool-based mechanical micro-machining processes such as diamond turning, micro-turning, micro-drilling, and micro-milling. Other micro-machining processes such as micro-grinding that utilize abrasive media in removing material are also discussed in this chapter.

In the last two to three decades, micro-manufacturing processes such as wet etching, plasma etching, ultrasonic micro-machining, and LIGA (*German acronym for lithography, electroplating, and molding*), which are a result of the explosion of activities in micro-electromechanical systems (MEMS), have been developed and widely used for the manufacture of micro-parts [1,2]. However, most of these methods are slow and limited to a few silicon-based materials [1]. Also, the MEMS-based methods are typically planar, that is, 2.5-dimensional processes, which are not capable of fabricating many of the miniature parts that consist of true three-dimensional (3D) features, for example, a micro-mold for a plastic injection of micro-parts [1]. Moreover, the majority of these processes require a high setup time and cost, and hence they are not economical for small-batch-size production. In short, the limitations of the MEMS-based methods in

Micro-Manufacturing: Design and Manufacturing of Micro-Products, First Edition.
Edited by Muammer Koç and Tugrul Özel.

terms of the choice of the material, part dimensions, and production sizes make these processes unsuitable for the manufacture of many complex miniature parts.

In the mean time, the demand for miniaturized meso- (1–10 mm)/micro- (1–1000 μm) devices having high aspect ratios and superior surfaces has been rapidly increasing in aerospace, automotive, biomedical, optical, military, and micro-electronic packaging industries [1,3].

There is a growing need for fast, direct, and mass manufacturing of miniaturized functional products from metals, polymers, composites, and ceramics. Since the MEMS-based methods are not capable of meeting every demand in micro-manufacturing, alternative processes have to be developed. For this reason, mechanical micro-machining as a scaled-down version of turning, milling, and drilling has been rapidly gaining momentum in industrial applications because of its viability to directly produce miniature 3D functional parts from a wide range of materials, with high precision [4–6].

Currently, mechanical micro-machining is capable of fabricating miniature parts as small as tens of micrometers to a few millimeters with very complex features and close tolerances, using energy-efficient small machine tools [5,7–9]. The major advantage of mechanical micro-machining compared to the other processes used to fabricate miniature parts is the process flexibility. Since there is no limitation on machining shapes, many complex features such as 3D cavities and arbitrary curvatures, or high-aspect-ratio features such as long shafts and micro-channels can be achieved using mechanical micro-machining. Even though deep X-ray lithography using synchrotron radiation beams (LIGA process) and focused ion beam machining process are capable of producing 3D submicron features with very high accuracy, these processes are far more expensive than mechanical micro-machining because of the need for very expensive and special facilities. Furthermore, the setup cost of a mechanical micro-machining process is very low and the material removal rate (MRR) is high compared to those of MEMS-based methods; thus it is very much suitable for a small batch production or even for a custom-made product. Also, mechanical micro-machining has no limitation in terms of the type of workpiece materials, unlike most of the lithography-based processes, which are limited to a few silicon-based materials.

Despite its benefits, scaling down the mechanical machining process from a macro-scale to a micro-scale is not as easy as it sounds. Many factors that can be neglected in macro-scale machining often become significant in micro-scale machining—for example, material structure, vibration, and thermal expansion [4,5,7,8]. Thus, application of mechanical micro-machining is still limited. Many technological obstacles need to be resolved, and many physical phenomena need to be well understood. In this chapter, the details and characteristics of mechanical micro-machining are presented.

8.2 MATERIAL REMOVAL AT MICRO-SCALE

Despite its success in manufacturing macro-scale parts, scaling down mechanical machining to micro-scale production encounters several difficulties. It is

important to note that as mechanical machining is scaled down, many physical and mechanical properties of the material removal process that are less pronounced in mechanical macro-machining play very important roles in mechanical micro-machining. As a result, there are some specific issues that occur only in micro-scale mechanical machining, for example, *size effect* and *minimum uncut chip thickness*. In this section, these issues regarding material removal on a micro-scale are addressed.

8.2.1 Size Effect

At small chip thicknesses, the specific energy required to remove a unit amount of material increases, and this phenomenon is referred to as the size effect [10,11]. The primary reasons include ploughing of the material under the tool due to large negative effective rake angles; the elastic recovery of the material and the normal and tangential pressure it applies to the flank face of the tool; the strain-rate dependency and dislocation density/availability of the workpiece material; and modified strain gradient in the primary deformation zone due to small uncut chip thicknesses. The size effect has been experienced during finish machining, ultraprecision machining (UPM), and grinding [12–14]. Machining at small chip thicknesses (compared to the edge radius) is considered to be ploughing dominated, rather than shearing dominated [15].

Kopalinsky and Oxley [16] have shown that in the chip formation process, as the undeformed chip-thickness decreases, the specific cutting pressure (force in cutting direction divided by cutting area) increases. They explained that the reason of this *size effect* is contributed to an increase of strain rate in chip formation zone in inverse proportion to undeformed-chip thickness. Since flow stress in most metals increases as strain rate increases, strain-rate sensitivity of flow stress also increases rapidly in the range applicable to processes ($>10^4$ s^{-1}) similar to machining; therefore, specific cutting pressure could increase as the undeformed-chip thickness decreases.

The term *size effect* in metal cutting (chip formation) processes is often defined as the nonlinear increase of the specific cutting energy with decrease in the undeformed-chip thickness. Vollertsen *et al*. [17] presented the decreasing trend in shearing energy per unit volume for machining processes with data for SAE 1112 steel from Backer [18] and tensile tests from Taniguchi [19] as shown in Fig. 8.1.

8.2.2 Minimum Chip (Undeformed) Thickness

Another phenomenon, usually referred to as the *minimum chip thickness*, also arises from the rounded edge geometry [20]. In mechanical micro-machining, owing to the limited strength of the edge of the micro-cutting tool, the uncut-chip thickness is constrained to be comparable to or even less than the tool edge size and, as a result, a chip will not be generated. The chips will be generated and material removal will be achieved only when the uncut chip thickness reaches a critical value, the *minimum chip thickness* [20]. *Minimum (or critical) uncut*

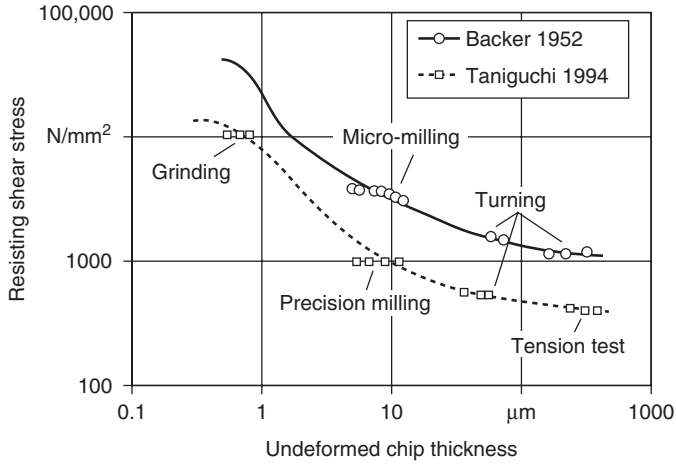

Figure 8.1 Increasing shear stress during material separation for decreasing undeformed-chip thickness in several micro-manufacturing processes [17].

chip thickness is often considered a measure of the highest attainable accuracy [12,13,21]. Below the critical chip thickness no chip is produced, and the entire material is forced under the tool and deformed. Especially in micro-milling, the elastic portion of the deformation recovers after the tool passes [22,23].

One of the major differences between mechanical micro-machining and macro-mechanical machining is the ratio between the undeformed-chip thickness and the tool edge radius. In macro-mechanical machining, this ratio is very large; thus the Merchant conventional sharp-edge cutting model, which assumes that the resultant force is affected only by shear along one shear plane and friction at the rake face, can always be applied. However, the assumption that the tool edge radius is perfectly sharp fails in the case of mechanical micro-machining, since the undeformed-chip thickness is comparable to or even less than the relatively large edge radius. In order to explain the mechanical micro-machining mechanism, Kim and Kim [14] have introduced the round-edge cutting model considering significant sliding along the clearance face of the tool due to the elastic recovery of the workpiece material, and ploughing due to the large effective negative rake angle resulting from the tool edge radius. Their experiment has shown that the cutting forces can be better approximated using the round-edge cutting model rather than the Merchant conventional sharp-edge cutting model, especially when the undeformed-chip thickness is less than 1 µm.

The term minimum chip thickness is used in mechanical micro-machining to explain the critical value of undeformed-chip thickness required to achieve chip formation. Aramcharoen and Mativenga's [24] explanation is that if the undeformed-chip thickness is lower than the minimum chip thickness, the material will be compressed by the cutting tool and then will recover back after the tool passes, as a result of elastic deformation (Fig. 8.2). Thus, there

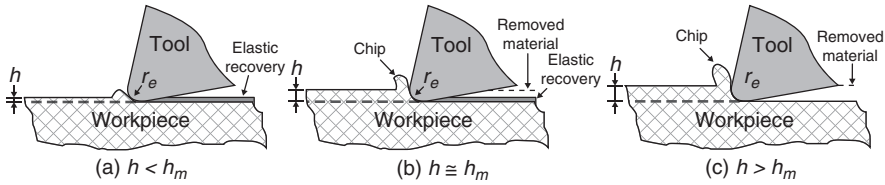

Figure 8.2 Chip formation relative to the minimum chip thickness in mechanical micro-machining [24].

is no material removal, and ploughing occurs. In another case in which the undeformed-chip thickness is equal to the minimum chip thickness, the chip starts to form through the shearing of the workpiece coupled with a portion of elastic deformation and recovery. Hence, the material removed is of less than the expected amount. The last case is when undeformed-chip thickness is greater than the minimum chip thickness, the chip is formed, and material is removed to the desired extent.

As mentioned earlier, when the minimum chip thickness is not reached, the shearing will not take place. Therefore, if the depth of cut (turning case) or the feed rates (milling and drilling case) are lower than the minimum chip thickness, ploughing will take place until the minimum chip thickness is reached and then the shearing will take place and the material is removed. In short, chip is not formed during every pass of the tool. Instead, cutting occurs only when the minimum chip thickness is reached and ploughing of the surface occurs when the minimum chip thickness is not achieved. Moreover, Weule *et al*. [25] have pointed out that this affects the surface roughness, especially when the ploughing is dominant. It is still a question of how much the minimum chip thickness should be and what factors affect the minimum chip thickness.

The minimum chip thickness is considered to be related to the resistivity of the material against plastic deformation, such as indentation hardness. It is found to be strongly dependent on the ratio of chip thickness to the cutting edge radius and on the workpiece material/tool combination. It was seen to be between 5% and 38% of the edge radius for different materials.

The minimum chip thickness requirement significantly affects the machining process performance in terms of cutting forces, tool wear, surface finish, process stability, etc. [22,23,25,26]. Hence, knowledge of the minimum chip thickness is important to the selection of appropriate machining conditions. Researchers have resorted to experimentation [22,23], molecular dynamics (MD) simulations [27,28], and micro-structure-level force models [29], as well as analytical slip-line plasticity-based models [30] to estimate the normalized minimum chip thickness.

8.2.3 Micro-Structure and Grain Size Effects

Most commonly used engineering materials, such as steel and aluminum, have their crystalline grain size between 100 nm and 100 μm, which is comparable

to the size of a micro-feature. Therefore, instead of shearing along the grain boundary as in macro-machining, in mechanical micro-machining the shearing takes place inside the individual grain (Fig. 8.3). It is widely reported that the *workpiece micro-structure* has a significant influence on the mechanical micro-machining process [29,31–34]. Characteristic dimensions of crystals (grains) on polycrystalline materials and phases on multiphase materials are commensurate with the tool dimensions and the uncut chip thickness values. Both elastic and plastic behavior of individual crystals are anisotropic, and therefore the cutting action experiences different mechanical properties when passing through different grains. Thus, machining force magnitudes, rake face friction, and elastic recovery will vary during the process [35–39]. Similar explanation can be offered for cutting multiphase materials [29]. A number of studies focused on micro-cutting characteristics and on the effect of crystalline orientation of soft and/or pure materials (e.g., copper and brass) [33,39–41]. Micro-cutting of multiphase materials (e.g., medium carbon steel) has also gained interest, including pioneering FEM modeling work on micro-cutting of pure materials [41] and heterogeneous steels [29,34,42].

The features of a micro-machined surface are influenced by the crystallographic orientation of the grains, with three distinct cases: (i) machining of amorphous materials; (ii) machining of single crystals; and (iii) cutting of polycrystalline materials [43–45].

The effect of the presence of micro-structures on the performance of mechanical micro-machining is more pronounced in materials with multiphase micro-structures such as steel. The structure of steel at the normalized state causes considerable difficulty in mechanical micro-machining because of a difference in hardness and ductility between the pearlitic and ferritic regions, which affects the constancy of the machining conditions. As a result, it is recommended that machining of steel be performed in the hardened state which has fine

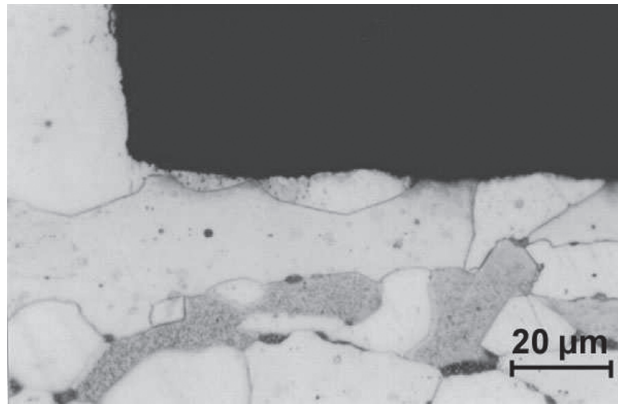

Figure 8.3 Grains on machined surface in micro-end-milling of brass with upmilling strategy ($f_z = 0.1$ mm, $a_e = 0.1$ mm, $V_c = 60$ m/ min) [43].

and equidistantly distributed carbides [46]. Multiphase materials also affect the surface generation of mechanical micro-machining. Vogler *et al*. [22] have investigated the surface roughness value (R_a) in micro-milling of multiphase ductile iron. They found that over the examined range of cutting conditions, the surface roughness of multiphase ductile iron is higher than that of single-phase iron. They claimed that the increase in surface roughness is due to interrupted chip formation that occurs as the cutting edge moves between the multiple phases.

8.3 TOOL GEOMETRY, TOOL WEAR, AND TOOL DEFLECTIONS

The tool wear mechanism in micro-end-milling is highly dependent on the bonding characteristics between the cobalt (Co) and tungsten-carbide (WC) grains. The WC grains are often randomly distributed within the Co matrix, given the average grain size of the carbide used for the micro-tools (400–700 nm). The wear in carbide micro-tools is mainly due to the harder WC grains dislodging from the softer Co matrix [33]. From this perspective, the wear behavior of micro-tools closely resembles that of grinding tools. The amount of dislodging-driven tool wear depends on the bonding strength and geometry and the cutting configuration (the part of the tool that is engaged with the workpiece), in addition to some minor thermal effects.

Tool breakage occurs under some cutting conditions, often unexpectedly. Crack propagation in areas of high stress concentration is mainly responsible for the tool breakage. Fracture mechanisms effective in the WC matrix are (i) transgranular fracture of WC, (ii) fracture across Co binder region, (iii) interfacial fracture along WC/Co boundary, and (iv) interfacial fracture along WC/WC boundary (Fig. 8.4).

8.3.1 Tool Geometry and Coatings for Micro-Mechanical Tools

Cutting tool geometry seems to be a major barrier limiting the capability of mechanical micro-machining. Conventional grinding can produce tools as small as 1–2 μm in edge radius; however, a normal feed per tooth in micro-machining is less than 1 μm to ensure a minimal tool deflection [9,48].

Fang *et al*. [49] have studied the performance of micro-end-mills with various types of geometry. Three types of micro-end-mills were studied, namely, two-flute (commercial type) end-mills, triangle-based (Δ-type) end-mills, and semicircle-based (D-type) end-mills (Fig. 8.5).

Triangle-based (Δ-type) end-mills with a tapered bodyand semicircle-based (D-type) end-mills with a tapered body were also included in the study to investigate the effect of tool deflection. Their experimental results showed that at low spindle speeds (20,000 rpm) and feed rates (<120 mm/min), all the three types of end-mills worked properly. When the spindle speed was increased, two-flute end-mills were unable to cut and were eventually broken. Nevertheless, Δ-type and D-type end-mills were only chipped and worn down but were never broken. This indicated that the rigidity of Δ-type and D-type end-mills is higher than

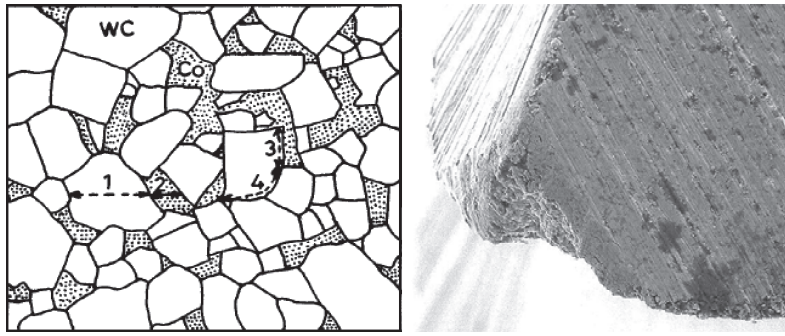

Figure 8.4 (a) Fracture mechanisms in WC: (1) transgranular fracture of WC, (2) fracture across Co binder region, (3) interfacial fracture along WC/Co boundary, (4) interfacial fracture along WC/WC boundary. (b) A worn micro-tool (250 μm radius) [47].

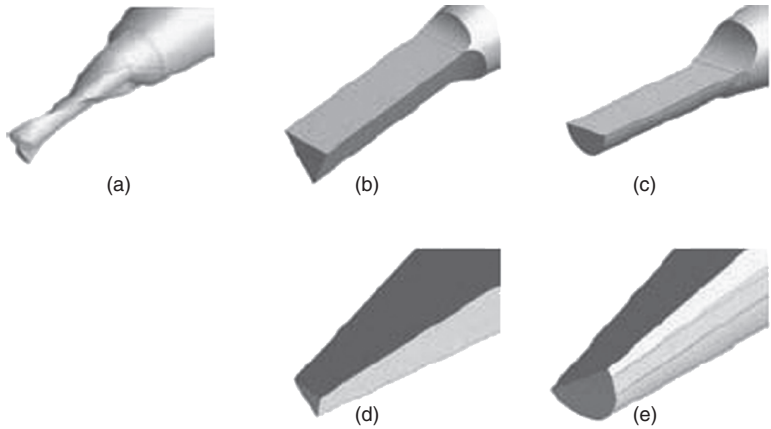

Figure 8.5 Various types of flat-bottom micro-end-mill geometry. (a) Two-flute end-mill with a helix angle, (b) Δ-type end-mill with a straight body, (c) D-type end-mill with a straight body, (d) Δ-type end-mill with a tapered body, and (e) D-type end-mill with a tapered body [49].

that of two-flute end-mills. The author also stated that the rigidity of Δ-type end-mills is much higher than that of the other two; however, the machining quality is poorer than that of the others [49]. In addition, they have presented failure studies for various tool geometries and suggested that D-type end-mills are more suitable for fabrication of micro-parts, since they have both rigidity and machining performance (Fig. 8.6).

Schmidt and Tritschler [50] presented the potentialities of focused ion beam cutting as an alternative to tool grinding. A WC two-flute micro-end-mill was fabricated using an ion milling strategy. However, the manufacturing result was

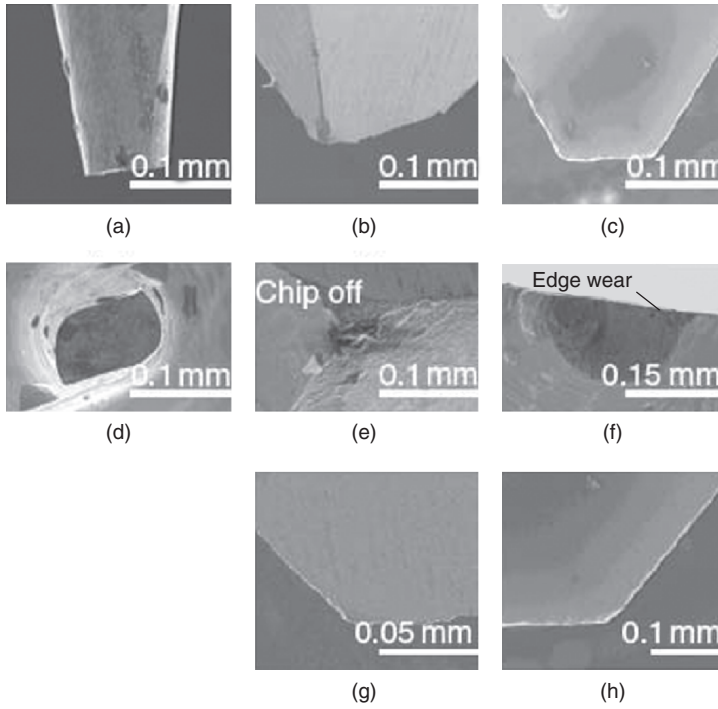

Figure 8.6 Tool failures of various tool geometries in mechanical micro-machining. (a, d) Two-flute end-mills 0.1 mm in diameter, (b, e, g) Δ-type end-mills 0.1 mm in diameter with a taper angle of 70.5°, and (c, f, h) D-type end-mills [49].

found unsatisfying with respect to burr formation. They also noted that with the optimized cutting parameters, better machining results may be achieved.

The geometries of micro-milling tools currently in use have been adopted from macro-tools, assuming that chip formation and process kinematics are analogous in both types of tools. However, micro-cutting is not a completely scaled-down version of macro-cutting; the requirements of the design of micro-tools are somehow different from those of macro-tools. Moreover, structural details such as rake angle and twist angle impede further minimization. Considering these points, Fleischer [51] has designed micro-milling tools based on the mechanism of the micro-cutting process (Fig. 8.7), and has proposed single-edged micro-milling tools, because the manufacturing tolerance of the tools is generally larger than the feed per tooth, which leads to high cutting forces, high wear, and breakage. The semicircular geometry was selected, since the result of FEM showed the highest rigidity for this geometry. The tool was successfully fabricated using wire electrical discharge grinding (WEDG). However, the machining results showed increase in burr formation potentially caused by high edge roundness and notchiness resulting from fabrication. Furthermore, the spiralization has not been optimized.

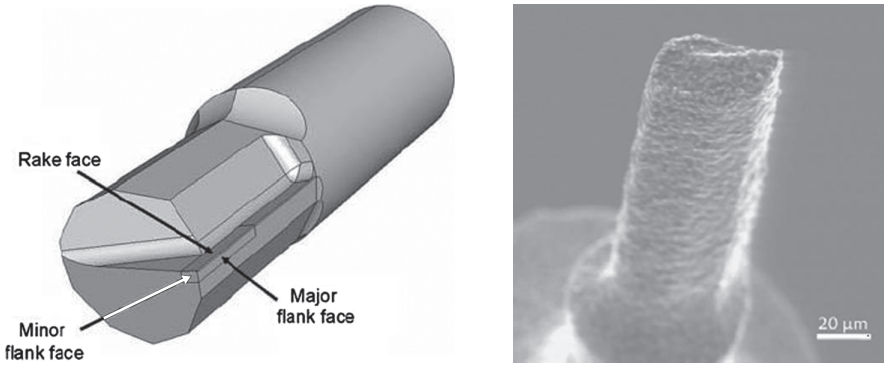

(a)

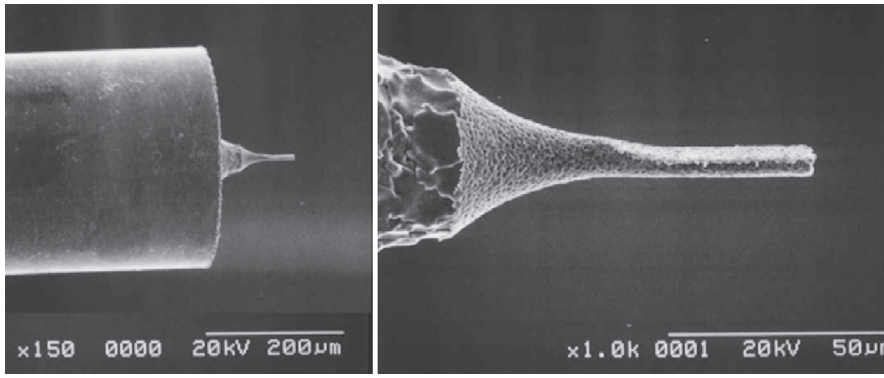

(b)

Figure 8.7 Micro-tool of (a) 50 µm diameter [51] and (b) 10 µm diameter [52].

It is generally known that coating can enhance tool performance; coated tools normally outperform uncoated tools in terms of tool life and machined surface quality. However, micro-tools for mechanical micro-machining suffer from the coating, since coating layer increases the size of the tool geometry, especially the cutting edge radius, which is the most critical tool geometry in mechanical micro-machining.

Heaney *et al*. [53] have shown the possibility of coating fine-grained diamond, of average grain size 30–300 nm, onto WC micro-end-mills (Fig. 8.8). The performance of the diamond-coated tools was improved dramatically when dry machining 6061-T6 aluminum. The fine-grained diamond coating reduced the trust and the main cutting forces by approximately 90% and 75%, respectively, compared with uncoated tools. The chip adhesion did not develop as long as the coating remained intact. Furthermore, the surface generated for the coated tools was uniform and no burr occurred.

Aramcharoen *et al*. [54] have studied the effect of micro-milling tool coating materials; they have reported that CrTiAlN-coated carbide micro-end-mills

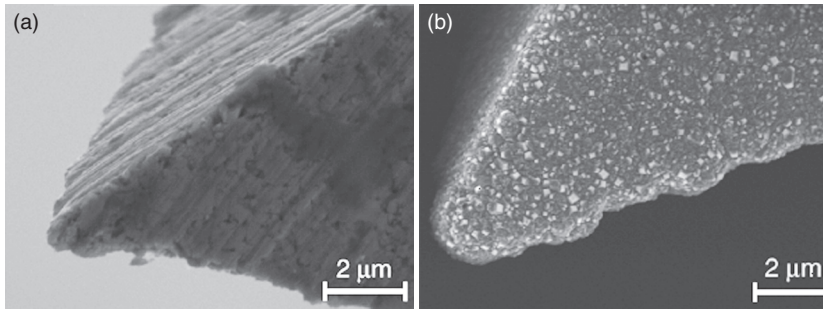

Figure 8.8 Comparison of fabricated tool edges: (a) uncoated WC tool and (b) fine-grained diamond-coated tool [53].

provide distinct advantages over uncoated carbide end-mills in terms of tool wear reduction and machined surface quality. They also compared the effect of coating materials on micro-carbide end-mills for machining-hardened H13 tool steel (45 HRC). TiN, TiCN, TiAlN CrN, and CrTiAlN were PVD coated on two-flute micro-carbide flat end-mills with a thin layer of 1.50 ± 0.15 µm, and then the cutting performance was evaluated under the same cutting conditions. The results indicated that TiN coatings offer the best performance in terms of tool wear and chipping reduction, surface roughness improvement, and decrease in burr size. Moreover, they found that at the beginning of cutting (burn-in-period) the coated tools did not outperform the uncoated tool in terms of the surface finish quality. Hence, it implied that an ultrafine coating surface or self-lubricating, low-friction top coat would be required for a better performance of coated carbide micro-end-mills.

8.3.2 Tool Wear Mechanisms in Micro-Cutting

Wear is a very critical issue in mechanical micro-machining; a small wear at one cutting edge of micro-tools would eliminate half of the cutting edge. As a result, the cutting force may be increased twofold at the other cutting edge, which leads to an increase in the stress at the shaft and tool breakage. Rahman *et al*. [55] have studied the tool wear in micro-milling of pure copper and investigated flank wear in micro-end-mills (Fig. 8.9). They found that the nonuniform wear occurs at the corner of the side and end cutting edge and mostly the tool fails before it is significantly worn out. Also, the helix angle plays an important role; they found that the life of the tool was increased considerably by using a 25° helix angle cutter. Moreover, tool life increases at higher depths of cut.

Malekian *et al*. [56] stated that factors that can be attributed to tool wear in mechanical micro-machining are elastic recovery of the workpiece, dynamic deflections, tool run-out, and low feed instability. The elastic recovery of the material will increase the cutting forces and the contact area between the tool and the workpiece at the flank face of the tool. This increased contact area

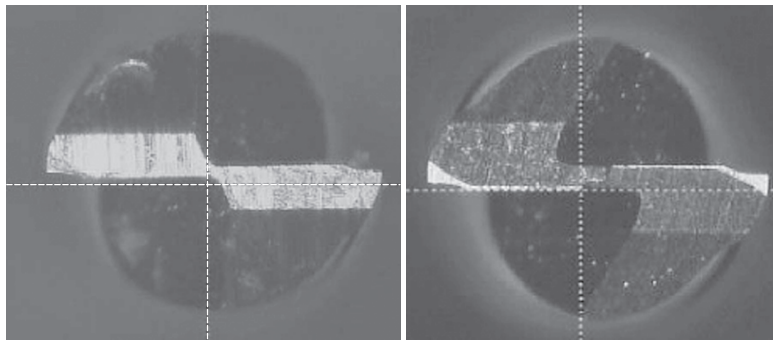

Figure 8.9 Typical flank wear in 1-mm-diameter micro-end-mills in machining of pure copper: (a) fine grain WC with a 25° helix angle and (b) fine grain WC with a 30° helix angle [55].

causes more flank wear to the micro-tools through more friction and rubbing. Tool deflection due to the dynamics of the tool tip and tool run-out affect the tool wear in several ways. Because of the tool deflection, the cutting process may not be uniform; some cutting edge may engage more with the workpiece and remove more material in one revolution. This usually results in an increase of cutting forces on the cutting edge that engages more with the workpiece, and consequently, the tool wears much faster on that cutting edge. Moreover, tool vibration caused by the transition of shearing and ploughing when cutting with a low feed rate generates intermittent impacts on the tool, resulting in cutting edge chipping or even tool breakage.

Even though tool wear is undesirable, tool breakage seems to be a more important problem in mechanical micro-machining. Unlike macro-mechanical machining, in which the tool gradually wears, causes undesirable surface effects, and eventually breaks, a tiny micro-tool can break when either the cutting edges become dull (because of material loss or material buildup) or a chip clogs. Tansel *et al*. [57] have studied the effect of wear in the micro-milling process. They found that micro-end-mills break quickly as they wear out. This is due to increased cutting forces of the dull tool causing the stress to exceed the strength of the small-diameter end-mills. In addition, König *et al*. [58] have indicated that the main reason for tool failure in the micro-drilling operation is chip clogging.

8.3.3 Tool Stiffness and Deflections under Dynamic Loading

Micro-tools, especially micro-end-mills and micro-drills, can be easily deflected because of their high aspect ratio. Therefore, the problems concerning the accuracy of mechanical micro-machining are much more pronounced compared to those of macro-mechanical machining.

Especially in the fabrication of dies for micro-molding and micro-forming applications, there is a need for the use of micro-end-mills with a high aspect ratio (ratio of the cutting length to the cutter diameter). However, the higher the ratio, the greater the tool deflections affecting the geometrical feature accuracy and tolerances. It was demonstrated that the tool deflections create serious deficiencies in feature accuracy [43] as shown in Fig. 8.10.

Dow *et al*. [48] identified a need for tool deflection compensation because the decreasing feature sizes required micro-mold designs. The long, small-diameter end-mills (diameters <1 mm) needed to create these high-aspect-ratio features exacerbate the error due to tool deflection and ball ends compound the problem even more because the force can be applied at different points and in different directions around the end of the tool. Because the tool stiffness is significantly different in the radial and axial directions, different deflections can be produced for the same applied load. They offered a force model that was combined with tool stiffness to calculate the deflection of the tool as a function of the depth of cut, feed per revolution, and the geometry of the part (Fig. 8.11).

8.4 MICRO-TURNING

Micro-turning is performed mostly as diamond turning (or often referred to as ultra precision machining), which is commonly used to produce very smooth surfaces with highly precise geometries for optical and many other applications [12,13,59–64]. As a cutting tool material, diamond is superb because of its high hardness, stiffness, thermal conductivity, low friction (in air), and relative inertness. This inertness ceases when the work material is readily able to absorb carbon and these materials are identified in Section 8.4.1. With these materials

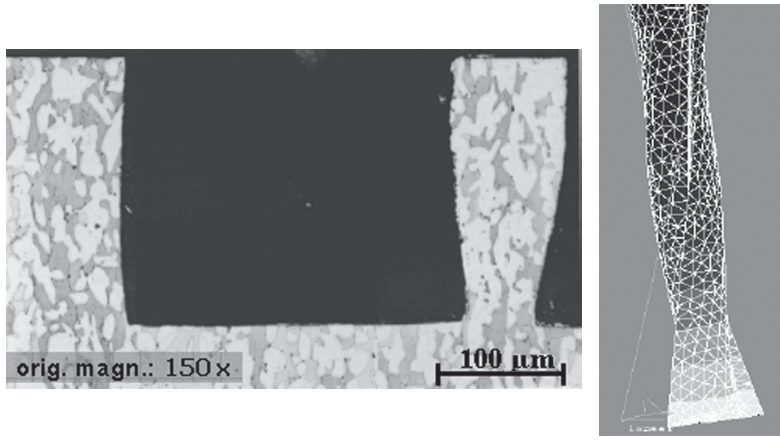

Figure 8.10 Tool deflections on the geometrical accuracy: (a) cross-sectional view of a groove fabricated with micro-end-milling, and (b) FEA of buckling in micro-end-mills [43].

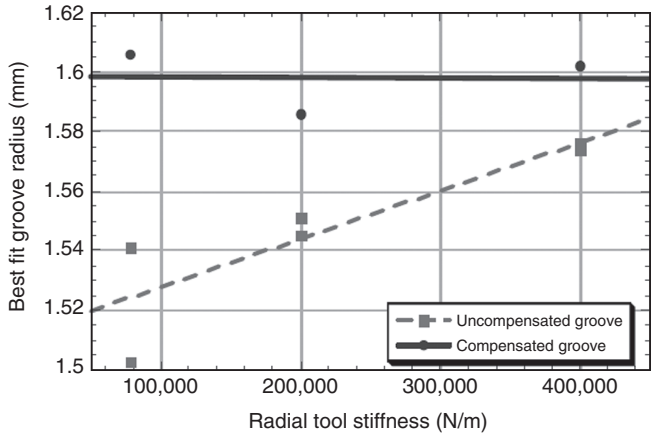

Figure 8.11 Tool deflection compensation using force modeling for micro-end-milling [48].

the diamond will be readily absorbed by the workpiece unless the diffusion rate can be significantly lowered, for example, by cryogenic cooling [60,65].

Elements with no unpaired d-shell electrons are regarded as diamond machinable. These elements include indium, tin, lead, zinc, plutonium, magnesium, aluminum, germanium, silver, gold, copper, beryllium, and silicon. Elements with unpaired d-shell electrons are regarded as non-diamond machinable. These elements include uranium, manganese, nickel, cobalt, iron, titanium, chromium, vanadium, rhodium, ruthenium, niobium, molybdenum, tantalum, rhenium, and tungsten [59,60,66–68].

8.4.1 Diamond as a Tool Material

Diamond has three different species that are used for machining. Natural single-crystal diamond is relatively expensive, has multiple crystal orientations thus giving differing machining results, and contains impurities. In any event, single-crystal diamond is heavily used in precision machining operations with compatible materials. Single-crystal diamonds are brazed to a steel tool shank for use. Although it varies widely depending on the precision of the cutting edge and the size of the diamond (radius of the cutting edge <0.5 μm), the cost of a single-crystal turning tool is typically on the order of several hundred to a thousand of US dollars [59,60,66–69].

Polycrystalline diamond consists of small particles of diamond (on the order of micrometers to tens of micrometers), which are mixed with a binder, normally cobalt based. The cermet-type mixture is then formed and sintered into the shape of the cutting tool. This is also brazed or attached to a steel shank for use in the machining operation. Polycrystalline diamond is not used for optical applications in a single-point turning operation because the material removal mechanism primarily involves grinding rather than conventional chip-making. This results

in a rougher surface and a "haze" in optical surfaces. Polycrystalline diamond wheels are used in grinding operations, though. Polycrystalline diamond tools generally cost more than other tool materials [59,60,66–68].

Synthetic diamond is used where the control on the impurities is important. It has been found over the years that impurities in natural diamond are correlated with variations in the wear rate of the cutting edge. Synthetic diamond is a more controllable and predictable tool material. The cost of synthetic diamond tools, though, is generally several times more than that of natural diamond tools [60,65].

Diamond has most of the properties desirable in a cutting tool material. It has the highest hardness, and hence is able to deform any other material. However, its brittleness makes machining with diamond less than desirable in all applications especially for interrupted cutting. Diamond has a high modulus of elasticity compared to tool steel, which gives it a high specific stiffness, which allows the tool to withstand high machining forces with less tool deformation. Smaller cutting edge deformation helps maintain precision machining. The critical tensile stress of diamond is comparable to that of high-strength steels but diamond can maintain this strength even at high temperatures, although it can transform into graphite at high temperatures. Over many years of machining experience, those materials that are generally machinable and those not machinable by diamond have been identified. Those materials that are readily machined by diamond include, but are not restricted to, aluminum, brass, gold, silver, tin, zinc, electroless nickel, most plastics including polycarbonate, fluoroplastics such as Teflon, acrylics including polymethyl methacrylate (PMMA), styrene, propylene, silicon, germanium, lithium niobate, zinc sulfide, gallium arsenide, and cadmium telluride [36,59,60,65–68].

Brittle materials cannot withstand tensile stress without the propagation of cracks within the material. This is one of the primary differences between the behavior of brittle crystals and more ductile metals [70]. To reduce the presence of residual cracks in the machined surface of crystals, a technique termed ductile-regime machining is normally used. This technique uses a very small depth of cut (uncut-chip thickness) to reduce the tensile stress induced in the surface of the machined material. If the local stress intensity factor, caused by the local tensile stress, is larger than the critical stress intensity factor, then a crack can begin at a micro-scale discontinuity or grow if the crack already exists. Therefore, a very small uncut chip thickness normally on the order of nanometers to submicrometer is required to maintain sufficiently low stress intensity.

Materials that are considered difficult to machine generally cause chipping of the diamond or dissolution of the diamond into the work material. These materials are nickel alloys, beryllium alloys, ferrous alloys including stainless steel, titanium alloys, and molybdenum alloys. The dissolution can be slowed and the tool life extended if the machining takes place at cryogenic temperatures (generally at a liquid nitrogen temperature of -150°C). At these temperatures, the ultimate material strength and the modulus of elasticity increase, while the thermal conductivity drops markedly [69].

Diamond has a very low coefficient of friction against many materials, in air. On metals, tests have shown that the friction coefficient is a function of sliding speed. Tests by Bowden and Freitag [71] of diamond on copper show a nearly step increase in the coefficient at about 100 m/s. The change is from a coefficient of about 0.03 to about 0.05. Similar tests of diamond on chromium show a jump from about 0.06 to about 0.4 at a speed of about 200 m/s. It was observed though that at higher speeds, the diamond was coated with a film of chromium and so the coefficient is more a measure of chromium on itself. The wear rate of diamond on plastics is also higher than on copper by several times. This is generally attributed to the high localized temperature during machining plastics because of the low thermal conductivity [12,13,61].

8.4.2 Diamond Micro-Machining

Diamond micro-machining is considered to be a finishing operation and diamond tools are generally used with a nominal rake angle near zero degrees. In metals, a slightly negative (a degree or two) rake angle can improve the surface finish, whereas in plastics a slightly positive rake angle has the same effect. Primary clearance angles are generally the same as for conventional machining, in the range of $6-10^{\circ}$ [12,13,61,69].

Micro-turning parameters are very different from those of conventional machining. For a micro-turning operation, the radial depth of cut (RDOC) for roughing is generally in the range of 50–15 μm for metals ranging from soft (copper and aluminum) to hard (steel, titanium, and nickel) [12,13,61]. Roughing cuts for plastic are generally on the order of several hundred micrometers in the RDOC. A roughing feed is typically in the range of 10–40 μm/rev. The finishing depth of cut is typically around 1 μm for hard metals and 3 μm for soft metals. For plastics, the finishing cut is generally about 15 μm [36,59,60,65–68].

Diamond micro-machined surfaces normally have optical qualities with a very low surface roughness (Ra $<$ 5 nm). However, optical systems are normally made of glass, which can withstand a relatively large amount of physical abuse without

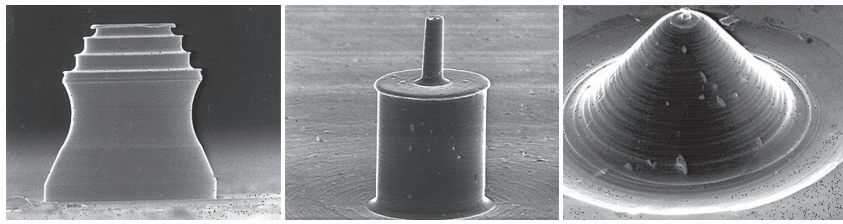

Figure 8.12 Diamond micro-turning of micro-mechanical components. (a) Profile turning with micro-meter dimensions. (b) Micro-shaft with two different diameters. (c) Aspherical press mold [72].

scratching. Diamond-machined metals though, particularly copper and aluminum, are very soft and can be easily damaged physically and chemically (Fig. 8.12).

8.5 MICRO-END-MILLING

As mechanical micro-machining has been gaining momentum because of its viability to directly produce miniature functional parts, micro-milling in numerically controlled machine tools has become a cost-effective alternative to rapidly fabricate mostly 3D parts from metals, ceramics, and plastics in small batch sizes, with an acceptable accuracy and precision (Fig. 8.13) [6,8,9,62,67,73,74].

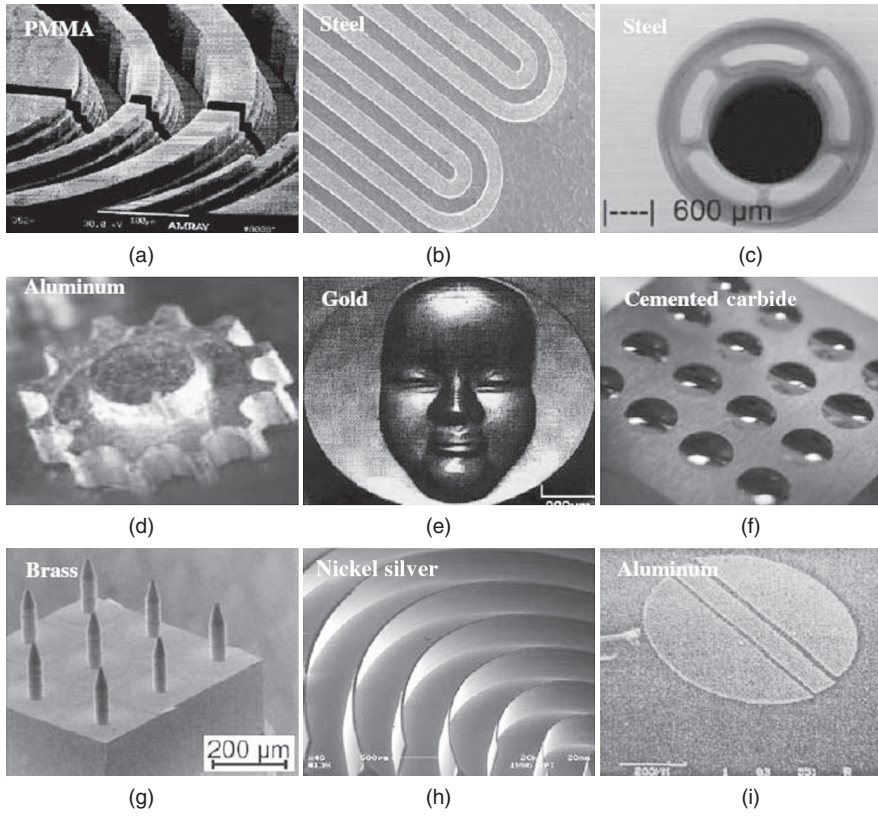

Figure 8.13 Examples of high-accuracy micro-milled components and micro-structures (adopted from Huo *et al*. [75]): (a) micro-trenches [73]; (b) micro-reactor (Courtesy of Fraunhofer Institute of Production Technology IPT); (c) micro-mold [25]; (d) micro-gear [4]; (e) 3D micro-machined part—Noh-mark (courtesy of Fanuc); (f) micro-projection array (courtesy of Fanuc); (g) micro-needles array [76]; (h) micro-wall [77]; and (i) target foil for nuclear fusion [78].

Micro-milling using flat-bottom- or ball-end-mills at high rotational speeds can achieve good accuracy, low surface roughness, and can provide high MRRs with feature sizes as small as 5–10 μm, particularly with the recently developed numerically controlled miniature machine tools [9,75,79].

Micro-end-mills (flat-bottom or ball-end) with diameters down to 25 μm, mostly made of tungsten carbide on a cobalt matrix (WC–Co), are available on the market. Some vendors offer micro-end-mills with diameters as small as 5 μm. Such micro-end-mills are utilized in the direct fabrication of micro-molds/dies from tool steels for injection molding and micro-forming applications [25,46,50,80].

Improving the productivity of micro-milling requires the use of high MRRs on a variety of materials. However, there are still issues associated with the dimensional accuracy, quality of the surfaces generated, and the efficiency of the tool—there may be a sudden tool failure.

Currently, uncoated and coated carbide micro-end-mills are utilized in direct fabrication of micro-molds/dies from tool steels for injection molding and micro-forming applications.

Increasing popularity of manufacturing of parts with micro-features has sparked the interest of researchers to study the mechanics and dynamics of micro-milling to improve the productivity and also to understand how it differs from conventional milling [81–83]. The fundamental difference between micro-milling and conventional milling lies in the scale of the operation, although they are kinematically the same. However, the ratio of the feed per tooth to the radius of the cutter is much greater in micro-milling than in conventional milling, which often leads to an error in predicting the cutting forces [81]. The run-out of the tool tip even within microns greatly affects the accuracy of micro-milling as opposed to the conventional milling [82]. Micro-milling is subject to sudden tool failure because of its highly unpredictable cutting action [83]. Chip formation in micro-milling depends upon a minimum chip thickness [20] and hence it does not always occur, whenever the tool and the workpiece are engaged, as opposed to conventional milling [32,84]. Tool deflection in micro-milling greatly affects chip formation and the accuracy of the desired surface, compared to conventional milling [48].

8.5.1 Micro-End-Mills

Micro-end-mills are made of sintered WC (some also with high-speed steel) [85], which is composed of fine grains (~0.4 μm) of WC (about 75%) embedded in a cobalt (15%) binder (Fig. 8.14). Since diamond grinding cannot create cutting edges smaller than the diameter of carbide grains, usually edge radii between 1.5 and 5 μm are fabricated on carbide micro-end-mills [86,87]. The relative size of the cutting edge radius has serious implications on the efficiency of mechanical micro-machining and on the overall tool performance as explained below.

The *tool edge radius* (typically between 1 and 5 μm) and its uniformity along the cutting edge are highly important as the chip thickness becomes comparable

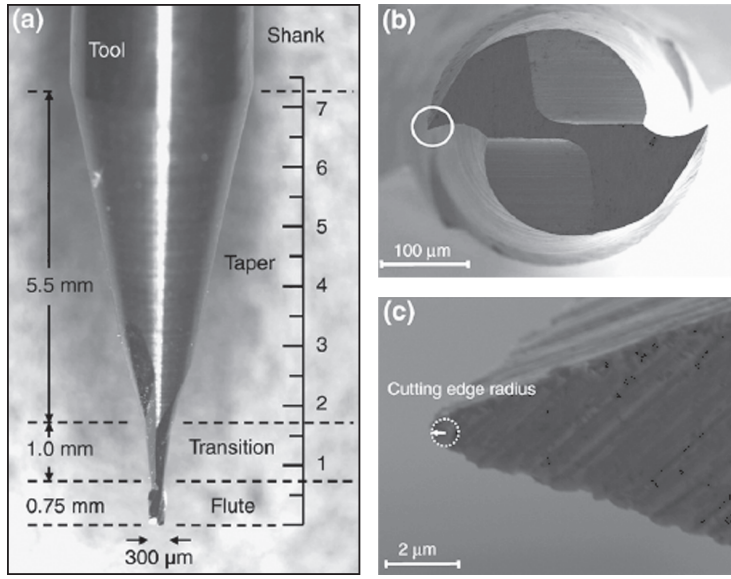

Figure 8.14 (a) Optical image of a typical micro-end-mill that is 300 µm in diameter; (b) SEM images of the bottom of the micro-end-mill; and (c) SEM image of a corner of the tool with edge radius [53].

in size to the cutting edge radius [61,88]. Since the chip load is small compared to the cutting edge radius, the size effect and ploughing forces become significant on both surface and force generation in micro-milling [22,23].

8.5.2 Mechanics of Micro-End-Milling

In terms of process characteristics, micro-end-milling is almost the same as macro-end-milling; the only difference is the size of tools. It is still the most flexible mechanical machining process, capable of fabricating complex 3D shapes such as a mold cavity. However, to successfully micro-machine miniature parts, something beyond what is required in macro-end-milling is needed, such as high spindle speed, high machine tool precision, low vibration. Reasons why factors that are negligible in macro-end-milling often become significant in micro-end-milling lie in its process mechanics and dynamics. Therefore, in order to successfully implement the micro-end-milling process, it is necessary to understand the mechanics and dynamics of micro-end-milling [89,90].

There are two main causes that result in fundamentally different mechanics and dynamics between micro-machining and macro-machining: *cutting process/tool geometry* and *workpiece material characteristics*.

In micro-end-milling, the ratio of the feed per tooth to the tool radius is considerably higher compared with conventional macro-end-milling. The current manufacturing method cannot fabricate end-mills, mostly made of WC–Co, with

sharp edges because of limitations on the structural strength of the tool at the edge. Widely available micro-tools have an edge radius ranging from 1 to 5 μm. As the tool diameter decreases, the rigidity of the tool also decreases, which leads to tool deflections under heavy chip load and sudden breakage of tool. This limits the chip load, especially in micro-milling, to a few microns per tooth. At low feed rates, the well-known size effect, originally discovered in ultraprecision diamond cutting [20], becomes prominent in micro-milling. Specific cutting forces also depend mostly on the ratio of the uncut-chip thickness to the tool edge radius.

The tool edge radius and small feed per tooth make the phenomenon of minimum chip thickness very dominant in micro-end-milling. A minimum chip thickness is observed where tool engagement with workpiece results in chip formation. In full-immersion micro-end-milling, uncut chip thickness of $t_u(\phi)$ varies from zero to a full feed per tooth value of f_t as shown in Fig. 8.15a. When the cutter engages with the workpiece at the tool tip, a very small uncut chip thickness is applied, which increases gradually as illustrated. The cutter rotation angle (ϕ) at which the minimum chip thickness is achieved and chip formation begins is termed the chip formation angle (CFA) as illustrated in Fig. 8.15b.

Hence the minimum chip thickness for micro-milling ($t_{c_{min}}$) can be defined as the formation of chip when the uncut chip thickness becomes greater than a minimum chip thickness ($t_u > t_{c_{min}}$) at a certain rotation angle. Unlike precision diamond turning, where diamond tools are up-sharp with a nanometric edge radius and the uncut chip thickness is often constant [21,61], the minimum chip thickness in micro-end-milling is greatly affected by the radius of the cutting edge (r_e), which is usually greater than 1 μm (Fig. 8.16). The chip is not formed and mostly

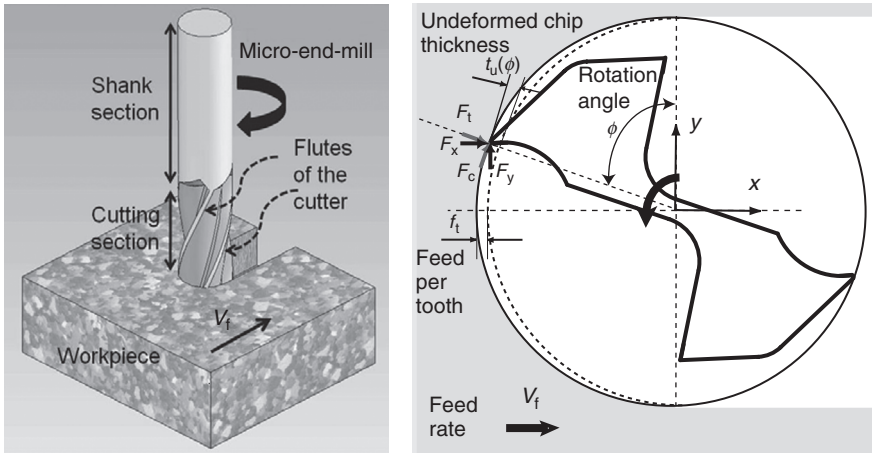

Figure 8.15 (a) Full-immersion micro-end-milling process and (b) chip thickness and planar forces during full immersion [91].

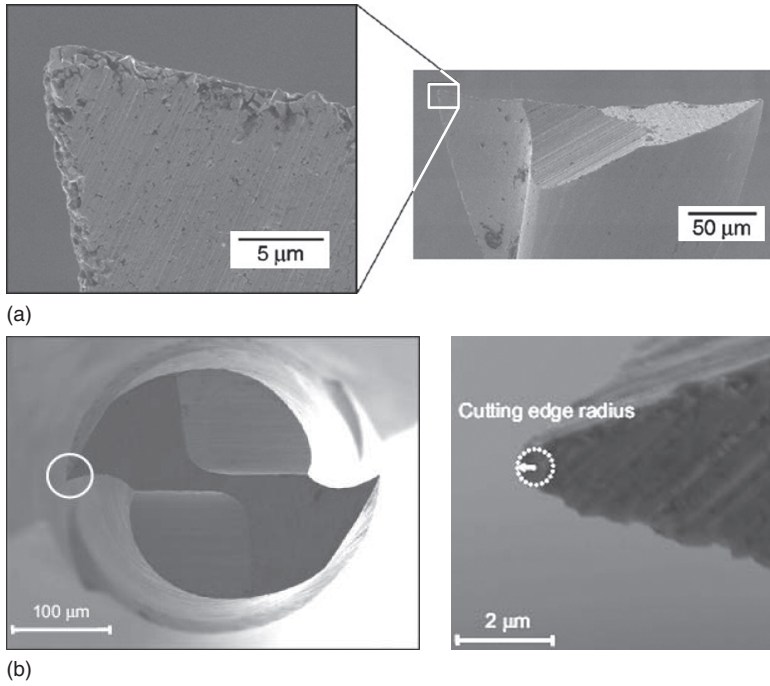

Figure 8.16 (a) Cutting edge of a tungsten-carbide (WC) micro-end-mill under SEM indicating large cutting edge and corner radius [33]; (b) 500 − µm-diameter micro-end-mill and edge radius (r_e) [92].

elastic deformations are induced to the workpiece until the tool reaches a certain rotation angle at which a minimum uncut chip thickness develops. A smaller edge radius causes early formation of the minimum chip thickness, whereas a larger edge radius will result in ploughing of the workpiece. Kim *et al*. [84] experimentally determined that the minimum chip thickness depends upon the ratio of the uncut-chip thickness to the cutting edge radius, which was claimed to be between 10% and 25% for the ductile metals. Liu *et al*. [30] calculated the minimum chip thickness and utilized a ratio $\lambda = t_{c_{min}}/r_e$ to describe it as function of the edge radius. In that study, the minimum chip thickness to tool edge radius ratio was found to be about 35–40% for micro-milling of 6082-T6 aluminum and 20–30% for AISI 1018 steel at a wide range of cutting speeds and edge radii.

8.5.3 Numerical Analysis of Micro-End-Milling

Attempts have also been made to understand the physics of the micro-machining process in micro-end-milling, using FEM-based modeling approaches (Fig. 8.17) [8]. Finite-element-based numeric models are created for micro-machining of

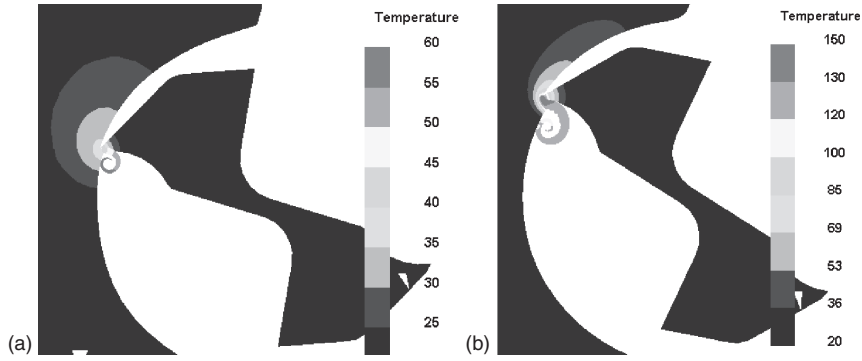

Figure 8.17 FEM simulation of micro-milling: (a) AL2024-T6 aluminum and (b) AISI 4340 steel [8]. (A full color version of this figure appears in the color plate section.)

aluminum and steels with the aim of understanding deformations including micro-structures and grain size effects. Micro-machining-induced plastic deformation, white layer formation, subsurface alteration, and residual stresses on the fabricated materials are analyzed through FEM-based process simulations. Furthermore, by using FEM-based process simulations, micro-end-mill tool geometry and machining parameters can be optimized.

Dhanorker and Ozel [8] have developed computational mechanics-based finite element simulations and predicted fully formed curly continuous chips at a tool rotation angle of 65° for micro-milling of AL2024-T6 aluminum as shown in Fig. 8.17a. They also observed a complete chip formation around a tool rotation angle of 53° in micro-milling of AISI 4340 steel as shown in Fig. 8.17b under the same cutting conditions. The predicted temperature distributions are also given in Fig. 8.18. The maximum temperature in the cutting zone is predicted to be around 60°C for AL2024-T6 aluminum and around 150°C for AISI 4340 steel under the same cutting conditions. Dhanorker and Özel [8] claimed that these temperatures are very low compared to the temperatures under meso-milling conditions because of the very small chip loads. They also claimed that tool failure is considered to be typically due to temperature-dependent accelerated wear rates in high-speed milling on a conventional scale. In contrast, temperature-dependent wear cannot be dominant in micro-milling as evident in the predicted temperature distributions shown in Fig. 8.18. They believed that highly fluctuating forces due to a continuous shift between ploughing- and shearing-dominated cutting modes in micro-milling are also responsible for the sudden tool failure and breakage [8].

In another study, Özel and Liu [91] investigated the influence of the edge radius on the minimum chip thickness for micro-milling of 2024-T6 aluminum by utilizing an analytical model developed by Liu *et al*. [30]. In their analytical model, a workpiece material model and a slip-line field analysis are utilized to estimate the minimum chip thickness for a given tool edge radius, feed rate, and surface cutting speed.

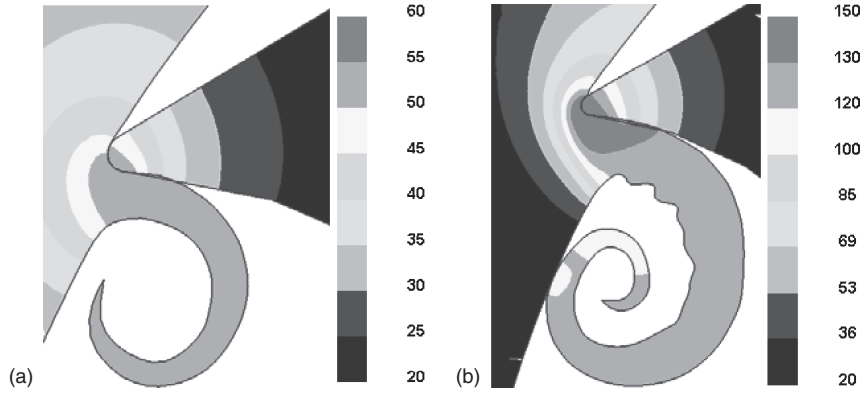

Figure 8.18 Predicted temperature distributions (°C) in the cutting zone during micro-milling: (a) AL2024-T6 aluminum and (b) AISI 4340 steel [8]. (A full color version of this figure appears in the color plate section.)

Özel and Liu [91] showed that the minimum chip thickness to edge radius ratio for the work material of AISI 4340 steel is estimated to be between 30% and 36% for the range of the edge radius 1–5 μm and for the range of the cutting speed 120–360 m/min. For the work material of AL 2024-T6 aluminum, the minimum chip thickness to edge radius ratio is estimated to be between 42% and 45% for the range of the edge radius 1–5 μm and for the range of the cutting speed 120–360 m/min as shown in in Fig. 8.19.

A particular cutter rotation angle at which the minimum chip thickness is achieved and chip begins to form is termed the chip formation angle (CFA) [91]. The CFA is found to be larger in micro-milling of AL2024-T6 aluminum compared to micro-milling of AISI 4340 steel as shown in Fig. 8.20. This may be due to the higher modulus of elasticity of AISI 4340 steel, in which case, elastic tool deformations are smaller. Hence, plastic flow begins at a lower uncut chip thickness [91].

In summary, Özel and Liu [91] showed that the minimum chip thickness to edge radius ratio is estimated to be between 42% and 45% for AL2024-T6 aluminum and between 30% and 36% for AISI 4340 steel for the given ranges of edge radius (1–5 μm) and the surface cutting speed (120–360 m/min). They also determined the CFA and its variation under micro-milling conditions [91].

In addition, micro-milling may result in generation of surfaces with burrs and increased roughness due to the ploughing-dominated cutting and the side flow of the deformed material when the cutting edge becomes worn and blunter [26].

8.5.4 Dynamics of Micro-End-Milling

Although the dynamics of micro-milling is similar to the dynamics of end-milling processes, cutter run-out at high rotational speeds, lower tool stiffness,

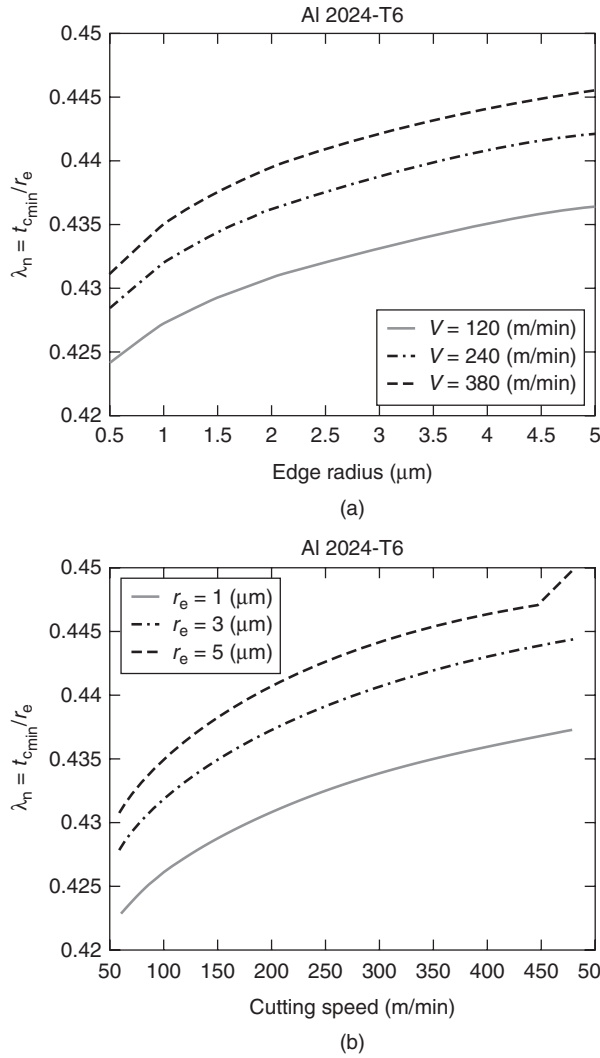

Figure 8.19 Predicted minimum chip thickness in micro-milling of AL 2024-T6 aluminum: (a) varying edge radius and (b) varying cutting speed [91].

and nonlinear forces due to shearing- and ploughing-related mix cutting action make micro-milling dynamics a significant factor in surface generation errors and tool performance. Several studies have investigated dynamic force generation in micro-milling [89,90]. However, the limiting factor is that the bandwidth of most force transducers and dynamometers is lower than the tooth-passing frequency at higher rotational speeds [8,33,56,93].

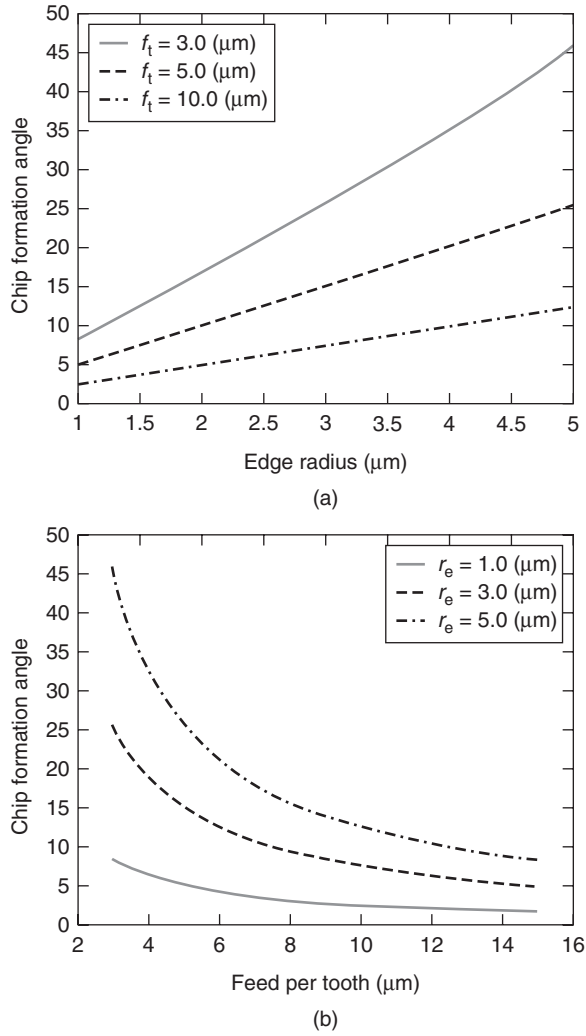

Figure 8.20 (a) Chip formation angle versus tool edge radius and (b) chip formation angle versus feed per tooth (AISI 4340 Steel) [91].

Various sensors such as acoustic emission (AE), accelerometer, and force sensors are widely utilized to monitor tool wear and tool breakage and identify stability diagrams (Fig. 8.21) in micro-end-milling. It is also well known that force sensors with limited frequency bandwidth (<1 kHz) are not suitable for monitoring micro-end-milling processes, in which tooth-passing frequencies are in the order of 1–5 kHz for two-flute end-mills rotating at a rate between 50,000

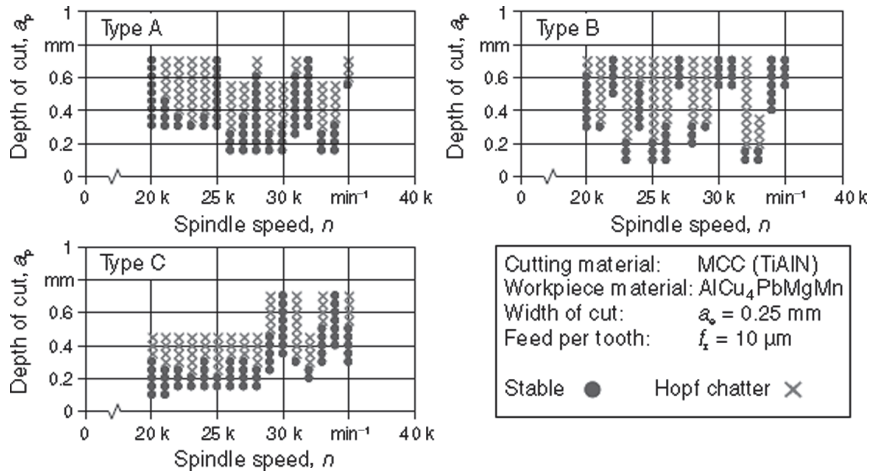

Figure 8.21 Stability diagrams for micro-milling using 1-mm-diameter end-mills [94].

and 150,000 rpm. However, an AE sensor bandwidth of 100 kHz–1 MHz provides an operating region well above the tooth-passing frequencies, and signal quality is not affected by the milling process dynamics [33,56,93,94].

8.5.5 Process Planning for Micro-End-Milling

In micro-milling, conventional strategies used in milling process planning become ineffective because of the intricacies of mechanical micro-machining [95]. The cutting forces with increased feed rate can easily snap the fragile micro-end-mills. Tool path planning and selection of machining parameters are highly important [96]. In addition, very low feed rates may not achieve minimum chip thickness requirements. Therefore, advanced process planning strategies are implemented for efficient micro-end-milling [91].

Özel and Liu [91] proposed a process planning guideline for successful micro-end-milling of cavities on metal molds. Interrelation between the process parameters (feed per tooth (f_t), axial depth of cut (ADOC), RDOC, spindle speed, (Ω)) and the achieved process performance has been analyzed for a variety of cutting tool edge radii. They introduced a sequential process planning consisting of a roughing and a finishing to achieve prescribed process performance specifications.

In their study, the constraint of the achievable maximum feed rate is first examined in terms of the machine tool capability. The manufacture of miniature parts involves the feed drive making a lot of segmented moves within a short distance, which allows an even smaller distance for the feed drive to accelerate from 0 to the programmed feed per tooth of f_t and to decelerate from, f_t back to 0. The maximum achievable feed per tooth ($f_{t\,max}$) is defined as the feed at which only a small fraction of the segmented distance (10%) is used for acceleration and

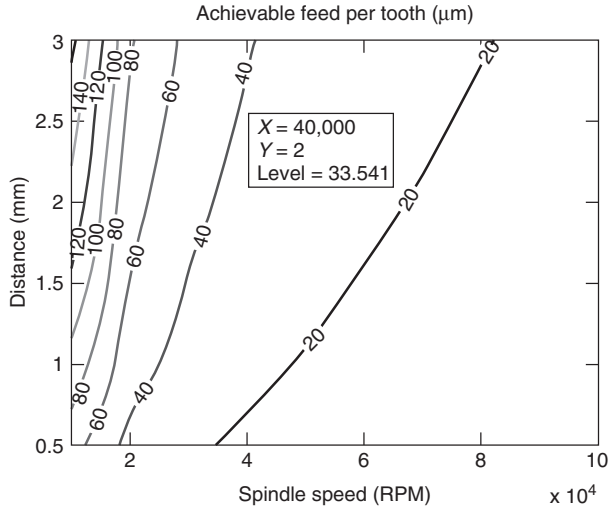

Figure 8.22 Contour plot of the achievable maximum feed per tooth [91].

deceleration. The maximum feed per tooth ($f_{t\,\max}$) is limited by the acceleration capability (a) of the feed drives, the segment length of the cut (d), the spindle speed (Ω), and the number of tooth of the micro-end-mill [91].

Figure 8.22 shows the maximum feed per tooth at different spindle speeds and segment distance, assuming that the feed drive acceleration is 1 g(9.8 m/s^2). It is seen that the maximum feed per tooth decreases when the spindle speed Ω increases and the segment distance d increases. For a spindle speed of 40,000 rpm and segment distance of 2 mm, as used in this case study, the maximum achievable feed rate is 33.5 μm/tooth [91].

In order to facilitate the process planning, time domain simulations were performed for both roughing and finishing 2024-T6 aluminum. In the roughing operation, the objective is to limit the cutting forces to avoid tool breakage and maximize the MRR. Fig. 8.23 shows the contour map of the peak-to-valley force in the normal to the feed (Y) direction. It is noted that the peak-to-valley forces increase rapidly as the ADOC increases beyond 140 μm for a range of feed rates (around 5–10 μm/tooth). This range of feed rate is likely to be the range in which low-feed-rate instability occurs. It is also noted that the cutting forces are much more sensitive to the increase in the ADOC than the feed per tooth. Since the ADOC and feed rate per tooth are both proportional to the MRR, the optimal strategy of limiting the cutting forces while maintaining high MRR is the combination of low ADOC and high feed rate. For example, to limit the cutting force below 5 N, an ADOC of 100 μm and a feed rate of 20 μm/tooth would be a good selection [91].

In the finishing operation, the objective is to minimize the form error, which was quantified by the surface location error (SLE). For all the simulations, a 3-μm

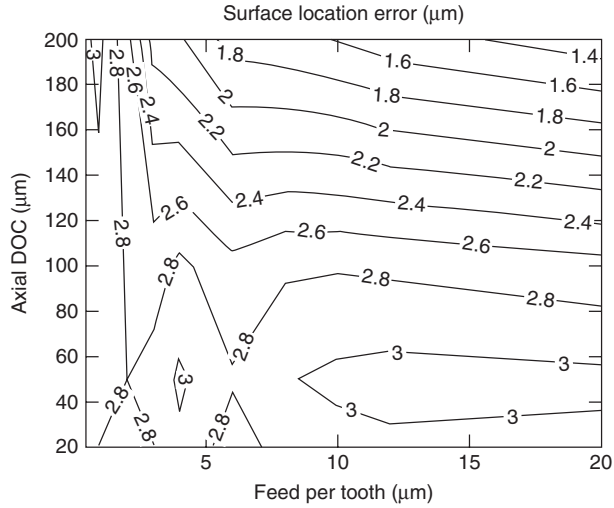

Figure 8.23 Contour plot of the peak-to-valley force in newtons for micro-milling of Al 2024-T6 [91].

spindle run-out is considered, which causes a 3-μm overcut. Figure 8.24 presents the contour plot of the SLE in the plane of feed per tooth and ADOC. Similar to the cutting forces, the SLE is also more sensitive to the ADOC. Because of the existence of the spindle run-out, the SLEs are positive (overcut) under all the conditions examined. The tool vibrations cancel part of the SLE caused by the spindle run-out. It is also noticed that at the lower right corner of the plot, there exists an isoline for an SLE of 3.0 μm, which indicates that the SLEs are not influenced by the tool vibrations under these conditions ($f_t = 10–20$ μm/tooth, ADOC $= 30–60$ μm). If the spindle run-out can be accurately measured and compensated, then the aforementioned process conditions are likely the optimal process conditions for minimizing the form error. From the above analysis, it is clearly seen that the spindle run-out plays a dominant role in the SLE. Therefore, the development of the on-line measurement technique for spindle run-out is crucial for improving the machining accuracy in micro-end-milling [91].

8.6 MICRO-DRILLING

Even though several methods exist for making micro-hole electrical discharge machining, ultrasonic machining, laser beam machining, electrochemical machining, and micro-mechanical drilling, micro-mechanical drilling is widely used because it can produce holes with good roundness, straightness, and surface roughness in a short processing time. It is especially useful for machining components with many holes, such as a nozzle, polarizing plate and photo-mask.

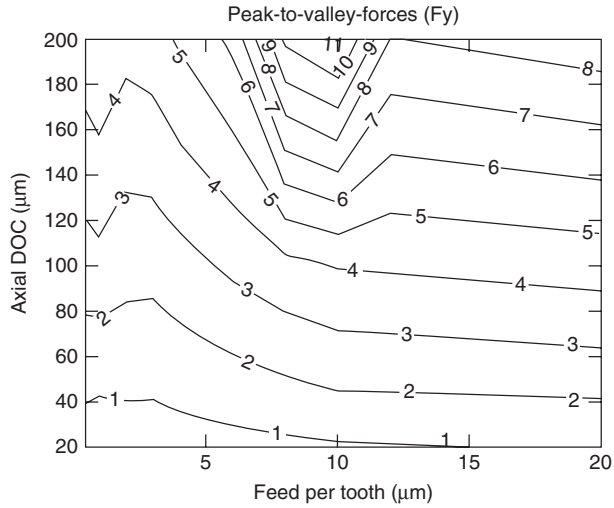

Figure 8.24 Contour plot of the surface location error for finishing operation on Al 2024-T6 [91].

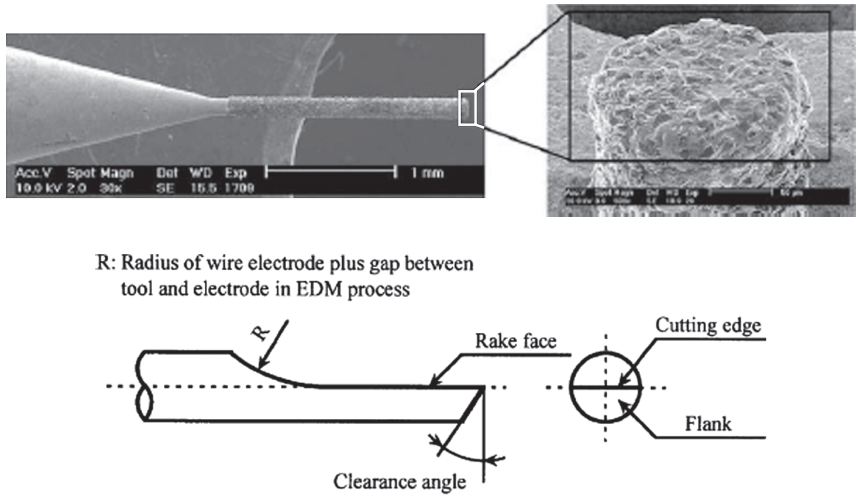

Figure 8.25 Microd-rill with diamond abrasives [97].

Mechanical micro-drilling is widely used in the manufacture of printed circuit boards (PCBs), in which numerous micro-trough-holes have to be drilled. Even though alternative methods such as laser or Electrical Discharge Machining (EDM) drilling can sometimes replace mechanical micro-drilling, their performances are not acceptable in PCB manufacture because of their inferior hole quality and accuracy [97].

Micro-drilling has important applications also in machining of ceramics. Ceramic plates containing many micro-holes are used in diverse applications such as catalytic converters, filters, MCPs (micro-channel plates) for electronic amplification, electrical insulators, and thermal conductors in integrated circuits. Lee *et al*. [97] have studied deep-hole micro-drilling of a ceramic green body. They used WC drills with 1000 mesh diamond abrasives nickel-electro-deposited on the surface (Fig. 8.25) [97]. Drilling was performed under the grinding lubricant to decrease cutting temperature and remove alumina particle chips. A feed rate of 10–80 mm/min and a fixed spindle speed of 150,000 rpm were used for the drilling test. Their results showed that tool life of micro-drills decreased linearly with feed rate because of abrasive wear and chip loading.

Another implementation of micro-drilling of brittle materials has been attempted in monocrystalline silicon by Egashira and Mizutani [98]. Micro-tools from WC with a D-shaped cross section and a cutting edge radius of 0.5 μm were designed and fabricated using WEDG. By using the self-fabricated micro-drills and utilizing ductile-regime cutting mode, the smallest machined hole of 6.7 μm diameter can be produced. Moreover, they also showed that a deep micro-hole (22-μm diameter and 90-μm depth) can be made using this technique (Fig. 8.26).

Three important problems associated with micro-drilling are increase of the cutting force, wandering motion of the drills, and tool breakage. As a drill bit penetrates the workpiece, the cutting forces acting on the drill bit increase. The friction between the flute and the cut surface of the workpiece caused from the chip produced during cutting is a primary cause of cutting forces increase. As a result, drilling of high-aspect-ratio holes becomes difficult. Micro-drilling suffers from wandering motion during the inlet stage more than macro-drilling; it generally takes a longer time until the wandering motion stabilizes. Maybe the most serious problem of micro-mechanical drilling is tool breakage, especially when drilling a deep hole. Because the rigidity of micro-drills is very low and the tendency for the chip to clog inside the hole is high, tool breakage occurs frequently, causing problems to manufacturers. Moreover, the use of cutting fluid seems to be ineffective in micro-drilling; cutting fluid cannot penetrate into the

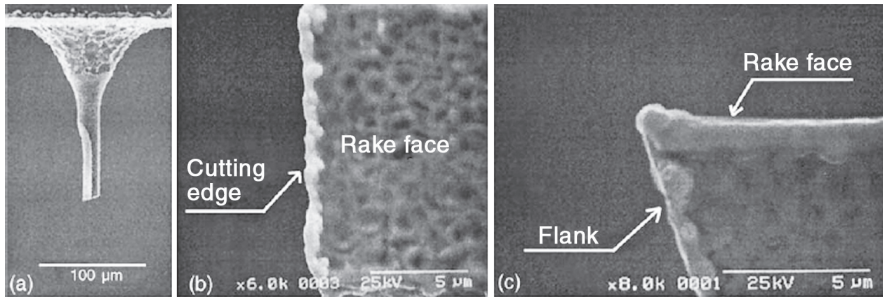

Figure 8.26 Micro-drill fabricated using wire electro-discharge grinding [99].

cutting zone, reducing the tool–chip friction and cutting temperature. In short, the increase of trust force during the micro-drilling process because of friction and chip clogging and the increase of temperature within the hole lead to premature tool breakage in micro-drilling.

To improve the tool life of micro-drilling, the use of peck drilling is recommended. Peck drilling has been successfully used in conventional macro-drilling, especially drilling of deep holes; it is a method in which a hole is drilled at an intermittent feed in order to facilitate chip removal and tool cooling. Kim *et al*. [99] have introduced peck drilling using trust force signal monitoring in deep micro-hole drilling of steel. Through the monitoring system, the proper one-step feed-length (OFSL) was determined to be about one-tenth of the tool diameter. Their results showed a significant improvement in terms of tool life when using peck drilling.

Despite the fact that peck drilling improves tool life in micro-drilling, it has lower productivity compared to continuous drilling. Therefore, Cheong *et al*. [100] have proposed an alternative to enhance the productivity of mechanical micro-drilling by controlling the spindle rotational frequency. They created a sliding mode control algorithm that can estimate the torque variation of the drill from the variation of the spindle angular velocity and perform the control accordingly. Since the increase of cutting forces was controlled, tool life, stabilization of the wandering motion, and positioning of the holes were improved.

8.7 MICRO-GRINDING

Micro-grinding is a material removal technique by means of mechanical force. It can provide a very good precision and surface finish to the produced parts. In terms of application, micro-grinding is used typically for machining cylindrical components and grooves with small dimensions and to obtain flat surfaces with very fine finish [2]. Several applications of micro-grinding for processing components include clock resonators, ferrite parts for electronic data recording devices, ceramic parts for engine and bearings, germanium aspherics, and infrared windows for optics application including fiber grating, pig tailing, lens, dispersion compensation, and optical interconnection [101]. One advantage of micro-grinding over other mechanical micro-machining processes is the ability to machine hard and brittle materials. For example, micro-grinding is a common technique used in the fabrication of WC micro-end-mills and micro-drill bits. In addition, many of those hard and brittle materials are poor conductors and have good chemical resistance, ceramic, for instance. Therefore, cutting by electrical and chemical processes is not an option.

Generally, micro-grinding is done using a grinding wheel consisting of an abrasive and a matrix. The abrasive type, abrasive grain size, and type of matrix materials vary on the basis of the workpiece materials and the purpose of grinding. It has been reported that by keeping the grain depth of cut less than 100 nm, smooth surfaces of less than 10 nm peak to valley roughness can be achieved [102]. This

can be done by two approaches. The first approach is to use a grinding wheel with an ultrafine abrasive grain size. This can be achieved by developing deposition techniques. The second approach is to maintain the small wheel depth of cut. This approach allows the use of coarse abrasive grain but high-precision machine tool and accurate wheel dressing are required. A special wheel dressing technique such as electrolytic in-process dressing (ELID) developed by Ohmori and Nakagawa [103] is a very successful technique to control the desired protrusion of the grains on the surface of the wheel.

Micro-grinding of the flat or curved surface can be done using the ultraprecision macro-grinding since the ultraprecision macro-grinding can achieve a nanoscale tolerance and surface roughness. However, there are limitations on micro-grinding of certain shapes such as grooves. A minimum tip radius of the wheel strongly influenced by the abrasive grain size limits the rounding radius when machining a concave shape such as V-grooves. The thickness and the diameter of grinding tools also limit the achievable feature size of micro-grinding. Micro-grinding of micro-grooves also suffers from severe edge chipping and coarse surface. Ramesh *et al*. [101] have proposed a new micro-grinding method using "high table reversal speeds" for reducing the grit cut load that complements the micro-deterministic grinding. Their experiment showed that the increase in the table reversal frequency reduced the grit cut load and thus enabled the production of fine features. The high table feed also facilitates the ductile cutting mode by maintaining the grit depth within the critical depth.

An extremely large-aspect-ratio cylindrical shape is very difficult to machine using micro-turning, since such parts can be bent easily by small forces applied from the tool tip. However, using ultrasonic-shoe centerless micro-grinding developed by Wu *et al*. [104], a micro-cylindrical component less than 100 μm in diameter with an extremely large aspect ratio can be achieved (Fig. 8.27).

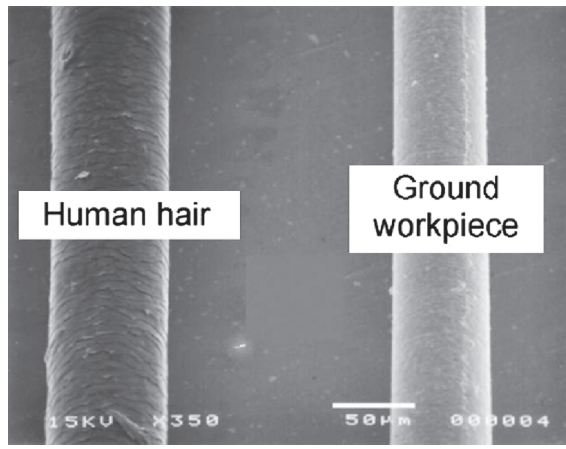

Figure 8.27 Tungsten-carbide workpiece fabricated with centerless micro-grinding [104].

Rather than using a regulating wheel as in conventional centerless grinding, a plate-shaped ultrasonic shoe was used to support the workpiece and control its rotational motion. The use of ultrasonic shoe eliminates the need for an extremely thin blade and the spinning problem (workpiece springs from the blade because of the surface tension of the grinding fluid adhering to the regulating wheel circumference surface); consequently, the micro-scale cylindrical component can be ground successfully.

Grinding of planar surface or cylindrical shape of micro-parts can be done using a macro-grinding wheel. However, to create a 3D micro-feature such as micro-channel, a small-diameter grinding tool or a so-called "micro-abrasive pencil" is needed. Aurich *et al*. [105] have presented a micro-shaft grinding tool with a cylindrical tool tip diameter between 13 and 100 μm (Fig. 8.28). To provide toughness to the tool body, the base material of the tool was ultrafine-grained carbide with an average grain size of 0.2 μm. Then, the carbide micro-pin was electroplated with diamond grains 1–3 μm in diameter. The grinding test on WC was performed at a spindle speed of 60,000 rpm, a feed rate of 1 mm/min, a depth of cut of 5 μm, and a tool diameter of 24 μm. The test indicated no significant size errors due to tool run-out and no significant burr, but produced very good surface roughness and very low edge radius. Furthermore, the individual WC grains were cut instead of being pulled out of the cobalt binder.

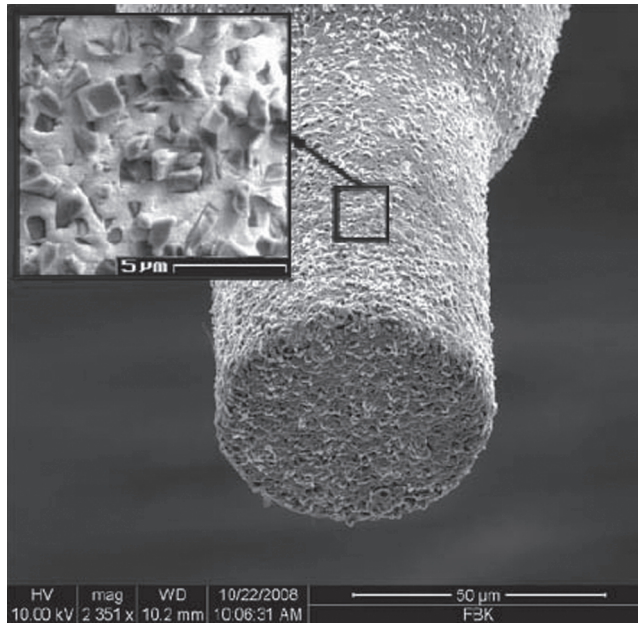

Figure 8.28 SEM image of a grinding tool with a diameter of 45 μm and a tool surface of 1–3 μm grit size [105].

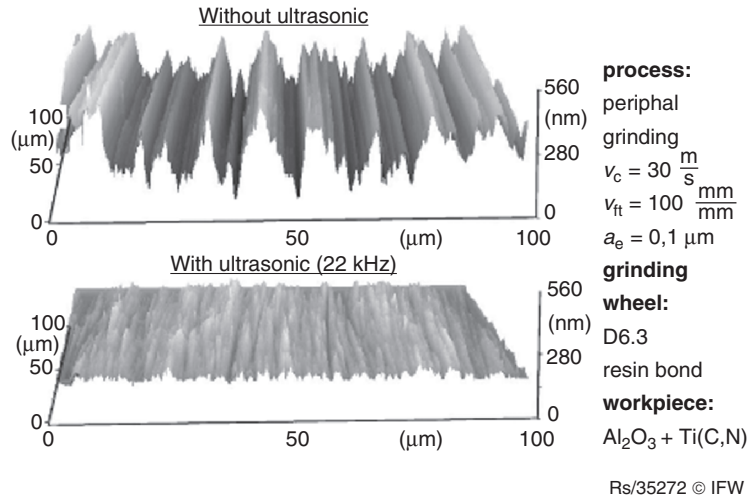

Figure 8.29 Influence of ultrasonic assistance in micro-grinding [106].

Denkena *et al*. [106] have used ultrasonic assistance to investigate the improvements in surface generation and found out that the ultrasonic assistance significantly affects and improves the surface roughness in ceramic finishing (Fig. 8.29).

8.8 MICRO-MACHINE TOOLS

In parallel to the fast-growing needs for direct and mass manufacturing of miniaturized functional products from metals, polymers, composites, and ceramics using mechanical micro-machining processes, the trend in machine tool technology has been moving toward developing ultraprecision machine tools with small footprints [5,9,75]. Miniaturization of machine tools has some obvious advantages such as reduction of energy consumption and saving space and resources. There are several industrial ultraprecision turning and milling machines available for the manufacture of high-precision components. However, most of these are aimed generally at the optical-components market and are not well suited to the manufacture of precision micro-components because of high investment costs and lack of flexibility. Figure 8.30 shows some examples of industrial precision machines with multiaxis micro-milling capabilities.

In this chapter, a brief overview of mechanical micro-machining processes, turning, milling, drilling, and grinding has been given and their characteristics are discussed with work cited from literature.

Mechanical micro-machining processes are being increasingly used in the production of parts and products with meso-/micro-/nanoscale features. Technological advancement of mechanical micro-machining is currently limited

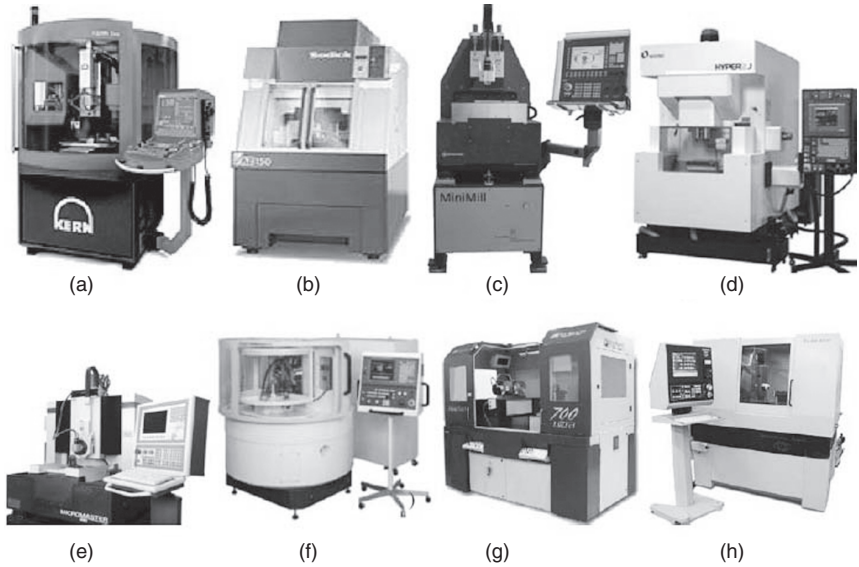

Figure 8.30 Industrial precision machine tools with micro-milling capabilities (adopted from Huo *et al*. [75]). (a) Kern micro (courtesy of Kern), (b) Sodick AZ150 (courtesy of Sodick), (c) Fraunhofer IPT Minimill (courtesy of Frounhoufer IPT), (d) Makino Hyper2J (courtesy of Makino, (e) Kuglar Micro-Master MM2 (courtesy of Kuglar), (f) Fanuc ROBOnano (courtesy of Fanuc), (g) Precitech freeform 700 Ultra (courtesy of Precitech), and (h) Moore Nanotech 350FG (courtesy of Moore Precision Tools).

by the size of the tools that can be produced cost effectively and used reliably in meso-/micro-manufacturing systems.

REFERENCES

1. Madou M. Fundamentals of microfabrication. Boca Raton (FL): CRC Press; 1997.
2. Alting L, Kimura F, Hansen HN, Bissacco G. Micro engineering. Ann CIRP 2003;52(2):635–657.
3. De Chiffre L, Kunzmann H, Peggs GN, Lucca DA. Surfaces in precision engineering, microengineering and nanotechnology. Ann CIRP 2003;52(2):561–577.
4. Liu XR, DeVor E, Kapoor SG, Ehmann KF. The mechanics of machining at the microscale: assessment of the current state of the science. J Manuf Sci Eng 2004;126:666–678.
5. Chae J, Park SS, Freiheit T. Investigation of micro-cutting operations. Int J Mach Tools Manuf 2006;46:313.
6. Dornfeld D, Min S, Takeuchi Y. Recent advances in mechanical micromachining. Ann CIRP 2006;55(2):745–768.
7. Asad ABMA, Masaki T, Rahman M, Lim HS, Wong YS. Tool-based micro-machining. J Mater Process Technol 2007;192–193:204–211.

8. Dhanorker A, Özel T. Meso/Micro scale milling for micromanufacturing. Int J Mechatron Manuf Syst 2008;1:23–43.
9. Liow JL. Mechanical micromachining: a sustainable micro-device manufacturing approach? J Clean Prod 2009;17:662–667.
10. Armarego EJA, Brown RH. On the size effect in metal cutting. Int J Prod Res 1961;1:75–99.
11. Nakayama K, Tamura K. Size effect in metal-cutting force. J Eng Ind Trans ASME 1968;90:119–126.
12. Lucca DA, Rhorer RL, Komanduri R. Energy dissipation in the ultraprecsion machining of copper. CIRP Ann Manuf Technol 1991;40:69–72.
13. Lucca DA, Seo YW, Rhorer RL, Donaldson RR. Aspects of surface generation in orthogonal ultraprecision machining. CIRP Ann Manuf Technol 1994;43:43–46.
14. Kim J, Kim DS. Theoretical analysis of micro-cutting characteristics in ultra-precision machining. J Mater Process Technol 1995;49:387.
15. Waldorf DJ, DeVor RE, Kapoor SG. A slip-line for ploughing during orthogonal cutting. ASME J Manuf Sci Eng 1998;120:693–699.
16. Kopalinsky EM, Oxley PLB. Size effects in metal removal processes. Institute of Physics Conference Series No 70; Bristol; 1984. pp 389–396.
17. Vollertsen F, Biermann D, Hansen HN, Jawahir IS, Kuzman K. Size effects in manufacturing of metallic components. CIRP Ann Manuf Technol 2009;58:566–587.
18. Backer WR, Marshall ER, Shaw MC. The size effect in metal cutting. Trans ASME 1952;74:61–72.
19. Taniguchi N. The state-of-the-art of nanotechnology for processing ultra-precision and ultra-fine products. Prec Eng 1994;16(1):5–24.
20. Ikawa N, Shimada S, Tanaka H. Minimum thickness of cut in micromachining. Nanotechnology 1992;3(1):6–9.
21. Yuan ZJ, Zhou M, Dong S. Effect of diamond tool sharpness on minimum cutting thickness and cutting surface integrity in ultraprecision machining. J Mater Process Technol 1996;62:327–330.
22. Vogler MP, DeVor RE, Kapoor SG. On the modeling and analysis of machining performance in micro-endmilling, Part I: surface generation. ASME J Manuf Sci Eng 2004;126:685–694.
23. Vogler MP, DeVor RE, Kapoor SG. On the modeling and analysis of machining performance in microendmilling, Part II: cutting force prediction. ASME J Manuf Sci Eng 2004;126:695–705.
24. Aramcharoen A, Mativenga PT. Size effect and tool geometry in micromilling of tool steel. Prec Eng 2009;33:402.
25. Weule H, Huntrup V, Tritschle H. Micro-cutting of steel to meet new requirements in miniaturization. Ann CIRP 2001;50(1):61–64.
26. Lee K, Dornfeld DA. An experimental study on burr formation in micro milling aluminum and copper. Trans NAMRI/SME 2002;30:255–262.
27. Shimada S, Ikawa N, Tanaka H, Ohmori G, Uchikoshi J. Molecular dynamics analysis of cutting force and chip formation process in micro cutting. Seimitsu Kogaku Kaishi/J Jpn Soc Prec Eng 1993;59:2015–2021.
28. Maekawa K, Itoh A. Friction and tool wear in nano-scale machining-a molecular dynamics approach. Wear 1995;188:115–122.

29. Vogler MP, DeVor RE, Kapoor SG. Microstructure-level force prediction model for micro-milling of multiphase materials. J Manuf Sci Eng Trans ASME 2003;125:202–209.
30. Liu X, DeVor RE, Kapoor SG. An analytical model for the prediction of minimum chip thickness in micromachining. ASME J Manuf Sci Eng 2006;128:474–481.
31. vonTurkovich BF, Black JT. Micro-machining of copper and aluminum crystals. J Eng Ind Trans ASME 1970;92:130–134.
32. Kim CJ, Bono M, Ni J. Experimental analysis of chip formation in micro-milling. Trans NAMRI/SME 2002;30:247–254.
33. Filiz S, Conley CM, Wasserman MB, Ozdoganlar OB. An experimental investigation of micro-machinability of copper 101 using tungsten carbide micro-endmills. Int J Mach Tools Manuf 2007;47:1088–1100.
34. Simoneau A, Ng E, Elbestawi MA. Grain size and orientation effects when microcutting AISI 1045 steel. CIRP Ann Manuf Technol 2007;56:57–60.
35. Furukawa Y, Moronuki N. Effect of material properties on ultra precise cutting processes. CIRP Ann Manuf Technol 1988;37:113–116.
36. Yuan ZJ, Lee WB, Yao YX, Zhou M. Effect of crystallographic orientation on cutting forces and surface quality in diamond cutting of single crystal. CIRP Ann Manuf Technol 1994;43:39.
37. To S, Lee WB, Chan CY. Ultraprecision diamond turning of aluminum single crystals. J Mater Process Technol 1997;63:157–162.
38. Zhou M, Ngoi BKA, Hock YS. Effects of workpiece material properties on microcutting process. Precision Engineering - Nanotechnology: Proceedings of the 1st International Euspen Conference, Volume 1;1999. pp 404–407, Bremen, Germany, 31 May-4 June, 1999.
39. Zhou M, Ngoi BKA. Effect of tool and workpiece anisotropy on microcutting processes. Proc Inst Mech Eng (IMechE) 2001;215:13–19.
40. Ueda K, Manabe K. Chip formation mechanism in microcutting of an amorphous metal. Ann CIRP 1992;41:129–132.
41. Moriwaki T, Sugimura N, Luan S. Combined stress, material flow and heat analysis of orthogonal micromachining of copper. Ann CIRP 1993;42:75–78.
42. Chuzhoy L, DeVor RE, Kapoor SG, Bammann DJ. Microstructure-level modeling of ductile iron machining. ASME J Manuf Sci Eng 2001;124:162–169.
43. Takacs M, Vero B. Material structural aspects of micro scaled chip removal. Mater Sci Forum 2003;414–415:337–342.
44. Ueda K, Iwata K, Nakajama K. Chip formation mechanism in single crystal cutting β-brass. CIRP Ann Manuf Technol 1980;29:41–46.
45. Shimada S, Ikawa N, Tanaka H, Ohmori G, Uchikoshi J, Yoshinaga H. Feasibility study on ultimate accuracy in microcutting using molecular dynamics simulation. Ann CIRP 1993;42:91–94.
46. Schmidt J, Spath D, Elsner J, Huntrup V, Tritschler H. Requirements of an industrially applicable microcutting process for steel micro-structures. Microsyst Technol 2002;8:402–408.
47. Chermant JL, Osterstock F. Fracture toughness and fracture of WC/Co composites. J Mater Sci 1976;11(10):1939–1951.

48. Dow TA, Miller EL, Garrard K. Tool force and deflection compensation for small milling tools. Prec Eng 2004;28:31–45.
49. Fang FZ, Wu H, Liu XD, Liu YC, Ng ST. Tool geometry study in micromachining. J Micromech Microeng 2003;13:726–731.
50. Schmidt J, Tritschler H. Micro cutting of steel. Microsyst Technol Micro Nanosyst Inf Storage Process Syst 2004;10:167–174.
51. Fleischer J. Design and manufacturing of micro milling tools. Microsyst Technol Micro Nanosyst Inf Storage Process Syst 2008;14:1771–1775.
52. Egashira K, Mizutani K. Microdrilling and micromilling of brass using a 10 μm diameter tool; 2010. Available at http://www.cis.kit.ac.jp/~egashira/pdf/10um-diameter_tool.pdf (last accessed 5 April, 2010).
53. Heaney PJ, Sumant AV, Torres CD, Carpick RW, Pfefferkorn FE. Diamond coatings for micro end mills: enabling the dry machining of aluminum at the micro-scale. Diamond Relat Mater 2008;17:223–223.
54. Aramcharoen A, Mativenga PT, Yang S, Cooke KE, Teer DG. Evaluation and selection of hard coatings for micro milling of hardened tool steel. Int J Mach Tools Manuf 2008;48:1578–1584.
55. Rahman M, Kumar AS, Prakash JRS. Micro milling of pure copper. J Mater Process Technol 2001;116:39–43.
56. Malekian M, Park SS, Jun MBG, Malekian M. Tool wear monitoring of micro-milling operations, micro milling of pure copper. J Mater Process Technol 2009;209:4903–4914.
57. Tansel I, Rodriguez O, Trujillo M, Paz E, Li W. Micro-end-milling–I. Wear and breakage. Int J Mach Tools Manuf 1998;38:1419.
58. König W, Kutzner K, Schehl U. Tool monitoring of small drills with acoustic emission. Int J Mach Tools Manuf 1992;32:487–493.
59. Eda H, Kishi K, Ueno H. Diamond machining using a prototype ultra-precision lathe. Prec Eng 1987;9:115–122.
60. Ikawa N, Donaldson RR, Komanduri R, Koenig W, Aachen TH, McKeown PA, Moriwaki T, Stowers IF. Ultraprecision metal cutting - the past, the present and the future. CIRP Ann Manuf Technol 1991;40:587–594.
61. Lucca DA, Seo YW. Effect of tool edge geometry on energy dissipation in ultra-precision machining. CIRP Ann Manuf Technol 1993;42:83–86.
62. Masuzawa T, Tonshoff HK. Three-dimensional micro-machining by machine tools. Ann CIRP 1997;46(2):621–628.
63. Arcona C, Dow TA. An empirical tool force model for precision machining. ASME J Manuf Sci Eng 1998;120:700–707.
64. Lu Z, Yoneyama T. Micro cutting in the micro lathe turning system. Int J Mach Tools Manuf 1999;39:1171–1183.
65. Moriwaki T, Okuda K. Machinability of copper in ultra-precision micro diamond cutting. CIRP Ann Manuf Technol 1989;38:115–118.
66. Ikawa N, Shimada S, Donaldson RR, Syn CK, Taylor JS, Ohmori G, Tanaka H, Yoshinaga H. Chip morphology and minimum thickness of cut in micromachining. Seimitsu Kogaku Kaishi/J Jpn Soc Prec Eng 1993;59:673–679.
67. Vasile MJ, Friedrich CR, Kikkeri B, McElhannon R. Micrometer-scale machining: tool fabrication and initial results. Prec Eng 1999;19:180–186.

68. Evans CJ, Paul E, Mangamelli A, Mc Glauflin ML. Chemical aspects of tool wear in single point diamond turning. Prec Eng 1996;18:4–19.
69. Friedrich CR, Kang D. Micro heat exchangers fabricated by diamond machining. J Prec Eng 1994;16(1):56–59.
70. Petch NJ. The cleavage strength of polycrystals. J Iron Steel Inst 1953;174:25–28.
71. Bowden FP, Freitag EH. The friction of solids at very high speeds I. Metal on metal; II. Metal on diamond. Proc R Soc Lond Ser A Math Phys Sci 1958;248:350–367.
72. Weck M, Fischer S, Vos M. Fabrication of microcomponents using ultraprecision machine tools. Nanotechnology 1997;8:145–148.
73. Friedrich CR, Vasile MJ. Development of the micro-milling process for high-aspect-ratio microstructures. J Microelectromech Syst 1996;5(1):33–38.
74. Schaller T, Bohn L, Mayer J, Schubert K. Microstructure grooves with a width of less than 50 micrometer cut with ground hard metal micro end mills. Prec Eng 1996;23:229–235.
75. Huo D, Cheng K, Wardle F. Design of a five-axis ultra-precision micro-milling machine—UltraMill. Part 1: holistic design approach, design considerations and specifications. Int J Adv Manuf Technol 2010;47:867–877.
76. Takeuchi Y, Suzukawa H, Kawai T, Sakaida Y. Creation of ultraprecision microstructures with high aspect ratio. Annals of the CIRP 2006;56(1):107–110.
77. Weck M, Hennig J, Hilbing R. Precision cutting processes for manufacturing of optical components. Proc SPIE 2001;4440:145–151.
78. Brinksmeier E, Riemer O, Stern R. Machining of Precision Parts and Microstructures. Proceedings of the 10th International Conference on Precision Engineering (ICPE), Initiatives of Precision Engineering at the Beginning of a Millennium, July 18–20, 2001, Yokohama, Japan: S. 3–1.
79. Vogler MP, Liu X, Kapoor SG, Devor RE, Ehmann KF. Development of meso-scale machine tool (mMt) systems. Soc Manuf Eng 2002;MS02-181:1–9.
80. Uhlmann E, Schauer K. Dynamic load and strain analysis for the optimization of micro end mills. Ann CIRP 2005;54(1):75–78.
81. Bao WY, Tansel IN. Modeling micro-end-milling operations. Part I: analytical cutting force model. Int J Mach Tools Manuf 2000;40:2155–2173.
82. Bao WY, Tansel IN. Modeling micro-end-milling operations. Part II: tool run-out. Int J Mach Tools Manuf 2000;40:2175–2192.
83. Bao WY, Tansel IN. Modeling micro-end-milling operations. Part III: influence of tool wear. Int J Mach Tools Manuf 2000;40:2193–2211.
84. Kim CJ, Mayor JR, Ni J. A static model of chip formation in microscale milling. ASME J Manuf Sci Eng 2004;126:710–718.
85. Friedrich C, Kikkeri B. Rapid fabrication of molds by mechanical micromilling: process development. Proc SPIE Int Soc Opt Eng 1995;2640:161–171.
86. Yin L, Spowage AC, Ramesh K, Huang H, Pickering JP, Vancoille EYJ. Influence of microstructure on ultraprecision grinding of cemented carbides. Int J Mach Tools Manuf 2004;44:533–543.
87. Yin L, Vancoille EYJ, Ramesh K, Huang H, Pickering JP, Spowage AC. Ultraprecision grinding of tungsten carbide for spherical mirrors. Proc Inst Mech Eng Part B (J Eng Manuf) 2004;218:419–429.

88. Melkote SN, Endres WJ. The importance of including the size effect when modeling slot milling. ASME J Manuf Sci Eng 1998;120:68–75.
89. Filiz S, Ozdoganlar OB. Microendmill dynamics including the actual fluted geometry and setup errors—Part I: model development and numerical solution. J Manuf Sci Eng Trans ASME 2008;130, Paper no. 031119 (13 pages).
90. Filiz S, Ozdoganlar OB. Microendmill dynamics including the actual fluted geometry and setup errors—Part II: model validation and application. J Manuf Sci Eng Trans ASME 2008;130, Paper no. 031120 (13 pages).
91. Özel T, Liu X. Investigations on mechanics based process planning of micro-end milling in machining mold cavities. Mater Manuf Process 2009;24:1274–1281.
92. Torres CD, Heaney PJ, Sumant AV, Hamilton MA, Carpick RW, Pfefferkorn FE. Analyzing the performance of diamond-coated micro end mills. Int J Mach Tools Manuf 2009;49:599–612.
93. Jemielniak K, Bombiński S, Aristimuno PX. Tool condition monitoring in micromilling based on hierarchical integration of signal measures. CIRP Ann Manuf Technol 2008;57(1):121–124.
94. Biermann B, Baschin A. Influence of cutting edge geometry and cutting edge radius on the stability of micromilling processes. Prod Eng 2009;3:375–380.
95. Dimov S, Pham DT, Ivanov A, Popov K, Fansen K. Micromilling strategies: optimization issues. Proc Inst Mech Eng Part B J Eng Manuf 2004;218:731–736.
96. Litwinsnski KM, Min S, Lee D, Dornfeld DA, Lee N. Scalability of tool path planning to micro machining. 1st International Conference on Micromanufacturing ICOMM; Paper No: 28; 2006 Sep 13–15; Urbana-Champaign (IL): 2006.
97. Lee DG, Lee HG, Kim PJ, Bang KG. Micro-drilling of alumina green bodies with diamond grit abrasive micro-drills. Int J Mach Tools Manuf 2003;43:551–558.
98. Egashira K, Mizutani K. Micro-drilling of monocrystalline silicon using a cutting tool. Prec Eng 2002;26:263–268.
99. Kim DW, Lee YS, Park MS, Chu CN. Tool life improvement by peck drilling and thrust force monitoring during deep-micro-hole drilling of steel. Int J Mach Tools Manuf 2009;49:246–255.
100. Cheong MS, Cho D, Ehmann KF. Identification and control for micro-drilling productivity enhancement. Int J Mach Tools Manuf 1999;39:1539–1561.
101. Ramesh K, Huang H, Yin L, Zhao J. Microgrinding of deep micro grooves with high table reversal speed. Int J Mach Tools Manuf 2004;44:39–49.
102. Ikeno J, Tani Y, Sato H. Nanometer grinding using ultrafine abrasive pellets—manufacture of pellets applying electrophoretic deposition. CIRP Ann Manuf Technol 1990;39:341–344.
103. Ohmori H, Nakagawa T. Mirror surface grinding of silicon wafers with electrolytic in-process dressing. CIRP Ann 1970;39:329–332.
104. Wu Y, Fan Y, Kato M. A feasibility study of microscale fabrication by ultrasonic-shoe centerless grinding. Prec Eng 2006;30:201–210.
105. Aurich JC, Engmann J, Schueler GM, Haberland R. Micro grinding tool for manufacture of complex structures in brittle materials. CIRP Ann Manuf Technol 2009;58:311–314.
106. Denkena B, Friemuth T, Reichstein M. Potentials of different process kinematics in micro grinding. Ann CIRP 2003;52(1):463–466.

CHAPTER 9

MICRO-FORMING

MUAMMER KOÇ
Center for Precision Forming (CPF-National Science Foundation IUCRC), Virginia Commonwealth University (VCU), Richmond, VA,
Istanbul Sehir University, Turkey

SASAWAT MAHABUNPHACHAI
National Metal and Materials Technology Center (MTEC), Pathumthani, Thailand

9.1 INTRODUCTION

Micro-forming is defined as the shaping of raw materials by plastic deformation into a geometry with at least two dimensions in the submillimeter range [1]. When a forming process is scaled down from conventional scale to the submillimeter range, some aspects of the workpiece, such as the micro-structure and the surface topology, remain unchanged. This causes the relation (or ratio) between the dimensions of the part (i.e., thickness, width, length, height) and the parameters of the micro-structure (i.e., grain size) or the surface (i.e., roughness) to change, and is commonly referred to as the *size effects*. The size effect alters almost all aspects of the forming process, including the material behavior, friction, heat transfer, and handling of the part. Therefore, the well-established metal-forming technology or the "know-how" meant for a macro-scale cannot be simply applied on a micro-scale.

On a micro-scale, materials used in the manufacturing processes are characterized only by a few grains located in the deformed area; thus, they can no longer be considered as a homogeneous continuum. Instead, the behavior of the material is greatly affected by the size and orientation of individual grains [2]. Therefore, mechanical properties (yield strength, flow stress, and elongation) obtained on a macro-scale are no longer used on a micro-scale for accurate analysis. Furthermore, the deformation mechanism on a micro-scale would be different because of large variations in the response of individual grains to applied loads. Surface

Micro-Manufacturing: Design and Manufacturing of Micro-Products, First Edition.
Edited by Muammer Koç and Tugrul Özel.

interactions and friction become more pronounced on a micro-scale as the ratio of the surface area to the volume increases [3,4]. These issues must be properly addressed to understand the "size effects" and scale down the forming processes to a micro-scale, in order to accurately predict process parameters such as forming force and spring-back, while reducing the scatter of the results.

As stated by the *similarity theory* proposed by Geiger *et al*. [5], when all the dimensions of the material specimen (i.e., workpiece) and tools are multiplied by a geometrical scale factor, λ, and the time scale is fixed to one, the strain, strain rate, and strain distribution will be scaled down by the same scale factor, λ. Postulating the similarity theory in elastic and plastic material behavior, stress and stress distribution should also be size invariant, that is, the same stress and strain curve should be obtained for different values of the geometrical scaling factor, λ. Nevertheless, while this theory may apply to the scaling down of the process and tooling design on a macro-scale, a number of material tests and forming experiments on a micro-scale have shown a significant deviation in the material response (i.e., material flow stress and hardness), which violates the similarity theory [6–9].

In the area of micro-scale sheet metal forming, decrease in flow stress with decrease in the thickness of the sheet material has been observed through tensile tests on different materials such as CuAl alloy [6], CuNi18Zn20 and CuZn15 [7], CuZn36 [8], and aluminum [9], as illustrated in Fig. 9.1. Several attempts were also carried out to investigate the effect of the tensile specimen size and geometry on the material flow curve. The specimen width was shown to have no significant effect on material response as reported by Michel and Picart [8] and Tseng [10]. However, in another study conducted by Sergueeva *et al*. [11], the gauge length of tensile specimen was found to significantly affect the maximum elongation values.

According to the well-known Hall–Petch equation, the material strength (i.e., flow stress) increases when the material grain size is reduced. However, Raulea *et al.* [9] have pointed out that when the grain size is close to the thickness of the sheet material (single-grain deformation), an inverse relation between the flow stress and the grain size is observed (i.e., the flow stress increases when the

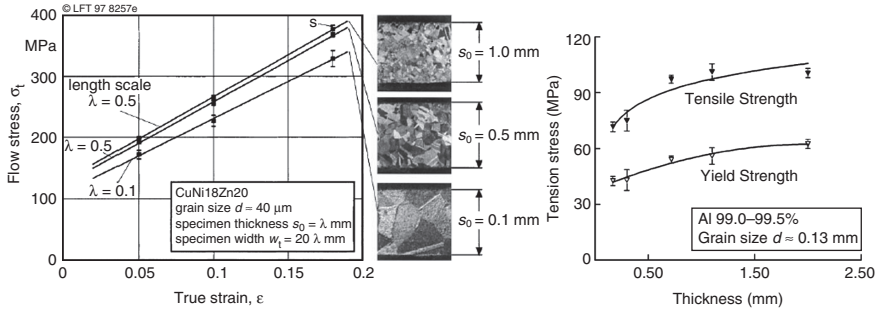

Figure 9.1 Feature size effect observed through tensile testing of thin sheet metals [7,9].

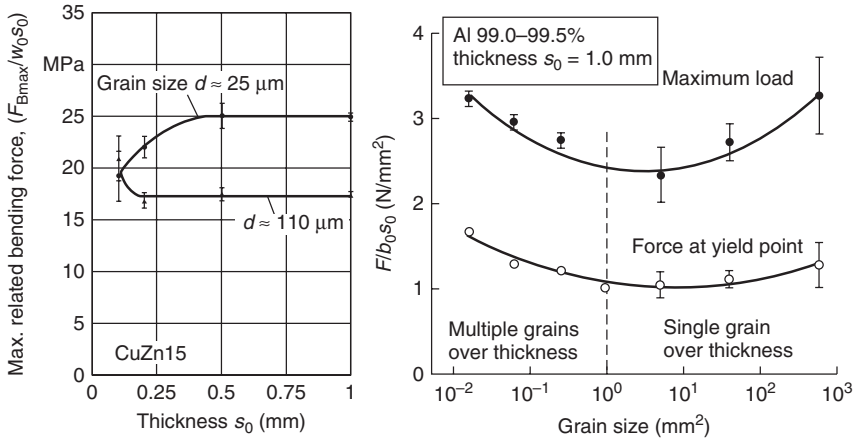

Figure 9.2 Grain size effect on bending force in bending experiment [7,9].

grain size becomes larger). This inverse relation was also reported by Kals and Eckstein [7] as illustrated in Fig. 9.2.

Another size-effect-related observation on the increase of scatter (variation) of the test results was reported for a single grain over thickness [2,12]. This large variation can be attributed to the pronounced effect of grain orientation; and hence, to its anisotropic behavior, on a micro-scale, where grain size is in the same range as the characteristic dimensions of a workpiece (i.e., thickness in sheet materials). Large data scattering was reported (Fig. 9.3) when the ratio of the sheet thickness to the grain size, ϕ, is less than 1 [9].

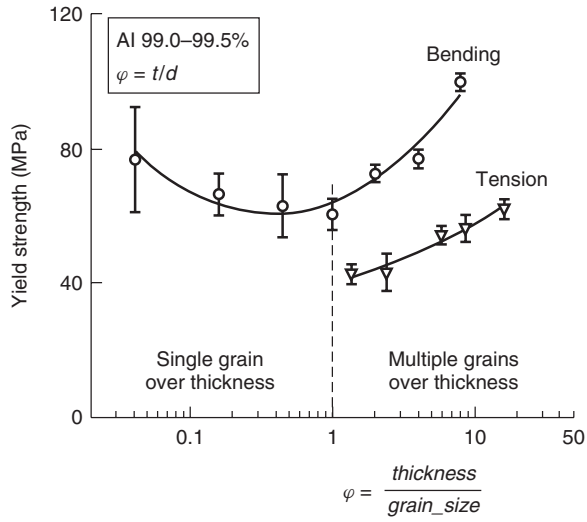

Figure 9.3 Large variations in the case of single-grain deformation [9].

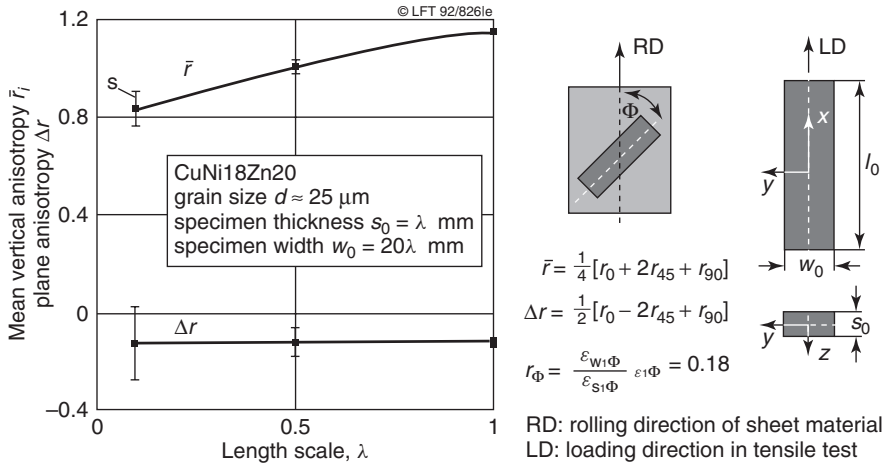

Figure 9.4 Strain anisotropy of CuNi18Zn20 versus length scale λ [7].

In a similar study by Kals and Eckstein [7], the effect of the miniaturization on material anisotropy was also studied. In their report, the vertical anisotropy ($\bar{r}$) was found to decrease with decreasing sheet thickness in tensile tests as shown in Fig. 9.4. This means that the forming characteristics become worse with reduction in sheet thickness, which could cause problems, especially in deep drawing application. However, the plane anisotropy, Δr, does not change significantly with scaling down of the specimen dimensions.

In the field of micro-scale bulk forming, upsetting and compression tests using copper alloys [12,13] have also shown a similar trend; that is, the flow stress decreases with increased miniaturization. Experimental results of the upsetting test of CuZn15 round billets are shown in Fig. 9.5.

Miyazaki *et al.* [6] as well as Engel and coworkers [1,2,7,12] explained the variation in the material flow curve due to the size effects, by using a so-called "surface layer model" (Fig. 9.6), and proposed the following: "the dislocation movements in the grains located at the surface are less restricted than grains inside the material; therefore, these surface grains show less hardening. Since the ratio of the free surface grain to the internal grain increases with miniaturization (i.e., thickness reduction or scaling-down of feature/part size), this would result in a decrease of the flow stress."

The size effects on the hardness of material were also investigated in a study by Chen and Tsai [13]. The measured hardness indicates that the hardness decreases as the specimen is downscaled to a small size. In addition, the material hardness values were shown to be proportional to the flow stresses; and thus, could be used to construct the material flow curve for downsized specimens where material data could not be acquired from tensile or compression tests (Fig. 9.7).

The effect of miniaturization on friction was investigated using ring compression and double-cup extrusion (DCE) tests [2]. The ring compression test is based

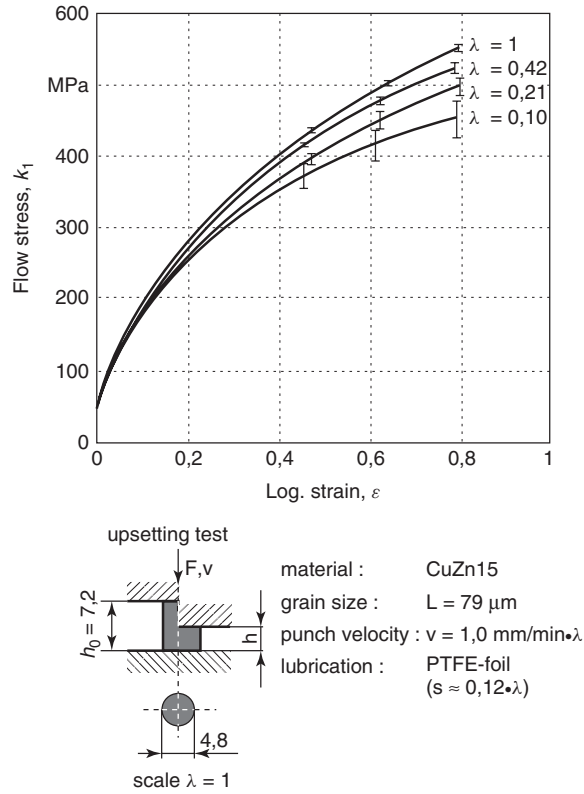

Figure 9.5 Feature size effects in bulk forming [12].

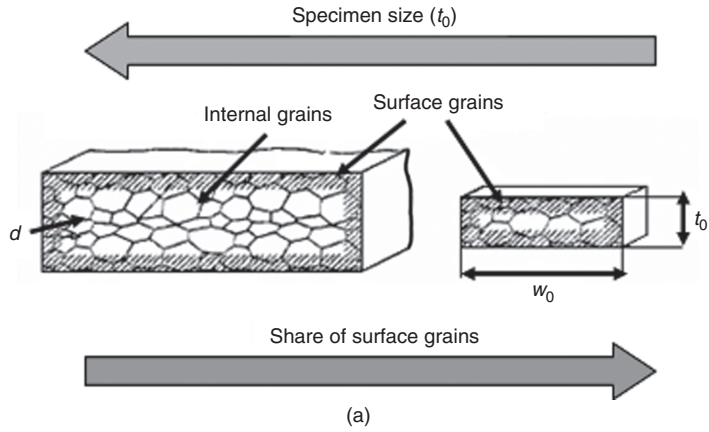

Figure 9.6 Surface layer model in (a) sheet metal (after [7]), and (b) bulk metal [1].

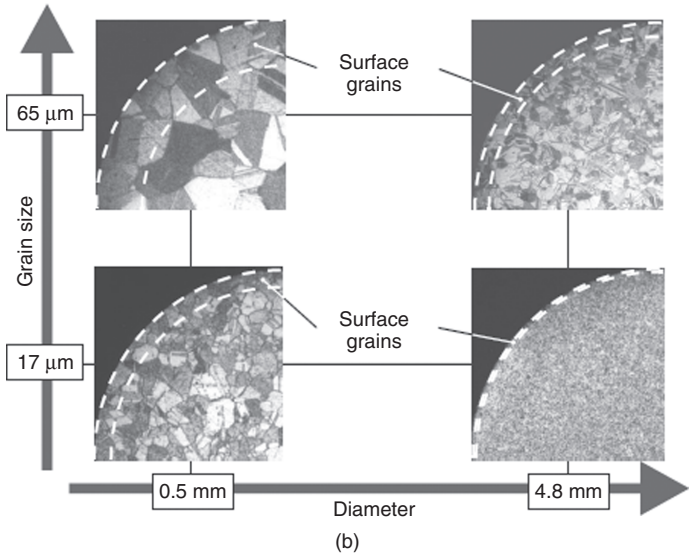

Figure 9.6 (continued)

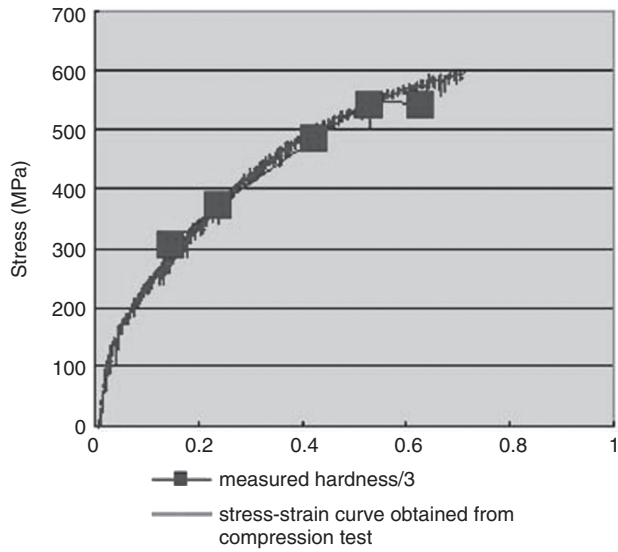

Figure 9.7 Comparison of hardness and flow curve for downscaled specimen [13].

on the fact that the evolution of the inner diameter of a ring during compression depends quite sensitively on friction. The results from the ring compression test showed an increase in friction with miniaturization when an oil lubricant was used. However, this trend was not observed in the case where no lubricant was applied during the ring compression test [12]. To extend the study of the friction

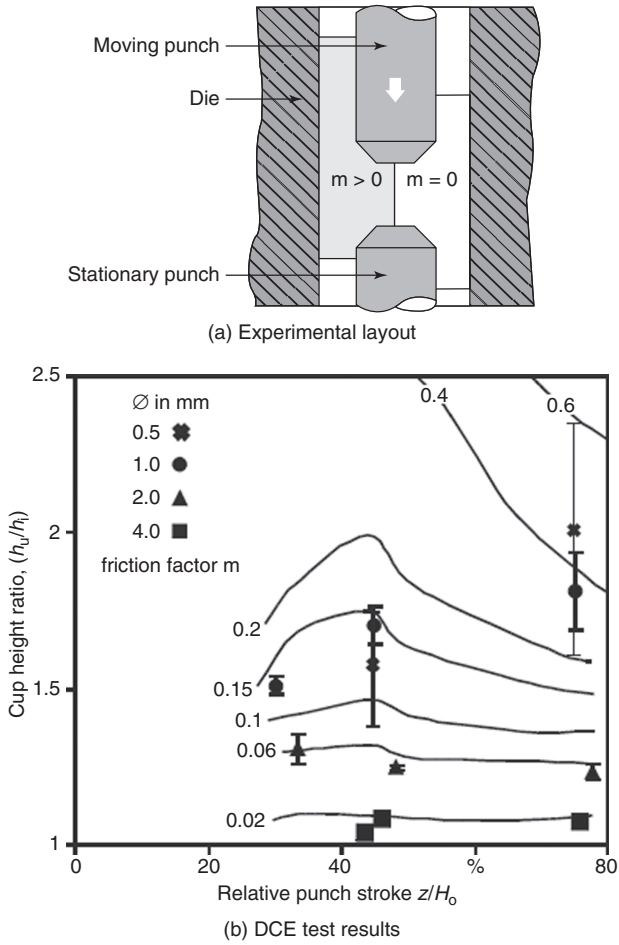

Figure 9.8 Double-cup extrusion (DCE) test [1].

and lubrication, DCE tests were performed as shown in Fig. 9.8a. The DCE test conditions are similar to those of the actual extrusion process because the test involves a large surface area, large strain, and high forming pressure. In the case of no friction ($m = 0$), both cups are expected to form to the same height value. However, when the friction on the contact surfaces is not zero, less forming is expected at the lower cup. The difference between the formed height values at the top and the bottom can be used to indicate the magnitude of the friction. The experimental results are shown in Fig. 9.8b. It can be seen that friction increases with a decrease in specimen size.

The increase of friction in both ring compression and DCE tests is explained by the model of "open and closed lubricant pockets," (Fig. 9.9a) by Tiesler [3]. Roughness valleys that have a connection to the edge of the surface cannot keep

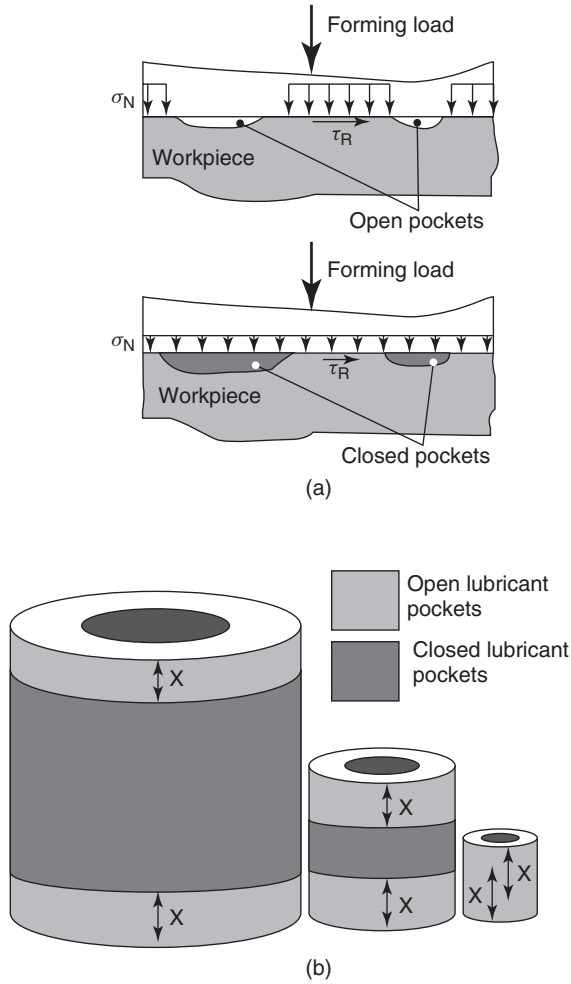

Figure 9.9 Effect of open and closed lubricant pockets on friction [1].

the lubricant. These open lubricant pockets fail to distribute the load, resulting in higher friction. On the other hand, closed lubricant pockets trap the lubricant, which helps transmit the load, thus reducing the normal pressure on the asperities. By reducing the size, the ratio of open to closed lubricant pockets increases as illustrated in Fig. 9.9b, thus resulting in an increase in the friction force. Another proof of the open and closed lubricant pockets model is the use of a solid lubricant instead of a fluid lubricant. In this case, the mechanism postulated by the open and closed lubricant pockets model is invalid, and consequently, size effects do not occur [3].

In the following sections, the aforementioned size effects are discussed in detail for different micro-forming processes.

9.2 MICRO-FORGING

Forging is a bulk metal forming process that uses compressive forces to deform a given workpiece into a desired shape. The feasibility of forging process on a micro-scale has been investigated by Saotome *et al.* [14,15] using V-grooved micro-dies of (100) silicon on superplastic material and amorphous alloys in supercooled liquid state. In their study, micro-scale dies were fabricated using photolithography and anisotropic etching techniques with the V-groove width between 0.1 and 20 μm. The experimental results show good micro-formability of both superplastic material and amorphous alloys in the supercooled liquid state under very low stresses in comparison with a conventional plastic deformation. They produced micro-pyramids and micro-gears of superplastic and amorphous alloys in supercooled liquid state using the silicon dies.

Cold and warm forging of micro-scale parts using CuZn15 specimens having a diameter of 0.5–4.8 mm was studied by Engel *et al.* [2]. The process was carried out between 100 and 450°C, being considered as a warm forming process for the CuZn15 material. As expected, the reduction of flow stress was observed with increasing temperature because of increasing recovery mechanism (Fig. 9.10). The scatter of data was also reduced with increasing temperature

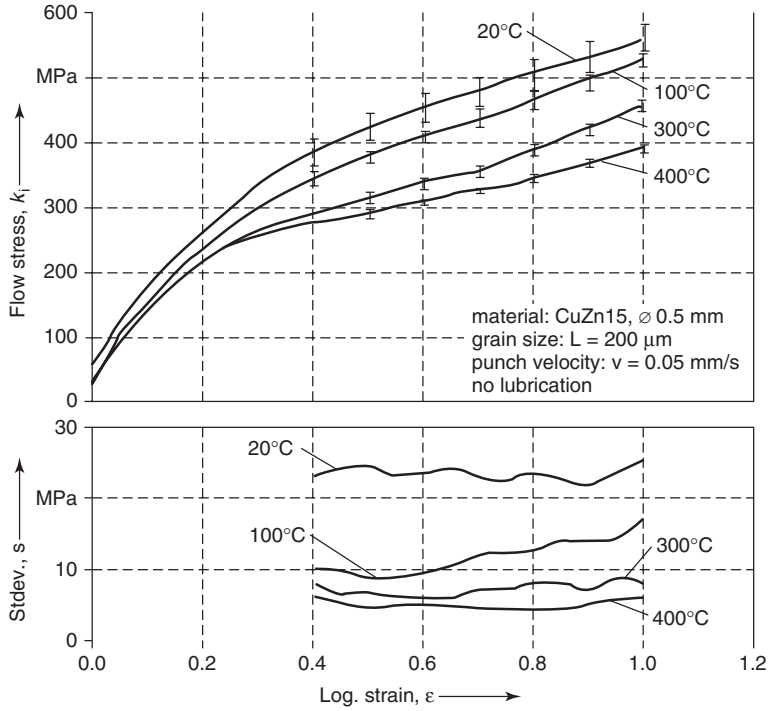

Figure 9.10 Flow stress and standard deviation of flow stress at different temperatures [2].

mainly because of the additional slip systems that were activated at elevated temperatures, enabling even grains of unfavorable orientation to deform, that is, less inhomogeneity flow of material.

9.3 MICRO-EMBOSSING/COINING

Embossing or coining is a form of bulk forming that uses a large amount of force to plastically deform only a small layer of surface on a workpiece to create precise surface structures. Micro-scale embossing was performed by Otto and Bohm [16,17] using a silicon die. Otto *et al.* embossed aluminum 99.5 material with straight channel feature dies at room temperature (Fig. 9.11). From this study, the

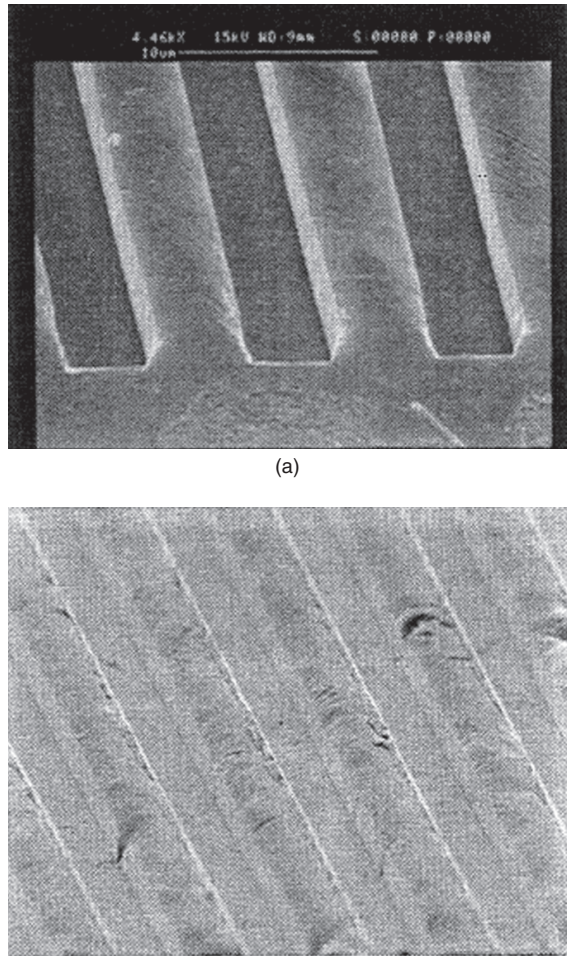

(a)

(b)

Figure 9.11 SEM images of (a) etched Si die and (b) embossed gratings with groove depth of 2.5 μm [16].

feasibility of embossing micro-features that are smaller than the material grain size without damaging the silicon die was verified. The second study by Bohm *et al.* focused on the forming precision and die-wear issues for different micro-geometries, applied loads, and workpiece materials. Specifically, two patterns of silicon die features were used: complex and straight channel structures. For the complex structure, aluminum, stainless steel, copper, and brass were used as the blank material. The results show that complex structures could be formed on all four materials with very high precision. However, in order to produce such precise geometries, the necessary compression stress must be much higher than the yield stress of the respective material. Moreover, for sharp edges at the bottom, a further increase of the pressing force would be required.

On the other hand, for the straight channel geometry, only aluminum was tested and the results had confirmed the feasibility of embossing micro-features that are smaller than the grain size of the material (i.e., aluminum grain size >3 μm, channel gap width $= 1$ μm). Finally, etched silicon dies were shown to be capable of providing accurate molding on a micro-level, but the range of use is limited to soft material and/or low compressive stresses. The life of silicon dies strongly depends on the design of the micro-geometry and coating. In another study by Hirt and Rattay [18], micro-coining of channel structures with achievable aspect ratios (height-to-width) up to three was reported, as illustrated in Fig. 9.12.

In a recent study by Wang *et al.* [19], coining experiments were carried out at 400°C on pure aluminum billets 3 mm in diameter and 2 mm in height with four different material grain sizes (16,37,75, and 98 μm), using dies with groove width varying from 40 to 120 μm. The plot of aspect ratios (rib height to groove width, *h/b*) and the groove width (*b*) for two material grain sizes is shown in Fig. 9.13. For a billet with grain size smaller than the groove width ($L = 16$ μm), *h/b* ratio increased with increasing groove width. However, when

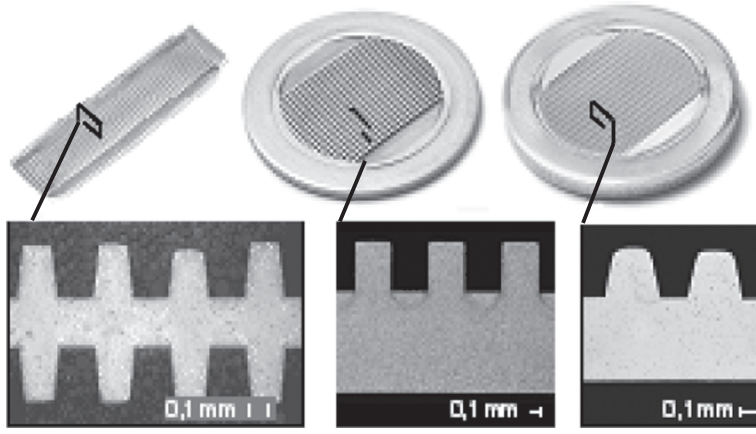

Figure 9.12 Micro-coined channels with achievable aspect ratios up to 3 [18].

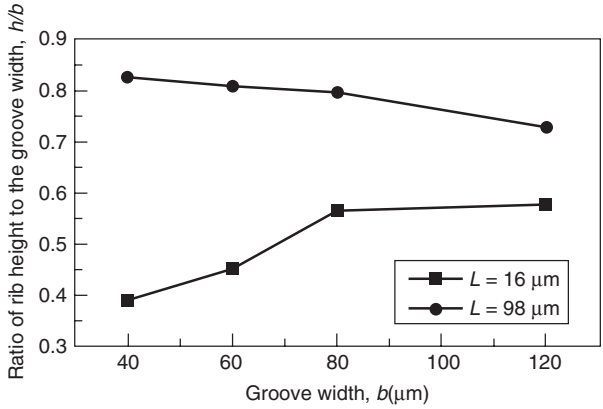

Figure 9.13 Ratio of rib height to groove width for various groove widths for two different grain sizes [19].

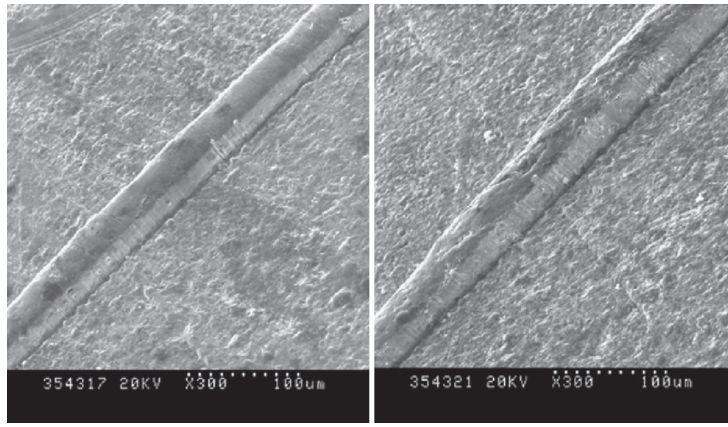

(a) $L = 37$ μm (b) $L = 98$ μm

Figure 9.14 SEM images of the ribs on billets with grain sizes of (a) 37 μm and (b) 98 μm [19].

a billet with grain size larger than the groove width ($L = 98$ μm) was used, *h/b* ratio decreased with increasing groove width. In other words, when the material grain size is larger than the groove width, the forming is considered as the single-grain deformation. The flow stress of the single grain is less than that of the polycrystalline material because of less constraint on the surface layer [19]. Finally, even though the billet with larger grains could be formed in an easier fashion (i.e., higher *h/b* ratio, regardless of groove width), the top of the rib was found to be less even when compared to the billet with smaller grains (Fig. 9.14).

9.4 MICRO-EXTRUSION

Geiger and Engel conducted experiments using the forward rod–backward can extrusion process to investigate the size effects [1,12]. In their studies, two billets of diameters 0.5 and 4 mm were used. As shown in Fig. 9.15, the ratio of cup height to shaft length (h_c/l_s) increased with miniaturization with fine grains (grain size of 4 μm), but did not increase with miniaturization with coarse grain (grain size of 120 μm). These observed results could be explained by the effect of the micro-structure of the specimen; that is, when the material grain size is larger than the thickness of the cup wall, it is easier for the material to flow into the shaft rather than into the cup wall. This example illustrates the importance of the exact knowledge of the miniaturization effects for part, process, and tool design.

The quality of the product is also affected by miniaturization. For example, in a backward micro-extrusion study by Engel and Egerer [2], irregular formation of the rim was observed to be caused by grains of different size and orientations passing through the clearance between the die and the punch, which is quite smaller than the mean grain size, thus yielding an inhomogeneous material flow and finally the observed irregular shape.

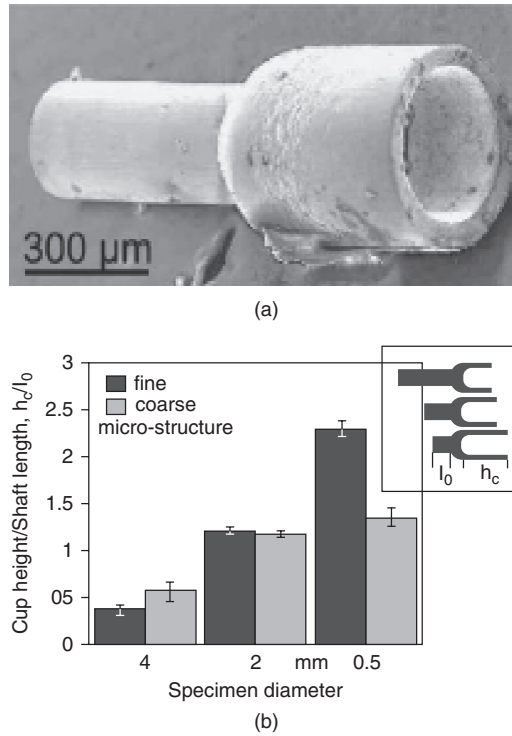

Figure 9.15 Forward rod–backward cup extrusion: effect of micro-structure [1,12]. (a) Part originally was ϕ of 0.5 mm diameter and (b) effect of micro-structure.

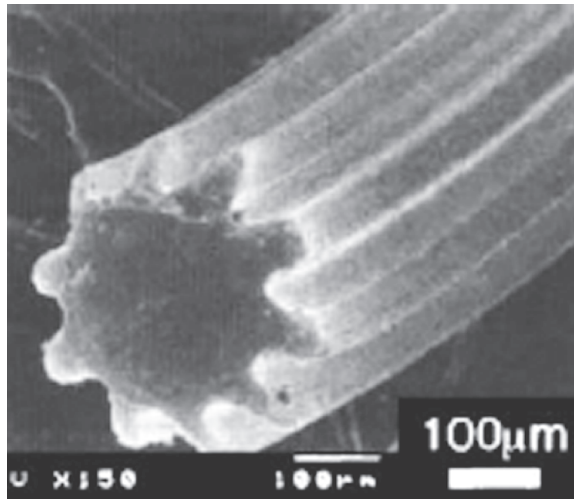

Figure 9.16 A forward-extruded micro-gear shaft: La60Al20Ni10Co5Cu5 amorphous alloy, gear module = 50 μm, number of teeth = 10 [16].

In other examples of micro-extrusion studies, micro-forward and backward extrusion of micro-gear shafts 50 μm in module and 500 μm in pitch diameter have been successfully produced on amorphous alloys at comparably low forces and high aspect ratios (Fig. 9.16). Amorphous alloys display perfect Newtonian viscous flow and are suggested for the fabrication of micro-machines [16]. Cao *et al.* extruded micro-pins of 0.48 and 1.2 mm diameter, using CuZn30 billets of three different grain sizes of 32, 80, and 200 μm [20]. The grain size effect on the flow stress was observed through the ram force. The results showed an increase in ram force for billets of smaller grain size. In other words, the flow stress of the material increases with decreasing grain size, a result that agrees with the Hall–Petch equation [21,22].

9.5 MICRO-BENDING

Similar size effects were also observed in bending on a micro-scale; that is, the material flow stress decreases with miniaturization (decreasing sheet thickness). This observation was found to be consistent down to the single-grain deformation region where the flow stress was observed to increase with further miniaturization (i.e., ratio of sheet thickness to grain size, t/d, is less than 1) as shown in Fig. 9.17 [1,9,23]. This means that in the single-grain deformation regime with a given sheet thickness, the flow stress would increase with increasing material grain size. This result clearly contradicts the theory of metal forming on a conventional scale, where the flow stress would decrease with increasing grain size according to the Hall–Petch relation [21,22].

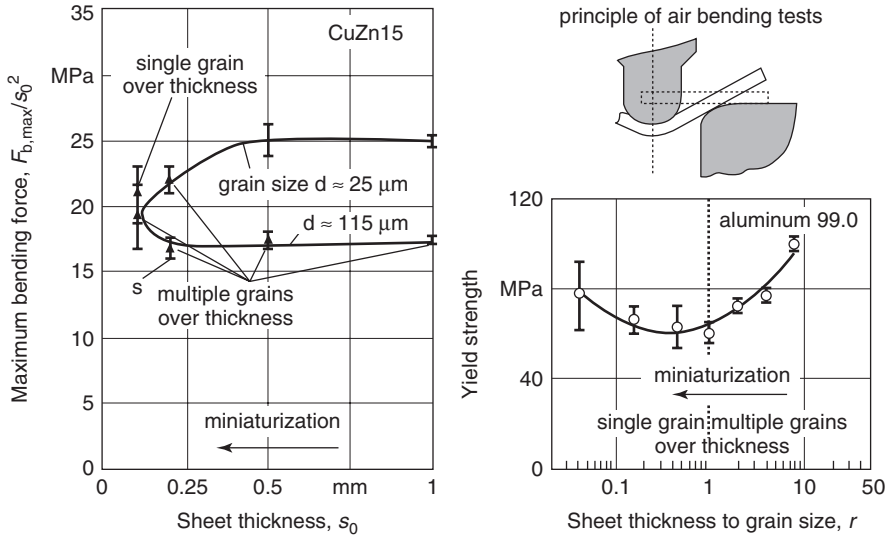

Figure 9.17 Bending forces and yield strength in bending tests [1].

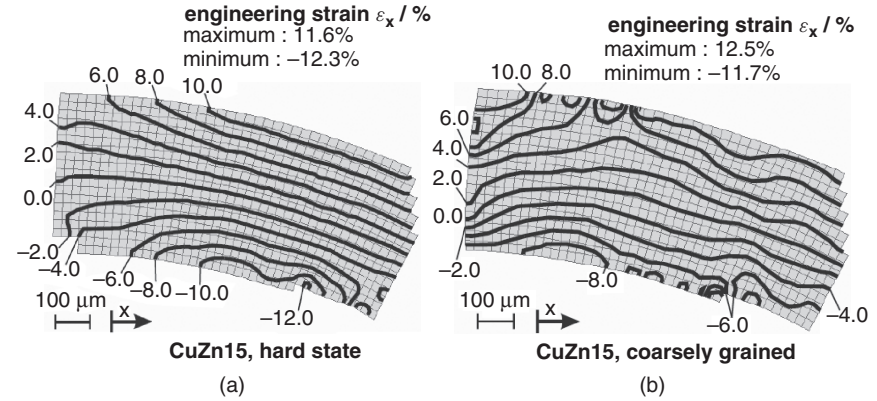

Figure 9.18 Strain distribution from bending experiment: (a) fine grain and (b) coarse grain [1].

The effect of grain size on the strain distribution in bent specimens was also discussed in the same study by Geiger *et al.* [1]. Sheet blanks of CuZn15 with an initial sheet thickness of 0.5 mm were bent and the strain distribution was plotted as shown in Fig. 9.18 for fine grains (10 µm) and coarse grains (70 µm). The fine grain blank (Fig. 9.18a) shows a typical distribution of strains as observed in a bending process, whereas the coarse grain blank (Fig. 9.18b) shows a disturbed strain distribution due to the irregular orientation of the grains. This may be the reason for an increase in bending force when only a single grain is located over the

thickness as the deformation mechanism will be minimized with a single-grain structure, as opposed to finer and multiple grains that would have additional deformation paths (i.e., more grain boundary motions and slip lines).

9.6 MICRO-STAMPING

Stamping is a process in which a metal sheet is formed by pressing it into the shape of a pair of dies (female and male dies), Fig. 9.19a. Mahabunphachai and Koç [24,25] conducted stamping experiments on thin blanks of SS304, SS316L, SS430, Ni270, and Ti grade 1 and 2, all with an initial thickness of 51 μm, by using rigid dies with micro-channel arrays 0.75 mm in width and height (Fig. 9.19b). The results showed the feasibility and process capability in producing micro-channel arrays from thin metal sheets (Fig. 9.19c). A similar study of micro-channel stamping was performed by Peng *et al.* [26], but instead of a rigid punch, polyurethane rubber was used as a soft punch with 0.1-mm-thick SS304 blanks. The effects of the material grain size, friction, and hardness of the soft punch on the formability were investigated numerically and experimentally.

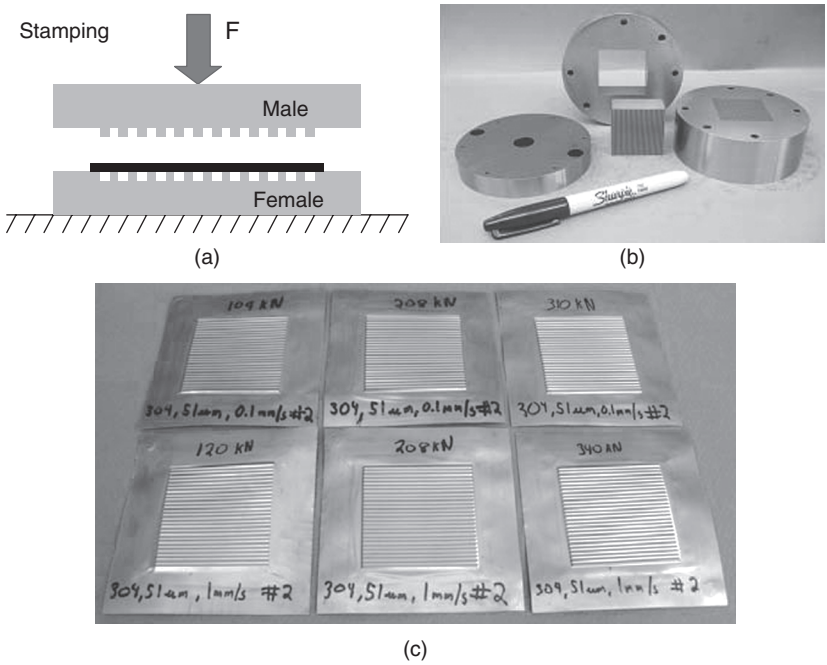

Figure 9.19 Micro-stamping basics, sample die set, and Bipolar Plates (BPPs) for fuel cells [26].

9.7 MICRO-DEEP DRAWING

Deep drawing is a sheet forming process in which a sheet blank is radially drawn into a forming die by a punch. At the micro-level, Saotome *et al.* [27] conducted a study of the micro-deep drawing process by using thin steel sheets of thickness (t) below 0.2 mm and punch diameter (D_p) ranging between 1 and 10 mm. The characteristic ratio, D_p/t, varied between 10 and 100 in their experiments. It was observed that the limiting drawing ratio (LDR) decreases with increasing D_p/t. The effect of the blank holder pressure (p) was clearly recognized above a D_p/t of 40. As D_p/t increased, the required blank holder pressure increased. In addition, the effect of punch radius (R_d) on drawability was observed only below a D_p/t of 15. Higher blank holder pressure was required as R_d/t decreased.

In order to investigate the applicability of the geometrical similarity law in the micro-deep drawing process, another set of experiments was conducted with specimen thicknesses of 0.05, 0.1, 0.2, and 1.0 mm in the same study. The results are shown in Fig. 9.20.

The ratio of the maximum punch force measured during the experiment (P_{exp}) to the maximum punch force calculated on the basis of Hukui's and Yoshida's equation (P_{cal}) is shown in Fig. 9.20. The results show that the value of P_{exp}/P_{cal} is very close to unity for D_p/t above 40. This suggests that the geometrical similarity is held true for D_p/t exceeding 40. However, when D_p/t is below 20, the P_{exp}/P_{cal} ratio deviates from unity, and the effect of the die radius becomes remarkable. Furthermore, in the case where $D_p/t = 10$ and $R_d/t = 5$, bending

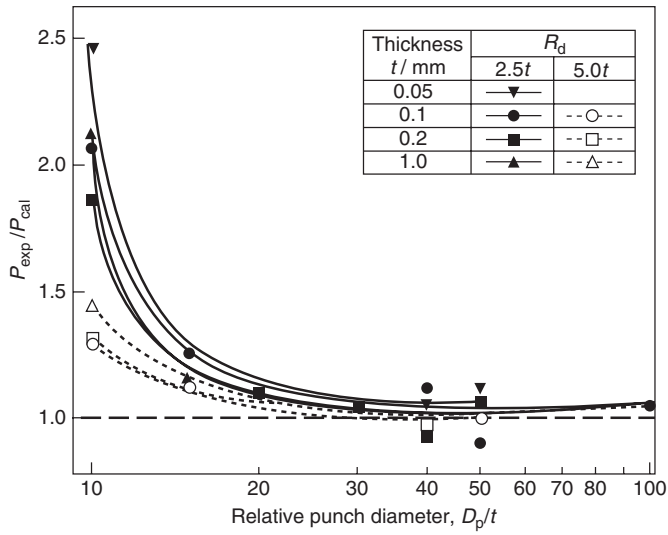

Figure 9.20 The P_{exp}/P_{cal} ratio under various conditions [27].

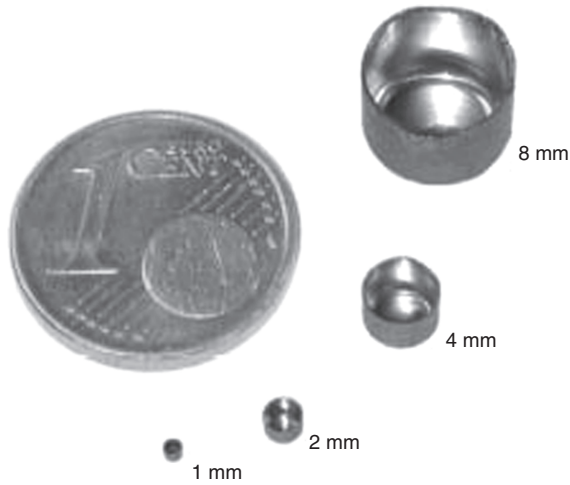

Figure 9.21 Micro-deep drawing cups with punch diameters between 1 and 8 mm [28].

is considered to be the dominant forming mechanism since the blank holder pressure has little effect on the drawability and no effect on the working material during the latter half of the drawing process.

Micro-deep drawing of cups of diameters between 1 and 8 mm on CuZn37 material (thickness between 80 and 300 μm) was performed in a more recent study by Witulski *et al.* [28]. The cups were drawn successfully as shown in Fig. 9.21. The punch force was measured during the experiments and the results later used for comparison with the simulation. The validated finite element models were further used to study the effects of other process parameters such as friction coefficient, transverse anisotropy, drawing gap, and blank holder gap, on the overall drawability.

Aluminum 99.5 foil with a thickness of 20 μm and mild steel foil with a thickness of 25 μm were deep drawn using a 1-mm-diameter punch by Vollertsen *et al.* [4]. The final shapes and the friction force measured during the deep drawing on a micro-scale were compared with those measured on a macro-scale in Figs. 9.22 and 9.23, respectively. Wrinkling was observed at the flange of the micro-cup and not found on the macro-scale. The friction force was found to decrease in both macro- and micro-cups when lubricant was applied; however, the amount of the decreased friction force was significantly higher in the micro-cup than that in the macro-cup.

Punch force was also compared between the two scales. It was found that the forming force was much higher than the calculated value for the micro-cup, while the force for the macro-cup was almost equal to the calculated value. Therefore, the friction coefficient in micro-forming is much greater than that in macro-forming. Vollertsen *et al.* also investigated the variation in the friction coefficient at the flange and the die radius by using strips of St14 material that is 1 mm

Material:	Al 99.5	Al 99.5
Blank thickness:	1.0 mm	0.02 mm
Drawing ratio:	1.8	1.8
Punch diameter:	50 mm	1.0 mm
Drawing depth:	25 mm	0.5 mm
Drawing velocity:	25 mm/s	1.0 mm/s

Figure 9.22 Comparison of macro- and micro-deep-drawn cups [4].

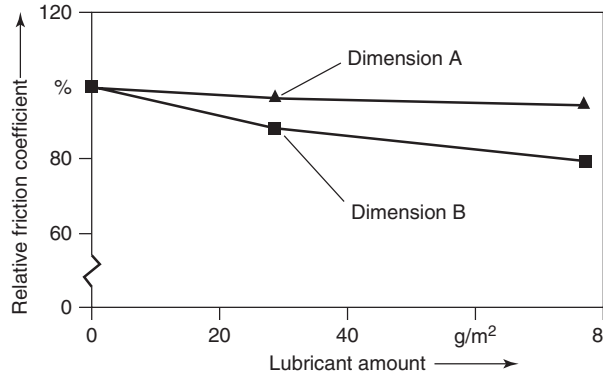

	Dimension A	Dimension B
Material :	St 15	1.0335
Blank thickness :	1.35 mm	0.025 mm
Drawing ratio :	1.7	1.7
Drawing velocity :	25 mm/s	1 mm/s
Lubricant :	HBO 947/11	HBO 947/11

Figure 9.23 Comparison of the effects of lubricant [4].

in thickness. They found that the friction coefficient was unequal at these two locations, and it depended on the applied normal pressure [4].

9.8 MICRO-HYDROFORMING

Hydroforming is a type of sheet/tube forming that uses a high pressurized fluid medium to press a piece of material into a die shape. At the micro-scale, the

first study of micro-hydroforming to fabricate micro-features (grooves) on thin foils of AISI304 stainless steel (2.5 μm thick) and pure copper (3.0 μm thick) was performed by Joo *et al.* [29]. Successful forming of thin foils into several micro-channel shapes with the channel dimensions of 10–20 μm in width and 5–10 μm in height, using a static pressure up to 250 MPa, was demonstrated as shown in Fig. 9.24. Nonetheless, only the copper foil could be fully formed into a concentric channel shape, while the stainless steel foil could not be fully formed into any channel shapes. Furthermore, the effect of interchannel distance (i.e., distance between two consecutive channels) was clearly seen from the thickness distribution in the case of copper foil. The results showed extreme thinning up to about 75% when a narrower interchannel distance of 1 μm was used compared to the wider channel spacing as shown in Fig. 9.25.

Recently, Mahabunphachai and Koç investigated the size effects on the material behavior and the formability of thin stainless steel sheets, using hydraulic bulge testing and micro-channel hydroforming [30,31]. In their study, thin blanks of SS304 of 51 μm thickness and three different grain sizes of 9.3, 10.6, and 17 μm were bulged into five different die diameters between 2.5 and 100 mm (Fig. 9.26a). The test results showed a decrease in flow stress with increasing grain size from 9.3 to 17 μm, and with decreasing bulge diameter from 100 to 10 mm. However, as the bulge diameter was decreased further from 10 to 2.5 mm, an opposite trend was observed; that is, the flow stress was found to increase with decreasing bulge diameter. Fabrication of micro-channel arrays

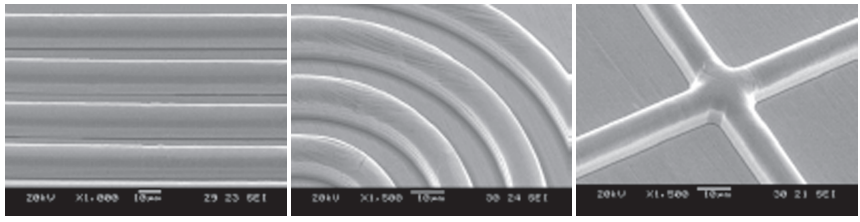

Figure 9.24 Hydroformed micro-channels on ultrathin copper foil [29].

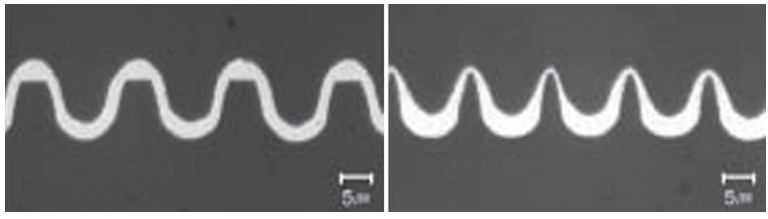

Figure 9.25 Effect of interchannel distance on the thickness distribution of the copper foil [29].

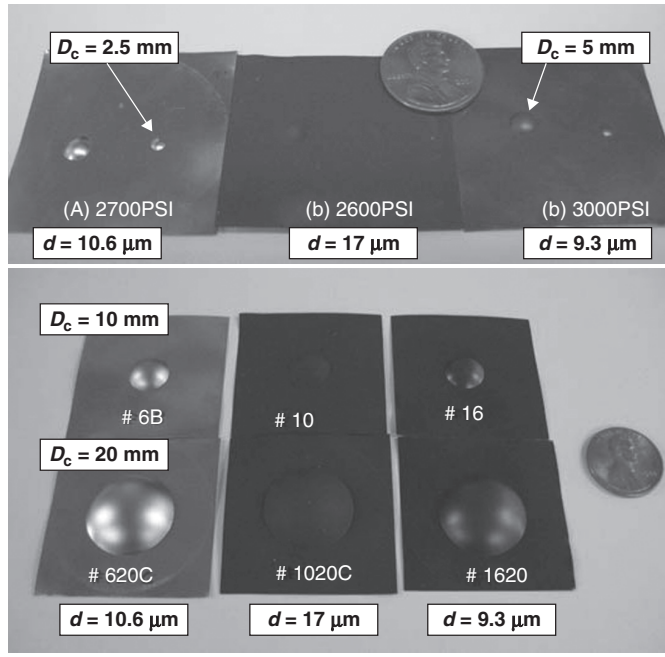

(a)

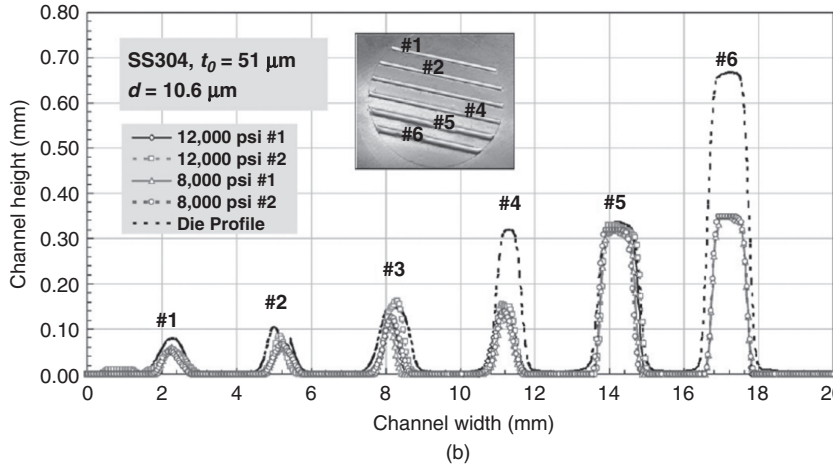

(b)

Figure 9.26 (a) Meso- and micro-scales bulging, and (b) micro-channel hydroforming on thin SS304 blanks [30,31]. (A full color version of this figure appears in the color plate section.)

using hydroforming on the same thin blanks of SS304 0.46–1.33 mm in width and 0.15–0.98 mm in height was also carried out by the same researchers. The results showed the insignificant effect of grain size on channel formability for the grain size range used in their study (9.3–17 μm). However, channel geometries were shown to significantly affect the overall formability of the micro-channels, as shown in Fig. 9.26b; and thus, were optimized using the FEA (finite element analysis) tool in the same study [31].

9.9 EQUIPMENT AND SYSTEMS FOR MICRO-FORMING APPLICATIONS

A micro-forming system is comprised of five major categories: material, process, tooling, machine/equipment, and product (Fig. 9.27). The size effects on material response and variation in several forming processes were previously discussed in this chapter. In this section, the scaling-down effects on tooling, machine/equipment, and product are discussed in detail.

In the design and fabrication of the tools for micro-forming, the small and complex geometries needed for the tools are difficult to achieve, especially when close tolerances and high surface quality are desired [32]. Special tool manufacturing techniques are required to overcome these difficulties. Carefully selected tool material and simple shaped/modular tools can help reduce the cost of tool making and the degree of difficulty involved in tool manufacturing, and increase tool life.

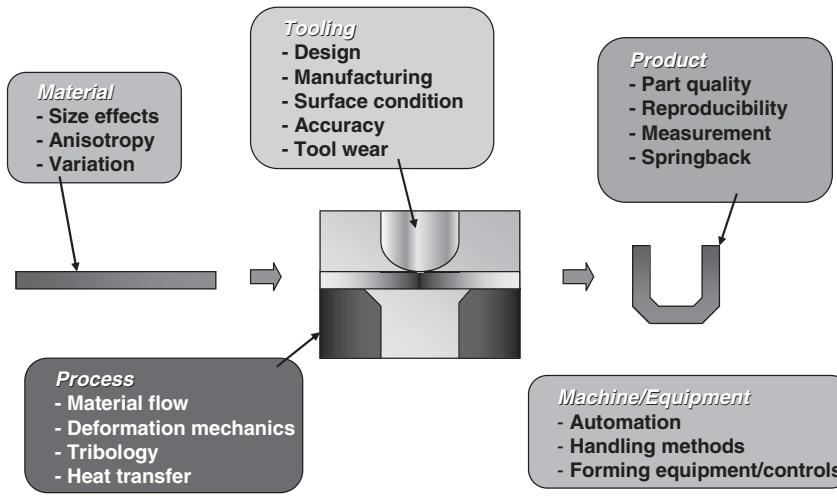

Figure 9.27 Basic elements of a micro-forming system. (A full color version of this figure appears in the color plate section.)

A major challenge with respect to machine and equipment in the micro-forming process arises from the need for high-precision and high-speed production. Specifically, positioning of the micro-parts during the production process requires an accuracy of the order of a few micrometers to submicrometers, depending on the part type and ultimate use. In addition, since the part size is extremely small and the part weight is too low, handling and holding of micro-parts becomes very difficult because of adhesive forces (van der Waals, electrostatic, and surface tension). Therefore, special handling and workholding equipment need to be developed to overcome these difficulties while placing, positioning, and assembling the micro-parts. Furthermore, the clearance or backlash between die and punch that could be negligible at the conventional scale can become a major problem when the total required stroke to form the micro-part and the clearance lie in the range of a few hundred micrometers [1]. Automation systems on a micro-level are another challenge that will eventually need to be studied and developed for the high-volume low-cost production process.

The last aspect of a micro-forming system that is affected by the miniaturization concerns part quality. With the part size in a few hundred micrometers, the measurement and inspection of the final micro-parts for quality assurance require special tools with high precision.

9.10 SUMMARY AND FUTURE WORK

It is believed by many engineers and researchers that micro-forming will be the future of mass production for micro-features/parts. A large number of studies have been carried out to investigate the size effects in different micro-forming processes as discussed in detail in this chapter. Nonetheless, more attempts are still required, especially in the area of material characterization on a micro-scale, in order to utilize a more accurate material model for part and process design using FEA. Another crucial aspect of micro-forming that requires special attention and fast development is the equipment suitable for micro-scale productions. With the downscaling of the parts, the use of conventional-scale tools and equipments is no longer economical because of the unnecessarily high machine power and machine space. Therefore, the development and utilization of micro-machines (table-top machines) and the concept of micro-factory are crucial and inevitable for mass-scale production of micro-features/parts.

REFERENCES

1. Geiger M, Kleiner M, Tiesler N, Engel U. Micro-forming. Ann CIRP 2001;50(2): 445–462. Keynote paper.
2. Engel U, Egerer E. Basic research on cold and warm forging of micro-parts. Key Eng Mater 2003;233–236:449–456.

3. Tiesler N, Engel U. Micro-forming-effects of miniaturization. Proceedings of the Eighth International Conference on Metal Forming. Rotterdam: Balkema; 2000.
4. Vollertsen F, Hu Z, Schulze Niehoff H, Theiler C. State of the art in micro forming and investigations into micro deep drawing. J Mater Process Technol 2004;151:70–79.
5. Geiger M, MeBner A, Engel U. Production of micro-parts-size effects in bulk metal forming, similarity theory. Product Eng 1997;4(1):55–58.
6. Miyazaki S, Fujita H, Hiraoka H. Effect of specimen size on the flow stress of rod specimens of polycrystalline Cu-Al alloy. Scr Metall 1979;13:447–449.
7. Kals TA, Eckstein R. Miniaturization in sheet metal working. J Mater Process Technol 2000;103:95–101.
8. Michel JF, Picart P. Size effects on the constitutive behaviour for brass in sheet metal forming. J Mater Process Technol 2003;141:439–446.
9. Raulea LV, Goijaerts AM, Govaert LE, Baaijens FPT. Size effects in the processing of thin metals. J Mater Process Technol 2001;115:44–48.
10. Tseng AA. Material characterization and finite element simulation for forming miniature metal parts. Finite Elem Anal Des 1990;6:251–265.
11. Sergueeva AV, Zhou J, Meacham BE, Branagan DJ. Gage length and sample size effect on measured properties during tensile testing. Mater Sci Eng A 2009;526:79–83.
12. Engel U, Eckstein R. Micro-forming—from basics to its realization. J Mater Process Technol 2002;125–126:35–44.
13. Chen FK, Tsai JW. A study of size effect in micro-forming with micro-hardness tests. J Mater Process Technol 2006;177:146–149.
14. Saotome Y, Akihisa I. Superplastic micro-forming of micro-structures. Proceedings of the 7th IEEE Workshop on Micro Electro Mechanical Systems. Oiso, Japan, January 1994. pp. 343–347.
15. Saotome Y, *et al*. The micro-nanoformability of Pt-based metallic glass and the nanoforming of three-dimensional structures. Intermetallics 2002;10:1241–1247.
16. Otto T, Schubert A, Bohm J, Gessner T. Fabrication of micro optical components by high precision embossing. Proc SPIE Int Soc Opt Eng 2000;4179:96–106.
17. Bohm J, Schubert A, Otto T, Burkhardt T. Micro-metalforming with silicon dies. Micro-syst Technol 2001;7(4):191–195.
18. Hirt G, Rattay B. Coining of thin plates to produce micro channel structures. 10th International Conference on Precision Engineering (ICPE) 2001; 2001 July 18–20; Yokohama, Japan. 2001. pp. 32–36.
19. Wang CJ, Shan DB, Zhou J, Guo B, Sun LN. Size effects of the cavity dimension on the Micro-forming ability during coining process. J Mater Process Technol 2007;187–188:256–259.
20. Cao J, *et al*. Micro-forming—experimental investigation of the extrusion process for micro-pins and its numerical simulation using RKEM. ASME Journal of Manufacturing Science and Engineering 2004;126:642–652.
21. Hall EO. Deformation and ageing of mild steel. Phys Soc Proc 1951;64:747–753.
22. Petch NJ. Cleavage strength of polycrystals. Iron Steel Inst 1953;174:25–28.
23. Kals RTA. Fundamentals on the Miniaturization of Sheet Metal Working Processes. Reihe Fertigungstechnik-Erlangen, Hrsg.: Geiger M. Meisenbach Bamberg; 87, 1999.

24. Mahabunphachai S, Koç M. Fabrication of PEMFC metallic bipolar plates with micro-channel arrays using stamping and hydroforming processes. International Conference on Multi-Material Micro-Manufacture (4M) and International Conference on Micro-Manufacture (ICOMM); Sep 23–25; Karslruhe, Germany. 2009.
25. Mahabunpachai S, Cora ON, Koç M. Effect of manufacturing processes on formability and surface topography of proton exchange membrane fuel cell metallic bipolar plates. J Power Sources 2010;195:5269–5277.
26. Peng L, Hu P, Lai X, Mei D, Ni J. Investigation of micro/meso sheet soft punch stamping process—simulation and experiments. Mater Des 2009;30:783–790.
27. Saotome Y, Kaname Y, Hiroshi K. Micro-Deep drawability of very thin sheet steels. J Mater Process Technol 2001;113:641–647.
28. Witulski N, Justinger H, Hirt G. Validation of FEM-simulation for micro deep drawing process modeling. NUMIFORM 2004; 2004 June 13–17; Columbus, OH. 2004.
29. Joo BY, Oh SI, Son YK. Forming of micro channels with ultra thin metal foils. CIRP Ann 2004;53(1):243–246.
30. Mahabunphachai S, Koç M. Investigation of size effects on material behavior of thin sheet metals using hydraulic bulge testing at micro/meso-scales. Int J Machine Tools Manufacture 2008;48:1014–1029.
31. Mahabunphachai S, Koç M. Fabrication of micro-channel arrays on thin metallic sheet using internal fluid pressure: investigations on size effects and development of design guidelines. J Power Sources 2008;175(1):363–371.
32. Qin Y. Micro-forming and miniature manufacturing systems—development needs and perspectives. J Mater Process Technol 2006;177:8–18.

CHAPTER 10

MICRO-ELECTRO DISCHARGE MACHINING (μEDM)

MUHAMMAD PERVEJ JAHAN, ABU BAKAR Md. ALI ASAD, MUSTAFIZUR RAHMAN, YOKE SAN WONG, and TAKESHI MASAKI

Mechanical Engineering Department, National University of Singapore (NUS), Singapore

10.1 INTRODUCTION

The very phenomenon of removal of material by electrical spark was first noticed around the year 1700 by Benjamin Franklin. The origin of electrical discharge machining (EDM) dates back to 1770, when English scientist Joseph Priestly discovered the erosive effect of electrical discharges [1]. However, the process of material removal by controlled erosion through a series of sparks, commonly known as electric discharge machining, was first started in the USSR in the 1940s, when a scientist couple, Doctors B.R. and N.I. Lazarenko, first applied it to a machine for stock removal [2]. One of the two principal types of EDM, the die-sinking process, was introduced as early as in the 1940s [2] and subsequently, various advanced features, including pulse generators, planetary and orbital motion techniques, Computer Numerical Controlled (CNC), and the adaptive control mechanism, were incorporated in it. The evolution of wire-EDM in the 1970s [3] was due to developments in generator technology, new wire tool electrodes, better mechanical concepts, improved machine intelligence, better flushing, etc. During the last few decades, this process has found wide applications in many industrial domains, such as mold and die manufacturing, and small and burr-free micro-hole drilling.

Even though micro-EDM is based on the same physical principle as spark erosion, it is not merely an adaptation of the EDM process for machining on a micron level. There are significant differences in the size of the tool

Micro-Manufacturing: Design and Manufacturing of Micro-Products, First Edition.
Edited by Muammer Koç and Tugrul Özel.

used, fabrication method of micro-sized tools, the power supply of discharge energy, movement resolution of the axes of the machine tools, gap control and flushing techniques, and also in the processing technique [4,5]. For example, *micro-EDM milling*, *wire electro-discharge grinding* (*WEDG*) and *repetitive pattern transfer* are commonly employed in and more specific to the micro-EDM process.

While the EDM process has found widespread applications in the industry over the last 70 years, the early demonstration of micro-EDM was done in 1968 by Kurafuji and Masuzawa [6], who achieved drilling of a minute hole of several microns in a 50-μm thick carbide plate. Since then, there has been much research effort on the development of micro-machining processes. Despite the effort, initially it had a rather slow industrial acceptance for production processes, until recently when the use of micro-EDM for micro-scale manufacturing became inevitable because of the demand for miniaturization.

With growing trends toward miniaturization of machined parts, developments in the area of micro-electromechanical systems (MEMS), and requirements for micro-features in difficult-to-cut materials, micro-EDM has become an important and cost-effective manufacturing process because of its noncontact machining capability due to micro-sized tools. Promising applications are not limited to the machining of hard materials for micro-molds, but also include the production of difficult-to-make features such as fuel injection nozzles, spinneret holes for synthetic fibers, electronic and optical devices, micro-mechatronic actuator parts, and micro-tools for producing these devices [7,8].

10.2 THE MICRO-EDM PROCESS

10.2.1 Physical Principles of Micro-EDM

10.2.1.1 Basic Mechanism of Micro-EDM. Micro-EDM is the process of machining electrically conductive materials in the form of micro-size craters by using precisely controlled sparks that occur between an electrode and a workpiece in the presence of a dielectric fluid [9]. The physical principle of the micro-EDM process is essentially similar to that of the EDM process with the differences mentioned above. The machining process is driven by an assigned and controlled gap, voltage, energy, and frequency of discharge. High frequencies ($>$200 Hz) and small energies (10^{-6} to 10^{-7} J) for every discharge (40–100 V) are required to obtain high accuracy and good surface qualities (roughness of about 0.1 μm) [10]. The discharge energy is supplied by a pulse generator and a servo system is employed to ensure that the electrode moves at a proper rate to maintain the right spark gap, and to retract the electrode if short-circuiting occurs. A dielectric circulation unit with pump, filter, and tank is used to supply the fresh dielectric in the gap and to maintain the proper flushing out of debris.

10.2.1.2 Sparking and Gap Phenomena in Micro-EDM. The sparking phenomena during micro-EDM can be divided into three important phases, namely, preparation phase for ignition, phase of discharge, and interval phase between discharges [11]. When the gap voltage is applied, an electric field or energy column is created, which gains highest strength once the electrode and the surface are closest. The electrical field eventually breaks down the insulating properties of the dielectric fluid. Once the resistivity of the fluid is lowest, a single spark is able to flow through the ionized flux tube and strike the workpiece. The voltage drops as the current is produced and the spark vaporizes anything in contact, including the dielectric fluid, encasing the spark in a sheath of gasses composed of hydrogen, carbon, and various oxides. The area struck by the spark melts quickly and may even vaporize. When the current at this point is switched off, which is during the pulse interval, the heat source is eliminated and the sheath of vapor around the spark implodes. Its collapse creates a void or vacuum and draws in fresh dielectric fluid to flush away debris and cool the area. Reionization also occurs, which provides favorable conditions for the next spark. Figure 10.1 illustrates the physical principle and the gap phenomena during the micro-EDM process.

10.2.2 Pulse Generators/Power Supply

Micro-EDM is probably the most promising micro-machining technique because of its noncontact nature of machining capability, as has been described in the introduction. While precision, rigidity, and repeatability of the machine tool structure are the cardinal factors from the machine tools point of view for conventional micro-machining processes, nonconventional micro-machining processes, such as micro-EDM, requires advanced process control capabilities in addition to the perfection of machine tool structure. For example, to realize precision micro-machining, one important point is that the smallest unit removal (UR) should be minimal, which is the volume or the size of the part removed from the workpiece by the unit of the removal phenomenon. For example, in micro-EDM, the UR is a crater produced by one pulse of discharge which is a kind of quanta [5,13–16], and to minimize the UR in micro-EDM, the pulse shape needs to be controlled such that less energy is discharged in every pulse as opposed to the cutting processes, where the UR consists of depth of cut, feed pitch, and the cut length corresponding to one chip. Because the UR controls surface roughness, smallest machinable feature, accuracy of feature control, and machining quality, the amount of energy released in every spark determines such output parameters in micro-EDM. The troubling fact is that the UR of micro-EDM is comparatively large but the cutting force is very small because of noncontact machining, and on the other hand for conventional micro-cutting, the UR can be quite small but the cutting force is comparatively very large. Therefore, for micro-machining by micro-EDM, it is essential to minimize the spark energy released from each spark

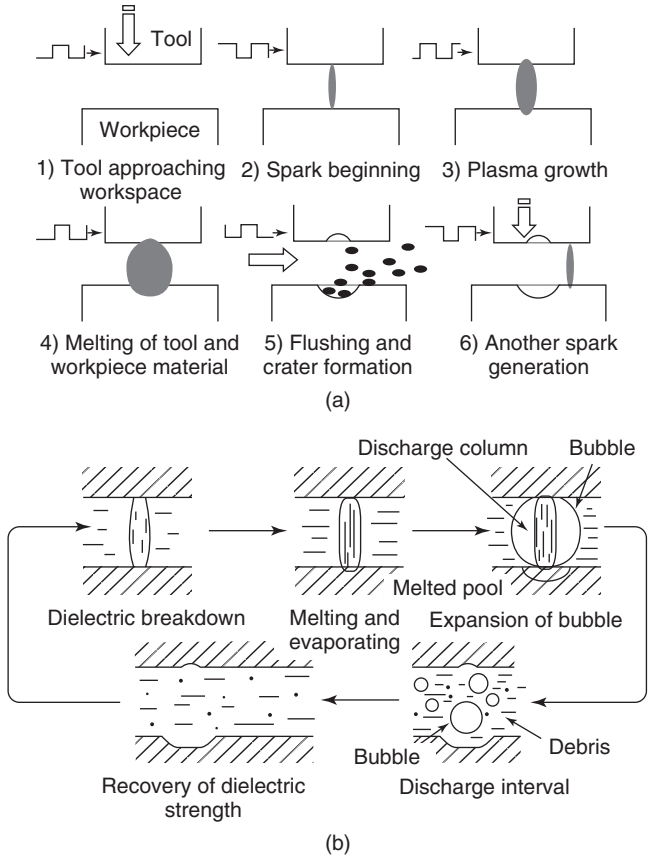

Figure 10.1 (a) Representation of sparking phenomena in EDM [8] and (b) Model of EDM gap phenomena [12].

to achieve smaller UR, which will result in smaller machinable feature size and finer surface roughness. But in addition to that, it is also important to maintain high machining throughput, and the problem in micro-EDM is that the UR frequency is more of a quantum in nature, which can vary significantly because of the sparking condition as opposed to the more-of-a-continuous UR frequency in conventional cutting process defined by the continuous feed rate.

Among the two major types of micro-EDM power supply, namely resistance—capacitance (RC) or relaxation-type and transistor-type pulse generator (Fig. 10.2), RC-based power supply has found widespread applications in micro-EDM, a rebirth after being replaced earlier by transistor-type power supply for conventional EDM power supply [12,17,18].

10.2.2.1 Transistor-Type Pulse Generator. In a transistor-type power supply (Fig. 10.2a), a series of resistances and transistors are connected in parallel

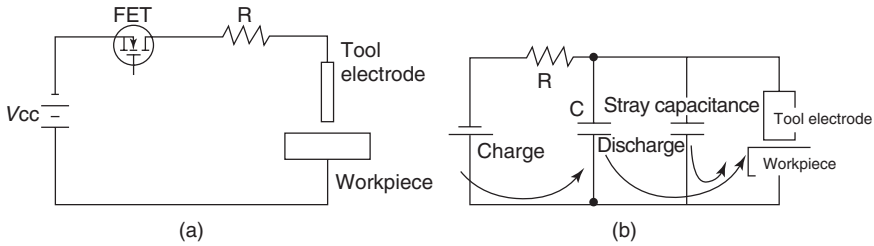

Figure 10.2 Schematic representation of basic circuit diagram of (a) transistor-type and (b) *RC*-type pulse generator.

between the direct current power supply and the discharge gap. The discharge current increases in proportion to the number of transistors, which are switched on at the same time. The switching ON–OFF of the gate control circuit is operated by the Field-effect transistor (FET). In order to generate a single pulse, the gap voltage is monitored to detect the occurrence of discharge and after the preset discharge duration, the FET is switched off.

The pulse duration and the discharge current can be arbitrarily changed in transistor-type pulse generators, depending on the machining characteristics required and provide for a very uniform pulse shape resulting in much better control of surface roughness. The discharge energy in every spark is controlled by the resistance across the circuit and the input voltage (R and Vcc in Fig. 10.2a). The smallest UR in transistor-type power supply is achieved by increasing the resistance with voltage settings at around 60 V, as voltages lower than 60 V result in unstable discharges [17,18]. Even though the UR could be minimized significantly in transistor-type circuits by increasing the resistance, difficulty arises in minimizing the UR frequency, as micro-EDM is essentially a discontinuous material removal process, as was mentioned earlier. The sparks generated from the transistor-type pulse generator can be controlled using electronics. The decision-making process of the electronics (or micro-controllers) are based on the set value of the ON/OFF time, the duty ratio, signal propagation delay as well as the inherent delay of the power transistor. All those processes contribute to more than few hundred nanoseconds, even very fast electronics are used in the setup [12,19]. This imposes a limit on the shortest pulse duration.

Transistor-type power supply is widely used in conventional EDM, where a much higher UR is acceptable for higher material removal rates (MRRs) and the achievable UR frequency is higher than the frequency that a *RC*-type circuit can provide. This is due to the fact that to provide for higher discharge energy, a larger capacitor is needed, which in turn requires a larger charging time and results in a small UR frequency.

10.2.2.2 RC-Type Pulse Generator. In an *RC*- or relaxation-type circuit, discharge pulse duration is dominated by the capacitance of the capacitor and

the inductance of the wire connecting the capacitor to the workpiece and the tool [7,8], and the discharge energy is determined by the used capacitance. In case of an ideal RC-type pulse generator shown in Fig. 10.2b, the repetition of the charging and discharging cycle occurs. During the charging cycle the capacitor C is charged through the resistor R, and discharged between the electrode and workpiece in the discharging cycle. The pulse energy E induced in the gap is calculated by using the following formula [14,18], assuming that the gap voltage V_g is constant during the discharge.

$$E = 2CV_g(V - V_g) \tag{10.1}$$

where C is the discharge capacitance and V is the supplied DC voltage. When $V = 2V_g$, the discharge energy is the maximum and equal to $0.5CV^2$, which is equal to the energy stored in the capacitor. For a more realistic case, the RC-type pulse supply will have a stray capacitance between the electric feeders, between the tool electrode holder and the work table, and between the tool electrode and the workpiece, and this results in the following modified form of the above equation:

$$E = 2(C1 + C2)V_g(V - V_g) \tag{10.2}$$

This means that the minimum achievable discharge energy per pulse is determined by the stray capacitance ($C2$) when discharge capacitance ($C1$) is set to 0, and thus, in order to reduce the pulse energy, it is important to reduce the stray capacitance between the wire and the workpiece. In the final finishing or while machining features at the lower boundary of micro-machining domain [4], a minimum discharge energy is necessary, and the capacitor is then not wired and machining is conducted with the stray capacitance only [7]. It can easily generate pulses with high peak current values and short duration, allowing efficient and accurate material removal, and meanwhile achieving the required surface quality. On a carefully designed equipment, the stray capacitance could be minimized to as small as around 10–12 pF, which can deliver 0.2-mA peak current and 30-ns wide pulse [20].

The frequency of discharge (discharge repetition rate) depends upon the charging time, which is decided by the resistor (R) used in the circuit and this provides for an additional advantage of the RC power supply: when the capacitance is reduced, the capacitor charging-up time is reduced following a first-order differential equation. The time taken for full charging-up of a capacitor is given by $5 \times RC$ and for the case of $R = 1$ kΩ and $C = 10$ pF, the full charging time of the capacitor would be around only 50 ns. Therefore, "R" should not be made very low, because arcing can occur instead of sparking and a critical resistance that will prevent arcing is desirable [21].

However, machining using the *RC* pulse generator usually has an extremely low removal rate, as the energy per spark is reduced significantly while relying on the uncontrolled spontaneous discharge frequency bottlenecked by the required capacitor charging time. In addition, uniform surface finish becomes difficult to obtain because the discharge energy varies depending on the electrical charge stored in the capacitor before dielectric breakdown. Moreover, thermal damage can occur easily on the workpiece if the dielectric strength is not recovered after the previous discharge and the current continues to flow through the same plasma channel in the gap without charging the capacitor [19].

The main reason why an *RC*-type power supply is still used in micro-EDM is the fact that the capacitor charging time for a very small capacitor is usually much smaller, around few tens of nanoseconds, than the smallest duration of the OFF time that can be reliably achieved using a transistor-type power supply designed using available electronic components. In addition, if an active control of power supply is expected upon short circuit detection, a transistor power supply would require additional tens of nanoseconds for the discharge current to diminish to zero. Therefore, in this mean time, the existing high current may pass through the circuit, causing damage to the fine features to be machined in the workpiece.

10.2.2.3 Research on Advanced Power Supply

10.2.2.3.1 Transistor-Type Isopulse Generator: Modification of Transistor-Type. The major problem of the transistor-type pulse generator is that the delay time in the transmission of detected signals is long. In order to shorten this delay time, the transistor-type isopulse generator for micro-EDM shown in Fig. 10.3a was developed [19]. Rough and semifinishing can be carried out by short-circuiting points P1 and P2, and finishing by inserting the supplementary circuit. In the case of roughing and semifinishing, the discharge current is cut off by FET1. The pulse current is monitored to detect discharge instead of monitoring the gap voltage. In addition, as the output of the current sensor is lower than 5 V, it can directly be input into the pulse control circuit, eliminating the use of the voltage attenuation circuit. As a result, the delay time in the new transistor-type isopulse generator developed was shortened to a considerable extent, and a minimum pulse duration of about 80 ns was obtained. In order to further shorten the pulse duration, it is necessary to shut off the discharge current without the use of a pulse control circuit and gate drive circuit. The circuit encircled by the dotted line shown in Fig. 10.3a was therefore developed. To shut off the discharge current immediately when discharge occurs in the gap, this circuit is activated by disconnecting points P1 and P2 and inserting the circuit between them. When discharge occurs in the gap, Tr1, Tr2, and Tr4 are turned on because of the discharge current, resulting in FET2 being turned off. Since FET2 is turned off, the discharge is stopped and the discharge current becomes zero. Hence, Tr1, Tr2, and Tr4 are turned off and FET2 is turned on, initializing the circuit autonomously.

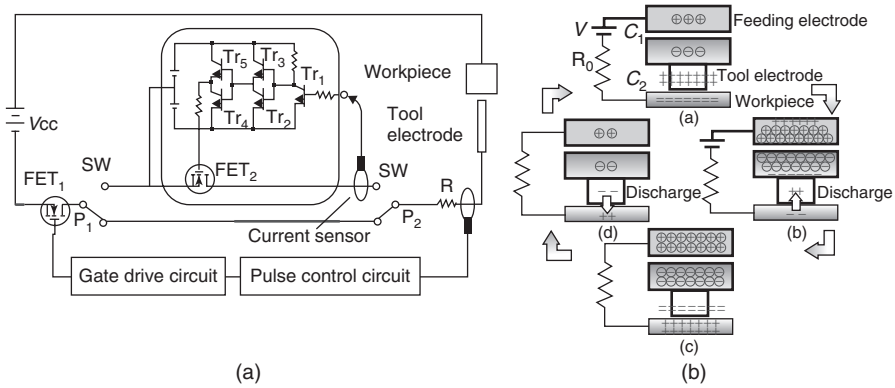

Figure 10.3 (a) Basic circuit diagram of transistor-type isopulse generator for micro-EDM [19]; (b) capacity-coupled pulse generator developed for nano-EDM [22].

10.2.2.3.2 Capacity Coupled Pulse Generator: Modification of RC-Type. During micro-EDM using RC-type pulse generator, the minimum electric discharge energy per pulse is determined by the stray capacitance, indicating a limit to miniaturization [23]. However, machining of micro-rods smaller than 1.0 μm in diameter has been found difficult because crater diameters of smaller than 2.0 μm cannot be obtained using the conventional RC-type pulse generator as the stray capacitance cannot be eliminated completely [24,25]. Therefore, a new pulse generator using the capacity coupling method was developed. With this method, as electric feeding can be carried out without contact with the tool electrode, the influence of the stray capacitance in the circuit can be eliminated, thereby realizing discharge craters of nanometer order.

As shown in Fig. 10.3b, the feeding electrode, tool electrode, and workpiece are coupled by capacity in series. In the figure, $C1$ is the capacitance of the feeding gap between the feeding electrode and the tool electrode, and $C2$ is the capacitance of the working gap between the tool electrode and workpiece. A pulse voltage V is applied between the feeding electrode and the workpiece with a constant pulse duration. R_0 is the internal electric resistance of the pulse generator. A definite distance is set between the feeding electrode and the tool electrode, in order to ensure that discharge does not occur and there is no conduction of electric charge between them. When the voltage of the pulse generator becomes V, the capacitances of both the feeding gap and the working gap, $C1$ and $C2$, are charged. In the working gap, the tool electrode and the workpiece are charged positive and negative respectively, creating a high electric field. Accordingly, discharge occurs and electrons are conducted from the workpiece to the tool electrode. As the discharge duration is significantly short, not longer than several tens of nanoseconds, the dielectric breakdown strength of the working gap is recovered immediately.

10.2.3 Variants of Micro-EDM

10.2.3.1 Die-Sinking Micro-EDM. Die-sinking micro-EDM is the earliest and most common type of micro-EDM. In die-sinking micro-EDM, electrodes with the desired micro-features are employed on the workpiece to produce corresponding mirror images. In die-sinking micro-EDM, the tool electrode has the complementary form of the finished workpiece and literally sinks into the workpiece, as can be seen in the illustration of Fig. 10.4a.

10.2.3.2 Milling Micro-EDM. Milling micro-EDM is a comparatively newer process, which eliminates the need for complex-shaped electrodes usually required in die-sinking. In this process, usually tubular or cylindrical micro-electrodes are employed to produce the desired complex shape by scanning. A cylindrical electrode rotates around its axis (Z-axis) with the scanning movements in the X and Y directions. The contour of a particular layer is specified in the part program of CNC. However, owing to tool wear, there exist serious issues in micro-EDM milling related to tool wear compensation, maintenance of tool shape from side wear while machining only by bottom wear, and control of the thickness of the layer to be machined, and therefore, quite a number of motion control strategies as well as wear compensation method have been evolved to handle such issues, each having unique advantages in specific situations [4,7]. For example, in one type of algorithm, the Z axis is expected to provide an up-and-down motion for the gap control based on the sampled gap voltage status while the X and Y axes are expected to make a linear or circular oscillatory motion [20], whereas in another algorithm, the Z axis is moved down at steps as in the milling process [7]. This is specially a challenging task from the motion control point of view to cater to all such different algorithms with the concern that a little delay in the sampling of the gap voltage can result in breakage of the fine electrode.

10.2.3.3 Micro-WEDM. Micro-WEDM (wire electrical discharge machining) is one of the variants of EDM technology that can be very well adapted for the

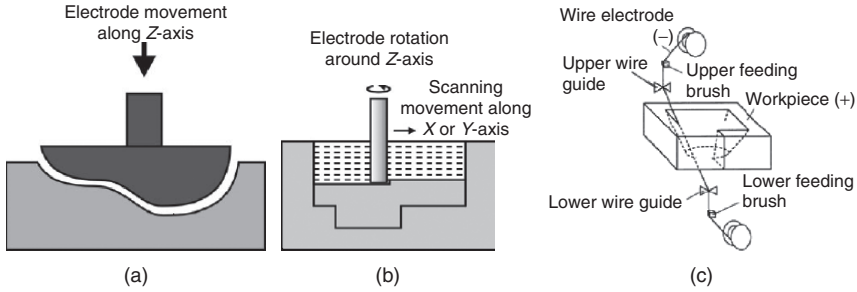

Figure 10.4 Schematic representation of (a) die-sinking micro-EDM, (b) milling micro-EDM [26], and (c) micro-WEDM [12].

micro-fabrication applications. In micro-WEDM, a continuously traveling micro-wire is used to cut through a conductive workpiece according to the programmed path. The basic mechanism of micro-WEDM is the same as that of micro-EDM as the material is removed by a series of electric sparks between the workpiece and wire electrode. Figure 10.4c schematically represents micro-WEDM.

10.2.3.4 Micro-EDG and Micro-WEDG. One of the most commonly used micro-EDM variants is the micro-electro-discharge grinding (micro-EDG). During micro-EDM, to fabricate a micro-electrode on-machine from an electrode thicker than the required one, micro-EDG with a sacrificial electrode is used. Different setup and trajectory control of the sacrificial electrode can be used in this process, such as using a "stationary block," "rotating disk," and "wire-EDG (WEDG)." In the stationary block' setup, due to dimensional changes in the sacrificial electrode, the diameter of the tool electrode fabricated is usually unpredictable, but provides a smooth surface. The use of a rotating disk involves a rather complicated setup, although it provides good shape accuracy. The WEDG process has the capability of producing extremely slender rods with good aspect ratio and has received wide industrial acceptance. The main advantage of the block electrode method is its capability to fabricate electrodes that are not cylindrical in shape (e.g., triangular or square electrode), in addition to being cheap, with lower operating costs [27]. Another important factor is that the diameter precision of commercially available brass wire commonly used for WEDG is usually ± 1 μm [28], which is added to the accuracy of micro-EDM process [23] and therefore, in some cases the surface finishing efficiency of WEDG was not found to be as high as that in the rotating disk fabrication method [29].

A process called "moving block EDG" has been developed to combine the advantages of both the "stationary block" and "rotating disk" electrode fabrication techniques. In this technique, while the tool electrode (Z-axis) controls the spark gap at the top surface of the sacrificial block, a to-and-fro relative translational motion between the block electrode and the tool electrode is provided along the longitudinal axis of the block electrode. The erosion is distributed uniformly over a larger area of the block electrode, which creates electrodes with very smooth surface and very good shape accuracy, and is not tapered. However, the length of the electrode produced is always smaller than the targeted length because of grooves created on the surface of the block electrode. Figure 10.5 shows different types of micro-EDG process for on-machine fabrication.

10.2.3.5 Micro-EDM Drilling. In micro-EDM drilling, micro-electrodes are used to "drill" micro-holes in the workpiece. However, the problem with deep small-hole drilling by micro-EDM is that forming and clamping the long electrode are difficult. Therefore, the micro-electrodes used are fabricated on-machine with high accuracy, using the different micro-EDG processes shown in Fig. 10.6. This also solves the clamping problem, because the electrode is clamped before the forming process and never reclamped until the hole is machined [13]. Figure 10.6 shows the consecutive process of on-machine electrode fabrication, measurement

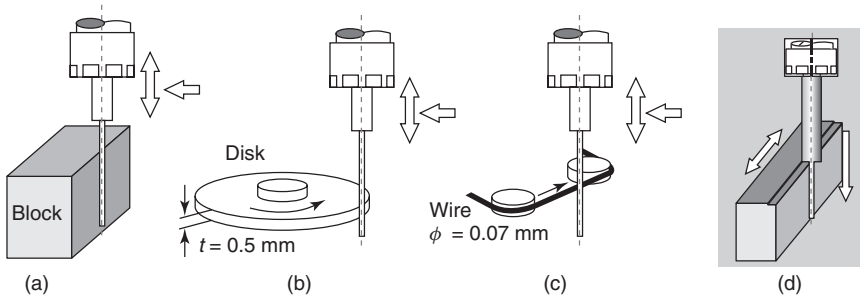

Figure 10.5 Different types of micro-EDG process using (a) stationary sacrificial block, (b) rotating sacrificial disc, (c) wire-EDG, and (d) moving BEDG process [30].

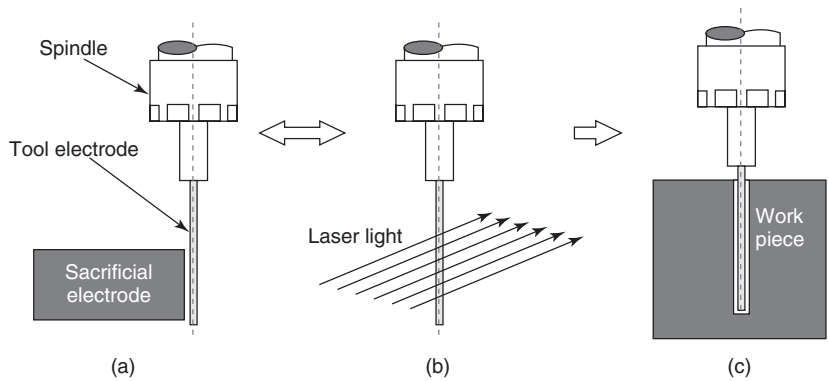

Figure 10.6 micro-EDM drilling process: (a) on-machine electrode fabrication by BEDG, (b) on-machine measure by laser, and (c) drilling of high-aspect-ratio micro-holes [29].

of micro-electrode and micro-EDM drilling with fabricated electrode. A comparison of the capabilities of five variants of micro-EDM is presented in Table 10.1.

Figure 10.6 micro-EDM drilling process: (a) on-machine electrode fabrication by Block Electro-Discharge Grinding (BEDG), (b) on-machine measure by laser, and (c) drilling of high-aspect-ratio micro-holes [29].

10.2.3.6 Planetary or Orbital Micro-EDM. One of the common problems during die-sinking micro-EDM or micro-EDM drilling is the debris accumulation, which becomes worst during machining high-aspect-ratio micro-structures. Therefore, adding a relative motion between the electrode and the workpiece, other than the electrode feeding motion, produces a wide clearance between them for fluid circulation and then reduces debris concentration, resulting in a high MRR, low electrode wear ratio, and higher machining accuracy. This results in lesser wear of the bottom edges of the tool and therefore, minimizes undesirable tapering and waviness at the bottom surface of the blind micro-hole [31]. The tool

TABLE 10.1 Comparison of the capabilities of the micro-EDM variants [8]

Micro-EDM Variant	Geometric Complexity	Minimum Feature Size	Maximum Aspect Ratio	Surface Quality, R_a (μm)
Drilling	2D	5 μm	~25	0.05–0.3
Die-sinking	3D	~20 μm	~15	0.05–0.3
Milling	3D	~20 μm	~10	0.5–1
WEDM	2.5D	~30 μm	~100	0.1–0.2
WEDG	Axi symmetric	3 μm	30	0.8

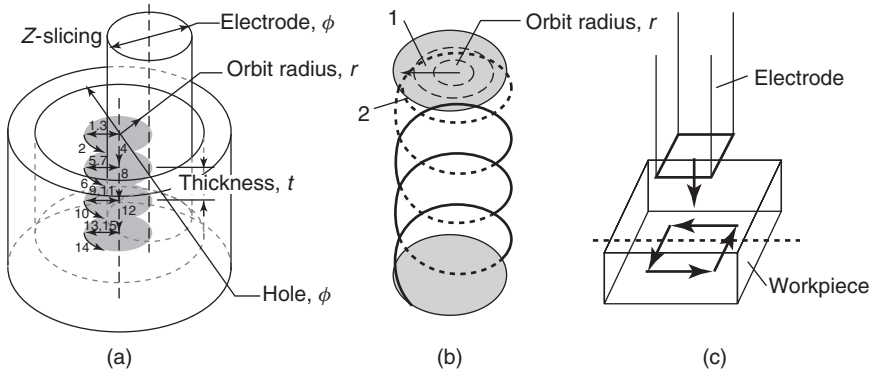

Figure 10.7 (a) Schematic representation of planetary micro-EDM, (b) the planetary movement of electrode for micro-hole [32], and (c) planetary movement for noncircular hole [31].

path depends on the complexity of the feature to be machined. Figure 10.7a–c represents the schematic of planetary micro-EDM, orbital movement for round micro-hole and for square micro-hole respectively.

10.2.3.7 Reverse Micro-EDM. Reverse micro-EDM [33] comprises different steps including fabrication of single micro-electrode, using micro-EDG; fabrication of arrays of micro-holes, which will act as the negative electrode during reverse EDM; and finally fabrication of multiple electrodes, using reverse micro-EDM. The polarity of the electrode and that of the sacrificial workpiece are interchanged during reverse micro-EDM, so that the electrode can be extruded among the arrays of micro-holes. In this process, the electrode is considered as the workpiece, and is fed down to the holes of the metal plate to be machined by electrical discharge that occurs within machining gap. However, the regions that correspond to the holes are not machined. Finally, micro-electrodes are machined as many as the holes. The principle of reverse micro-EDM is presented schematically in Fig. 10.8. Consecutive application of this reverse micro-EDM process is also known as micro-EDM^n and is capable of doing batch processing by performing repetitive pattern transfer, which is discussed in more detail in Section 10.5.4.

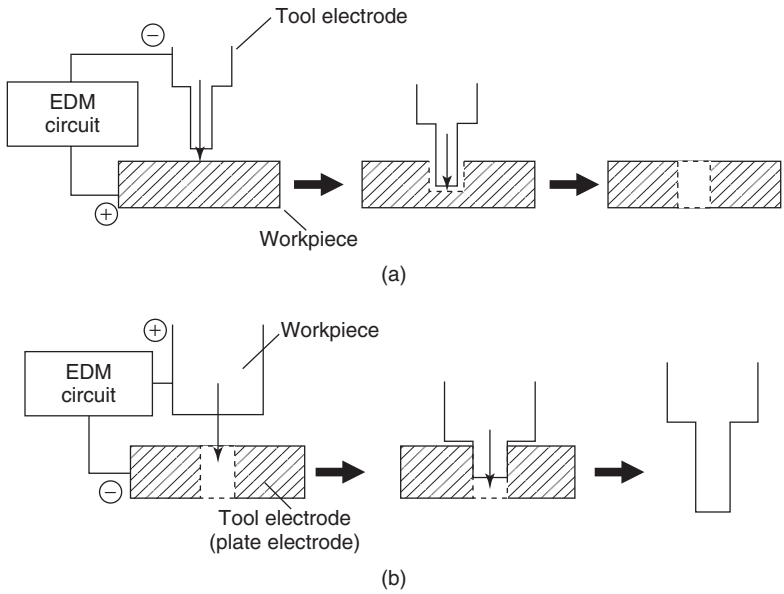

Figure 10.8 Principle of reverse micro-EDM: (a) fabrication of micro-hole using normal micro-EDM and (b) fabrication of micro-electrode using reverse micro-EDM [33].

10.3 MICRO-EDM PROCESS CONTROL PARAMETERS

10.3.1 Electrical Parameters

10.3.1.1 Pulse Waveform and Discharge Energy. The pulse shape and the discharge energy for micro-EDM depend mainly on the type of pulse generator. Figure 10.9a and b shows the ideal voltage and current signals for transistor and RC-type pulse generator respectively. The discharge energy of a pulse generator can be determined from its electrical and discharge parameters. The higher the discharge energy is, the higher the MRR will be. However, the relative electrode wear (RWR) also increases, and surface finish deteriorates with the increase in the discharge energy. The pulse shape used in micro-EDM is normally rectangular, but generators with other pulse shapes have also been developed for various functions [34]. For example, generating trapezoidal pulses during micro-EDM was found to provide reduced relative tool wear to very low values [35].

In the transistor-type pulse generator, when the transistors are switched on, the open voltage, u_e, is applied between the tool electrode and the workpiece, but discharge does not occur immediately but occurs after the ignition delay time. After the dielectric breakdown, a discharge current, i_e, is passed through the gap. The gate control circuit keeps the transistors on for the discharge duration, t_e, after the dielectric breakdown, resulting in a uniform discharge crater size. Then after the fixed discharge interval, t_0, the transistors are again switched on and the open voltage is applied between the electrodes. The discharge energy per single

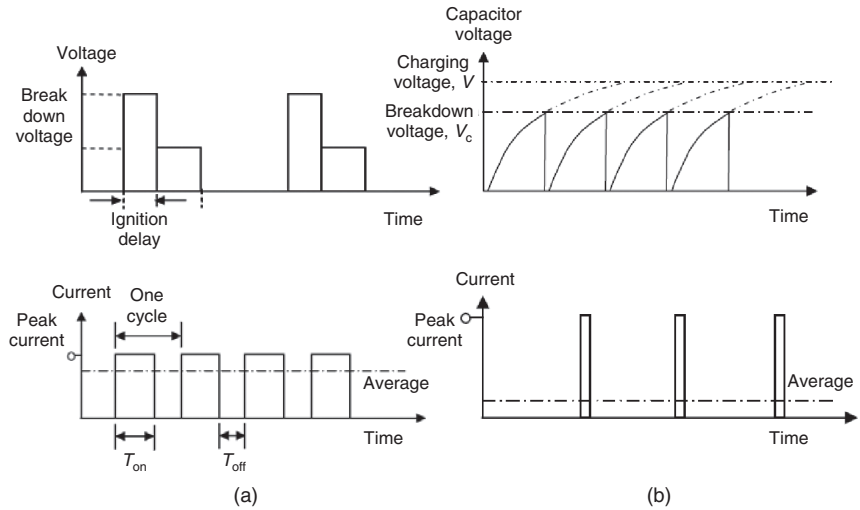

Figure 10.9 Ideal voltage–time (top) and current–time (bottom) characteristics curve/waveform for (a) transistor-type and (b) RC-type pulse generator [36–40].

pulse, q, is expressed as

$$q = u_e \times i_e \times t_e \tag{10.3}$$

where u_e is the discharge voltage, i_e is the discharge current, and t_e is the pulse duration [12].

For the RC-type, the charging time of capacitor (C) is considered as the OFF time or the pulse interval, whereas the discharging time is considered as the pulse ON time. One of the important characteristics of RC-type pulse generator is that the breakdown or discharging voltage (V) is lower than the charging voltage, and therefore, sometimes discharging starts before the capacitor is fully charged [19], which creates nonuniform discharge energy. The peak current is the amount of current that reaches before discharging starts. Considering $V = 2V_g$ in Eq. (10.1), a simplified form of the discharge energy per single pulse, q, is expressed as

$$q = (1/2)CV^2 \tag{10.4}$$

where C is the capacitance used for machining and V is the discharging voltage [15].

10.3.1.2 Discharging, Breakdown, Open-Circuit, and Gap Voltage. Discharge voltage in micro-EDM is related to the spark gap and the breakdown strength of the dielectric. Breakdown voltage is the threshold voltage at which the initiation of breakdown occurs. However, before the current can flow, the open gap voltage increases until it has created an ionization path through the dielectric. Once the current starts to flow, voltage drops and stabilizes at the working gap

level. The voltage at the gap between the electrode and the workpiece is known as gap voltage. The applied voltage determines the total energy of the spark. Higher voltage settings increase the gap, which improves the flushing conditions and helps to stabilize the machining and increase the MRR. But at the same time, higher voltage will also contribute to poor surface roughness.

10.3.1.3 Peak Current. The term "peak current" is often used to indicate the highest current during the machining. The higher the peak current is, the higher the discharge energy will be. During each ON-time pulse, the current increases until it reaches a preset level, which is expressed as the peak current. Higher currents will improve the MRR, but at the cost of surface finish and tool wear.

10.3.1.4 Pulse Duration. This is the duration of time for which the current is allowed to flow per cycle. The discharge energy is really controlled by the peak current and the length of the pulse on time. It is the "work" part of the spark cycle, when the current flows and work is done only during this time. Material removal is directly proportional to the amount of energy applied during this time. With longer period of spark duration, the resulting craters will be broader and deeper; therefore, the surface finish will be rougher. Shorter spark duration, on the other hand, helps to obtain fine surface finish. However, excessive pulse duration can be counterproductive [34].

10.3.1.5 Pulse Interval. This is the duration of time between two successive sparks when the discharge is turned off. Pulse off time is the duration of rest or pause required for reionization of the dielectric. This time allows the molten material to solidify and to be washed out of the spark gap. If the pulse off time is too short, it will cause sparks to become unstable, and then more short-circuiting will occur. On the other hand, a higher pulse off time results in higher machining time, but it can provide the stability required to successfully EDM a given application. When the pulse OFF-time is insufficient compared to the ON-time, it will cause erratic cycling and retraction of the advancing servo motors, slowing down the operation.

10.3.1.6 Duty Ratio or Duty Factor. Duty factor is a percentage of the pulse duration relative to the total cycle time. It is a measure of efficiency and is calculated by dividing the on time by the total cycle time. Generally, a higher duty factor means increased cutting efficiency. It is calculated in percentage by dividing the pulse duration by the total cycle time (ON-time + OFF-time).

10.3.1.7 Pulse Frequency. Pulse frequency is the number of cycles produced across the gap in one second. The higher the frequency is, the finer the surface finish that can be obtained will be. With an increase in the number of cycles per second, the length of the ON-time decreases. Short ON-times remove very little material and create smaller craters. This produces a smoother surface finish with less thermal damage to the workpiece. Pulse frequency is calculated by dividing 1000 by the total cycle time (ON-time + OFF-time) in microseconds [34].

10.3.1.8 Electrode Polarity. Generally, during the micro-EDM process electrons are emitted from the cathode and move toward the anode. After reaching the anode, the electrons strike the anode surface and as a result cause the metal ions to be removed from the anode material. Therefore, it is the anode that loses more weight because of more material removal from its surface. This is a more common reason for getting high MRRs when the workpiece is the anode and an electrode is used as the cathode (negative polarity) [37–41].

10.3.2 Material Parameters

10.3.2.1 Electrode Tool Material. Because micro-EDM is a thermal process, the influence of the thermal properties of the electrode materials on its performanceis significant. When the heat fluxes from the arc column are equal, higher heat conductivity results in lower temperatures on the electrode surface [12]. Hence materials with higher heat conductivity are suitable as tool electrodes. Materials with higher melting point and boiling point are also suitable as tool electrodes. The important properties of the electrode materials, including thermal and electrical conductivity, melting and boiling temperatures, and specific heat, influence the micro-EDM process [37–40].

10.3.2.2 Wire Materials for Micro-WEDM. The performance of micro-WEDM, that is, MRR, wire breakage, and speed of the machining, is influenced by the electrical properties, thermal properties, as well as tensile strength of the wire materials. The wire materials should possess high discharge capacity, low electrical resistance, and high tensile strength, at high temperatures and at a reasonably low cost. In addition, the thermal characteristics of the wire materials such as specific heat, heat conductivity, melting point, and boiling point should also be taken into consideration when selecting proper wire materials for micro-WEDM.

10.3.2.3 Dielectric Material. During the micro-EDM process, as the machining zone is immersed in the dielectric media, the properties of dielectrics such as chemical compositions, viscosity, dielectric strengths, and cooling rates play an important role. Moreover, the dielectric fluid also serves several functions such as flushing of debris from the machined zone and acting as a coolant. The higher the flash point temperature and the dielectric strength are, the safer and finer the controlled sparking will be. The lower the viscosity of the dielectric fluid is, the better the accuracy and finishing will be. Lower specific gravity and colorless dielectric are more desirable for better performance [42].

10.3.2.4 Workpiece Material. The workpiece materials should have sufficient electrical conductivity so that they can be machined by micro-EDM. The EDM machinability of a workpiece material depends on the thermal conductivity, specific heat, melting point, and evaporation point [43].

10.3.3 Mechanical and Motion Control Parameters

10.3.3.1 Gap Control and Servo Feed. Unlike other micro-machining processes, the electrode feed is not continuous during micro-EDM. The main purpose of the servo feed control is to maintain proper spark gap or gap width during the machining, in addition to ensuring that the process is more stable by minimizing the open circuit, arcing, and short-circuiting during machining. A stable gap control system enables better dimensional accuracy of micro-machined features by predicting the gap distance and offsetting tool position [8]. Larger gap width causes longer ignition delays, resulting in a higher average voltage. Tool feed speed increases when the measured average gap voltage is higher than the preset servo reference voltage and vice versa [12]. Other than the average gap voltage, the average delay time can also be used to monitor the gap width. In some cases, the average ignition delay time is used in place of the average gap voltage to monitor the gap width [44]. In addition, gap-monitoring circuits can also identify the states and ratios of gap open, normal discharge, transient arcing, harmful arcing, and short circuit [8].

10.3.3.2 Positioning Accuracy and Repeatability. During micro-EDM, the accuracy and repeatability of positioning of the machine employed is a major source of errors [45]. For both the fabrication of micro-electrodes and fabrication of micro-features, using on-machine fabricated micro-electrodes with high dimensional accuracy and repeatability, proper positioning accuracy should be maintained. The accuracy and repeatability of positioning of a micro-EDM machine can be measured using a laser interferometer. To machine a micro-hole at a specific position, the accuracy of positioning of the machine will affect mainly the position of the hole, while the repeatability of positioning will impact the size and shape of the hole. The accuracy of measurement is dependent on the speed of approach to the workpiece surface. The lower it is in relation to the speed of rotation of the electrode, the smaller the error will be.

10.3.3.3 Electrode Shape and Rotation. Electrode rotation can significantly enhance the flushing process in micro-EDM and significantly improve the overall performance of micro-EDM as well as improve dimensional accuracy and surface finish. With the increase in the electrode rotational speed, the tangential velocities of the electrode increase, which promotes the disturbance of the dielectric [46]. The increased flow speed of the dielectric helps to separate the debris from the machined zone, thus facilitating further material removal from the workpiece. The RWR decreases with increase in the electrode rotational speed.

The electrode shape can certainly improve the flushing condition and the overall performance of micro-EDM. Improved flushing of debrishas been reported with the use a single-side notch electrode compared to cylindrical electrodes [47]. Using a helical micro-tool electrode for micro-EDM combined with ultrasonic vibrations can substantially reduce the EDM gap, taper, and machining time for deep micro-hole drilling [49].

10.3.3.4 Wire Tension and Wire Speed in Micro-WEDM. The amount of wire tension affects the dynamic stability condition of the micro-WEDM process. The deflection of the wire happens because of different kinds of forces working on it, such as electromagnetic force, flushing pressure, and pressure of the spark. If tension is less, there is a greater chance of wire bending and inaccuracy in machining. Because of continuous motion of the wire, if proper tension is not maintained, there could be high vibration at the machining area. This can cause undesirable gap width, excessive short circuit, and even wire breakage. Too high wire tension again can cause the wire to break often.

Wire speed is the relative velocity of the wire at which it moves across the workpiece during machining. The speed of the wire should not be too high so as to reduce the usage of the wire. At very low speeds, the wire tends to break more often, as the same region gets eroded more, reducing the tensile strength of the wire.

10.3.3.5 Flushing Pressure and Flushing Mechanism. During micro-EDM to maintain stable machining, it is critical to flush debris particles and cool the working gap in order to prevent the localization and concentration of discharge locations [12]. High flushing pressure can improve the overall flushing mechanism, machining stability, and MRR, especially in micro-EDM drilling. However, very high pressure can increase position error, in addition to reducing dimensional accuracy due to deflection of the thin electrode used in micro-EDM. On the other hand, the particles generated in micro-EDM can quickly accumulate because of the lack of flushing pressure and create an electrical short circuit condition between the electrodes. This is aggravated by the fact that in moderate settings of micro-EDM voltage, the spark gap can be as small as 3–4 μm. Pressure or suction flushing through the holes in the electrode or workpiece remains one of the most efficient flushing methods at least if those holes have to be provided anyway, or does not harm the workpiece.

A special rotary electrode movement has been applied to enhance the pumping action of the dielectric fluid during the lifting motion [50]. Orbiting of the tool or workpiece has also been found to assist flushing and improve machining conditions. In addition, the flushing direction can have significant influence on the performance of machining. Flushing from one direction can cause increased density of debris particles in the downstream, resulting in an uneven distribution of gap width, deteriorating the machining accuracy [51]. Therefore, sometimes flushing from both sides, alternate flushing, and sweeping flushing are preferable.

10.4 MICRO-EDM PROCESS PERFORMANCE MEASUREMENTS

10.4.1 Material Removal Rate

MRR in micro-EDM is defined as the amount of material that is removed in unit time. MRR can be calculated from the volume of material removed or from the

weight difference before and after machining. It is an indication of how high or low the machining rate is and an important performance parameter in micro-EDM, as this is usually a very slow process. Higher machining productivity must also be achieved with a desired accuracy and surface finish. MRR greatly depends on the process parameters.

Higher discharging voltage, peak current, pulse duration, and duty cycle, and lower pulse interval can result in higher MRRs. In addition to these electrical parameters, other nonelectrical parameters and material properties have a significant influence on MRR. Since material is removed by sparks that are applied in discontinuous mode, the product of the crater size created by a single discharge, the sum of the pulse width and the required capacitor charging time provides an estimate of the maximum achievable MRR. However, the practically achievable MRR is smaller than maximum achievable MRR by orders of magnitude, mainly due to the stochastic nature of the formation of suitable sparking site, gap control system of the equipment, and flushing condition.

10.4.2 Tool Electrode Wear Ratio

The tool electrode wear ratio is defined as the ratio of the volume of tool electrode wear to the volume of workpiece removal. High tool wear rates result in inaccurate machining and add considerably to the expense, as the tool electrode itself must be first accurately machined. During micro-EDM, the pulse condition with shorter discharge duration and lower peak current brings about both lower tool electrode wear ratio and better surface roughness. However, the lower heat fluxes due to the lower current density at the discharge spot result in lower energy efficiency of material removal. It is seen that the tool wear characteristics are associated with material properties, specially the boiling point [52]. The volumetric wear ratio of the electrode becomes small for the electrode material with high boiling point, high melting point, and high thermal conductivity, which is independent of the workpiece materials. Corner wear of electrode is related to diffusion of heat and is more obvious in lower thermal conductivity electrodes. The wear of the electrode is also related to such factors as the distribution of discharge power between both electrodes and the thermodynamic constants of materials. To reduce the influence of electrode wear, it is necessary either to feed an electrode of thickness larger than the workpiece thickness in the case of making through-holes, or to prepare several electrodes for roughing and finishing, as in the current technology [52].

10.4.3 Surface Quality

The term surface quality comprises average surface roughness, peak-to-valley roughness, surface topography, crater characteristics, and overall surface integrity. In micro-EDM, the surface topography and roughness are determined largely by eroded crater size and crater uniformity related to discharge pulse energy [8,37–40]. Smaller pulse duration results in generation of smaller craters on the

surface. The recast layer caused by micro-EDM can be reduced by changing the tool path or layer depth, or can be removed using powder-mixed dielectric. The addition of conductive or semiconductive micro/nano powders to the dielectric in a suitable concentration can significantly reduce the surface roughness, in addition to making the surface glossy. The depth of the recast layer is influenced by the resistance and the capacity in the circuit, both of which impact on the discharge energy. Higher energy leads to thicker recast layer [53]. Low open-circuit voltage, shorter pulse duration with higher frequency, and enough higher pulse interval produce small craters and hence lesser surface roughness [16]. The roughness of the electro-discharge machined surface improves with the increase of dielectric fluid pressure. However, very high dielectric pressure may not be favorable for better surface finish of the machined product [37–40].

10.4.4 Spark Gap/Kerf Width/Gap Width

For micro-EDM, there must always be a small space between the electrode and the workpiece, known as the spark gap in die-sinking micro-EDM. For micro-WEDM, the spark gap is more commonly referred to as kerf width or gap width. It is equal to half of the value obtained by subtracting the tool/wire diameter from the diameter of the machined periphery. This spark gap or kerf width affects the ability to achieve dimensional accuracy and surface finishes. The lower and more consistent the size of the gap is, the more predictable the resulting dimension and machining accuracy will be. During micro-EDM, in order to achieve micro-features, the spark gap should be very small [45]. It has been found that the spark gap has a proportional relationship with the gap voltage [54]. However, the spark gap and surface roughness are also influenced by pulse width. The peak current and the applied energy also influence the spark gap. Therefore, the main parameters affecting spark gap were identified as open-circuit voltage, peak current, and pulse ON time.

10.4.5 Tolerances and Limitation of Miniaturization Based on Micro-EDM

As micro-EDM has much promise for the fabrication of micro-features, it is important to understand the various factors affecting the minimal dimensions achievable by micro-EDM. The minimum feature size attainable by a micro-EDM setup is not limited merely by the precision of the motion devices and electrodes used, but mainly coupled to the spark energy delivered in every quanta and can be estimated by simple knowledge of the roughness of a surface created by every crater at the applied energy being employed. It is postulated that feature size is unachievable when there is no material left in some places of a machined feature because of overlapping of valleys from one surface with the valleys of the

adjacent surface and therefore, minimum attainable feature size can be estimated from the accuracy of the motion control system and a delta amount added to two times R_z—average distance between the highest peak and lowest valley formed from the spark energy provided by the power supply settings. This has been illustrated in Fig. 10.10, taking the case of machining a vertical wall as a feature and therefore, milling micro-EDM is performed on both sides of the wall. In the schematic, a top view of a wall is shown, which experienced micro-EDM on both sides of the wall. When the two rough surfaces overlap, as in the second case, the machined structure becomes discontinuous because of overlapping of valleys causing formation of holes in the wall, resulting in an unsuccessful machining of the feature.

In addition, the limitations and tolerances of miniaturization in micro-EDM depend greatly on residual stress, subsurface layer damages, and material structure of the workpiece [12]. It was found that cemented tungsten carbide micro-rods (grain size 0.4 μm) smaller than 2.3 μm in diameter could not be obtained by micro-EDM even after a large number of repeated experiments [23–25,55]. The minimum diameter of the micro-rod was found to be almost the same whether the rod is used as the anode or the cathode in WEDG. By reducing the open-circuit voltage to 20 V, a minimum rod diameter of 1 μm was obtained [8]. The minimum machinable thickness of a micro-wall was smaller when monocrystal tungsten was used compared with polycrystal tungsten. However, as cracks were generated parallel to it, it is not always true that the monocrystal is more suitable for miniaturization than polycrystal.

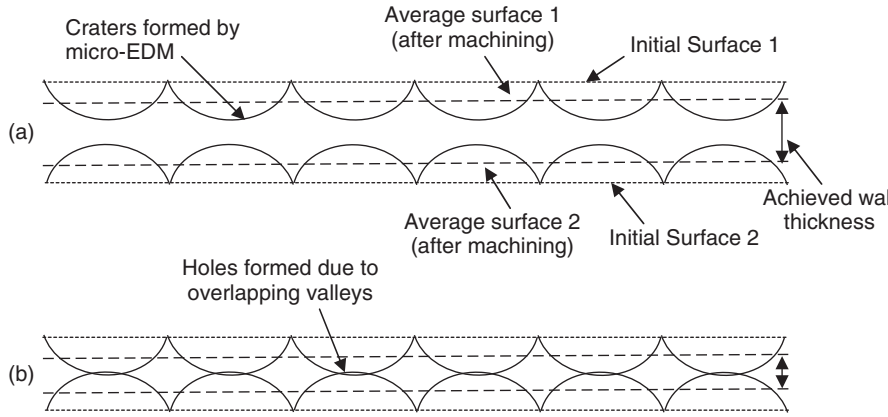

Figure 10.10 Schematic showing the simplified estimation of minimum achievable feature size from crater size of micro-EDM: (a) shows a top view of a case of forming a thin wall by micro-EDM milling on both sides of the wall and (b) shows failure in machining because of the expected wall thickness being smaller than twice the average crater size.

10.5 MICRO-EDM PROCESS APPLICATIONS AND EXAMPLES

10.5.1 On-Machine Electrode Fabrication

The noncontact nature of micro-EDM makes it possible to use a very long and thin electrode for machining tough die materials. However, during micro-EDM, changing the micro-electrode during machining is not recommended, because it incurs inaccuracy due to the change in the setup or reclamping of the micro-electrode. From an electrode thicker than the required diameter, a cylindrical electrode is fabricated by EDG, using a sacrificial electrode. Different types of setup and trajectory control of the sacrificial electrode can be used in this process, such as "stationary block," "rotating disk," "wire-EDG (WEDG)," and moving BEDG. Figure 10.11 shows the fabricated micro-electrodes using stationary BEDG, moving BEDG, and micro-WEDG and rotating disk EDG. It has been reported that, among the various micro-EDM techniques used for on-machine fabrication, micro-WEDG and moving BEDG can produce dimensionally more accurate micro-electrodes with better surface finish. However, micro-electrodes with a lowest diameter of 4.3 μm diameter were obtained by micro-WEDG process.

10.5.2 On-Machine Cutting Tool Fabrication Using Micro-EDM

10.5.2.1 Ultrasharp Micro-Turning Tool Fabrication by Micro-EDM. Commercially available polycrystalline diamond (PCD) inserts, designed for light finishing cut, have a relatively large tool nose radius, for example, 100-μm (Fig. 10.12a). This tool nose resolves the cutting force on the shaft into two components, namely F_x and F_y, as can be seen in Fig. 10.12a. The F_y component of the cutting force does the actual cutting, while the F_x component causes deflection of the micro-shaft. A commercially available PCD insert can be modified to achieve a very sharp cutting edge, so as to reduce the F_x component of the cutting force significantly, which is illustrated in Fig. 10.12b. Thus, this makes it possible to achieve a straight shaft of a much smaller diameter. A comparison of micro-shafts fabricated with round tool nose and modified tool nose is shown in Fig. 10.12.

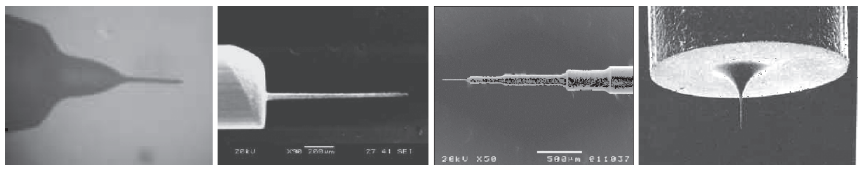

(a) (b) (c) (d)

Figure 10.11 On-machine fabricated micro-electrodes obtained by (a) 44.5-μm CuW electrode by stationary BEDG, (b) 45-μm W electrode by moving BEDG process [30], (c) 10-μm electrode fabricated by micro-WEDG process [56], and (d) 4.3-μm diameter shaft by micro-WEDG process [24].

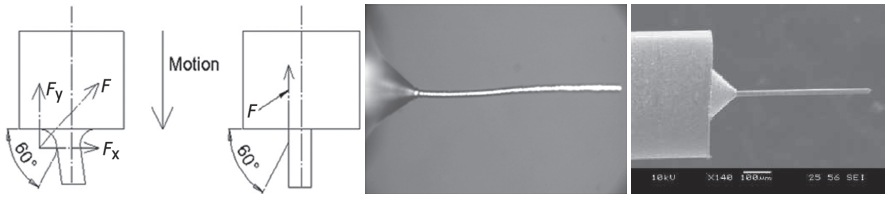

Figure 10.12 (a) Resolution of cutting force components (F_x and F_y) in commercial PCD cutting tool, (b) cutting force component after modification of cutter, (c) fabricated 100-μm shaft by conventional μ-turning, and (d) 19-μm electrode of 500-μm fabricated by modified PCD cutter [30].

10.5.2.2 Fabrication of Milling Tool. The use of micro-WEDG for the production of milling tools has several advantages. The geometry can be changed quite easily and the potential of scaling down the size of the milling tools is very high. In comparison to other contactless machining technologies, micro-EDM has an acceptable machining time and the resulting costs for the machining are tolerable in comparison to machining with ion beam. An advantage of using the micro-EDM for the milling process is the prevention of inaccuracy by rechucking processes [57]. Figure 10.13 shows the fabricated milling tool, the machined slot, and chips generated during milling. Moreover, fabrication of micro-end-mill with a single flute using micro-WEDG for milling has been reported by Morgan *et al*. [58] for milling soft materials such as brass and aluminum. Figure 10.14a shows a SEM micro-graph of a 100-μm diameter tungsten carbide micro-tool. The fabricated micro-slot and surface roughness in aluminum after mechanical cutting are shown in Fig. 10.14b and c, respectively. Tungsten carbide was chosen as the tool material because of its high hardness and low wear rate. Three-fourths of the cylinder was removed to provide a single cutting edge, and then a 45° slice was also removed from the nose of the tool to provide clearance for various micro-milling applications. Micro-tools fabricated by WEDG have been used to

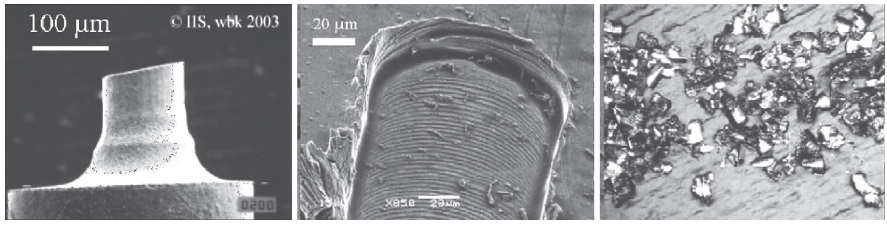

Figure 10.13 (a) 100-μm-diameter milling tools in tungsten carbide fabricated by micro-WEDG, (b) surface finish and edge of the slot machined by fabricated milling tool, (c) chips generated during micro-milling.

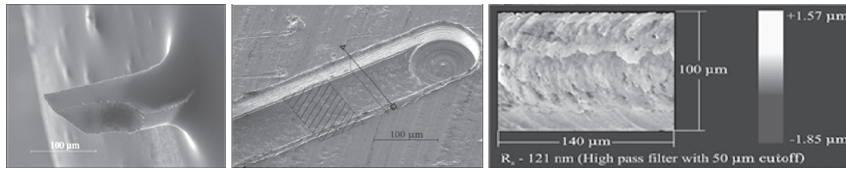

(a) (b) (c)

Figure 10.14 (a) 100-μm-diameter tungsten carbide micro-tools fabricated by micro-WEDG, (b) micro-graph of square groove machined in AA3003 aluminum, and (c) R_a of 121 nm on the bottom of the groove [58].

remove material by mechanical cutting, rather than by electrical discharges, to achieve better surface finish and higher MRR.

10.5.2.3 Fabrication of Micro-Grinding Tools. Another important application of micro-EDM is the fabrication of micro-grinding tools, using PCD or tungsten carbide materials. PCD, which can be shaped with WEDG, is emerging as a tool material for micro-grinding hard and brittle materials. The cobalt binder provides an electrically conductive network that can be removed with EDM [58]. The diamond cutting edges are exposed as the discharges erode away the cobalt binder. Figure 10.15a shows a SEM micro-graph of a 95-μm-diameter PCD grinding tool (grain size of 0.5-μm) with a flute to allow swarf when reaming holes. The ground surface of the micro-hole after reaming is shown in Fig. 10.15b. The resulting R_a is 41 nm, as against 388 nm achieved by micro-EDM alone. The MRR is approximately half that obtainded by micro-EDM alone, but the surface finish is improved by one order of magnitude.

In addition to reaming of micro-holes, grinding of micro-slots and machining of V-grooves with fabricated PCD tool have been reported [59]. Figure 10.16a shows an example of 95-μm-diameter PCD tool fabricated by micro-EDM. The fabricated groove with a pitch of 100 μm, a length of 90 μm, and a depth of 35 μm in tungsten carbide machined by the PCD tool, and V-grooves with a groove width of 30 μm were cut to form a cross pattern in nickel, as shown in Fig. 10.16b and c, respectively.

10.5.3 Fabrication of Micro-Rods Using Self-Drilled Holes (Holes Drilled by the Same Micro-Rods)

An interesting technique of fabricating micro-rods using micro-EDM is that using the rod electrode to first machine a specific feature hole and then using the machined feature hole to shape the same rod electrode [60]. After the rod electrode returns to the initial position, the axis of the rod electrode is off-centered from the center of the hole at a certain distance. The polarity of the rod electrode is then reversed, and the rod electrode is fed into the plate electrode, with or without rotation. Because holes are formed by the rod electrode itself, the rod electrode

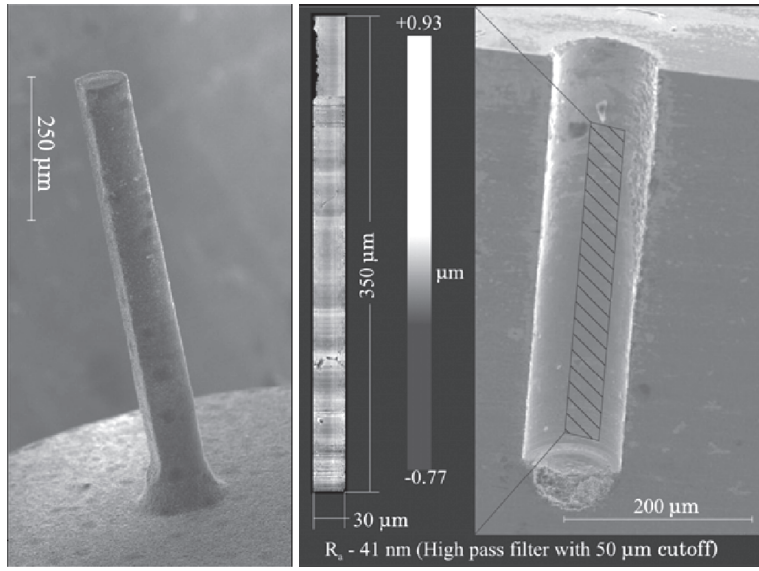

(a) (b)

Figure 10.15 (a) SEM micro-graph of a D-shaped PCD micro-tool used to ream holes and (b) micro-graph of holes ground with a D-shaped PCD tool [58].

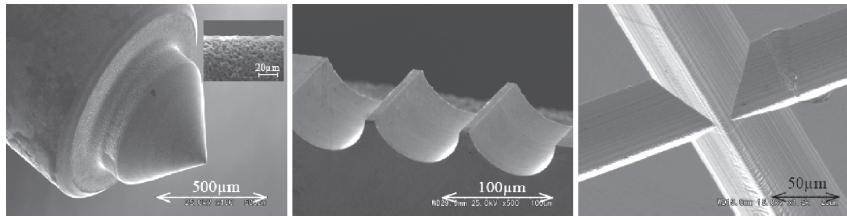

(a) (b) (c)

Figure 10.16 (a) Tool fabricated by micro-EDM, (b) micro-machined groove in WC, and (c) V-groove on Ni surface [59].

can be machined precisely (i.e., without need for alignment). As this method does not need initial positioning of the tool electrode with respect to the plate electrode, the operation is easy and short. Figure 10.17 shows micro-electrodes with different structures using this method.

10.5.4 Repetitive Pattern Transfer and Batch Processing

In recent years, micro-EDM has been found to be a flexible technique for repetitive pattern transfer batch processing. Micro-structures that are commonly found

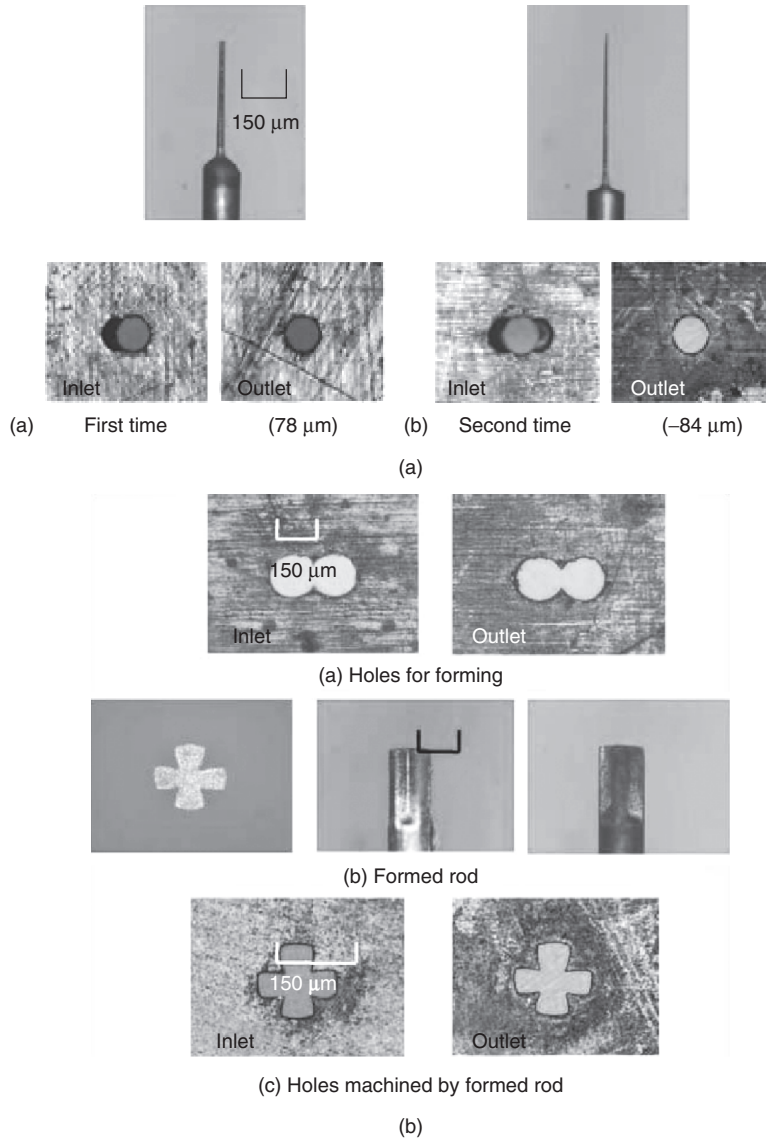

Figure 10.17 (a) Micro-electrodes obtained by double forming, (b) micro-electrode and micro-hole obtained by cross-shaped section, and (c) micro-electrode and micro-hole obtained by cross-shaped right-angled rod [60].

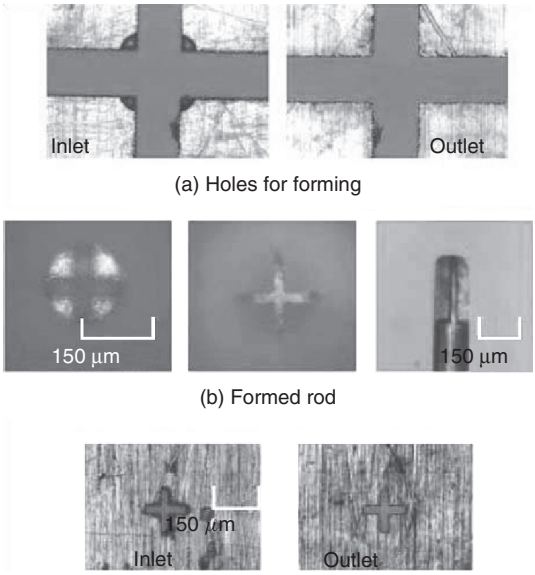

Figure 10.17 (*Continued*)

to be patterned using micro-EDM are arrays of micro-holes, micro-disk, or micro-slit. The major advantage of micro-EDM as a pattern transfer and batch mode processing technique over Lithographie, Galvanoformung, Abformung (Lithography, Electroplating, and Molding, LIGA) and other photographic technique is that it can be applied to a wide range of materials. Miniature parts with high-density micro-holes are often used in the micro-mask in the MEMS process, biochips for handling individual embryo cells, ultrasonic-vibration-assisted atomizer for the treatment of medicine and the micro-device in aerostatic air bearing systems [61]. A large number of micro-holes are needed for biomedical parts, ink-jet nozzles, and micro-droplet spraying parts.

There are several micro-EDM-based techniques that have been applied successfully for the batch mode production. Figure 10.18 shows a novel approach to improving the throughput in micro-EDM [62]. In the first step ($n = 1$), a single micro-cylindrical electrode is made by WEDG. In the second step ($n = 2$), a plate electrode is perforated to have a pattern of holes, using the cylindrical electrode made in the first step. In the third step ($n = 3$), using the plate electrode as tool electrode, the pattern is replicated to a block workpiece. In the next step ($n = 4$), the workpiece is used as the tool electrode to make many patterns of holes precisely and efficiently. After this, steps 3 and 4 may be repeated to obtain numerous holes.

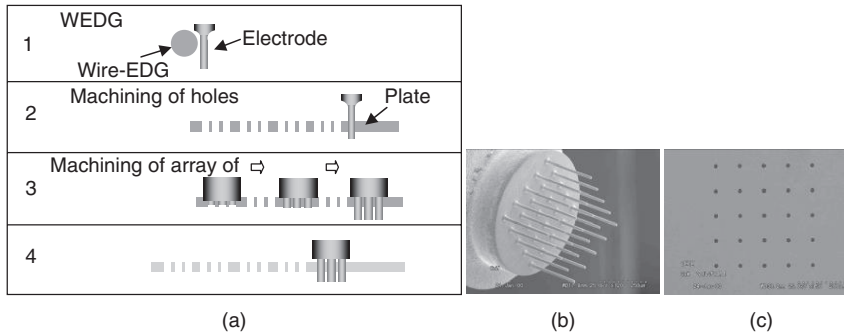

Figure 10.18 (a) Schematic representation of micro-EDM^n, (b) fabricated arrays of micro-electrodes, and (c) array of micro-holes obtained by pattern transfer [62,63].

Another micro-WEDM-based technique used for the fabrication of arrays of micro-electrodes and upward batch micro-EDM drilling for fabrication of micro-holes were developed [61]. In order to drill the micro-hole arrays in an efficient manner, the miniature of high-aspect-ratio micro-structure arrays with a (10 × 10) squared micro-batch of electrodes is designed. The micro-electrode arrays are made of tungsten carbide with a diameter of 800 μm cut with a horizontal wire from top to bottom (Fig. 10.19a and b). To provide the electrode with an adequate length during discharging, each micro-pillar is fabricated to have a length greater than 700 μm. Thereafter, the arrays of micro-electrodes are used to fabricate arrays of micro-holes, using upward batch micro-EDM (Fig. 10.19c and d).

In recent years, for the fabrication of multiple electrodes or arrays of micro-electrodes, a newer technique named as reverse micro-EDM has been found very useful. In this process, the electrode is considered as the workpiece, and is fed down to the holes of the metal plate to be machined by electrical discharge that occurs within the machining gap. However, the regions that correspond to the holes are not machined. Finally, as many microelectrodes are machined as there are holes. Figure 10.20a and b shows the plate electrode used for reverse micro-EDM with arrays of micro-holes and fabricated arrays of micro-electrodes, respectively.

Besides arrays of micro-holes, fabricating series-pattern micro-disk electrode by micro-WEDG and its application in machining micro-slit by micro-EDM was developed [64]. First, a raw pin clamped at the mandrel and rotated horizontally on the bearing surface is machined into the required length and diameter. Then, the wire traveling on the wire guide can be fed toward the radial direction of pin up to the required depth. The disk thickness is dominated by tracking path of wire electrode. The fabricated single micro-rotating disk electrode (MRDE) can also act as a tool electrode for fabricating arrays of micro-slits. The MRDE can then be fed into the workpiece from the surface upto the appropriate depth. A straight line with a micro-slit can therefore be formed by moving the Y-stage carrying the workpiece and an array of micro-disks is generated by micro-EDM (Fig. 10.21).

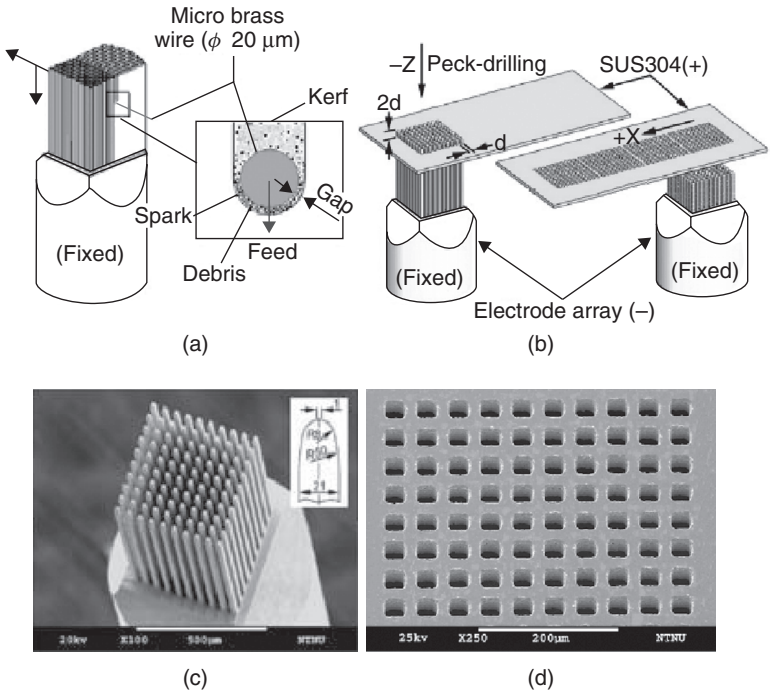

Figure 10.19 (a) Schematic illustration of micro-electrode arrays using micro-WEDM, (b) illustration of upward batch micro-EDM, (c) fabricated arrays of micro-electrodes, and (d) pattern transfer by upward batch micro-EDM [61].

10.5.5 Micro-Cavity and Micro-Structure Formation by Die-Sinking

Micro-die-sinking using microstructured form electrodes is used mainly for the manufacture of replication tools for micro-injection molding or hot embossing, where micro-mechanical parts can be produced in large numbers. High wear resistant composites based on refractory materials such as tungsten–copper or cemented carbide are preferred in micro-die-sinking EDM. Conventional flushing strategies cannot be used in micro-die-sinking EDM, as flushing through the electrodes is not possible because of their small dimensions. Together with the extremely small gap width, the poor flushing conditions put great demands on feed control in die-sinking micro-EDM [65]. Figure 10.22 shows different micro-die-sinking electrodes and fabricated micro-structures using complex-shaped electrodes.

10.5.6 3D Micro-Features and Micro-Mold Fabrication by Micro-EDM-Milling

Micro-moulds with widely spread micro-structures, such as those needed in glass embossing processes for flat panel displays, can often not be structured

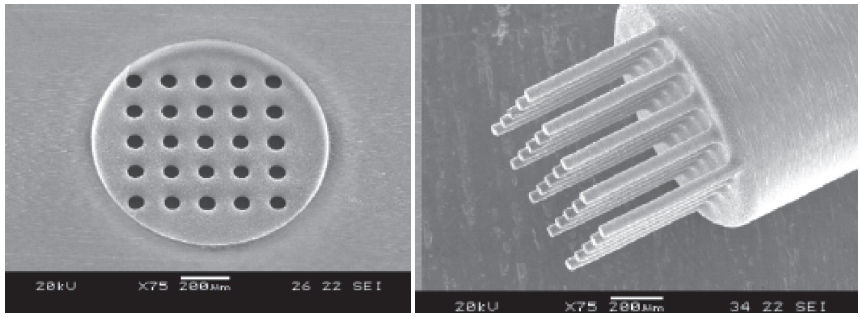

(a) (b)

Figure 10.20 (a) Plate electrodes for Reverse Electro-Discharge Machining (REDM) and (b) 5 × 5 arrays of multiple (diameter 35 μm, length 1.5 mm) micro-electrodes machined by reverse micro-EDM [33].

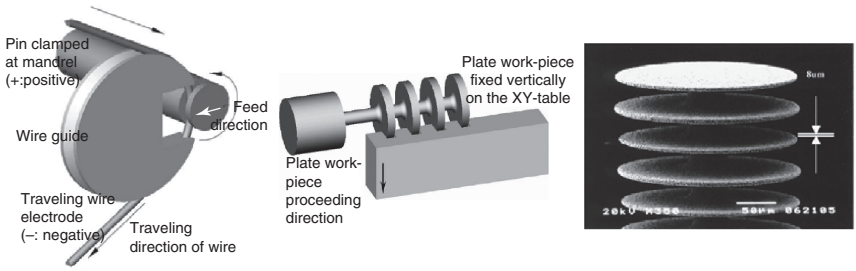

(a) (b) (c)

Figure 10.21 (a) The schematic representation of fabrication of the single micro-disk using micro-WEDG mechanism, (b) schematic representation for cutting the arrays of micro-slit using the MRDE, and (c) the photograph of series-pattern micro-disk [64].

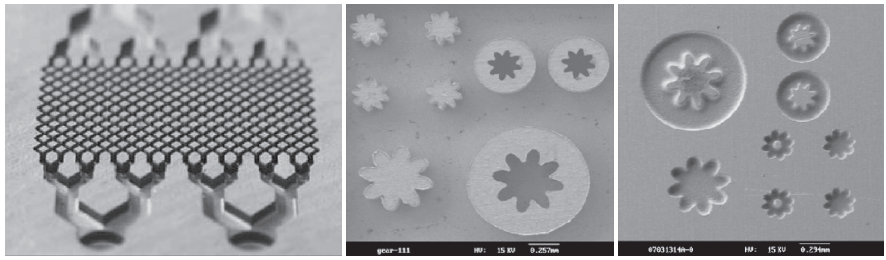

(a) (b) (c)

Figure 10.22 (a) Micro die-sinking electrode for micro-mixing device made of fine-grained graphite machined [65], (b) fabricated micro-gear-electrodes, and (c) gear-array micro-structures by die-sinking micro-EDM [66].

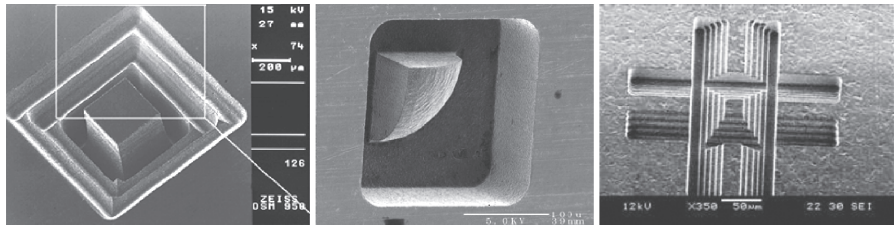

(a) (b) (c)

Figure 10.23 (a) Micro-cavity in hot forming tool steel using a simple electrode of 100 µm [65], (b) 1/8 ball in a square cavity [67], and (c) small pyramid (L: 25 mm, W: 25 mm, H: 35 mm, step size 7 mm) by micro-EDM milling [30].

by micro-WEDM or die-sinking micro-EDM because of their dimensions. Micro-EDM milling is mainly used when large and complex geometries are required. As an alternative, micro-EDM milling can be used in which a path-controlled multiaxis feed motion is performed between the rotating tool electrode and the workpiece. The use of geometrically simple rotating electrodes significantly decreases effort and costs for electrode production. Either commercially available micro-electrodes can be used or micro-electrodes can be machined on-machine by micro-EDG. The minimum structural dimensions are determined by the diameter of the pin electrodes and the gap width. Figure 10.23 shows the various micro-cavities fabricated by using milling micro-EDM with on-machine-fabricated electrode.

During micro-EDM milling of 3D micro-structures, a specific CAD/CAM system is needed for generating tool path and related machining process. When a 3D microstructure is machined, it is necessary to compensate for the worn length of the electrode. Compensation of electrode wear can be obtained though evaluating the electrode wear ratio. However, when a 3D cavity has an irregular geometry and the surface is very hard to describe by the general mathematical equation, the evaluation of electrode wear ratio becomes very difficult. Furthermore, the machining environment is not uniform in the various parts of the workpiece with a complicated cavity. Therefore, the on-line measurement of the electrode wear is necessary for maintaining the machining accuracy. Two tool wear compensation methods namely, the linear compensation [26,68] and uniform wear method [69], have been used in micro-EDM. The linear compensation consists in feeding the tool toward the workpiece and compensating for tool wear length after it moves along a certain distance. It is suitable for generation of 3D cavities with straight side walls. The uniform wear method includes tool path design rules and tool wear compensation. Tool paths designed on the basis of the uniform wear method can keep tool wear uniform at the tool tip. This method has been verified by generating 3D micro-cavities with inclined side surfaces and spherical surfaces successfully as shown in Fig. 10.24.

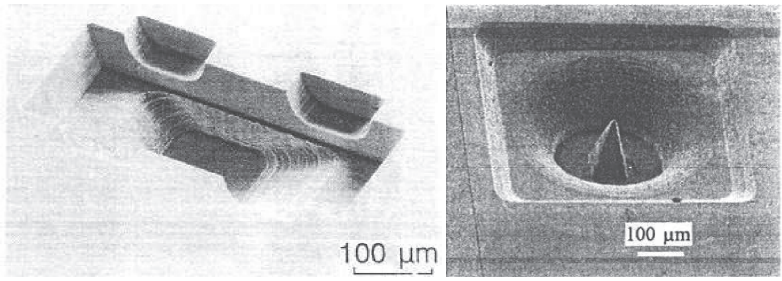

(a) (b)

Figure 10.24 (a) 3D cavities using uniform wear method: micro-mould of a car [69] and (b) 3D Micro-EDM using CAD/CAM [7].

10.5.7 Fabrication of Fine Features Using Micro-EDM Milling

Micro-EDM milling can also fabricate fine micro-features with sharp and smooth edges and thus can replace the need for setting up micro-WEDM attachment and can save machining time. Moreover, these micro-features with especial shapes can be fabricated more easily compared to die-sinking, where the electrodes need to be fabricated. Figure 10.25 shows various fine features with sharp and burr-free edges, fabricated by micro-EDM milling.

10.5.8 Smaller and High-Aspect-Ratio Micro-holes and Nozzle Fabrication

Micro-holes are the most basic machined features of micro-machining. Micro-holes are found in various applications such as fuel injection nozzles, spinneret holes, standard defects for testing material, and biomedical filters [15]. In recent years, micro-EDM has been found inevitable in the fabrication of high-aspect-ratio micro-holes in difficult-to-cut materials, where conventional micro-drilling process is found difficult. However, the micro-electrodes have to be fabricated

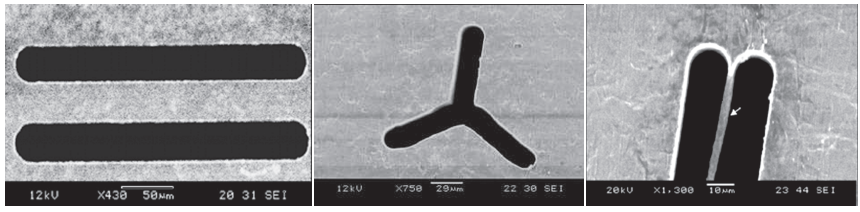

(a) (b) (c)

Figure 10.25 Fine features (through) fabricated by micro-EDM milling; micro-slots of 30 μm width, (b) micro spinneret of 12 μm width, and (c) two 10-μm slots with 2.5-μm-thick separating wall on a 50-μm-thick SUS 304 stainless steel [30].

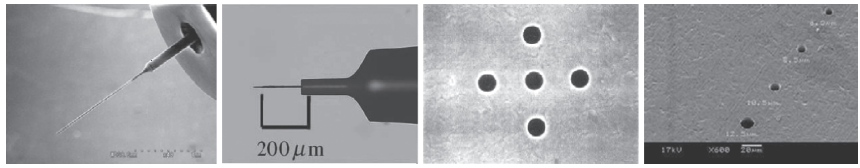

Figure 10.26 (a) 4.3-μm micro-electrode fabricated on-machine by micro-WEDG, (b) 4-μm micro-electrode fabricated by self-drilled hole [60], (c) 5-μm-diameter holes in stainless steel 10 μm in thickness, and (d) 6.5-μm hole machined on 50-μm stainless steel plate [30].

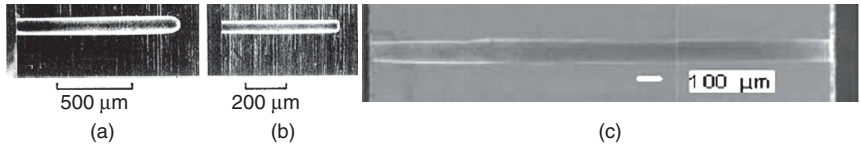

Figure 10.27 Cross section of high-aspect-ratio micro-holes: (a) 80 μm diameter, (b) 40 μm diameter [13], and (c) 120 μm diameter [31].

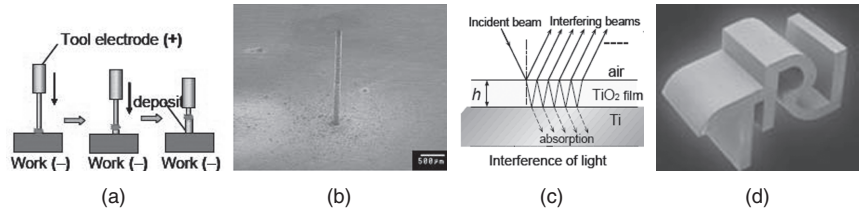

Figure 10.28 Innovative application of micro-EDM: (a) principle of micro-EDM deposition technique, (b) deposited micro-electrode [70], (c) principle of coloring technique by micro-WEDM, and (d) coloring of titanium alloy after micro-WEDM [71].

on-machine using any of the micro-EDG processes in order to maintain high accuracy and reducing clamping and position error. In most of the cases, micro-EDM drilling is vertical drilling with the assistance of electric spark. Figure 10.26 shows some examples of very fine micro-electrodes and micro-holes obtained by micro-EDM drilling.

Besides vertical-type micro-EDM drilling, horizontal-type drilling was also established in order to remove the debris easily and improve the flushing conditions, especially for deep-hole drilling [13]. Using the developed horizontal system, 50-μm-diameter micro-holes with 10 times the usual aspect ratio were fabricated (Fig. 10.27a and b). In addition, high-aspect-ratio blind micro-holes of aspect ratio upto 18 with sharp edges are fabricated using micro-EDM drilling with planetary tool movement (Fig. 10.27c) [69].

10.5.9 Other Innovative Applications of Micro-EDM

Hayakawa *et al*. [70] fabricated a microstructure shown in Fig. 10.28b, using EDM deposition in air. The suitable discharge conditions for this process were predicted from the transient temperature analysis of the tool electrode and the workpiece. To enhance the wear of the tool electrode, its polarity was set positive, which is opposite to the above coating and alloying methods, because removal rate of the anode is higher than that of the cathode in air. The process is considered similar to dry EDM where the air is used as dielectric medium and the deposition is done using EDM conditions. Minami *et al*. [71] developed a new method of coloring titanium alloys, using the WEDM process. Because deionized water is normally used in WEDM, an oxide layer is formed over the surface of the anode workpiece because of electrolysis. It is known that the surface of titanium alloy and stainless steel can be colored by anodic oxidation due to the interference of light in the oxide film formed by electrolysis (Fig. 10.28c and d). The process is considered as an EDM process, as deionized water is used instead of an electrolyte in addition to other EDM conditions. However, the effect of coloring can be considered as a result of cocurrent EDM and Electro-Chemical Machining (ECM), as the coloring is due to the formation of an oxide layer.

10.6 RECENT DEVELOPMENTS AND RESEARCH ON MICRO-EDM

Although micro-EDM is found to be capable of machining any conductive material regardless of hardness, micro-EDM alone cannot fulfill many requirements of the performance of the machined part owing to several disadvantages like slow machining rate, high tool wear, and defective surface finish. Therefore, to establish micro-EDM as an effective process and to overcome the shortcomings of micro-EDM process alone, recent research trends have focused on the development of micro-EDM-based compound and hybrid machining processes. Compound micro-machining can be defined as a combination of two different machining processes in a single setup one after another. Some recent developments in compound processes include LIGA and micro-EDM, micro-EDM and micro-grinding, micro-EDM and micro-ECM, and micro-EDM and micro-USM. On the other hand, the hybrid process can be defined as an integrated application or combination of different physical active principles in a single process. Some current research trends in micro-EDM-based hybrid processes are vibration-assisted micro-EDM, powder-mixed micro-EDM, and micro-ECDM.

10.6.1 LIGA and Micro-EDM

LIGA [a German acronym for "Lithographie, Galvanoformung, Abformung," in English (X-ray) Lithography, Electroplating, and Molding] can produce high-aspect-ratio micro-structures with ultrafine patterns and very smooth sidewall surfaces, but electroplating is limited to a few metals, such as copper,

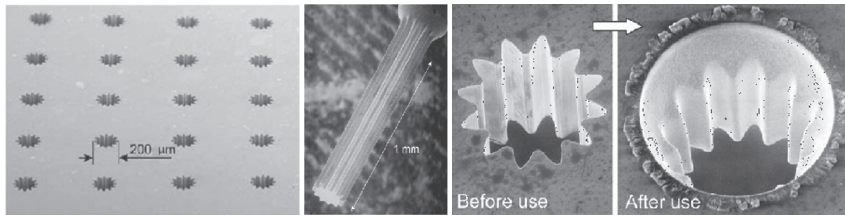

Figure 10.29 (a) arrays of negative-type nickel electrodes fabricated by LIGA, (b) high-aspect-ratio WC–Co micro-structures produced by micro-EDM, (c) initial negative-type electrode before micro-EDM, and (d) negative-type electrode after micro-EDM [72].

and their alloys. On the other hand, micro-EDM can produce 3D micro-structures in any electrically conductive material. Therefore, in this compound process, first an array of negative-type electrodes with gear pattern was fabricated in nickel, using the LIGA process. After that, a positive-type patterned structure is produced by feeding WC–Co workpiece into one of the electrodes with discharging. Therefore, a very hig h aspect ratio patterned micro-structure is obtained, which can be used for further fabrication of patterned micro-holes using micro-EDM. Figure 10.29 presents the sequence of the LIGA and micro-EDM compound process and fabricated micro-structure.

10.6.2 Micro-EDM and Micro-Grinding

In this process, a PCD tool is fabricated on-machine to a desired shape using the micro-EDM process. Thereafter, the fabricated micro-electrode is used for grinding brittle and hard glass materials with the help of diamond particles that extrude from the matrix metal and act as cutter. When the PCD tool is fabricated by EDM, the binder material (usually Nickel or WC) is removed as it is conductive, thus making the diamond particles, which are nonconductive, protrude. The randomly distributed protrusions of diamond with dimensions around 1 μm serve as the cutting edges for micro-machining on glass. The scratches were found to produce ductile chips that were attached to the edge of the groove, and subsurface damage was not visible in the glass workpiece. This suggested that the PCD material could be suitable for grinding nonconductive brittle materials. Figures 10.30 and 10.31 show two different studies of glass micro-grinding using on-machine-fabricated PCD tool, where the PCD tool is prepared by micro-EDM before micro-grinding.

10.6.3 Micro-EDM and Micro-ECM

The surface machined by micro-EDM is relatively rough especially on a micro-level because of micro-craters and cracks produced by the micro-discharges. Therefore, a micro-EDM-based hybrid process consisting of micro-EDM

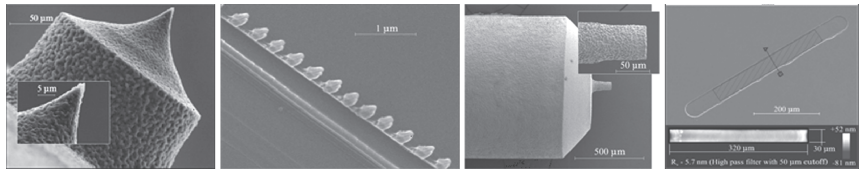

(a) (b) (c) (d)

Figure 10.30 (a) PCD scratch tool produced with the WEDG process, (b) scratch in Ultra Low Expansion glass produced with tool shown in (a), (c) a cylindrical 50-μm PCD tool used to cut pockets in ULE glass, and (d) slot ground in ULE glass using the tool shown in (c) [58].

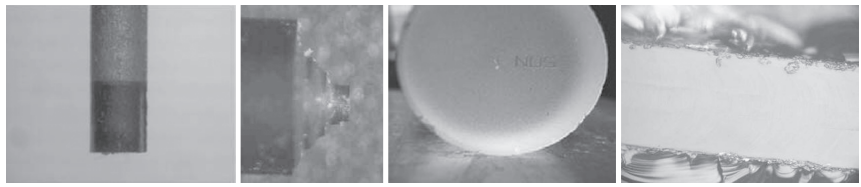

(a) (b) (c) (d)

Figure 10.31 (a) commercially available PCD rod (500 diameter, 1 mm length), (b) 150-μm micro-grinding tool *in situ* fabricated by μ-EDG, (c) "NUS" (slot width 150 μm × depth 50 μ m) machined on BK-7 glass by micro-grinding process, and (d) 100 μm (W) × 100 μm (D) × 5 mm (L) Slot machined by micro-grinding process on BK-7 glass [30].

followed by micro-ECM or electropolishing can be a suitable solution to improve the machined surface. The deionized water used in the micro-EDM process can serve as an electrolyte solution for micro-ECM under low-current-density conditions between the electrode and the workpiece. After the application of micro-ECM, the surface becomes much smoother and peak-to-valley distances of craters (R_{max}) reduce significantly compared to those in micro-EDM after applying micro-ECM. Micro-ECM can also be applied for finishing the slot machined by micro-EDM milling. Figure 10.32a shows the finishing of micro-hole surface by electropolishing after micro-EDM. The comparison of surface roughness for compound micro-EDM and micro-ECM and micro-EDM alone is presented in Fig. 10.32b.

10.6.4 Micro-EDM and Micro-USM

A newly developed machining process combining micro-EDM and micro-ultrasonic machining (MUSM) has been found to improve the performance of micro-EDM alone [74]. The process is a compound process combining fabrication of micro-electrode using micro-WEDG and fabricating micro-holes in nonconductive glass materials using MUSM [75]. This combined process is used mainly for micro-EDM drilling (Fig. 10.33a and b). The material removal

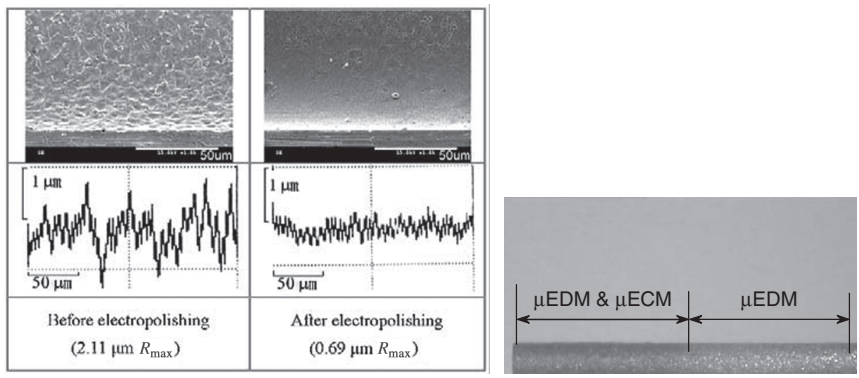

Figure 10.32 (a) Electropolishing of micro-hole surface followed by micro-EDM [48] and (b) Micro-ECM of machined slot followed by Micro-EDM [73].

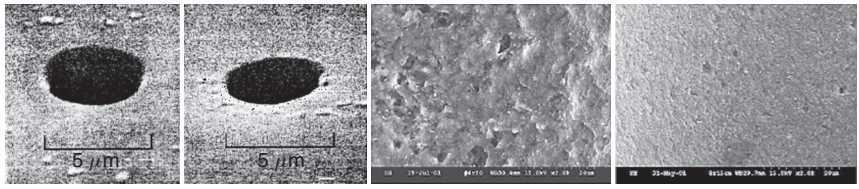

Figure 10.33 (a) Micro-hole with a diameter of 5 μm and a depth of 10 μm in quartz glass (4 μm tool fabricated by micro-WEDG) [75], (b) micro-hole of a diameter of 5 μm and a depth of 6 μm (4 μm tool fabricated by micro-WEDG) [75], (c) inner surface of the micro-holes fabricated in MUSM using 3-μm particles [47], and (d) inner surface of the micro-holes fabricated in MUSM using 1.2 μm particles [47].

is from both the electrical discharging and mechanical polishing of abrasive slurry [47]. The high-frequency pumping action of the vibrating surface of the electrode accelerates the slurry circulation, making machining times shorter. The pressure variations in the gap lead to more efficient discharges, which remove more melted metal. Therefore, the surface of the heat-affected layer that has resulted from micro-EDM is reduced, thermal residual stresses are modified, less micro-cracks are observed, and fatigue resistance is increased because of abrasive action of slurries. The MRR and the surface finish of the process depend on the size of the abrasive particles used in MUSM (Fig. 10.33b and c).

10.6.5 Vibration-Assisted Micro-EDM

This process is considered as a hybrid process as it combines micro-EDM and vibration to the workpiece or the electrode at the same time. The process improves the flushing conditions and removal of debris, improves the machining

stability, and thus reduces the machining time significantly. The process is suitable for deep-hole drilling in hard and difficult-to-cut materials. Depending on the experimental design and objective, the vibration can be applied to the tool electrode [76] or the workpiece [66]. A tool electrode is attached to a holder, which is joined to a Piezoelectric Transducer (PZT) actuator, which is subjected to vibration. The feed direction on the tool electrode can be parallel to the direction of vibration of the PZT or perpendicular to the direction of vibration of the PZT. In the method of tool electrode vibration, owing to the suction and vibration, dielectric circulation and debris removal are improved significantly. Tool vibration is comparatively more difficult to apply in micro-EDM, as the diameter of the tool electrode is only several microns; hence, there is a chance of tool deflection. Therefore, in recent years research on the feasibility of workpiece-vibration-assisted EDM has been carried out for the fabrication of micro-parts, especially during deep-hole drilling. During workpiece-vibration-assisted micro-EDM, the signal generator generates the sine-wave signal at a certain frequency and amplitude to the power supply of the PZT actuator for the required vibration [66]. For low-frequency workpiece vibration, the electric power is supplied periodically to the electromagnet with the help of a power transistor switch. The ON–OFF sequence of the power transistor is controlled by a frequency-controllable pulse generator. There is a pull and release action of vibration pad by the flexure beam with the ON–OFF sequence, which generates the low-frequency vibration to the workpiece [37]. Figure 10.34 shows the different devices developed for generating tool vibration and workpiece vibration during machining. The main application of vibration-assisted micro-EDM is the fabrication of small and high-aspect-ratio micro-structures and micro-holes (Figs. 10.35 and 10.36).

10.6.6 Powder-Mixed Micro-EDM

Powder-mixed micro-EDM is one of the recent innovations for the enhancement of micro-EDM. In recent years, to improve the quality of the EDM-ed surface

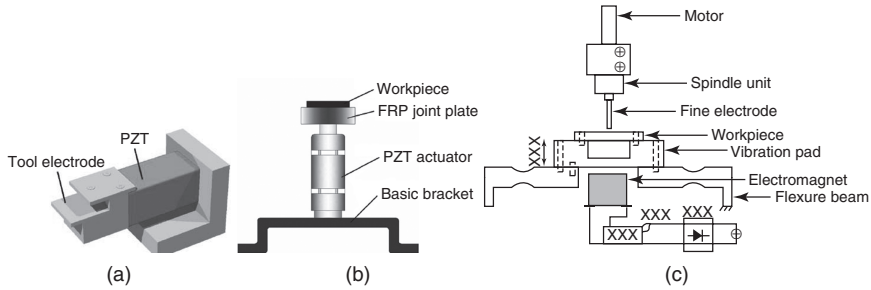

Figure 10.34 (a) Mechanism of applying vibration to the tool electrode [76], (b) mechanism of applying vibration to the workpiece [66], and (c) mechanism of generating low-frequency vibration on workpiece [37].

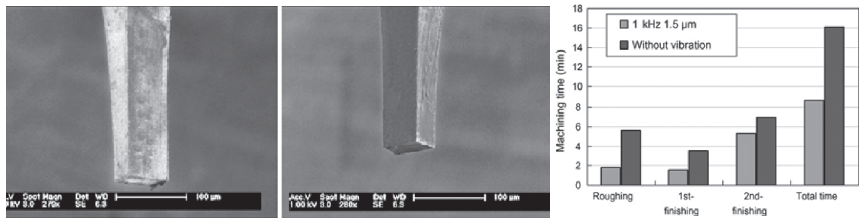

Figure 10.35 (a) Fabrication of square shaft without vibration, (b) with vibration, and (c) comparison of machining time for fabricating square shaft without and with vibration [76].

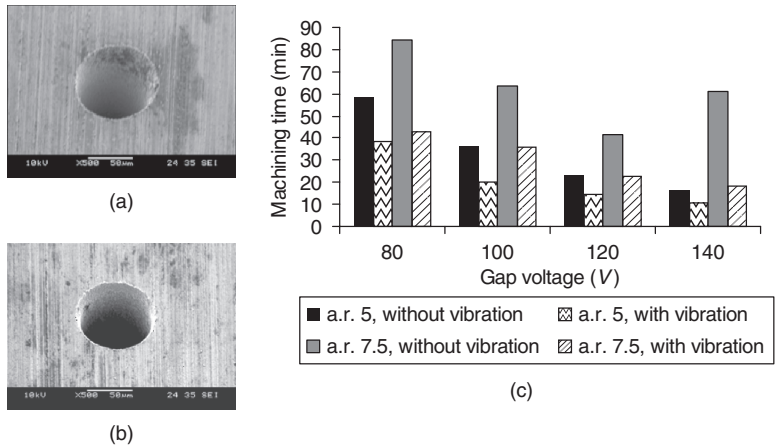

Figure 10.36 (a) Micro-hole (diameter 60 µm, depth 0.5 mm) without vibration, (b) micro-hole (diameter 60 µm, depth 1.0 mm) with vibration, and (c) comparison of machining time without and with vibration [37].

and also to reduce the surface defects, several investigators have found this process effective. In this hybrid process, the electrically conductive powder is mixed with the dielectric, which reduces the insulating strength of the dielectric fluid and increases the spark gap between the tool and the workpiece [77]. Enlarged spark gap makes the flushing of debris easier. As a result, the process becomes stable, improving the MRR and the surface finish. The sparking is uniformly distributed among the powder particles in the spark gap, thus reducing the intensity of a single spark, which results in the formation of uniform shallow craters instead of a single broader crater. Thus, the surface finish improves. There are some abrasive actions of the powder particles during finishing, which reduce the crater boundaries, thus making the surface shiny. Figure 10.37a and b shows the schematic illustration of lower spark gap and crater sizes, which are seen

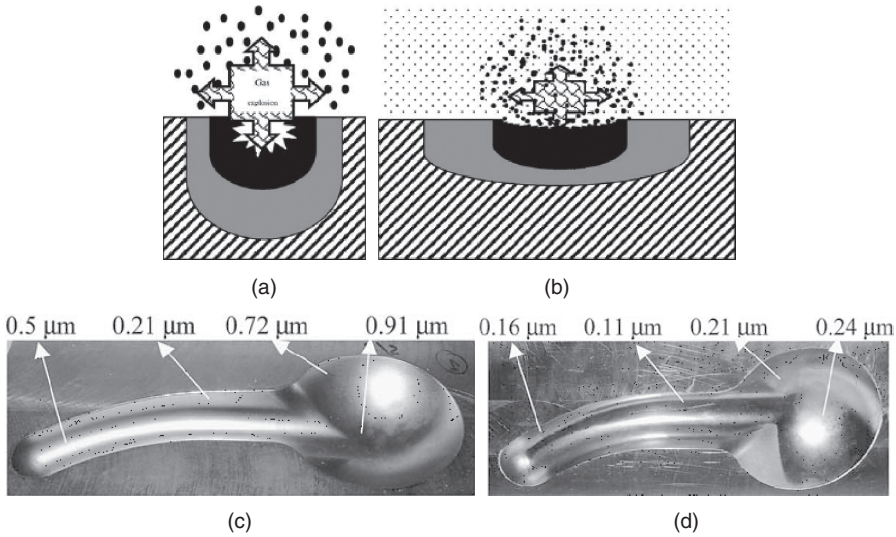

Figure 10.37 (a) Lower spark gap, higher gas explosive pressure, and higher single crater size without powder; (b) larger spark gap, lower gas explosive pressure, and lower single crater size in powder-mixed micro-EDM [78]; (c) mould cavity surface without powder; and (d) significant reduction of roughness after application of silicon powder [79].

in powder-mixed micro-EDM. The improvement in surface finish after applying powder-mixed dielectric is shown in Fig. 10.37c and d.

10.6.7 Micro-ECDM

In recent years, Micro-ECDM (electrochemical discharge machining), an important modification of micro-EDM, has been found to be useful for machining nonconductive and ceramic materials. Micro-ECDM is an attractive micro-machining method for fabricating micro-hole, micro-channel, and micro-structure, because it can be applied to nonconducting materials such as silicon and glass [80]. The process involves a complex combination of an electrochemical (EC) reaction and electro-discharge (ED) action. The electrochemical action helps in the generation of the positively charged ionic gas bubbles, for example, hydrogen (H2). The electrical discharge action takes place between the tool and the workpiece because of the breakdown of the insulating layer of the gas bubbles as the DC power supply voltage is applied between the tool (or cathode) and the anode, resulting in material removal due to melting, vaporization of the workpiece material, and mechanical erosion [81]. An expanded version of micro-ECDM with conductive powder-mixed electrolyte has been found to produce improved surface finish and integrity compared to micro-EDM alone [55]. Figure 10.38 shows a comparison of the surface finish between ECDM and abrasive mixed ECDM.

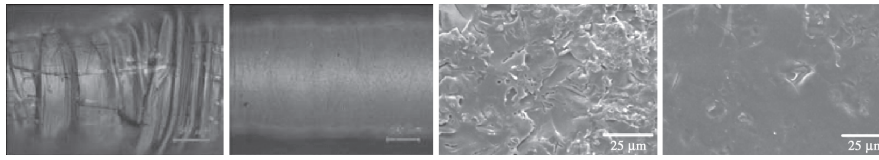

Figure 10.38 Surface improvement in powder-mixed ECDM: (a) Borosilicate glass, ECDM without powder (R_a:4.86 μm); (b) graphite powder in NaOH: 0.5 wt% (R_a:1.63 μm) [55]; (c) Pyrex glass, without powder (R_a:1.8 μm), and (d) SiC powder in KOH, 300 g/L (R_a:1.0 μm) [82].

10.7 SUMMARY

The capability of micro-EDM in machining intricate micro-features with high dimensional accuracy in hard and difficult-to-cut materials has made it an inevitable and one of the most popular micro-machining processes. In recent years, micro-EDM has found important industrial applications, such as fabrication of automotive nozzles, spinnerets, micro-moulds and dies, fiber-optics and MEMS, aerospace, medical and biomedical applications, micro-electronics, and micro-tools.

This chapter presents a detailed overview of the micro-EDM process, including the physical principle of micro-EDM, power supply, different process control parameters such as electrical, nonelectrical, mechanical, and motion control parameters, and the overall performance measures of the process. The current research trends on the improvement and varieties of micro-EDM and their application in the fabrication of micro-structures are presented comprehensively. Advanced research and developments in the area of micro-EDM are also presented in the final section of the chapter. The current research trend shows that micro-EDM alone sometimes cannot fulfill all of the process requirements because of its limitations of lower machining speed and comparatively inferior surface finish. Therefore, compound and hybrid micro-machining based on micro-EDM has been found to be very useful in solving the problems of micro-EDM alone. The hybrid micro-machining technologies have the potential to combine the strength and to complement the weakness of different processes. However, one of the challenges in hybrid micro-machining is the requirement of a multiprocess universal machine tool, in which different machining processes can be performed only by changing attachments suitably. Therefore, development of multipurpose miniature machine tool can significantly improve the advanced research on the areas of micro-EDM and micro-EDM-based compound and hybrid micro-machining.

Although in recent years extensive research on several areas of micro-EDM has been carried out, a significant number of issues remain. Some of the future directions for research and development include improving the positioning accuracy, machine intelligence, and advanced on-line monitoring of the process,

developing knowledge-based systems, and developing multifunctional machine tool and machining centers.

REFERENCES

1. Webzell S. That first step into EDM. Machinery, 159, (4040). Kent, UK: Findlay Publications Ltd.;2001. p. 41.
2. Ho KH, Newman ST. State of the art electrical discharge machining (EDM). Int J Mach Tools Manuf 2003;43:1287–1300.
3. Ho KH, Newman ST, Rahimifard S, Allen RD. State of the art wire electrical discharge machining. Int J Mach Tools Manuf 2004;44:1247–1259.
4. Rahman M, Asad ABMA, Masaki T, Saleh T, Wong YS, Senthil Kumar A. A multi-process machine tool for compound micromachining. Int J Mach Tools Manuf 2010;50(4):344–356.
5. Masuzawa T. State of the art micromachining. Ann CIRP 2000;49(2):473–488.
6. Kurafuji H, Masuzawa T. Micro-EDM of cemented carbide alloys. Jpn Soc Electr Mach Eng 1968;2(3):1–16.
7. Rajurkar KP, Yu ZY. 3D micro-EDM using CAD/CAM. Ann CIRP 2000;49(1):127–130.
8. Rajurkar KP, Levy G, Malshe A, Sundaram MM, McGeough J, Hu X, Resnick R, De Silva A. Micro and nano machining by electro-physical and chemical processes. Ann CIRP 2006;55(2):643–666.
9. Jameson EC. Description and development of electrical discharge machining (EDM). Electrical discharge machining. Dearbern (MI): Society of Manufacturing Engineers; 2001. p 12.
10. Gentili E, Tabaglio L, Aggogeri F. Review on micromachining techniques, courses and lectures; 2005, www.dimgruppi.ing.unibs.it (last accessed on January 17, 2011).
11. Schumacher BM. After 60 years of EDM the discharge process remains still disputed. J Mater Process Technol 2004;149:376–381.
12. Kunieda M, Lauwers B, Rajurkar KP, Schumacher BM. Advancing EDM through fundamental insight into the process. Ann CIRP 2005;54(2):599–622.
13. Masuzawa T, Tsukamoto J, Fujino M. Drilling of deep microholes by EDM. Ann CIRP 1989;38(1):195–198.
14. Masuzawa T, *et al*. Three-dimensional micromachining by machine tools. Ann CIRP 1997;46(2):621–628.
15. Masuzawa T. Micro-EDM. In: Proceedings of the 13th International Symposium for Electromachining; 2001. pp 3–19.
16. Masuzawa T, Yamaguchi M, Fujino M. Surface finishing of micropins produced by WEDG. Ann CIRP 2005;54(1):171–174.
17. Masaki T, *et al*. Electric discharge machining method and apparatus for machining a microshaft. US patent 4,900,890. 1990.
18. Masaki T, *et al*. Micro electro-discharge machining and its applications. Proceedings of Micro Electro Mechanical Systems; 1990. pp 21–26.

19. Han F, Yamada Y, Kawakami T, Kunieda M. Improvement of machining characteristics of micro-EDM using transistor type isopulse generator and servo feed control. Prec Eng 2004;28:378–385.
20. Rahman M, Asad ABMA, Masaki T, Wong YS, Lim HS. Integrated hybrid Micro/Nano-machining. Proceedings of the 2007 International Manufacturing Science and Engineering Conference; 2007 Oct 15–18; Atlanta -Georgia; 2007.
21. Wong YS, Rahman M, Lim HS, Han H, Ravi N. Investigation of micro-EDM material removal characteristics using single RC-pulse discharges. J Mater Process Technol 2003;140(1–3):303–307.
22. Kunieda M, Hayasaka A, Yang XD, Sano S, Araie I. Study on nano EDM using capacity coupled pulse generator. Ann CIRP 2007;56(1):213–216.
23. Kawakami T, Kunieda M. Study on factors determining limits of minimum machinable size in micro EDM. Ann CIRP 2005;54(1):167–170.
24. Han F, Yamada Y, Kawakami T, Kunieda M. Investigations on feasibility of submicrometer order manufacturing using micro-EDM. ASPE Ann Meet 2003;30:551–554.
25. Egashira K, Mizutani K. EDM at low open- circuit voltage. IJEM 2005;10:21–26.
26. Bleys P, Kruth JP, Lauwers B. Sensing and compensation of tool wear in milling EDM. J Mater Process Technol 2004;149:139–146.
27. Ravi N, Chuan SX. The effects of electro-discharge machining block electrode method for microelectrode machining. J Micromech Microeng 2002;12:532–535.
28. Masaki T, Kuriyagawa T, Yan J, Yoshihara N. Study on shaping spherical poly crystalline diamond tool by micro-electro-discharge machining and micro-grinding with the tool, Inter-national. J Surf Sci Eng 2007;1(4):344–359.
29. Lim HS, Wong YS, Rahman M, Lee EMK. A study on the machining of high-aspect ratio micro-structures using micro EDM. J Mater Process Technol 2003;140:318–325.
30. Asad ABMA, Masaki T, Rahman M, Lim HS, Wong YS. Tool-based micromachining. J Mater Process Technol 2007;192–193:204–211.
31. Yu ZY, Rajurkar KP, Shen H. High aspect ratio and complex shaped blind micro holes by micro EDM. CIRP Ann Manuf Technol 2002;51(1):359–362.
32. Bamberg E, Heamawatanachai S. Orbital electrode actuation to improve efficiency of drilling micro-holes by micro-EDM. J Mater Process Technol 2009;209:1826–1834.
33. Kim BH, Park BJ, Chu CN. Fabrication of multiple electrodes by reverse EDM and their application in micro ECM. J Micromech Microeng 2006;16(4):843–850.
34. Kumar S, Singh R, Singh TP, Sethi BL. Surface modification by electrical discharge machining: A review. J Mater Process Technol 2009;209:3675–3687.
35. Bruyn HEDe. Slope control—a great improvement in spark erosion. Ann CIRP 1968;16:183–186.
36. McGeough JA. Advanced methods of machining. 1st ed. USA: Chapman & Hall; 1988. ISBN 0-412-31970-5.
37. Jahan MP, Saleh T, Wong YS, Rahman, M. Study of micro-EDM of tungsten carbide with workpiece vibration. Advances in Materials and Processing Technologies conference (AMPT 2009); 2006 Oct 26–29. Kuala Lumpur, Malaysia: 2006.
38. Jahan MP, Wong YS, Rahman M. A study on the fine-finish die-sinking micro-EDM of tungsten carbide using different electrode materials. J Mater Process Technol 2009;209:3956–3967.

39. Jahan MP, Anwar MM, Wong YS, Rahman M. Nanofinishing of hard materials using micro-EDM. Proc Inst Mech Eng Part B J Eng Manuf 2009;223(9):1127–1142.
40. Jahan MP, Wong YS, Rahman M. A study on the quality micro-hole machining of Tungsten Carbide by micro-EDM process using Transistor and RC-type pulse Generator. J Mater Process Technol 2009;209(4):1706–1716.
41. Lee SH, Li XP. Study of the effect of machining parameters on the machining characteristics in EDM of tungsten carbide. J Mater Process Technol 2001;115:344–355.
42. Guitrau EB. The EDM handbook. Cincinnati: Hanser Gardner Publications; 1997.
43. Mahardika M, Tsujimoto T, Mitsui K. A new approach on the determination of ease of machining by EDM processes. Int J Mach Tools Manuf 2008;48:746–760.
44. Altpeter F, Perez R. Relevant topics in wire electrical discharge machining control. J Mater Process Technol 2004;149(1–3):147–151.
45. Pham DT, Dimov SS, Bigot S, Ivanov A, Popov K. Micro-EDM - recent developments and research issues. J Mater Process Technol 2004;149:50–57.
46. Yan BH, Huang FY, Chow HM, Tsai JY. Micro-hole machining of carbide by electrical discharge machining. J Mater Process Technol 1999;87:139–145.
47. Yan BH, Wang AC, Huang CY, Huang FY. Study of precision micro-holes in borosilicate glass using micro-EDM combined with micro ultrasonic vibration machining. Int J Mach Tools Manuf 2002;42:1105–1112.
48. Hung J-C, Yan B-H, Liu H-S, Chow H-M. Micro-hole machining using micro-EDM combined with electropolishing. J Micromech Microeng 2006;16:1480–1486.
49. Hung JC, Lin JK, Yan BH, Liu HS, Ho PH. Using a helical micro-tool in micro-EDM combined with ultrasonic vibration for micro-hole machining. J Micromech Microeng 2006;16:2705–2713.
50. Masuzawa T, Heuvelman CJ. A self-flushing method with spark-erosion machining. Ann CIRP 1983;32(1):109–111.
51. Masuzawa T, Cui X. Improved jet flushing for EDM. Ann ClRP 1992;41(1):239–242.
52. Tsai Y-Y, Masuzawa T. An index to evaluate the wear resistance of the electrode in micro-EDM. J Mater Process Technol 2004;149:304–309.
53. Klocke F, Lung D, Antonoglou G, Thomaidis D. The effects of powder suspended dielectrics on the thermal influenced zone by electrodischarge machining with small discharge energies. J Mater Process Technol 2004;149(1–3):191–197.
54. Amorim FL, Weingaertner WL. The influence of generator actuation mode and process parameters on the performance of finish EDM of a tool steel. J Mater Process Technol 2005;166(3):411–416.
55. Han M-S, Min B-K, Lee SJ. Improvement of surface integrity of electro-chemical discharge machining process using powder-mixed electrolyte. J Mater Process Technol 1999;95:145–154.
56. Kim YT, Park SJ, Lee SJ. Micro/Meso-scale shapes machining by micro EDM process. Int J Prec Eng Manuf 2005;6(2):5–11.
57. Fleischer J, Masuzawa T, Schmidt J, Knoll M. New applications for micro-EDM. J Mater Process Technol 2004;149:246–249.
58. Morgan CJ, Vallance RR, Marsh ER. Micro-machining and micro-grinding with tools fabricated by micro electro-discharge machining. Int J Nanomanuf 2006;1(2):242–258.

59. Wada T, Masaki T, Davis DW. Development of micro grinding process using micro EDM trued diamond tools. Proceedings of the Annual Meeting of ASPE; 2002.
60. Yamazaki M, Suzuki T, Mori N, Kunieda M. EDM of micro-rods by self-drilled holes. J Mater Process Technol 2004;149:134–138.
61. Chen ST. Fabrication of high-density micro holes by upward batch micro EDM. J Micromech Microeng 2008;18:085002, 9.
62. Masaki T, Wada T. Micro electro discharge machining. J JSAT 2002;46(12):610–613, (in Japanese).
63. Masaki T, *et al*. Repetitive pattern transfer process of micro EDM. Int J Electro Mach 2006;11:33–34.
64. Kuo C-L, Huang J-D. Fabrication of series-pattern micro-disk electrode and its application in machining micro-slit of less than 10 μm. Int J Mach Tools Manuf 2004;44:545–553.
65. Uhlmann E, Piltz S, Doll U. Machining of micro/miniature dies and moulds by electrical discharge machining—Recent development. J Mater Process Technol 2005;167:488–493.
66. Tong H, Li Y, Wang Y. Experimental research on vibration assisted EDM of micro-structures with non-circular cross-section. J Mater Process Technol 2008;208(1–3):289–298.
67. Narasimhan J, Yu Z, Rajurkar KP. Tool wear compensation and path generation in micro and macro EDM. Trans NAMRI/SME 2004;32:151–158.
68. Bleys P, Kruth J-P, Lauwers B, Zryd A, Delpretti R, Tricarico C. Real-time tool wear compensation in milling EDM. Ann CIRP 2002;51(1):157–160.
69. Yu ZY, Masuzawa T, Fujino M. Micro- EDM for three-dimensional cavities—development of uniform wear method. Ann CIRP 1999;47(1):169–172.
70. Hayakawa S, Ori RI, Itoigawa F, Nakamura T, Matsubara T. Fabrication of microstructure using EDM deposition. ISEM 2001;13:783–793.
71. Minami H, Masui K, Tsukahara H, Hagino H. Coloring method of titanium alloy using EDM process. Proceedings ISEM 12; 1998. pp 503–512.
72. Takahata K, Shibaike N, Guckel H. High-aspect-ratio WC-Co microstructure produced by the combination of LIGA and micro-EDM. Microsyst Technol 2000;6(5):175–178.
73. Wong YS, Rahman M, Lim HS, Senthil kumar A. Computer controlled multi process machine tool for flexible micromachining. AUN/SEED Net 3rd Fieldwise Seminar on Manufacturing and Material Processing Technology; 2004 Mar 17–18; University of Malaya, Kuala Lumpur, Malaysia: 2004.
74. Egashira K, Masuzawa T, Fujino M, Sun XQ. Application of USM to micromachining by on the machine tool fabrication. Int J Electr Mach 1997;2:31–36.
75. Egashira K, Masuzawa T. Microultrasonic machining by the application of workpiece vibration. Ann CIRP 1999;48(1):131–134.
76. Endo T, Tsujimoto T, Mitsui K. Study of vibration-assisted micro-EDM-the effect of vibration on machining time and stability of discharge. Prec Eng 2008;32(4):269–277.
77. Wong YS, Lim LC, Rahuman I, Tee WM. Near-mirror-finish phenomenon in EDM using powder-mixed dielectric. J Mater Process Technol 1998;79:30–40.

78. Tzeng Y-F, Chen F-C. Investigation into some surface characteristics of electrical discharge machined SKD-11 using powder-suspension dielectric oil. J Mater Process Technol 2005;170:385–391.
79. Pecas P, Henriques EA. Influence of silicon powder mixed dielectric on conventional electrical discharge machining. Int J Mach Tools Manuf 2003;43:1465–1471.
80. Wuthrich R, Fascio V. Machining of non-conducting materials using electrochemical discharge phenomenon-an overview. Int J Mach Tools Manuf 2005;37:1095–1108.
81. Sorkhel SK, Bhattacharyya B, Mitra S, Doloi B. Development of electrochemical discharge machining technology for machining of advanced ceramics. International Conference on Agile Manufacturing; 1996 Feb. 1996. pp 98–103.
82. Yang CT, Song SL, Yan BH, Huang FY. Improving machining performance of wire electrochemical discharge machining by adding SiC abrasive to electrolyte. Int J Mach Tools Manuf 2006;46:2044–2050.

CHAPTER 11

METAL INJECTION MOLDING AT MICRO-SCALES (μMIM)

GANG FU, NGIAP HIANG LOH, SHU BENG TOR, and BEE YEN TAY
Mechanical Engineering Department, Nanyang Technological University (NTU), Singapore

11.1 INTRODUCTION TO METAL INJECTION MOLDING (MIM)

Powder injection molding (PIM) is a process used to produce net-shaped/near-net-shaped parts from metal or ceramic powders. It combines the benefits of plastic injection molding (complex shapes and high productivity) with the advantages of powder metallurgy (nearly unlimited choice in alloy-composition and isotropic properties) [1]. PIM has been used for several decades, originally with ceramic powders and then with metal powders. PIM can be classified into ceramic injection molding (CIM) and metal injection molding (MIM). CIM was developed in the 1920s, but MIM remained relatively uncommon until the latter half of the 1970s. MIM patent holders, Rivers (1976) and Weich (1980), were the first to apply thermoplastics to binders [2]. Since the 1980s, MIM has been undergoing rapid development. However, there are regional differences with North America showing the highest attention to ceramic but metal in Europe and Asia. Even in MIM, 17-4PH is the most commonly used stainless steel powder used in the United States, whereas in Europe it is 316L [3].

A typical MIM process includes the following four processing steps: mixing, injection molding, debinding, and sintering. The MIM process begins by mixing the selected powder and the binder—the mixture of powder and binder is termed "feedstock." The powder particles are small to aid the sintering process and usually have their sizes between 0.1 and 20 μm with near-spherical shapes [4]. The binder is usually based on a common thermoplastic, but food-grade polymers, cellulose, gels, silanes, water, and various inorganic substances are also in use. Generally, the binder consists of several components.

Micro-Manufacturing: Design and Manufacturing of Micro-Products, First Edition.
Edited by Muammer Koç and Tugrul Özel.

The granulated feedstock is injection molded into the desired shape on an injection molding machine. The molded part is termed "green part." After injection molding, the binder has to be removed from the green part. Depending on the binder used, a wide array of options exist for binder extraction, but mainly consist of three methods: thermal, solvent, and catalytic [4]. The last step is sintering, in which the void space remaining after removal of the binder is eliminated with appreciable shrinkage. Sintering often occurs in a protective atmosphere or vacuum at an elevated temperature. In sintering, the particles in the debound part are bonded into a coherent, solid mass whose density may reach or near the theoretical density.

Today, markets for MIM are found for small complex parts. Being a process that produces net-shaped/near-net-shaped parts, it is cost effective, as secondary operations are reduced or eliminated. In addition, MIM is able to produce complex parts in high productivity. MIM has three key attributes—shape complexity, high performance, and low cost [4]. Despite the numerous advantages, MIM also has disadvantages and there are hurdles to further growth: (i) the raw materials, especially metal powders, are expensive; (ii) for shapes with simple or axial-symmetric geometries, it is not competitive in contrast to other shaping technologies; (iii) it is difficult to achieve tight dimensional tolerance in sintered parts and therefore in some cases secondary operation is a must, which increases the production costs.

As the demand for complicated-shaped metal components increased rapidly in recent years, MIM has become one of the popular methods that meet the requirements. It is highly preferred to slurry techniques such as dry pressing, cold isostatic pressing, slip casting, and tape casting, in the aspect of mass production [4]. MIM has been widely used in various industries such as automobile, defense, aerospace, electronics, household appliances, and medical/dental appliances.

11.2 MICRO METAL INJECTION MOLDING (μMIM)

In the last decade, micro-systems and related products have seen an ever increasing number of applications in various markets. The demand for micro-components and micro-structures has also increased accordingly. Currently, the production of micro-components or micro-structures is dominated by materials based on silicon or polymers [5]. However, in many other applications, metal micro-components and micro-structures are required because of their superior mechanical properties and thermal stability. MIM on a micro-scale, also termed micro metal injection molding (μMIM), is a suitable process for the mass production of complex metal micro-components or micro-structures [6–11]. μMIM is adapted from MIM. It comprises the same four processing steps as MIM: mixing, injection molding, debinding, and sintering, as shown in Fig. 11.1 [12]. μMIM inherits the features and advantages of MIM and micro plastic injection molding such as low production cost, shape complexity, and applicability to many materials (compared with

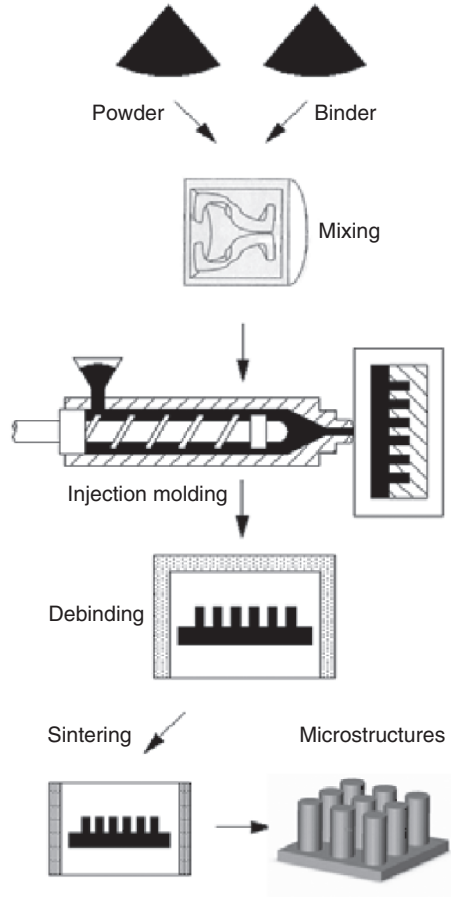

Figure 11.1 Schematic drawing of processing steps of μMIM.

other fabrication methods for metal or ceramic micro-structures such as electroplating, Lithography, Electroplating, and Molding (LIGA), and other material removal methods).

11.3 FEEDSTOCK PREPARATION

The feedstock for injection molding is produced by mixing the powder and the binder.

11.3.1 Powder

Generally, the selection of a powder is essential to achieve defect-free green parts (i.e., molded part) and final sintered parts as well as for the successful control of

μMIM. Thus, an understanding of the characteristics of the powder is important. Particle size and particle shape are two important powder characteristics. Particle size is measured by determining the dimensions of a particle. The size is dependent on the measurement technique and particle shape. Coherent (laser) light scattering is a suitable measurement technique [2]. Usually, size determinations are based on detecting discontinuities in the properties of a fluid stream (air or water) carrying dispersed particles [4]. The particle size distribution can be shown as a histogram of the amount of powder in the measured size increments as shown in Fig. 11.2. Or more typically, a plot of the cumulative particle size distribution gives the amount of powder smaller than a given size. As shown in Fig. 11.2, the percentage of 316L stainless steel powder particles by mass smaller than a given size is plotted versus the particle size on a logarithmic scale. Three points on the distribution curve, designated as d_{10}, d_{50}, and d_{90}, that correspond to the particle size at 10%, 50%, and 90% on the cumulative distribution are typically considered. A wide particle size distribution gives a higher packing density that leads to less shrinkage, and easier process, as well as dimensional control. However, in the case of a wide particle distribution, special care must be taken during feedstock mixing. Owing to the size difference between particles, there will be segregation in the mixed powder. This can lead to uneven packing densities and distortion in sintering.

In μMIM, the particle size of the metal powder is a very important parameter that limits the producible structure dimensions and the aspect ratio. For this reason, feedstock of high strength with smaller powder with the mean particle size far below 3 μm is desirable. In Germany, carbonyl iron powder with particle size down to $d_{50} = 1.5$ μm was used at the Karlsruhe Institute of Technology [13]. At the Nanyang Technological University (Singapore), 316L stainless steel powder with particle size down to $d_{50} = 2.4$ μm was used to produce 3D metal

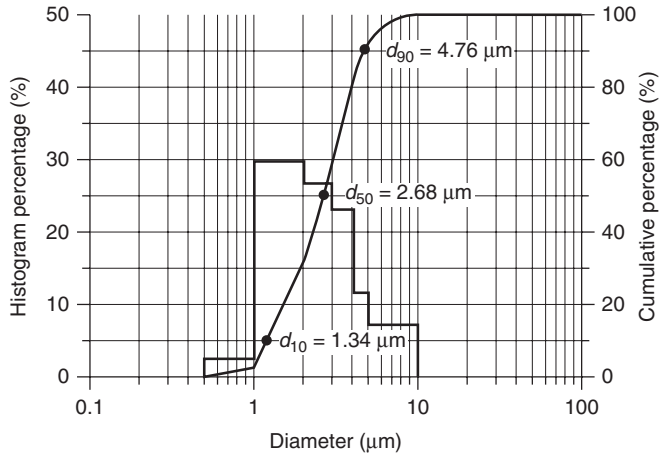

Figure 11.2 Particle size distribution of 316L stainless steel powder.

micro-structures [6,14,15]. The smaller particles help to avoid molding defects and produce finer structures and sharper corners. Smaller particles have higher surface areas, which provide higher sintering activation energy and faster sintering, as well as higher density after sintering.

However, metal powders in the submicron range, which is almost standard for ceramics, are not very easily available. The reason for this lies in the ductility and reactivity of metals, which make it difficult and very expensive to produce fine powders [16]. The handling of fine powder becomes difficult as it tends to oxidize. Fine powder also agglomerates very easily and it is more difficult to break the agglomeration during mixing. Furthermore, owing to particle agglomeration, the smaller the powder size, the lower the packing density, especially for particles below 1 μm. Because the shrinkage in sintering to full density depends on the particle packing density after binder removal, the smaller particles lead to greater sintering shrinkage, which increases the possibility of defects such as warpage and cracks. On the other hand, the processing of powders becomes more difficult as the higher surface area of smaller powders necessitates a large amount of binder. This again increases the shrinkage during sintering and often leads to cracks and distortion. Thus, a balance between particle size and an appropriate mixture of very small powders is needed [16].

Particle shape has a great effect on the success of the μMIM process. Generally speaking, a spherical-shaped powder is preferable as it gives the feedstock better moldability compared with a powder having an irregular shape. Irregular shape particles exhibit better part shape retention during debinding, however the packing coordination number and density decreases due to irregular particle shape [17]. Thus, more densification is needed in sintering to compensate for the poor initial packing. A compromise is to combine some spherical-shaped and irregular-shaped particles to attain the benefits of each shape [2]. Figure 11.3 shows a micro-graph of water-atomized 316L stainless steel powder taken using a scanning electron micro-scope [18].

11.3.2 Binder

A binder is a key component in MIM, which provides the feedstock with the fluidity necessary for molding. Many binders are being used industrially and can be categorized into thermoplastic compounds, thermosetting compounds, water-based systems, gelation systems, and inorganics. Although many binders are available on a production basis, thermoplastics are by far the most widely used and understood [4]. In μMIM, considering the small dimensions and high aspect ratio of micro-components or micro-structures, an appropriate binder must be selected in order to give higher green strength for demolding, lower viscosity for easy filling of mold cavity during molding, as well as good shape retention and lower shrinkage during debinding and sintering [14,19,20].

Most binders are multiple-component systems whose constituents will be removed in a progressive extraction cycle. Usually, the binder has three components—a backbone polymer that provides strength (some commonly

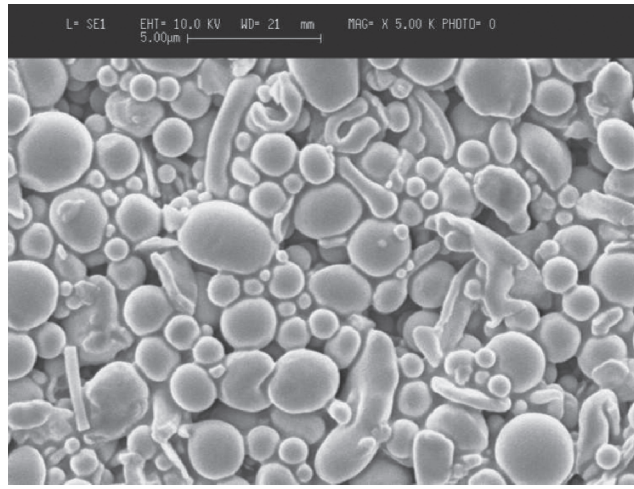

Figure 11.3 SEM photo of 316L stainless steel powder.

used backbone polymers are Polyoxymethylene (POM), Polyvinyl alcohol (PVA/PVOH), Polyethylene (PE), Ethylene vinyl acetate (EVA), and Polypropylene (PP), a filler phase that is easily extracted in the first phase of debinding (e.g., wax), and a surfactant to bridge the binder and the powder. Often, the surfactants reduce the mixture viscosity and increase the solid content of the mixing by creating an interfacial bridge between the powder and the binder. During debinding, the binder components are removed progressively. The primary binder components such as filler phases and surfactants are removed first to partially open the pores. The fully debound but unsintered structure becomes so fragile that it becomes impossible to handle. The secondary polymer component, which usually remains in the green part serving as the backbone, retains the shape of the part, preventing slumping and distortion [4,14]. Eventually, the backbone polymers are removed during debinding, which occurs as part of the heating process before the sintering temperature is reached.

11.3.3 Mixing of Feedstock

After the mixing of the powder and the binder, the resulting mixture is granulated or pelletized to form the feedstock for injection molding. Five factors determine the attributes of the feedstock—powder characteristics, binder composition, the ratio of the amount of the powder to that of the binder (powder loading), mixing method, and pelletization techniques [4]. The flow properties of the feedstock should permit good rheological behavior and good filling of the mold cavity. The powder-to-binder ratio largely determines the success or failure of the subsequent processes. Generally, the feedstock is prepared using a minimum binder

content, which gives rise to high green density and little shrinkage during sintering. The optimal powder loading for molding has less powder than the critical powder loading (the critical powder loading is the composition where particles are packed as tightly as possible without external pressure and all the space between the particles is filled with the binder), typically a value of 60 vol% for MIM [4]. At this point, the feedstock has a sufficiently low viscosity for molding but exhibits good particle–particle contact to ensure shape preservation during processing.

The purpose of mixing is to coat the particles with the binder and break up the agglomerates to get a homogeneous feedstock. Failure to disperse or evenly distribute the powder in the binder may result in powder–binder separation, segregation, and agglomeration in the feedstock. These may be translated into nonuniform shrinkage during sintering and cause inhomogeneities in the final properties [2,4]. A properly mixed feedstock has a homogeneous powder dispersion in the powder with no internal porosity or agglomerates.

A small-scale mixer can be used to evaluate whether the mixed feedstock is homogeneous or not by monitoring the torque of the mixing blade. This is very important during the stage of developing new feedstock and determining the suitable powder loading. Figure 11.4 shows a small-scale mixer with two roller blades and a maximum mixing volume of 69 cm^3. A typical mixing torque curve is shown in Fig. 11.5. A constant torque value can be achieved if the mixed feedstock is homogeneous. If the torque value keeps increasing during mixing, the feedstock should not be used for injection molding.

After the small-scale mixing, the feedstock can be mixed in a large-scale mixer. Several types of high-shear mixers are used for MIM feedstock preparation, which include double planetary mixer, single-screw extruder, plunger extruder, twin-screw extruder, twin-cam extruder, shear roll compounder, sigma-blade mixer, and Z-blade mixers. Figure 11.6 shows a Z-blade mixer for laboratory use.

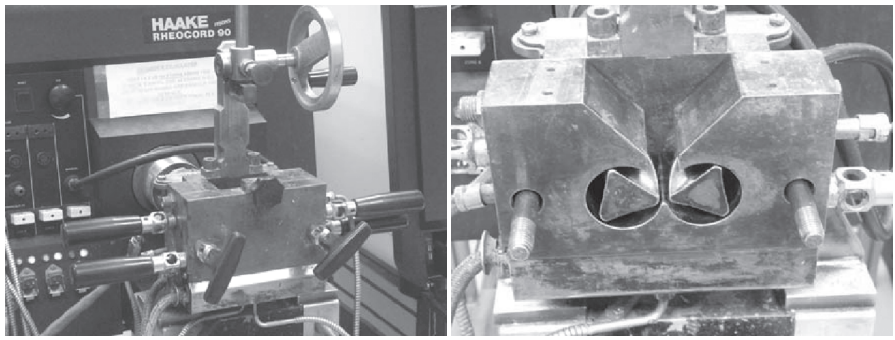

Figure 11.4 Small-scale mixer with torque measurement function.

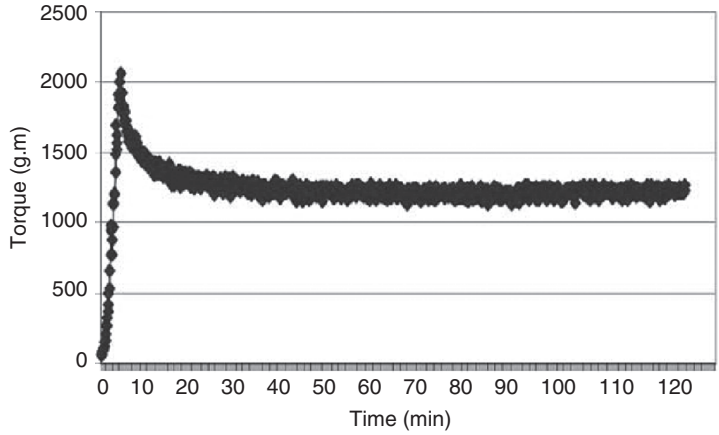

Figure 11.5 Torque curve during mixing.

Figure 11.6 Z-blade mixer for laboratory use.

11.4 INJECTION MOLDING

11.4.1 Equipment and Processing Parameters for μMIM

Injection molding is one of the key processing methods used for molding plastics. It is suitable for the mass production of parts with a complex shape. In MIM, the procedure of injection molding is similar to that of plastics injection molding. The defects and problems associated with plastic injection molding apply also to MIM. In addition, higher heat conductivity and different feedstock rheological characteristics give more problems.

Some dedicated micro injection molding machines meant for plastics are made applicable also to μMIM by using wear-resistant hardened plasticating unit, for example, Battenfeld Micro-system 50. In most cases of μMIM, a number of equipment modifications based on conventional plastic injection molding machine and a specially designed mold are required. This is mainly due to the small dimensions of the molded micro-components and the high aspect ratio of the micro-structures as well as the demand for submicron precision. Typically, they include

- The surfaces in contact with the feedstock such as reciprocating injection screw and mold inserts have to be hardened to resist the abrasive metal feedstock.
- *Separate Plasticating and Injection Unit:* For injection of milligram-shot weight, metering and dosing have to be very exact. In this aspect, separate plasticating (metering and dosing) units can be used, and smaller metering screw and smaller injection plungers can be used to guarantee exact metering and fast injection [21,22].
- *Cavity Vacuum System:* In conventional molding process, air vent slots facilitate the escape of air in the mold cavity during mold filling. However, these slots are close to the size of the micro-structures. Therefore, the cavity has to be evacuated using an external evacuation system [23]. Further, the incorporation of vacuum system is necessary to avoid air getting entrapped and "diesel effect" in the blind micro-cavity during molding, and to enhance the mold-filling process. In some cases, a pressure of 2.7 Pa is used [24].
- *Variotherm Mold Heating/Cooling System:* In micro plastic injection molding, the extreme aspect ratio in combination with the small dimensions of the micro-structures requires a mold temperature variation technology termed variotherm [21]. In the case of high-aspect-ratio micro-structure injection molding using conventional mold, the rapid heat loss often leads to incomplete filling of the mold cavity. Thus, it is necessary to increase the mold temperature to an elevated temperature for easy filling. After filling, the mold is then cooled to a demolding temperature that allows a safe and defect-free demolding of the micro-structures [25]. The principle of the variotherm mold is applicable also to μMIM.
- *High Mold Alignment Tolerance:* Although during micro injection molding, the temperature changes and high clamping force is applied, dimensional stability has to be ensured. An effective and extremely precise dimension alignment device with an alignment quality of ± 10 μm has been used [25]. Further, high-tolerance requirements on the closing joint, ejector pins, and the mold inserts are also required. During production, tolerance smaller than 1 μm must be observed [25].
- *Separation or Substrate Unit:* Typical micro-structures exhibit dimensions in the range of some tens of microns and a large aspect ratio. To facilitate separation of these micro-structures from the mold insert, a separation or substrate unit is needed to demold the micro-structures [26].

Molding conditions for μMIM are different from those used for conventional plastic injection molding and MIM. Higher barrel temperature and mold temperature are necessary to ensure that the feedstock has a sufficiently low viscosity to fill the mold cavity completely. Higher injection speeds can avoid rapid heat lost from the feedstock as the feedstock has a high thermal conductivity. This can prevent premature solidification. The injection pressure and the packing pressure need to be high, for example, an injection pressure of 200–250 MPa is used [27,28]. Further, lower ejection speeds are needed to prevent the micro-structures from breaking and sticking inside the cavity.

11.4.2 Mold Inserts for μMIM

The potential of molding minimum structural details is determined by the method selected for manufacturing the micro-structured mold inserts, their quality, as well as by the particle (powder) size. A number of methods are capable of producing micro-components and micro-structures in the micron range. The resulting micro-structures may be used directly or serve as mold inserts for the mass production of micro-structures in micro injection molding of plastics and μMIM [29].

The following processes and materials are used for the production of mold inserts used in metal or ceramic micro-components and micro-structures:

- LIGA. Nickel mold, Nickel mold insert coated with approximately 500 nm of gold, Ni–Fe alloy and tungsten–cobalt alloy [30–32].
- Laser ablation. Hard metal [13] and polyimide film mold-pattern ablated by excimer laser [33].
- Precision engineering techniques (micro-milling, Micro Electrical Discharge Machining (μEDM), wire-cut erosion, etc.) [34]. For example, Fig. 11.7 shows a μEDM mold insert for molding micro-gears 1 mm in diameter.
- Nitinol and stainless steel [19,30].
- Brass for simpler micro-structure by micro-mechanical processing [5].
- Silicone rubber. Usually used in low-pressure PIM, good demolding property [35].
- Plasma etching of silicon [6,14,36]. Silicon has physical and chemical properties that make it a promising material for MEMS (micro-electromechanical systems) and micro-system technology. Silicon is very strong, similar to steel with respect to the modulus of elasticity; has no mechanical hysteresis; and possesses good thermal conductivity and a low thermal expansion coefficient [37]. Silicon mold inserts made by plasma dry etching of silicon wafer (e.g., DRIE—deep reactive ion etching) were used as in the mold insert in μMIM [6]. The DRIE technology allows the attainment of relatively vertical sidewalls at a high anisotropy and better sidewall surface roughness by selecting a suitable wafer temperature and the addition of oxygen. The photos of silicon mold inserts etched by DRIE and the details of micro-cavities and micro-channels are shown in Fig. 11.8 [38].

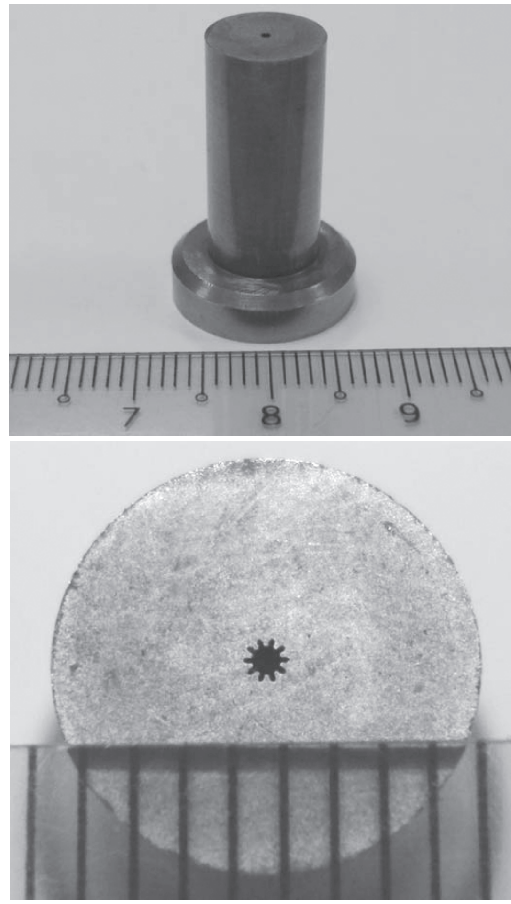

Figure 11.7 μEDM mold insert for molding micro-gears 1 mm in diameter.

- μMIM. Iron (Fe), 316L stainless steel, and hard metal (WC–Co10). Limitation: high surface roughness compared with DRIE silicon mold inserts and LIGA mold inserts, but are comparable to micro laser ablation and micro-cutting [39].

11.4.3 Variotherm Mold for μMIM

As mentioned in section 11.4.1, the problem of incomplete filling when molding tiny micro-component or high-aspect-ratio micro-structures can be resolved by using a variotherm mold. A Variotherm mold with a rapid heating–cooling system was utilized to fabricate high-aspect-ratio 316L stainless steel micro-structures [24]. The variotherm mold heating–cooling system has advantages such as good filling of high-aspect-ratio micro-structures, adjustable demolding temperature,

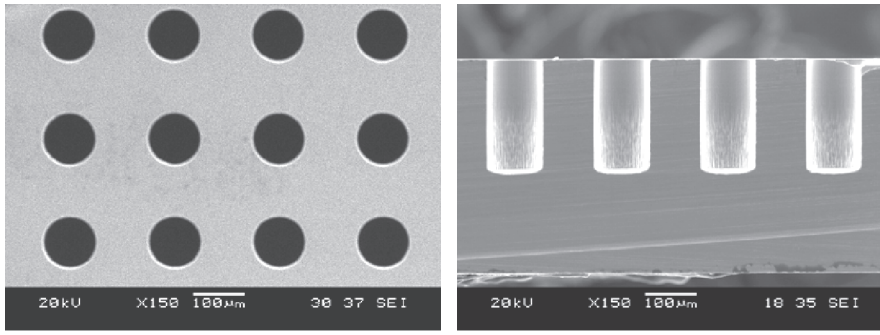

Micro-cavities

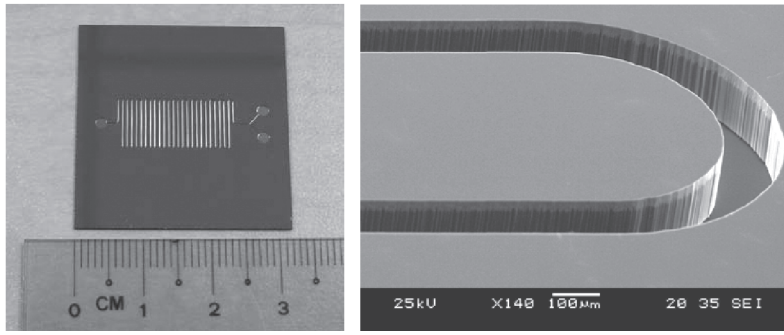

Micro-channels

Figure 11.8 Silicon inserts with micro-cavities and micro-channels etched by DRIE.

and reduced cycle time. The variotherm mold comprises mold body, heating system, cooling system, vacuum system, hot sprue system, and measuring system (cavity pressure and cavity temperature), as shown in Fig. 11.9. The actual variotherm mold and cross-sectional drawing are shown in Fig. 11.10. As shown in Fig. 11.11, ϕ40 μm × height 174 μm micro-structures with an aspect ratio of 4.4 and ϕ20 μm × height 160 μm micro-structures with an aspect ratio of 8 were successfully molded using the variotherm mold.

11.5 DEBINDING

After injection molding, the next step in the μMIM process is debinding, in which the binder is removed from the green part. Currently, the following debinding methods or a combination of the methods are used in μMIM:

1. Debinding by thermal degradation of the organic binder components.
2. Solvent debinding using organic solvent to remove the binder.

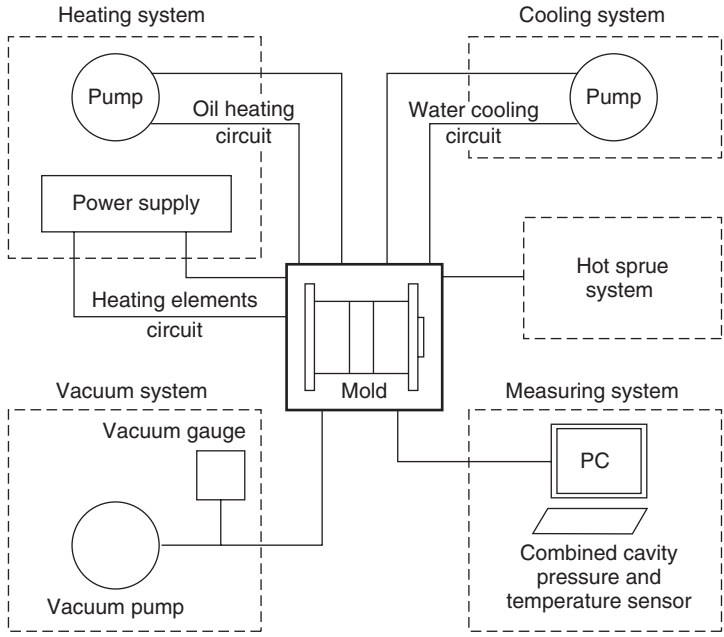

Figure 11.9 Variotherm mold design layout.

3. Catalytic debinding in an atmosphere containing a catalyst such as nitric acid vapor, which is usually applied for polyacetal binders.

Thermal debinding involves the removal of the binder from the green part at elevated temperatures. The binder may be thermally decomposed into low-molecular-weight species such as water, methane, and carbon oxide and subsequently removed from the green part by diffusion or by permeation [40,41].

Figure 11.12 shows a thermal debinding schedule for a 316L stainless steel feedstock in μMIM. The green part was debound in a tube furnace with a flowing gas mixture of 95% argon and 5% hydrogen.

Considering the small dimensions and the high aspect ratio of the micro-structures, appropriate binder components and their composition must be selected in order to achieve good shape retention during debinding. In the debinding, the green micro-structures may slump or deform as the binder reaches its softening point during thermal binder removal. Figure 11.13 shows micro-structures slumped because of an insufficient strength of the feedstock during debinding.

In addition to thermal debinding, catalytic debinding is also used in μMIM. The emergence of catalytic debinding with polyacetal-based binder makes it possible to remove the polymer at a higher debinding rate. In catalytic debinding, the reaction depends on permeation of the catalyst vapor (e.g., 100% nitric acid) into the pores and permeation of the decomposition product out of the pores. In the

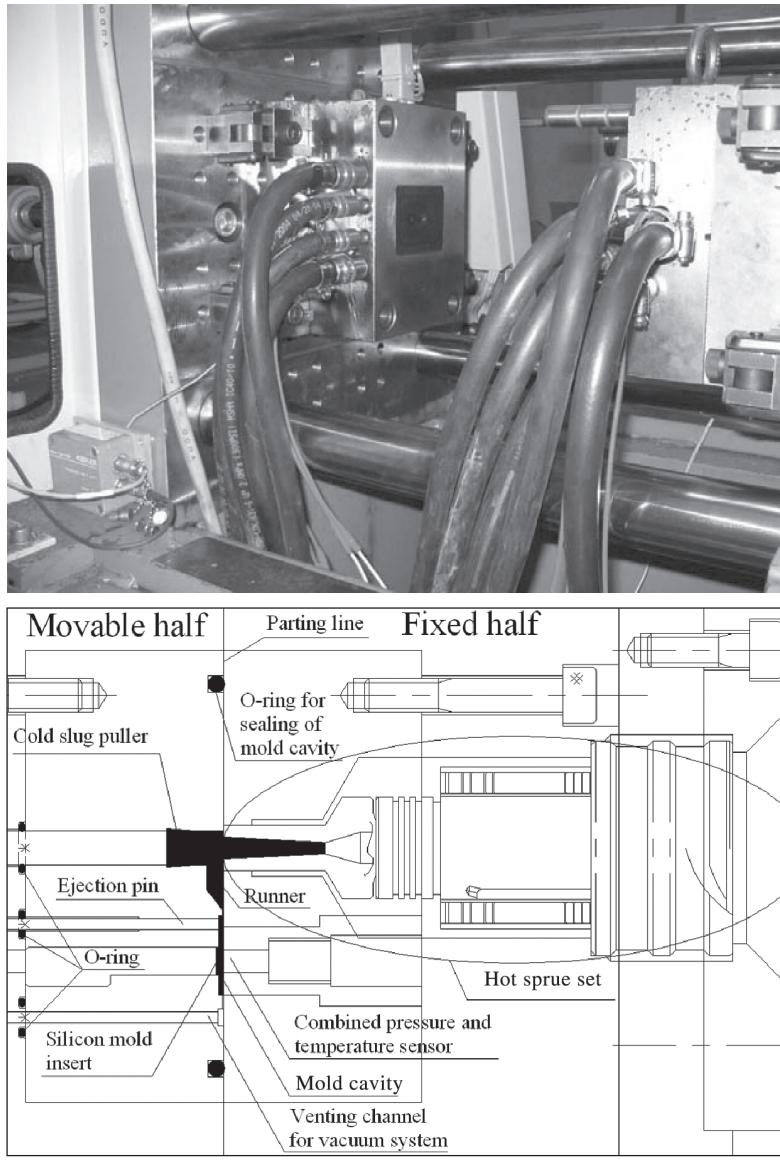

Figure 11.10 Variotherm mold and its cross-sectional drawing.

presence of an acid vapor, the binder decomposes predominantly to formaldehyde well below its softening point, that is, in the solid state. These occur in nitrogen at atmospheric pressure and at a temperature of 110–140°C [42]. The relatively low debinding temperature below the softening point of the binder gives the debound part good shape retention. The debinding rate depends on the

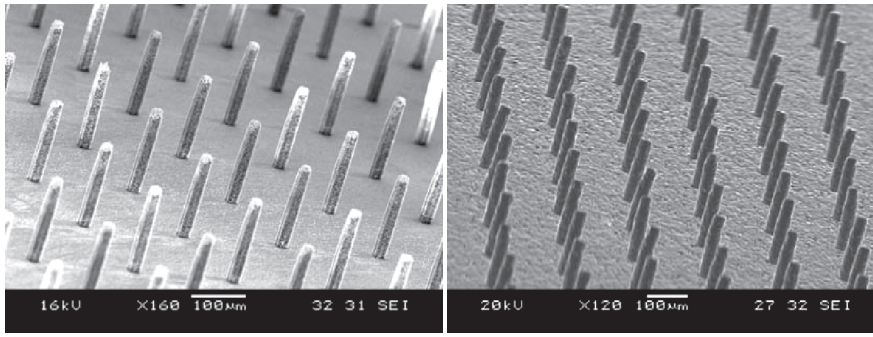

Figure 11.11 ϕ20 µm × height 160 µm green micro-structures and sintered ϕ40 µm × height 174 µm micro-structures (seating on a ϕ16 mm × thickness 1.5 mm disc).

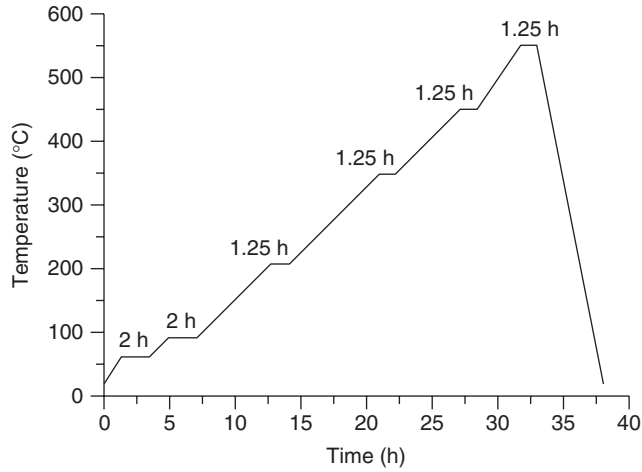

Figure 11.12 Schematic debinding schedule for 316L feedstock.

debinding temperature and catalyst concentration. Usually, the depolymerization rate is the controlling factor, not the permeation rate. Normally, the debinding rate is almost constant and is 2 mm/h.

11.6 SINTERING

Sintering is the last processing step of µMIM. The sintering study in this chapter is mainly focused on 316L stainless steel micro-structures and micro-gears. A typical sintering schedule for a 316L stainless steel debound part is shown in Fig. 11.14 [12]. Sintering was conducted in a tube furnace. First, the debound part was heated from room temperature (25°C) to 600°C at a heating rate of

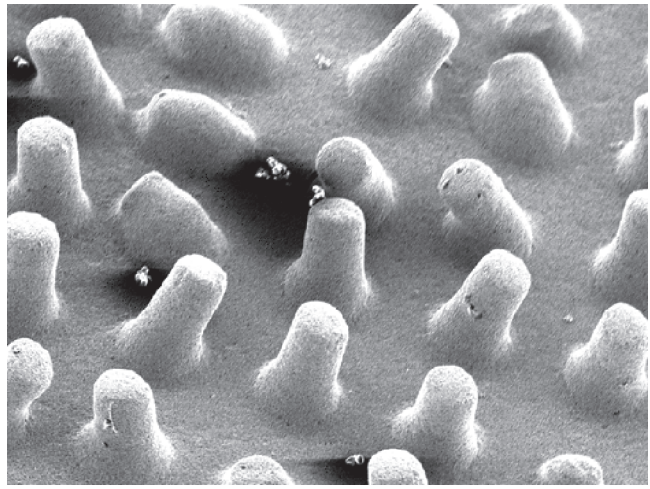

Figure 11.13 Slumped micro-structures after debinding.

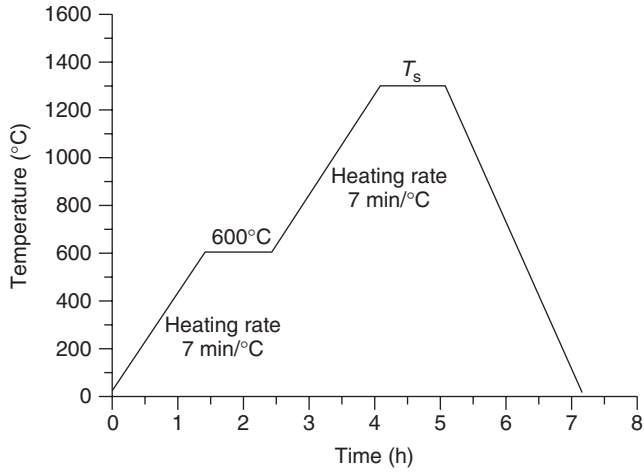

Figure 11.14 Sintering temperature profile.

7°C/min, and was held at 600°C for 1 h. After debinding, there may be some remaining organic matter, dispersants, and some polymer fragments, which can be removed quickly by pyrolysis at 600°C at the first stage of the sintering process. A high amount of carbon will be kept in the sintered parts if higher heating rates are used. This is because sintering occurs before all of the organic components have been removed from the part [2]. The part was then heated from 600°C to the sintering temperature T_s and held at T_s for 1 h. After that, the sintered part was naturally cooled down in the furnace to room temperature.

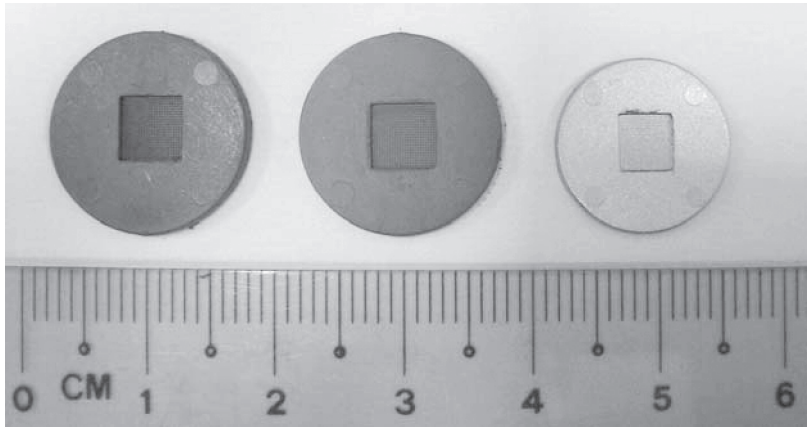

Figure 11.15 Green, debound, and sintered parts (with ϕ100 μm × height 200 μm micro-structures).

11.6.1 Sintering of Micro-Structures

The part was a round disc of ϕ16 mm and thickness 1.5 mm in thickness with an array of 24 × 24 (total of 576) micro-structures in the center of the disc, as shown in Fig. 11.15. Two types of debinding and sintering methods were used. The first feedstock was developed in-house. The molded micro-structures were debound by thermal debinding and sintered in an atmosphere of pure hydrogen. The second feedstock is a commercial feedstock. The green micro-structures were debound using the catalytic debinding method and sintered in vacuum condition (0.67 Pa).

In the case of the in-house feedstock, near-isotropic shrinkages are achieved in the directions of the diameter and the height of the micro-structure, and in the directions of the diameter and the thickness of the base after sintering at 1300°C for 1 h. However, the measured shrinkage of the micro-structure is 19.6–19.7%, which is higher than that for the base (14.0–15.1%). The different shrinkage between the micro-structure and the base did not result in any cracks in the sintered part. Accordingly, the average fractional density of the micro-structure (97.1%) is higher than that of the base (89.55%). As shown in Fig. 11.16, there is a dense layer in the region adjacent to the surface of the micro-structure. The use of fine powder and the presence of the oxides on the debound parts may be responsible for the formation and progression of the dense layers on the sintered micro-structures [43,44].

However, in the case of the commercial feedstock, isotropic shrinkage of around 16% and a fractional density of 95.6% were achieved after sintering at 1300°C in vacuum. No dense layer appeared. Figure 11.17 shows that the grain size increases as the sintering temperature increases [12]. At a low temperature of 1200°C, grain growth had taken place. A higher sintering temperature of 1300°C

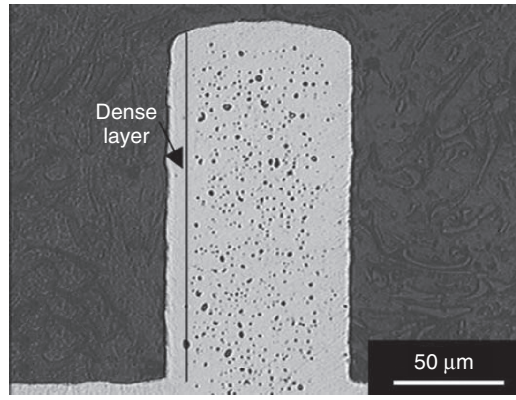

(a)

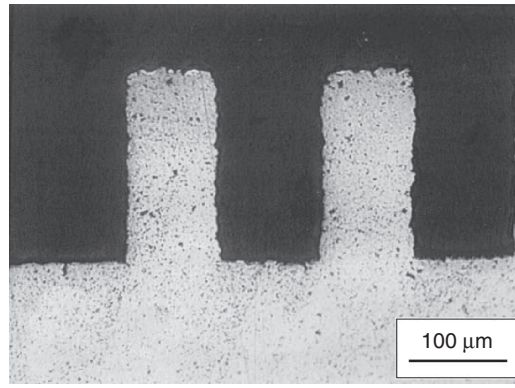

(b)

Figure 11.16 Micro-graphs of the polished micro-structures sintered in (a) hydrogen and (b) vacuum.

results in higher densification and smaller pore size, and some isolated pores in the grain hinder further densification.

11.6.2 Sintering of Micro-Gear

Figure 11.18 shows a 316L stainless steel micro-gear 1-mm in diameter after sintering. Sintering was conducted in hydrogen gas at 1250°C for 1 h. The grain structure of the micro-gear was examined using EBSD (electron backscatter diffraction) system as shown in Fig. 11.19 [45]. The annealing twin content at the tooth is significantly higher than that at the hub. The average grain size of the outer layer of the tooth (Region Z) (35 μm) is larger than that of the hub (Region Y) (5 μm). Similar to the case in the sintering of the micro-structures depicted in Section 11.6.1, the so-called "dense layer" exists on the surface of

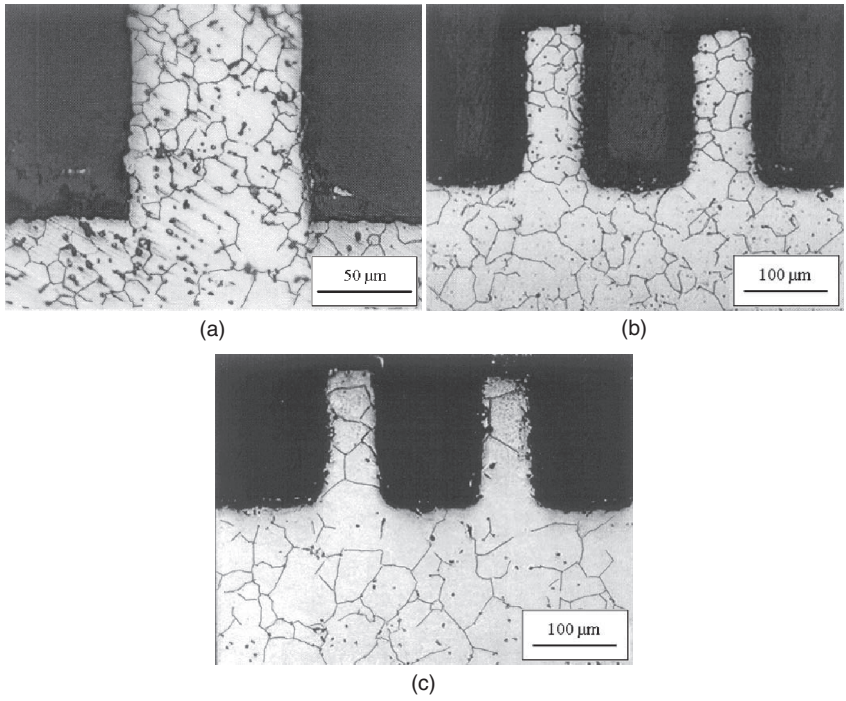

Figure 11.17 Micro-graphs of etched sintered micro-structures: sintering temperature of (a) 1200, (b) 1250, and (c) 1300°C.

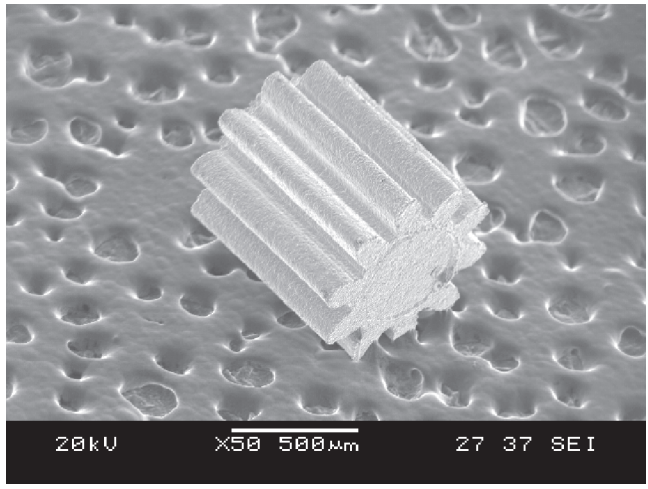

Figure 11.18 Micro-gear 1 mm in diameter.

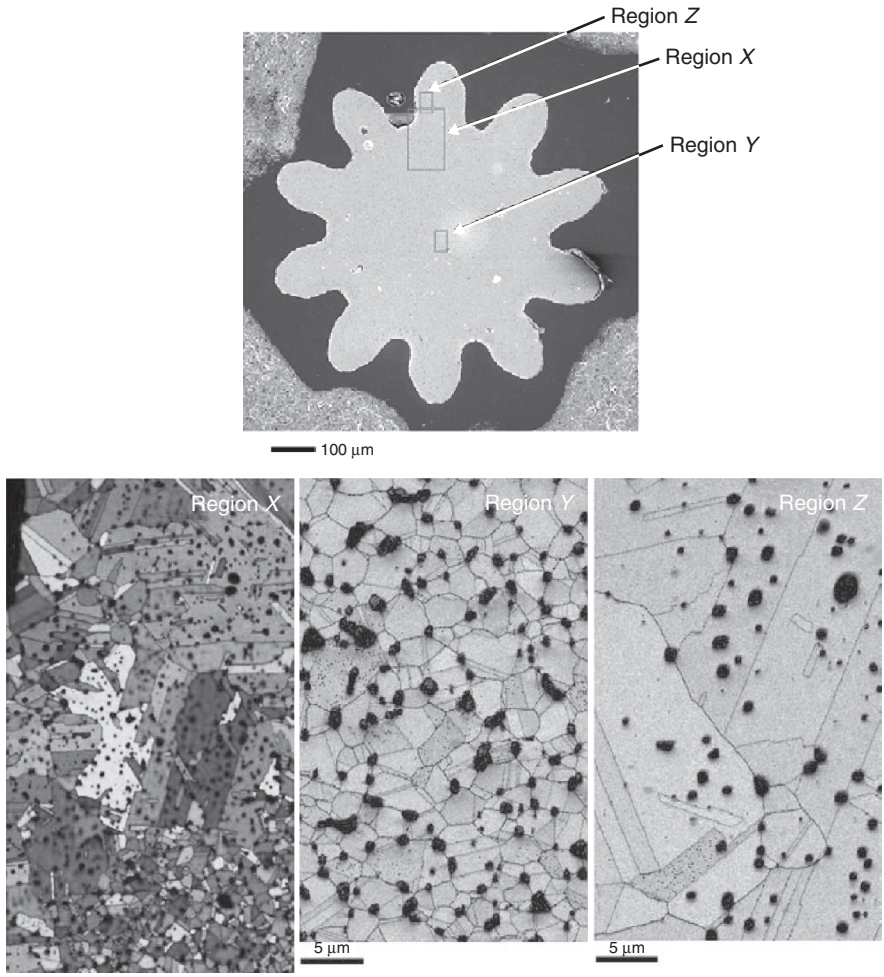

Figure 11.19 Micro-graphs of the micro-gear.

the micro-gear. The reason may also be the presence of the oxide from the binder residue [43,44].

11.7 SUMMARY

μMIM is a relatively new technology suitable for the mass production of metallic micro-components or micro-structures. Since the last decade, it has found wide applications such as stainless steel invasive surgery implant, mold insert for plastic micro-molding, micro-gear, heat sink, and structural micro-components. However, there are still problems and constraints to be resolved. These include

smaller metal powder, binder with high green strength and good shape retention during debinding, mold insert with good surface finish for ease of demolding (especially for high-aspect-ratio micro-structure), development of dedicated μMIM machine and tools, reduction of tolerances in shrinkage due to sintering, better surface quality, and improved economic efficiency.

REFERENCES

1. Schatt W, Wieters KP. Powder metallurgy processing and materials. Shrewsbury, UK: European Powder Metallurgy Association (EPMA); 1997.
2. German RM. Powder injection molding. Princeton (NJ): MPIF; 1990.
3. Wohifromm H. Novel stainless steel for metal injection molding. Volume 3, Proceedings of Powder Metallurgy World Congress & Exhibition. Granada, Spain: European Powder Metallurgy Association; 1998. pp. 1–8.
4. German RM, Bose A. Injection molding of metals and ceramics. Princeton (NJ): Metal Powder Industries Federation; 1997.
5. Piotter V, Haneman T, Ruprecht R, Hausselt J. Injection molding and related techniques for fabrication of micro-structures. Microsyst Technol 1997;3:129–133.
6. Liu ZY, Loh NH, Tor SB, Khor K, Murakoshi Y, Maeda R, Shimizu T. Micro-powder injection molding. J Mater Process Technol 2002;127:165–168.
7. Piotter V. PIM looks for role in the micro world. Metal Powder Report 1999; 54:36–39.
8. Piotter V, Benzler T, Hanemann T, Woellmer H, Ruprecht R, Hausselt J. Innovative molding technologies for the fabrication of components for micro-systems. Proc SPIE—Int Soc Opt Eng 1999;3680:456–463.
9. Piotter V, Gietzelt T, Merz L. Micro powder-injection moulding of metals and ceramics. Sadhana—Acad Proc Eng Sci 2003;28:x299–306.
10. Merz L, Rath S, Piotter V, Ruprecht R, Hausselt J. Powder injection molding of metallic and ceramic micro-parts. Microsyst Technol 2004;10:202–204.
11. Tay BY, Liu L, Loh NH, Tor SB, Murakoshi Y, Maeda R. Injection molding of 3D micro-structures by μPIM. Microsyst Technol 2005;11:210–213.
12. Fu G, Loh NH, Tor SB, Tay BY, Murakoshi Y, Maeda R. Injection molding, debinding and sintering of 316L stainless steel micro-structures. Appl Phys A: Mater Sci Process 2005;81:495–500.
13. Ruprecht R, Gietzelt T, Mueller K, Piotter V, Haußelt J. Injection molding of micro-structured components from plastics, metals and ceramics. Microsyst Technol 2002;8:351–358.
14. Liu ZY, Loh NH, Tor SB, Khor K, Murakoshi Y, Maeda R. Binder system for micro-powder injection molding. Mater Lett 2001;48:31–38.
15. Tay BY, Liu L, Loh NH, Tor SB, Murakoshi Y, Maeda R. Injection molding of 3D micro-structures by μPIM. Microsyst Technol 2005;11:210–213.
16. Hartwig T, Veltl G, Petzoldt F, Kunze H, Scholl R, Kieback B. Powders for metal injection molding. J Eur Ceram Soc 1998;18:1211–1216.

17. Miura H, Ritsu D, Takamori S, Seiji N. Effects of powder characteristics on flowability of feedstock and deformation during thermal debinding in MIM. J Jpn Soc Powder Powder Metall 1993;40(5):479–483.
18. Liu L, Loh NH, Tay BY, Tor SB, Murakoshi Y, Maeda R. Mixing and characterisation of 316L stainless steel feedstock for micro powder injection molding. Mater Characterization 2005;54:230–238.
19. Guber E, Herrmann D, Muslija A. Fabrication of metal and polymer micro-structures. Med Device Technol 2001;12(3):22–26.
20. Liu L, Loh NH, Tay BY, Tor SB, Murakoshi Y, Maeda R. Mixing and characterisation of 316L stainless steel feedstock for micro-powder injection molding. Mater Characterization 2005;54:230–238.
21. Ruprecht R, Finnah G, Piotter V. Micro-injection molding—principles and challenges. In: Löhe D, Haußelt J, editors. Advanced micro and nanosystems, Volume 3: micro-engineering of metals and ceramics, Part I: design, tooling and injection molding., Weinheim, Germany: Wiley-VCH Verlag GmbH & Co. KGaA; 2005. pp 253–288.
22. Michaeli W, Spennemann A, Gaertner R. New plastification concepts for micro injection moulding. Microsyst Technol 2002;8:55–57.
23. Heckele M, Schomburg WK. Review on micro molding of thermoplastic polymers. J Micromech Microeng 2004;14:R1–R14.
24. Fu G, Tor S, Loh N, Tay B, Hardt DE. A micro powder injection molding apparatus for high aspect ratio metal micro-structure production. J Micromech Microeng 2007;17:1803–1809.
25. Menges G, Michaeli W, Mohren P. How to make injection molds. Munich: Carl Hanser Verlag; 2001.
26. Huber N, Tsakmakis C. Finite element simulation of micro-structure demolding as part of the LIGA process. Microsyst Technol 1995;2:17–21.
27. Spennemann A, Michaeli W. Process analysis and injection molding of micro-structures. In: Heim HP, Potente H, editors. Specialized molding techniques. New York: Plastics Design Library, William Andrew Inc.; 2001. pp 157–162.
28. Merz L, Rath S, Piotter V, Ruprecht R, Ritzhaupt-Kleissl J, Hausselt J. Feedstock development for micro powder injection molding. Microsyst Technol 2002;8:129–132.
29. Bacher W, Bade K, Matthis B, Saumer M, Schwarz R. Fabrication of LIGA mold inserts. Microsyst Technol 1998;2:117–119.
30. Weber L, Ehrfeld W, Freimuth H, Lacher M, Lehr H, Pech B. Micro molding—a powerful tool for the large scale production of precise micro-structures. SPIE 1996; 2879:156–167.
31. Benzler T, Piotter V, Ruprecht R, Hausselt J. Fabrication of micro-structure by MIM and CIM. Volume 3, Proceedings of Powder Metallurgy World Congress & Exhibition. Granada, Spain: European Powder Metallurgy Association; 1998. pp 9–14.
32. Guttmann M, Schulz J, Saile V. Lithographic fabrication of mold inserts. In: Löhe D, Haußelt J, editors. Advanced micro and nanosystems, Volume 3: micro-engineering of metals and ceramics, Part I: design, tooling and injection molding. Weinheim, Germany: Wiley-VCH Verlag GmbH & Co. KGaA; 2005. pp 187–220.

33. Shimizu T, Murakoshi Y, Sano T, Maeda R, Sugiyama S. Fabrication of micro parts by high aspect ratio structuring and metal injection molding using the supercritical debinding method. Microsyst Technol 1998;5:90–92.
34. Loh NH, Tor SB, Tay BY, Murakoshi Y, Maeda R. Fabrication of micro gear by micro powder injection molding. Microsyst Technol 2008;14:43–50.
35. Bauer W, Knitter R, Emde A, Bartelt G, Goehring D, Hansjosten E. Replication techniques for ceramic micro-components with high aspect ratios. Microsyst Technol 2002;9:81–86.
36. Bohm J. Micro-metalforming with silicon dies. Microsyst Technol 2001;7:191–195.
37. Rangelow IW. Reactive ion etching for high aspect ratio silicon micro-machining. Surf Coat Technol 1997;97:140–150.
38. Fu G, Loh NH, Tor SB, Murakoshi Y, Maeda R. Replication of metal micro-structures by micro powder injection molding. Mater Des 2004;25:729–733.
39. Rota A, Duong T-V, Hartwig T. Wear resistant tools for reproduction technologies produced by micro powder metallurgy. Microsyst Technol 2002;7:225–228.
40. German RM. Theory of thermal debinding. Proceedings of the Powder Metallurgy World Congress & Exhibition. Granada, Spain: European Powder Metallurgy Association; 1998. pp 159–167.
41. Nash P. Kinetics of binder burnout and oxide reduction in injection moulded iron parts. Metal Powder Rep 1998;53(12):42.
42. Catamold—the range to suit your needs, BASF AG. Catalogue, Business Division Inorganics, Marketing Powder Injection molding, Ludwigshafen, Germany, 2002.
43. Tay BY, Liu L, Loh NH, Tor SB, Murakoshi Y, Maeda R. Characterization of metallic micro rod arrays fabricated by μMIM. Mater Characterization 2006;57:80–85.
44. Liu L, Loh NH, Tay BY, Tor SB, Murakoshi Y, Maeda R. Densification and grain growth of stainless steel micro-size structures fabricated by μMIM. Appl Phys A: Mater Sci Process 2006;83:31–36.
45. Tay BY, Loh NH, Tor SB, Ng FL, Fu G, Lu XH. Characterisation of micro gears produced by micro powder injection moulding. Powder Technol 2009;188:179–182.

INDEX

Micro-Manufacturing: Design and Manufacturing of Micro-Products, First Edition.
Edited by Muammer Koç and Tugrul Özel.